NASA CR-80018

INTERPLANETARY GUIDANCE SYSTEM REQUIREMENTS STUDY FINAL REPORT

VOLUME I

April 1967

Distribution of this report is provided in the interest of information exchange and should not be construed as endorsement by NASA of the material presented. Responsibility for the contents resides with the organization that prepared it.

Prepared under Contract No. NAS 12-7 by
AC ELECTRONICS DIVISION
GENERAL MOTORS CORPORATION
Milwaukee, Wisconsin 53201

Electronics Research Center

NATIONAL AERONAUTICS AND SPACE ADMINISTRATION

FACILITY FORM 602

N67-37180
(ACCESSION NUMBER)

(THRU)

435
(PAGES)

1
(CODE)

CR-80018
(NASA CR OR TMX OR AD NUMBER)

21
(CATEGORY)

Mr. Stephen O'Neil
Technical Monitor
NAS 12-7
Electronics Research Center
575 Technology Square
Cambridge, Massachusetts 02139

Requests for copies of this report should be referred to:

NASA Scientific and Technical Information Facility
P. O. Box 33, College Park, Maryland 20740

NASA CR-80018

INTERPLANETARY GUIDANCE SYSTEM REQUIREMENTS STUDY FINAL REPORT

VOLUME I

April 1967

Prepared under Contract No. NAS 12-7 by
AC ELECTRONICS DIVISION
GENERAL MOTORS CORPORATION
Milwaukee, Wisconsin 53201

Electronics Research Center

NATIONAL AERONAUTICS AND SPACE ADMINISTRATION

7111A

ABSTRACT

A two-volume report has been compiled by the Systems Engineering Section of the R and D Laboratories of AC Electronics Division of General Motors Corporation, El Segundo, California, from studies performed under Contract NAS 12-7.

The main objective of this study was to aid quantitatively in the determination of research and development requirements in the area of guidance technology for future interplanetary missions. Two steps were necessary to accomplish these objectives: first, the development of digital simulations for the mission phases under consideration in order to translate quantitatively the mission requirements:into guidance system requirements; second, the employment of the developed simulations in trade-off studies involving typical mission profiles and system configurations.

The accomplishments of this study are documented in two separate volumes. Volume I contains the findings of the trade-off studies, which cover free-fall; powered-flight and atmospheric-entry phases using conventional short-term, high-thrust propulsion; and low-thrust missions in the spiral-out, heliocentric-transfer and spiral-in phases using constant-magnitude, variable-direction thrust acceleration. An appendix to the final report contains an outline of the mathematical model which was used as a basis for the development of large digital simulations.

Volume II contains a detailed description of the digital computer programs, their underlying mathematical models, and a user's guide for the trade-off studies. It is divided into the following eleven parts:

Part 1	Program Descriptions for Interplanetary Free-fall Trajectories
Part 2	Performance Assessment of Midcourse Guidance Systems
Part 3	Nominal Powered Flight Trajectories
Part 4	Performance Assessment of All-Inertial Guidance Systems
Part 5	Nominal Atmospheric Entry Trajectories, Version I
Part 6	Nominal Atmospheric Entry Trajectories, Version II
Part 7	Performance Assessment of Atmospheric Entry Guidance Systems

Part 8	Computer Program Description for Matched Interplanetary Free-fall Trajectories
Part 9	Low Thrust Trajectory Design Using a Neighboring Optimum Iteration Process
Part 10	Program Description for Performance Assessment of Low-Thrust Space Guidance Systems, Version I
Part 11	Program Description for Performance Assessment of Low-Thrust Space Guidance Systems, Version II

TABLE OF CONTENTS

SECTION	TITLE	PAGE
I	INTRODUCTION AND SUMMARY	1-1
II	OUTLINE OF PERFORMANCE ASSESSMENT TRADE-OFF STUDIES	2-1
	2.1 Performance Assessment Technique	2-1
	2.2 Missions and System Configurations Studied	2-2
	2.3 General Trade-off Study Plan	2-4
	2.3.1 Free-Fall Mission Phase Studies	2-4
	2.3.2 Atmospheric Entry Mission Phase Studies	2-5
	2.3.3 Powered Flight Mission Phase Studies	2-6
	2.3.4 Low Thrust Mission Phase Studies	2-6
III	GUIDANCE SYSTEM STUDY RESULTS	
	3.1 Midcourse Guidance and Navigation	3-1
	3.1.1 Objectives of the Investigation	3-1
	3.1.2 Technical Approach, Simulation Techniques	3-1
	3.1.3 Performance Assessment of Mission Category 1 — Total Missions	3-5
	3.1.4 Performance Assessment of Mission Category 2 — Planetary Approach	3-13
	3.1.5 Performance Assessment of Mission Category 3 — Planetary Reconnaissance	3-26
	3.1.6 Special Studies	3-29
	3.1.7 Conclusions and Suggestions for Future Investigations	3-39
	3.2 Guidance and Navigation for Atmospheric Entry	3-42
	3.2.1 Objectives of the Investigation	3-42
	3.2.2 Atmospheric Entry Guidance and Navigation Prior to Landing	3-43
	3.2.3 Guidance and Navigation During Atmosphereic Braking	3-51
	3.2.4 Exploration of Planetary Atmospheres	3-55
	3.2.5 Atmospheric Entry Corridor Width Studies	3-60
	3.2.6 Conclusions	3-61
	3.3 Guidance and Navigation During Powered Flight	3-63
	3.3.1 Objectives of the Investigation	3-63
	3.3.2 Deboost Prior to Reentry (Trajectory Index 9)	3-69
	3.3.3 Launch from Mars into Circular Parking Orbit (Trajectory Index 8)	3-71

TABLE OF CONTENTS (Continued)

SECTION	TITLE	PAGE
	3.3.4 Trajectory Change Maneuvers	3-71
	3.3.5 Conclusions	3-72
	3.4 Guidance and Navigation for Low-Thrust Missions	3-73
	3.4.1 Objectives of the Investigation	3-73
	3.4.2 Trade-off Studies Using Version I of the Digital Simulation Program	3-74
	3.4.3 Trade-off Studies Using Version II of the Digital Simulation Program	3-86
IV	SUMMARY OF CONCLUSIONS AND RECOMMENDATIONS FOR FUTURE STUDIES	4-1
	4.1 Free-Fall Study Conclusions	4-1
	4.2 Atmospheric Entry Study Conclusions	4-3
	4.3 Powered Flight Phase Study Conclusions	4-5
	4.4 Low Thrust Study Conclusions	4-5
	REFERENCES	
APPENDIX		
A	MATHEMATICAL MODEL FOR PERFORMANCE ASSESSMENT OF SPACE GUIDANCE SYSTEMS	A-1
B	SUPPORT DATA FOR SECTION III	B-1

LIST OF ILLUSTRATIONS

FIGURE	TITLE	PAGE
3-1	Re-entry Capability After a Slow (12.02 km/sec) Earth Approach from the Three Planet Grand Tour (Earth → Venus → Mars → Venus → Earth)	3-16
3-2	Re-entry Capability After a Moderate Speed (13.95 km/sec) Earth Approach from Venus-Mars Swingby (Earth → Venus → Mars → Earth)	3-17
3-3	Re-entry Capability After a High Speed (15.67 km/sec) Earth Approach from a Martian Capture Mission	3-18
3-4	Re-entry Capability After a Slow (5.67 km/sec) Martian Approach from Martian Capture Mission	3-19
3-5	Re-entry Capability After a Fast (12.63 km/sec) Martian Approach from Martinal Flyby (Earth → Mars → Earth)	3-20
3-6	Re-entry Capability (after Navigation with State-of-the-Art Ground-Tracking) as a Function of Velocity at the Re-entry Sphere of Earth	3-21
3-7	Re-entry Capability (after Navigation with State-of-the-Art Horizon Sensor) as a Function of Velocity at the Re-entry Sphere of Earth	3-22
3-8	Re-entry Capability (after Navigation with State-of-the-Art Horizon Sensor) as a Function of Velocity at the Re-entry Sphere at Mars	3-23
3-9	Boost Trajectory Characteristics for Launch from Mars Mission (Trajectory Index 8)	3-68
3-10	Final Position Eigenvalues Using Planet Tracker Only	3-83
3-11	Final Position Eigenvalues Using IG1 Plus Plant Tracker	3-84
3-12	Miss in Position Versus Iteration Number	3-88
3-13	Miss in Velocity Versus Iteration Number	3-89
3-14	Terminal Versus Initial Miss in Position	3-90
3-15	Terminal Versus Initial Miss in Velocity	3-91

LIST OF TABLES

TABLE	TITLE	PAGE
2-1	Mission Classes and Associated Mission Phases	2-3
3-1	Performance Parameters, Mission Category	3-8
3-2	Re-entry Corridor Widths for Trajectories Investigated	3-14
3-3	Performance Parameters, Mission Category 2 —Planetary Approach	3-25
3-4	Performance Parameters, Mission Category 3 —Planetary Reconnaissance	3-27
3-5	Effect of Orbital Rectification upon Navigation System Performance	3-30
3-6	Diagonal Matrix of Initial Covariance	3-31
3-7	Observation Schedules	3-32
3-8	Variable-Time-of-Arrival System Configuration and Performance Parameters (Total Missions Category)	3-34
3-9	System Configurations and Performance Parameters Summary	3-35
3-10	Performance Parameters	3-39
3-11	Characterization of Initial Errors for First Atmospheric Reentry at Earth (P_{nom})	3-46
3-12	Definition of Guidance Systems for Performance Assessment Studies on Reentry Trajectories	3-46
3-13	Summary of Guidance System Performance Assessment Studies for Earth Reentry Trajectories	3-47
3-14	Trade-Off Results for Guidance and Navigation Performance Assessment of Navigation with Electromagnetic Sensors Only on the Manned Earth Single Pass Entry Trajectory	3-50
3-15	Performance Assessment Results for Direct Reentry at Mars	3-52
3-16	Trade-off Results for Guidance and Navigation Performance Assessment Studies on the Martian Atmospheric Braking Trajectory	3-53
3-17	Results of Studies Indicating the Range of Linearity for Various Parameters for the Martian Atmospheric Braking Trajectory	3-54
3-18	Strapdown System Error Budget	3-64
3-19	Gimballed IMU Error Budgets	3-65
3-20	Description of Boost Trajectories Used in Performance Assessment Studies	3-66
3-21	Definition of Inertial Guidance Systems Used in Boost Trajectory Performance Assessment Studies	3-67
3-22	All-Inertial Guidance System, Performance Indices for Space Boost Trajectories	3-70

LIST OF TABLES (Continued)

TABLE	TITLE	PAGE
3-23	Systems, Configurations, and Missions Studied	3-76
3-24	Initial Error Covariances	3-77
3-25	Effect of Initial Covariance in Position and Velocity on Terminal Accuracy	3-79
3-26	Summary of Terminal Accuracy of Typical Systems for Trajectory HTR2	3-80
3-27	Summary of Terminal Accuracy of Typical Systems for Trajectory MO	3-81
3-28	Summary of Terminal Accuracy of Typical Systems for Trajectory EO	3-81
3-29	Summary of Terminal Accuracy for Trajectory MI	3-81
3-30	Terminal Accuracy as a Function of Bias for Nonzero Finite Random Noise	3-85
3-31	Terminal Accuracy as a Function of Random Noise for Bias Zero	3-85
4-1	Performance Assessment Summary for Planetary Approach	4-2
4-2	Summary of All-Inertial Reentry Guidance Performance Assessment Results	4-4
4-3	Summary of Performance Assessment Results for Single-Skipout Trajectories Which Use Aiding Navigation in Free-Fall (Nominal Initial Errors)	4-6
4-4	Performance Assessment Study Results for Powered Flight Phases	4-7
4-5	Summary of Terminal Accuracy of Typical Navigation Systems for Earth-Mars Low-Thrust Trajectory HTR2	4-8

SECTION I

INTRODUCTION AND SUMMARY

This report presents the results of a study conducted by the AC Electronics Division of General Motors Corporation under Contract NAS 12-7. The main objective of this study was to translate the guidance and navigation requirements for future interplanetary missions into guidance and navigation system requirements to identify areas of hardware and software technology in which further research and development may be needed.

The study was conducted in three steps. The first of these was the selection of a representative set of mission profiles and vehicle configurations. The second step was the development of mathematical models for the mission profiles, vehicle dynamics, and the navigation and guidance systems that can be used to analyze navigation and guidance system performance. The third step was the conduct of navigation system performance assessment trade-off studies using the mathematical models.

The mathematical models, and the corresponding digital computer programs, represent the most voluminous portion of the output of this study. Detailed descriptions of these make up Volume II of this report. There are separate digital programs for the determination of trajectories and for the assessement of guidance and navigation performance during each of four different types of mission phase. These phases are free-fall, atmospheric entry, powered flight, and low thrust. A general outline of the mathematical models for the assessment of navigation and guidance system performance is given in Appendix A of this volume of the report.

Section II of this volume outlines the performance assessment trade-off studies in terms of missions and system configurations. The details of the studies and the results are described in Section III, and Section IV summarizes the results and presents the conclusions to be drawn from them.

Because interplanetary travel is still in a relatively primitive state, the specific objectives of interplanetary missions and the quantitative navigation performance are not fully defined. The results and conclusions of this study, therefore, should not be considered absolute, but rather indicative of relative capabilities of different systems and of mission sensitivities to navigation and guidance parameters. Nevertheless, it is felt that the results are obtained are illuminating and should add to present understanding of the problems of navigation and guidance for interplanetary travel. In addition, the tools developed in the form of the mathematical models and computer programs should be useful in more refined future analyses as specific missions, spacecraft, and navigation sensor capabilities are defined.

SECTION II

OUTLINE OF PERFORMANCE ASSESSMENT TRADE-OFF STUDIES

The study results are of two types. The first type includes a set of mathematical models and digital simulation programs for the analysis of interplanetary guidance and navigation. The second type includes the results of performance studies of guidance and navigation for a representative set of space missions. The mathematical models and simulation programs are Volume II of this report. The performance trade-off studies make up the major portion of this volume.

The rest of this section outlines the techniques employed in the performance assessment studies, the specific system configurations analyzed, and the missions studied.

2.1 PERFORMANCE ASSESSMENT TECHNIQUE

The trade-off studies were performed by mission phase, employing the methods described in Appendix A. First an appropriate trajectory was determined for each mission to be studied, using the programs described in Volume II. Trajectories for each mission consist of a series of trajectory phases of the following possible types.

1. Free-Fall.
2. Atmospheric Entry.
3. Powered Flight.
4. Low Thrust.

Volume II includes programs for the calculation of nominal trajectories of each of these types. The calculation of these nominal trajectories is based upon:

1. The specified mission objective in terms of where and when the vehicle should go,
2. The physical environmental data, including solar system ephemeris data, gravitational data, and planetary atmospheric data,
3. The vehicle data, including thrust, mass, and aerodynamic force data.

The nominal trajectory data consists of time histories for position, velocity, and —for non-free-fall phases — attitude and acceleration of the spacecraft.

Next the navigation and guidance system configurations whose performance is to be studied are selected, and values or ranges of values of the various trade-off parameters are specified. These parameters may include:

1. Navigation sensor accuracies,
2. Data processing rate,
3. Data processing techniques or equations,
4. Guidance law.

The performance assessment programs (such programs exist for each trajectory phase included in Volume II) are then used to calculate the resulting performance for each configuration being studied. The resulting performance is given in terms of navigational accuracy (position and velocity uncertainty) and required control effort (for example, probable amount of propulsion needed to effect orbit corrections). Finally this performance is compared with the specified requirement.

2.2 MISSIONS AND SYSTEM CONFIGURATIONS STUDIED

Studies were performed for the following six mission classes.

1. Martian Landing Mission.
2. Planetary Stopover.
3. Single Planetary Flyby.
4. Multiple Planetary Flyby.
5. Planet Atmospheric Exploration Mission.
6. Low Thrust Planetary Stopover Mission.

Each mission starts from an Earth parking orbit and terminates with Earth re-entry, with the exception of the Planet Atmospheric Exploration Mission. This mission, which is to provide data on the Martian atmospheric density and pressure, is ended when the vehicle has passed through the Martian atmosphere on a near encounter. The stopover missions involve staying in an orbit about the target planets and the flyby missions involve only passing near the target planets. The different mission phases associated with each of the mission classes are indicated in Table 2-1. Specific quantitative descriptions of the trajectory profiles are given in Section III, in which the studies and their results are described.

MISSION PHASES		MISSION CLASSES					
		1 Martian Landing	2 Planetary Stopover	3 Single Planetary Flyby	4 Multiple Planetary Flyby (Grand Tour)	5 Exploration of Martian Atmosphere	6 Low Thrust Planetary Stopover
Free-fall	Planetary Departure	x	x	x	x	x	
	Heliocentric Transfer	x	x	x	x	x	
	Planetary Approach	x	x	x	x	x	
	Orbital Phase	-	x	-	-	-	x
Powered Flight	Trajectory Change Maneuver	x	x	x	x	x	
	Miscourse Correction	x	x	x	x	x	
	Launch from Mars	x	-	-	-	-	-
	Deboost prior to Atmospheric Entry	x	x	x	x	x	-
Atmos-pheric Entry	Atmospheric Entry Prior to Landing	x	x	x	x	-	x
	Atmospheric Braking	-	-	x	x	x	-
	Entry for Nonlifting Scientific Probe	-	-	-	-	x	-
Low Thrust	Spiral Out - Spiral In	-	-	-	-	-	x
	Heliocentric Transfer	-	-	-	-	-	x

Table 2-1. Mission Classes and Associated Mission Phases

The navigation systems analyzed for these different missions had the following types of navigation sensors.

1. Inertial Measurement Units.
2. Ground Tracking Systems (DSIF).
3. Space Sextants.
4. Horizon Scanners.
5. Planet Trackers.
6. Radio Altimeters.
7. Star Trackers (for Inertial System Alignment).

For navigation the sensor data is processed using a Kalman linear estimation technique, except for phases with all-inertial navigation (since there is no redundant measurement information for these phases). The guidance laws investigated include lambda matrix, neighboring optimum, and, for midcourse phases, both fixed — and variable-time-of-arrival impulsive guidance.

2.3 GENERAL TRADE-OFF STUDY PLAN

Since the trade-off studies were performed by mission phase, the detailed descriptions of the studies and results are organized in this way. The free-fall, atmospheric entry, powered flight, and low thrust mission phase studies are described in Paragraphs 3.1 and 3.4, respectively. The following paragraphs outline these studies.

2.3.1 FREE-FALL MISSION PHASE STUDIES

The free-fall studies include three categories of phases:

1. Complete flyby missions, designated as "Total Missions",
2. Planetary approach phases,
3. Planetary reconnaissance or planetary orbit phases.

Two missions of Category 1 were studied: a Mars flyby mission and a Mars-Venus multiple flyby mission. For each of them, the navigation performance was determined throughout the entire mission, from Earth escape to Earth atmospheric re-entry. Navigation by ground tracker, by horizon scanner, by sextant, and by a combination of

horizon scanner and ground tracker was evaluated. Two guidance laws were used, both fixed-time-of-arrival. One of these laws, constrains terminal position, the other terminal altitude and flight path direction. These studies are described in Paragraph 3. 1. 3.

Because planetary approach is the most critical free-fall mission phase, five different approach phase trajectories were studied (Category 2). Three of them are the Earth approach phases from a Mars capture mission and from two multiple planet flyby missions. These three trajectories represent slow, medium, and fast approach speeds. The other two are Mars approach trajectories taken from a Mars close flyby mission and a Mars capture mission. They represent slow and fast Mars approach speeds. The same types of system configurations were simulated as for the first category missions. The details are in Paragraph 3. 1. 4.

For planetary reconnaissance missions, the vehicle remains in orbit about the target planet for some time. Two mission phases of this type were studied (Category 3). They are Martian orbits, one at high altitude (8, 200 km) and one at low altitude (125 km). Navigation by means of horizon scanner was evaluated. The study is detailed in Paragraph 3. 1. 5.

In addition, several special free-fall studies were conducted. These include the effects of orbit rectification, star selection criteria (for use with sextant navigation), and variable-arrival-time guidance versus fixed-arrival-time guidance. These studies are described in Paragraph 3. 1. 6.

2. 3. 2 ATMOSPHERIC ENTRY MISSION PHASE STUDIES

The atmospheric entry studies include atmospheric entry at Earth and at Mars, atmospheric braking (for a close planet flyby), exploration of planet atmospheres, and studies to determine atmospheric-entry corridor requirements.

For Earth entry, performance assessment studies for all-inertial guidance were made for four different trajectories: two direct entry and two single skipout trajectories. For the two skipout entry phases, inertial navigation in combination with either horizon scanner or ground tracker navigation was also evaluated. All-inertial guidance was evaluated for the Mars direct entry phase of the Martian landing mission. All trajectory phases were for an Apollo Command Module type of entry vehicles. These studies are described in detail in Paragraph 3. 2. 2.

The performance attainable with different navigation configurations and guidance parameters (lambda matrix) was studied for a Martian atmospheric braking maneuver and is described in Paragraph 3. 2. 3.

A study of the feasibility of obtaining better information about Mars' atmosphere by "flying" a spacecraft through it and observing its effect on the trajectory of the spacecraft is described in Paragraph 3. 2. 4.

Finally, a series of special studies to determine the acceptable Earth and Mars entry corridor widths for a variety of entry conditions and entry vehicle configurations is described in Paragraph 3. 2. 5.

2. 3. 3 POWERED FLIGHT MISSION PHASE STUDIES

For powered flight or thrusting mission phases, only all-inertial navigation was evaluated. Six different trajectory phases were studied:

1. Injection from Earth orbit to Mars transfer,
2. Injection from Earth-Mars transfer to Mars orbit,
3. Trajectory change at Mars pericenter in flyby mission,
4. Midcourse orbit correction,
5. Launch from Mars surface to Mars parking orbit,
6. Deboost prior to Earth entry.

These studies are described in Paragraph 3. 3.

2. 3. 4 LOW THRUST MISSION PHASE STUDIES

The low thrust mission phases are interplanetary or midcourse phases in which the spacecraft is continuously accelerated at a very low level ($\leq 10^{-3}$ g). For such mission phases continuous guidance is required; consequently, continuous navigation is also required. Two Earth-Mars low thrust mission phases — a fast (79 day, $\sim 10^{-3}$ g) and a slow (166 day, $\sim 10^{-5}$ g) trajectory — were studied using various combinations of planet tracker, ground tracker, and inertial measurement unit navigation. The studies are described in Paragraph 3. 4. 2.

Paragraph 3. 4. 3 describes studies of the performance of neighboring optimum guidance for a fast Earth-Mars low thrust mission phase and for a slow Mars-Earth mission phase.

SECTION III

GUIDANCE SYSTEM STUDY RESULTS

3.1 MIDCOURSE GUIDANCE AND NAVIGATION

3.1.1 OBJECTIVES OF THE INVESTIGATION

The objectives of the midcourse guidance and navigation study were the following:

1. The construction of the mathematical model to provide guidelines for the development of digital computer simulation programs.
2. The development of the digital computer simulation program necessary to analyze and assess the performance of the guidance and navigation system requirements for future interplanetary space missions.
3. The performance of trade-off studies using the computer programs to aid in the selection of the optimal and suboptimal guidance and navigation system configurations for future space missions.

3.1.2 TECHNICAL APPROACH, SIMULATION TECHNIQUES

The technical approach and the simulation techniques employed in this study are outlined briefly in the paragraphs which follow. For more detailed information, refer to Appendix A of this volume and Part 2 of Volume II.

3.1.2.1 Construction of Mathematical Models and Development of the Digital Computer Programs

The mathematical model upon which the midcourse guidance assessment computer program was based contains a set of basic assumptions. These assumptions are summarized as follows.

1. The equations describing the dynamics and the measurement systems are known (the nominal mission profiles are defined).
2. Linear perturbation theory holds (deviations from the nominal profiles are small and of first order).
3. The statistical character of the noise processes in the dynamics and measurements are known and are assumed to be Gaussian.
4. The performance criterion is quadratic.
5. The design of interplanetary nominal free-fall trajectories is based upon sphere-of-influence techniques. This means that the motion is described by different "matched" two-body orbits in different portions of the flight.

These assumptions are fundamental in the construction of the mathematical model. The validity of the first two is of paramount importance in the conclusions that are derived from the computer programs.

One additional aspect should be noted. The estimation and control problem has been formulated as a time-discrete model. Because the time-discrete formulation is employed, the dynamics equation must be reduced to a difference equation. This is accomplished by using well-established techniques involving the state transition matrix. Because of the discrete nature of the problem, the character of the dynamics and measurement noise sequences of Assumption 3 can be described further; the noises shall be assumed to be uncorrelated between sampling times; furthermore, the dynamics noise will not be correlated with the measurement noise.

3.1.2.2 Application of Digital Computer Simulations to Investigate Different Trajectory Profiles and a Variety of System Configurations

The overall approach to the studies can be illustrated by considering three aspects of the performance assessment problem:

1. Mission specification and nominal trajectory generation,
2. Specification of the sensor system configuration,
3. Performance assessment based on linear techniques.

The specification of missions is essentially governed by a set goal and technological capabilities. There are several mission categories that could be investigated. Among them are: planetary landing, planetary stopover and reconnaissance, single planetary flyby, and multiple planetary flyby. After the mission has been defined, the necessary computations relating to the determination of the nominal are performed. Next, the sensor system configuration is established. Specific system configurations may be selected from either present or projected state-of-the-art guidance hardware. A particular configuration can be categorized according to the inertial instruments and electromagnetic sensors used. The free-fall performance assessment program does not include an IMU; however, a number of electromagnetic sensors can be used either singly or in combination. These sensors include:

- Space sextant: measures the angle between a prescribed star and the limb or center of a prescribed planet (SS),
- Horizon sensor: measures the angle subtended by a prescribed planet and the direction of the local vertical (HS),
- Planet tracker: measures the direction from a spacecraft to the center of a prescribed planet,
- Ground tracking: measures the range, range-rate, and direction of the spacecraft relative to the tracker. The capability of using three trackers simultaneously is included (GT).

After the tasks implied by (1) and (2) above have been completed, the performance assessment begins. This is accomplished through the application of linear guidance and navigation techniques, that is, Kalman filtering. For the midcourse studies, the assessment involves two types of calculations. The first of these, and the one which consumes the least computer time, is to calculate the statistics, in terms of error covariance matrices, of the probable navigational error as a function of the statistics of the assumed error sources such as instrument errors and plant noise. Such a calculation involves "mapping" the error covariances along the nominal trajectory by means of the linearized equations of motion; therefore, the results are valid only within the range of linearity. The second type of calculation includes the simultation of specific, actual trajectories with specific simulated measurement input errors. This type of simulation allows Monte Carlo analyses and accounts for non-linear effects in the equations of motion and observation processes. For additional details, refer to Appendix A.

3.1.2.3 The Computer Programs

The digital computer simulation programs employed in the study of free-fall trajectories are summarized in the following five paragraphs.

The program designated 281 is a program for the determination of position, velocity, and flight time of planetocentric hyperbolic orbits. The output of this program determines initial conditions for nominal planetocentric orbits as used in the performance assessment of space guidance systems, see Volume II, Part 1 for a more detailed description of this program.

The program designated 291 is a digital computer program for the design of interplanetary nominal free-fall trajectories based upon two-body sphere-of-influence techniques. In combination with Program 281, it provides the initial conditions of the nominal trajectory for the performance assessment simulation of aided-inertial space guidance systems during the free-fall phases of an interplanetary mission; see Volume II, Part 1 for a more detailed description of this program.

The program designated 284 is a digital computer simulation program for the performance assessment of midcourse guidance systems. The program can be used to study and assess the performance of space guidance systems during free-fall phases of interplanetary missions. Program 284 is organized in such a manner that a desired system configuration involving different combinations of aiding instruments can be easily simulated. Thus, comparative studies using ground-based and/or onboard aiding instruments, as well as different sensor accuracies, can be performed.

The aiding instruments presently programmed in 284 are: three ground trackers capable of simulating the measurement of range, range-rate, and azimuth and elevation angles; a horizon sensor capable of simulating the onboard measurement of the subtended angle and the two local vertical angles; a planet tracker, that is, a horizon sensor capable of operating in a planet tracker mode; and a space sextant capable of simulating the measurement of a planet's limb-to-star angle or the planet's center-to-star angle. The space sextant has the capability of using different star selection options including realistic stars selected from a star catalog in an "optimum" fashion.

Linear guidance laws that incorporate different end constraints with fixed and variable time of arrival can be simulated in this program. Five different guidance laws are available. They cover the possibility of controlling the terminal position vector or terminal altitude and velocity direction (for both fixed and variable time of arrival), as well as the possibility of controlling altitude, flight path angle, and trajectory plane for variable time of arrival; see Volume II, Part 2 for a more detailed description of Program 284.

3.1.2.4 Simulation Techniques

Detailed discussions of the simulation techniques employed in this study are given in the user's guides of the respective program descriptions in Volume II. The discussion which follows relates to the observation schedules employed in the simulations of this study. If an observation schedule which is in a one-to-one correspondence to the correlation of times of the instruments were used (for example, 1 minute for ground tracking and 10 minutes for onboard instruments), the computer cost would be extreme. In an effort to conserve computer time, "equivalent" observation schedules were selected empirically in this study. These modified schedules have the property that the relationship $\sigma^2 \Delta t$ = constant is preserved throughout a simulation run. Thus, this method introduces an "equivalent" instrument accuracy in the simulations, and the variance of the equivalent instrument is given by σ^2 = constant/Δt; Δt being the observation interval.

3.1.2.5 Interface of Free-Fall Missions with the Powered Flight Missions and Atmospheric Entry Missions

There exists a relationship between the boost powered flight trajectory simulation and the free-fall interplanetary simulation at the injection point. This relationship lies in the use of the terminal covariance matrix obtained in the boost simulation as the initial convariance matrix in the performance assessment of the midcourse guidance systems. Another relationship also exists between the midcourse simulation and the re-entry simulation. The initial conditions for the re-entry are generally obtained from the midcourse performance assessment simulation.

3.1.3 PERFORMANCE ASSESSMENT OF MISSION CATEGORY 1 — TOTAL MISSIONS

Two missions were investigated in this category. The two were selected as representative missions from a number of standpoints — one being their Earth approach velocities. The first, mission number VI in Table B-6, is from the multiple planetary flyby class. The second, mission number VII, is from the single planetary flyby class.

In the total mission category, the overall trajectory is subdivided into trajectory legs. Each leg normally consists of three conics. The first has as its central body the departure planet, the second the sun, and the third the approach planet. Each trajectory leg is simulated separately, the target conditions being defined as the end of the third conic. This trajectory subdivision makes the overall problems easier to handle, as well as affords some flexibility in the selection of the next trajectory leg.

3.1.3.1 Nominal Trajectory Data for the Missions Investigated

Table B-6 gives the nominal trajectory data for the two missions. Note that mission number VI has three trajectory legs; whereas mission number VII has only two legs. The position and velocity components given are the initial values for each conic in equatorial coordinates centered at the implied central body. For example, VI.1.2 implies the heliocentric conic of the first (Earth to Venus) leg of trajectory number VI. For a graphical illustration of portions of trajectory VII in the ecliptic plane, refer to Figures B-1 through B-4 in Appendix B.

3.1.3.2 System Configurations Investigated

The system configurations investigated in mission category 1 are summarized in Table B-7. This table is divided into three separate aspects of the overall problem — navigation, data processing, and guidance information.

Under the heading navigation is the information relating to the instruments with their error budgets, the initial covariance matrices, and the reference bodies used. The error budgets are further defined in Table B-8. In this table, the state-of-the-art and beyond-state-of-the-art instrument error budgets are stated in more detail. More detailed information relating to initial covariance matrices and the reference bodies used by the onboard instruments is given in Tables B-9 and B-10.

Note that Tables B-7 through B-11 contain additional information which is used in subsequent mission categories. This was done to keep repetition to a minimum.

In the simulation, there exists the capability of processing the data via either the square root Kalman filter formulation or the regular Kalman filter formulation. In the total mission category the regular filter was used exclusively. In the formulation of the Kalman filter navigation model, it is necessary to account for uncertainties in the state or trajectory equations of motion. That is, the motion of the spacecraft is subject to various unknown forces, and there are uncertainties or errors in the assumed equations of motion. In the filter formulation, the notation Q_1 represents the assumed covariance matrix of these errors. For a more detailed discussion of the Q matrix see Appendix A. Table B-11 gives the different Q values used in all the mission categories.

In the guidance information columns of Table B-7 are given the different variables affecting the velocity corrections. No attempt will be made here to justify theoretically or explain these quantities; refer to Appendix A for that. Some of these quantities are defined below for convenience. They are

R_V = velocity correction ratio criterion

V_{min} = minimum velocity correction magnitude before a correction is permitted

$(1 - \kappa) t_A$ = time before arrival at target in which velocity corrections are not allowed

Law = one of five linear guidance laws used for midcourse guidance and navigation:

Guidance Law 1

- Fixed time of arrival
- Fixed magnitude of terminal position vector

Guidance Law 2

- Variable time of arrival
- Fixed magnitude of terminal position vector

Guidance Law 3

- Fixed time of arrival
- Fixed magnitude of terminal position vector
- Fixed terminal flight path angle
- Fixed plane of terminal velocity vector

Guidance Law 4

- Variable time of arrival
- Fixed magnitude of terminal position vector
- Fixed terminal flight path angle
- Fixed plane of terminal velocity vector

Guidance Law 5

- Variable time of arrival
- Fixed magnitude of terminal position vector
- Fixed terminal flight path angle
- Actual and nominal terminal orbit planes are identical

In addition to the above information, there are also engine characteristics. The 1σ engine errors employed throughout the entire midcourse study are:

1 percent in velocity correction magnitude

0.1 degree in velocity direction

3.1.3.3 Performance Parameters

The total missions performance parameters are given in Table 3-1. Before proceeding with a discussion of the findings and conclusions, a definition of the symbols is in order:

$RSS(\tilde{x}) = [\tilde{x}_1^2 + \tilde{x}_2^2 + \tilde{x}_3^2]^{1/2}$ x_i being the ith component of the error in the estimate of position at the target point.

$RSS(\tilde{\dot{x}}) = [\tilde{x}_4^2 + \tilde{x}_5^2 + \tilde{x}_6^2]^{1/2}$ where x_i is the ith component of the error in the estimate of velocity.

$\sqrt{TR\ P1}$ = square root of the trace of the covariance matrix of the error in the estimate of position at the target point, that is, $[P11 + P22 + P33]^{1/2}$

$\sqrt{TR\ P4}$ = square root of the trace of the covariance matrix error in the estimate of the velocity at the target point.

MISSION PROFILE		SYSTEM CONFIGURATION	GUIDANCE INFORMATION: CONTROL EFFORT: TOTAL ΔV (m/sec)	GUIDANCE INFORMATION: CONTROL EFFORT: NO. OF ΔV's	GUIDANCE INFORMATION: GUIDANCE LAW	NAVIGATION INFORMATION: ERROR BUDGET	NAVIGATION INFORMATION: COMMENTARY ON AIDING INSTRUMENT ERROR BUDGET	TERMINAL CONDITIONS: ESTIMATED ERROR: RSS $(\tilde{X})$ (km)	ESTIMATED ERROR: $\sqrt{TRP_1}$ (km)	ESTIMATED ERROR: RSS $(\tilde{X})$ (m/sec)	ESTIMATED ERROR: $\sqrt{TRP_4}$ (m/sec)	ACTUAL DEVIATION: RSS $(\tilde{X})$ (km)	ACTUAL DEVIATION: $\sqrt{TRM_1}$ (km)	ACTUAL DEVIATION: RSS $(\tilde{X})$ (m/sec)	ACTUAL DEVIATION: $\sqrt{TRM_4}$ (m/sec)	TERMINAL ACCURACY: δr (km)	TERMINAL ACCURACY: $\sigma_{\delta r}$ (km)	TERMINAL ACCURACY: σ_{γ}* (mrad)	COMMENTS
EARTH-VENUS-MARS-EARTH MISSION PROFILE VI	VI. 1 E → V	TM1	9.6	3	1	G11	S.O.A. Ground Tracking and Instrument Bias	6.0	21.6	0.7	2.7	24.0	120.0	3.4	54.6				
	VI. 2 V → M	TM2	8.0	3	1	G11		365.0	63.0	60.0	15.4	1,200.0	1,400.0	250.0	325.0				Probably would impact on planet.
	VI. 3 M → E	TM3	27.0	4	3	G11		1.4	3.9	1.2	3.2					3.3	10.3	6.1	
	VI. 1 E → V	TM4	140.0	7	1	H11	S.O.A. Horizon Sensor and Instrument Bias	20.0	16.0	2.1	1.9	172.0	160.0	76.0	80.6				
	VI. 2 V → M	TM5	260.0	5	1	H11		5.0	7.5	1.6	2.3	210.0	170.0	200.0	143.0				
	VI. 3 M → E	TM6	1,300.0	3	3	H11		3,000.0	12.0	1,500.0	10.6					4,500.0	156.0		Statistics not compatible with actual results.
	VI. 1 E → V	TM7	27.0	5	1	H32	B.S.O.A. Horizon Sensor and Instrument Bias	2.3	2.0	0.3	0.4	15.0	20.0	5.5	50.8				
	VI. 2 V → M	TM8	45.0	3	1	H32		0.5	0.85	0.2	0.4	60.0	62.0	40.0	50.0				
	VI. 3 M → E	TM9	1,220.0	6	3	H32		0.3	2.0	0.5	2.7					28.6	30.5	17.7	Reentry angle error outside allowable corridor.
	VI. 1 E → V	TM10	385.0	6	1	S11	S.O.A. Space Sextant and Instrument Bias	11.4	23.0	2.3	2.9	90.0	136.0	100.0	176.0				
	VI. 2 V → M	TM11	100.0	6	1	S11		7.0	11.0	1.9	2.9	14.0	192.0	33.1	116.8				
	VI. 3 M → E	TM12	100.0	5	3	S11		7.2	30.0	12.2	26.7					84.0	103.0	96.0	Reentry angle error outside allowable corridor.
	VI. 1 E → V	TM13	31.0	6	1	S31	B.S.O.A. Space Sextant and Instrument Bias	0.8	2.2	0.06	0.3	12.5	16.6	10.0	15.7				
	VI. 2 V → M	TM14	16.0	3	1	S31		0.7	1.4	0.30	0.4	30.0	29.0	6.4	25.8				
	VI. 3 M → E	TM15	35.0	6	3	S31		7.0	6.2	12.2	26.7					6.5	7.0	5.8	
EARTH-MARS-EARTH MISSION PROFILE VII	VII. 1 E → M	TM16	99.4	5	1	G11	S.O.A. Ground Tracking and Instrument Bias	210.0	55.5	55.0	17.6	260.0	229.0	16.0	79.6	37.0			Probably would impact on planet. To observe the effects of tracker bias, compare with TM18 and see Figures B-25 through B-28 in Appendix B.
	VII. 2 M → E	TM17	24.0	5	3	G11		0.9	1.3	0.8	1.1	29.0	62.4	2.8	33.0	4.5	4.9	4.2	
	VII. 1 E → M	TM18	17.0	4	1	G10	S.O.A. Ground Tracking; No Instrument Bias	2.3	9.5	1.0	3.0	18.0	11.6	4.2	4.0	10.5			
	VII. 2 M → E	TM19	12.0	4	3	G10		0.08	0.08	0.08	0.06	3.3	10.6	7.3	9.4	0.24	0.20	0.2	
	VII. 2 M → E	TM20	337.0	5	3	H11	S.O.A. Horizon Sensor and Instrument Bias	8.0	13.5	7.9	9.7	447.0	405.0	396.0	390.0	54.0	70.0	60.2	Reentry angle error outside allowable corridor.
	VII. 1 E → M	TM21	297.0	5	1	H10	S.O.A. Horizon Sensor; No Instrument Bias	1.3	4.7	1.4	5.5	250.0	318.0	250.0	593.0	9.5			Probably would impact on planet.
	VII. 2 M → E	TM22	106.0	5	3	H10		10.3	13.3	5.1	9.5	71.0	331.0	48.5	299.0	13.8	53.0	45.6	Reentry angle error outside allowable corridor.
	VII. 1 E → M	TM23	236.0	5	1	H41	B.S.O.A. Horizon Sensor and Instrument Bias	2.1	0.35	1.6	0.8	7.6	133.0	92.0	126.0	2.2			
	VII. 2 M → E	TM24	23.7	4	3	H41		0.7	0.8	0.4	0.6	6.8	55.0	13.0	46.4	1.4	8.6	7.4	Reentry angle error marginal.
	VII. 1 E → M	TM25	145.0	5	1	H40	B.S.O.A. Horizon Sensor; No Instrument Bias	2.1	0.34	0.65	0.72	34.0	21.7	77.0	109.6	3.3			
	VII. 1 E → M	TM26	70.0	5	1	H40		2.2	0.34	0.95	0.72	15.8	21.4	8.3	100.0	0.02			
	VII. 2 M → E	TM27	20.4	4	3	H40		0.35	0.75	0.3	0.5	11.4	31.2	15.0	28.7	1.3	4.6	3.9	
	VII. 1 E → M	TM28	181.0	5	1	S11	S.O.A. Space Sestant and Instrument Bias	1.7	1.9	2.0	0.8	42.5	48.0	145.0	55.0	5.1			
	VII. 1 E → M	TM29	157.5	5	1	S10	S.O.A. Space Sextant; No Instrument Bias	2.7	2.2	2.1	0.9	38.0	45.0	71.5	74.5	2.7			
	VII. 2 M → E	TM30	11.0	3	3	S41	B.S.O.A. Space Sextant and Instrument Bias	0.7	1.3	0.47	0.75	54.5	54.6	33.6	37.8	7.3	8.2	7.0	Reentry angle error marginal.
	VII. 2 M → E	TM31	24.6	4	3	S40	B.S.O.A. Space Sextant; No Instrument Bias	0.7	1.2	0.45	0.71	15.4	48.0	15.0	35.7	0.8	6.5	5.6	
	VII. 1 E → M	TM32	35.5	4	1	G11+H41	S.O.A. Ground Tracking; B.S.O.A. Horizon Sensor and Instrument Bias	2.0	2.32	0.80	0.36	4.0	14.8	20.0	14.0	1.6			
	VII. 1 E → M	TM33	13.0	4	1	G10+H40	S.O.A. Ground Tracking; B.S.O.A. Horizon Sensor; No Instrument Bias	2.1	0.18	0.93	0.05	19.0	5.6	5.8	2.0	8.0			To observe the effects of adding horizon sensor to ground tracking, compare with TM18 and see Figures B-21 through B-24 in Appendix B.
	VII. 2 M → E	TM34	10.0	4	3	G10+H40		0.5	0.5	0.2	0.5	7.8	38.9	8.4	26.7	2.0	3.6	3.1	

(S.O.A.) State of the art; (B.S.O.A.) Beyond the State of the Art.

(E → V) Earth to Venus; (V → M) Venus to Mars; (M → E) Mars to Earth; (E → M) Earth to Mars

4643

Table 3-1. Performance Parameters, Mission Category I — Total Missions

The defintions for the actual deviations are analogous to the estimated errors.

$$|\delta r| = |R(t_A) - R^*(t_A)|$$

$$\sigma^*_\gamma = C\left[\left(\frac{\cot\gamma^*}{R^*(t^*_A)}\sigma_{\delta r}\right)^2 + \frac{\cot\gamma^*}{R^*(t^*_A)}\sigma_{\delta r}\sigma_{\delta\gamma} + \sigma^2_{\delta\gamma}\right]^{1/2} C t_A$$

where C is a function of the entry velocity and

$$\cos\gamma^* = \frac{\underline{R}^*(t^*_A)\cdot\underline{V}^*(t^*_A)}{R^*(t^*_A)V^*(t^*_A)}$$

It should be noted that σ^*_γ is the 1 σ error in the actual flight-path angle, not the 1 σ error in the estimate of the flight-path angle. $\sigma_{\delta r}$ and $\sigma_{\delta r}$ are obtained from the terminal constraint covariance matrix T_E, program 284.

Earth-Venus-Mars-Earth Mission Profile

State-of-the-Art Radar Tracker

In this mission profile, it was found that with S. O. A. (state-of-the-art) ground tracking accuracies, the first and third legs of the trajectory (TM1 and TM3) gave satisfactory results. The behavior of the error in the estimate, the actual deviation, and their statistics is quite good in these legs. The resulting error in the flight path angle (re-entry angle) on the third leg is sufficient to insure that the vehicle would be within the appropriate re-entry corridor defined by the ϕ (roll angle) - γ (flight path angle) domain. In the middle trajectory leg (TM2), Venus to Mars, the results point to a possible inadequacy of the ground tracking. In this leg, the vehicle could probably impact the planet, as can be seen from the actual deviations. The reason for this poor performance by ground tracking is attributed to the fact that it was assumed that only range-rate information is available for this leg.

State-of-the-Art Onboard Instruments

As can be seen from Table 3-1 the S. O. A. onboard instrument accuracies studied (TM4, 5, 10, 11) were adequate for the first two legs (VI. 1 and VI. 2) of trajectory VI; however, in the last leg, the S. O. A. accuracies (TM6, 12) were insufficient to ensure proper re-entry. The flight path angle error (σ_{γ}^{*}) obtained was too large to be within the appropriate re-entry corridor defined in the $\phi - \gamma$ domain. In system configuration TM6, the statistics and actual results are not compatible. The incompatibility in this case can be attributed to improper Q election. However, even with proper compensation, re-entry would still be questionable with S. O. A. accuracies as can be seen from mission Category 2 (A4) in Section 3. 1. 4. Note also that in this case if one would examine only the statistics $\sqrt{TR\ P1}$ and $\sqrt{TR\ P4}$, ignoring the other information available, the conclusions would probably be different. This illustrates the pitfalls one could get into by looking just at the statistics of the error estimate and ignoring the actual error estimate.

Beyond State-of-the-Art Instruments

In the B. S. O. A. (beyond the state-of-the-art) onboard instrument accuracies studied (TM7, 8, 9, 13, 14, and 15), it was found that all the systems yielded satisfactory results except for TM9. In this latter system, the error in flight path angles as well as the total control effort were unsatisfactory. This undesirable result can probably be attributed to the improper selection of the velocity spacing, R_V.

Earth-Mars-Earth Mission Profile

Radar Tracker (S. O. A. and B. S. O. A.)

In this mission profile, it was found that S. O. A. ground tracking (TM16, 17) gave unsatisfactory results at the end of the first leg and satisfactory results in the second trajectory leg. The reason for the good results in the second leg (TM17) is attributable to the fact that an orbit rectification was assumed at the perifocal passage and that the initial conditions were based on good first leg results obtained with the other instrumentation. As can be seen in Table 3-1 the B. S. O. A. ground tracking (TM18, 19) yielded exceptionally good results in both legs of the trajectory. In this table only the terminal accuracies are given. Refer to Figures B-5 through B-12 for a graphical presentation of the behavior of the error in the estimate, actual deviation, and their respective statistics as a function of time for systems TM16 and TM18. In these graphs, the abscissas (the time from injection*) are in seconds, and the position and

*The time is not uniformally distributed along the abscissa. The specific inbetween time points can be obtained from Table B-10, Sheet 2.

velocity ordinates are in km and km/sec, respectively. The velocity correction requirements for the first leg were 99.4 m/sec with S.O.A. and 17 m/sec with B.S.O.A. ground tracking. For the second leg, the velocity correction requirements were 24 m/sec and 12 m/sec, respectively. The 1σ re-entry angle errors at Earth are 4.2 mrad for S.O.A. and 0.26 mrad for the B.S.O.A. case. These are well within the re-entry corridor.

Onboard Instruments (S.O.A. and B.S.O.A.)

As can be seen from Table 3-1, self-contained horizon sensor/planet tracker instrument accuracies used for TM20, 21, 22 are not adequate to assure mission success. These accuracies are within the present state of the art. When B.S.O.A. accuracies were used, (TM23, 24, 25, 26, and 27) it was found that system configuration TM24 was slightly marginal in its re-entry angle error; whereas the other configurations yielded satisfactory results. Typical behavior of the error in the estimate, actual deviations, and their statistics (for systems TM21 and TM25) are given in Figures B-13 through B-20 as functions of time. In the space sextant case, it was found that B.S.O.A. instrument accuracies gave satisfactory results except that the re-entry angle error in TM30 is marginal.

Combination of Onboard Instruments and Ground Tracking

As can also be seen TM32, 33, and 34 combinations of ground tracking and onboard horizon sensor/planet tracker yield satisfactory results. The degree of improvement due to the horizon sensor addition can be seen by comparing TM32 with TM16 and TM33 with TM18. The statistics of the errors in the estimate in the latter two are also compared graphically in Figures B-25 through 28. From these figures it can be observed that in the system studied: (1) the horizon sensor reduced the error in the estimate of position in the early and terminal stages of the trajectory leg; (2) the error in the estimate of velocity was not affected appreciably by the addition of the horizon sensor. From this result one might conclude that it would suffice to use combinations of instruments only in the departure and approach conics.

3.1.3.3.1 Instrument Bias Effects upon the Results. The effects of ground tracker biases can be observed by comparing system configurations TM16 with TM18 and TM17 with TM19. A graphical comparison of the statistics of the error in the estimate for TM16 and TM18 is also given in Figures B-25 through B-28. Note that significant improvements are obtained if there are no tracker biases. The total control effort is about 3 to 5 times less than with bias, and the statistics of the terminal error in the estimate are more than 10 times better.

The effect of horizon sensor/planet tracker biases can be observed by comparing TM23 with TM26 and TM24 with TM27. A graphical comparison of the statistics of the error in the estimate is also given in Figures B-29 through B-32. In the horizon sensor case studied, it can be seen that the bias effects are negligible. It should, however, be kept in mind that the value of the bias used was small (0.01 degree).

3.1.3.3.2 Reference Body Effects upon the Horizon Sensor/Planet Tracker Results. The effect of changing the reference body in the total mission profile can be seen by comparing system configurations TM25 and TM26 in Table 3-1. The only difference between these two systems was the reference body. Table B-10, Sheet 2, shows this difference as a function of time from injection.

Figures B-33 through B-36 demonstrate graphically this effect upon the statistics of the error in the estimate. Figure B-2 shows that the path of the vehicle in the initial stage of the heliocentric phase is almost a straight line between Earth and Mars. Thus, switching between the two bodies (schedule R2) does not add more information content. However, employing the Sun in this initial stage (although it is further away than Earth) yields additional information. Note that the terminal accuracies attainable with either schedule R2 or R3 are about the same. However, the significantly better behavior of the estimate in the initial stages of the heliocentric phase (Figures B-33 through B-36) reduces the total control effort by a factor of 2.

As can be seen from Figure B-1 the Moon could have also been used as the reference body in the Earth departure phase to further improve the estimate. This was actually done in mission Category 2 system configurations A4, 6, 8, and 9 are significant improvements were obtained. (See Paragraph 3.1.4.)

Examination of the reference body effects in the horizon sensor/planet tracker case indicates that this body should be selected judiciously. Whether "optimum" body selection — as in the space sextant case — is desirable will have to be investigated further. In any such investigation, the vehicle window constraints should also be considered. In this study, such constraints were not considered.

3.1.3.3.3 Horizon Sensor Instrument Accuracy Effects upon the Statistics. Typical effects of changing the horizon sensor/planet tracker random errors can be observed by comparing TM21 and TM25. Figures B-37 through B-40 illustrate graphically the behavior of the statistics in the two cases. The larger control effort required in the less accurate case is directly attributable to the larger errors in the estimate.

3.1.4 PERFORMANCE ASSESSMENT OF MISSION CATEGORY 2 — PLANETARY APPROACH

As can be seen from the total mission investigations, the most important phase of any trajectory is the approach phase. This is a fortunate consideration from the point of view of computer time consumption, since it permits studying the approach (prior to direct atmospheric entry) problem in more detail without squandering computer time. Thus, in the performance assessment of planetary approaches, only the last portion of the trajectories (from the sphere of influence of the target planet to the re-entry sphere) was investigated.

3.1.4.1 Nominal Trajectory Data for Missions Investigated

Planetary approach portions from five different missions were investigated. The planetary approach portion is considered to be that part of the trajectory from the sphere of influence to the re-entry sphere. The three approach trajectories prior to direct atmospheric re-entry at Earth were a high-, a moderate-, and a low-speed approach. They were taken from a Martian Capture mission (VIII) and from two multiple planet flyby missions (VI and I). The two approach trajectories prior to direct atmospheric entry at Mars were taken from a Martian Flyby (III) and a Martian capture mission (II), and modified so as to be appropriate for atmospheric entry. They are high- and low-speed approaches, respectively.

The nominal trajectory data are summarized in Table B-12.

3.1.4.2 System Configurations Investigated

Systems investigated included state-of-the-art and beyond state-of-the-art onboard and ground-based instruments, as well as combinations of these instruments. The system configurations used to investigate planetary approach are summarized and defined in Table B-13.

3.1.4.3 Performance Parameters

The primary objective of studying the planetary approach phase is to ascertain whether or not particular systems can meet a set of re-entry constraints. The re-entry constraints are considered to be satisfied if the 6σ error (3σ from the nominal value which is assumed to be the center of corridor) in the flight path angle elevated at the re-entry sphere is less than the corridor width. These corridor widths are defined in Paragraph 3.2.5, and the pertinent values are repeated in Table 3-2.

The simulation results compiled in Table 3-12 will be discussed from several points of view. The first will be simply to point out which systems were accurate enough to assure the proper flight path angle upon arrival at the re-entry sphere and to indicate typical propulsion requirements. The second will be to illustrate three of the

TRAJECTORY	TARGET PLANET	VELOCITY AT RE-ENTRY SPHERE (km/s)	CORRIDOR WIDTH (mrad) A	B
I. 4. 3 (Slow)	Earth	12. 02	30	58
VI. 3. 3(Medium)	Earth	13. 95	25	47
VII. 2. 3 and VIII. 2. 3 (Fast)	Earth	19. 66	21	39
II. 1. 3 (Slow)	Mars	5. 69	100	130
III. 1. 3 (Fast)	Mars	12. 63	4	-

Table 3-2. Re-entry Corridor Widths for Trajectories Investigated

four obvious ways to improve performance in the approach phases. They are: (1) to increase sensor accuracy, (2) to select missions with lower approach speeds, and (3) to select judiciously a program of reference bodies for an onboard horizon sensor. The fourth way is orbit rectification which will be discussed under the heading, "Special Studies."

3. 1. 4. 3. 1 Simulation Results for Approach Phase. In the low-speed Earth approach (A1, A2, A3), it can be seen that while the ground tracking gives excellent terminal accuracy with a low velocity correction requirement (13 m/sec), neither the S. O. A. nor the B. S. O. A. onboard instruments were accurate enough to ensure re-entry. The onboard instruments also required a significantly larger total velocity correction.

In the moderate-speed Earth approach (A4 through A9), it is seen again that the S. O. A. horizon sensor is not accurate enough, and it is also seen that three of the four system configurations using B. S. O. A. horizon sensors are not accurate enough. The two systems employing a 10-arc-second horizon sensor in conjunction with B. S. O. A. ground tracking, and a 10-arc-second horizon sensor alone were both adequate to insure re-entry. Both systems require approximately 44 m/sec in velocity corrections.

In the high-speed Earth approach, the two horizon sensor systems studied were far from adequate and the system employing ground tracking was only marginal.

In the low-speed Martian approach (A13 through A18), both the S. O. A. horizon sensor and space sextant proved to be marginally adequate. The propulsion requirement was slightly over 100 m/sec, which is high. When ground tracking was used in conjunction with the S. O. A. horizon sensor, there was a very marked improvement in performance. The error in the flight path angle was well within the corridor and the

propulsion requirement was reduced from over 100 m/sec (horizon sensor without ground tracking) to approximately 25 m/sec (horizon sensor with ground tracking).

In the high-speed Martian approach, the results were much less encouraging. None of the systems investigated were accurate enough to ensure entry. There are two obvious reasons for this: first, the shorter time resulted in less information from the navigation instruments; second, the corridor itself is a great deal smaller.

Some of the simulation results mentioned above are illustrated in Figures 3-1 through 3-5.

.1.4.3.2 Effect of Increasing Sensor Accuracy. In Figures 3-1 through 3-5 the terminal error in the flight path angle is shown for systems of various accuracies. In each figure at least one system is accurate enough to ensure entry. Although it is interesting to vary the parameter "instrument accuracy," it is obvious that simply specifying that a particular accuracy is required is not necessarily a feasible solution to the re-entry problem since that accuracy may be too far beyond the state of the art to be realizable.

3.1.4.3.3 Effect of Decreasing Approach Speed. As can be observed from the results so far, the higher the approach velocity the more difficult it is to enter. Obviously, a solution is then to decrease this velocity. The approach speed can be decreased in the following ways:

1. Select a nominal trajectory that has a low speed due to the swingby through the gravitational field of another planet as was done in the multiple planetary flyby case — mission class I.
2. Perform a retrobraking maneuver prior to the approach phase. Such a maneuver would, however, introduce larger vehicle propulsion requirements which might prove undesirable.

By examination of Figures 3-6 through 3-8 it becomes clear that reducing the approach speed increases the re-entry capability of the systems considered. However, this increase would not be adequate for the S. O. A. horizon sensor in the Earth approach case, as is illustrated in Figure 3-7. In this case there is no velocity in the range attainable by a swingby through a gravitational field that would make re-entry practicable.

3.1.4.3.4 Effect of Varying the Reference Body. It has been observed that the judicious selection of a program of reference bodies to be used by the horizon sensor can result not only in a marked improvement in the accuracy of the estimate of the state throughout the flight, but in some cases also in an improvement in the terminal accuracy. It has been seen also that an improvement in the estimate throughout the flight goes hand in hand with a reduction in the propulsion requirements.

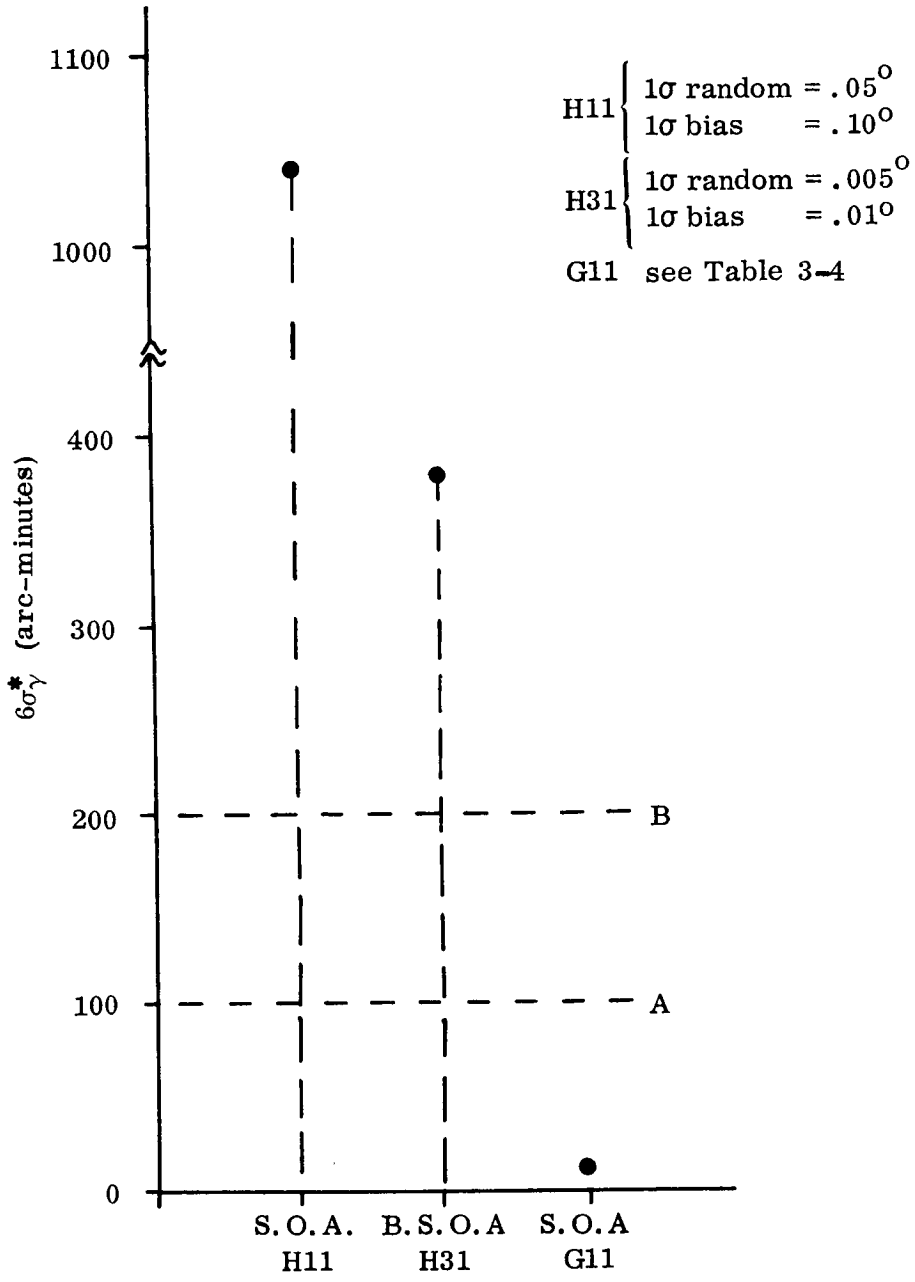

Figure 3-1. Re-entry Capability After a Slow (12.02 km/sec) Earth Approach from the Three Planet Grand Tour (Earth → Venus → Mars → Venus → Earth)

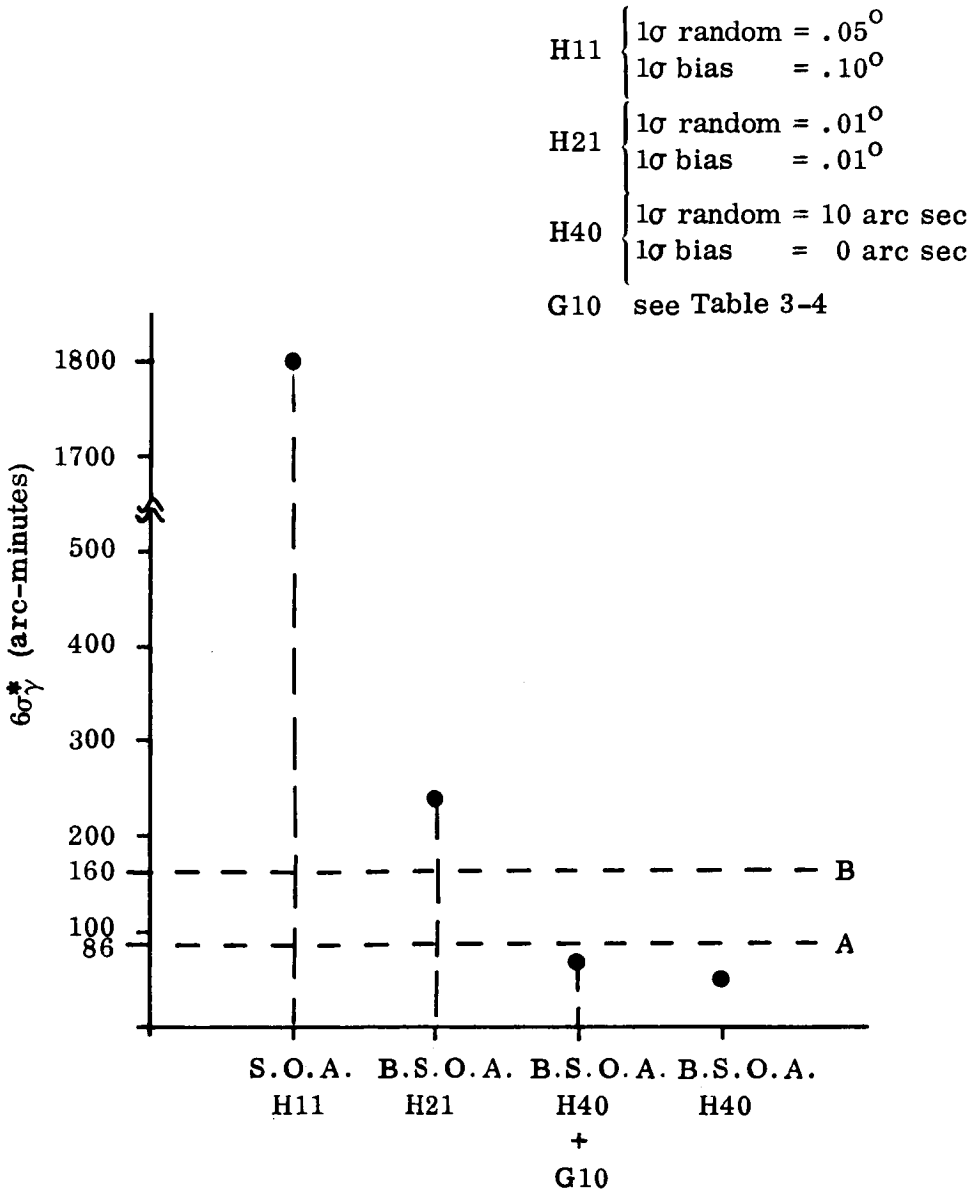

Figure 3-2. Re-entry Capability After a Moderate Speed (13.95 km/sec) Earth Approach from Venus-Mars Swingby (Earth → Venus → Mars → Earth)

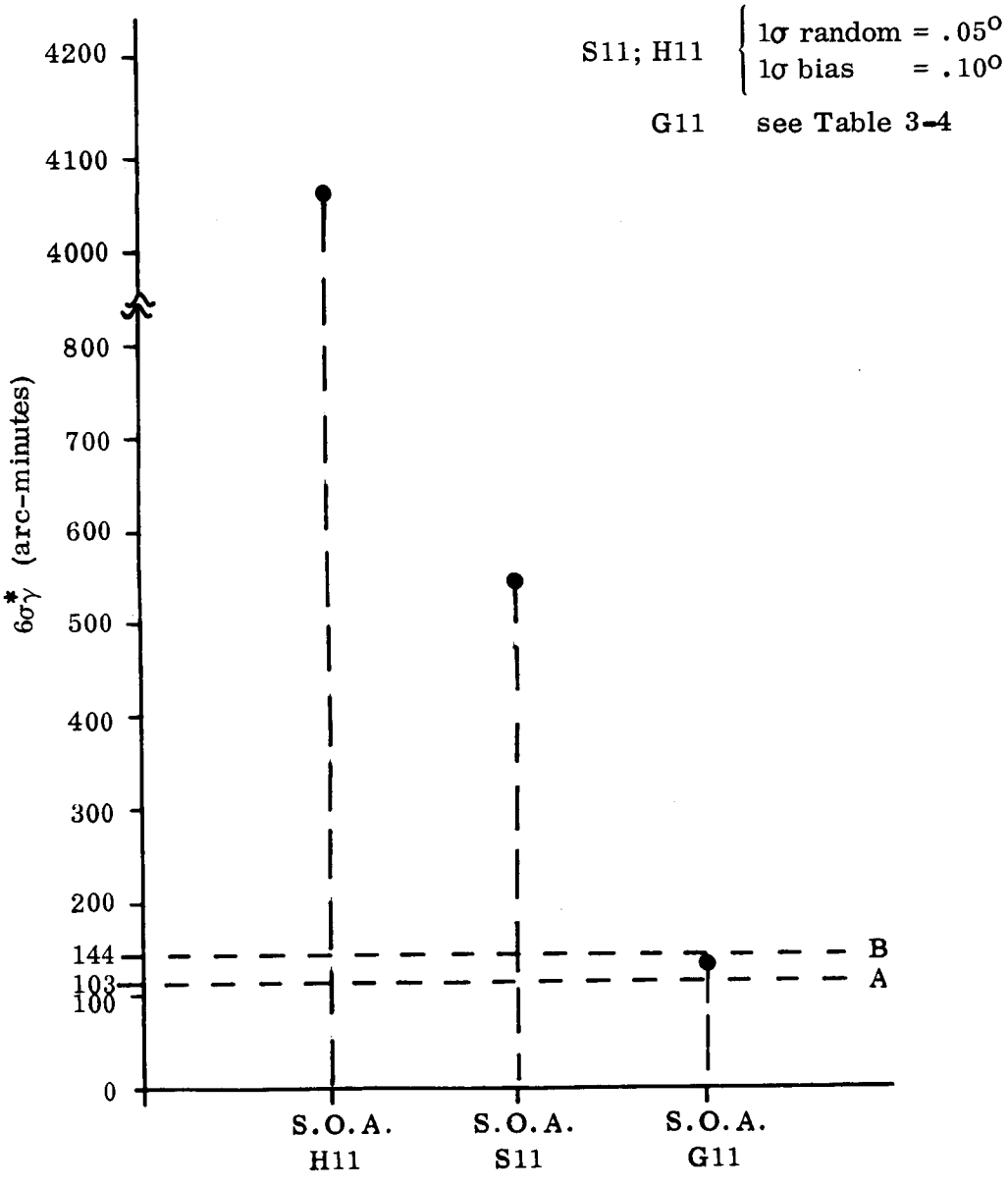

Figure 3-3. Re-entry Capability After a High Speed (15.67 km/sec) Earth Approach from a Martian Capture Mission

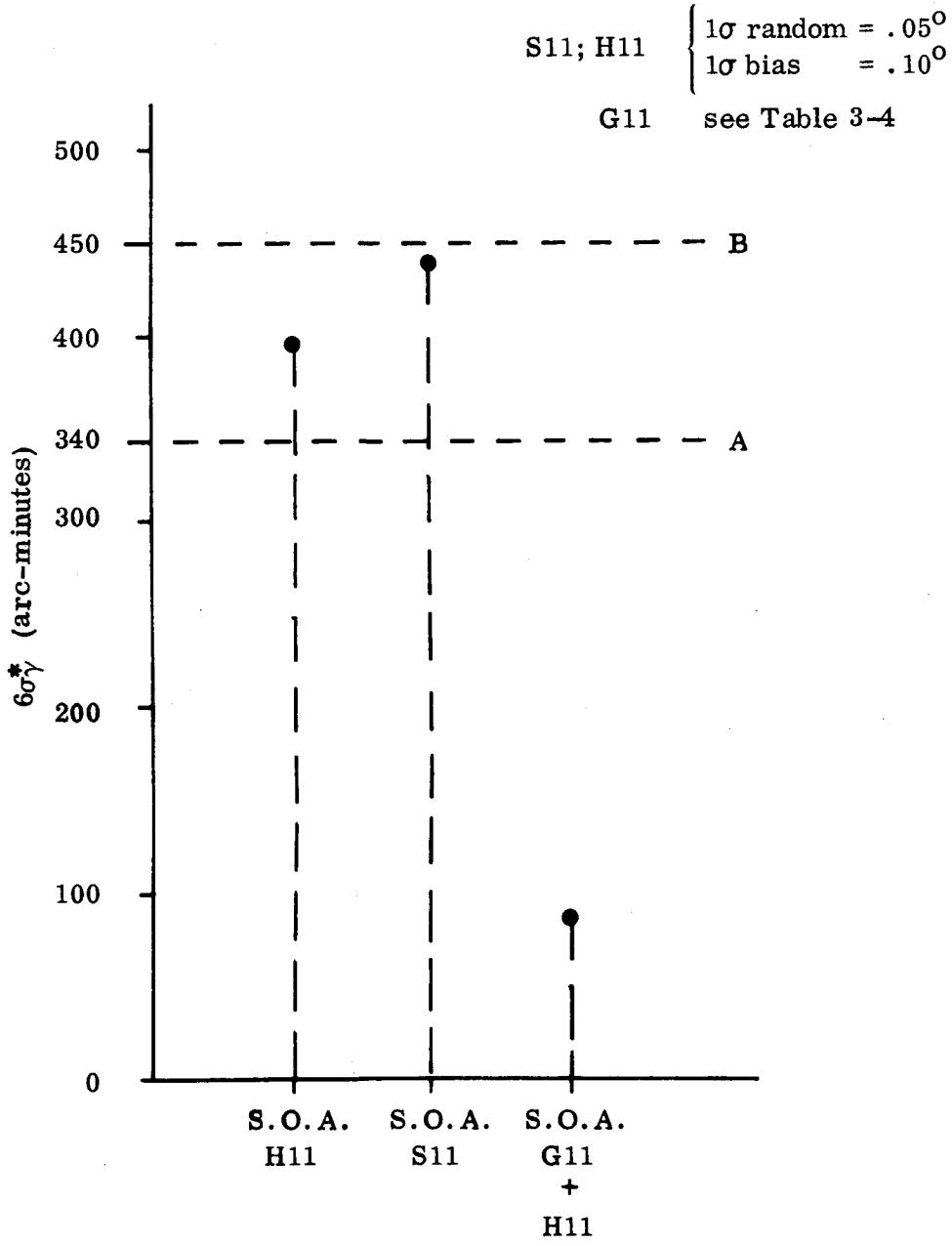

Figure 3-4. Re-entry Capability After a Slow (5.67 km/sec) Martian Approach from Martian Capture Mission

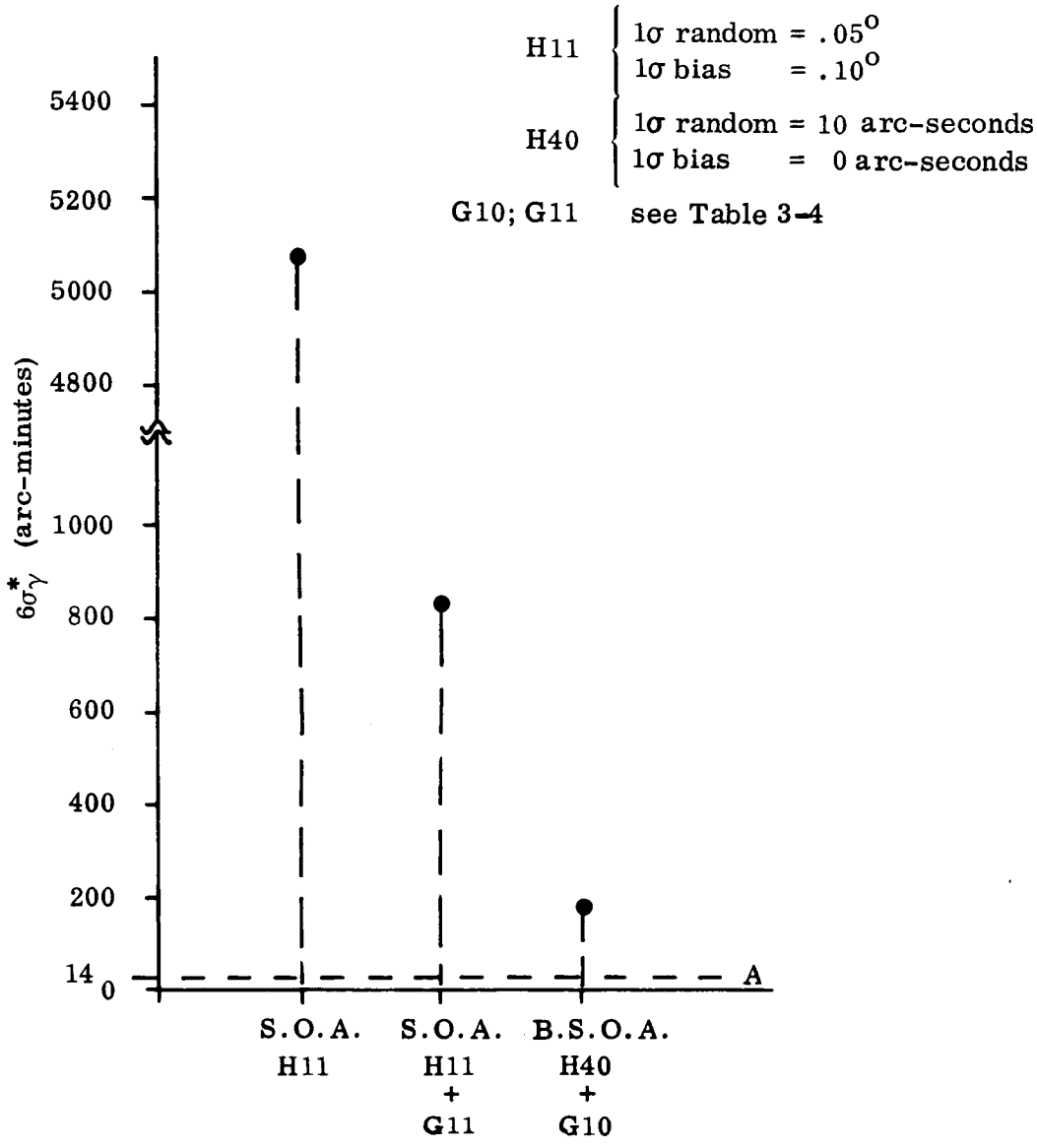

Figure 3-5. Re-entry Capability After a Fast (12.63 km/sec) Martian Approach from Martinal Flyby (Earth → Mars → Earth)

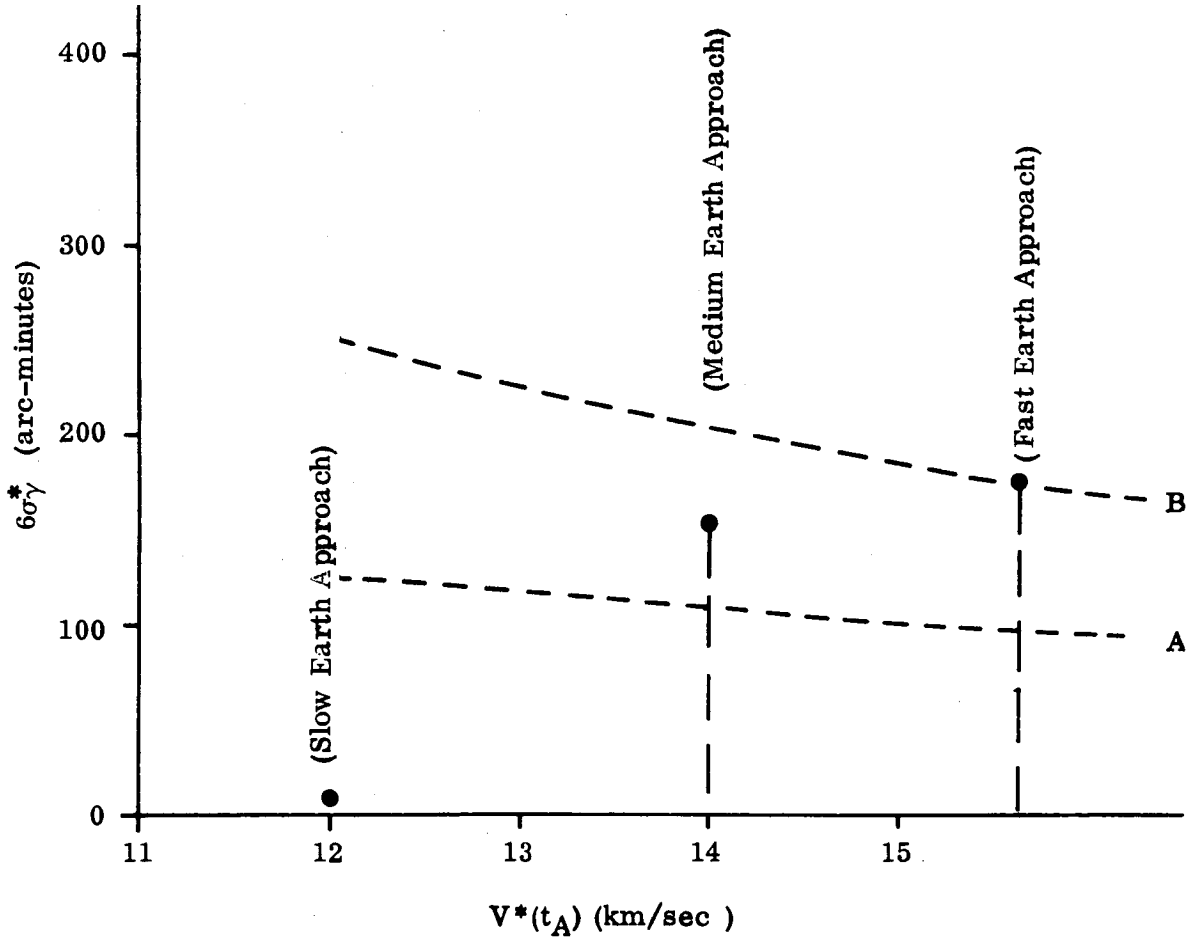

Figure 3-6. Re-entry Capability (after Navigation with State-of-the-Art Ground-Tracking) as a Function of Velocity at the Re-entry Sphere of Earth

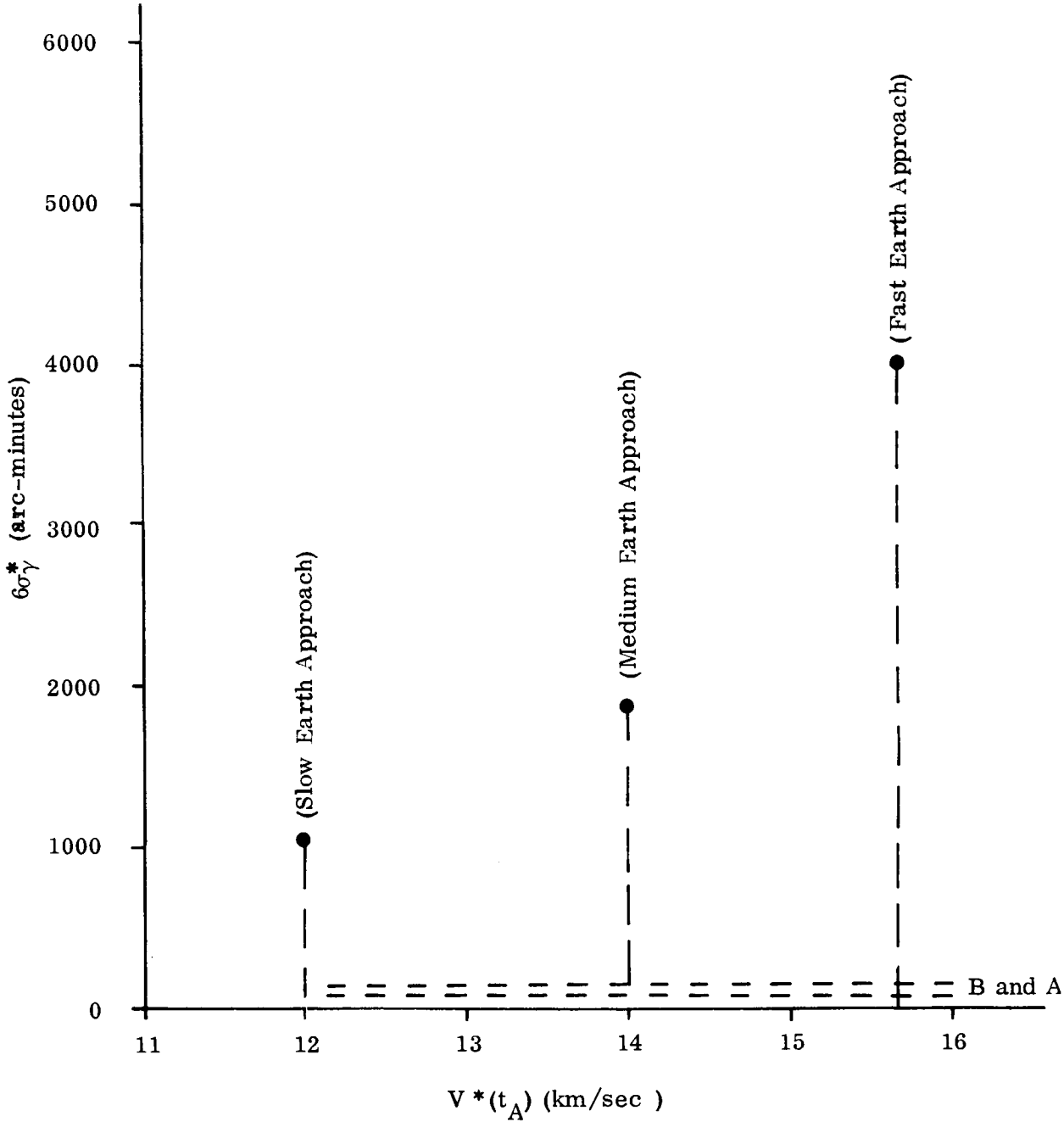

Figure 3-7. Re-entry Capability (after Navigation with State-of-the-Art Horizon Sensor) as a Function of Velocity at the Re-entry Sphere of Earth

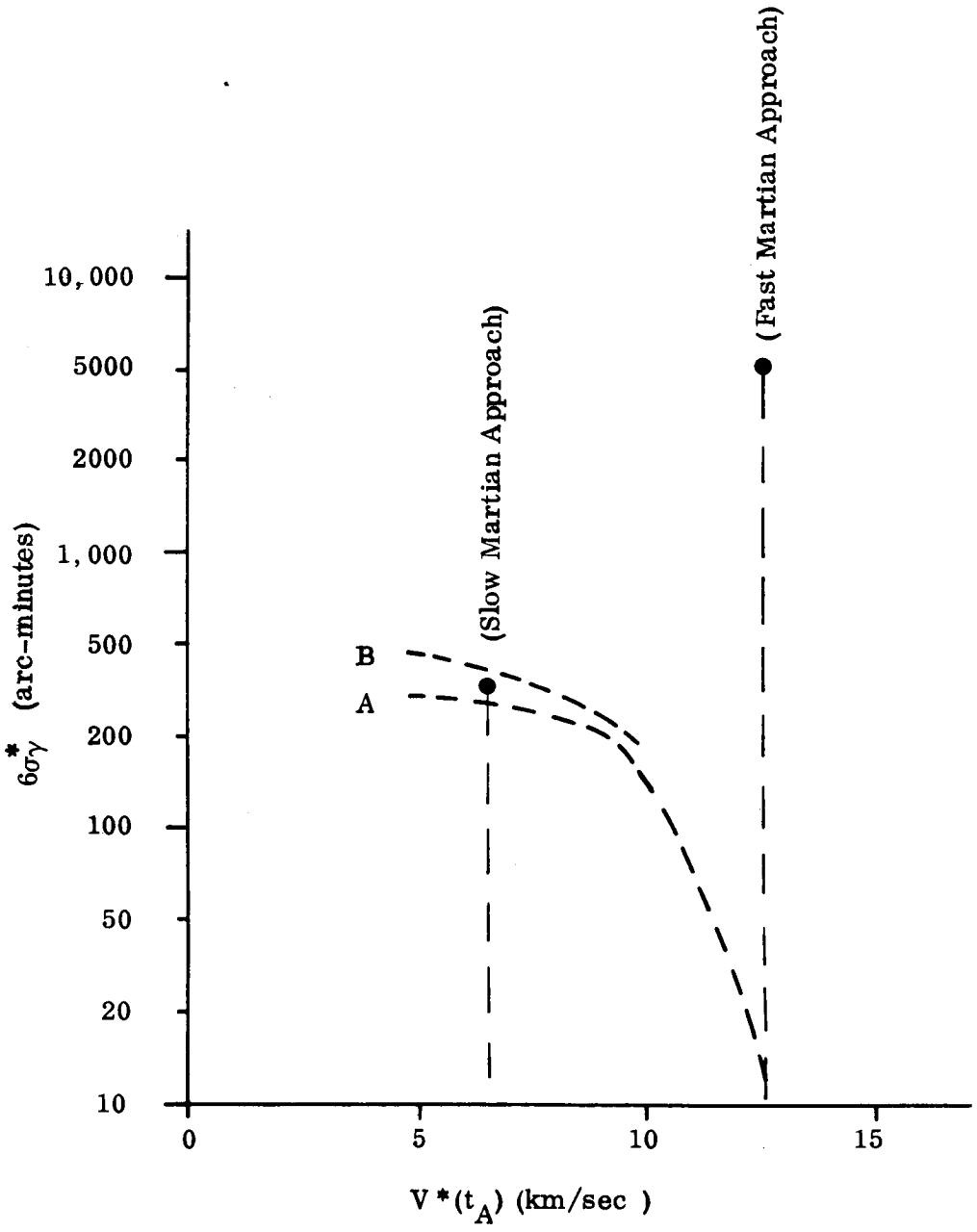

Figure 3-8 Re-entry Capability (after Navigation with State-of-the-Art Horizon Sensor) as a Function of Velocity at the Re-entry Sphere at Mars

The moderate speed Earth approach (VI. 3. 3) was chosen to illustrate these improvements. As shown in Figure B-41, the Earth and the Moon are approximately 90 degrees from each other when viewed from the probe. The reference body was alternated from the Earth to the Moon every 0.7 hours (see R5, Table B-10, Sheet 1) until the probe was close enough to the earth to enable use of subtended angle information. The results of using this reference body schedule are to be compared with the results using only the earth as a reference body. Two different B.S.O.A. horizon sensors were used, H21 and H40. These were systems A5 through A8 (Table B-13. It can be seen that using the "good" reference body schedule (R5) instead of the usual one (R1) resulted in a decrease in the error in the flight path angle from 22.1 mrad to 11.3 mrad when H21 was used. When H40 was used, the decrease was from 10.2 mrad to 2.6 mrad. In both cases the use of R5 instead of R1 resulted in a decrease in the propulsion requirement from a value of over 360 m/sec to a value less than 60 m/sec.

It is interesting to note the trade-off attainable between instrument accuracy and observation geometry. Almost as much improvement can be obtained by changing the observation geometry while keeping the instrument accuracy constant as can be obtained by increasing the instrument accuracy but keeping the same observation geometry. Systems A5, A6, and A7 illustrate this and Figures B-42 through B-45 show the time history of the error in the estimate, the state, and their associated statistics for these systems.

It should also be pointed out that in simulating the different observation geometry no window constraints were taken into account. Generally speaking, such window constraints would incur some attitude propulsion penalty; however, the penalty is not considered significant in this case.

	MISSION PROFILE	SYSTEM CONFIGURATION	GUIDANCE INFORMATION: CONTROL EFFORT: TOTAL ΔV (m/sec)	GUIDANCE INFORMATION: CONTROL EFFORT: NO. OF ΔV's	GUIDANCE INFORMATION: GUIDANCE LAW	NAVIGATION INFORMATION: ERROR BUDGET	NAVIGATION INFORMATION: COMMENTARY ON AIDING INSTRUMENT ERROR BUDGET	TERMINAL CONDITIONS: ESTIMATED ERROR: RSS (x) (km)	TERMINAL CONDITIONS: ESTIMATED ERROR: $\sqrt{TRP}$ (km)	TERMINAL CONDITIONS: ESTIMATED ERROR: RSS (x) (m/sec)	TERMINAL CONDITIONS: ESTIMATED ERROR: $\sqrt{TRP}$ (m/sec)	TERMINAL CONDITIONS: TERMINAL ACCURACY: δr	TERMINAL CONDITIONS: TERMINAL ACCURACY: $\sigma_{\delta r}$	TERMINAL CONDITIONS: TERMINAL ACCURACY: σ_{γ}*	COMMENTS
EARTH APPROACH	I. 4. 3 Slow	A1	13	3	3	G11	S. O. A. Ground Tracking and Instrument Bias	0.2	0.5	0.17	0.73	0.12	0.69	0.3	See Figures B-42 Through B-45 in Appendix B
		A2	165	3	3	H11	S. O. A. Horizon Sensor and Instrument Bias	17.0	8.7	21.2	12.5	51.0	59.0	50.6	
		A3	88	3	3	H31	B. S. O. A. Horizon Sensor and Instrument Bias	1.6	1.4	2.8	2.4	29.0	22.0	18.3	
	VI. 3. 3 Medium	A4	70	3	3	H11	S. O. A. Horizon Sensor and Instrument Bias	36.0	8.2	28.0	10.0	95.0	145.0	87.3	
		A5	364	6	3	H21	B. S. O. A. Horizon Sensor and Instrument Bias	3.7	2.1	2.9	3.1	20.0	27.0	22.1	
		A6	53	4	3	H21	B. S. O. A. Horizon Sensor and Instrument Bias	3.3	1.8	3.0	1.9	38.4	18.7	11.3	
		A7	375	6	3	H40	B. S. O. A. Horizon Sensor and Instrument Bias	1.1	0.5	1.2	0.50	23.0	9.7	10.2	
		A8	44	4	3	H40	B. S. O. A. Horizon Sensor; No Instrument Bias	0.3	0.4	0.28	0.37	3.3	2.5	2.6	
		A9	44	3	3	G10 + H40	S. O. A. Ground Tracking; B. S. O. A. Horizon Sensor; No Instrument Bias	0.3	0.4	0.18	0.30	4.4	4.5	3.2	
	VIII. 2. 3 Fast	A10	40	3	3	G11	S. O. A. Ground Tracking and Instrument Bias	0.3	0.5	10.0	4.1	0.6	7.7	6.7	
		A11	91	1	3	H11	S. O. A. Horizon Sensor and Instrument Bias	200.0	16.0	158.0	15.0	Not Available	228.0	197.3	
		A12	250	2	3	H31	B. S. O. A. Horizon Sensor and Instrument Bias	3.0	2.4	0.4	0.4	22.0	27.0	26.2	
MARTIAN APPROACH	II. 1. 3 Slow	A13	120	3	3	H11	S. O. A. Horizon Sensor and Instrument Bias	5.0	4.8	9.1	5.4	5.0	35.0	19.2	
		A14	20	3	3	H20	B. S. O. A. Horizon Sensor; No Instrument Bias	1.5	1.0	0.9	0.7	3.1	Not Available		
		A15	105	3	3	S11	S. O. A. Space Sextant and Instrument Bias	31.0	37.0	18.1	20.5	12.0	37.0	20.9	
		A16	45	2	3	S20	B. S. O. A. Space Sextant; No Instrument Bias	3.9	14.2	2.0	7.0	15.0	Not Available		
		A17	53	3	3	H20 + S20	B. S. O. A. Horizon Sensor; B. S. O. A. Space Sextant; No Instrument Bias	0.41	0.8	0.51	0.6	2.9	Not Available		
		A18	25	4	3	G11 + H11	S. O. A. Ground Tracking; S. O. A. Horizon Sensor and Instrument Bias	1.2	1.9	0.18	2.3	6.0	8.0	4.1	
	III. 1. 3 Fast	A19	32	1	3	H11	S. O. A. Horizon Sensor and Instrument Bias	25.0	8.0	2.8	5.2	210.0	170.0	253.0	
		A20	0	0	3	S11	S. O. A. Space Sextant and Instrument Bias	55.0	32.0	30.0	8.8	620.0	377.0	443.0	
		A21	101	2	3	H11 + G11	S. O. A. Horizon Sensor; S. O. A. Ground Tracking and Instrument Bias	11.4	6.3	7.7	3.6	51.0	50.0	40.1	
		A22	47	3	3	H40 + G10	B. S. O. A. Horizon Sensor; B. S. O. A. Ground Tracking; No Instrument Bias	0.8	0.42	0.22	0.16	11.5	6.0	10.5	
		A23	52	3	3	H40 + G10	B. S. O. A. Horizon Sensor; B. S. O. A. Ground Tracking; No Instrument Bias	0.3	0.42	0.11	0.18	0.7	5.2	9.3	

870316

Table 3-3. Performance Parameters, Mission Category 2 — Planetary Approach

3.1.5 PERFORMANCE ASSESSMENT OF MISSION CATEGORY 3 — PLANETARY RECONNAISSANCE

Circular orbits can be of interest for a few different reasons, the most obvious of which is just for the observation of a planet. They can also be used prior to atmospheric entry to reduce the uncertainties after the approach phase, in a flyby mission to reduce uncertainties at the beginning of the return leg, and of course, the probe can remain in a parking orbit until a favorable date for the return leg of a mission. Since most of these uses are primarily concerned with reducing the uncertainty in position and velocity, most of the flights were simulated in the navigation mode only, that is, without midcourse velocity corrections.

3.1.5.1 Nominal Trajectory Data for Missions Investigated

Two circular trajectories around Mars were chosen to be studied — one at a high altitude (8,200 km) and one at a low altitude (140 km). The high altitude orbit was chosen to be compatible with the altitude at the perifocal passage at Mars in Trajectory II.1, Mars capture mission. The other trajectory was planned to be at an altitude slightly above the top of the mean Martian atmosphere. The nominal trajectory data for these trajectories are summarized in Table B-14.

3.1.5.2 System Configurations Investigated

For this study, only horizon sensors of various accuracies were employed, and Mars was the only reference body used. The system configurations are defined in Table B-15

3.1.5.3 Performance Parameters

High Altitude Orbit

The performance parameters, which will be discussed next, are presented in Table 3-4. In the high altitude orbit, the initial uncertainty in position was reduced from 100 km to approximately 18 km after two revolutions using the S.O.A. horizon sensor. The same instrument without bias errors reduced the uncertainty to approximately 3 km. The radial component of the error in the estimate (XRWIGL) $\tilde{x}$ and its corresponding 1σ statistical measure ($\sqrt{P11}$) are plotted as functions of time and are presented in Figures B-46 and B-47. The normal and tangential components exhibit the same type of behavior and therefore are not presented. The B.S.O.A. horizon sensor with and without bias reduced the same initial uncertainty (100 km) to 12 km and 0.5 km, respectively.

From just the terminal results, it is tempting to deduce that the bias errors had a very strong effect throughout the flight, but inspection of Figures B-46 and B-47 lead to a different conclusion. It can be seen that the effect of the bias errors is effectively removed before the completion of one revolution and that the errors are approximately the same for the rest of the flight.

MISSION PROFILE		SYSTEM CONFIGURATION	GUIDANCE INFORMATION			NAVIGATION INFORMATION		TERMINAL CONDITIONS						COMMENTS
			CONTROL EFFORT		GUIDANCE LAW	ERROR BUDGET	COMMENTARY ON AIDING INSTRUMENT ERROR BUDGET	ESTIMATED ERROR				TERMINAL ACCURACY		
			TOTAL ΔV (m/sec)	NO. OF ΔV's				RSS ($\tilde{x}$) (km)	$\sqrt{TRP1}$ (km)	RSS ($\tilde{x}$) (m/sec)	$\sqrt{TRP4}$ (m/sec)	δr	$\sigma_{\delta r}$	
LOW ALTITUDE MARTIAN ORBIT	XII	P1				H11	S.O.A. Horizon Sensor and Instrument Bias	20.0	18.0	2.4	2.2			See Figure B-46 in Appendix B.
		P2				H10	S.O.A. Horizon Sensor and Instrument Bias	4.1	2.6	0.45	0.38			See Figure B-47 in Appendix B.
		P3				H51	B.S.O.A. Horizon Sensor and Instrument Bias	11.5	2.1	2.2	0.25			
		P4				H50	B.S.O.A. Horizon Sensor and Instrument Bias	0.5	0.05	0.27	0.007			
HIGH ALTITUDE MARTIAN ORBIT	IX	P5				H11	S.O.A. Horizon Sensor and Instrument Bias	3.1	4.0	2.8	3.0			See Figure B-48 in Appendix B.
		P6				H11	S.O.A. Horizon Sensor and Instrument Bias	1.5	4.3	1.9	3.3			
		P7	14.0	1	3	H11	S.O.A. Horizon Sensor and Instrument Bias	2.1	4.0	1.2	3.0	1.2	0.9	
		P8				H11	S.O.A. Horizon Sensor and Instrument Bias	336.2	114.0	334.9	113.8			
		P9				H10	S.O.A. Horizon Sensor, No Instrument Bias	1.0	1.3	0.58	1.2			
		P10				H10	S.O.A. Horizon Sensor, No Instrument Bias	2.3	1.8	1.8	1.7			
		P11				H10	S.O.A. Horizon Sensor, No Instrument Bias	2.3	1.8	1.8	1.8			
		P12				H10	S.O.A. Horizon Sensor, No Instrument Bias	1.1	1.3	0.7	1.2			See Figure B-49 in Appendix B.
		P13				H20	B.S.O.A. Horizon Sensor, No Instrument Bias	1.4	0.26	0.14	0.24			See Figure B-51 in Appendix B.
		P14				H20	B.S.O.A. Horizon Sensor, No Instrument Bias	0.22	0.26	0.22	0.24			
		P15	5.8	1	3	H20	B.S.O.A. Horizon Sensor, No Instrument Bias	1.4	0.30	1.3	0.20	0.02	0.3	
		P16				H21	B.S.O.A. Horizon Sensor and Instrument Bias	0.61	0.67	0.61	0.50			See Figure B-50 in Appendix B.
		P17				H21	B.S.O.A. Horizon Sensor and Instrument Bias	524.0	121.2	515.7	120.0			
		P18				H21	B.S.O.A. Horizon Sensor and Instrument Bias	0.61	0.81	0.50	0.70			
		P19				H50	B.S.O.A. Horizon Sensor, No Instrument Bias	0.11	0.03	0.17	0.02			
		P20				H50	B.S.O.A. Horizon Sensor, No Instrument Bias	0.20	0.03	0.26	0.03			
		P21				H50	B.S.O.A. Horizon Sensor, No Instrument Bias	0.17	0.03	0.24	0.03			
		P22				H50	B.S.O.A. Horizon Sensor, No Instrument Bias	0.13	0.03	0.17	0.02			

4645

Table 3-4. Performance Parameters, Mission Category 3 — Planetary Reconnaissance

Low Altitude Orbit

In the low altitude orbit, the S.O.A. horizon sensor reduced the initial uncertainty ($\sqrt{TR\ P1}$ from 10 km to 4 km after three revolutions (P5), and the same instrument without bias errors (P12) reduced the uncertainty to 1.3 km. A more accurate system (P16) reduced the uncertainty to 0.7 km and that instrument without its bias errors (P13) effected a reduction to 0.3 km. The radial component and its 1σ statistical measure are presented in Figures B-48 through B-51, respectively, for the aforementioned systems. Navigation with a very accurate instrument (P19) resulted in statistics which indicated a 1σ error in the estimate of .03 km, but the actual error was about four times that large. It is presumed that these errors are on the order of magnitude of the nonlinearities in the system, since the discrepancy could not be removed by adjusting the plant dynamics covariance Q.

In this low altitude orbit, it is again seen by inspection of Figures B-48 and B-49 that the bias errors can be removed before one revolution has been completed. Since the bias error was small in the B.S.O.A. instrument used in the generation of Figure B-50, there is not much difference between that figure and Figure B-51, which was generated using the same instruments with no bias error at all.

The square root formulation of the Kalman filter was exercised in this portion of the study, as well as in the Special Studies. It was observed here, as there, that when the state is augmented in order to estimate the bias errors, the square root filter gives very poor results in comparison to the nonsquare root filter. This is because of the greater volume of computation required by the square root formulation. When bias errors were not simulated, the results for the square root and the conventional filter (P19 and P22) were almost identical.

3.1.6 SPECIAL STUDIES

In conjunction with the midcourse guidance performance assessment studies, several special studies were initiated. The paragraphs below summarize these studies and their findings.

3.1.6.1 Orbit Rectification

Rectification (the policy of updating the nominal trajectory at each observation with the best estimate) was found to extend significantly the range of linear theory and provided the most satisfactory results in those cases where Kalman filter estimation using a single prespecified nominal was found to be inadequate.

In practical applications of the developed guidance and navigation theory, the question of the effect of the neglected nonlinear terms upon the filter performance is of great importance. These effects will be felt most strongly in strongly nonlinear regions of interplanetary space, that is, close to the planets and for large initial deviations. On the other hand, one has to expect that orbit rectification improves the filter performance over a navigation mode without it. Such a situation was simulated using a horizon sensor with 1σ error of 0.1 degree, and an observation interval of 600 sec in a 100 nmi earth orbit. The initial deviations were of the order of 10 nmi and 100 ft/sec. The response of the navigation system with and without orbit rectification are shown in Table 3-5. The application of the orbit rectification scheme, which was used in this simulation at each observation, shows a significant improvement even under these large initial deviations. It can be concluded that linear navigation theory will be adequate for a wide range of mission profiles and instrument errors.

3.1.6.2 Optimum Star Selection

In an effort to determine the minimum size of a star catalog (from which stars are selected in an optimal* fashion at each observation time), the use of which results in an accuracy which cannot be improved merely by increasing the size of the catalog, flights were simulated along selected trajectories using star catalogs containing the following combinations of stars:

1. Two stars, one parallel to the plane of motion, one perpendicular** to the plane of motion,
2. Five stars, selected randomly,
3. Ten stars, selected randomly,
4. "Ideal" stars; an infinite catalog.

*See Appendix A, Optimal Star Routine

**By perpendicular to the plane of motion, it is meant that the line of sight from the probe to the star is approximately 90 degrees from the plane of motion.

TIME	Position/ Velocity	NO RECTIFICATION		RECTIFICATION	
		Error in Estimate	Eigenvalues of Error Covariance	Error in Estimate	Eigenvalues of Error Covariance
5400 sec (approximately 1 revolution)	X, ft	-36,783	4,352	5,450	4,021
	Y, ft	-52,744	18,118	-1,685	17,306
	Z, ft	10,600	16,562	10,460	16,510
	$\dot{X}$, fps	59.9	20.1	2.9	19.5
	$\dot{Y}$, fps	-23.7	4.7	-4.5	4.2
	$\dot{Z}$, fps	-24.8	19.6	-23.5	19.6
10,800 sec (approximately 2 revolutions)	X, ft	-137,028	2,852	1,809	2,523
	Y, ft	-93,000	15,504	-3,604	15,092
	Z, ft	18,163	12,035	18,487	11,992
	$\dot{X}$, fps	106.9	17.5	1.7	17.2
	$\dot{Y}$, fps	-123.3	3.3	0.6	2.8
	$\dot{Z}$, fps	-19.6	14.4	-17.8	14.4
27,000 sec (approximately 5 revolutions)	X, ft	-11,896,883	11,131	-3,721	11,142
	Y, ft	14,777,479	1,732	993	1,519
	Z, ft	4,998	7,736	7,041	7,704
	$\dot{X}$, fps	-16,318.1	12.7	-3.5	12.8
	$\dot{Y}$, fps	-14,123.4	2.0	-1.8	1.8
	$\dot{Z}$, fps	-7.2	9.3	-4.0	9.4

Table 3-5. Effect of Orbital Rectification upon Navigation System Performance

3.1.6.2.1 Nominal Trajectory Data. Three trajectories were chosen for the study: a Martian approach trajectory (III.1.3, Table B-12 and two circular orbits (IX and X, Table B-13). One of the circular trajectories is at a low altitude of 140 km, the other at a medium altitude of 1000 km. In order to demonstrate the efficacy of having one star plane of motion and one normal to it, the simulations were repeated with the plane of motion rotated 45 degrees around the X axis. Thus, the stars were neither in the plane nor normal to it. The low-altitude trajectory is designated A_0 and the trajectory with plane of motion rotated is designated A_{45}. The medium altitude orbits are likewise designated B_0 and B_{45}.

3.1.6.2.2 System Configuration. The space sextants studied were S20 and S50 (see Table B-8). The initial covariance matrices employed are given in Table 3-6.

Trajectory Number	σ_x (km)	σ_y (km)	σ_z (km)	$\sigma_{\dot{x}}$ (m/sec)	$\sigma_{\dot{y}}$ (m/sec)	$\sigma_{\dot{z}}$ (m/sec)
1 (III.1.3)	200	150	130	2.1	2.6	3.0
A (IX)	30	30	30	30	30	30
B (X)	30	30	30	30	30	30

Table 3-6. Diagonal Matrix of Initial Covariance

In this study only the navigation mode was employed; no velocity corrections were made. The conventional Kalman filter was used without Q compensation. The observation schedules are given in Table 3-7.

It should be noted that in the study the assumption was made that the vehicle has an unrestricted window.

3.1.6.2.3 Performance Parameters. The simulation results are presented in Figures B-52 through B-61. The following symbols are used in the figures.

σ_T ◇ Standard deviation of the error in the estimate of the tangential component of position propagated from t_k to time of arrival

σ_N □ Standard deviation of the error in the estimate of the normal component of position propagated from t_k to time of arrival

σ_R ⬡ Standard deviation of the error in the estimate of the radial component of position propagated from t_k to time of arrival

In the analysis of the results, attention must be paid not only to the error at the end of the flight, but also to the errors throughout the flight because they strongly affect fuel consumption.

For the Martian approach trajectory, it can be seen from Figures B-52 through that while there is an appreciable improvement in using five stars over using two, there is only very slight improvement to be gained in using ten stars over five. When the results of navigating with ten stars is compared with that of using "ideal" stars (Figure B-55), it is clear that the use of "ideal" stars gave no improvement in this trajectory.

For the circular trajectories, attention is directed to Figures B-56 through B-61. For the low-altitude orbit, if Figure B-56 is compared with Figure B-57. it can be seen that having one star in the plane of motion and one normal to it is superior to having two stars removed from the plane of motion. Comparison of Figures B-56 and B-58 shows that the use of five stars gives improved results over the use of two stars; however, Figures B-58 and B-59 indicate that there is no appreciable improvement in navigational accuracy to be gained by using ideal stars instead of using a catalog of five stars.

Mission Profile	Number of Observations	Interval Between Observations	
		Time (sec)	Angular (degrees)
Martian Approach (1) (III. 1. 3, 1)	1 6 8 20	500 4000 2000 500	N.A.
Low-Altitude (140 km) Martian Circular Orbit (IX, A)	60	319.2	18
Medium Altitude (1,000 km) Martian Circular Orbit (X, B)	60	442.3	18

Table 3-7. Observation Schedules

For the high-altitude orbit, Figures B-60 and B-61 demonstrate again that one star in the plane and one start normal to the plane yield better results than do two stars located arbitrarily.

It is important to note that the following conclusions were reached under the assumption of an unrestricted window.

In an effort to establish realistic star catalog sizes, studies were performed in which the number of stars available for observation was varied. From these studies it was

found that for both the approach trajectory and the circular trajectories a catalog of five stars with an unrestricted window would suffice in the cases that were investigated. The results using five stars show a significant improvement over those for one star or for two stars; however, the results for ten stars and for "ideal" stars do not show appreciable improvement in the terminal errors over those for five stars.

3.1.6.3 Fixed Versus Variable Time-of-Arrival Guidance Laws

In this study, several of the mission categories and system configurations were investigated using variable time-of-arrival guidance laws. Generally speaking, when the terminal constraints (such as time-of-arrival) are relaxed, a savings in the propulsion requirements occurs. The objective of this study was, therefore, to determine the propulsion savings and to evaluate the overall performance.

In the total mission category, some problems were found when variable time-of-arrival laws were used. It was observed that the linearity assumption in the onboard measurements was violated in the terminal phase of the trajectories. This violation is a natural consequence when large changes in the time of arrival (δt_A) are computed because the time is used as the independent variable in advancing both the nominal and actual trajectories. The time is also used in establishing the observation schedules. The sketch below illustrates this problem for mission profile VII. 1 system configuration TM25 (Guidance Law 2). The first point in this sketch corresponds to approximately 4,000 sec before the actual time of arrival. Table 3-8 summarizes some of the other results obtained in the total mission category. Note that the geometric disparities in the unsketched results would be even worse since δt_A is larger in those cases.

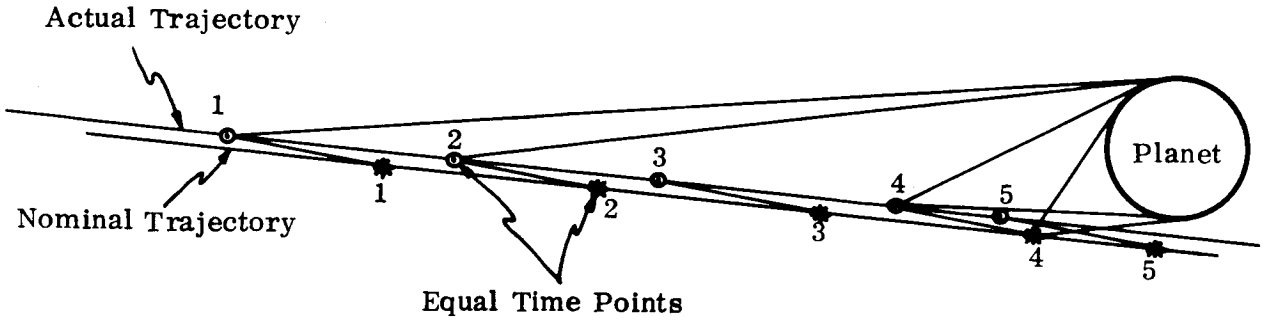

The measurement linearity problems encountered in the total mission category should be investigated further with inclusion of orbit rectification. If the problem persists, even when orbit rectification is employed, it would probably be necessary to use the arc length as the independent variable in advancing the trajectories. Even if the measurement linearity problems are eliminated in future studies, but the changes in time-of-arrival remain as given in Table 3-8, the effect of such large changes on the reentry problem should be investigated further.

MISSION PROFILE		SYSTEM CONFIGURATION	GUIDANCE INFORMATION				NAVIGATION INFORMATION	COMMENTS
			TOTAL ΔV (m/sec)	CHANGE IN t_A $\lvert \delta t_A \rvert$ (sec)	GUIDANCE LAW	ERROR BUDGET	COMMENTARY ON AIDING INSTRUMENT ERROR BUDGET	
Earth - Mars	VII. 1	TM25	12-20	640-760	2	H40	B. S. O. A. Horizon Sensor, No Instrument Bias	Measurement Linearity Problem on Approach Trajectory to Mars
	VII. 1	TM23	90-190	3,500-3,800	2	H41	B. S. O. A. Horizon Sensor and Instrument Bias	Measurement Linearity Problem on Approach Trajectory to Mars
Mars-Earth	VII. 2	TM27	4-6	1,160-2,460	4	H40	B. S. O. A. Horizon Sensor, No Instrument Bias	Measurement Linearity Problem on Approach Trajectory to Earth
	VII. 2	TM24	6	1,550-2,200	4	H41	B. S. O. A. Horizon Sensor and Instrument Bias	Measurement Linearity Problem on Approach Trajectory to Earth

4661

Table 3-8. Variable-Time-of-Arrival System Configurations and Performance Parameters (Total Missions Category)

In the single conic planetary approach phases studied, the results were more favorable. No measurement linearity problems were encountered in these studies. Table 3-9 summarizes the results obtained for the system configurations that were investigated.

The values for the terminal flight path angle accuracies were within the re-entry corridor as defined by the $\phi - \gamma$ domain for an Apollo vehicle (see Table 3-2). Considerable propulsion savings were also achieved by using variable-time-of-arrival (VTA) guidance laws in both the Earth approach and Martian flyby without affecting the terminal accuracies, as can be seen in Table 3-9.

	MISSION PROFILE	INITIAL COVARIANCE MATRIX	GUIDANCE INFORMATION			NAVIGATION INFORMATION	
			TOTAL ΔV (m/sec)	CHANGE IN t_u $\lvert \delta t_u \rvert$ (sec)	GUIDANCE LAW	ERROR BUDGET	COMMENTS
EARTH APPROACH	VIII. 2. 3	M15	10-30	160	4	G10	S. O. A. ground tracking no instrument bias
			30-50	0	3	G10	S. O. A. ground tracking no instrument bias
	I. 4. 3	M16	8-20	105	4	G10	S. O. A. ground tracking no instrument bias
			12-25	0	3	G10	S. O. A. ground tracking no instrument bias
MARTIAN APPROACH	III. 1. 3	M17	15-20	38-46	2	H50	B. S. O. A. horizon sensor no instrument bias
			60-85	0	1	H50	B. S. O. A. horizon sensor no instrument bias
		M17	20-45	15-46	2	H20	B. S. O. A. horizon sensor no instrument bias
			18-120	0	1	H20	B. S. O. A. horizon sensor no instrument bias

4655

Table 3-9. System Configurations and Performance Parameters Summary

3.1.6.4 Comparison of Performance of Square Root Kalman Filter and Conventional Kalman Filter

Two results were obtained using DSIF in an earth-approach phase. First, the square root filter kept the covariance matrix positive throughout the entire flight, whereas the conventional filter did not if no bias errors were considered. Second, the square root filter gave nonpositive covariance matrices if the bias errors were included, whereas the conventional filter yielded positive-definite covariance matrices throughout the entire flight if appropriate noise was included in the dynamical equations.

The explanation of the behavior of the square root Kalman filter lies in the fact that the bias errors increase the state vector; therefore, many more computations are required at each observation point. This increases the computer-generated errors to the extent that the covariance matrix becomes nonpositive.

3.1.6.5 Some Computational Aspects of Sequential Estimation in Space Navigation

Theoretically, the error covariance matrix (see Appendix A) in Kalman filtering is a nonnegative definite symmetric matrix. Because of computational inaccuracies, such as computer roundoff and truncation errors in the simulation and perhaps model errors, the covariance matrix may lose these properties if these computational inaccuracies are not properly accounted for. To properly account for these effects, appropriate values for the Q matrices, which represent the assumed covariances of these error sources, must be employed.

The specific Q values used are indicated in the system configuration tables. The selection of the Q's was done empirically, based upon estimated values for the computation and model errors, in such a way that consistent results were obtained from the navigational filter. By consistent results, it is meant that the filter converges properly so that the behavior of the estimate is consistent with its statistics.

Typical results obtained for a ground-tracking case when improper Q compensation was employed are depicted in Figures B-62 through B-65. These results were obtained from system configuration TM18 when Q1 was used in place of Q4. As can be observed in Figure B-62, the error in the estimate and the corresponding statistics are initially compatible for TM18 (Q1). The magnitude of the error in this case, however, is significantly larger throughout the flight than with TM18 (Q4); see Figure B-66. The larger values can be attributed to improper Q compensation. In the last phase, it can be seen that the error in the estimate starts diverging very rapidly. The dramatic divergence of the error in the estimate in the Mars approach phase is a direct result of the actual deviation being too large so that the linearity assumption is violated. It should be observed that the actual position deviation, Figure B-64, starts diverging and becomes incompatible with its statistical measure at a much earlier time. This divergence is also due to improper Q compensation for the following reasons.

When the "bad" Q1 was used, it affected the velocity correction statistics and the velocity correction ratio R_V in such a manner that only two velocity corrections were made in the Earth departure conic. No subsequent velocity corrections were made in the remaining conics. Thus, the error introduced by these early corrections, due to improper Q compensation, affected the subsequent actual deviation results more dramatically in the early stages than the error in the estimate results.

When proper Q compensation is employed, all of these problems are eliminated. Figures B-66 through B-69 illustrate the superior behavior obtained for system TM18 when Q4 replaces Q1. To facilitate comparison, Figures B-70 through B-73 are also included.

Figures B-74 through B-77 depict typical results that were obtained for system configuration TM23 (horizon sensor) when the Q schedule was changed from Q1 to Q2. Observe that when Q1 was used, the errors in the estimate and their statistics were incompatible in the first half of the heliocentric conic, that is, the errors were outside the 3σ statistics. By changing the Q schedule in the interval in question (see Q1 and Q2 in Table B-11), the statistics are approximately doubled and they represent more closely the actual situtation. The larger Q value in this interval tends to give more weight to the current measurements (through the gain matrix), thus forcing the better agreement between the errors in the estimate and their statistics.

It should be pointed out that the empirical experimentation to establish the Q values is an undesirable and sometimes expensive proposition. It is very desirable either that future studies concern themselves with devising other compensation techniques or that analytical investigations be initiated that lead to an optimal way of selecing the Q matrix.

3.1.6.6 Study of the Initial Covariance Matrix Effects upon the Results

A brief study was performed to establish the filter performance dependency on the initial covariance matrix. Three different initial covariance matrices (M9, M10, M11 of Table B-9) were employed in the study, and no parameters other than the initial M were varied. Even the initial random number noise sequence was the same in the generation of the initial conditions for the actual. Naturally, the actual initial conditions generated were different in the three cases since the variances of the initial M's were different. For additional information concerning the system configuration reference should be made to Table B-7 in the total mission category.

Table 3-10 summarizes some of the performance parameters obtained in this study. As can be seen from the table the terminal accuracies hardly changed in the first and last cases. In the third case, TM19 (M11), the change was somewhat larger in the actual deviations but still well within tolerable limits. The error in the estimate, however, is incompatible with the corresponding statistics. This result would seem to indicate a need for some Q compensation (see Paragraph 3.1.6.5). If Q compensation would not remedy the situation, it is then possible that M11 is on the verge of being too large so that the linearity assumption is almost violated; however, the latter is doubtful for this particular system configuration.

The control effort in this third case is also larger by a factor of 3. This could probably be attributed to the larger initial M and also the fact that the velocity correction ratio (R_V) behavior was such that two additional velocity corrections were introduced.

Figures B-78 through B-89 illustrate graphically the behavior of the error in the estimate and the actual deviation statistics for ground tracking (TM19), and Figures B-90 and B-91 illustrate the behavior for the horizon sensor (TM24). It should be observed that the initial covariance affected the results only in the first part of the trajectory — up to about the first velocity correction. Subsequently, its effects were negligible.

In a previous study (Reference 1) that employed only a statistical analysis (which assumed that the linear system described exactly the perturbations), it was found that the initial covariance appreciably affected the filter response only in the initial phase of the trajectory. The terminal accuracies were hardly affected. In order to establish whether these conclusions are also valid in a complete Monte Carlo simulation, this study was performed. From the limited scope of this study it can be concluded that the initial covariance matrix does not affect the terminal accuracies attainable with a particular system configuration. However, with larger initial covariances a larger control effort has to be exerted. It should also be kept in mind that too large an initial

MISSION PROFILE	SYSTEM CONFIGURATION	INITIAL COVARIANCE MATRIX SEE TABLE 5-5	GUIDANCE INFORMATION				NAVIGATION INFORMATION	TERMINAL CONDITIONS								COMMENTS
			TOTAL ΔV (m/sec)	NO. OF ΔV's	GUIDANCE LAW	ERROR BUDGET	COMMENTARY ON AIDING INSTRUMENT ERROR BUDGET	RSS (σ) (km)	√TRP1 (km)	RSS (m/sec)	√TRP4 (m/sec)	RSS (σ) (km)	√TRM1 (km)	RSS (σ) (m/sec)	√TRM4 (m/sec)	
Martian Flyby VII.2 Mars — Earth Leg	TM19	M9	9.0	4	3	G10	S.O.A. Ground Tracking, No Instrument Bias	0.07	0.05	0.09	0.04	5.2	4.7	2.9	3.8	Initial Covariance Matrix is Spherically Distributed with Each Position Component 250 m, and Each Velocity Component 0.7 m/sec.
	TM19	M10	12.0	4	3	G10	S.O.A. Ground Tracking, No Instrument Bias	0.08	0.06	0.08	0.06	3.3	10.6	7.3	9.4	Initial Covariance Matrix is Spherically Distributed with Each Position Component 4.2 km and Each Velocity Component 1.6 m/sec.
	TM19	M11	31.5	6	3	G10	S.O.A. Ground Tracking, No Instrument Bias	0.70	0.06	0.51	0.06	11.7	7.4	10.8	5.9	Initial Covariance Matrix is Spherically Distributed with Each Position Component 10 km and Each Velocity Component 3.2 m/sec.
	TM24	M9	20.4	4	3	H41	B.S.O.A. Horizon Sensor and Instrument Bias	0.35	0.75	0.28	0.54	11.4	31.2	15.0	28.7	Initial Covariance Matrix is Spherically Distributed with Each Position Component 250 m and Each Velocity Component 0.7 m/sec.
	TM24	M10	16.5	4	3	H41	B.S.O.A. Horizon Sensor and Instrument Bias	0.98	0.74	0.50	0.53	37.0	46.4	14.5	31.5	Initial Covariance Matrix is Spherically Distributed with Each Position Component 4.2 km and Each Velocity Component 1.6 m/sec.

Table 3-10. Performance Parameters

covariance would force the generation of actual deviations in a Monte Carlo simulation which would violate the linearity assumption. Apparently this was not the case in this limited study. Further study in this area might prove fruitful, especially with respect to what should be done in the case where no initial navigation information exists and an infinite initial error covariance is assumed.

3.1.7 CONCLUSIONS AND SUGGESTIONS FOR FUTURE INVESTIGATIONS

From this study the following conclusions can be drawn. State-of-the-art ground tracking (DSIF) accuracies used in this study were sufficient to assure Earth entry in the low- and moderate-speed Earth approach trajectories. In the high-speed Earth approach, the state-of-the-art ground tracking was only marginal. However, if an orbit rectification is assumed at the perifocal passage of the departing planet, state-of-the-art ground tracking gives satisfactory results.

All of the state-of-the-art and most of the beyond-the-state-of-the-art onboard instrumentation accuracies yielded insufficient accuracy to assure an acceptable Earth atmospheric entry at any of the approach speeds (12 to 20 km/sec). Only the following beyond-the-state-of-the-art onboard instrumentation accuracies gave satisfactory results:

- 10 arc-second horizon sensor/planet tracker (H40),
- 10 arc-second space sextant (S40).

For a low-speed Martian approach (6 km/sec), both the state-of-the-art horizon sensor and space sextant gave marginal results for a Mars atmospheric entry. When state-of-the-art ground tracking was combined with the state-of-the-art horizon sensor, the accuracy was well within the Martian reentry corridor for the low-speed approach. In the high-speed Martian approach, however, none of the systems investigated were sufficiently accurate to assure safe entry.

The overall results significantly improved when there were no tracker biases. In the Martian flyby case, elimination of ground tracker biases reduced the total velocity correction requirements from 99 m/sec to 17 m/sec in the first leg and from 24 m/sec to 12 m/sec in the second leg.

Judicious selection of the reference body schedule to be used in the horizon sensor/planet tracker case improves the overall performance and reduces the required control effort.

Rectification (the updating of the nominal trajectory at each observation with the best estimate) significantly extends the range of applicability of linear guidance theory and Kalman filter estimation.

It was determined that for an approach trajectory and some circular trajectories, a catalog of five stars with an unrestricted window would suffice. The results using five stars show a significant improvement over those obtained with one or two stars; however, no appreciable navigational improvement in the terminal errors were obtained when either 10 stars or an "ideal" (infinite) number of stars were used.

Considerable propulsion savings were obtained when variable-time-of-arrival guidance laws were employed with respect to fixed time-of-arrival guidance laws. However, some problems with the variable-time-of-arrival guidance laws will have to be solved before any credence can be given to the results; for example, in the total mission categories, it was discovered that linearity of measurements was violated in the terminal leg of the trajectory.

It was found that for a Mars-Earth trajectory the initial error covariance matrix does not affect the terminal accuracies attainable with a particular system as long as the linearity assumption is not violated. However, as would be expected with larger initial errors, a large control effort has to be exerted.

Further program improvements and investigations associated with the performance assessment of midcourse guidance systems can be carried out along the following lines:

1. Incorporation of double-precision routines in the state transition block, the linear guidance law, and filter computations,

2. Modification of the orbit rectification to include its capability at each observation point,

3. Modification of the velocity correction spacing to include the capability of spacing the corrections as a function of time. Here the spacing techniques developed by D. F. Lawden (Reference 2) and J. Breakwell (Reference 3) could also be incorporated,

4. Further investigation to establish the adequacy of ground tracking (when only range rate is used) in the Venus-to-Mars leg of the swingby trajectory,

5. Further investigation of the high-speed Martian entry problem to establish the conditions under which entry is possible,

6. Incorporation of additional aiding instruments such as radio altimeter and theodolite,

7. Use of universal variables in the solution of two body motion to simplify trajectory calculations and enhance the program capability. It is suggested that the method of Reference 4 yields the most satisfactory results.

3.2 GUIDANCE AND NAVIGATION FOR ATMOSPHERIC ENTRY

3.2.1 OBJECTIVES OF THE INVESTIGATION

The reentry systems investigation has four objectives:

1. Assess the performance of all-inertial and aided-inertial guidance and navigation systems as applied to various reentry mission profiles such as single-pass entry, single-skipout, and atmospheric braking trajectories.

   This was done using two different computer programs.

   - The program for Performance Assessment of Atmospheric Entry Guidance Systems (Volume II, Part 7 of the Interplanetary Guidance System Requirements Study) is used. The actual trajectory of a vehicle through the atmopsphere and also the statistics describing the error in the navigation data are computed. This program uses a Kalman filter for optimal data processing of IMU and/or electromagnetic sensor observations for navigational purposes and Lambda Matrix Control for perturbative guidance. This program is complex and uses modern data processing and guidance techniques for flight through the atmosphere and was developed as a part of the study. Most of the time allocated to the study was devoted to the development and subsequent checkout of the program. As a consequence, there was not time available for a comprehensive performance assessment study and, while valid comparative data is presented, the study should be viewed in the light of a tutorial example indicating how the program may be used to perform the indicated future studies.

   - The program for Performance Assessment of All-Inertial Guidance Systems (Volume II, Part 4 of Interplanetary Guidance Systems Requirements Study), is used to make trade-off studies of inertial guidance systems for reentry trajectories at Earth and Mars. The program calculates the statistics of the navigation function as a function of the statistics of the inertial measurement system components. The program does not calculate a trajectory and a control function as does the program of 1a. A representative selection of reference trajectories, inertial guidance systems, and optical or electromagnetic aiding instruments was made and trade-off studies performed. These studies are intended to provide a measure of the relative effects of trajectory, guidance system, and guidance system statistics upon the navigation system performance.

2. Evaluate the reentry performance assessment program described in 1a above.

   As a consequence of the experience gained during the operation of the program during the performance assessment studies, certain minor changes to the computer program are suggested to improve its capabilities.

3. Perform feasibility study of improving the knowledge of a distant planet's atmosphere by using data obtained from a navigation system traveling through the atmosphere.

4. Define and study atmospheric reentry corridors and the effect of different nominal control philosophies and vehicular constraints upon the width of these corridors.

   The program, Nominal Atmospheric Entry Trajectories Version II, (Volume II, Part 6 of the Interplanetary Guidance System Requirements Study) was used. The study results are reported in Appendix B.

3.2.2 ATMOSPHERIC ENTRY GUIDANCE AND NAVIGATION PRIOR TO LANDING

3.2.2.1 Atmospheric Entry at Earth

3.2.2.1.1 All-Inertial Guidance System Studies. The studies reported in this paragraph are statistical and use the simulation program, Performance Assessment of All-Inertial Systems, (Interplanetary Guidance System Requirements Study, Volume II, Part 4). The navigation statistics for free-fall portions of skipout reentry trajectories, in which horizon scanners or ground trackers are used are obtained using the program described in Volume II, Part 2 of the Interplanetary Guidance System Requirements Study.

3.2.2.1.1.1 Description of Inertial Guidance Systems. Both strapdown and gimballed inertial measurements units were selected for evaluation of reentry trajectories. Two gimballed systems are modeled. One system is representative of current Apollo-class inertial measurements units and the other system has improved instrument accuracies but still within near-future state-of-the-art capabilities. The error budgets for the two gimballed systems designated Budget A and Budget B, are shown in Table B-16, Appendix B, Section II.

Two strapdown systems were modeled, one with rate gyros the other with rate-integral gyros (RIG). These RIG gyros are characteristized by single-axis stabilized mounting which stabilizes the input axis with respect to rotations about the input axis. The rate gyro system is considered to be representative of current strapdown inertial measurement units. The system with RIG gyros is categorized as a near-future state-of-the-art unit. Error budgets for the strapdown systems are enumerated in Table B-17, Section II of Appendix B.

The error budget magnitudes are somewhat arbitrary and do not, except for gimballed system A, have any reference to particular existing systems. The values selected are considered to be representative values in order that the numerical data generated by the study have application to current and future design studies.

The initial orientation of the sensitive axes triad, for both gyros and accelerometers, is taken along the initial pitch, yaw, and roll body axes of the reentry vehicles. The roll axis is aligned along the initial velocity vector and the pitch and yaw axes are 45 degrees above the local horizontal at the initial reentry point.

For the skipout trajectories, navigation accuracy can be improved by the employment of some form of electromagnetic sensor, or tracking information during the skip phase. All inertial, ground tracking and three horizon scanners with 1σ accuracies in angle of 0.005 degree, 0.01 degree, and 0.05 degree were evaluated for the free-fall portions of such trajectories (Table B-21). A total of 19 distinct guidance systems were evaluated; corresponding to various combinations of the inertial systems alone or in combination with the 4 free-flight navigation devices.

3.2.2.1.1.2 Reentry Reference Trajectories. Four reentry reference trajectories were selected to provide a comparison of the effect of trajectory type and reentry vehicle control on the performance of the inertial navigation system. The trajectory parameters are given in detail in Table B-18.

All four reentry trajectories have the same initial reentry conditions of velocity, position, and attitude. The reentry vehicle parameters were those of the Apollo reentry vehicle for all trajectories. The guidance and control parameters were varied to obtain four very different trajectories.

1. Trajectory 10A: single-pass, direct reentry with pitch modulation controls.
2. Trajectory 10B: single-pass, direct reentry without pitch modulation control.
3. Trajectory 11A: single-skipout trajectory with pitch modulation control, free-fall central angle of 280 degrees.
4. Trajectory 11B: single-skipout trajectory with pitch modulation control, free-fall central angle of 80 degrees.

The trajectories were terminated when the vehicle speed was reduced to 304.8 m/sec.

3.2.2.1.1.3 Performance Assessment Results. Realistic initial conditions, defined by ground tracker navigation during the free-fall trajectory prior to reentry, are defined statistically by a 1σ covariance matrix of position and velocity uncertainties. This matrix, P_{nom}, is described by the 1σ position and velocity error ellipsoid parameters of Table 3-11.

The guidance systems studied are tabulated in Table 3-12. All-inertial guidance systems were evaluated twice, once with the initial navigational error assumed to be zero, and once with the initial error represented by P_{nom}. This is to separate the navigation error due to the inertial measurement unit from that due to the initial conditions. The performance indices selected were the maximum semi-axis of the position and velocity 1σ error ellipsoids at the terminal point of the trajectory. These two parameters are magnitudes and have no significance as to any critical direction of velocity or position error. The simulation output does contain a complete description of such properties, but its inclusion here would distract from the studies intent to demonstrate relative performance. Table 3-13 gives the tabulation of performance indices as a function of trajectory, guidance system,and initial conditions.

3.2.2.1.2 Inertial Systems with Realignment Capability. Improvement of navigation accuracy for all-inertial navigation systems is obtained if periodic realignment of the platform inertial coordinates is made. The reentry at earth occurs at the end of an interplanetary mission, and knowledge of the inertial instrument parameters is certainly significantly degraded.

Therefore, an investigation to determine the amount of the improvement provided by periodic realignment of the platform inertial coordinate system by optical observations (for example, two-star sightings), assuming such observations were possible, was undertaken.

3.2.2.1.2.1 Definition of Study Parameters. Two reference trajectories were employed; namely, direct entry with pitch modulation control, trajectory 10A, and a single-skipout (280 degrees central angle) entry trajectory, 11A. A strapdown IMU, employing rate integral gyros (RIG), defined in Paragraph 3.2.2.1.1.1 was selected.

The navigation model utilized the realignment information in a simple direct fashion in that only accelerations sensed subsequent to a realignment were sensed in the realigned, but still drifting platform coordinates. No correction was applied to previously gathered information. The realignment 1σ accuracy was 30 arc-seconds about each of the three axes.

The realignment schedule was varied by changing the number of realignments made during the reentry trajectory. One to five realignments were made in the direct reentry trajectory; one to eight realignments were made in the reentry portions of the single-skipout trajectory. The realignments were made on regular 90-second intervals following reentry: (1) one realignment at 90 seconds after reentry, (2) two realignments at 90 and 180 seconds after reentry, and so on.

	Principle Axes Magnitude	Direction Cosines		
		N_x	N_y	N_z
Position (km)	3.4357610	-.41488146	.90593878	.084547052
	1.7222726	.90487565	.40108867	.14257569
	1.0377096	-.095253982	-.13565658	.98616626
Velocity (m/sec)	3.1596481	-.25163381	-.14260361	.95725888
	1.1421311	-.75209684	.65131757	-.10067576
	0.72261197	.60912284	.74528482	.27114527

Table 3-11. Characterization of Initial Errors for First Atmospheric Reentry at Earth (P_{nom})

	Navigation System Index																		
	1	2	3	4	7	8	9	10	11	12	13	14	15	16	17	18	19	20	21
Class 1 Systems																			
Gimballed IMU																			
Budget A	x				x	x	x	x											
Budget B		x							x	x	x	x							
Strapdown IMU																			
Rate Gyro System			x														x	x	x
RIG Gyro System				x									x	x	x	x			
EMS																			
Horizon Sensor																			
$\sigma_\theta = .05^o$					x				x				x				x		
$\sigma_\theta = .01^o$						x				x				x				x	
$\sigma_\theta = .005^o$							x				x				x				
Ground Tracker								x				x				x			x

4686

Table 3-12. Definition of Guidance Systems for Performance Assessment Studies on Reentry Trajectories

Mission Phase	Navigation System Index	P_o	Maximum Semi Axis of Terminal Error Ellipsoid	
			Position (km)	Velocity (m/sec)
10A	1	0	1.70	8.37
	1	P_{nom}	4.02	8.73
	2	0	1.16	5.49
	2	P_{nom}	3.99	6.05
	3	0	71.75	454.08
	3	P_{nom}	71.77	454.08
	4	0	1.51	7.05
	4	P_{nom}	3.99	7.50
10B	1	0	2.95	8.39
	1	P_{nom}	4.66	8.68
	2	0	2.06	5.71
	2	P_{nom}	4.60	6.19
	3	0	243.76	932.95
	3	P_{nom}	243.77	932.95
	4	0	3.49	10.17
	4	P_{nom}	4.67	10.36
11A	1	0	26.82	23.33
	1	P_{nom}	49.42	42.58
	2	0	22.75	19.74
	2	P_{nom}	47.34	40.72
	3	0	106.52	446.62
	3	P_{nom}	106.53	446.63
	4	0	27.59	23.67
	4	P_{nom}	49.81	42.77
	7	P_{nom}	7.23	6.69
	8	P_{nom}	3.82	4.61
	9	P_{nom}	1.21	4.15
	10	P_{nom}	1.01	4.13
	11	P_{nom}	7.19	6.34
	12	P_{nom}	3.80	3.88
	13	P_{nom}	1.13	3.21
	14	P_{nom}	.81	3.07
	15	P_{nom}	7.66	6.76
	16	P_{nom}	4.70	4.39
	17	P_{nom}	1.70	3.62
	18	P_{nom}	.89	3.39
11B	1	0	6.22	6.30
	1	P_{nom}	10.73	10.36
	2	0	5.00	4.97
	2	P_{nom}	10.06	9.66
	3	0	64.76	234.83
	3	P_{nom}	65.12	234.84
	4	0	5.24	5.31
	4	P_{nom}	10.35	10.04
	7	P_{nom}	1.72	4.07
	8	P_{nom}	.68	3.92
	10	P_{nom}	.52	3.91
	11	P_{nom}	1.62	2.87
	12	P_{nom}	.61	2.65
	14	P_{nom}	.41	2.63
	15	P_{nom}	1.70	2.65
	16	P_{nom}	.60	2.31
	18	P_{nom}	.42	2.31
	19	P_{nom}	27.74	234.76
	20	P_{nom}	27.67	234.76
	21	P_{nom}	27.67	234.76

Table 3-13. Summary of Guidance System Performance Assessment Studies for Earth Reentry Trajectories

As for all-inertial reentry studies, the platform is initially aligned before each atmospheric reentry phase.

Initial position and velocity errors are included at the first reentry point and are propagated to the terminal point of the trajectory. The inertial system errors add to these initial errors during reentry portions of the trajectories. During the free-fall portion of the single-skipout trajectory, the inertial sensors output is not used.

3.2.2.1.2.2 Study Results. The entire inertial instrument error budget for the RIG strapdown IMU system was degraded by factors of 3 and 10 to simulate IMU degradation for the direct reentry trajectory 10A.

The performance index is the maximum dimension of the position or velocity error ellipsoid at the terminal point of the trajectory, which is defined as the point when the speed is 304.8 meters per second and altitude is about 20 kilometers.

The study results are summarized in Figure B-92 for the direct reentry trajectory, and Figure B-93 for the single-skipout trajectory.

For the direct entry trajectory, 10A, the successive alignments reduce the terminal error for a 10× degraded budget, from an unacceptable 14 kilometers (1σ) to an acceptable 5 kilometers (1σ). Periodic realignment does reduce the terminal error for the single skipout trajectory, 11A, from 27 kilometers (1σ) to 18 kilometers (1σ), but this is inadequate because the nominal altitude is 20 kilometers at this point.

This realignment technique provides sufficient improvement only for extremely degraded IMU's (10× budget), on direct entry trajectories. Aided free-fall navigation is still required for single-skipout trajectories. It is concluded that this technique does not offer enough correction capability to warrant further study.

3.2.2.1.3 Navigation with Electromagnetic Sensors. Although the feasibility of employing electromagnetic sensors in the atmosphere entry environment has not been completely established, a study of the navigational performance attainable with such devices, assuming they can be made to work, was conducted. The trajectory and the guidance system configuration are defined in Tables B-19, B-20, and 3-14.

The injection conditions for the nominal trajectory are the terminal conditions for the earth approach trajectory designated VI.3.3 in Table B-12. These conditions were used, along with vehicle, environmental, and nominal control in the simulation called Nominal Atmospheric Entry Trajectories — Version II described in Volume II, Part 6 of this report, to obtain a nominal trajectory which could be used for the performance assessment of guidance and navigation systems. The same input was used to generate

the nominal trajectory tape with the performance assessment program. Performance Assessment of Atmospheric Entry Guidance Systems described in Volume II, Part 7 of this report. The results for six different simulation cases are summarized in Table 3-14.

The specific definitions of the system configurations for each of these cases are given in Appendix B. Time histories of navigation performance parameters for some of the results summarized in Table 3-14 are also shown in graphical form in Appendix B, Section II.

Two conclusions may be made from observation of Table 3-14.

1. Most accurate performance,in terms of deviation of the state from the nominal trajectory and in terms of error in the estimate,is accomplished by the system with the most accurate instruments as seen by comparing runs 3001, 3002, and 3003 — Table 3-14.
2. The addition of control noise significantly degrades performance as seen by comparing runs 3002 and 3006, Table 14.

Areas for possible future investigation in the single-pass atmospheric entry mission class are listed below.

1. Use of irregular schedules for electromagnetic sensor observations to account for possible problems associated with ionization and resultant sensor dropout.
2. Use of IMU during entry.
3. Single-pass entry at other planets at variety of injection speeds.
4. Effect of initial uncertainty of state on performance.
5. Different combinations of electromagnetic sensors and error budget.
6. Additional studies using uncertainties in both atmospheric and aerodynamic coefficients.

3.2.2.2 Atmospheric Entry at Mars

A statistical performance assessment study was made using the atmospheric and gravitational properties of Mars. The same Apollo vehicle and guidance and control systems were used as for the Earth entry. The Martian atmosphere density can be accurately approximated by an exponential function of altitude, as can Earth's atmospheric density. The relative performance capabilities of the inertial measurement units is expected to be the same. The studies used the same statistical simulation as used for the studies of Paragraph 3.2.2.1.1.

Mission	Identification	Error in Estimate ($\tilde{x}$) and Statistics (σ_x)				Deviation from Nominal Trajectory		Maximum Control	
		Position		Velocity				Pitch	Roll
		$\Delta\tilde{R}$ (km)	σ_R (km)	$\Delta\tilde{V}$ (m/sec)	σ_V (m/sec)	ΔR (km)	ΔV (m/sec)	$\delta\alpha$ (rad)	$\delta\rho$ (rad)
Manned Earth Single Pass Entry	3001	.32	0.14×10^{-4}	1.2	0.11×10^{-4}	1.3	.44	.15	.15
	3002	1.5	.85	.78	1.4	1.7	1.8	.16	.16
	3003	.61	.20	.13	.26	1.5	1.4	.16	.17
	3004, 3005	These runs terminate prematurely (t = 156 sec)							
	3006	2.1	.89	1.8	1.2	2.8	2.1	.17	.17

Note: ΔR = magnitude of terminal position perturbation.
ΔV = magnitude of terminal velocity perturbation.
$\Delta\tilde{R} = \Delta R$ — best estimate of ΔR
$\Delta\tilde{V} = \Delta V$ — best estimate of ΔV

Table 3-14. Trade-Off Results for Guidance and Navigation Performance Assessment of Navigation with Electromagnetic Sensors Only on the Manned Earth Single Pass Entry Trajectory

3.2.2.2.1 Definition of Study Parameters. A direct entry trajectory was selected with initial speed of 5,690 meters per second at 125 kilometers altitude with an entry angle of 0.234 radians below the local horizontal. These initial conditions are taken from a capture mission to Mars (II.1.3). The trajectory was terminated at a speed of 304.8 meters per second. The Mars atmospheric model was the Mars II model. Trajectory duration was 533 seconds.

Maximum acceleration level was 51 meters per second^2 and maximum angular rates were 0.69213 radians per second. Pitch modulation control was used, set to maintain a 5 g aerodynamic acceleration. The plane control parameter, ϵ_s was 10^{-4}.

The same four guidance systems and budgets used in the performance assessment studies for Earth atmospheric entry, Paragraph 3.2.2.1.1, are used for the Mars entry trajectory.

The initial covariance matrix of velocity and position errors, P_{nom}, is characterized by 1σ position error ellipsoid semi-axes of 1.5, 0.7, and 0.1 kilometer and 1σ velocity error ellipsoid semi-axes of 2.3, 2.3, and 0.004 meters per second. These initial errors are principally in the plane of the incoming trajectory.

3.2.2.2.2. Study Results. Table 3-15 shows the position and velocity performance indices for the four guidance systems evaluated with P_0 set to either P_{nom} or to zero. The results show that both gimballed systems and the RIG strapdown system give the same navigational accuracy. The cases where $P_0 = 0$ indicate that guidance system errors are about half of the corresponding values for direct entry at Earth. This is consistent with the observation that the net velocity loss in the Mars trajectory is about half of the velocity loss during the Earth entry trajectories reported in Paragraph 3.2.2.1.

3.2.3 GUIDANCE AND NAVIGATION DURING ATMOSPHERIC BRAKING

Atmospheric braking in this report is defined as the maneuver consisting of the entry, path through, and subsequent departure from the atmosphere with the intent of modifying (by aerodynamic means only) the direction and magnitude of the exit velocity vector with respect to the value it would have had if the atmosphere had not been present. It is a form of the flyby trajectory which may be used effectively to reduce the entry speed at earth during the final phase of an interplanetary mission. The nominal trajectory and vehicle is described by the data in Appendix B, Table B-25. The nominal injection conditions are obtained from Table B-12 under the heading of Fast Martian Approach.

Guidance System	P_o	Maximum Semi Axis Magnitude of 1σ Error Ellipsoid	
		Position (km)	Velocity (m/sec)
Gimballed Budget A	0	.63	2.14
	P_{nom}	2.04	3.14
Gimballed Budget B	0	.57	1.96
	P_{nom}	2.02	3.02
Strapdown RIG Gyros	0	.52	1.83
	P_{nom}	2.00	2.93
Strapdown Rate Gyros	0	120.61	463.53
	P_{nom}	120.61	463.53

Table 3-15. Performance Assessment Results for Direct Reentry at Mars

The results of the preliminary study indicate that the maneuver is feasible and that more detailed studies are required. These further studies are outlined in the performance assessment section which is presented below along with linearity studies.

3.2.3.1 Range of Linearity

Since both the guidance and navigation are based on linear theory and because the dynamical system is nonlinear, it is pertinent to consider the range over which the linear approximations are valid. This was accomplished by perturbing the parameters listed in Table 3-17 from nominal values by at least two values and comparing the terminal state deviations from the nominal trajectory. The nonguided version of the atmospheric braking trajectory is particularly well suited for this type of analysis since the nominal control during this maneuver is open loop (not a function of the state of the vehicle). This is in contrast to performing the analysis during a single-pass entry in which case the vehicle is required to maintain constant altitude for a time. The nominal control system then generates guidance commands as a function of the radial speed of the vehicle which obscures the determination of terminal deviations as a function of initial perturbations.

The data in Table 3-17 indicates that fairly large deviations in initial position, velocity, aerodynamic and atmospheric coefficients are possible without exceeding the linear range; that is, when the parameter is varied by a factor of x, the terminal deviation is also varied by the same factor. The perturbative control does not fall into this category as indicated by the data, and perturbative control magnitudes of 10

Mission	Identification	Error in Estimate ($\tilde{x}$) and Statistics (σ_x)				Deviation from Nominal Trajectory		Maximum Control	
		Position		Velocity				Pitch	Roll
		$\Delta\tilde{R}$ (km)	σ_R (km)	$\Delta\tilde{V}$ (m/sec)	σ_V (m/sec)	ΔR (km)	ΔV (m/sec)	$\delta\alpha$ (rad)	$\delta\rho$ (rad)
Manned Atmospheric Braking at Mars	511					$.34\times10^{-1}$	$.25\times10^{-2}$	0	0
	540	$.61\times10^{-1}$	$.25\times10^{-2}$	.57	$.12\times10^{-1}$	$.18\times10^{-1}$	$.38\times10^{-1}$	$.4\times10^{-1}$	$.53\times10^{-2}$
	546	.36	$.25\times10^{-2}$	$.88\times10^{-1}$	$.12\times10^{-1}$	.91	$.86\times10^{-1}$	-.44	-.11
	534	.14	$.25\times10^{-2}$	$.23\times10^{-1}$	$.12\times10^{-1}$	$.14\times10^{-1}$	$.11\times10^{-2}$	-.27	-.07
	550	.49	$.25\times10^{-2}$	$.58\times10^{-1}$	$.12\times10^{-1}$	$.12\times10^{-1}$	$.96\times10^{-1}$	.24	-.31
	600	.97	$.33\times10^{-1}$	$.21\times10^{-2}$	.38	.66	$.18\times10^{-2}$	-.38	$-.9\times10^{-1}$
	601	.90	$.33\times10^{-1}$	$.21\times10^{-2}$	.42	.64	$.19\times10^{-2}$	-.36	$-.9\times10^{-1}$
	602	$.11\times10^{-1}$	$.42\times10^{-1}$	$.26\times10^{-2}$	.97	.59	$.29\times10^{-2}$	-.32	.14
	603	$.15\times10^{-1}$	$.44\times10^{-1}$	$.32\times10^{-2}$	$.11\times10^{-1}$	.93	$.37\times10^{-2}$	-.22	-.29
	604	.39	.77	$.50\times10^{-1}$	$.41\times10^{-1}$	$.18\times10^{-1}$	$.11\times10^{-2}$	.42	-.15
	605	.39	.77	$.50\times10^{-1}$	$.41\times10^{-1}$	$.18\times10^{-1}$	$.11\times10^{-2}$	.42	-.15
	606	.31	.78	$.84\times10^{-1}$	$.53\times10^{-1}$	$.17\times10^{-1}$	$.93\times10^{-1}$	.62	-.18
	607	$.91\times10^{-1}$	.84	$.13\times10^{-2}$	$.73\times10^{-1}$	$.16\times10^{-1}$	$.72\times10^{-1}$	.8	-.25
	608	$.14\times10^{-1}$	.40	$.86\times10^{-1}$	$.27\times10^{-1}$	$.28\times10^{-1}$	$.19\times10^{-2}$	.21	-.18

Note: ΔR = magnitude of terminal position perturbation.
ΔV = magnitude of terminal velocity perturbation.

Table 3-16. Trade-off Results for Guidance and Navigation Performance Assessment Studies on the Martian Atmospheric Braking Trajectory

Identification	Initial Perturbation from Nominal		Aerodynamic Perturbation	Atmospheric Perturbation	Control Perturbation (rad)	Terminal Deviation from Nominal		Range of Linearity
	Position (km)	Velocity (m/sec)				Position (km)	Velocity (m/sec)	
509	.0173	.0173				.0333	.28	excellent
510	.173	.173				.339	2.8	
511	1.73	1.73				3.40	29.	
512	17.3	17.3				34.81	300.	
514					$\delta\varphi = .08725$	.11	2.	poor
526					$\delta\varphi = .1745$	.435	8.	
515					$\delta\alpha = .08725$	4.82	127.	fair
527					$\delta\alpha = .1745$	14.1	242.	
516				$\delta\rho_o = .1\,\rho_o$		4.24	60.	good
517				$\delta\rho_o = .005\,\rho_o$		.22	3.6	
518				$\delta\beta' = .1\,\beta'$		20.1	300.	
519				$\delta\beta' = .005\,\beta'$		1.0	18.	
520			$\delta C_i = .1\,C_i$			5.01	78.	good
521			$\delta C_i = .2\,C_i$			9.85	153.	
			$i = D_o$, N					

Table 3-17. Results of Studies Indicating the Range of Linearity for Various Parameters for the Martian Atmospheric Braking Trajectory

degrees are large with respect to maintaining a linear relationship. The latter fact has implications for the choice of the guidance law matrices used since they must be defined so that the perturbative control does not exceed 10 degrees or the navigation suffers.

3.2.3.2 Performance Assessment Results for Atmospheric Braking Maneuver at Mars

The results of the performance assessment for the atmospheric braking maneuver are summarized in Table 3-16. The data defining the guidance (lambda matrix) parameters employed and the navigation system configurations is specified in Appendix B, Table B-26. The systems employed ground tracker, radio altimeter and horizon scanner navigation.

The first case in Table 3-16 (case numbered 511) represents no guidance or navigation so that comparing the results of the various other cases with it indicates the performance improvement possible by closed loop guidance during the maneuver.

Time histories of performance parameters for some of the results summarized in Table 3-16 are contained in Appendix B, Paragraph 2.2

3.2.4 EXPLORATION OF PLANETARY ATMOSPHERES

In order to make an atmospheric entry at a planet, it is essential to have an accurate knowledge of the atmosphere of that planet. This is clearly demonstrated by the entry corridors shown in Appendix B, Figure B-138 through B-140 .for the different versions of the Martian atmosphere which indicate that there is little overlap of the reentry corridors at injection speeds in excess of parabolic, that is, 1.4 times circular speed.

Since the uncertainty in our knowledge of the atmosphere is large enough to make all three of these Martian atmospheric models feasible, only two courses are open in order to assure atmospheric entry. The first consists of entry at low speed with the injection flight path angle in the overlap region. This may not be feasible from a fuel consumption standpoint. This leaves only the second possibility; improve the knowledge of the atmosphere of the entry planet.

A number of approaches to the solution of the problem of obtaining this information is available including the injection of an unmanned vehicle into the planet's atmosphere. It would transmit observations after landing to the "mother ship" which could process the data or transmit the data back to earth for processing. Another approach would consist of making observations during or after passage through the fringes of the atmosphere as in atmospheric braking.

In either approach some form of barometric or dynamic pressure measurements would be made, but these could be supplemented by the use of observations made with electromagnetic sensors or an IMU such as described in this report, followed by the processing of this data using the equations programmed in the navigation block of the reentry guidance and navigation performance assessment program.

3.2.4.1 Description of Trade-Off Study Parameters and Techniques

The data presented in this section is the result of a study using the observations made with electromagnetic sensors and/or an IMU to obtain an estimate of the augmented state vector (position, velocity aerodynamic, and atmospheric coefficients). Two trajectories are considered. (See Table B-27, Appendix B.) These are:

1. 10 g unmanned Martian single-pass entry at low injection speed. This trajectory would result from a deboost from a circular parking orbit around Mars. The deboost phase was not one of the missions studied so detailed information about the uncertainty in the estimate of position and velocity is not available, but it is clear that the uncertainty must be very small due to the possibility of extensive navigation while in the parking orbit and during the low-speed approach to the injection point.

2. The atmospheric braking trajectory which uses the terminal conditions of the interplanetary mission identified by number III. 1.3 in Table 3-3 as reentry injection conditions. The uncertainty in these terminal conditions is also defined in Table 3-3 for various system configurations.

Trade-off studies were conducted using the various system configurations defined in Table B-28. The results of the study are tabulated in Table B-29. For all of the runs, the error in the estimate of the magnitude of the position deviation, $\Delta\tilde{R}$ = root sum square of the error in the estimate of position components is tabulated, followed by the standard deviation, σR, of that quantity. Similarly, $\Delta\tilde{V}$, the root sum square of the error in the estimate of the velocity components, and its standard deviation, σV is tabulated. Since these are unguided flights, the maximum value of the nominal control is zero. With respect to estimation on the aerodynamic and atmospheric coefficients, the runs are divided into three categories.

1. Estimation is made only on aerodynamic coefficients.

2. Estimation is made only on atmospheric coefficients.

3. Estimation is made on both aerodynamic and atmospheric coefficients simultaneously.

Blanks appearing in Table B-29 imply that no estimation was attempted. No estimation was made on the lift coefficient C_N in the 10g unmanned trajectory since a non-lifting vehicle was used.

Two models of the atmospheric uncertainty were simulated. In the first, an uncertainty in the sea-level density, $\delta\rho_o$, was assumed so that the density, ρ, was described by the following equation

$$\rho = (\rho_o + \delta\rho_o)e^{-\beta' h}$$

where β' is the atmospheric decay factor and h is the altitude. In this formulation, $\delta\rho_o$ is a constant random variable and the state of the vehicle is augmented by the addition of this quantity. In the second,formulation density was given by the equation

$$\rho = \rho_o e^{-\beta' h} + \delta\rho$$

where $\delta\rho$ is the uncertainty in the atmospheric density and is correlated in altitude. Under these circumstances, the state is augmented by the addition of a variable, $\delta\rho$. Runs 416, 420, and 423 were made with this formulation. The error in the estimate is much smaller than with the $\delta\rho_o$ formulation but this does not imply superior performance since the density is smaller (i.e., density at terminal point of a braking trajectory is small compared to sea-level density). Estimation on sea-level density has the advantage of including directly in the estimation process a constant which is used in the mathematical model describing the atmosphere. It has the disadvantage, however, of having uncertainties in this quantity indistinguishable, in a dynamical sense, from uncertainties in the aerodynamic coefficients, unless pitch modulation is used for nominal control. This can be shown easily by writing the perturbation in force dF (directly proportional to acceleration perturbation) as a function of the perturbation in aerodynamic coefficients, dC, and sea-level atmospheric coefficients, $d\rho_o$, as follows:

$$F = C\rho_o e^{-\beta' h} V^2 S/2$$

$$dF = F\left(\frac{dC}{C} + \frac{d\rho_o}{\rho_o}\right)$$

where

C = aerodynamic coefficient

V = speed

S = area

The dynamical effect due to the quantities in the parenthesis cannot be separated if both C and ρ_0 are constant. If estimation on both of these is desired simultaneously, it is necessary to make one of them a variable. C is a variable if pitch modulation is used; i.e., modifying the angle of attack as a part of the nominal control philosophy (see description in Paragraph 3.2.5) since C is a function of the angle of attack.

If the second formulation of atmospheric density is used, the observability problem does not exist since $d\rho_0/\rho_0$ in the equation above is replaced by $d\rho/\rho$, which is varible. However, this formulation estimates the deviation from the nominal atmosphere at the current altitude which is not as useful in specifying the true atmospheric model as an estimation on constants used in the formula for that model. Only runs 416, 420, and 423 in Table B-29 have this second formulation.

3.2.4.2 Description of Results

The data resulting from computer runs used in the study of atmospheric exploration with the guidance and navigation performance assessment program is presented in Table B-29. In the runs, in which estimation was made on $\delta\rho_0$ and the aerodynamic coefficients, the ratio of the statistics describing the uncertainty in these quantities is the same at the terminal point as at the initial point, although the magnitude is less at the terminal point. This is a consequence of the fact that the perturbation due to the combined effect of these can be measured. Since the Kalman filter cannot attribute the effect to one or the other of the coefficients, it uses the initial statistics to decide the amount of uncertainty associated with each quantity.

The highlights of the data in Table B-29 are listed in the following paragraphs.

1. 10 g unmanned entry. The purpose of this series of runs is to compare the effectiveness of an IMU with the radio altimeter for three different values of initial position and velocity perturbations. The estimation on the atmospheric and aerodynamic coefficients is as described in the preceding paragraph. The statistics describing the uncertainty in the magnitude of the position deviation, σR, are comparable for both instruments, but the uncertainty in the magnitude of the velocity deviation is less when the IMU is used. This is expected since the IMU measures the integral of nongravitational acceleration.

2. Estimation during atmospheric braking - Part I

a. Initial state uncertainty and covariance. The use of state-of-art horizon sensor and ground trackers during planetary approach results in an uncertainty of 6.3 kilometers in position and 3.6 meters per second in velocity (Table 3-3, Mission III.1.3) at the entry sphere. Runs 448 and 449, which have initial uncertainties of this order are compared with runs 445 and 446, which have considerably smaller uncertainties. It is seen that the uncertainty in terminal position and velocity is strongly affected by initial conditions, but that the uncertainty in terminal atmospheric and aerodynamic coefficients is relatively insensitive to these quantities.

b. Choice of aiding instrument. An evaluation of the relative effectiveness of a particular aiding instrument can be made by comparing the statistics of the following runs.

Run Number	Instrument	Effectiveness
427, 428	IMU	Most accurate for position and velocity. Not quite as good as radio altimeter for aerodynamic coefficients.
433, 434	Horizon Sensor	Least accurate in all respects.
436, 437	Radio Altimeter	Comparable in position but inferior in velocity to IMU.
439, 440	Horizon Sensor and Radio Altimeter	Accurate for aerodynamic and atmospheric coefficients. Slightly better than radio altimeter by itself.

c. Observation time interval. If runs 436 and 437 are compared with runs 445 and 446, it is seen that a change in observation interval from 10 to 5 seconds reduces the statistics describing the error in the estimate by

about 20 percent for the radio altimeter. A comparison of runs 424 and 425 with 439 and 440, and with 445 and 446 gives similar results.

3. Estimation during atmospheric braking—Part II. If the uncertainty in the initial position and velocity is small compared to the sea-level atmospheric density uncertainty (small meaning that the deviation in the terminal position and velocity due to the initial perturbation in these quantities is small compared to the final state perturbation caused by uncertainties in the sea-level atmospheric density), then estimation may be made on the atmospheric and aerodynamic coefficients by making observation after the vehicle has left the atmosphere. The advantage of this approach consists primarily in the fact that electromagnetic sensors may be used without ionization problems associated with these measurements during passage through the atmosphere.

   The two runs tabulated in Part II of Table B-29 reflect this technique. The results are comparable with results obtained by making observations in the atmosphere. Although the observations were made every 20 seconds for over 1,000 seconds, only the first few were required and no further improvement occurred after these were made. As mentioned earlier, pitch modulation during passage through the atmosphere would have been required to separate the effects of the aerodynamic and atmospheric effects.

3.2.4.3 Future Studies

Additional data should be collected to properly evaluate the effectiveness of the procedures described in preceding paragraphs. The following items should be incorporated into the future studies.

1. Include dynamic pressure or barometric measurements in the observations.
2. The atmospheric model should have uncertainties in the sea-level density and the atmospheric decay factor.
3. Pitch modulation should be employed to improve the estimation on simultaneous aerodynamic and atmospheric studies.
4. The observation schedule for electromagnetic sensors should be modified to account for possible problems due to ionization.

3.2.5 ATMOSPHERIC ENTRY CORRIDOR WIDTH STUDIES

The program described in Volume II, Part 6 of the Interplanetary Guidance System Requirements Study was used to determine atmospheric entry corridors at Earth and at Mars. The variation in corridor width due to changes in entry speed, attitude,

entry vehicle, aerodynamics, vehicle control parameters, and atmospheric models was measured. The resulting corridor widths were used to establish standards for free-fall planetary approach trajectories. Data demonstrating the influence of the aforementioned factors is presented graphically in Appendix B, Paragraph 2.2, where the study parameters are tabulated. A total of 26 distinct entry corridor studies were made. Principle results demonstrate the strong effect of initial roll angle upon entry corridor width and the need for a better definition of the Martian atmosphere before manned entry at Mars can be attempted. With the three versions of Martian atmosphere used in these studies, only a 24-milliradian wide corridor is common to the three corridors corresponding to the three atmospheric models at a low (3,962 meters per second) entry speed. At higher speeds, the reentry corridors are disjoint (Figures B-138, B-139, and B-140 in Appendix B) and are narrower than Earth corridors for corresponding entry speeds.

3.2.6 CONCLUSIONS

Results of the atmospheric study are summarized below.

For guidance and navigation during direct atmospheric entry, state-of-the-art gimballed inertial measurement units (like the Apollo IMU) give adequate performance.

For entry trajectories employing skipout phases, navigation using some form of electromagnetic tracking data must be employed during the skip phase.

Providing the capability of realignment of the inertial reference during entry improves the performance somewhat; however, this may be very difficult to implement. The improvement available is not adequate to negate the requirement for electromagnetic tracking data for skipout entry, consequently, this approach does not appear very worthwhile.

The performance assessment programs seemed to function satisfactorily. These revisions are suggested to increase their usefulness even more.

- Include pitch modulation for nominal control. Not only is the entry corridor wider but simultaneous estimation on atmospheric and aerodynamic coefficients is also possible.
- Rewrite the atmospheric model so that uncertainties in sea-level density and the atmospheric decay factor are constant random variables which are added to the augmented state vector.
- Limit the magnitude of the perturbative control to values near the limit of linearity to improve the navigation.

- Reformulate the plant noise model so that noise proportional to the perturbative control vector is used. This will weight observations by the aiding instruments more whenever large perturbative control degrades the navigation.
- Replace the best estimate of the state by the deviation from the nominal trajectory in the guidance block whenever evaluation of the weighting matrices is to be made.

The technique of using navigation systems to determine distant planet atmospheric characteristics as a spacecraft passes through the atmosphere seems feasible, based on this study, and should receive further consideration for future possible missions.

Safe-entry corridor widths are extremely narrow for Mars entry, due mainly to the uncertainties in the Martian atmosphere.

Safe-entry corridor widths are considerably larger for vehicles having both roll and pitch control than for those with roll control only.

3.3 GUIDANCE AND NAVIGATION DURING POWERED FLIGHT

3.3.1 OBJECTIVES OF THE INVESTIGATION

The investigation of the guidance and navigation during powered flight is intended to establish reference performance criteria for the guidance and navigation system during powered flight phases of interplanetary missions. Inertial measurement systems consisting of gyroscopes and accelerometers in either a gimballed or strapdown configuration are required for powered flight navigation and guidance where "instantaneous" navigation data is required for the guidance and control function.

The study results discussed in this section provide data on the performance capability of current and near-future inertial guidance and navigation systems when assessed on a representative set of powered flight phases of the reference mission classes. These results provide practical data for guidance systems and trajectories of current interest.

3.3.1.1 Reference Inertial Guidance Systems

Four reference inertial guidance systems, two strapdown systems and two gimballed systems with error budgets defined in Tables 3-18 and 3-19,were selected for performance assessment studies with the set of six reference boost trajectories given in Table 3-20. The two gimballed systems differ only in the error budget magnitude. The two strapdown systems differ in budget and in the type of gyro; one strapdown system uses a rate gyro that has scale factor and scale factor nonlinearity uncertainties, while the other strapdown system has a rate-integral (RIG) gyro that is servo-stabilized to maintain zero angular rate along its input axis.

Error budget magnitudes are chosen with reference to current and near-future inertial measurement unit accuracies. The more conservative gimballed budget (Budget A) is modeled from current Apollo standards. The other budgets represent engineering estimates of possible representative systems, not modeled after any particular system or instrument.

Table 3-21 defines the inertial guidance systems used in the boost-trajectory performance-assessment studies.

The selected instrument orientation placed the instrument's sensitive axes along the initial orientation of the reference pitch, yaw, and roll axes. The pitch and yaw gyros had their output axes aligned along the initial roll axis to minimize gyro drifts due to mass unbalance.

Error Source	Units	Rate Gyro System	RIG Gyro System
GYROS			
Random Drift			
X-gyro	meru	20	6
Y-gyro	meru	20	6
Z-gyro	meru	20	6
g-Dependent Drifts			
acceleration along input axes			
X-gyro	meru/g	50	10
Y-gyro	meru/g	50	10
Z-gyro	meru/g	50	10
acceleration along spin axes			
X-gyro	meru/g	30	10
Y-gyro	meru/g	30	10
Z-gyro	meru/g	30	10
g^2-Dependent Drifts			
acceleration along input and spin axes			
X-gyro	meru/g^2	20	5
Y-gyro	meru/g^2	20	5
Z-gyro	meru/g^2	20	5
Input Axes Misalignments			
X-gyro input → output	arcsec	20	10
X-gyro input → spin	arcsec	20	10
Y-gyro input → output	arcsec	20	10
Y-gyro input → spin	arcsec	20	10
Z-gyro input → output	arcsec	20	10
Z-gyro input → spin	arcsec	20	10
Scale Factor (rate gyro only)			
X-gyro	10^{-6}	16.6	
Y-gyro	10^{-6}	16.6	
Z-gyro	10^{-6}	16.6	
Non-linearity (rate gyro only)			
X-gyro	10^{-6}/(rad/sec)	2666.6	
Y-gyro	10^{-6}/(rad/sec)	2666.6	
Z-gyro	10^{-6}/(rad/sec)	2666.6	
ACCELEROMETERS			
Bias			
X-accelerometer	μg	300	200
Y-accelerometer	μg	300	200
Z-accelerometer	μg	300	200
Scale Factor			
X-accelerometer	μg/g	210	100
Y-accelerometer	μg/g	210	100
Z-accelerometer	μg/g	210	100
Non-Linearity			
X-accelerometer	μg/g^2	60	10
Y-accelerometer	μg/g^2	60	10
Z-accelerometer	μg/g^2	60	10
Input Axes Misalignment			
X → Y	arcsec	30	18
X → Z	arcsec	30	18
Y → Z	arcsec	30	18
Y → X	arcsec	30	18
Z → X	arcsec	30	18
Z → Y	arcsec	30	18
INITIAL ALIGNMENT			
φ_X	arcsec	30	30
φ_Y	arcsec	30	30
φ_Z	arcsec	30	30

Table 3-18. Strapdown System Error Budget

Error Source	Units	Budget A	Budget B
GYROS			
Random Drift			
X-gyro	meru	5	2.5
Y-gyro	meru	5	3
Z-gyro	meru	5	3
g-Dependent Drifts			
acceleration along input axes			
X-gyro	meru/g	15	10
Y-gyro	meru/g	10	3
Z-gyro	meru/g	15	3
acceleration along spin axes			
X-gyro	meru/g	15	5
Y-gyro	meru/g	10	8
Z-gyro	meru/g	15	8
g^2-Dependent Drift			
acceleration along input and spin axis			
X-gyro	meru/g^2	1	0.5
Y-gyro	meru/g^2	1	0.5
Z-gyro	meru/g^2	1	0.5
ACCELEROMETERS			
Bias			
X-accelerometer	μg	204	200
Y-accelerometer	μg	204	200
Z-accelerometer	μg	204	200
Scale Factor			
X-accelerometer	μg/g	100	50
Y-accelerometer	μg/g	100	50
Z-accelerometer	μg/g	100	50
Non-Linearity			
X-accelerometer	μg/g^2	10	10
Y-accelerometer	μg/g^2	10	10
Z-accelerometer	μg/g^2	10	10
Sensitive Axis Misalignments			
X → Y	arc-sec	41	35
X → Z	arc-sec	41	50
Y → Z	arc-sec	41	15
INITIAL ALIGNMENT			
φ_X	arc-sec	41	41
φ_Y	arc-sec	41	41
φ_Z	arc-sec	41	41

Table 3-19. Gimballed IMU Error Budgets

Nominal Trajectory Description	Mission Phase					
	5A	5B	6	7	8	9
Description	Inject into Mars transfer from 185 km Earth parking orbit	Deboost into 4633 km parking orbit at Mars	Trajectory change at Mars peri-center in fly-by mission	Midcourse correction	Launch from Mars surface into 345 km parking orbit	Deboost prior to atmospheric re-entry at Earth
Environmental Data						
Central Body	Earth	Mars	Mars	Earth	Mars	Earth
Atmosphere Model					Mars II	1962 U S
Highest Harmonic in Gravity Model	4th	0th	0th	4th	0th	4th
Trajectory Data						
Initial Conditions						
R (km)	6560.	11619.	8065.	87926.	3415.	8017.
V (m/sec)	7794.9	3925.3	11195.	5251.1	242.	12934.6
X (km)	1235.	-7235.	7298.	41925.	3415.	-2881.
Y (km)	4150.	-3562.	2699.	46972.	0	-4186.
Z (km)	4928.	-8365.	2120.	61375.	0	6200.
$\dot{X}$ (m/sec)	7639.4	2866.7	2217.1	1694.1	0	10619.2
$\dot{Y}$ (m/sec)	5569.1	-2429.	9756.3	3070.9	242.	3937.4
$\dot{Z}$ (m/sec)	1445.5	1135.7	5023.0	3908.1	0	6247.6
Terminal Conditions						
Time of Flight (sec)	392.	244.6	10.3	4.94	637.3	418.
R (km)	6805.	11594.	8065.	87952.	3757.	6494.
V (m/sec)	11646.3	1924.7	11135.8	5228.7	3382.4	9227.3
X (km)	4583.	-6664.	7275.	41933.	3502.	1094.
Y (km)	3414.	4039.	2800.	46987.	1360.	-5314.
Z (km)	3694.	8584	2069.	61395.	0	3568.
$\dot{X}$ (m/sec)	9976.3	1415.5	2203.7	1669.8	-1232.4	7233.6
$\dot{Y}$ (m/sec)	3297.6	1185.4	9705.2	3061.6	3150.	1049.9
$\dot{Z}$ (m/sec)	5023.4	543.8	4996.0	3895.8	0	5631.6
Inertial Velocity Increment ΔV (m/sec)	3851.4	-2000.5	-59.3	-22.4	31617.	-3707.3
Re-entry Angle γ (rad) (measured at 123 km altitude)	—	—	—	—	—	-.11053
IMU Environmental Data						
Maximum Thrust Acceleration (m/sec^2)	23.93	11.08	5.86	5.81	36.1	26.87
Minimum Thrust Acceleration (m/sec^2)	5.75	5.75	5.75	5.75	9.26	5.75
Maximum Angular Body Rate (rad/sec)	0.00415	.075	.087	0.0	.087	0.001
Propulsion System						
Vacuum Specific Impulse (sec)	312.	312.	312.	312.	{282.8, 309.0}	312.
Mass Rate (kilograms/sec)	-23.263	-23.263	-23.263	-23.263	{-759.73, -147.62}	-23.263

Table 3-20. Description of Boost Trajectories Used in Performance Assessment Studies

Navigation System Description	Mission Phase																							
	5A				5B				6				7				8				9			
Navigation System Index	1	2	3	4	1	2	3	4	1	2	3	4	1	2	3	4	1	2	3	4	1	2	3	4
Class 1 Systems																								
Gimballed IMU																								
Budget A	x				x				x				x				x				x			
Budget B		x				x				x				x				x				x		
Strapdown IMU																								
Rate Gyro System			x				x				x				x				x				x	
RIG Gyro System				x				x				x				x				x				x

Table 3-21. Definition of Inertial Guidance Systems Used in Boost Trajectory Performance Assessment Studies

3.3.1.2 Reference Boost Trajectories

The reference boost trajectory phases were selected from boost phases of interplanetary missions. The boost trajectories are described in detail in Table 3-20. These trajectories, which form a representative array of boost trajectories for interplanetary missions, were generated using the program described in Volume II, Part 3, Nominal Powered Flight Trajectories, wherein a detailed description of the generation of these trajectories is given. The initial and terminal conditions of the boost trajectories are specified by data taken from the interplanetary mission class designated in Table 3-20.

For performance assessment purposes, the output of the trajectory program consists of a time history of nongravitational acceleration, body angular rates and attitudes, and a state transition matrix recorded on magnetic tape for use with the performance assessment simulation.

Boost phases of interplanetary trajectories are, in general, characterized by adding a velocity increment in a constant direction. Except for planetary launches and landings, angular rates during inertial navigation phases are quite small. The acceleration levels are low and vary in an almost linear fashion for small velocity changes. A significant exception is the acceleration profile for the launch from Mars trajectory where thrust levels are higher and propellent mass expended is a significant portion of total missile mass. Figure 3-9 shows trajectory parameters including the acceleration profile for the launch from Mars trajectory.

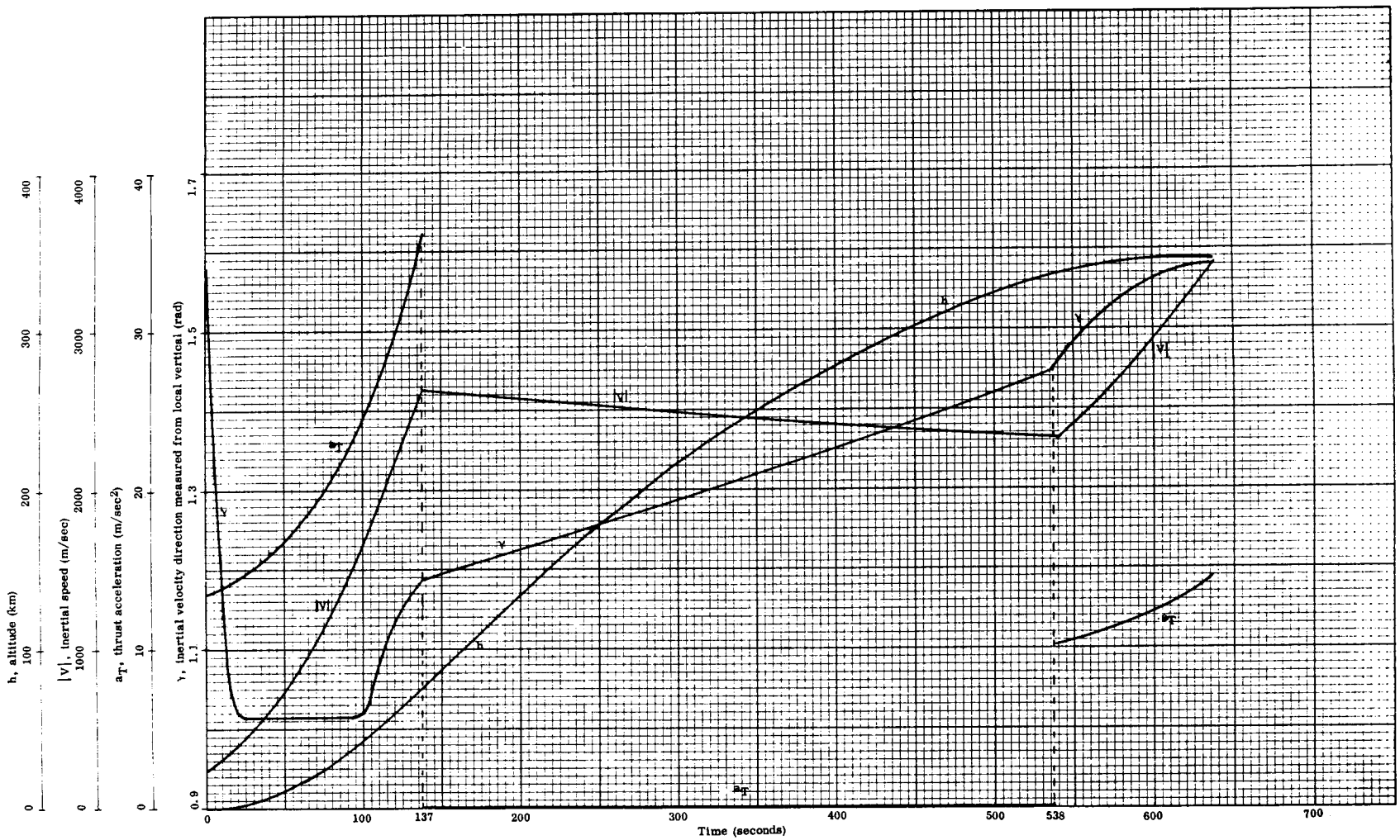

Figure 3-9. Boost Trajectory Characteristics for Launch from Mars Mission (Trajectory Index 8)

3.3.1.3 Performance Assessment

A statistical performance assessment of all-inertial guidance systems is made using the digital program defined in Volume II, Part 4, Performance Assessment of All-Inertial Guidance Systems. This computer program for performance assessment of all-inertial guidance systems is capable of simulating an inertial measurement unit in either a gimballed, strapped-down, or Carousel mode of operation. A total of three gyro error models and two accelerometer error models are currently programmed, with provision for additional instrument error models included in the program structure. As many as 51 independent error sources may be represented in the inertial guidance system model.

The performance indices used for the study are the maximum semi-axis magnitudes of the position and velocity error ellipsoids measured at the end of the boost phase. These values are a measure of the statistical properties of the injection initial condition for the succeeding free-fall trajectory. The values do not contain information regarding the deviation in position and velocity at this point due to guidance and control actions during the boost trajectory. A summary of performance assessment results is shown in Table 3-22.

3.3.2 DEBOOST PRIOR TO REENTRY (TRAJECTORY INDEX 9)

Most boost phases of interplanetary trajectories are followed by relatively long free-flight trajectories. Injection errors can be compensated by optimal navigation during these phases when correction velocities are defined and implemented. Velocity budgets for interplanetary missions are computed with allowances for such injection errors.

However, deboost for ballistic atmospheric reentry does not permit later correction in time to effect a successful and safe reentry. The reentry point and, in particular, the reentry angle are initial conditions that must be achieved with high accuracy almost immediately at the end of the powered trajectory. This trajectory occurs at the end of an interplanetary mission when the calibration accuracy of the inertial instruments has the largest uncertainties.

The performance assessment indices of the four reference inertial guidance systems for this trajectory are shown in Table 3-22. These navigational uncertainties are small and do not significantly affect the reentry angles.

An investigation of the effects due to degraded inertial guidance systems was conducted for this trajectory. The inertial instrument package consisted of three rate gyros and three proof-mass accelerometers, evaluated in both a strapdown and gimballed configuration. The acceleration independent components in the error budget — accelerometer bias, constant random gyro-drift rate, and initial misalignment — can easily be calibrated

Mission Phase	Navigation Class	Navigation System Index	Maximum Semi Axis of Terminal Error Ellipsoids	
			Position (km)	Velocity (m/sec)
5A	1	1	0.202	1.25
		2	0.207	1.20
		3	0.295	2.02
		4	0.208	1.27
5B	1	1	0.080	0.66
		2	0.079	0.64
		3	0.108	0.93
		4	0.080	0.66
6	1	1	0.00012	0.024
		2	0.00012	0.023
		3	0.00017	0.033
		4	0.00012	0.024
7	1	1	0.00003	0.011
		2	0.00003	0.011
		3	0.00004	0.016
		4	0.00003	0.011
8	1	1	0.603	1.841
		2	0.570	1.737
		3	1.956	3.868
		4	0.512	1.55
9	1	1	0.240	1.41
		2	0.234	1.35
		3	0.350	2.41
		4	0.243	1.45

Table 3-22. All-Inertial Guidance System, Performance Indices for Space Boost Trajectories

during the long periods of free-fall that separate the short phases of high navigational accelerations in which the IMU can play a primary role. Therefore, only the acceleration-sensitive error terms were assumed to be degraded for this study. The numerical results of this study are shown in Appendix B, Section III. These results indicate that even with a degradation factor of 20 on all acceleration sensitive errors, the inertial system errors will not degrade the entry corridor miss by more than a few arc-minutes.

3.3.3 LAUNCH FROM MARS INTO CIRCULAR PARKING ORBIT (TRAJECTORY INDEX 8)

The launch-from-Mars trajectory is a two-stage boost trajectory with a coast period between the two stages of thrust. Figure 3-9 gives trajectory parameters as a function of flight time. Table 3-20 lists other pertinent trajectory data.

This boost trajectory has been somewhat arbitrarily defined but does have high accelerations, high angular rates and a long flight time. Hence, it does provide a relatively severe test of the inertial-navigation-system performance characteristics that will be associated with any such launch phase. The performance indices given in Table 3-22 show that the navigational errors at the end of this trajectory are 2 to 3 times as large as navigational errors of the other boost phases. The errors are, however, in every case tolerable in terms of the allowable errors at the initiation of midcourse navigation.

3.3.4 TRAJECTORY CHANGE MANEUVERS

3.3.4.1 Trajectory Change at Mars (Trajectory Index 6)

Martian flyby missions require a small velocity change at Martian pericenter to inject into an acceptable Earth return trajectory. This particular trajectory requires only 59.3 meters/second speed change over a 10.3 second interval for the required boost maneuver. Table 3-20 gives the pertinent trajectory data. The performance indices for this trajectory are given in Table 3-22 and are very small values.

3.3.4.2 Injection into Mars Transfer from 185 kilometers Earth Parking Orbit (Trajectory Index 5A)

This trajectory is a boost phase of the 3-planet flyby (Grand Tour) mission number I and has the largest inertial velocity increment among the set of reference boost trajectories. It is a typical space boost trajectory, characterized by almost constant thrust direction, slow angular rates, and relatively low acceleration levels (<3 g). The performance indices are given in Table 3-22 and the trajectory characteristics are given in Table 3-20.

3.3.4.3 Deboost into Circular Parking Orbit at Mars (Trajectory Index 5B)

This boost trajectory is also a boost phase of the Grand Tour mission. The physical trajectory characteristics are similar to the trajectory of Paragraph 3.3.4.2, but the inertial velocity and flight time are about half the values of the preceeding boost trajectory (Table 3-20), and the corresponding performance indices are slightly less than half the value of the preceeding trajectory (Table 3-22).

3.3.4.4 Midcourse Correction (Trajectory Index 7)

This trajectory is a standard boost maneuver for all interplanetary missions. Despite the short time and small velocity increment, the accuracy requirements on the inertial measurement system are still quite high because of the high terminal sensitivity to velocity errors at points where midcourse corrections are made. The principle error source for such maneuvers is the initial alignment accuracy, which accounts for the uniformity of the performance indices shown in Table 3-22 for this trajectory.

3.3.5 CONCLUSIONS

The inertial measurement systems evaluated in this study are considered to be representative of current and near-future inertial measurement systems. Their performance for boost phases, which are followed by free-fall trajectories in which recursive optimal navigation is performed, is sufficiently accurate to assure the validity of the linear assumptions of such navigation.

The boost trajectory that deboosts for ballistic atmospheric reentry at Earth where the reentry angle is the critical parameter is the most severe test of inertial guidance performance. Here even degraded rate-gyro strapdown systems provide adequate accuracy margins for entry at approximately circular speed. It was demonstrated in Paragraph 3.2 that navigation during maneuvering atmospheric entry imposes the most severe requirements upon the inertial measurement unit. The relatively benign acceleration and angular rate environments of interplanetary trajectory boost phases permit use of inertial measurement systems with current performance standards to obtain satisfactory navigational accuracy. Thus, even the strapdown system with rate gyros, the least accurate system considered, could be used satisfactorily on the powered flight trajectories considered in this study, although it is not adequate for atmospheric entry inertial navigation.

3.4 GUIDANCE AND NAVIGATION FOR LOW-THRUST MISSIONS

A low-thrust mission is one in which the propulsion is supplied by thrusters operating continuously over most or all of the mission at very low thrust levels (less than or equal to 10^{-3}g). Such thrust devices are the electric propulsion systems that are currently in early stages of development and appear attractive for future extended space travel. The guidance and navigation for such a mission differs from that for the most conventional high-thrust, free-fall mission in that the trajectory equations of motion must account for the thrust (that is, there is no free-fall trajectory), and the control action is continuous rather than impulsive.

Two different low-thrust performance-assessment simulation programs have been developed: Version I is a simplified two-dimensional, statistical model, while Version II is a more complete, three-dimensional model. These programs are described in Volume II Parts 10 and 11, respectively.

The objectives of the low-thrust guidance and navigation studies are described below, followed by a discussion of the trade-off studies made using the two different digital simulation programs.

3.4.1 OBJECTIVES OF THE INVESTIGATION

The overall objective of the study is to investigate the requirements for low-thrust interplanetary navigation. The following are specific objectives.

1. To develop methods of obtaining optimum low-thrust heliocentric transfer trajectories.
2. To study guidance sensitivities for low-thrust missions, including the following:
   a. The dependence of system response on trajectory profile,
   b. The effects of the initial uncertainty in position and velocity,
   c. The sensitivity of the navigational procedure to errors in the a priori statistics of the instruments,
   d. The accuracy of a neighboring optimum guidance scheme.
3. To make a performance assessment study of alternate guidance system configurations, including the following:
   a. The effects of combining an IMU with electromagnetic sensors, plus determining the necessary precision for the IMU,
   b. The effects of rotation of the IMU on system response,
   c. The effects of ground tracking; that is, trade-off between onboard instrumentation and onboard and ground tracking.

3.4.2 TRADE-OFF STUDIES USING VERSION I OF THE DIGITAL SIMULATION PROGRAM

This section details the results of a series of trade-off studies made with the simplified digital simulation program. For a complete description of this mathematical model and computer program, see Volume II Part 10. Briefly, it is a two-dimensional simulation of low-thrust trajectory phases which computes only the statistical quantities related to the navigation problem.

3.4.2.1 Nominal Mission Profiles

The parameters for the optimum nominal Earth heliocentric-transfer trajectories and tangential-thrust spiral-in and spiral-out trajectories at Earth and Mars are presented and discussed in this section.

3.4.2.1.1 Heliocentric Transfer Trajectories. HTR2 — This trajectory is a fast (79 day = 6.8258×10^6 sec) Earth-to-Mars trajectory with a Julian launch date of 2439491.5. The Earth-to-Mars transfer angle is 93 degrees. A (normalized) initial thrust acceleration of 1.18411×10^{-5} km/sec^2 and a (normalized) mass flow rate of 3.0×10^{-8} sec were used. The trajectory was integrated for 1 million seconds to define the escape phase, and the heliocentric transfer was integrated for 5 million seconds to the start of the Mars approach phase. Table B-33 shows the initial conditions at the start of this heliocentric phase.

HTR4 — This trajectory is a slow (166 day = 1.43424×10^7 sec) Earth-to-Mars trajectory with a Julian launch date of 2441067.5. The Earth-to-Mars transfer angle for this case is 135 degrees. A (normalized) initial thrust acceleration of 0.95347×10^{-7} km/sec^2 and a (normalized) mass flow rate of 1.0×10^{-8} sec were used for this case. This trajectory, being slower, was integrated for 2 million seconds to provide for the escape phase, and then integrated for 10 million seconds to the start of the Mars approach. The renormalized initial conditions at the start of this phase are also shown in Table B-33.

These optimum heliocentric-transfer trajectories were obtained using the program described in Volume II, Part 9. It was necessary to input planetary ephemeris information for each trajectory. Since the planets are assumed to move in circular orbits, it is sufficient to input R, ω, T_o for each trajectory. Table B-34 summarizes these values.

3.4.2.1.2 Planetocentric Escape Trajectories. Two spiral-out trajectories were run, one at Earth and one at Mars. Each was truncated after 200,000 seconds. Table B-35 shows the initial conditions used for each trajectory. As this table shows, the vehicle was assumed to spiral out under tangential thrust from a circular orbit around the respective planet.

3.4.2.1.3 Planetocentric Capture Trajectories. The initial conditions of the two spiral-in trajectories were determined from the terminal conditions of the spiral-out trajectories, with 200,000 seconds flight time. Table B-36 summarizes the initial conditions used.

3.4.2.2 System Configurations

In this section the available systems are discussed in terms of the sensors employed and the associated error budgets. Table 3-23 details the systems used in the course of these studies. Details of the specific error budgets represented by each of the designated system symbols are given in Table B-37. The following notational conventions are used.

1. Instruments — indicated by initials

   G Ground tracker — measures range, range-rate, and angle.

   P Planet tracker — measures space angle (may be switched between Earth, Sun, and Mars).

   IG Gimballed IMU

   IC Carousel IMU

2. Error Budgets — indicated by subscripting initials by 1, 2,3, and so on.

3. Systems — indicated by combining subscripted initials separated by dashes, as P1-G1, P1-G1-IG1, and so on.

4. Correlation time, switching times for the planet tracker, and dynamic noise values when the IMU is not present are also specified by the subscript.

5. Variance

   σ^2 indicates a noise variance.

   b^2 indicates a bias variance.

   Subscripts indicate components of measurement to which they apply; that is, σ^2_α for noise variance of angle for planet tracker, b^2_α for the bias variance.

For this study it was necessary to develop a reference set of values for the bias in the propulsion parameters, and also a set of reference values for the initial uncertainty in position and velocity for the heliocentric transfer trajectories and the planetocentric spiral-out trajectories. For the planetocentric spiral-in, the terminal accuracy of the heliocentric transfer trajectory, using the corresponding system, was used to initialize the error in the estimate of position and velocity. The program allows for a bias to be present on the control angle, but this option was not used, therefore $b^2 = 0$ for the control angle. Table 3-24 shows the reference values used for HTR2, HTR4,

SYSTEM	CONFIGURATION	MISSIONS				
		HTR2	HTR4	MO	EO	MI
I	G1	X			X	
II	G1-IG1	X			X	
III	G1-IC1	X				
IV	P1	X	X	X		X
V	P1-IG1	X	X	X		X
VI	P1-IC1	X		X		
VII	G1-P1	X			X	
VIII	G1-P1-IG1	X	X		X	
IX	G1-P1-IC1	X				
X	P2	X		X		
XI	P2-IG1	X		X		
XII	P2-IC1	X		X		
XIII	P3	X				
XIV	P3-IG1	X				
XV	P4	X				
XVI	P4-IG1	X				
XVII	P5	X				
XVIII	P5-IG1	X				
XIX	P2-IC2	X				
XX	P2-IC3	X				
XXI	P6	X				
XXII	P7	X				
XXIII	P8	X				
XXIV	P9	X				
XXV	P10	X				

HTR — Heliocentric trajectory

MO — Mars Out planetocentric escape trajectory

EO — Earth Out planetocentric escape trajectory

MI — Mars In planetocentric capture trajectory

Table 3-23. Systems, Configurations, and Missions Studied

and the planetocentric escape phase. Escape from Mars used the same values as were used for HTR2, since they were assumed to use the same propulsion system. Escape from Earth used a slightly different set of values. Propulsion errors are approximately 1 percent values.

TRAJECTORY	POSITION		VELOCITY		PROPULSION	
	σ^2_{x1} $(km)^2$	σ^2_{x2} $(km)^2$	σ^2_{x3} $(km/sec)^2$	σ^2_{x4} $(km/sec)^2$	$\sigma^2_{a_o}$ $(km/sec)^2$	$\sigma^2_{\dot{m}}$ $(/sec)^2$
HTR2 (MO)	1.0	1.0	0.1×10^{-5}	0.1×10^{-5}	0.25×10^{-14}	0.1×10^{-17}
HTR4	1.0	1.0	0.1×10^{-5}	0.1×10^{-5}	0.134×10^{-16}	0.1×10^{-18}
EO	1.0	1.0	0.1×10^{-5}	0.1×10^{-5}	0.169×10^{-13}	0.9×10^{-19}

Table 3-24. Initial Error Covariances

3.4.2.3 Trade-Off Parameters

For the heliocentric phase, in addition to studying the effects of combining various instruments with different error budgets, it was also desired to study the effects of changing the trajectory profile and of changing the initial error covariance of the position, velocity, and parameters to be estimated. The change in accuracy as a function of the rotational rate of the Carousel IMU was also studied. In addition, sensitivity studies to errors in the a priori statistics were run as described in Paragraph I. 4 of Volume II, Part 10.

For the planetocentric phase it was desired to investigate the effects of the IMU and also the ground tracking on the error in the estimate of position and velocity. Also, the effects of planet tracker accuracy were investigated with and without the IMU.

3.4.2.4 Study Results

In this section the studies of the various mission phases are summarized. Tables of terminal accuracies are included for many cases. In the box format of these tables, the top line represents the position eigenvalues and the bottom line the velocity eigenvalues; that is, the semi-major and semi-minor axes for the position and velocity ellipses, respectively. Graphical time histories of these eigenvalues are also presented in some cases, the scales being km for position, km/sec for velocity, and sec for time.

3.4.2.4.1 Heliocentric Transfer Phase. Most of the heliocentric phase trade-off studies were made with trajectory HTR2. This was done because the system responses were found to be relatively trajectory independent. Figures B-147 and B-148 (Appendix B) illustrate the correctness of this assumption. Figure B-147 shows the time history of the more accurate position eigenvalue for trajectory HTR2 using system P1-IG1. Figure B-148 shows the time history of the more accurate position eigenvalues for trajectory HTR4 using the same system with the time scale shrunk by a factor of 2 (since HTR4 takes twice as long as HTR2). Note that the shape of the two time histories is virtually identical, and that the peak error for each trajectory is of the same order of magnitude. Indeed, the terminal accuracies are also very close, and the fluctuations are believed to be primarily due to geometrical differences of the position and velocity of the target relative to the vehicle in the final approach phase.

Figure B-149 shows the time history of the more accurate eigenvalue when the planet tracket P2 is used by itself. Note the abrupt changes at $T = 0.15 \times 10^7$ and $T = 0.35 \times 10^7$ due to the change in the body being observed at these points. Since one goal of this study was to determine the improvements in accuracy obtained with various types of IMU's Figures B-150, B-151, and B-152 show the same time history when P2 is combined with the gimballed IMU IG1, the Carousel IMU IC1, and the more rapidly rotating IMU IC3. An immediate improvement in accuracy by a factor of 5 and a smoothing effect occur with the addition of the gimballed IMU. Rotating the IMU reduces the error by another factor of 2.5, even though the IMU rotates only 10 times during the entire flight. As Figure B-152 shows, only a very slight improvement is noted when the IMU is rotated 100 times during the flight, so it appears that even a very slow rotational rate is adequate to reap the majority of the benefits of the Carousel configuration.

Figure B-153 adds the ground tracker G1 which measures range-rate and angle information to the system P1-IG1 of Figure B-147. Although a similar shape is retained, it is seen that the peak error is reduced by more than an order of magnitude when the ground tracker is used. Thus it appears very desirable to have accurate ground tracking whenever possible, at least during the early phases of the flight.

Another topic of interest is the dependence of system accuracy on the initial covariance of the error in position and velocity. If PO2 and PO3 are the covariance of position and velocity for HTR2 in Table 3-24 multiplied by 10^4 and 10^6, respectively, where the covariance of the propulsion errors remain the same, then Figures B-154, B-155, and B-156 show the time history of the more accurate eigenvalue for system P1, when the initial covariance in position and velocity is set equal to the normal values PO2 and PO3, respectively. Note in particular that the maximum error is only doubled when the 1σ value of initial position and velocity error is raised 2 or 3 orders of magnitude. Table 3-25 summarizes the terminal accuracies of these three systems. As the table shows, the maximum change for any eigenvalue is less than 20 percent, even with a 3-order-of-magnitude change in the initial position and velocity uncertainty. Thus it appears that the filtering process is relatively insensitive to the initial error in the state.

P1	P1-PO2	P1-PO3
3760, 268 4.77×10^{-2}, 5.83×10^{-3}	4320, 269 5.55×10^{-2}, 5.84×10^{-3}	4370, 287 5.63×10^{-2}, 6.02×10^{-3}

Table 3-25. Effect of Initial Covariance in Position and Velocity on Terminal Accuracy

Table 3-26 summarizes the terminal accuracy of typical systems for trajectory HTR2. As mentioned before, the top line of each box shows the position axes, the bottom line the velocity axes. This table shows the dramatic improvement when an IMU is added to an EMS, and also the further improvement when the IMU is rotated at a constant angular velocity. Also, the improvement obtained by combining the ground tracker with the onboard planet tracker is clear from the numerical results.

In Paragraph I.4 of Volume II, Part 10 of this report, a statistical measure of sensitivity to errors in the a priori statistics is discussed. Briefly, the sensitivity coefficients are defined by the ratio of the eigenvalues of the covariance matrix (computed using the "true" statistics and the a priori filter-gain matrix) to the eigenvalues of the "true" covariance matrix for the state. Figures B-159 and B-160 are examples of the time history of the degradation in performance which might be expected due to errors in the a priori assumptions about the random and bias errors of the various instruments.

Figure B-157 shows the sensitivity coefficient for one position component if the bias and random errors of P1 are four times as great as assumed. The terminal performance is only about 75 percent as good as that with accurate knowledge of the statistics.

Since it was found that the filter is almost totally insensitive to errors in the initial conditions, including the IMU covariance, Figures B-158 and B-159 combine IG1 and IC1 with 5σ bias errors with P1 with 4σ bias and random errors. With the gimballed IMU the terminal accuracy was found to be over 97.5 percent of optimum, and with the Carousel IMU over 99.5 percent of optimum, indicating that these aided-inertial systems are very insensitive to errors in the a priori statistics as far as filter performance is concerned.

Figure B-160 shows the sensitivity to a 4σ ground tracker coupled with the 5σ gimballed IMU. Again, the terminal accuracy is over 99.5 percent of optimum, and thus ground tracker-IMU systems are also rather insensitive to errors in the a priori statistics.

EMS \ IMU	0	IG1	IC1
G1	1780, 1.14 1.88×10^{-2}, 3.0×10^{-5}	66.4, 1.13 2.0×10^{-5}, 9.88×10^{-7}	45.4, 1.13 9.22×10^{-6}, 3.03×10^{-7}
P1	3760, 268 4.77×10^{-2}, 5.83×10^{-3}	40.3, 1.28 3.85×10^{-4}, 1.86×10^{-5}	25.2, 0.902 1.87×10^{-4}, 6.35×10^{-6}
G1-P1	5.57, 1.05 3.08×10^{-4}, 1.06×10^{-6}	1.15, 0.644 2.99×10^{-6}, 1.25×10^{-7}	1.14, 0.640 2.66×10^{-7}, 1.04×10^{-7}
P2	5550, 548 6.24×10^{-2}, 1.17×10^{-2}	571, 28.1 4.19×10^{-3}, 4.55×10^{-4}	519, 22.8 3.37×10^{-3}, 8.24×10^{-5}

Table 3-26. Summary of Terminal Accuracy of Typical Systems for Trajectory HTR2

3.4.2.4.2 Planetocentric Escape Phase. For the planetocentric spiral-out phase, cases with a ground tracker were run at Earth, and cases without a ground tracker were run at Mars. Of particular interest were the effects of the IMU and the effects of the ground tracker since the planet tracker may be present at Mars, whereas the ground tracker may not and the IMU may be present at either planet.

An explanation of the figures follows. Due to the fact that the nominal trajectory is a spiral, the roles of the larger and smaller eigenvalues are interchanged due to the rotation of the eigenvectors. Thus, when features of the figures are referred to, the larger eigenvalue (that is, the upper envelope of each graph) is applicable. The terminal accuracies for the cases are shown in Tables 3-27 and 3-28, and the time histories of the error eigenvalues are shown in Figures B-161 through B-163 of Appendix B.

As mentioned previously, the outward spirals were run arbitrarily for 200,000 seconds and then truncated. Figure B-161 shows the Martian spiral-out with only the planet tracker P1. Note that the error is still increasing at T = 200,000 and the filter has not converged. Figure B-162 shows the same run with the addition of the gimballed IMU IG1. The error here also increases for a time (although not as rapidly), but at T = 100,000, the filter rapidly begins to converge as the estimate of the bias errors begins to improve. Figure B-163 shows an Earth-centered spiral-out with the system G1-P1-IG1. In particular, this shows that with the addition of ground tracking the error in the estimate does not increase, but instead is a monotonic decreasing function of time.

Tables 3-27 and 3-28 and the figures in Appendix B show that the addition of the IMU greatly improves system performance and that the ground tracker at the Earth is also extremely valuable.

3.4.2.4.3 Planetocentric Capture Phase. Since the planetocentric spiral-out and planetocentric spiral-in systems responses are so similar, only a very few spiral-in cases were run. Table 3-29 presents these results. Since the vehicle is moving toward the planet, instead of away, the increase in error using the planet tracker only, which was observed in the spiral-out case, does not occur, because moving closer to the target decreases error and moving away increases error when the planet tracker is used. As before, however, the IMU is seen to improve the system accuracy significantly.

EMS \ IMU	0	IG1	IC1
P1	216, 8.03 9.7×10^{-3} 8.41×10^{-4}	0.138, 4.00×10^{-3} 4.31×10^{-6}, 7.70×10^{-6}	0.105, 1.77×10^{-3} 3.98×10^{-6}, 2.13×10^{-6}
P2	219, 8.20 9.83×10^{-3}, 1.01×10^{-3}	3.20, 0.102 1.00×10^{-4}, 1.97×10^{-6}	2.55, 4.48×10^{-2} 9.38×10^{-5}, 4.72×10^{-5}

Table 3-27. Summary of Terminal Accuracy of Typical Systems for Trajectory MO

EMS \ IMU	0	IG1
G1	1.83, 6.16×10^{-3} 6.99×10^{-4}, 1.77×10^{-4}	2.50×10^{-1}, 1.68×10^{-3} 9.03×10^{-5}, 4.66×10^{-7}
G1-P1	2.76×10^{-1} 6.15×10^{-3} 1.01×10^{-4}, 1.97×10^{-5}	2.05×10^{-1} 7.35×10^{-4} 7.42×10^{-5}, 2.59×10^{-7}

Table 3-28. Summary of Terminal Accuracy of Typical Systems for Trajectory EO

EMS \ IMU	0	IC1
P1	0.982, 0.304 9.53×10^{-4}, 2.93×10^{-4}	9.06×10^{-3} 2.21×10^{-4} 8.71×10^{-6}, 2.12×10^{-7}

Table 3-29. Summary of Terminal Accuracy for Trajectory MI

3.4.2.4.4 Approximate Determination of Acceptable Navigation System Classes. During the study it was decided to seek an empirical relationship between terminal accuracy and instrument error budgets that would eliminate the necessity of a large number of computer runs for determining classes of adequate systems. In particular, it was desired to find a family of acceptable instruments as a function of bias and random error that would give terminal errors smaller than a specified value.

This problem is attacked by expressing the terminal accuracy λ as an expansion about λ_o given by

$$\lambda = \lambda_o + \left.\frac{\partial f}{\partial \sigma_\alpha}\right|_o \delta\sigma_\alpha + \left.\frac{\partial f}{\partial b_\alpha}\right|_o \delta b_\alpha + 0\left(\frac{1}{t}\right)$$

Note that the variations in all parameters except the planet tracker bias and random noise are neglected. These expressions then allow determination of acceptable regions in σ_α, b_α space for λ in the neighborhood of λ_o.

Figure 3-10 shows the terminal errors for a system using only planet tracking for various random noise values and a fixed nonzero bias error. Both the larger and smaller eigenvalues are plotted to show that the terminal error is nearly linear over the range of more than an order of magnitude of random error. Figure 3-11 shows a similar graph when an IMU is present with the same result of linearity over the range shown. Thus, for a given bias, an acceptable level of random noise may be chosen over a limited range, using only a few runs by interpolation or extrapolation.

Table 3-30 shows the terminal accuracy of a planet tracker with a fixed random error and various biases. For a change in bias of two orders of magnitude it is seen that the change in terminal accuracy is less than 10 percent. Thus $\partial f/\partial b_\alpha$ also appears to be fairly small. However, it is known that the filter has a singularity at $\sigma_\alpha = 0$, and from Table 3-31 it appears that this also presents a problem for $b_\alpha = 0$. As the table shows, the eigenvalues do not appear to be linear functions of the random noise for $b_\alpha = 0$.

It is suggested, however, that the determination of a family of hyperplanes whose "interior" would provide the family of acceptable systems for a given terminal accuracy requirement might be possible for small regions, at least away from the origin which is the region of practical importance. This would be a very important simplification of the problem of choosing a system to satisfy any given set of terminal accuracies.

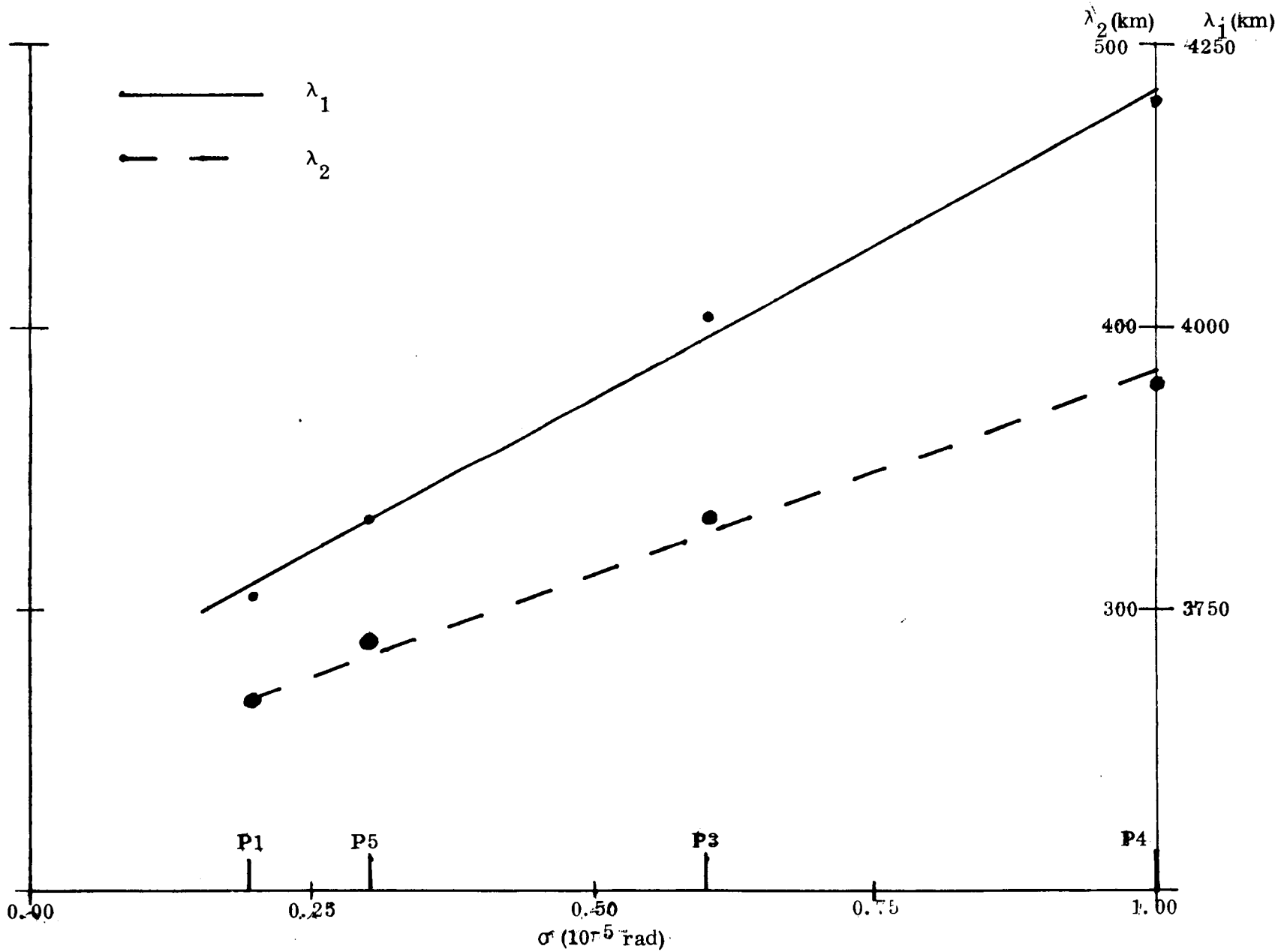

Figure 3-10. Final Position Eigenvalues Using Planet Tracker Only

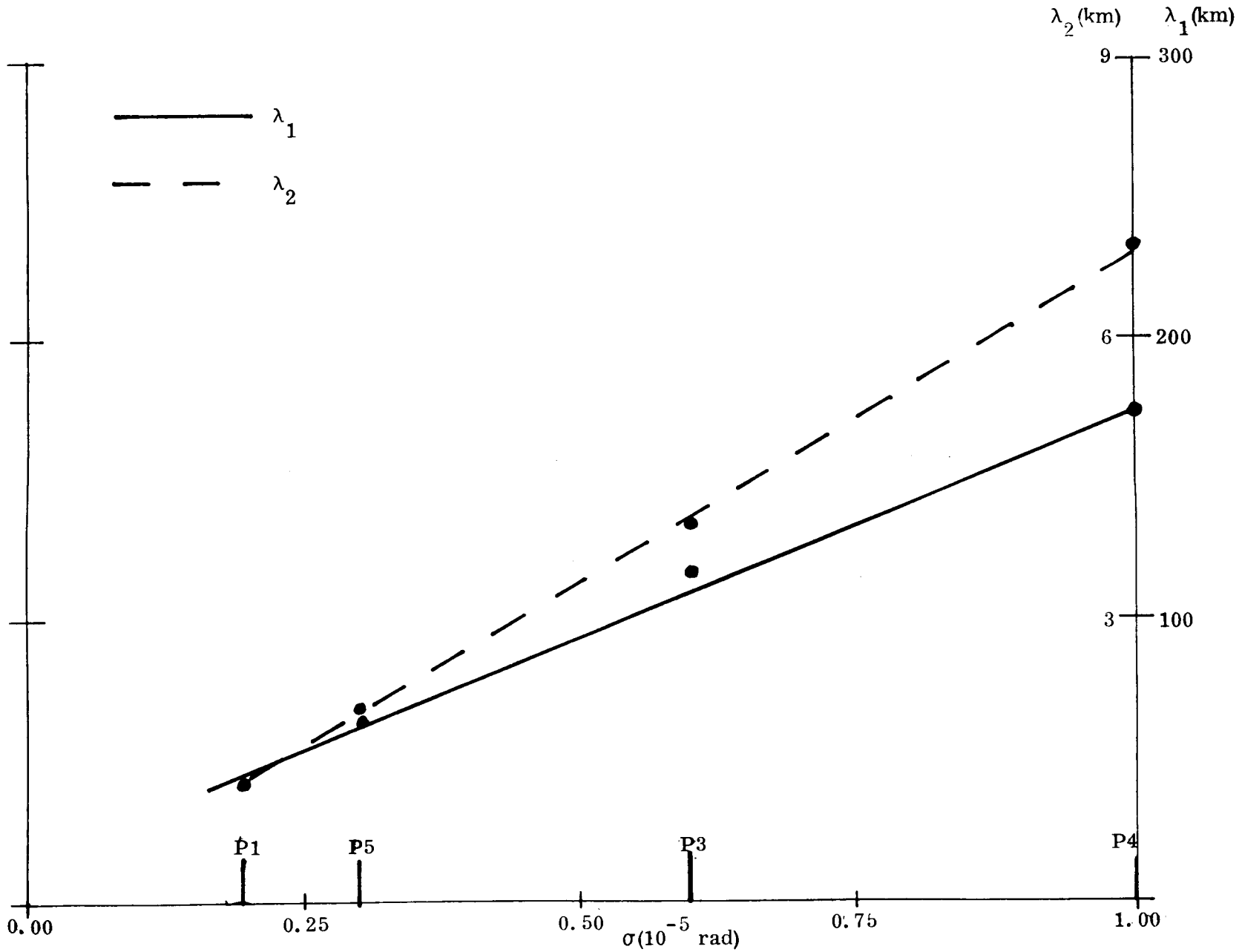

Figure 3-11. Final Position Eigenvalues Using IG1 Plus Planet Tracker

b rad	λ_1 km	λ_2 km	$\lambda_1\lambda_2$ km^2
5.5×10^{-2}	3.8×10^{3}	2.7×10^{2}	1.0×10^{6}
5.5×10^{-3}	3.8×10^{3}	2.7×10^{2}	1.0×10^{6}
5.5×10^{-4}	3.7×10^{3}	2.4×10^{2}	8.9×10^{6}

Table 3-30. Terminal Accuracy as a Function of Bias for Nonzero Finite Random Noise

σ rad	λ_1 km	λ_2 km	$\lambda_1\lambda_2$ km^2
1.9×10^{-4}	6.5×10^{3}	1.1×10^{2}	7.15×10^{5}
1.9×10^{-5}	3.1×10^{3}	1.5×10^{1}	4.65×10^{4}
1.9×10^{-6}	2.1×10^{3}	1.7	3.57×10^{3}

Table 3-31. Terminal Accuracy as a Function of Random Noise for Bias Zero

3.4.2.4.5 Conclusions. From the results presented previously it is seen that the IMU appears to be the key to an adequate onboard system. As the tables show, the addition of an IMU to a reasonably accurate planet tracker brings the terminal error down to acceptable values. Also, as the graphs show, the system is far less sensitive to errors in the a priori statistics when the IMU is included. The ground tracker also reduces the terminal error, but this is difficult to assess due to the extreme distances over which the tracker must be accurate. For the planetocentric phase, however, the ground tracker is extremely accurate and extremely desirable.

Also, since the terminal error was found to be relatively insensitive to the initial error in position and velocity, and almost totally insenstive to the trajectory, it appears that the approximate procedure outlined in Paragraph 3.4.2.4.4 would be a very fruitful topic for future investigation into the simplification of error analysis techniques.

Another conclusion of this study is that an extremely accurate IMU is not essential for low-thrust navigation, as the tables and graphs show. In fact, present state-of-the-art inertial instrumentation appears to be adequate, particularly in the Carousel configuration, even if the IMU is rotated at very low frequencies. The estimation of the IMU bias error appears, therefore, to be an extremely good substitute for building very high precision inertial instruments, and so low-thrust navigation does not appear to need the extremely accurate accelerometers which have been postulated for the future.

3.4.3 TRADE-OFF STUDIES USING VERSION TWO OF THE DIGITAL SIMULATION PROGRAM

The more exact (and more costly in computer time) Version II of the low-thrust computer program is described in Volume II, Part 9. It has been exercised relative to the following specific objectives.

1. To determine the range of linearity of the equations of motion about a nominal low-thrust trajectory. Within this range, linear perturbative methods would be applicable.
2. To determine, within the linear range, the accuracy of a neighboring optimum guidance scheme in a deterministic application; that is, assuming perfect navigation and no control noise.

3.4.3.1 Description of Study

Two trajectories with constant continuous thrust were selected for the study:

1. HTR_2 - a fast Earth-to-Mars trajectory with a thrust level of 5.8×10^{-4} g and a flight time of 79 days.
2. HTR_{32} - a slow Mars-to-Earth trajectory with a thrust level of 6.2×10^{-5} g and a flight time of 193 days.

These trajectories are described in more detail in Volume II, Part 9.

In the design of each trajectory a neighboring optimum iteration scheme was used. First, an initial guess of the trajectory parameters was made. With these values, an initial optimum reference trajectory was established by integrating the equations of motion from the initial position and velocity out to the end of the flight time. The resulting final position and velocity missed the desired target. Attempt was then made to establish a neighboring optimum trajectory as the desired trajectory by guiding to the target with the neighboring optimum guidance scheme. If the terminal miss was still too large, then the process was repeated with the neighboring optimum trajectory as the reference trajectory.

If the initial target miss was outside the range of linearity, only a fraction at a time could be corrected until the residual miss was within the range. This fact enables the range of linearity to be established by making successive computer runs with increasing fractions of the initial miss to be corrected in the first iteration. Consider the first run made in which the iterative process does not converge. The initial fractional miss to be corrected for is outside the linear range. Furthermore, the initial fractional miss in the prior run is within the linear range.

For the latter series of runs, only HTR_{32} was used because its long flight time would give a conservative estimate of the range of linearity.

Iterations in which total corrections of the miss were attempted, provide results to establish the guidance accuracy. The accuracy required to correct for a terminal miss is comparable to the accuracy required to correct for an initial deviation. Correcting for an initial deviation, is, of course, the true guidance problem.

3.4.3.2 Results

Figures 3-12 and 3-13 contain the results of the study in determining the range of linearity. The initial miss in position and velocity was 5.37×10^7 kilometers and 5.13 kilometers/second. In the broken line labeled NSTEPS = 3, the initial fraction of the miss corrected was 1/3. Similarly, in the line labeled NSTEPS = 2, the initial fraction was 1/2. The latter definitely appears to be diverging while the former converged. Consequently, the range of linearity extends to about 2×10^7 kilometers in position and about 2 kilometers/second in velocity.

Figures 3-14 and 3-15 contain the results of the study in determining the accuracy of a neighboring optimum guidance scheme. As can be seen, the accuracy that can be expected for initial deviations up to 50,000 kms in position and 5 meters/second in velocity is 100 kilometers and 0.01 meters/sec (at least in the deterministic case), respectively.

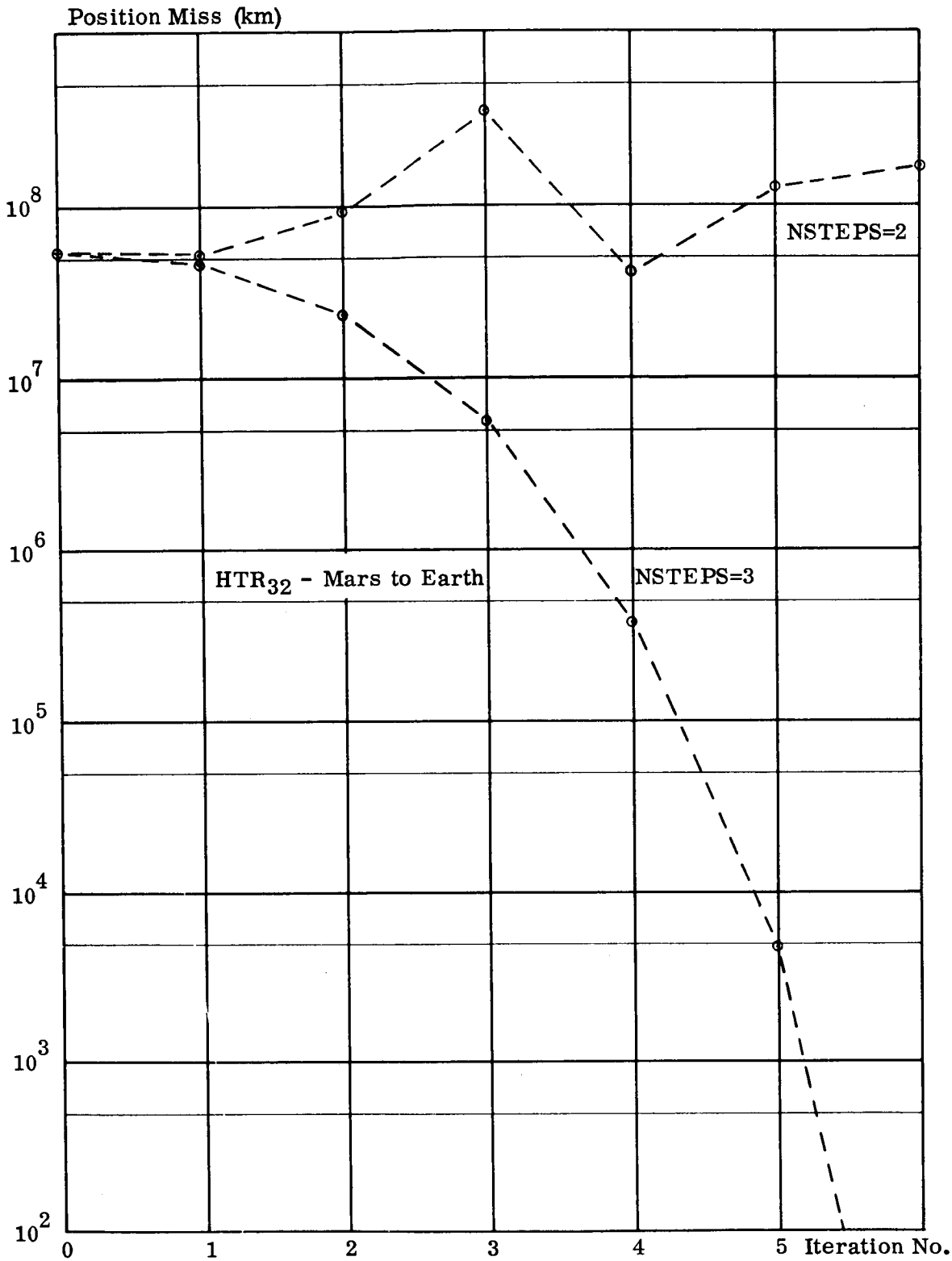

Figure 3-12. Miss in Position Versus Iteration Number

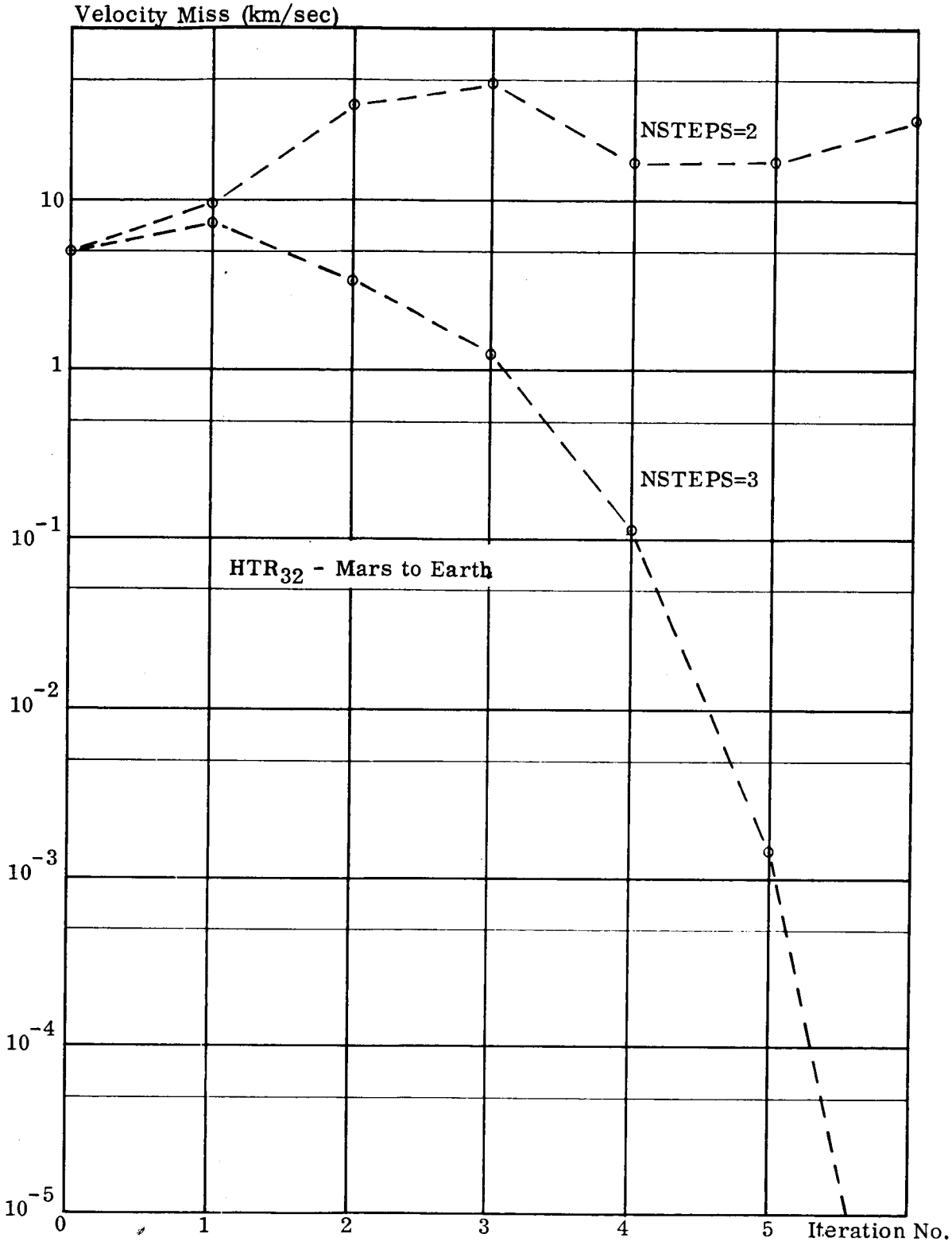

Figure 3-13. Miss in Velocity Versus Iteration Number

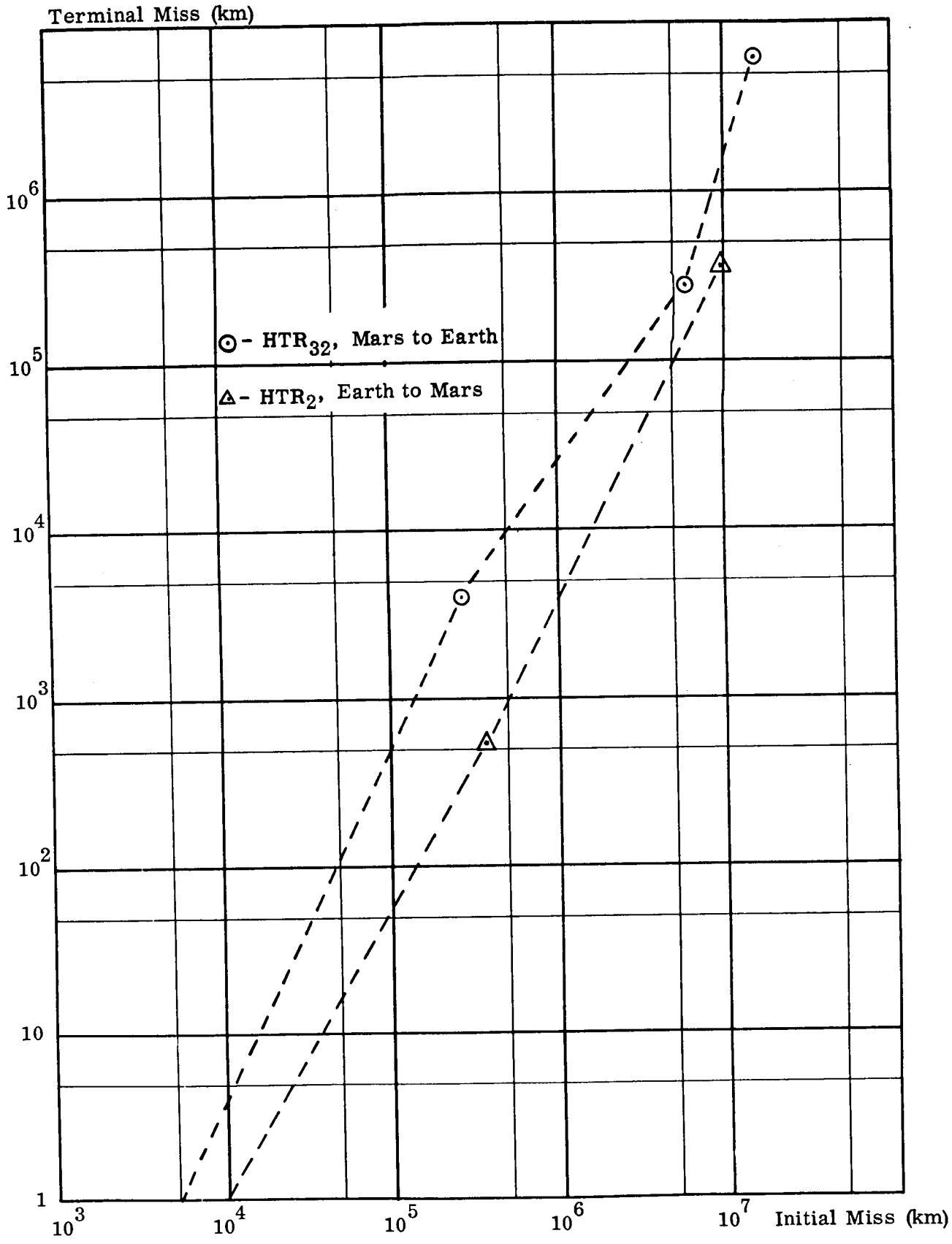

Figure 3-14. Terminal Versus Initial Miss in Position

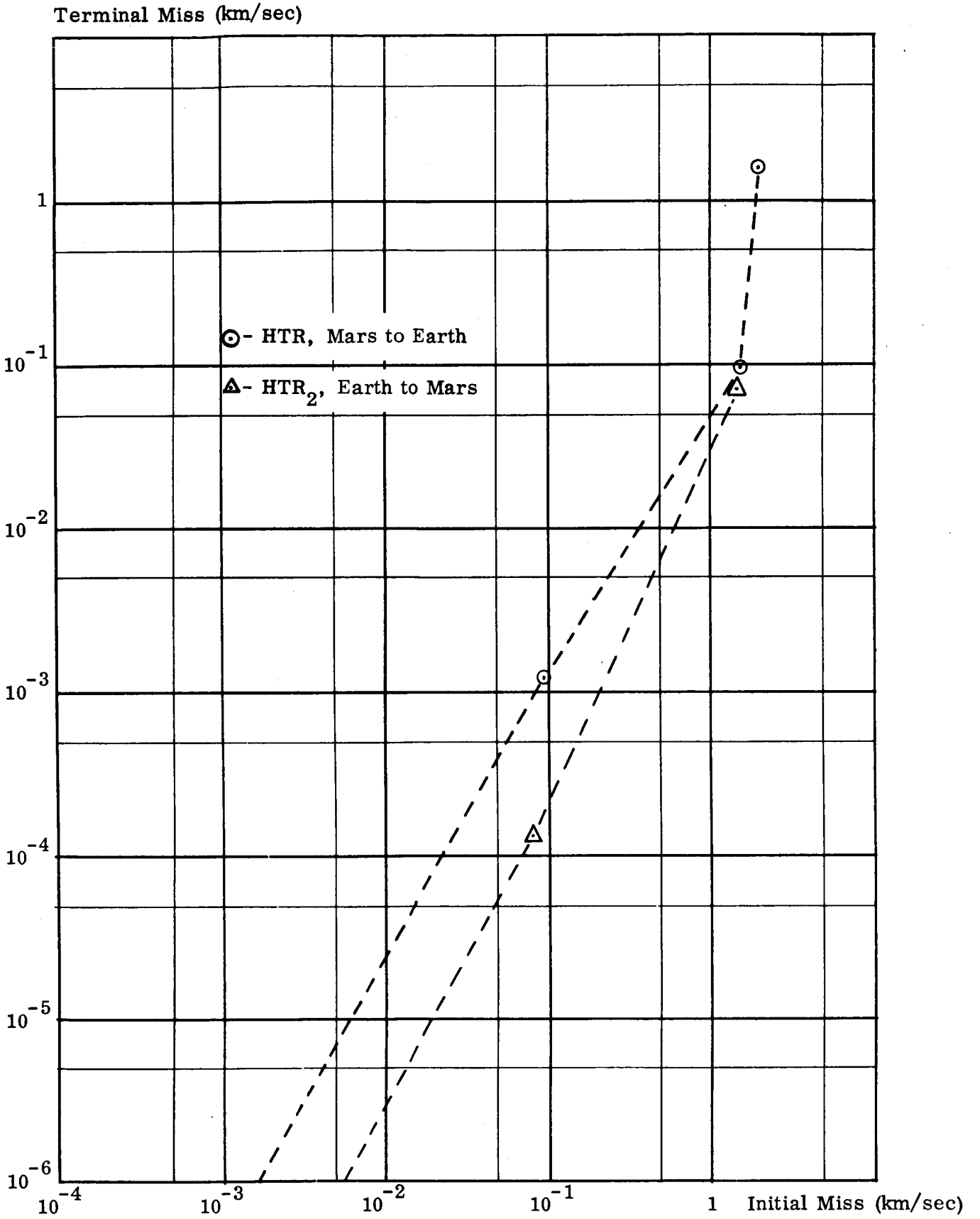

Figure 3-15. Terminal Versus Initial Miss in Velocity

SECTION IV

SUMMARY OF CONCLUSIONS AND RECOMMENDATIONS FOR FUTURE STUDIES

The performance studies have treated classes of missions rather than specific missions. This is because interplanetary travel is still in such a primitive state that for many missions, specific quantitative objectives and requirements do not exist; however, the analysis programs should be useful when specific missions are defined. These are the general conclusions reached in this study:

Atmospheric entry requires the highest level of navigation system performance. The meeting of entry corridor constraints requires the greatest accuracy during free-fall or midcourse phases, and navigating during atmospheric entry requires the most accuracy of inertial systems (during non-free-fall phases).

State-of-the-art navigation performance levels appear adequate for all mission phases except preentry approach to a distant planet (Mars). In particular, present DSIF performance seems adequate for all free-fall phases except Martian preentry approach.

State-of-the-art inertial systems are adequate for high thrust and atmospheric entry phases, but they are not sufficiently accurate for unaided inertial guidance of skipout reentry.

State-of-the-art onboard electromagnetic sensors (trackers and sextants) are adequate for planetary orbit navigation but not for those interplanetary midcourse phases which lead directly to atmospheric entry.

The rest of this section discusses these conclusions and the supporting data for each mission phase.

4.1 FREE-FALL STUDY CONCLUSIONS

The free-fall performance studies are described in Paragraph 3.1. The analysis of two complete interplanetary missions, described in Paragraph 3.1.3, indicates that the most critical phases of these missions is the approach to atmospheric entry; therefore, additional studies of approach phases were made. They are described in Paragraph 3.1.4, and representative results are summarized in Table 4-1.

The safe-entry-angle corridor widths shown in the table are for an Apollo Command Module type of entry vehicle. The navigation position and velocity uncertainties have been converted to uncertainty in entry angle, and the numbers in the table are 6σ entry angle uncertainties, so there is an attainable $\pm 3\sigma$ corridor to compare with the safe corridor.

MISSION PHASE	NAVIGATION CONFIGURATION (See Table B-8 for Error Budget)	NAVIGATION UNCERTAINTY IN REENTRY ANGLE γ (arc-minutes)	ENTRY ANGLE SAFE CORRIDOR WIDTH (arc-minutes)
Earth approach at 12.02 km/sec from Three-Planet Grand Tour	SOA Horizon Sensor (H 11)	2150	200
	BSOA Horizon Sensor (H 31)	900	
	SOA Ground Tracking (G 11)	25	
Earth approach at 13.95 km/sec from Venus-Mars Swing-by	SOA Horizon Sensor (H 11: σ = 3.0 arc-minutes; σ_b = 6.0 arc-minutes)	3600	160
	BSOA Horizon Sensor (H 21: σ = 0.6 arc-minutes; σ_b = 0.6 arc-minutes)	480	
	BSOA Horizon Sensor (H 40: σ = 0.17 arc-minutes; σ_b = 0)	84	
Martian approach at 5.67 km/sec from Capture Mission	SOA Horizon Sensor (H 11: σ = 3.0 arc-minutes; σ_b = 6.0 arc-minutes)	1050	450
	SOA Space Sextant (S 11: σ = 3.0 arc-minutes; σ_b = 6.0 arc-minutes)	975	
	SOA Horizon Sensor and Ground Tracker (H 11 and G 11)	210	
Martian approach at 12.63 km/sec from Martian Flyby	SOA Horizon Sensor (H 11)	5750	14
	SOA Horizon Sensor and Ground Tracker (H 11 and G 11)	900	
	BSOA Horizon Sensor and Ground Tracker (H 40 and and G 10)	210	

Table 4-1. Performance Assessment Summary for Planetary Approach

The table shows that ground tracking (DSIF) provides a wide safety margin for Earth entry, but that onboard horizon-scanner navigation is not adequate. It also shows that for approach to Mars, no present methods are adequate unless the approach speed is drastically reduced (below Mars escape speed).

Special studies concerning free-fall navigation were described in Paragraph 3.1.6, and the results suggest certain conclusions:

The navigation computation employed for free-fall should incorporate orbit rectification capability. This is indicated by the results (Table 3-5) of the simulations in earth orbit. These show that, without orbit rectification, the navigation errors attributable to nonlinearity are extremely large (approximately 10 kilometers) after only one revolution for an initial perturbation from nominal of about 30 meters per second and that, beyond one orbit, they increase very rapidly. With rectification, the errors due to this nonlinearity effect appear to be bounded and masked by the effects of observation errors.

A study of free-fall navigation by sextant indicates that the use of a star catalog of five "optimally" selected stars yields performance notably better than that of fewer stars, but that increasing this even to a very large star catalog does not improve navigation accuracy.

The principal guidance-and-navigation obstacle to successful travel to Mars (and to other planets, although travel to them should be studied using the programs developed in this study) is the inaccuracy of navigation in the Mars approach phase. Therefore, navigation during the Mars approach phase should be studied further to establish more precise performance levels for a greater range of system configurations, and a thorough state-of-the-art survey of all sensor types that might be used during approach to track or scan Mars directly from a spacecraft should be conducted.

A study of a wider variety of entry vehicle configurations should also be undertaken to determine how much the entry corridor width restrictions at Mars might be relaxed.

4.2 ATMOSPHERIC ENTRY STUDY CONCLUSIONS

The atmospheric entry and powered flight phases of interplanetary flight are the only phases which involve sustained nongravitational accelerations and are thus the phases which establish the accuracy requirements for inertial measurement systems. The studies described in Paragraphs 3.2 and 3.3 have shown that atmospheric entry requires inertial system performance greater than that required for the powered flight (thrusting) phases.

In particular, it can be concluded that current inertial system capability is adequate for unaided inertial navigation of direct (single pass) entry trajectories but inadequate for skipout entry. This is shown in the study results summarized in Table 4-2.

MISSION PHASE	INERTIAL NAVIGATION SYSTEM DEFINITION	MAXIMUM SEMI-AXIS OF TERMINAL ERROR ELLIPSOID			
		Position (km)		Velocity (m/sec)	
		$P_o = 0$	$P_o = P_{nom}$	$P_o = 0$	$P_o = P_{nom}$
10A Single-pass reentry with pitch modulation control	Gimballed Budget A	1.70	4.02	8.37	8.73
	Gimballed Budget B	1.16	3.99	5.49	6.05
	Strapdown, Rate Gyro	71.75	71.77	454.08	454.08
	Strapdown, RIG	1.51	3.99	7.05	7.50
10B Single-pass reentry without pitch modulation control	Gimballed Budget A	2.95	4.66	8.39	8.68
	Gimballed Budget B	2.06	4.60	5.71	6.19
	Strapdown, Rate Gyro	243.76	243.77	932.95	932.95
	Strapdown, RIG	3.49	4.67	10.17	10.36
11A Skipout with 280° central angle	Gimballed Budget A	26.82	49.42	23.33	42.58
	Gimballed Budget B	22.75	47.34	19.74	40.72
	Strapdown, Rate Gyro	106.52	106.53	446.62	446.63
	Strapdown, RIG	27.59	49.81	23.67	42.77
11B Skipout with 80° central angle	Gimballed Budget A	6.22	10.73	6.30	10.36
	Gimballed Budget B	5.00	10.06	4.97	9.66
	Strapdown, Rate Gyro	64.76	65.12	234.83	234.84
	Strapdown, RIG	5.24	10.35	5.31	10.04

Table 4-2. Summary of All-Inertial Reentry Guidance Performance Assessment Results

In this table the terminal errors are 1σ errors at the point at which the vehicle has slowed to Mach 1, or about 20 kilometers altitude. The trajectory data is given specifically in Table B-18 and the error budgets in Tables B-16 and B-17. The Budget A system represents an Apollo type of inertial measurement capability. The conclusion stated above is based on this data, and the assumption that a 1σ error of about 5 kilometers is the maximum permissible. The figures in the column headed "$P_0 = P_{nom}$" include the effect of initial uncertainties assuming DSIF navigation in free-fall.

The results of studying the performance of aided-inertial systems for the skipout trajectories are summarized in Table 4-3. This data supports the conclusion that ground tracking during the skipout provides adequate performance for these trajectories but that current horizon scanner performance is marginal for longer skipouts (Trajectory 11A). These results also suggest that alternative navigation configurations for use during skipouts should be studied further since the skipout approach to entry has many advantages and since it would seem desirable to have complete onboard capability to navigate and guide during such entry phases.

It can be concluded from studies of atmospheric braking at Mars that such a maneuver can measure the Martian atmosphere. The specific results of these studies are listed in Tables B-28 and B-29 of Section III. Specifically, these results indicate that the uncertainty in Martian atmospheric "sea level" density would be reduced by about one order of magnitude using inertial measurement unit data together with the free-fall navigation data (preceding the entry) and would be reduced even more if radio altimeter (range and range rate) measurements could be made during the pass through the atmosphere.

4.3 POWERED FLIGHT PHASE STUDY CONCLUSIONS

The results of the powered-flight guidance and navigation studies, described in Paragraph 3.3, indicate that the requirements for these phases of interplanetary travel are less demanding than the atmospheric phases. A summary of results is shown in Table 4-4. The system error budgets are given in Tables 3-18 and 3-19 , and the trajectory data is given in Table 3-20 .

4.4 LOW THRUST STUDY CONCLUSIONS

The navigation performance assessment studies for low thrust interplanetary flight phases are represented by the results for an Earth-Mars transfer phase summarized in Table 4-5. The results are shown for various combinations of electromagnetic sensors and inertial systems. In the table, G1 represents present DSIF and P_1 , P_2 represent state-of-the-art planet tracker performance, P_2 representing a tracker with considerably greater random noise but with the same bias uncertainty. The

MISSION PHASE	INERTIAL GUIDANCE SYSTEM	FREE-FALL NAVIGATION SENSOR	MAXIMUM SEMI-AXIS TERMINAL ERROR ELLIPSOID	
			Position (km)	Velocity (m/sec)
11A	Gimballed Budget A	Horizon Scanner ($1\sigma = 0.05°$)	7.23	6.69
		Horizon Scanner ($1\sigma = 0.01°$)	3.82	4.61
		Horizon Scanner ($1\sigma = 0.005°$)	1.21	4.15
		Ground Tracker (SOA)	1.01	4.13
	Gimballed Budget B	Horizon Scanner ($1\sigma = 0.05°$)	7.19	6.34
		Horizon Scanner ($1\sigma = 1.01°$)	3.80	3.88
		Horizon Scanner ($1\sigma = 0.005°$)	1.13	3.21
		Ground Tracker (SOA)	0.81	3.07
	Strapdown (RIG)	Horizon Scanner ($1\sigma = 0.05°$)	7.66	6.76
		Horizon Scanner ($1\sigma = 0.01°$)	4.70	4.39
		Horizon Scanner ($1\sigma = 0.005°$)	1.70	3.62
		Ground Tracker (SOA)	0.89	3.39
11B	Gimballed Budget A	Horizon Scanner ($1\sigma = 0.05°$)	1.72	4.07
		Horizon Scanner ($1\sigma = 0.01°$)	0.68	3.92
		Ground Tracker (SOA)	0.52	3.91
	Gimballed Budget B	Horizon Scanner ($1\sigma = 0.05°$)	1.62	2.87
		Horizon Scanner ($1\sigma = 0.01°$)	0.61	2.65
		Ground Tracker (SOA)	0.41	2.63
	Strapdown (RIG)	Horizon Scanner ($1\sigma = 0.05°$)	1.70	2.65
		Horizon Scanner ($1\sigma = 0.01°$)	0.60	2.31
		Ground Tracker (SOA)	0.42	2.31
	Strapdown (Rate Gyros)	Horizon Scanner ($1\sigma = 0.05°$)	27.74	234.76
		Horizon Scanner ($1\sigma = 0.01°$)	27.67	234.76
		Ground Tracker (SOA)	27.67	234.76

Table 4-3. Summary of Performance Assessment Results for Single-Skipout Trajectories Which Use Aiding Navigation in Free-Fall (Nominal Initial Errors).

POWERED FLIGHT PHASE	GUIDANCE SYSTEM	MAXIMUM SEMI-AXIS OF TERMINAL ERROR ELLIPSOID	
		Position (km)	Velocity (m/sec)
5A Inject into Mars transfer from 185 km Earth parking orbit	Gimballed Budget A Gimballed Budget B Strapdown Rate Gyro Strapdown Rate-Integral Gyro	0.202 0.207 0.295 0.208	1.25 1.20 2.02 1.27
5B Deboost into 4633 km parking orbit at Mars	Gimballed Budget A Gimballed Budget B Strapdown Rate Gyro Strapdown Rate-Integral Gyro	0.080 0.079 0.108 0.080	0.66 0.64 0.93 0.66
6 Trajectory change at Mars pericenter in flyby mission	Gimballed Budget A Gimballed Budget B Strapdown Rate Gyro Strapdown Rate-Integral Gyro	0.00012 0.00012 0.00017 0.00012	0.025 0.023 0.033 0.024
7 Midcourse Correction	Gimballed Budget A Gimballed Budget B Strapdown Rate Gyro Strapdown Rate-Integral Gyro	0.00003 0.00003 0.00004 0.00003	0.011 0.011 0.016 0.011
8 Launch from Mars surface into 345 km parking orbit	Gimballed Budget A Gimballed Budget B Strapdown Rate Gyro Strapdown Rate-Integral Gyro	0.603 0.570 1.956 0.512	1.841 1.737 3.868 1.55
9 Deboost prior to atmospheric reentry at Earth	Gimballed Budget A Gimballed Budget B Strapdown Rate Gyro Strapdown Rate-Integral Gyro	0.240 0.234 0.350 0.243	1.41 1.35 2.41 1.45

Table 4-4. Performance Assessment Study Results for Powered Flight Phases

EMS	Maximum Terminal Error	IMU		
		0	IG1	IC1
G1	Position (km)	1780.	66.4	45.4
	Velocity (m/sec)	18.8	0.02	0.009
P1	Position (km)	3760.	40.3	25.2
	Velocity (m/sec)	47.7	0.38	0.19
P2	Position (km)	5550.	571.	519.
	Velocity (m/sec)	62.4	4.2	3.4
G1 - P1	Position (km)	5.6	1.2	1.1
	Velocity (m/sec)	0.3	0.003	0.0003

Table 4-5. Summary of Terminal Accuracy of Typical Navigation Systems for Earth-Mars Low-Thrust Trajectory HTR2

inertial systems IG1 and IC1 have Apollo level error budgets, but IC1 refers to a system for which the instruments are rotated slowly in an attempt to average out bias errors.

It can be concluded that the rotation is not very helpful. It can also be concluded that, for this mission, combining at least two measurement sources provides much better performance than any single type of measurement; in particular, DSIF combined with either an inertial measurement unit or a planet tracker should provide adequate performance.

The study of neighboring optimum guidance for low thrust travel indicates that this guidance law yields convergent results over a very wide range of departure from the optimal trajectory, up to departures as large as 1/20 astronomical unit at the terminus of the trajectory. These results are shown in Figure 3-14 and 3-15 of Section III.

REFERENCES

1. Sorenson, H. W., Z. Solomon, and T. Kido, "Application of Weiner-Kalman Filter Theory to Orbit Determination," AC Spark Plug Report, August 1963.

2. Lawden, D. F., "Optimal Programme for Corrective Manoeuvres," Astronautica Acta, Volume VI, 4th Quarter, pp. 195-205.

3. Breakwell, J. V., "The Spacing of Corrective Thrusts in Interplanetary Navigation," Advances in Astronautical Sciences, Volume V, Plenum Press (New York, 1960).

4. Goodyear, W. H., "A General Method for the Computation of Cartesian Coordinates and Partial Derivatives of the Two Body Problem," NASA CR-522 (Greenbelt, September 1966).

APPENDIX A

MATHEMATICAL MODEL

FOR

PERFORMANCE ASSESSMENT OF SPACE GUIDANCE SYSTEMS

ABSTRACT

This appendix contains the description of the mathematical model which provided the guidelines for the development of digital computer programs employed in the Performance Assessment of Aided-Inertial Space Guidance Systems. A general discussion concerning the basic assumptions of the general structure of the mathematical model is followed by a detailed description for different mission phases. Powered flight, free-fall, and re-entry are considered for space missions using conventional high-level chemical propulsion. The last section contains a description of the mathematical model used for low thrust space missions.

TABLE OF CONTENTS

SECTION	TITLE	PAGE
1.	INTRODUCTION	A-1
2.	GENERAL DISCUSSION	A-2
	2.1 BASIC ASSUMPTIONS	A-2
	2.2 THE GUIDANCE AND NAVIGATION PROBLEMS AND THEIR SOLUTION	A-6
	2.3 THE GENERAL STRUCTURE OF THE MATHEMATICAL MODEL	A-8
	2.4 SENSORS	A-13
	2.4.1 Electromagnetic Sensors	A-13
	2.4.2 Observation Matrices for Electromagnetic Sensors	A-18
	2.4.3 Inertial Measurement Unit (IMU)	A-24
	2.5 MISCELLANEOUS REMARKS	A-27
3.	PERFORMANCE ASSESSMENT OF ALL-INERTIAL BOOST AND RE-ENTRY GUIDANCE SYSTEMS	A-28
	3.1 NOMINAL POWERED FLIGHT TRAJECTORY	A-28
	3.1.1 Coordinate Systems	A-28
	3.1.2 Environmental Models	A-30
	3.1.3 Missile Dynamics	A-31
	3.1.4 Autopilot Model	A-33
	3.1.5 Guidance Schemes	A-33
	3.2 IMU ERROR MODEL	A-37
	3.2.1 Inertial Measurement Unit Configuration	A-38
	3.2.2 Instrument Error Models	A-39
	3.3 ERROR ANALYSIS	A-43
4.	FREE-FALL MISSIONS	A-46
	4.1 TRAJECTORY	A-46
	4.1.1 Nominal Trajectory	A-46
	4.1.2 Linear System Matrices	A-50
	4.1.3 Actual Trajectory	A-54
	4.2 SENSORS	A-55

TABLE OF CONTENTS

SECTION	TITLE	PAGE
4.3	NAVIGATION	A-55
4.3.1	The State Vector	A-56
4.3.2	Orbit Rectification	A-57
4.3.3	Square-root Kalman Filter	A-58
4.3.4	Compensation for Computational Errors	A-58
4.3.5	Variable Computer Word-length	A-58
4.4	GUIDANCE	A-58
4.4.1	Determination of the Desired Velocity Correction	A-59
4.4.2	Timing of the Velocity Corrections	A-60
4.4.3	Implementation of the Correction	A-61
4.4.4	Relation to the General Guidance Problem	A-62
5.	RE-ENTRY MISSIONS	
5.1	TRAJECTORY	A-63
5.1.1	Nominal Trajectory	A-63
5.1.2	Linear System Matrices	A-72
5.1.3	Actual Trajectory	A-78
5.2	SENSORS	A-78
5.2.1	Measurement Errors	A-79
5.2.2	IMU Error Model	A-79
5.3	NAVIGATION	A-81
5.3.1	The State Vector	A-82
5.3.2	Miscellany	A-82
5.4	GUIDANCE	A-83
6.	LOW-THRUST MISSIONS	A-84
6.1	TRAJECTORY	A-84
6.1.1	Nominal Trajectory	A-84
6.1.2	Linear System Matrices	A-87
6.1.3	Actual Trajectory	A-88
6.2	SENSORS	A-89
6.2.1	Electromagnetic Sensor Errors	A-89
6.2.2	IMU Error Model	A-90

TABLE OF CONTENTS

SECTION		TITLE	PAGE
	6.3	NAVIGATION	A-90
	6.3.1	Form of the Filter Equations	A-90
	6.3.2	The State Vector	A-93
	6.4	GUIDANCE	A-94
	6.4.1	Lambda Matrix Control	A-95
	6.4.2	Neighboring Optimum Control	A-95

SECTION I

INTRODUCTION

One of the objectives of this study has been to develop the digital computer programs required to analyze and assess the performance of the guidance and navigation systems for future interplanetary space missions. This report states and describes the assumptions and mathematical model upon which these programs are based.

The programs are designed to deal with several different types of missions, and it is natural to discuss the programs in these terms. There are four general mission phases that have been considered. They are referred to hereafter as boost, free-fall, re-entry, and low-thrust. These terms are defined briefly below. The general formulation of the mathematical model for these phases is described in general in Section II and more specifically in Sections III through VI.

BOOST: The term "boost" is meant to encompass phases of those missions that require the utilization of a vehicle with an engine capable of producing a large acceleration (i.e., accelerations of the same order of magnitude as the gravitational acceleration or greater). This would include the launch phase from Earth or some other planet, injection into an interplanetary trajectory, trajectory change maneuvers in flyby missions, and deboost for planetary capture.

FREE-FALL: The term "free-fall" refers to those portions of a mission in which the motion of the vehicle is influenced primarily by the gravitational attractions of the Sun and the planets. These missions can include small midcourse corrections that are determined according to some guidance criterion and which are implemented by thrust devices aboard the vehicle.

RE-ENTRY: The re-entry phase of a mission begins when the vehicle enters the atmosphere of a planet (e.g., Earth or Mars) and terminates at the start of the final descent phase. In this phase, the vehicle is controlled aerodynamically rather than by propulsive devices.

LOW-THRUST: In some projected missions of long duration, the vehicle is to be subjected to a small but continual acceleration (i.e., less than 10^{-3} g's) resulting from an electrical propulsion system. Vehicles containing a device of this nature are referred to as low-thrust vehicles.

The specific details relating to the guidance and navigation systems differ from one phase to the next because of the varying requirements of each. But all of these phases do have a common basis and many of the same general techniques can be utilized. In Section II, the general assumptions and mathematical formulation are discussed. In this section, the commonality is emphasized. Details regarding the four mission phases are presented in Sections III through VI.

SECTION II

GENERAL DISCUSSION

Before becoming too involved with the discussion, the meaning of the terms "guidance system" and "navigation system" as used herein are defined.

GUIDANCE SYSTEM: It is the function of the guidance system to determine the control action that is required to cause the vehicle to satisfy prespecified trajectory constraints. For example, in a free-fall trajectory, the midcourse corrections can be determined so that the position of the spacecraft at the terminal time assumes prespecified values. As another example, the angle of attack and roll angle during re-entry must be chosen so that the deceleration of the spacecraft does not exceed certain limits during the flight and must also cause terminal constraints on the position and velocity to be satisfied.

In a spacecraft, the guidance system will determine the desired control action, but it is the control system that actually transforms the guidance commands into signals that activate the physical control devices (e.g., the propulsive unit). In the simulations described here, the errors introduced by the control system are treated as random forces acting upon the dynamical system. The character of the control system is implicitly contained in the statistical model of these random errors.

NAVIGATION SYSTEM: The commands computed by the guidance system are based upon knowledge of the current state of the vehicle. It is the function of the navigation system to determine the state of the vehicle, which is not necessarily restricted to the position and velocity, from available measurement data. These data are imprecise because of inaccuracies inherent in the physical devices, so the determination provides at best an approximation of the true situation. As described below, optimal filtering techniques are used to estimate the state.

With these general definitions in mind, a statement and discussion of the basic assumptions and the general mathematical model follows. The assumptions are stated and discussed in Section 2.1, and the general solution of the guidance and navigation problem is presented in Section 2.2. In Section 2.3, the general structure of the mathematical model is discussed. The sensors considered in the study are to a major extent phase-independent. They are discussed in Section 2.4.

2.1 BASIC ASSUMPTIONS

Reference is made frequently in the succeeding discussion of the state of the system. The state of the system at each time is considered to be described by a collection of quantities, including at least the position and velocity of the spacecraft. This collection

is referred to as the state vector. The additional components of the state vector will depend upon the mission phase and sensor configuration. For example, for the re-entry phase, the lift and drag coefficients are included as state variables. The description of the state vector for each phase is contained in the appropriate section below. In some instances when the state vector contains components in addition to the position and velocity, it is referred to as the augmented state.

There are two fundamental equations that describe the system for each phase. First, the state $\underline{X}$ is assumed to evolve according to a known relation

$$\dot{\underline{X}} = \underline{f}(\underline{X}, \underline{U}) + \underline{w} \tag{A-1}$$

where the p-dimensional vector $\underline{U}$ represents the control parameters and the n-dimensional vector $\underline{w}$ describes the stochastic effects acting upon the plant. Second, the measurement data $\underline{Z}$ are assumed at each time to be related to the state according to

$$\underline{Z} = \underline{h}(\underline{X}) + \underline{v} \tag{A-2}$$

where $\underline{v}$ describes the stochastic effects that cause the measurement data to be imprecise. More specific descriptions of (A-1) and (A-2) will appear below. A more general form could be assumed for (A-1) and (A-2) but would not be relevant to this study.

From (A-1) and (A-2) two basic assumptions are made.

ASSUMPTION 1

Equations (A-1) and (A-2) provide the general form for the plant and measurement systems. This further implies that the relations $\underline{f}$ and $\underline{h}$ are precisely known.

ASSUMPTION 2

The statistical character of the noise processes $\underline{w}$ and $\underline{v}$ are known gaussian processes.

The requirement that $\underline{w}$ and $\underline{v}$ be gaussian is somewhat artificial but reflects the fact that it is well nigh impossible to obtain information about the third and higher order moments of a physical device.

Certainly, the statement that $\underline{w}$ and $\underline{v}$ are gaussian does not complete the description of the noise processes. However, it is assumed that the remaining characteristics are known and their discussion is deferred until later in this section.

It is now possible to formulate the general navigation and guidance problems more precisely. But it is not possible to solve the estimation and control problems that result. A complete theory is available only when the system equations are linear, so it becomes necessary to approximate (A-1) and (A-2) in order to obtain a more tractable problem.

Suppose that values for the control variables $\underline{U}^*(t)$, $t_o \leq t < t_f$, and for the initial state $\underline{X}(t_o)$ exist that provide a solution of the deterministic equation

$$\dot{\underline{\xi}} = \underline{f}(\underline{\xi}, \underline{U}^*) \tag{A-3}$$

Let the solution of (A-3) be denoted by $\underline{X}^*(t)$ and be designated as the <u>nominal</u> or <u>reference</u> trajectory.

Then, suppose that $\underline{f}$ can be rewritten in a Taylor Series relative to the nominal values $\underline{X}^*$, $\underline{U}^*$ such that deviations of any actual trajectory can be described by

$$\dot{\underline{x}} = F(t)\,\underline{x} + G(t)\,\underline{u} + \underline{w} \tag{A-4}$$

where

$$\underline{x} \overset{Df}{=} \underline{X} - \underline{X}^*$$

$$\underline{u} \overset{Df}{=} \underline{U} - \underline{U}^*$$

The F(t) and G(t) are matrices whose elements are partial derivatives.

$$F(t) \overset{Df}{=} \left(\frac{\partial \underline{f}}{\partial \underline{X}}\right) \Big/ \text{evaluated with } \underline{X}^*,\ \underline{U}^*$$

$$G(t) \overset{Df}{=} \left(\frac{\partial \underline{f}}{\partial \underline{U}}\right) \Big/ \text{evaluated with } \underline{X}^*,\ \underline{U}^*$$

The determination of these matrices constitute one of the major computations in the computer program.

Next, the nonlinear measurement equation must also be written as the first order Taylor Series expansion relative to $\underline{X}^*$. Then,

$$\underline{z} = H(t)\,\underline{x} + \underline{v} \tag{A-5}$$

where

$$\underline{z} \overset{Df}{=} \underline{Z} - \underline{Z}^*$$

and the (m x n) matrix H(t) is composed of partial derivatives.

$$H(t) = \left(\frac{\partial \underline{h}}{\partial \underline{X}} \right) \Big/ \text{evaluated with } \underline{X}^*, \ \underline{U}^*.$$

This matrix will also play an important role.

ASSUMPTION 3

Nominal values for the state $\underline{X}^*$ and control $\underline{U}^*$ must exist that permit (A-1) and (A-2) to be described by the linear perturbation Equations (A-4) and (A-5).

These three assumptions are fundamental to the entire study. The validity of the third is certainly of paramount importance in all of the conclusions that derive from these computer programs.

One additional aspect of the problem should be noted. At this point, it is possible to formulate the estimation and control problems relative to either a time-continuous or a time-discrete model. The time-continuous version would be natural since the plant is described by differential equations. Several reasons led to the use of a primarily time-discrete model. (The low-thrust phase belies this statement to a certain extent, but this exception will be dealt with in Section VI.) The principal reasons for using the time-discrete model are the following.

1. Measurement data are usually available only at discrete times
2. The control is determined with the aid of a digital computer, so it is changed only at discrete times
3. In the time-continuous case, the $\underline{w}$ and $\underline{v}$ are assumed to be white noise processes. But such processes are physically unrealizable and as such seem to be unnecessarily restrictive.

Because the time-discrete formulation is utilized, (A-4) must be reduced to a difference equation. This is accomplished using well-established techniques involving the state-transition matrix, $\Phi_{k,k-1}$, to yield

$$\underline{x}_k = \Phi_{k,k-1}\underline{x}_{k-1} + \Gamma_{k,k-1}\underline{u}_{k-1} + \underline{w}_{k-1} \qquad \text{(A-6)}$$

Acknowledging the discrete nature of the measurement data, (A-5) can be restated as

$$\underline{z}_k = H_k \underline{x}_k + \underline{v}_k \tag{A-7}$$

The character of the noise sequences $\underline{w}_k$ and $\underline{v}_k$ can now be made more explicit. The noise is assumed to be uncorrelated from one sampling time to the next; furthermore, the plant noise will not be correlated with the measurement noise. The statistics of the plant noise are established from physical considerations and can be assumed to arise from control system errors, uncertainties in the physical model (e.g., radiation pressure), errors arising from computational inaccuracies, etc. The statistics of the measurement noise are determined from the characteristics of the measurement devices.

2.2 THE GUIDANCE AND NAVIGATION PROBLEMS AND THEIR SOLUTION

In this study, the performance of the guidance and navigation systems is assessed relative to the linear systems (A-6) and (A-7). To navigate, an estimate $\hat{x}_k$ of the state perturbation $\underline{x}_k$ is obtained so the estimate of the state $\underline{X}_k$ is given as

$$\hat{\underline{X}}_k = \underline{X}_k^* + \hat{\underline{x}}_k$$

The guidance problem entails the determination of the control perturbation $\underline{u}_k$ so the actual control is

$$\underline{U}_k = \underline{U}_k^* + \underline{u}_k$$

The problem of estimating the state perturbation as considered here can be stated in the following manner.

NAVIGATION PROBLEM: Determine the estimate $\hat{\underline{x}}_k$ of the state perturbation $\underline{x}_k$ as that function of all past and current measurement data, denoted* as $\underline{z}^k$, that minimizes the mean-square error

$$E[(\hat{\underline{x}}_k - \underline{x}_k)^T (\hat{\underline{x}}_k - \underline{x}_k)]$$

The solution of this problem is well-known and is discussed next.

---

* The superscript k is used to denote the collection $\underline{z}_o, \underline{z}_1, \ldots, z_k$

The guidance problem is posed in terms of determining the control perturbation $\underline{u}_k$. The nominal control policy $\underline{U}^*$ is generally established under the requirement that certain terminal conditions be satisfied exactly. This is reasonable since the problem of establishing the nominal trajectory is deterministic in nature. However, the actual trajectory contains stochastic effects so it does not appear entirely desirable to require the vehicle to satisfy these constraints exactly. Instead, it could be considered more practical to minimize the deviation in some sense and thereby require only that the vehicle be in a neighborhood of the target. This aspect is further emphasized because terminal control laws generally tend to become unstable as the terminal time is approached and some rather violent maneuvers could be commanded. Thus, the primary guidance problem is stated in the following manner.

GUIDANCE PROBLEM: Choose the control perturbation $\underline{u}_k$ as a function of the measurement data so that the expected value of the performance index

$$V_N = \sum_{i=1}^{N} (\underline{x}_i^T W_i^X \underline{x}_i + \underline{u}_{i-1}^T W_{i-1}^U \underline{u}_{i-1}) \tag{A-8}$$

is minimized. The non-negative definite, symmetric matrices W_i^X and W_{i-1}^U are arbitrary and can be selected to limit the amount of control and/or state perturbation along the trajectory.

The solution of this guidance problem is well-known and is stated in the next section. The control policy that results is referred to as <u>Lambda Matrix Control</u>.

When the nominal control policy is optimal in some well-defined sense, the perturbation control can be selected so that the actual control (i.e., $\underline{U}^* + \underline{u}$) is optimal in the same sense. The control policy resulting from this criterion has been referred to as <u>Neighboring Optimal Control</u> and is considered in the low-thrust program. The Lambda Matrix Control policy is also included in this program so that the effectiveness of the two can be compared directly.

It has been shown that the solution of the stochastic linear control problem with the quadratic performance index (A-8) is described in the following manner.

SEPARATION PRINCIPLE: For the model described by Equations (A-6), (A-7), and (A-8), the optimal stochastic control law is described by

$$\underline{u}_k = -\Lambda_{k+1} \Phi_{k+1,k} \hat{\underline{x}}_k \tag{A-9}$$

where:

1. The form of the guidance law as given by (A-9) and the precise definition of the Λ_{k+1} can be obtained by considering the related deterministic control. That is, suppose that the plant is described by

$$\underline{x}_k = \Phi_{k,k-1}\underline{x}_{k-1} + \Gamma_{k,k-1}\underline{u}_{k-1}$$

and that the state is measured exactly

$$\underline{z}_k \equiv \underline{x}_k.$$

Then, choose the control to minimize (A-9) without stochastic considerations. The guidance law for this problem involves $\underline{x}_k$ directly. As indicated by (A-9), the stochastic control problem is obtained by replacing $\underline{x}_k$ with the mean-square estimate $\hat{\underline{x}}_k$. The equations defining the Λ_{k+1} will be stated in Section 2.3.

2. The mean-square estimate $\hat{\underline{x}}_k$ for a system containing control is obtained by treating the $\Gamma_{k,k-1}\underline{u}_{k-1}$ as a known function. The control terms then enter in a trivial manner. The general filter equations are stated in Section 2.3.

Then, under the assumption that the linear model is valid, the navigation and guidance is achieved in an optimal manner insofar as the stated performance indices are concerned.

2.3 THE GENERAL STRUCTURE OF THE MATHEMATICAL MODEL

The discussion of the preceding sections has covered the salient features involved in the performance assessment of the guidance and navigation system of space vehicles. In this section, the general structure of the mathematical model for the free-fall, re-entry, and low-thrust programs will be made more precise. The character of the boost programs is less sophisticated than these programs and is discussed in Section III.

The structure can be exhibited by considering three aspects of the performance assessment problem. These are:

1. Mission and control policy specification and nominal trajectory generation.
2. Specification of the sensor configuration.
3. Performance assessment based on linear techniques.

The specification of the mission essentially establishes the program that must be used for the performance assessment (i.e., boost, free-fall, re-entry, or low-thrust).

The basic control policy that is utilized is defined by the choice of mission. These policies are discussed in more detail in Sections III through VI. For each mission phase the following computations relating to the determination of the nominal as required by Assumption 3 are performed.

1. Based on the nonlinear equations of motion

$$\dot{\underline{\xi}} = \underline{f}\,(\underline{\xi}, \underline{U})$$

a nominal control function $\underline{U}^*(t)$, $t_o \leq t \leq t_N$, must be determined that will produce a nominal trajectory with prespecified characteristics. For example, for the free-fall phase, the vehicle may be required to arrive at some position relative to a planet at a specific time. A more stringent requirement might be imposed on a re-entry vehicle. For example, it might be required to arrive at a desired position with a given velocity and, moreover, would not be permitted to violate heating and deceleration constraints along the trajectory.

2. After the nominal trajectory is established, the matrices associated with the linear systems (A-4) can be computed (i.e., the F(t) and G(t) matrices). These matrices are entirely determined by the nominal trajectory. Then the differential equation must be solved and rewritten as a difference equation. This requires the calculation of the state-transition matrix $\Phi_{k,k-1}$ and the control gain matrix $\Gamma_{k,k-1}$.

As stated in Item B, the sensor configuration must be defined. This defines the quantities that are to be measured and leads to the following computations.

3. The nature of the sensor defines the relation $\underline{h}$ of Equation (A-2). Based on the nominal trajectory data and the sampling schedule, the nominal measurement values

$$\underline{Z}_k^* = \underline{h}\,(\underline{X}_k^*)$$

can be determined.

4. The observation matrix H of (A-7) is determined from the sensor characteristics and is evaluated using the nominal values of the state. The sensors are discussed further in Section 2.4.

After the tasks implied by Items A and B have been completed, the performance assessment can proceed. This is accomplished through the application of linear guidance and navigation techniques.

For this study, the assessment has involved two types of calculations. The first type, a linear variance analysis, involves the calculation of the statistics — in terms of covariances — of the trajectory perturbations, and of the errors in the estimated (via the simulated navigation method) state.

A linear variance analysis would be adequate if the linear system were an exact description of the perturbations. Since it is only approximate, actual trajectories are simulated. This simulation utilizes noise generators to simulate the plant and measurement noise and provides the capability of a complete Monte Carlo simulation. The calculation of an actual simulated trajectory requires the following calculations.

1. The initial conditions for the actual trajectory are established using a gaussian random number generator according to the a priori statistics defined for $\underline{x}_0$. Generally, the mean value of $\underline{X}_0$ is the initial condition of the nominal trajectory $\underline{X}^*_0$ so that the expected value of the perturbation $\underline{x}_0$ is zero. The covariance of the perturbation is denoted as the non-negative-definite, symmetric matrix M_0.

2. The nonlinear equations of motion are used to compute the actual trajectory. The control is established as the sum of the nominal control $\underline{U}^*$ and the perturbation $\underline{u}$ determined from the linear perturbation equations. The calculation and utilization of $\underline{u}$ results in a stochastic feedback control system. The determination of the control perturbation $\underline{u}$ is an integral part of the overall performance assessment.

3. At each sampling time (i.e., at times that new measurement data are available), measurements based on the actual trajectory are determined. These measurement data include the noise values $\underline{v}$ which are obtained from a gaussian random number generator with prescribed statistics. The measurements processed by the linear filter are obtained by differencing the nominal and actual values

$$\underline{z}_k = \underline{h}(\underline{X}_k) - \underline{h}(\underline{X}^*_k) + \underline{v}_k$$

Note that the linear analysis assumes that

$$\underline{h}(\underline{X}_k) - \underline{h}(\underline{X}^*_k) = H_k \underline{x}_k .$$

4. The state perturbation is estimated from the Kalman filter equations using these data. In general, the estimate $\hat{\underline{x}}_k$ is given by

$$\hat{\underline{x}}_k = \hat{\underline{x}}'_k + K_k(\underline{z}_k - H_k \hat{\underline{x}}'_k) \qquad \text{(A-10)}$$

where

$$\hat{\underline{x}}'_k = \Phi_{k,k-1} \hat{\underline{x}}_{k-1} + \underline{f}_{k-1}$$

$$K_k = P'_k H_k^T [H_k P'_k H_k^T + R_k]^{-1}$$

$$P'_k = \Phi_{k,k-1} P_{k-1} \Phi^T_{k,k-1} + Q_{k-1}$$

$$P_k = P'_k - K_k H_k P'_k$$

The R_k and Q_{k-1} are the covariance matrices associated with measurement and plant noises, respectively.

The $\underline{f}_{k-1}$ is treated in two different ways in the programs. In the re-entry performance assessment program, the $\underline{f}_{k-1}$ represents the control effects (i.e., $\Gamma_{k,k-1}\underline{u}_{k-1}$), whereas in the low-thrust performance assessment program, the $\underline{f}_{k-1}$ represents the acceleration measured by the inertial measurement unit (hereafter denoted as the IMU). These aspects are discussed in greater depth in Sections V and VI.

The $\hat{\underline{x}}_k'$ represents the estimate of the state perturbation at t_k based on the data $\underline{z}^{k-1}$. This prediction is computed in a slightly different manner in the low-thrust performance assessment program. See Section VI for additional details.

One aspect relative to the treatment of data from several instruments should be considered. If at a sampling time several instruments provide a total of m measurements, the observation matrix H_k would have an overall dimension of m x n. The matrix $[H_k P_k' H_k^T + R_k]$ would then have dimension (m x m). This matrix must be inverted so if m is large, a numerical problem of significant importance is engendered. Fortunately, this problem can be circumvented because the data from each particular instrument can be processed independently of the data from any other instrument. The maximum dimension of H for any single instrument considered in this study (i.e., the radar) is (4 x n), so only a 4 x 4 matrix has to be inverted. The matrix could be reduced to a scalar except that this would not permit correlation at a specified time between the measurements from the single instrument.

The matrix P_k represents the covariance of the error in the estimate, and as such, provides the basic statistical measure of the adequacy of the navigation system. This matrix is (n x n) where n represents the dimension of the state vector. Since n is at least equal to six, it is not entirely satisfactory to examine the individual elements of the P_k to establish the behavior of the navigation system. Instead, the axes of the associated error ellipsoids are determined and used as the basic measure.

5. The control perturbation is determined from the estimate $\hat{\underline{x}}_k$. As was stated in Section 2.2, the control is

$$\underline{u}_k = - \Lambda_{k+1} \Phi_{k+1,k} \hat{\underline{x}}_k \qquad \text{(A-11)}$$

The control matrix Λ_{k+1} that results from the minimization of (2.4) is

$$\Lambda_{k+1} = (\Gamma^T_{k+1,k}\, \Pi'_{k+1}\, \Gamma_{k+1,k} + W^U_{k-1})^{-1}\, \Gamma^T_{k+1,k}\, \Pi'_{k+1}$$

$$\Pi'_{k+1} = \Phi^T_{k+2,k+1}\, \Pi_{k+2}\, \Phi_{k+2,k+1} + W^X_{k+1}$$

$$\Pi_{k+1} = \Pi'_{k+1} - \Pi'_{k+1}\, \Gamma_{k+1,k}\, \Lambda_{k+1}$$

The similarity between the control equations and the Kalman filter equations has been referred to as a "Duality Principle."

The matrix Π_{N-k} is the dual of the error covariance matrix P_k for an N-stage control policy. It provides one of the important measures of the behavior of the control system. However, the primary consideration of the evaluation of the linear guidance law resides in its ability to satisfactorily meet the original constraints imposed upon the trajectory in the specification of the mission. Since the deviation from the nominal is the basic criterion for evaluating the performance of the guidance system, the covariance of this deviation is computed from

$$M_k \overset{Df}{=} E[\underline{x}_k \underline{x}_k^T]$$

$$= \Phi_{k,k-1}\, (I - \Gamma_{k,k-1}\, \Lambda_k)(M_{k-1} - P_{k-1})(I - \Gamma_{k,k-1}\, \Lambda_k)^T \Phi^T_{k,k-1}$$

$$+ \Phi_{k,k-1}\, P_{k-1}\, \Phi^T_{k,k-1} + Q_{k-1}$$

Thus, the P_k and M_k provide the basic statistical measures of the performance of the navigation and guidance systems.

As mentioned earlier, the low-thrust performance assessment program contains the capability of using a linear control law in addition to the Lambda Matrix controller described above. The Neighboring Optimal Control law is discussed in Section VI.

This completes the general description of the mathematical model and the structure of the computer programs. Specific details for each mission phase are given in Sections III through VI regarding the equations of motion, nominal control policy, and the linear

guidance and navigation equations. The sensors are discussed in Section 2.4 since they are to a major extent phase-independent.

2.4 SENSORS

The sensors that have been included in the performance assessment programs are discussed in this section. Many of the other details (e.g., the equations of motion) are phase-dependent but this is not particularly true of the sensors that provide navigational data. The sensors are separated into two major classes. The acceleration-related measurements obtained from an inertial measuring unit (IMU) constitute one class and all other sensors form the second class. These sensors are referred to as electromagnetic sensors or, occasionally, as aiding instruments. The distinction arises because of the differences between the manner in which the sensors enter the linear model. The electromagnetic sensors enter in the most direct way and are considered first.

In this section every sensor that is simulated in any of the programs is described. Each program uses a subset of the sensors described here. For example, the free-fall performance assessment program does not directly include the IMU since there is no nongravitational acceleration to be measured.

2.4.1 ELECTROMAGNETIC SENSORS

The following electromagnetic sensors can be simulated.

1. Space sextant: measures the angle between a prescribed star and the limb or center of a planet.
2. Horizon sensor: measures the angle subtended by a planet and the direction of the local vertical.
3. Planet tracker: measures the direction from the spacecraft to the center of a distant planet.
4. Ground tracking: measures the range, range rate, and direction of the spacecraft relative to the tracker. The capability of simulating three trackers simultaneously is included.
5. Radio altimeter: measures the radial distance and radial speed from a near planet.

These instruments are described by establishing the relationship between the measured quantities and the state. Once this relation $\underline{h}$ is defined, the observation matrix is determined as the partial derivatives of $\underline{h}$ with respect to $\underline{X}$. These derivatives are evaluated with nominal values of the state at each sampling time to establish H_k. The measured quantities are defined below. The observation matrices are stated thereafter.

Space Sextant

This instrument measures the angle between a star and the edge of a planet. The equations expressing these measurements are

$$\theta_{pb}(t_k) = \cos^{-1}\{\underline{s}(t_k) \cdot \underline{e}_{pb}(t_k)\} - \varkappa\, {}_S\beta^S_{pb}(t_k)$$

where

$$\underline{e}_{pb}(t_k) = -\frac{\underline{R}_{pb}(t_k)}{R_{pb}(t_k)}$$

$$\beta^S_{pb}(t_k) = \sin^{-1}\frac{r_b}{R_{pb}(t_k)}$$

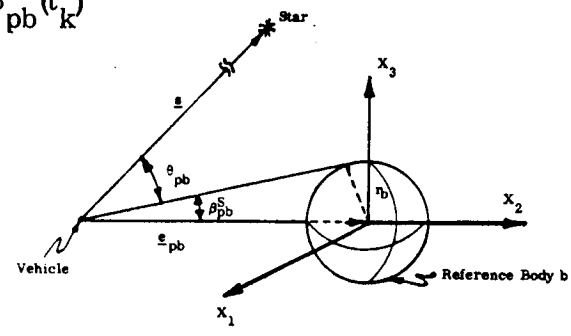

Figure A-1. Space Sextant Measurement Geometry

$$\underline{R}_{pb}(t_k) = \underline{R}\,(t_k) - \underline{R}_{bc}(t_k) \qquad \underline{R}_{bb} = 0$$

r_b = radius of reference body $\qquad b \overset{Df}{=}$ BODY

$\underline{R}_{bc}(t_k)$ = position of reference body b with respect to central body c

and the unit vector from the vehicle to the star is

$$s_j(t_k) = \begin{bmatrix} s_{j1} \\ s_{j2} \\ s_{j3} \end{bmatrix} = \begin{bmatrix} \cos\alpha_j & \cos\delta_j \\ \sin\alpha_j & \cos\delta_j \\ \sin\delta_j & \end{bmatrix}$$

The α_j and δ_j define the right ascension and declimation of the star.

The star that is used at a particular sampling time can be specified arbitrarily or it can be selected to minimize the mean-square error in a prescribed quantity. The optimal star selection option will not be discussed here.

Horizon Sensor

This instrument provides information about three angles.

Local elevation angle:

$$\alpha = -\sin^{-1} \frac{X_3(t_k)}{|\underline{R}(t_k)|}$$

Local azimuth angle:

$$\delta = \sin^{-1} \frac{X_2(t_k)}{[X_1^2(t_k) + X_2^2(t_k)]^{1/2}}$$

Half-subtended angle:

$$\beta^H = \sin^{-1} \frac{r_\ell}{|\underline{R}(t_k)|}$$

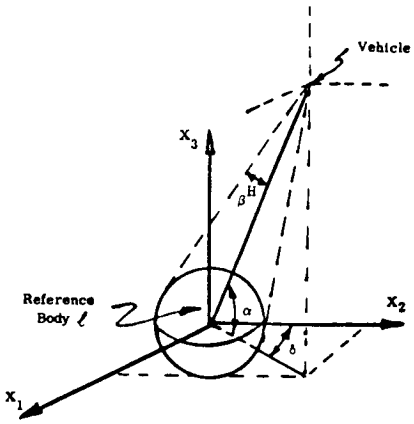

Figure A-2. Horizon Sensor Geometry of Angular Measurements

Planet Tracker

The horizon sensor equations can be reinterpreted as equations for a planet tracker if the information about the subtended angle is ignored.

Ground Tracking

Range, range rate, and angular information is provided according to the following equations.

The range and range rate vector equations are given by

$$\underline{\rho}_i(t_k) = \underline{R}(t_k) - \underline{r}_{iT}(t_k) + \underline{R}_{\ell o}(T_k)$$

$$\dot{\underline{\rho}}_i(t_k) = \underline{V}(t_k) - \dot{\underline{r}}_{iT}(t_k) + \dot{\underline{R}}_{\ell o}(T_k)$$

$$i = 1, 2, 3$$

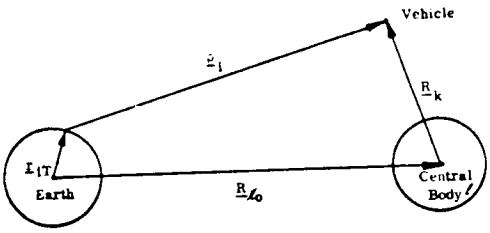

Figure A-3. Range Vector Relationships

where

$$\underline{R}(t_k) \overset{Df}{=} [X_1(t_k),\ X_2(t_k),\ X_3(t_k)]^T \text{ and } \underline{V}(t_k) \overset{Df}{=} [X_4(t_k),\ X_5(t_k),\ X_6(t_k)]^T$$

$\underline{R}_{\ell o}(T_k)$ and $\dot{\underline{R}}_{\ell o}(T_k)$ are the position and velocity of the ℓth planet with respect to the Earth (in equatorial coordinates) obtained from an ephemeris at each epoch time $T_k \longleftrightarrow t_k$.

$$\underline{r}_{iT}(t_k) \overset{Df}{=} \begin{bmatrix} X_{iT}(t_k) \\ Y_{iT}(t_k) \\ Z_{iT}(t_k) \end{bmatrix} = \begin{bmatrix} r_{iT} \cos \varphi_i \cos (\theta_i + \omega t_k) \\ r_{iT} \cos \varphi_i \sin (\theta_i + \omega t_k) \\ r_{iT} \sin \varphi_i \end{bmatrix}$$

and

$$\dot{\underline{r}}_{iT}(t_k) \overset{Df}{=} \begin{bmatrix} -\omega Y_{iT}(t_k) \\ \omega X_{iT}(t_k) \\ 0 \end{bmatrix}$$

are the tracker position and velocity in an Earth-centered system, see Figure A-4.

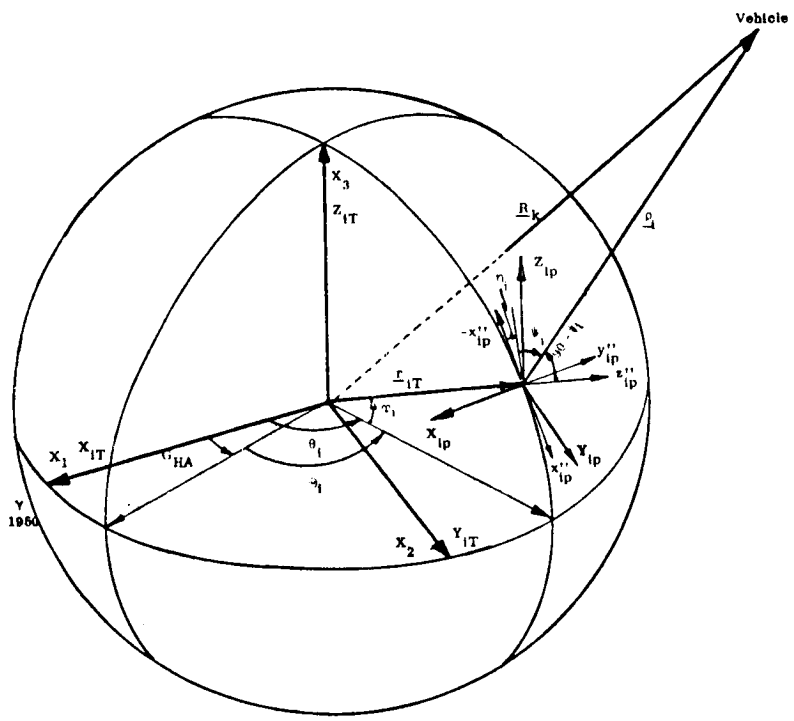

$(r_{iT}, \theta_i, \varphi_i)$	Earth fixed tracker coordinate system
$(x''_{ip}, y''_{ip}, z''_{ip})$	Earth fixed azimuth-elevation tracker coordinate system
(X_1, X_2, X_3)	Non-rotating right-handed planet centered equatorial coordinate system with X_1 along the vernal equinox of 1950
(X_{iT}, Y_{iT}, Z_{iT})	Non-rotating right-handed Earth centered tracker coordinate system parallel to the (X_1, X_2, X_3) system
(X_{ip}, Y_{ip}, Z_{ip})	Non-rotating right-handed tracker centered coordinate system parallel to the (X_1, X_2, X_3) system

Figure A-4. Definition of Tracker Coordinate Systems

Defining the vehicle, with respect to tracker location, position vector as

$$\underline{\rho}_i(t_k) \overset{Df}{=} \begin{bmatrix} X_{ip}(t_k) \\ Y_{ip}(t_k) \\ Z_{ip}(t_k) \end{bmatrix}$$

Then the range and range rate from the trackers are given by

$$\rho_i = [X_{ip}^2 + Y_{ip}^2 + Z_{ip}^2]^{1/2}$$

$$\dot{\rho}_i = \frac{\underline{\rho}_i^T \, \dot{\underline{\rho}}_i}{\rho_i}$$

and elevation and azimuth angle of probe with respect to the tracker are

$$\psi_i = \sin^{-1}\left[\frac{\underline{r}_{iT}^T \, \underline{\rho}_i}{r_{iT} \, \rho_i}\right] \quad -90° < \psi_i < 90°$$

$$\eta_i = \begin{cases} \cos^{-1}\left[\dfrac{-x''_{ip}}{\rho_i \cos \psi_i}\right] \\ \sin^{-1}\left[\dfrac{y''_{ip}}{\rho_i \cos \psi_i}\right] \end{cases} \qquad 0 \le \eta_i \le 360°$$

where

$$\begin{bmatrix} x''_{ip} \\ y''_{ip} \end{bmatrix} = \begin{bmatrix} \sin \varphi_i \cos(\theta_i + \omega t_k) & \sin \varphi_i \sin(\theta_i + \omega t_k) & -\cos \varphi_i \\ -\sin(\theta_i + \omega t_k) & \cos(\theta_i + \omega t_k) & 0 \end{bmatrix} \begin{bmatrix} X_{ip} \\ Y_{ip} \\ Z_{ip} \end{bmatrix}$$

Radio Altimeter

This instrument measures the radial altitude h and radial speed $\dot{r}$ of the spacecraft relative to a planet.

$$h = R - r_o$$

$$\dot{r} = \frac{\underline{R} \cdot \dot{\underline{R}}}{R}$$

where $\underline{R}$ and $\dot{\underline{R}}$ are the position and velocity of the spacecraft relative to the planet and r_o is the radius of the body.

All of these instruments can be subject to two different types of error sources: bias errors and random errors (i.e., errors that are uncorrelated between samples). The bias errors are considered to be constant during the interval of interest. Whenever they are present, these parameters are included as additional state variables. This leads to a state vector having an increased dimension and results, in the computation of estimates of the bias errors.

2.4.2 Observation Matrices for Electromagnetic Sensors

In this section, the observation matrices H_k for the electromagnetic sensors, are stated. The elements of these matrices are determined in a straightforward manner from the defining relations given in Paragraph 2.4.1. Refer to that section for definitions of the quantities appearing below.

Space Sextant

The space sextant provides the measurement of the angle θ_{pb} between a star and the limb or center of a planet. Thus, the H_k for this device has the dimension (1x6). Since the angle does not depend upon the velocity* the partial derivatives involving

*It is presumed here that the small, but possibly important, angular shift due to abberation is compensated in the sextant mechanization. The compensation angle, $\theta'_{pb} - \theta_{pb_1}$ may be computed from

$$\theta'_{pb} - \theta_{pb} = \sin^{-1} \sin\theta'_{pb} \frac{(1 - \sqrt{1 - \beta^2})\cos\theta'_{pb} + \beta}{1 + \beta\cos\theta'_{pb}}$$

$$\beta = (X_4^2 + X_5^2 + X_6^2)^{1/2}/C$$

C = speed of light in vacuo

θ'_{pb} = angle defined in Figure A-1, uncompensated for relativistic effects.

The compensation angle would be almost 0.7 arc-minutes for a vehicle speed of 40 miles/sec. Errors in compensation due to velocity errors, however, would be second order.

velocity are identically zero. The remaining elements are found to be

$$h_{11}(t_k) = \frac{1}{A}\left[\cos\left\{\varkappa_S \beta^S_{pb}(t_k)\right\} s_{j1}(t_k) - \cos\left\{\theta_{pb}(t_k)\right\} e_{pb1}(t_k)\right]$$

$$h_{12}(t_k) = \frac{1}{A}\left[\cos\left\{\varkappa_S \beta^S_{pb}(t_k)\right\} s_{j2}(t_k) - \cos\left\{\theta_{pb}(t_k)\right\} e_{pb2}(t_k)\right]$$

$$h_{13}(t_k) = \frac{1}{A}\left[\cos\left\{\varkappa_S \beta^S_{pb}(t_k)\right\} s_{j3}(t_k) - \cos\left\{\theta_{pb}(t_k)\right\} e_{pb3}(t_k)\right]$$

where $h_{1i}(t_k) = \dfrac{\partial\theta_{pb}}{\partial X_i}$

and $A = R_{pb}(t_k) \cos\left\{\varkappa_S \beta^S_{pb}(t_k)\right\} \sin\left\{\theta_{pb}(t_k) + \varkappa_S \beta^S_{pb}(t_k)\right\}$

The partial derivatives are evaluated with nominal values of the state.

Horizon Sensor

The horizon sensor is assumed to provide three angles α, δ, β^H so the H_k has the dimension (3x6). The velocity partials are identically zero so the nontrivial portion of the observation matrix has the dimension (3x3). It follows from the relations of Paragraph 2.4.1 that

$$\begin{bmatrix} h_{11} & h_{12} & h_{13} \\ h_{21} & h_{22} & h_{23} \\ h_{31} & h_{32} & h_{33} \end{bmatrix} \underline{\underline{Df}} \begin{bmatrix} \frac{\partial\alpha}{\partial X_1} & \frac{\partial\alpha}{\partial X_2} & \frac{\partial\alpha}{\partial X_3} \\ \frac{\partial\delta}{\partial X_1} & \frac{\partial\delta}{\partial X_2} & \frac{\partial\delta}{\partial X_3} \\ \frac{\partial\beta^H}{\partial X_1} & \frac{\partial\beta^H}{\partial X_2} & \frac{\partial\beta^H}{\partial X_3} \end{bmatrix}$$

$$= \begin{bmatrix} \frac{-\sin\alpha\cos\delta}{R_{pb}(t_k)} & \frac{\sin\alpha\sin\delta}{R_{pb}(t_k)} & \frac{-X_{pb2}(t_k)}{R^2_{pb}(t_k)\sin\delta} \\ \frac{-\sin^2\delta}{X_{pb2}(t_k)} & \frac{\cos^2\delta}{X_{pb1}(t_k)} & 0 \\ \frac{-X_{pb1}(t_k)\tan\beta^H}{R^2_{pb}(t_k)} & \frac{-X_{pb2}(t_k)\tan\beta^H}{R^2_{pb}(t_k)} & \frac{-X_{pb3}(t_k)\tan\beta^H}{R^2_{pb}(t_k)} \end{bmatrix}$$

where

$$\tan \beta^H = \frac{r_b}{\sqrt{R_{pb}^2(t_k) - r_b^2}}$$

Nominal values of the state are used to evaluate these partials.

Ground Tracking

The ground trackers measure the range ρ_i and range rate $\dot{\rho}_i$ of the vehicle and its elevation ψ_i and azimuth η_i angles. This leads to a basic observation matrix that is (4x6). The H_k for each of the three trackers has the form

$$H_{iT1} \overset{Df}{=} \begin{bmatrix} \frac{\partial \rho_i}{\partial X_1} & \frac{\partial \rho_i}{\partial X_2} & \frac{\partial \rho_i}{\partial X_3} & 0 & 0 & 0 \\ \frac{\partial \dot{\rho}_i}{\partial X_1} & \frac{\partial \dot{\rho}_i}{\partial X_2} & \frac{\partial \dot{\rho}_i}{\partial X_3} & \frac{\partial \dot{\rho}_i}{\partial X_4} & \frac{\partial \dot{\rho}_i}{\partial X_5} & \frac{\partial \dot{\rho}_i}{\partial X_6} \\ \frac{\partial \psi_i}{\partial X_1} & \frac{\partial \psi_i}{\partial X_2} & \frac{\partial \psi_i}{\partial X_3} & 0 & 0 & 0 \\ \frac{\partial \eta_i}{\partial X_1} & \frac{\partial \eta_i}{\partial X_2} & \frac{\partial \eta_i}{\partial X_3} & 0 & 0 & 0 \end{bmatrix} \quad i = 1, 2, 3$$

where

$$\frac{\partial \rho_i}{\partial X_1} = \frac{\partial \dot{\rho}_i}{\partial X_4} = \frac{X_{ip}(t_k)}{\rho_i(t_k)}$$

$$\frac{\partial \rho_i}{\partial X_2} = \frac{\partial \dot{\rho}_i}{\partial X_5} = \frac{Y_{ip}(t_k)}{\rho_i(t_k)}$$

$$\frac{\partial \rho_i}{\partial X_3} = \frac{\partial \dot{\rho}_i}{\partial X_6} = \frac{Z_{ip}(t_k)}{\rho_i(t_k)}$$

$$\frac{\partial \dot{\rho}_i}{\partial X_1} = \frac{1}{\rho_i(t_k)} \left[\dot{X}_{ip}(t_k) - \dot{\rho}_i(t_k) \frac{\partial \rho_i}{\partial X_1} \right]$$

$$\frac{\partial \dot{\rho}_i}{\partial X_2} = \frac{1}{\rho_i(t_k)} \left[\dot{Y}_{ip}(t_k) - \dot{\rho}_i(t_k) \frac{\partial \rho_i}{\partial X_2} \right]$$

$$\frac{\partial \dot{\rho}_i}{\partial X_3} = \frac{1}{\rho_i(t_k)} \left[\dot{Z}_{ip}(t_k) - \dot{\rho}_i(t_k) \frac{\partial \rho_i}{\partial X_3} \right]$$

$$\frac{\partial \psi_i}{\partial X_1} = \frac{1}{\cos \psi_i} \left[\frac{X_{iT}}{r_{iT}\rho_i} - \frac{X_{ip}}{\rho_i^2} \sin \psi_i \right]$$

$$\frac{\partial \psi_i}{\partial X_2} = \frac{1}{\cos \psi_i} \left[\frac{Y_{iT}}{r_{iT}\rho_i} - \frac{Y_{ip}}{\rho_i^2} \sin \psi_i \right]$$

$$\frac{\partial \psi_i}{\partial X_3} = \frac{1}{\cos \psi_i} \left[\frac{Z_{iT}}{r_{iT}\rho_i} - \frac{Z_{ip}}{\rho_i^2} \sin \psi_i \right]$$

$$\frac{\partial \eta_i}{\partial X_1} = \frac{1}{x''_{ip}} \left[\sin(\theta_i + \omega t_k) + \frac{y''_{ip}}{\rho_i} \left(\frac{\partial \rho_i}{\partial X_1}\right) - y''_{ip} \left(\frac{\sin \psi_i}{\cos \psi_i}\right) \left(\frac{\partial \psi_i}{\partial X_1}\right) \right]$$

$$\frac{\partial \eta_i}{\partial X_2} = \frac{1}{x''_{ip}} \left[-\cos(\theta_i + \omega t_k) + \frac{y''_{ip}}{\rho_i} \left(\frac{\partial \rho_i}{\partial X_2}\right) - y''_{ip} \left(\frac{\sin \psi_i}{\cos \psi_i}\right) \left(\frac{\partial \psi_i}{\partial X_2}\right) \right]$$

$$\frac{\partial \eta_i}{\partial X_3} = \frac{1}{x''_{ip}} \left[\frac{y''_{ip}}{\rho_i} \left(\frac{\partial \rho_i}{\partial X_3}\right) - y''_{ip} \left(\frac{\sin \psi_i}{\cos \psi_i}\right) \left(\frac{\partial \psi_i}{\partial X_3}\right) \right]$$

In addition to these partial deviatives tracker location errors and bias errors are included. Each tracker location is described by the vector components X_{iT}, Y_{iT}, Z_{iT}. In order to include these constant errors, an observation matrix relating errors

in the measured quantities ρ_i, $\dot{\rho}_i$, ψ_i, η_i to the tracker errors must be established. The bias errors are assumed to enter additively so the observation matrix for the tracker errors is defined as

$$H_{iT2} \overset{Df}{=} \begin{bmatrix} \frac{\partial \rho_i}{\partial X_{iT}} & \frac{\partial \rho_i}{\partial Y_{iT}} & \frac{\partial \rho_i}{\partial Z_{iT}} & 1 & 0 & 0 & 0 \\ \frac{\partial \dot{\rho}_i}{\partial X_{iT}} & \frac{\partial \dot{\rho}_i}{\partial Y_{iT}} & \frac{\partial \dot{\rho}_i}{\partial Z_{iT}} & 0 & 1 & 0 & 0 \\ \frac{\partial \psi_i}{\partial X_{iT}} & \frac{\partial \psi_i}{\partial Y_{iT}} & \frac{\partial \psi_i}{\partial Z_{iT}} & 0 & 0 & 1 & 0 \\ \frac{\partial \eta_i}{\partial X_{iT}} & \frac{\partial \eta_i}{\partial Y_{iT}} & \frac{\partial \eta_i}{\partial Z_{iT}} & 0 & 0 & 0 & 1 \end{bmatrix} \quad i = 1, 2, 3$$

$$\frac{\partial \rho_i}{\partial X_1} = - \frac{\partial \rho_i}{\partial X_{iT}}$$

$$\frac{\partial \rho_i}{\partial X_2} = - \frac{\partial \rho_i}{\partial Y_{iT}}$$

$$\frac{\partial \rho_i}{\partial X_3} = - \frac{\partial \rho_i}{\partial Z_{iT}}$$

$$\frac{\partial \dot{\rho}_i}{\partial X_{iT}} = - \frac{\partial \dot{\rho}_i}{\partial X_1} - \frac{\omega Y_{ip}}{\rho_i}$$

$$\frac{\partial \dot{\rho}_i}{\partial Y_{iT}} = - \frac{\partial \dot{\rho}_i}{\partial X_2} + \frac{\omega X_{ip}}{\rho_i}$$

$$\frac{\partial \dot{\rho}_i}{\partial Z_{iT}} = - \frac{\partial \dot{\rho}_i}{\partial X_3}$$

$$\frac{\partial \psi_i}{\partial X_{iT}} = \frac{1}{\cos \psi_i} \left[\frac{X_{ip}}{r_{iT} \rho_i} - \frac{X_{iT}}{r_{iT}^2} \sin \psi_i \right] - \frac{\partial \psi_i}{\partial X_1}$$

$$\frac{\partial \psi_i}{\partial Y_{iT}} = \frac{1}{\cos \psi_i} \left[\frac{Y_{ip}}{r_{iT} \rho_i} - \frac{Y_{iT}}{r_{iT}^2} \sin \psi_i \right] - \frac{\partial \psi_i}{\partial X_2}$$

$$\frac{\partial \psi_i}{\partial Z_{iT}} = \frac{1}{\cos \psi_i} \left[\frac{Z_{ip}}{r_{iT} \rho_i} - \frac{Z_{iT}}{r_{iT}^2} \sin \psi_i \right] - \frac{\partial \psi_i}{\partial X_3}$$

$$\frac{\partial \eta_i}{\partial X_{iT}} = \frac{1}{x''_{ip}} \left[- \sin (\theta_i + \omega t_k) - \frac{AY_{iT}}{X_{iT}^2 + Y_{iT}^2} + \frac{y''_{ip}}{\rho_i} \left(\frac{\partial \rho_i}{\partial X_{iT}} \right) - y''_{ip} \left(\frac{\sin \psi_i}{\cos \psi_i} \right) \left(\frac{\partial \psi_i}{\partial X_{iT}} \right) \right]$$

$$\frac{\partial \eta_i}{\partial Y_{iT}} = \frac{1}{x''_{ip}} \left[\cos (\theta_i + \omega t_k) + \frac{AX_{iT}}{X_{iT}^2 + Y_{iT}^2} + \frac{y''_{ip}}{\rho_i} \left(\frac{\partial \rho_i}{\partial Y_{iT}} \right. - y''_{ip} \left(\frac{\sin \psi_i}{\cos \psi_i} \right) \left(\frac{\partial \psi_i}{\partial Y_{iT}} \right) \right]$$

$$\frac{\partial \eta_i}{\partial Z_{iT}} = \frac{1}{x''_{ip}} \left[\frac{y''_{ip}}{\rho_i} \left(\frac{\partial \rho_i}{\partial Z_{iT}} \right) - y''_{ip} \left(\frac{\sin \psi_i}{\cos \psi_i} \right) \left(\frac{\partial \psi_i}{\partial Z_{iT}} \right) \right]$$

where $A = X_{ip} \cos (\theta_i + \omega t_k) + Y_{ip} \sin (\theta_i + \omega t_k)$

All of these terms are evaluated with the nominal values of the state and tracker locations.

Radio Altimeter

The radio altimeter is assumed to provide measurements of the radial altitude r and radial speed $\dot{r}$ so the H_k is (2×6)

$$H_k \overset{Df}{=} \begin{bmatrix} \frac{\partial r}{\partial X_1} & \frac{\partial r}{\partial X_2} & \frac{\partial r}{\partial X_3} & 0 & 0 & 0 \\ \frac{\partial \dot{r}}{\partial X_1} & \frac{\partial \dot{r}}{\partial X_2} & \frac{\partial \dot{r}}{\partial X_3} & \frac{\partial \dot{r}}{\partial X_4} & \frac{\partial \dot{r}}{\partial X_5} & \frac{\partial \dot{r}}{\partial X_6} \end{bmatrix}$$

$$\frac{\partial r}{\partial X_1} = \frac{\partial \dot{r}}{X_4} = \frac{X_{1k}}{R_k}$$

$$\frac{\partial r}{\partial X_2} = \frac{\partial \dot{r}}{\partial X_5} = \frac{X_{2k}}{R_k^*}$$

$$\frac{\partial r}{\partial X_3} = \frac{\partial \dot{r}}{\partial X_6} = \frac{X_{3k}}{R_k}$$

$$\frac{\partial \dot{r}}{\partial X_1} = \frac{1}{R_k} \left[X_{4k} - \dot{r}_k \frac{X_{1k}}{R_k} \right],$$

$$\frac{\partial \dot{r}}{\partial X_2} = \frac{1}{R_k} \left[X_{5k} - \dot{r}_k \frac{X_{2k}}{R_k} \right]$$

$$\frac{\partial \dot{r}}{\partial X_3} = \frac{1}{R_k} \left[X_{6k} - \dot{r}_k \frac{X_{3k}}{R_k} \right]$$

This completes the quantitative description of the electromagnetic sensors.

2.4.3 INERTIAL MEASUREMENT UNIT (IMU)

It was possible in the case of the electromagnetic sensors to establish an algebraic relation between the measured quantities and the state directly from physical considerations. The accelerometers measure nongravitational acceleration so it is somewhat more difficult to establish the relation to the state in a form compatible with the navigation model. Two distinctly different formulations have been developed. For the Re-entry Performance Assessment Program the IMU has been formulated so that these data are treated in an identical manner to the electromagnetic sensors. That is, the

IMU data enters the filter equation as components of the measurement perturbation vector $\underline{z}$. This formulation appears to be unique to this program. An approach that has appeared in other investigations involves the introduction of the IMU data as forcing terms in the plant equation. This formulation results in the requirement that an aiding instrument (i.e., an electromagnetic sensors) must be present in order for any filtering to be accomplished. These two formulations are described below.

The output of an accelerometer is actually the integral of the nongravitational acceleration and these data are available at discrete times (the interval between times is generally small). For the moment neglect errors that exist in the measurements. It can be shown, using the general solution of (A-4) that the difference between the actual and nominal IMU outputs is approximately described by

$$\underline{s}_k = {}_aJ_k \underline{x}_k + \underline{\sigma}_k + \underline{n}_k \tag{A-12}$$

where

$${}_aJ_k = {}_aJ_{k-1} \Phi_{k-1,k} + \int_{t_{k-1}}^{t_k} F(t)\, \Phi(t, t_k)dt$$

Also,

$$\underline{\sigma}_k = \underline{\sigma}_{k-1} + \gamma_{k-1} \underline{u}_{k-1}$$

where

$$\gamma_{k-1} = A_{k-1} + \int_{t_{k-1}}^{t_k} G(t)dt$$

and

$$A_{k-1} = -{}_aJ_{k-1} \Phi_{k-1,k} \Gamma_{k,k-1} + \int_{t_{k-1}}^{t_k} F(t) \int_{t_k}^{t} \Phi(t, \tau)\, G(\tau)d\tau\, dt$$

In addition

$$\underline{\eta}_k = \underline{\eta}_{k-1} + \beta_{k-1} \underline{w}_{k-1}$$

where

$$\beta_{k-1} = C_{k-1} + (t_k - t_{k-1})I$$

and

$$C_{k-1} = -\, {}_aJ_{k-1} \Phi_{k,k-1} \int_{t_{k-1}}^{t_k} \Phi(t_k, t_{k-1})dt + \int_{t_{k-1}}^{t_k} F(t) \int_{t_k}^{t} \Phi(t, \tau)d\tau\, dt$$

The $\underline{\sigma}_k$ involves the known guidance commands, so it is a deterministic quantity. The $\underline{\eta}_k$ is a function of the plant noise, so it is a random variable. The $\underline{\eta}_k$ is described by a linear difference equation, and this three-dimensional vector can be treated as additional state variables. Thus, when the IMU is included, the state vector has at least nine components.

The matrix ${}_aJ_k$ provides the observation matrix for the IMU model. It is the equivalent for this instrument of the matrix H_k that arises in deriving the linear model for the electromagnetic sensors.

The model for the IMU data is completed by considering the error sources. Primarily, the measurement inaccuracies are believed to arise from instrument imperfections that change very slowly and are usually considered to be constant. These errors are caused by such things as initial platform misalignment, gyro drift, accelerometer bias, etc. These errors depend upon the mission phase and consequently will not be discussed here. The error model is discussed again in Sections III, V, and VI.

Other errors that arise can be considered to be uncorrelated between sampling times. These errors are generally insignificant compared to the constant errors. The model for the IMU, when treated directly as measurement data, can be seen to be described by

$$\underline{z}_k = \underline{s}_k - \sigma_k + \left[\int_{t_o}^{t_k} B(t)dt\right] \underline{\epsilon} + \underline{v}_k$$

The $\underline{\epsilon}$ and $\underline{v}_k$ represent the constant and random errors. The matrix $\int_{t_o}^{t_k} B(t)\, dt$ relates the constant error sources to the resultant errors in the integrated acceleration. This matrix is discussed below. The specific application of this model to the re-entry problem is described in Section VI.

Another formulation is possible if the IMU output is treated as nongravitational acceleration rather than as its integral. Assume that the control term $G(t)\underline{u}$ and the noise $\underline{w}$ appearing in (A-4) represent the linear approximation of the nongravitational acceleration. The output of the accelerometer (after subtracting the nominal values) including errors is then

$$\underline{\zeta}(t) = G(t)\underline{u} + \underline{w} + B(t)\underline{\epsilon} + \underline{v}$$

Using this relation, (A-4) can be rewritten as

$$\dot{\underline{x}} = F(t) + \underline{\zeta}(t) - B(t)\underline{\epsilon} - \underline{v} \qquad \text{(A-13)}$$

The $\underline{\zeta}$ is the <u>known</u> output of the IMU. Since $\underline{\epsilon}$ is a constant vector, it can be treated as additional state variables. Thus (A-13) assumes the desired form for the plant. It can then be rewritten as a difference equation. In order to estimate the state using the Kalman filter it is imperative that electromagnetic sensor data be available. This formulation is utilized in the low-thrust performance assessment program and is discussed again in Section VI.

In either formulation it is important to note that the constant error sources are included as additional state variables. Thus, it becomes important to restrict attention only to the more important effects in order to prevent the dimension of the state vector from becoming too large. Thus, the error model described in Sections V and VI is considerably simpler than the model used in the Boost program.

2.5 MISCELLANEOUS REMARKS

The general description of the structure underlying the mathematical model for the individual performance assessment programs is essentially complete. The remaining aspects are specialized to the requirements of the mission phases and are covered in the remaining sections. Before proceeding to the specialized discussion a few additional remarks appear to be in order.

The trajectory calculations described for the free-fall, re-entry, and low-thrust missions are not based upon the most general possible equations of motion. For example, the planets, including Earth, are assumed to be spherical with a spherical gravity potential. In the free-fall and low-thrust programs only one attracting body is considered to act on the spacecraft at a particular time. In the re-entry program the atmospheric density is described by a single exponential function.

The approximations used to describe the equations of motion should not significantly degrade the validity of the results from the linear analysis of the guidance and navigation systems. Most of the simplifications omit second-order effects and would, therefore, not have a strong influence.

The discussion in the remaining sections is restricted to the major aspects of the particular phase. The reader is directed to Volume II, Parts 1 through 11 of the final report for more detailed discussions of the programs.

The analysis of a mission entails two principal steps. First, a nominal trajectory must be generated and then, using this trajectory, the performance assessment program must be exercised. Implicit in the generation of the nominal trajectory is the prespecification of the mission constraints and objectives.

SECTION III

PERFORMANCE ASSESSMENT OF ALL-INERTIAL BOOST AND RE-ENTRY GUIDANCE SYSTEMS

Methods for the performance assessment of all-inertial guidance systems as they are used in powered flight phases and during atmospheric entry are described in this section. The techniques for establishing nominal trajectories during powered flight are described in Paragraph 3.1. For the determination of appropriate re-entry trajectories the reader is referred to Paragraph 5.1. The IMU error models are described in Paragraph 3.2, and the mathematical techniques for the evaluation of the guidance systems are presented in Paragraph 3.3.

This part of the mathematical model is, to a certain extent, outside the general framework inasmuch as it represents an "open-loop" analysis which considers the navigation function of the system alone and does not include the errors introduced by the guidance and control loop. This is the conventional approach to the performance assessment of all-inertial guidance systems.

3.1 NOMINAL POWERED FLIGHT TRAJECTORY

Inertial instrument errors can be mathematically represented as a power series expansion of the nongravitational acceleration and, in the case of strapdown systems, angular body rates. Within a first-order analysis, nominal values of the thrust accelerations and angular body rates can be used. It is, therefore, necessary to generate these nominal trajectory data first.

3.1.1 COORDINATE SYSTEMS

Most coordinate systems are right-handed cartesian coordinate systems with the right-hand convention for positive rotations. Exceptions will be noted.

3.1.1.1 Inertial Coordinate Systems

3.1.1.1.1 PCI Coordinates (X, Y, Z). The reference coordinate system is a planet-centered, inertial (PCI), cartesian coordinate system (X, Y, Z), oriented with the X-Y plane coincident with the planets equatorial plane, the Z-axis along the planet's positive axis of rotation. A reference launch point is automatically defined in the X-Z plane by inputs of launch point geographic coordinates. All forces, acceleration, velocities, positions, and reference trajectory planes are ultimately defined as vector componenents in this coordinate system.

3.1.1.1.2 Launch Level Coordinates (P_{I0}, Y_{A0}, R_{00}). The initial orientation of the reference body axes is defined by the inertial cartesian coordinate system (P_{I0}, Y_{A0}, R_{00}). The orientation of this coordinate system, with respect to the PCI system, is defined by input of the geographic coordinates of the launch point and the figure of the

reference planet. The R_{00} axis is directed outward from the reference planet, along the direction of launch local vertical, the P_{I0}-Y_{A0} plane is parallel to the local level plane at the launch site. $-Y_{A0}$ is oriented in the direction defined by the input azimuth, ψ_p, measured positively in an eastward direction from true North. This inertial coordinate system is used as a reference for the gimbal angles α_1, α_2, and α_3 which describe the time-varying orientation of the missile body fixed axes (P_I, Y_A, R_0).

3.1.1.1.3 Velocity Profile Steering Coordinates (P, Q, R). The desired velocity profile of velocity profile guidance is defined in the (P, Q, R) inertial coordinate system. The (P, Q, R) coordinate system is geometrically related to the (P_{I0}, Y_{A0}, R_{00}) coordinate system by a positive rotation, θ_{cc}, about the P_{I0} axis. θ_{cc} is normally selected to align the R axis along an average thrust direction.

3.1.1.2 Noninertial Coordinate System

3.1.1.2.1 Geographic Coordinates. A reference launch point is defined by the input coordinates of geodetic or geographic latitude (λ_L), the geographic longitude (λ_L), the equatorial radius (a_e), ellipticity of the reference spheroid, (ϵ); geoidal altitude (H_L), and launch point geoidal separation (N_L). The local vertical at the launch site and the launch level plane are defined by additional inputs of the astronomic latitude and longitude (λ_{LA}, μ_{LA}), which account for local deflections of the vertical.

The sign convention for latitude and longitude is that North latitudes and East longitudes are positive. The geographic coordinate system is clearly not a cartesian coordinate system, but rather one that conforms to conventional planet-fixed geographic coordinates currently employed in Earth-mapping procedures.

3.1.1.2.2 (P_I, Y_A, R_0) Coordinates. The time-varying missile body attitude is defined by a reference missile body-fixed coordinate system (P_I, Y_A, R_0), and is employed to conveniently resolve missile aerodynamic and thrust forces. The initial orientation is coincident with the (P_{I0}, Y_{A0}, R_{00}) coordinate system, and its orientation at other times is specified by the time history of the missile body angular rates ω_{PI}, ω_{YA}, ω_{R0}.

3.1.1.2.3 Gimbal Angle Coordinates (α_1, α_2, α_3). An alternate representation of the missile time-varying body axis orientation in inertial space is given by the three Euler angles, α_1, α_2, and α_3 which are gimbal angles in a roll, yaw, and pitch order. These Euler angles are initially referenced to the (P_{I0}, Y_{A0}, R_{00}) coordinate system and are calculated by a trigonometric resolution of angles between the unit coordinate vectors of the (P_I, Y_A, R_0) and (P_{I0}, Y_{A0}, R_{00}) coordinate systems.

3.1.1.2.4 Trajectory Plane Coordinates ($\overline{U}_r$, $\overline{U}_v$, $\overline{U}_w$). An instantaneous trajectory plane coordinate system is defined by an input unit vector $\overline{U}_{wj}$, which is normal to a desired trajectory plane, oriented so that $\overline{U}_r$, the unit instantaneous position vector,

and $\overline{U}_v = \overline{U}_{wj} \times \overline{U}_r$ form the right-handed triad $(\overline{U}_r, \overline{U}_v, \overline{U}_{wj})$. The required velocity, $(\overline{V}_{REQ})$, is defined in this coordinate system for both modes of explicit guidance and for trim steering guidance. The index j refers to a particular guidance mode.

3.1.1.2.5 Planet-fixed Cylindrical Coordinates (r, θ, z). The program has the option of inputting aim point coordinates in either the reference PCI coordinate system or in planet-fixed cylindrical coordinates (r, θ, z). The z-axis is parallel to the Z-axis of the PCI system, r is normal to Z and θ is the angle measured in a positive sense about z from the meridian plane containing the missile at t = 0. Components of the aim point in this coordinate system at t = 0 are j-dependent and are designated by (C_{1j}, C_{2j}, C_{3j}).

3.1.2 ENVIRONMENTAL MODELS

3.1.2.1 Figure of Planets

A reference surface, corresponding to the physical surface of the planet, is defined as an oblate spheroid by inputs of equatorial radius, ellipticity and stellar angular rate. The figure is oriented with the Z-axis of the PCI coordinate along the reference axis of rotation.

3.1.2.2 Gravitational Potential

The gravitational potential of the reference planet is defined by a series representation in Legendre polynomials including the zero, second, third, and fourth harmonics. The gradient of this potential function defines the gravitational forces in the PCI coordinate system. Input parameters are GM, the universal gravitational constant times the mass of the planet; the second, third, and fourth harmonics in the conventional J, H, and D form; and the position vector PCI components.

3.1.2.3 Planetary Atmosphere

The atmosphere of a planet is assumed to be affixed to the planet, rotating with the planet's inertial angular rate. The atmosphere is defined to exist between the planet's surface and an input altitude above which atmospheric properties are considered to have insignificant affects upon the missile trajectory. The atmospheric models and properties thereof are discussed in greater detail in the following paragraphs.

3.1.2.3.1 Earth Atmosphere. The mathematical model defining the earth's atmospheric properties such as pressure, density, and speed of sound is based on the fundamental data and computational procedures used to generate "U.S. Standard Atmosphere 1962" (1). (See Appendix A, Reference 1.) Briefly, the atmosphere is assumed to be in hydrostatic equilibrium with respect to the Earth. A geopotential function due to mass attraction, including the second harmonic, and centrificial forces is calculated. This potential function, divided by the reference sea-level value of

gravity, defines a "geopotential altitude." The variation of molecular-scale temperature with geopotential altitude is the fundamental defining property of the atmosphere, and all other properties are derived from this data. The data, as employed by COSEA in generating the "U.S. Standard Atmosphere 1962," defined the molecular-scale temperature as a series of connected line segments, linear in geopotential altitude up to 90 km and linear in geometric altitude above 90 km. The AC Electronics molecular-scale temperature model employe segments linear in geopotential altitude for all altitudes. The geopotential altitude range encompassed by the input data is -5 km to 630 km (-5 km to 700 km geometric altitude). The speed of sound has been held constant at geopotential altitudes greater than 88.743 km for purposes of mathematical continuity, although it is not a well-defined physical property of the atmosphere at higher altitudes.

3.1.2.3.2 Atmosphere Model of Planets other than Earth. Simple exponential models for atmospheric pressure and density are employed when near a planet other than Earth for powered flight trajectories. The speed of sound is defined as a constant.

3.1.3 MISSILE DYNAMICS

3.1.3.1 Propulsion Model

The total thrust force acting on the missile is calculated as the product of the specific impulse (I_{sp}), the mass rate ($\dot{M}$), and the sea-level value of gravity (g'_o). $g'_o I_{sp}$ is a phase-dependent tabulated function of atmospheric pressure. $\dot{M}$ is a phase-dependent tabulated function of the expended mass in each phase. A very arbitrary time-varying thrust function can be simulated with this model. One of the principal requirements of boost guidance is to compensate for propulsion variations, therefore, provision for perturbing either $g'_o I_{sp}$ or $\dot{M}$ or both is included. Thus, total impulse and/or time duration of the impulse can be perturbed. For powered flight out of the atmosphere, the thrust force is directed along the missile roll axis, R_0.

During flight in the atmoshpere, a thrust force normal to the missile roll axis, (F_{MN}), is defined to be that which exactly nulls the moment due to the normal aerodynamic force. The remaining component of thrust force, (F_{MA}), is defined to be directed along the missile roll axis, R_0.

3.1.3.2 Aerodynamic Model

Aerodynamic forces on the missile are calculated in the body-fixed coordinates (P_I, Y_A, R_0) and utilize standard approximations appropriate to slender cylindrical bodies and small angles of attack. The axial drag force (F_{DA}) is defined as the product of dynamic pressure (q), the reference area (S), and the drag coefficient (C_D), a tabulated function of mach number. This drag force is directed along the negative R_0 axis.

The aerodynamic force normal to the roll axis, (F_{DN}), is in the plane defined by the missile roll axis, (R_0), and the missile velocity vector with respect to the planet's air mass. The normal force magnitude is defined by the product of the dynamic pressure (q), reference area (S), the normal drag coefficient (C_N), which is a tabulated function of mach and angle of attack, and the angle of attack (α) which is approximated by sin α in the simulation program. This normal aerodynamic force acts at a point along the missile longitudinal axis, termed the center of pressure (C_p), which is defined by a tabular function of mach and angle of attack.

3.1.3.3 Equations of Motion

The inertial velocity and position of the center of mass of the missile in the PCI coordinate system are obtained by integrating the inertial accelerations defined by the sum of gravity and the specific force-to-mass ratio.

$$\ddot{\vec{X}} = \vec{g} + \frac{\left[\vec{F}_{MA} + \vec{F}_{MN} + \vec{F}_{DA} + \vec{F}_{DN}\right]}{M}$$

The initial conditions $\dot{\vec{X}}_0$ and $\vec{X}_0$ are computed by the initialization block for planet surface conditions, or are directly input in PCI components for initialization for other start conditions.

The time-varying missile mass, per phase, is expressed as

$$M(t) = M_o + \int_{t_o}^{t} \dot{M}\,(M_o - M(\tau))d\tau$$

where M_o, t_o, and $\dot{M}\,(M_o - M(\tau))$, a tabulated function of the expended mass, are phase-dependent values.

The orientation of the vehicle reference body axes is specified by three mutually orthogonal unit vectors in the PCI coordinates along the (P_I, Y_A, R_0) coordinate axes; namely, $\overline{P}_I$, $\overline{Y}_A$, $\overline{R}_0$. The vehicle angular rates in the P_I, Y_A, R_0 coordinate system, denoted by ω_{PI}, ω_{YA}, and ω_{RO}, respectively, are employed to calculate $\dot{\overline{Y}}_A$ and $\dot{\overline{R}}_O$. These six first-order differential equations are integrated to define $\overline{Y}_A$ and $\overline{R}_O$, while $\overline{P}_I$ is defined by a vector cross-product

$$\dot{\vec{Y}}_A = \omega_{PI}\vec{R}_O - \omega_{RO}\vec{P}_I$$

$$\dot{\vec{R}}_O = \omega_{YA}\vec{P}_I - \omega_{PI}\vec{Y}_A$$

$$\vec{P}_I = \vec{Y}_A \times \vec{R}_O$$

3.1.4 AUTOPILOT MODEL

The definition of body angular rates as a function of a guidance error signal is accomplished with a "perfect" autopilot model in which the angular rates about the (P_I, Y_A, R_O) coordinate axes are defined to be directly proportional to appropriately resolved guidance error signals. The guidance calculations of this simulation define gimbal angle commands. These gimbal angle commands are differenced with the computer gimbal angles to define a gimbal angle error which is resolved through the gimbal angle coordinate system to obtain an error signal in body axis coordinates. This error signal is limited in magnitude and the body angular rates are defined to be directly proportional to it, e.g., $\omega_{PI} = K\theta'_{EC'}$ etc.

3.1.5 GUIDANCE SCHEMES

3.1.5.1 General Guidance and Steering Concepts

Each guidance scheme defines a particular trajectory objective, a mathematical statement of the objective, and a measure of the missile's error in attaining that objective. If, in the mathematical statement of the objective, the criteria is defined in terms of quantities measured by the missile guidance system, a closed-loop guidance system is said to exist. If the criteria is defined otherwise, it is referred to as an open-loop guidance scheme; e.g., attitude vs time program. In most closed-loop guidance systems the guidance objective is stated in terms of a vector required velocity. A control is effected by "cross-product" steering that is, steering so as to reduce to zero the angular misalignment of the missile's actual velocity with respect to the required velocity. Thus achievement of the guidance requirement is reduced to determining the velocity magnitude error, as the angular errors are theoretically eliminated by the steering function.

3.1.5.2 β^* Guidance

The β^* guidance scheme is an open-loop trajectory design guidance scheme used to generate data required for the definition of one of the closed-loop guidance schemes, especially for that portion of the trajectory which is in the sensible atmosphere.

The objective of the β^* steering scheme is to obtain a constant $q\alpha$ during the initial portion of the atmospheric flight, followed by a zero angle of attack during the latter portion of the trajectory. This is accomplished by computing a pitch gimbal angle command of the form

$$\alpha_{3c} = \beta^* + \frac{K_\alpha}{q} = \tan^{-1}\left[\frac{\vec{V}_A \cdot \vec{Y}_{Ao}}{\vec{V}_A \cdot \vec{R}_{Oo}}\right] + \frac{K_\alpha}{q}$$

where V_A is the computed inertial velocity with respect to the planet-fixed atmosphere, K_α is the desired value of $q\alpha$ (usually set to zero in the latter portion of the trajectory).

A vertical rise phase preceeds this form of guidance so that $\vec{V}_A$ and q are physically (and numerically) well defined, nonzero values.

3.1.5.3 Velocity Profile Guidance

The velocity profile guidance scheme is a closed-loop guidance scheme. Its objective is to control the angle of attack of the missile while in the significant atmosphere by steering the missile along a nominal pitch-plane velocity profile of accelerometer measured velocities. Data required to define this profile is obtained from a β^* guided reference trajectory. The pitch plane profile is defined in the (P, Q, R) coordinate system; the Q-R plane being the pitch plane. The nominal value of the "normal" velocity, $\dot{Q}_a$, is curve fit by a cubic polynomial in the nominal "tangential" velocity, $\dot{R}_a$. The nominal value of the pitch gimbal command α_{3c}, is also curve fit by a cubic polynomial in $\dot{R}_a$. The closed-loop pitch gimbal angle command is then defined to be of the form

$$\alpha_{3c} = \alpha_{3c(\text{nominal})} + K\left[\dot{Q}_a - \sum_{j=1}^{3} K_j \dot{R}_a^j\right]$$

where

$$\alpha_{3c(\text{nominal})} = \sum_{j=1}^{3} C_i \dot{R}_a^j$$

and $\dot{R}_a$, $\dot{Q}_a$ are the measured values of the thrust velocity components. The thrust velocity component normal to the pitch plane is nulled. Velocity profile steering is initiated following a vertical rise phase. The thrust velocities, viz., the integrated accelerometer outputs, are utilized for steering to permit the steering loop to operate independently of the navigation equations during that portion of the trajectory in the effective atmosphere where this mode of guidance is generally employed.

3.1.5.4 Explicit Guidance with Time of Flight Constraint

The explicit guidance scheme defined in this simulation is employed above the effective atmosphere where no atmospheric steering constraints need be considered. The explicit guidance equations define a unique ellipse between the present position of the vehicle and a defined target point. The ellipse is unique because a time of flight between the launch and the interception of the target point is specified. The time constraint is introduced into the Keplarian explicit equations by the following relationship, defining the semi-latus rectum, p, of the ellipse.

$$p_{i+1} = p_i + [K_{13} + K_{14}\, p_i][T_A - (t_i + T_i)]$$

where K_{13}, K_{14} are curve fit constraints derived from a reference trajectory. T_A is the specified time of flight, T_i is the current estimate of the time of flight from Lambert's equation, and t_i is the time since launch.

After a few iterations the orbital parameters are in a reasonably close neighborhood of the desired orbital parameters and p_i is estimated by a nonlinear logic which selects the value determined by either a linear extrapolation, the previous value, or redetermined by the above relationship. This logic is based upon the preceding changes in (p_i) and in $(t_i + T_i)$.

For each major guidance cycle the position of the missile is determined and a velocity, V_{REQ}, is determined as the instantaneous elliptical velocity which satisfies the fixed total time of flight constraint

$$\vec{V}_{REQ} = K\left[\left(\frac{e \sin v}{\sqrt{p}}\right)\vec{U}_r + \frac{\sqrt{p}}{r}\vec{U}_v\right]$$

where K is gravitational constant (GM); e, the eccentricity; v, the true anomaly of vehicle; r, the radial position; $\vec{U}_r$ and $\vec{U}_v$ are orbit plane unit vectors.

The velocity to be gained is defined as

$$\vec{V}_g = \vec{V}_{REQ} - \vec{V}$$

At each guidance index change, (j), during the explicit guidance mode, a reference set of gimbal angles $(\alpha_{1vg}, \alpha_{3vg})$, corresponding to the alignment of the roll vector along V_g are computed. A reference unit vector along $\overline{V}_g$, $\overline{U}_{vgj}$, is also computed at this time. A cross-product steering error function is defined by

$$\overrightarrow{\Delta R} = \vec{V}_g \times \vec{U}_{vgj}$$

and is resolved into appropriate gimbal angle components.

$$\Delta\alpha_{1c} = -K_{2j}\,(\overrightarrow{\Delta R} \cdot \vec{R}_{Oo}) - K_{3j}\,\Sigma(\overrightarrow{\Delta R} \cdot \vec{R}_{Oo})\,\Delta t$$

$$\Delta\alpha_{2c} = 0$$

$$\Delta\alpha_{3c} = -K_{4j}\,(\overrightarrow{\Delta R} \cdot \vec{P}'_I) - K_{5j}\,\Sigma(\overrightarrow{\Delta R} \cdot \vec{P}'_I)\,\Delta t_i$$

where P'_I is along the current pitch axis of the missile.

The gimbal angle commands are

$$\alpha_{1c} = \Delta\alpha_{1c} + \alpha_{1vgj} + \vec{\theta}_K \cdot \vec{R}_{Oo}$$

$$\alpha_{2c} = 0$$

$$\alpha_{3c} = -\Delta\alpha_{3c} + \alpha_{3vgj} + \vec{\theta}_K \cdot \vec{P}'_I$$

where $$\vec{\theta}_K = F(V_g)\,[\vec{U}_r \times \vec{U}_{vgj}]$$

$F(V_g)$ is a curve fit function of V_g which offsets the gimbal angle commands to compensate for gravitational and centrifugal acceleration. Powered flight is terminated when V_g is zero. This is an iterated condition which is calculated to a precision specified by an input ϵ, and is not restricted to a time specified by a multiple of either major or minor computational cycles.

3.1.5.5 Explicit Guidance with Velocity Direction Constraints

This formulation of explicit guidance is perhaps the most useful form of explicit guidance, as the terminal direction of the velocity vector at the target point is a very convenient parameter for direct-injection-into-orbit trajectories. The guidance model is exactly the same as the explicit time of flight constraint guidance except that the semi-latus rectum, p, is defined using the desired velocity angle, $K_{\gamma j}$, and the calculated angle, γ_A.

$$\gamma_A = \sin^{-1}\left[\frac{e \sin V_A}{1 + 2\,(e \cos V_A) + e^2}\right]$$

$$p_{i+1} = p_i + [K_{13} + K_{14}\, s][K_{\gamma j} - \gamma_A]$$

where s is the sine of the range angle between the present position and the target point; K_{13}, K_{14} are curve fit constants, taken from a reference trajectory. A nonlinear logic is again employed to select p_{i+1}; either p_i, a linear extrapolated value, or the value defined by the equation above is chosen, depending upon the prior values p_i and γ_A. The same steering logic as described in Paragraph 2.5.4 is employed with this guidance mode.

3.1.5.6 Trim Steering Guidance

Trim steering guidance is designed to guide a vehicle into a specified plane with specifications on the following end conditions:

- desired radial position r_c
- desired radial speed $\dot{r}_c$
- desired "tangential" speed $(r\dot{v}_c)$ where $\dot{v}$ is the time derivative of the true anomaly.

The quantities r_c, $\dot{r}_c$, and $(r\dot{v}_c)$ are curve fit second-order polynomials in time, measured from the initiation of trim steering.

The orbit plane is specified by an input vector normal to the desired orbital plane, $\vec{U}_{wj}$, and an inplane unit vector is defined by the cross-product relationship $\vec{U}_v = \vec{U}_{wj} \times \vec{U}_r$.

$\vec{V}_{REQ}$ is defined as

$$\vec{V}_{REQ} = \dot{r}_c \vec{U}_r + (rv)_c \vec{U}_v + K_{Aj} [\dot{r}_c - \dot{r} + K_{Hj} (r_c - r)] \vec{U}_r$$

The difference $\vec{V}_{REQ} - \vec{V}$ is defined as $\vec{V}_g$ and the same V_g cross-product steering scheme that was employed in the explicit guidance schemes is used for this guidance scheme.

The validity of the time polynomial expressions for r_c, $\dot{r}_c$, and $(r\dot{v}_c)$ is restricted to a reasonably small neighborhood of the desired injection conditions, insofar as the simultaneous realization of <u>all three</u> of the conditions will result in the desired orbit.

For most applications of this steering, it is inititated when the vehicle radial position is close to the desired value, and V_{REQ} is essentially along U_v.

3.2 IMU ERROR MODEL

The error models representing inertial guidance systems are discussed in the following paragraphs.

The error models are a mathematical representation of the factors that cause errors in the guidance system outputs as a function of the mission profile being simulated. The output errors are in the form of errors in the measured velocity and position; the error model must thus provide a valid method of calculating the errors in position and velocity for each mission profile for the guidance system being simulated. The results are handled statistically in terms of the covariance of the output errors as a function of the covariance of the guidance system errors in terms of the system error parameters as defined by the system model.

Inertial guidance systems employ two types of basic inertial sensors, namely, gyroscopes and accelerometers. Gyroscopes are sensitive to, and hence measure, angular motion relative to an inertial or non-accelerating coordinate frame. Accelerometers respond to or measure the difference between total acceleration and acceleration due to gravitational forces, again with respect to an inertial coordinate frame. The system determines its position and velocity by calculating and "remembering" all changes from its initial position and velocity using the angular and acceleration measurements from the system sensors. The gravitational accelerations are calculated as functions of position using the known gravitational fields of the appropriate celestial bodies.

The inertial guidance system accuracy is thus dependent upon its accurate determination of position and velocity changes, or of acceleration. The system error model, therefore, calculates the (vector) error in measured acceleration due to each of the error parameters incorporated in the model. The resultant position and velocity errors are obtained by integration of these acceleration errors along the mission trajectory profile.

The specific models by which system errors are related to acceleration errors and by which the acceleration errors are integrated into position and velocity errors are discussed in the following subparagraphs.

3.2.1 INERTIAL MEASUREMENT UNIT CONFIGURATION

Inertial instruments are subject to errors from a variety of causes, some of which are mission- and trajectory-independent and others that are functions of the mission-dependent environment in acceleration and angular rate, the inputs to which the instruments are sensitive. Thus, the errors will depend not only on the instrument error parameters but also on the trajectory profile. Furthermore, the errors will also be dependent upon the angular orientation of each instrument; that is, upon how it is oriented with respect to the impressed accelerations and angular rates.

The basic coordinate system in which all errors are calculated in the simulation programs is a planet-centered, inertially fixed (PCI), coordinate frame with reference axes denoted by X, Y, and Z. The trajectory data for the mission being simulated is input with respect to this coordinate frame. The pertinent trajectory data for inertial system error analyses consists of the components of acceleration, $a_X(t)$, $a_Y(t)$, and $a_Z(t)$, and the components of angular rate $\omega_X(t)$, $\omega_Y(t)$, and $\omega_Z(t)$, and/or the vehicle orientation relative to the PCI coordinates in terms of Euler angles, $\alpha_1(t)$, $\alpha_2(t)$, and $\alpha_3(t)$. The acceleration error from each error source and the resultant position and velocity errors are calculated in PCI coordinates.

In the present inertial system error model, it is possible to evaluate three different types of inertial measurement units. These are the gimballed, strapped-down and carousel. From the point of view of inertial component errors, these are different in the manner in which the instrument orientation varies. These are discussed briefly as follows.

3.2.1.1 Gimballed

In a conventional gimballed inertial measurement unit, the instrument package or platform remains fixed with respect to inertial space. In the error model, the instrument package orientation is thus fixed in PCI coordinates. In the notation used in Sections III and IV, the orientation of the platform with respect to X, Y, Z coordinates is specified by means of an orthonormal 3 x 3 matrix $[A_4]$, the orientation

of each accelerometer with respect to the platform by an orthonormal matrix $[J_i]$, and the orientation of each gyro with respect to the platform by a matrix $[M_i]$. Thus, for a gimballed system, the orientation of all instruments with respect to the trajectory-dependent parameters (acceleration) is specified by the 3 x 3 matrices $[J_i]$, $[M_i]$, and $[A_4]$.

3.2.1.2 Strapped-Down

In a strapped-down inertial system, the instrument package remains fixed with respect to the vehicle, and thus its orientation changes with angular motion of the vehicle. The initial orientation of the instrument package is specified in the same manner as for the gimballed system, but the orientation changes as a function of time are given by a trajectory-dependent attitude time history in terms of Euler angles $\alpha_1(t)$, $\alpha_2(t)$, and $\alpha_3(t)$.

3.2.1.3 Carousel

A carousel inertial measurement unit is essentially a gimballed unit in which the instrument package or platform is rotated with respect to an inertial reference according to a prespecified time program, usually a constant angular rate. Inertial systems of this type are employed in some missions, usually missions involving extended time periods, because the effect of many component errors, particularly bias errors, is reduced by virtue of the "geometric averaging" effect. This system is analyzed very much like the strapped-down system except that the time-varying platform attitude is specified by a non-trajectory-dependent, time-varying program of Euler angles, $\eta_1(t)$, $\eta_2(t)$, and $\eta_3(t)$.

3.2.2. INSTRUMENT ERROR MODELS

The determination of measured acceleration error attributable to the various error parameters for each instrument type is discussed below: gyro errors in Paragraph 2.2.1 and accelerometer errors in Paragraph 2.2.2. In addition to instrument errors, inertial systems are subject to errors due to initial misalignment. These are incorporated in the model in a manner similar to the treatment of gyro errors.

3.2.2.1 Gyro Error Models

Gyroscopes serve to measure orientation or direction relative to an inertial frame, and thus all gyro errors will result in attitude errors that cause the system to measure the impressed acceleration along the wrong direction. For each gyro error model, the instantaneous misalignment, $\varphi(t)$, due to each error parameter, is calculated along the mission profile. The vector

$$\underline{\varphi(t)} = \begin{bmatrix} \varphi_X(t) \\ \varphi_Y(t) \\ \varphi_Z(t) \end{bmatrix}$$

is computed in PCI coordinates and is based on a small angle representation, each element representing the misalignment about one of the reference axes, X, Y, Z.

The resultant measured acceleration error, $\Delta\underline{a}$, is then given by

$$\Delta\underline{a} = \underline{a(t)} \times \underline{\varphi(t)}$$

where $\underline{a}(t)$ is the acceleration vector in PCI coordinates from the mission trajectory profile.

There are currently error models for three single-degree-of-freedom gyros included in the simulation program. It should be pointed out that there are a number of types of gyros, some of unique or exotic design, for which none of the included error models is exactly correct. However, the models described are representative of the majority of gyroscope types likely to be employed in space missions.

3.2.2.1.1 Single-axis Rate Gyro. A single-axis gyro has a mutually orthogonal axis system consisting of spin, (S), output (O), and input, (I), axes. The ideal single-axis rate gyro exactly measures rotation about its input axis. The error terms that are accounted for in the model include a random or non-trajectory-dependent drift, acceleration-dependent drifts caused by mass unbalances within the gyro, second-order acceleration-dependent drifts caused by anisoelasticity of the gyro structure, errors due to the gyro's sensing axes being mechanically misaligned, and first- and second-order scale factor errors. In particular, there are error parameters denoted in the notation of Sections III and IV, as $K_1 \ldots, K_8$ that result in drift rates about the gyro's input axis proportional to the magnitude of the parameters and to 1, a_I, a_S, $a_I a_S$, ω_O, ω_S, ω_I, and ω_I^2, where a represents acceleration, ω represents angular rate, and subscripts I, S, and O indicate gyro input, spin, and output axes, respectively.

In addition, the error model incorporates a gyro parameter denoted by K_0 that represents the "stiffness" of the constraint torque about the gyro output axes. The gyro axes tilt about the output axis an amount proportional to ω_I, and K_0 is the proportionality factor. This effect is incorporated in the model.

The drift rate about the input axis due to each of the error parameters $K_1, \ldots, K_8$ is resolved into PCI coordinates and integrated to obtain the appropriate misalignment vector, $\underline{\varphi}$.

3.2.2.1.2 Single-axis Torque-rebalanced Gyro. This is a single-axis rate gyro with a torque feedback servo loop. It is represented by an error model of the same type as the single-axis rate gyro above except that because of the feedback loop the "stiffness" of the constraint torque is essentially infinite, that is, equivalent to having the parameter $K_0 = 0$.

3.2.2.1.3 Single-axis Platform. This instrument consists of a single-degree-of-freedom gyro mounted in a single-axis stabilized platform; that is, the gyro is stabilized or isolated from rotation about its input axis. The output of this instrument is the measured angular displacement about its input axis between the outer instrument case and the stabilized gyro element. This angle, θ, is equal to the integral of the angular rate about the instrument's input axis; that is,

$$\theta = \int_{t_o}^{t} \omega_I \, dt$$

Instruments of this type are used primarily in strapped-down system applications.

Since this instrument is based upon a single-axis gyro, its error model will include some of the same type of error parameters as the previous gyros. In this instrument the gyro element's spin (S) and output (O) axes do not remain fixed with respect to the instrument package or platform, but, in fact, rotate about its input axis by the angle θ. Thus, the error model for this instrument must resolve the acceleration and angular rate inputs into the platform fixed initial gyro axis system and then through the angle θ into the instantaneous gyro instrument axis system to determine the drift rate attributable to the various error parameters.

The error parameters incorporated in this model are the same as the parameters, $K_1, \ldots, K_8$ in the previous models, except for the omission of K_7 and K_8. These were the first- and second-order scale factor errors and this type of gyro is not subject to these errors because the gyro element is isolated from the angular rate about its input axis. That is, the ω_I experienced by the gyro element is zero.

3.2.2.2 Accelerometer Error Models

There are mathematical error models for two different types of accelerometers included in the simulation programs. One of these is the pendulous integrating gyro accelerometer, or PIGA, and the other model represents a torque feedback, pendulum type of accelerometer. The following paragraphs discuss the error parameters for each of these error models and the resultant acceleration error for each of them.

3.2.2.2.1 PIGA-type Accelerometer (see Reference in Section V). This accelerometer is actually a single-axis stabilized platform, like the third type of gyro instrument discussed above, in which the gyro instrument has a delibrate and calibrated unbalance along its spin axis. That is, it is made to have a large "drift" sensitivity to acceleration along its input axis. Therefore, the rate at which it drifts, or rotates about its input axis relative to an inertial frame,is a measure of the acceleration along its input axis. The measurement output of this instrument is the rotation of the "stabilized" gyro element relative to the instrument case. If the instrument is being used in a configuration other than a gimballed IMU, then the angular output must be corrected for the rotation of the accelerometer case in inertial space.

The error sources for this accelerometer are to a certain extent related to the error sources in the single-axis platform gyro instrument. The residual torques that result in a random or bias drift cause a bias or random acceleration error. In the notation employed in Sections III and IV, this error parameter is called K_9. Errors in the "drift" sensitivity to acceleration, that is, in the ratio of the gyro angular momentum to the mass unbalance, result in first-order scale factor errors, denoted by K_{10}. There are second-order scale factor, or nonlinearity, errors and errors due to misalignment of the accelerometer input axis. In addition, there will be an acceleration measurement error proportional to the angular rate about the input axis due to errors in measuring and/or compensating for this rotation.

In summary, there are in the model error parameters that result in acceleration measurement errors proportional to 1, a_I, a_I^2, $a_C + K_1' \omega_C$, $a_N + K_1' \omega N$, and ω_I, where subscripts I, C, and N represent the instrument's input axis, cross axis, and normal axis, respectively. The cross and normal axes are mutually orthogonal reference axes that are normal to the input axis. The terms $a_C + K_1'\omega_C$ and $a_N + K_1'\omega_N$ represent errors due to input axis misalignments about the N and C axes, respectively. The K_1' terms reflect the fact that the instrument actually measures angular rotation.

3.2.2.2.2 Torque Restrained Pendulum Accelerometer. The torque restrained pendulum accelerometer is a simple pendulum with a mass unbalance and a feedback torque device to balance the torque due to acceleration. The instrument has an input axis, I, and output or normal axis, N, and a "cross" axis, C. There is an unbalanced mass along the cross axis such that an acceleration along the input axis causes a torque about the output axis. A torque feedback loop employing an electrical torque mechanism serves to null the rotation about the output axis by providing a counter torque. The output of the instrument is an electrical signal proportional to the feedback torque.

For this type of instrument, the error model provides error parameters that represent bias acceleration errors and acceleration errors proportional to a_I and a_I^2, these errors being due primarily to lack of linearity in the torque electronics. There is provision for an error parameter yielding an acceleration error proportional to $a_I a_C$. This is due to the fact that the torque feedback loop does not have infinite stiffness and therefore the input axis will tilt about the normal axis an amount proportional to a_I. The model also includes the effect of input axis misalignments about the C and N axes, these resulting in acceleration measurement errors proportional to a_N and a_C, respectively.

3.3 ERROR ANALYSIS

The preceding paragraphs have described how the mathematical error model calculates the acceleration error $\Delta \underline{a}(t)$ in PCI coordinates due to each error parameter as a function of time along the reference trajectory. To describe how these errors result in position and velocity errors, the equations of motion for the mission trajectory must be considered.

Let $\underline{X}(t)$ represent the six-element position-velocity vector along the trajectory in PCI coordinates; that is,

$$\underline{X}(t) = \begin{bmatrix} X(t) \\ Y(t) \\ Z(t) \\ \dot{X}(t) \\ \dot{Y}(t) \\ \dot{Z}(t) \end{bmatrix}$$

Then the differential equations of motion may be written as

$$\dot{\underline{X}} = \underline{g}(\underline{X}) + \underline{a}$$

where

$$\underline{g}(\underline{X}) = \begin{bmatrix} \dot{X} \\ \dot{Y} \\ \dot{Z} \\ g_X(X, Y, Z) \\ g_Y(X, Y, Z) \\ g_Z(X, Y, Z) \end{bmatrix}$$

$$\underline{a} = \begin{bmatrix} 0 \\ 0 \\ 0 \\ a_X \\ a_Y \\ a_Z \end{bmatrix}$$

and g_X, g_Y, and g_Z are the PCI components of the gravitational acceleration.

Then, if there is an error, $\Delta\underline{a}$ in the measured acceleration, the guidance system will calculate an erroneous position and velocity, $\underline{X} + \Delta\underline{X}$, satisfying the equation

$$\dot{\underline{X}} + \Delta\dot{\underline{X}} = \underline{g}(\underline{X} + \Delta\underline{X}) + \underline{a} + \Delta\underline{a},$$

where

$$\Delta\underline{a} = \begin{bmatrix} 0 \\ 0 \\ 0 \\ \Delta a_X \\ \Delta a_Y \\ \Delta a_Z \end{bmatrix}$$

Thus, the position and velocity error $\Delta\underline{X}$ satisfies the equation

$$\Delta\dot{\underline{X}} = \underline{g}(\underline{X} + \Delta\underline{X}) - \underline{g}(\underline{X}) + \Delta\underline{a}$$

Making first-order approximations, this becomes

$$\Delta\dot{\underline{X}} = \left[\frac{\partial\, \underline{g}\,(\underline{X})}{\partial\underline{X}}\right] \Delta\underline{X} + \Delta\underline{a}$$

where

$$\left[\frac{\partial\underline{g}(\underline{X})}{\partial\underline{X}}\right] = \left[\begin{array}{c|c} O\ (3 \times 3) & I\ (3 \times 3) \\ \hline \dfrac{\partial g_{X,Y,Z}}{\partial X,Y,Z} & O\ (3 \times 3) \end{array}\right] \quad (6 \times 6)$$

The matrix $[\partial\underline{g}/\partial\underline{X}]$ may be evaluated along the nominal mission trajectory so that the differential error equations are linear with time-varying coefficients.

The error, $\Delta\underline{X}(t)$, resulting from a particular acceleration error time history, $\Delta\underline{a}$, may then be obtained in terms of the integral expression

$$\Delta\underline{X}(t) = \Phi_1(t,t_o) \int_{t_o}^{t} \Phi_1^{-1}(\tau, t_o)\, \Delta\underline{a}\,(\tau)\, d\tau$$

in which t_o is the trajectory start time and $\Phi_1(t,t_o)$ is the state transition matrix given by

$$\dot{\Phi}_1(t,t_o) = \left[\frac{\partial \underline{g}}{\partial \underline{X}} \right] \Phi_1(t,t_o), \quad \Phi_1(t_o,t_o) = I \text{ (identity)}.$$

The simulation model provides an option whereby the state transition matrix Φ_1 may be approximated by

$$\Phi_1^{-1}(t,t_o) = \left[\begin{array}{c|c} I\ (3 \times 3) & (t_o - t)\ I\ (3 \times 3) \\ \hline O\ (3 \times 3) & I\ (3 \times 3) \end{array} \right]$$

This is quite accurate for relatively short mission times, or for situations where the gravitational field is very small.

For each error parameter simulated, there is a resultant acceleration error vector,

$$\Delta \underline{a}\ (t) = \begin{bmatrix} 0 \\ 0 \\ 0 \\ \Delta a_X \\ \Delta a_Y \\ \Delta a_Z \end{bmatrix}$$

The 6 x 51 matrix G(t) denotes the matrix of $\Delta \underline{a}$ error vectors, each column being the error associated with a unit value of a particular error parameter. It follows then that the covariance matrix of errors [P] resulting from all simulated error sources is given by

$$[P] = \Phi_2(t,t_0)\ [P_I]\ \Phi_2^T(t,t_0),$$

where $[P_I]$ represents the covariance matrix of all of the error parameters being simulated and

$$\Phi_2(t,t_o) = \Phi_1(t,t_0) \int_{t_0}^{t} \Phi_1^{-1}(\tau, t_0)\ G(\tau)\ d\tau\ .$$

The simulation model also provides for the incorporation of initial position and velocity errors at the start of the mission, in which case the resultant error covariance matrix is given by

$$[P(t)] = \Phi_1(t,t_0)[P_0]\Phi_1^T(t,t_0) + \Phi_2(t,t_0)\ [P_I]\ \Phi_2^T(t,t_0),$$

where $[P_0]$ is the covariance matrix of initial errors.

SECTION IV

FREE-FALL MISSIONS

In this section, a detailed description of the mathematical model used for the performance assessment of the guidance and navigation systems for free-fall vehicles is given. The trajectory calculations are described in Paragraph 4. 1 and relate both to the nonlinear model (i. e., as described in general by Eq. (A-1) and the perturbation equations. The sensors that are considered in the performance assessment program are stated in Paragraph 4. 2. The navigation equations are given in Paragraph 4. 3, and several computational aspects relating to the use of these relations are discussed. The guidance policy is described in Paragraph 4. 4 and is related to the general problem introduced in Paragraph 2. 2.

4. 1 TRAJECTORY

4. 1. 1 NOMINAL TRAJECTORY

There are two conceptually different methods of determining the nominal free-fall trajectory for an interplanetary mission. The first method uses the "exact" dynamical equations; i. e., the influence of all heavenly bodies upon the space vehicle are taken into account at each time during the entire mission. In this case, no "closed-form" analytical solutions exist and the analyst has to rely solely upon numerical integration. The second method is an approximate one. It utilizes the fact that the vehicle's motion in different portions of free-fall is essentially determined by the gravitational attraction of a single central body. This means that the motion can be described by different two-body orbits in different portions of the flight, namely, heliocentric ellipses determined by the initial conditions and the sun in the transfer phase, and planetocentric ellipses or hyperbolas during planet approach, planet departure phase, and periodic orbits around a planet. If the two-body orbits are appropriately "matched", the resulting orbit constitutes, as experience has shown, an excellent approximation to the precise orbit. This method is employed here for the mathematical model. The conics are matched at the sphere-of-influence in a manner similar to that described in the reference stated below. (Reference 2)

Since the differential equations for the two-body problem can be solved in closed form, nominal position and velocity at a desired time are obtained from explicit analytical expressions rather than by numerical integration. The steps involved are the following:

1 At the beginning of the m-th conic, position and velocity are obtained in an equatorial coordinate system. They are defined by the symbols

$$\underline{R}^*(t_o^m) \overset{Df}{=} \begin{pmatrix} X_1^*(t_o^m) \\ X_2^*(t_o^m) \\ X_3^*(t_o^m) \end{pmatrix} ; \qquad \underline{V}^*(t_o^m) \overset{Df}{=} \begin{pmatrix} X_4^*(t_o^m) \\ X_5^*(t_o^m) \\ X_6^*(t_o^m) \end{pmatrix}$$

2. The corresponding angular momentum

$$\underline{h}^*(t_o^m) = \underline{R}^*(t_o^m) \times \underline{V}^*(t_o^m)$$

is computed.

3. From the vis-viva

$$\alpha^*(t_o^m) = \frac{2}{R^*(t_o^m)} - \frac{\underline{V}^*(t_o^m) \cdot \underline{V}^*(t_o^m)}{\mu_\ell}$$

is computed, where μ_ℓ is the gravitational constant of the body ℓ. The sign of this quantity defines the character of the orbit. For closed orbits $\alpha^*(t_o^m)$ is positive; for hyperbolic orbit, it becomes negative.

4. Unit vectors $(\underline{\zeta}_1, \underline{\zeta}_2, \underline{\zeta}_3)$ in the direction of $\underline{R}^*$ (the t_o^m is dropped in the following equations for the sake of brevity) $\underline{h}^*$ and $\underline{h}^* \times \underline{R}^*$ define the local coordinate system and the orientation of the orbital plane at t_o^m, that is,

$$\underline{\zeta}_1 = \frac{\underline{R}^*}{R}; \quad \underline{\zeta}_2 = \underline{\zeta}_3 \times \underline{\zeta}_1; \quad \underline{\zeta}_3 = \frac{\underline{R}^* \times \underline{V}^*}{|\underline{R}^* \times \underline{V}^*|}$$

A second, right-handed, planet-centered, orbital in-plane coordinate system (ξ_1, ξ_2, ξ_3) is defined such that $\underline{\xi}_1$ points along the pericentron and $\underline{\xi}_3$ is perpendicular to the trajectory plane; i.e.,

$$\underline{\xi}_3 \overset{Df}{=} \underline{\zeta}_3$$

The transformation between the (ξ_1, ξ_2, ξ_3) and the (X_1, X_2, X_3) coordinates at $t = t_k^m$ is given by

$$\begin{pmatrix} X_1 \\ X_2 \\ X_3 \end{pmatrix}_{t_k^m} = \mathcal{R}^*(t_o^m) \begin{pmatrix} \xi_1 \\ \xi_2 \\ \xi_3 = 0 \end{pmatrix}_{t_k^m}$$

where

$$\mathcal{R}^*(t_o^m) = (\zeta_1\, \zeta_2\, \zeta_3)_{t_o^m} \begin{pmatrix} \cos\nu & \sin\nu & 0 \\ -\sin\nu & \cos\nu & 0 \\ 0 & 0 & 1 \end{pmatrix}_{t_o^m}$$

The coordinate system is shown in Figure A-5.

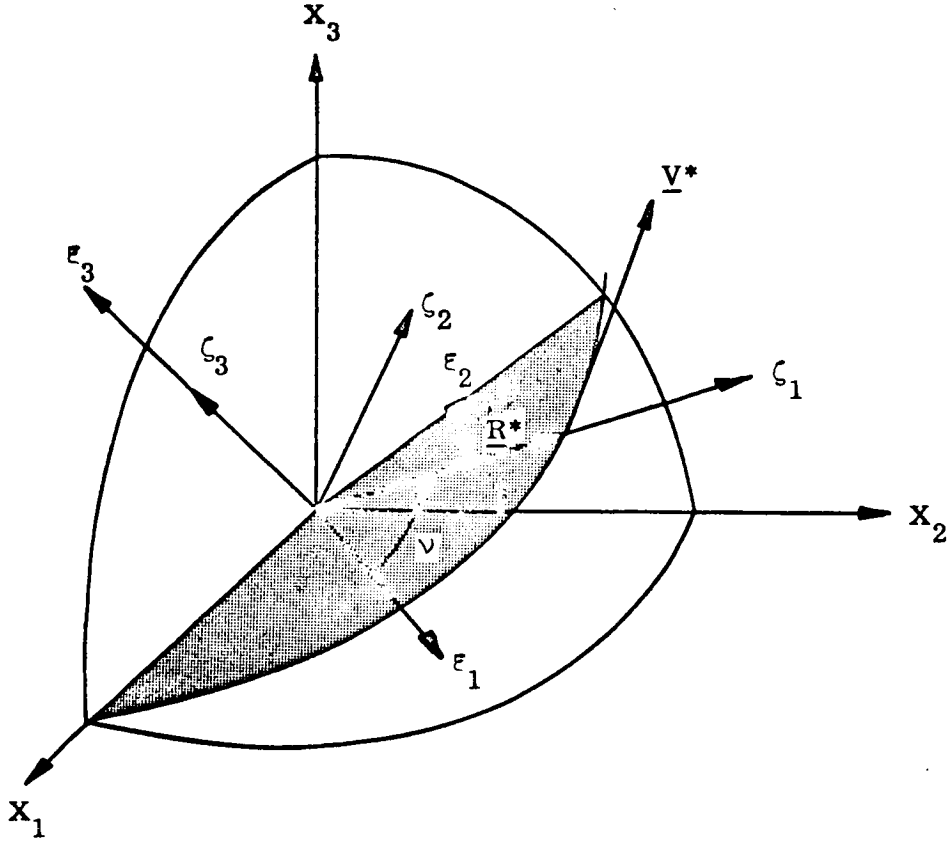

γ_{1950}

Figure A-5. Definition of Coordinate Systems

5. In this orbital plane, the trajectory is specified in the case of an elliptical orbit in the following way:

$$\alpha^* > 0 \Rightarrow \text{elliptic case}$$

The semi-major axis is given by

$$a = \frac{1}{\alpha}$$

The eccentricity is given by

$$e = \left\{\left(1 - \frac{R}{a}\right)^2 + \frac{[\underline{R} \cdot \underline{V}]^2}{\mu_\ell \, a}\right\}^{1/2}$$

The eccentric anomaly can be expressed in terms of the previously defined quantities as

$$E = \begin{cases} \cos^{-1} \dfrac{1}{e} \left[1 - \dfrac{R}{a}\right] \\ \sin^{-1} \dfrac{1}{e} \left[\dfrac{\underline{R} \cdot \underline{V}}{[\mu_\ell \, a]^{1/2}}\right] \end{cases}$$

The mean motion, n, is given by

$$n = \sqrt{\frac{\mu_\ell}{a^3}}$$

The true anomaly is given by

$$\cos \nu = \frac{\cos E - e}{1 - e \cos E}$$

$$\sin \nu = \frac{\sqrt{1 - e^2} \, \sin E}{1 - e \cos E}$$

Time of perifocal passage is given by

$$\tau = \frac{1}{n} [E - e \sin E]$$

The equations for the hyperbolic orbits are very similar and are not stated here.

6. For each time point, Kepler's equation

$$n\tau = E - e \sin E$$

if solved and the in-plane position and velocities are computed relative to a coordinate system with the ζ_1-axis pointing towards pericenter according to the equations,

$$\xi_1(t_k^m) = a(t_o^m)\,[\cos E(t_k^m) - e(t_o^m)]$$

$$\zeta_2(t_k^m) = a(t_o^m)\,\sqrt{1 - e^2(t_o^m)}\,\sin E(t_k^m)$$

$$\dot{\zeta}_1(t_k^m) = a(t_o^m)n(t_o^m)\,\left[\frac{-\sin E(t_k^m)}{1 - e(t_o^m)\cos E(t_k^m)}\right]$$

$$\dot{\zeta}_2(t_k^m) = a(t_o^m)n(t_o^m)\,\sqrt{1 - e^2(t_o^m)}\,\left[\frac{\cos E(t_k^m)}{1 - e(t_o^m)\cos E(t_k^m)}\right]$$

7. Since the guidance and navigation analysis is done in an equatorial coordinate system, the nominal position $\underline{R}^*(t_k^m)$ and velocity $\underline{V}^*(t_k^m)$ are obtained from the in-plane $(\xi_1(t_k);\ \xi_2(t_k);\ \dot{\xi}_1(t_k);\ \dot{\xi}_2(t_k))$ coordinates by the transformation $\mathcal{R}^*(t_o^m)$.

This completes the description of the mathematical model for the calculation of the nominal trajectories. Based on these equations, trajectories are generated that satisfy prescribed mission objectives and constraints.

Because of the nature of these missions, the nominal control policy is very simple. In essence, it consists of choosing the initial conditions of each phase in such a manner that the trajectory constraints are satisfied. For example, consider a round-trip mission to Mars. The distance from Earth at departure and return, as well as the closest approach to Mars, will be specified. Then, the times of departure, Martian passage, and return are chosen to satisfy these constraints so that the injection velocity requirements are as small as possible.

4.1.2 LINEAR SYSTEM MATRICES

As is evident from the preceding section, the equations of motion for the free-fall phase have the general form

$$\dot{\underline{X}} = \underline{f}(\underline{X})$$

It follows then that the linear perturbation equation is simply

$$\dot{\underline{x}} = F(t)\,\underline{x}$$

where F has the form

$$F = \begin{bmatrix} 0 & 0 & 0 & 1 & 0 & 0 \\ 0 & 0 & 0 & 0 & 1 & 0 \\ 0 & 0 & 0 & 0 & 0 & 1 \\ \frac{\partial^2 V}{\partial X_1^2} & \frac{\partial^2 V}{\partial X_1^2 \partial X_2} & \frac{\partial^2 V}{\partial X_1 \partial X_3} & 0 & 0 & 0 \\ \frac{\partial^2 V}{\partial X_2 \partial X_1} & \frac{\partial^2 V}{\partial X_2^2} & \frac{\partial^2 V}{\partial X_2 \partial X_3} & 0 & 0 & 0 \\ \frac{\partial^2 V}{\partial X_3 \partial X_1} & \frac{\partial^2 V}{\partial X_3 \partial X_2} & \frac{\partial^2 V}{\partial X_3^2} & 0 & 0 & 0 \end{bmatrix}$$

where V is the potential of the central body. Because of the assumptions, the potential is described by

$$V = \frac{\mu}{r}$$

The perturbation equations can be solved in a closed form for this system, so it is not necessary to use the matrix F in the calculations in the computer program. The solution requires the state transition matrix to be known and is

$$\underline{x}(t) = \Phi(t, t_o)\, x(t_o)$$

As described above, the basic calculations are performed in an <u>in-plane</u> coordinate system so the Φ has the following structure.

$$\Phi = \left[\begin{array}{c|c} \Phi_1 & \Phi_2 \\ \hline \Phi_3 & \Phi_4 \end{array}\right]$$

where the submatrices have the form

$$\Phi_1 = \begin{bmatrix} \Phi_{11} & \Phi_{12} & 0 \\ \Phi_{21} & \Phi_{22} & 0 \\ 0 & 0 & \Phi_{33} \end{bmatrix} ; \qquad \Phi_2 = \begin{bmatrix} \Phi_{14} & \Phi_{15} & 0 \\ \Phi_{24} & \Phi_{25} & 0 \\ 0 & 0 & \Phi_{36} \end{bmatrix}$$

$$\Phi_3 = \begin{bmatrix} \Phi_{41} & \Phi_{42} & 0 \\ \Phi_{51} & \Phi_{52} & 0 \\ 0 & 0 & \Phi_{63} \end{bmatrix} ; \qquad \Phi_4 = \begin{bmatrix} \Phi_{44} & \Phi_{45} & 0 \\ \Phi_{54} & \Phi_{55} & 0 \\ 0 & 0 & \Phi_{66} \end{bmatrix}$$

Elliptic, parabolic, and hyperbolic trajectories can occur in the range of missions considered and the form of the elements Φ_{ij} depends upon the type of conic. The solution for elliptic trajectories is stated. The reader is directed to the program definition for a more complete statement.

Letting $\sin E_k = S_k \qquad \cos E_k = C_k$

then the elements of the submatrices are

$$\Phi_{11} = \frac{1}{(1-e)^2(1-e\,C_k)} \left[C_k^2(1+e-e^2) + C_k(2+e+2e^2-e^3) - 2 - 5e + 2e^2 + 3E_kS_k\right]$$

$$\Phi_{12} = \frac{\sqrt{1-e^2}}{(1-e)(1-e\,C_k)} S_k\,(1-C_k)$$

$$\Phi_{21} = \frac{\sqrt{1-e^2}}{(1-e)^2(1-e\,C_k)} \left[S_kC_k(1+e) + S_k(2-e) - 3E_kC_k\right]$$

$$\Phi_{22} = \frac{1}{(1-e)(1-e\,C_k)} \left[C_k^2 + C_k(-1-2e+e^2) + 1\right]$$

$$\Phi_{33} = \frac{(C_k - e)}{(1-e)}$$

$$\Phi_{14} = \frac{(1-e)}{n(1-e\,C_k)}\; S_k[-C_k(1+e) + 2]$$

$$\Phi_{15} = \frac{\sqrt{1-e^2}}{(1-e)n(1-e\,C_k)}\; [C_k^2(2-e) + 2C_k(1+e) - 4 - e + 3E_kS_k]$$

$$\Phi_{24} = \frac{\sqrt{1-e^2}}{n(1-e\,C_k)}\; [1 - C_k]^2$$

$$\Phi_{25} = \frac{1}{n(1-e\,C_k)}\; [S_kC_k(2+e+e^2) + 2S_k - 3(1+e)E_kC_k]$$

$$\Phi_{36} = \frac{S_k(1-e)}{n}$$

$$\Phi_{41} = \frac{n}{(1-e)^2(1-e\,C_k)^3}\; [S_kC_k^{\,2}(e+e^2-e^3) + S_kC_k(-2-5e+2e^2) + S_k(1+e+3e^2-e^3) + 3E_k(C_k-e)]$$

$$\Phi_{42} = \frac{n\sqrt{1-e^2}}{(1-e)(1-e\,C_k)^3}\; [e\,C_k^3 - 2C_k^2 + C_k + 1 - e]$$

$$\Phi_{51} = \frac{n\sqrt{1-e^2}}{(1-e)^2(1-e\,C_k)^3}\; [-C_k^3(e+e^2) + C_k^2(2+5e) - C_k(1+e) - 1 - 3e + e^2 + 3E_kS_k]$$

$$\Phi_{52} = \frac{n\,S_k}{(1-e)(1-e\,C_k)^3}\; [e\,C_k^2 - 2C_k + 1 + e - e^2]$$

$$\Phi_{63} = \frac{-n\,S_k}{(1-e)(1-e\,C_k)}$$

$$\Phi_{44} = \frac{1-e}{(1-e\,C_k)^3}\; [C_k^3(e+e^2) - 2C_k^2(1+e) + 2C_k + 1 - e]$$

$$\Phi_{45} = \frac{\sqrt{1-e^2}}{(1-e)(1-e\,C_k)^3}\,[S_k C_k^2(2e-e^2) - S_k C_k(4+e) + S_k(1+e)^2 + 3E_k(C_k-e)]$$

$$\Phi_{54} = \frac{S_k\sqrt{1-e^2}}{(1-e\,C_k)^3}\,[e\,C_k^2 - 2C_k + 2 - e]$$

$$\Phi_{55} = \frac{1}{(1-e\,C_k)^3}\,[-C_k^3(2e+e^2+e^3) + C_k^2(4+5e+5e^2)$$
$$-C_k(1+3e) - 2 - 3e - e^2 + 3(1+e)E_k S_k]$$

$$\Phi_{66} = \frac{(1-e)\,C_k}{(1-e\,C_k)}$$

The transition matrix is the only linear system matrix computed in the program that is related to the plant. The observation matrices for the electromagnetic sensors are also required, and they are discussed in Paragraph 4. 2

The transition matrix for this phase has been recognized as being a symplectic matrix. It has, therefore, an easily obtained inverse

$$\Phi^{-1} = \begin{bmatrix} \Phi_4^T & -\Phi_2^T \\ -\Phi_3^T & \Phi_1^T \end{bmatrix}$$

4. 1. 3 ACTUAL TRAJECTORY

The actual trajectory is computed according to the same equations and in the same manner as the nominal trajectory. No plant noise is assumed, so the only unknown relative to the actual trajectory is the initial state. In the program, the $\underline{X}_o$ can be specified by the engineer or can be obtained by establishing the perturbation $\underline{x}_o$ using a random noise generator and the a priori statistics. Then,

$$\underline{X}_o = \underline{X}_o^* + \underline{x}_o$$

4.2 SENSORS

The Free-fall Performance Assessment Program has the capability of simulating several instruments. They are

1. Space sextant
2. Horizon sensor
3. Planet tracker
4. Ground-based radar — three radar stations can be included simultaneously.

These instruments are discussed in Paragraph 2.4. The facility has been included in the program to consider bias errors in the measurement data. When this option is utilized, the biases are considered as additional state variables.

The bias errors are random quantities and are described as having a mean value of zero and covariance matrix B_o. In the simulation, the B_o is used in conjunction with a noise generator to obtain numerical values for the bias errors. The measurement data also are corrupted by random noise. These random errors are defined as having zero mean. At each sampling time, the covariance matrix of the noise is assumed to be known and is denoted by R_k. Random noise is obtained from a noise generator using these statistics.

4.3 NAVIGATION

The Kalman filter is used to estimate the state perturbations from the measurement data. The plant model is simpler than the general form described in Section II, so the filter equations can also be simplified. In the Free-fall Performance Assessment Program, the general form of the Kalman filter is given by

$$\hat{\underline{x}}_k = \hat{\underline{x}}'_k + K_k (\underline{z}_k - H_k \hat{\underline{x}}'_k)$$

where

$$\hat{\underline{x}}'_k = \Phi_{k,k-1} \hat{\underline{x}}_{k-1}$$

$$K_k = P'_k H_k^T [H_k P'_k H_k^T + R_k]^{-1}$$

$$P'_k = \Phi_{k,k-1} P_{k-1} \Phi_{k,k-1}^T + Q_{k-1}$$

$$P_k = P'_k - K_k H_k P'_k$$

Although the plant does not explicitly contain any noise, the matrix Q_{k-1} has been included in the equations. This feature is discussed below.

The only difference between these equations and A-10 occurs in the absence of the known plant term $\underline{f}_{k-1}$. There are several aspects relating to these general equations that are not immediately apparent. First, the state vector must be defined. The error covariance matrix P_k is of the same order as the dimension of the state. Theoretically, the P_k is a non-negative definite, symmetric matrix. Because of computational inaccuracies, it can happen that the P_k loses both of these properties. Techniques have been devised that delay or prevent this from occurring. The inaccuracies result from the finite word-length of a digital computer. Capability has been included that allows the simulation of the effects of a reduced word-length. These topics are discussed briefly in the subsequent paragraphs.

4.3.1 THE STATE VECTOR

The state vector is at least six-dimensional and always contains the position and velocity as components. In this program, the bias errors of the electromagnetic sensors provide the other possible components of the state vectors. The most general state vector occurs when every instrument is included and has the following form.

X_1, X_2, X_3	position of the spacecraft
X_4, X_5, X_6	velocity of the spacecraft
X_7, X_8, X_9	errors in location of Tracker No. 1
X_{10}, X_{11}, X_{12}, X_{13}	bias errors in measurements from Tracker No. 1
X_{14}, X_{15}, X_{16}	errors in location of Tracker No. 2

X_{17}, X_{18}, X_{19}, X_{20}	bias errors in measurements from Tracker No. 2
X_{21}, X_{22}, X_{23}	errors in location of Tracker No. 3
X_{24}, X_{25}, X_{26}, X_{27}	bias errors in measurements from Tracker No. 3
X_{28}, X_{29}, X_{30}	bias errors in horizon sensor measurements
X_{31}	bias error in space sextant measurement.

Thus, the maximum dimension of the state vector in this program is thirty-one.

4.3.2 ORBIT RECTIFICATION

Orbit rectification is the process of updating the nominal trajectory of each observation with the best estimate. This process is designed to extend the range of linear theory and provide satisfactory results in those cases where Kalman filter estimation using a single perspecified nominal trajectory was found to be inadequate.

4.3.3 SQUARE-ROOT KALMAN FILTER

Since P_k is non-negative definite and symmetric, it is always possible to write it in terms of a matrix factor Π_k

$$P_k = \Pi_k \Pi_k^T$$

When there is no plant noise and when each measurement is processed individually, it is possible to obtain recursion relations for the Π_k. Then the computations can be based on the Π_k. Since P_k is then the product of a matrix and its transpose, the P_k will remain symmetric and non-negative definite. This formulation of the Kalman filter is included in the program.

4.3.4 COMPENSATION FOR COMPUTATIONAL ERRORS

The matrix Q_{k-1} that appears in the filter equations generally represents the covariance of the plant noise. To assume that there is no plant noise ($Q_{k-1} = 0$) is to assume that the actual state obeys the linear equations of motion exactly; that is, that once the state is known exactly (or almost exactly) at some time, t_i, that it can then be determined exactly (or almost exactly) at any other time by use of the state transition matrix.

Intuitively, it would seem that if this were so, then each additional measurement would reduce the state error, and nothing would tend to increase the error; therefore the resultant error would tend to approach zero. This, in fact, does happen mathematically in that if Q_{k-1} is assumed equal to 0, then P_k approaches 0. This causes a singularity problem which reflects the fact that ultimately the model assumes that the state is already so well known that it should give zero weight to any new measurements.

This is clearly an unrealistic assumption and therefore assumed values for Q_{k-1} are incorporated. These represent errors in the model and computational errors. The effect of increasing the magnitude of the Q_{k-1} is to cause the filter to "wash out" the effect of past measurements more rapidly.

4.3.5 VARIABLE COMPUTER WORD-LENGTH

Provision has been made to examine some of the effects of a reduced computer word-length. This is accomplished by setting a specified number of bits of the elements of P_k, K_k, and $\hat{\underline{x}}_k$ equal to zero at the end of every computational cycle.

4.4 GUIDANCE

It is assumed that the trajectory corrections that are required for this type of mission will be small and that they can be adequately represented by an instantaneous change in the velocity of the vehicle. Based on this assumption, the guidance policy involves two primary considerations.

1. The time of the velocity correction must be established. Needless to say, a velocity correction will not be made at every sampling time. It is, in fact, desirable to introduce as few corrections as is necessary to accomplish the mission objectives.

2. The velocity correction itself must be determined according to some criterion.

The policy used in the program is presented below. The guidance law is then discussed in terms of the general statements of Section 2.

4.4.1 DETERMINATION OF THE DESIRED VELOCITY CORRECTION

The guidance laws are determined by the terminal conditions required for the mission. At each correction time, the velocity that is required to completely null the error in specified terminal constraints is computed using the linear perturbation theory and the current best estimate. In general, the correction is determined according to

$$\Delta \hat{\underline{V}}_k = \Lambda_k \hat{\underline{x}}_k$$

where $\hat{\underline{x}}_k$ represents the best estimate of the basic six-dimensional state. The guidance matrix Λ_k is established in a deterministic manner to accomplish the objective. In some cases, the time of arrival at the target is allowed to be different than that of the nominal. The change is computed from

$$\delta T = C_T \hat{\underline{x}}_k$$

Five different control laws have been considered and are listed below. They are classified by the nature of the terminal constraints.

1. <u>Fixed position - fixed time of arrival</u>

   The spacecraft is required to reach a specified position at a given time.

2. <u>Fixed position - variable time of arrival</u>

   The spacecraft is required to arrive at a specified position; the time at which it accomplishes this objective is not restrained. In this case, the magnitude of the velocity correction is minimized through the choice of the time of arrival.

3. <u>R, γ, θ - fixed time of arrival</u>

   The spacecraft is required to achieve a desired radial distance, flight path angle, and velocity direction at the nominal time of arrival.

4. R, γ, θ - variable time of arrival

This control law is similar to the preceding one except the time of arrival is not specified. It is chosen to minimize the magnitude of the velocity correction.

5. R, γ, $\underline{u}$ - variable time of arrival

In addition to the radial distance and flight path angle, the position and velocity of the vehicle is required to lie in a desired plane. The time of arrival is used to satisfy the fourth constraint that is introduced by the constraint on $\underline{u}$.

The specified form of the Λ and C_T are given in the Program Definition.

4.4.2 TIMING OF THE VELOCITY CORRECTIONS

Several techniques have been suggested in the literature. In this program, the variance ratio criteria suggested by Battin is used. Using this approach, the time of the correction is based upon statistics relating to the velocity correction.

The covariance of the estimated correction is

$$V(t_k) = E[\Delta\hat{\underline{V}}(t_k)\,\Delta\hat{\underline{V}}^T(t_k)]$$

$$= \Lambda(t_k)\,[M_k - P_k]\,\Lambda^T(t_k)$$

where

$$M_k = \Phi_{k,k-1} M_{k-1} \Phi^T_{k,k-1}$$

$$P_k = \Phi_{k,k-1} P_{k-1} \Phi^T_{k,k-1}$$

The trace of this matrix is defined as $\overline{\Delta V^2(t_k)}$.

The error in the estimate of the velocity correction is characterized statistically by its covariance matrix

$$D(t_k) = E[(\Delta\hat{\underline{V}}(t_k) - \Delta\hat{\underline{V}}_e(t_k))\,(\Delta\hat{\underline{V}}(t_k) - \Delta\hat{\underline{V}}_e(t_k))^T]$$

$$= \Lambda(t_k)\,P(t_k)\,\Lambda^T(t_k)$$

where $\Delta\underline{V}_e(t_k)$ would be the velocity correction if the state were known perfectly. The trace of this matrix is defined as $\overline{d^2(t_k)}$.

A velocity correction is commanded according to the variance ratio criterion below. This test is accomplished by comparing the quantity

$$R_V = \frac{\overline{d^2(t_k)}}{\overline{\Delta V^2(t_k)}}$$

with some arbitrary constant R_V min. When $R_V < R_V$ min, a correction is made.

4.4.3 IMPLEMENTATION OF THE CORRECTION

The control system will, in general, not perform guidance corrections exactly. The errors in the control system and non-nominal engine performance are assumed to combine to result in actual velocity corrections whose magnitude are proportional to the estimate.

$$|\Delta \underline{V}(t_k)| = (1 + \eta)\ |\Delta \hat{\underline{V}}(t_k)|$$

The η is a Gaussian random variable with mean zero and variance $\overline{\eta^2}$. It is selected from a Gaussian number generator. The angle between the actual and estimated corrections is δ and is a Gaussian random variable with mean zero and variance $\overline{\delta^2}$.

The difference between the estimated and actual velocity corrections is characterized statistically by the covariance matrix

$$\begin{aligned} N(t_k) &= E[(\Delta \hat{\underline{V}}(t_k) - \Delta \underline{V}(t_k))\ (\Delta \hat{\underline{V}}(t_k) - \Delta \underline{V}(t_k))^T] \\ &= \overline{\eta^2} V(t_k) + \frac{\overline{\delta^2}}{2} [v(t_k)\ I - V(t_k)] \end{aligned}$$

where

$$v(t_k) = \sum_{i=1}^{6} \sum_{j=1}^{6} \beta_{ij} [m_{ij}(t_k) - p_{ij}(t_k)]$$

and the m_{ij} and p_{ij} are elements of M_k and P_k. The β_{ij} are elements of the matrix $\Lambda^T(t_k)\ \Lambda(t_k)$.

At velocity correction times, the navigation statistics and state vector estimate must be modified to include the effects of the correction.

$$P_k = P'_k + J\, N_k\, J^T$$

$$M_k = [I + J\,\Lambda(t_k)]\,[M(t_k) - P(t_k)]\,[I + J\,\Lambda(t_k)]^T + P'(t_k)$$

$$\hat{\underline{x}}_k = \Phi_{k,k-1}\,\hat{\underline{x}}_{k-1} + J\,\Delta\hat{\underline{V}}(t_k)$$

and

$$J = \begin{pmatrix} 0 \\ I \end{pmatrix}$$

The 0 and I represent 3 x 3 zero and identity matrices, respectively.

It should be noted that when a velocity correction occurs, no measurement data is processed. Thus, the $\hat{\underline{x}}_k$ and P_k given above provide the best available navigational data.

4.4.4 RELATION TO THE GENERAL GUIDANCE PROBLEM

The guidance policy described above does not bear a close resemblance to the problem described in Section II. It is interesting to note that the same guidance laws are obtained by formulating the velocity correction $\Delta\underline{V}$ as the control variables, assuming that only one correction will be made, and by then minimizing the expected value of the square of the terminal constraint errors. The requirement that the derivation assume that only one correction will occur illustrates the suboptimal character of this common guidance policy. Policies of this general character (i.e., policies which ignore the fact that additional data and corrections are to be available) are referred to as open-loop feedback control. One might expect that a closed-loop policy in which the total number of corrections is specified and thus is considered in the determination of each $\Delta\underline{V}_k$ would be superior. However, the present policy is used because of its common application in other space guidance studies.

SECTION V

REENTRY MISSIONS

In this section a detailed description of the mathematical model for the performance of aided-inertial re-entry guidance systems is given. The nominal trajectory calculations are described in Paragraph 5.1. It includes the nonlinear differential equations of motion the nominal control policy, and the linear perturbation equations. The mathematical description of the IMU configurations and electromagnetic sensors for re-entry guidance systems are presented in Paragraph 5.2. The navigation equations are formulated in Paragraph 5.3, and the guidance policy is described in Paragraph 5.4.

5.1 TRAJECTORY

5.1.1 NOMINAL TRAJECTORY

5.1.1.1 Basic Assumptions and General Structure of Trajectory Profile

The model for the nominal re-entry trajectory, which provides acceleration, velocity, position, and attitude as a function of time for the performance assessment of aided-inertial re-entry guidance systems as described below, is based upon the following general assumptions.

1. Physical Environment

   A nonrotating planet with a spherically symmetric gravitational potential and an exponential nonrotating atmosphere constitutes the physical environment.

2. Vehicle Configuration

   A rigid lifting vehicle without any thrusting capability outside that required for attitude changes is assumed.

3. Nominal Control

   Aerodynamic control is achieved through a change of the roll angle and angle of attack of the vehicle. The specific character of the control law depends upon the trajectory phase.

The mathematical model is formulated in such a fashion that at most 7 phases can be encountered in one trajectory. On the other hand, it is possible that the starting point can lie in any of these phases. These phases are schematically depicted in Figure A-6.

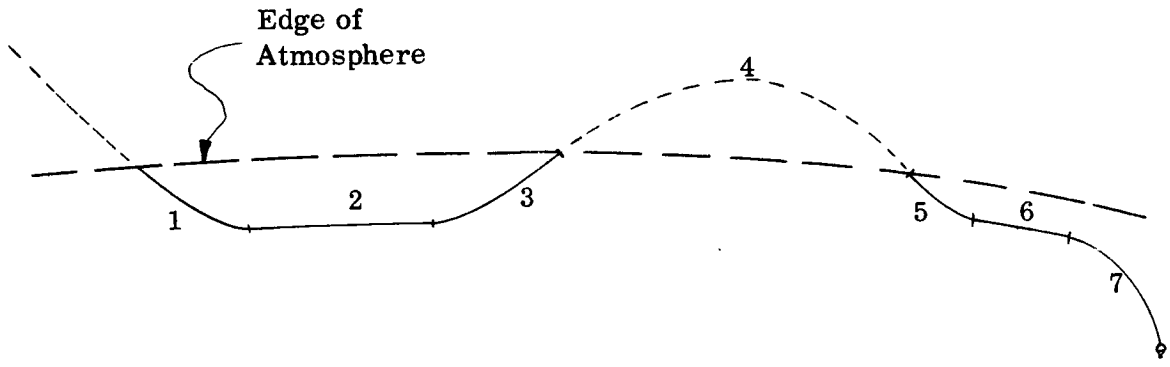

Figure A-6

The model describes the following major mission profiles.

1. Single-pass trajectories. This class encompasses those trajectories in which the vehicle does not leave the atmosphere after it entered it once.

2. Single-skipout trajectories. This class encompasses those trajectories for which two atmospheric phases are connected with each other by a free-fall orbit.

In addition to these two major classes the model provides the possibility of describing other trajectories such as those encountered in atmospheric braking maneuvers. The latter can be simulated by starting the program in Phase 3.

For the sake of clarity, the different phases as numbered in Figure A-6 (i.e., assuming a single-skipout trajectory) are defined as follows.

Phase 1: Initial entry phase. The roll angle and the angle of attack can be used for nominal control.

Phase 2: "First" constant altitude phase. The control technique, using the roll angle as the only control variable, attempts to keep the vehicle at constant altitude above the planet.

Phase 3: Pullout phase. Characteristic for skipout trajectories. In this phase, using the roll angle as a control variable, the vehicle is brought back into the vacuum and put on an elliptic orbit.

Phase 4: Skipout phase. No trajectory control is provided since it is assumed that thrust is only available for vehicle attitude control.

Phase 5: "Second" entry phase. Control variables are the roll angle and the angle of attack.

Phase 6: "Second" constant altitude phase. The same control variable (roll angle) as in Phase 2 is used.

Phase 7: Final descent phase. The vehicle is kept at constant roll angle and angle of attack. The roll angle can change signs in order to provide out-of-plane control.

5.1.1.2 Coordinate System

The motion of the re-entry vehicle is described in two different coordinate systems, namely:

1. Orthogonal, nonrotating, cartesian coordinate system ($\underline{i}$, $\underline{j}$, $\underline{k}$) with the origin at the center of the planet. The differential equations of motion are integrated in this coordinate system.
2. Spherical coordinate system. This coordinate system is used in connection with the performance assessment program, primarily because the linear system matrices have a simpler form in such a coordinate system. It is defined with respect to the initial flight plane, thus providing a natural measure for out-of-plane errors.

The spherical coordinate system is shown in Figure A-7, and is referenced to an irrotational orthogonal cartesian coordinate system ($\underline{i}_t$, $\underline{j}_t$, $\underline{k}_t$). The relation of this system to the cartesian system ($\underline{i}$, $\underline{j}$, $\underline{k}$) as described under (a), is shown in Figure A-8.

5.1.1.3 Differential Equations of Motion

This section states the differential equations of motion, resulting from the following basic assumptions.

1. The vehicle is represented by a point mass.

   This assumption concerns only the motion of the vehicle along the trajectory. The 6-dimensional dynamical character of the problem is taken into account through the model for the nominal control policy, as described in the next section. It enters the differential equations directly through the control variables, which are the roll angle, φ, and the angle-of-attack, α.
2. Ablation effects are ignored resulting in a constant mass for the vehicle.
3. Exponential nonrotating atmosphere and spherical earth is assumed.

Under these assumptions the differential equations of motion in the cartesian ($\underline{i}$, $\underline{j}$, $\underline{k}$) coordinate systems become

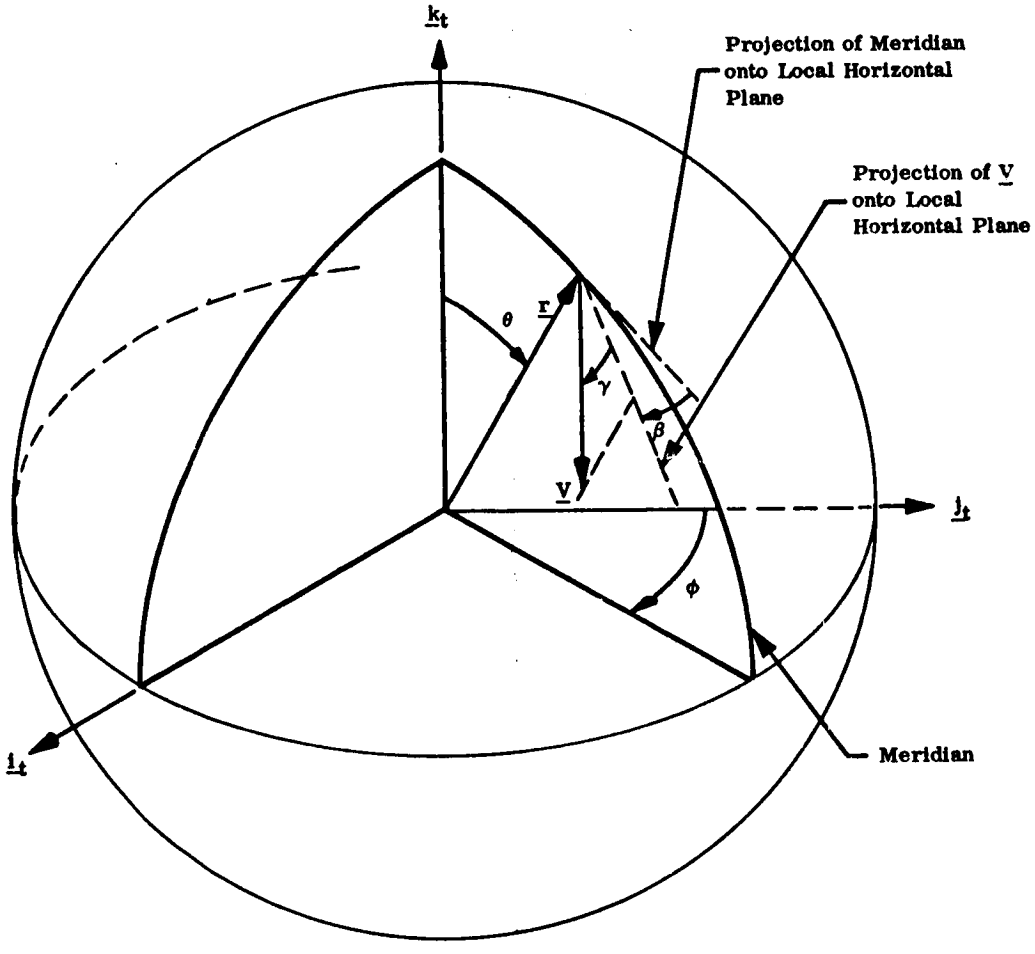

Figure A-7. Relation Between Spherical Coordinate System (r, ϕ, θ, V, γ, β) and $\underline{i}_t$, $\underline{j}_t$, $\underline{k}_t$ System

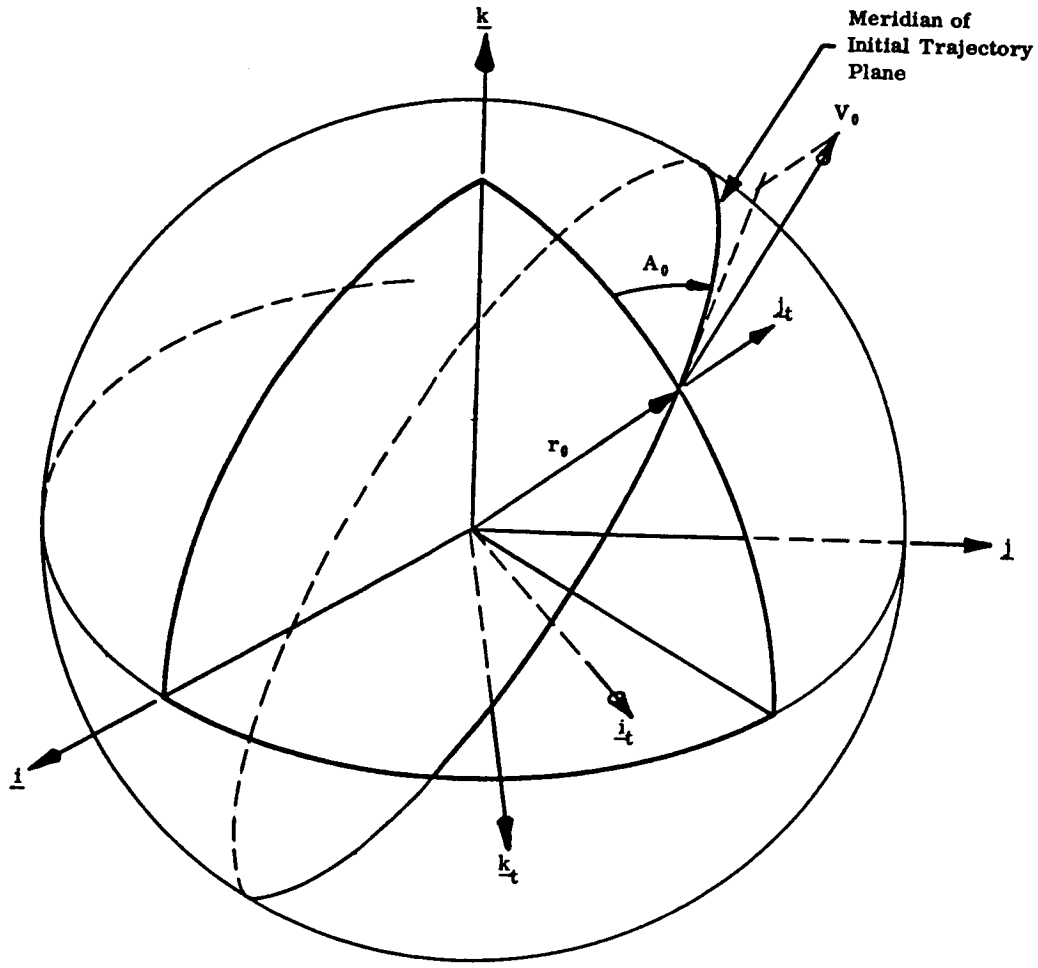

Figure A-8. Cartesian Basis for Output Spherical Coordinate System at $t = t_o$ ($\underline{i}_t$, $\underline{j}_t$, $\underline{k}_t$) Related to $\underline{i}$, $\underline{j}$, $\underline{k}$ System

$$\underline{a} = \frac{1}{M}(\underline{D} + \underline{N}) - \underline{g}$$

$\underline{a}$ is the total acceleration, M the mass of the vehicle, $\underline{g} = g_o(\frac{R}{r})^2 \underline{U}_r$ is the gravitational acceleration with

g_o	=	sea level gravitational acceleration of re-entry planet
R	=	radius of re-entry planet
r	=	radial distance of re-entry vehicle from center of re-entry planet
$\underline{U}_r$	=	unit position vector of vehicle in the Newtonian reference cartesian coordinate system, $\underline{i}$, $\underline{j}$, $\underline{k}$.

The aerodynamic drag forces $\underline{D}$ and the aerodynamic normal force $\underline{N}$ are given by

$$\underline{D} = -C_D \rho \frac{V^2 S}{2} \underline{U}_v$$

$$\underline{N} = C_N \rho \frac{V^2 S}{2} (\cos \omega \underline{U}_u - \sin \omega \underline{U}_p)$$

The dependence of the aerodynamic drag and normal force coefficients C_D and C_N on the angle of attack α is assumed as

$$C_D = C_{D_o} + C_2 \alpha^2 + C_4 \alpha^4$$

$$C_N = C_{N_\alpha} \alpha + C_3 \alpha^3 + C_5 \alpha^5$$

where C_{D_o}, C_{N_α}, and C_i $(i = 2, \ldots, 5)$ are properly chosen constants.

The atmosphere density has the form

$$\rho = \rho_o e^{-\beta'(r - R)}$$

V indicates the speed, S the aerodynamic area of the vehicle, and the orthogonal (u, v, p) coordinate system is defined as

$\underline{U}_u$	unit vector perpendicular to $\underline{U}_v$ and in instantaeious trajectory plane.
$\underline{U}_v$	unit vector in direction of velocity.

$$\underline{U}_p = \underline{U}_u \times \underline{U}_v$$

This completes the description of the differential equations in the ($\underline{i}$, $\underline{j}$, $\underline{k}$) coordinate system. The equations of motion are always integrated with respect to this coordinate system.

In the spherical coordinate system, as defined in Figure 2, the differential equations assume the form

$$\begin{bmatrix} \dot{r} \\ \dot{\theta} \\ \dot{\phi} \\ \dot{V} \\ \dot{\gamma} \\ \dot{\beta} \end{bmatrix} = \begin{bmatrix} V \sin \gamma \\ (V/r) \cos \gamma \cos \beta \\ \dfrac{V \cos \gamma \sin \beta}{r \sin \theta} \\ -\dfrac{D}{M} - g \sin \gamma \\ \dfrac{N \cos \varphi}{MV} + \left(\dfrac{V}{r} - \dfrac{g}{V}\right) \cos \gamma \\ \dfrac{N \sin \varphi}{MV} + \dfrac{V \cos \gamma \sin \beta \cos \theta}{r \sin \theta} \end{bmatrix}$$

This set of equations forms the basis for the derivation of the linear system matrices.

5.1.1.4 Nominal Control

For the Nominal Trajectory Generation Program, the roll angle φ and the angle of attack α can be used for aerodynamic control of the vehicle in the different phases as explained in the first section. The nominal trajectory for the Performance Assessment Program is restricted to the use of the roll angle as the control variable. The angle of attack serves as a control variable for the actual trajectory calculations, however. The quantitative details are discussed phasewise below.

5.1.1.4.1 Nominal Control During First and Second Re-entry Phase. A constant roll angle is used in these two phases and is changed in sign if the direction of the velocity vector deviates from the initial nominal trajectory plane by more than ϵ_s. Thus

$$\varphi_{ci} = \text{sign}_i \, \varphi_c$$

$$\text{sign}_i = \begin{cases} \text{sign}_{i-1} & \text{if } |\underline{U}_{po} \cdot \underline{U}_v| < \epsilon_s \\ \text{sign}\,(\underline{U}_{po} \cdot \underline{U}_v) & \text{if } |\underline{U}_{po} \cdot \underline{U}_v| \geq \epsilon_s \end{cases}$$

where

$$\underline{U}_{po} = (\underline{U}_u \times \underline{U}_v)_{t_o}$$

defines the unit vector normal to the initial trajectory phase.

During a flipover maneuver the change in the roll angle is assumed to be

$$\varphi_i = \varphi_{i-1} + \omega\varphi_{i-1} \Delta t$$

and the rate of the vehicle is computed according to

$$\omega\varphi_i = K_\varphi (\varphi_{ci} - \varphi_i)$$

K_φ is a preselected constant, representing in a gross fashion the vehicle response to the control system.

The commanded angle of attack is assumed as

$$\alpha_c = \alpha_{i-1} + \left(\frac{d\alpha}{da}\right) \Delta a$$

where

$$\Delta a = a_o - a$$

a_o is a prespecified acceleration and a represents the present acceleration. Thus, the angle of attack control tends to increase the velocity losses during these phases as much as possible.

The differential quotient $\frac{d\alpha}{da}$ is given by

$$\frac{d\alpha}{da} = \frac{2M}{q} \frac{\left[C_{D_o}^2 + \sum_{i=1}^{5} A_{2i}\, \alpha^{2i}\right]^{1/2}}{\sum_{i=0}^{4} A_{2i+1}\, \alpha^{2i+1}}$$

q is the dynamic pressure, M the total sum of the vehicle, and the A_i are given as

$$A_1 = 4\, C_{D_o}\, C_2 + 2\, C_{N_\alpha}^{\;2}$$

$$A_2 = 2\, C_{D_o}\, C_2 + C_{N_\alpha}^{\;2}$$

$$A_3 = 4\, C_2^{\;2} + 8\, C_{D_o}\, C_4 + 8\, C_{N_\alpha}\, C_3$$

$$A_4 = 2\, C_{D_o}\, C_4 + C_2^{\;2} + 2\, C_{N_\alpha}\, C_3$$

$$A_5 = 12\, C_2 C_4 + 12\, C_{N_\alpha}\, C_5 + 6\, C_3^{\;2}$$

$$A_6 = 2\, C_2 C_4 + 2\, C_{N_\alpha}\, C_5 + C_3^{\;2}$$

$$A_7 = 8\, C_4^{\;2} + 16\, C_3 C_5$$

$$A_8 = C_4^{\;2} + 2\, C_3 C_5$$

$$A_9 = 10\, C_5^{\;2}$$

$$A_{10} = C_5^{\;2}$$

In contrast to the roll control, it is assumed that there is no delay in the commanded angle of attack and the actual angle of attack, i.e.,

$$\alpha_i = \alpha_{c_i}$$

This assumption is justified by the small changes in this control variable.

5.1.1.4.2 Nominal Control During the Constant Altitude Phase. The roll angle control is given by

$$\varphi_c = \text{sign}_i \left[\frac{\pi}{2} + \sin^{-1}(K_1\, \Delta\dot{r} + K_2\, \Delta r) + \frac{\pi}{2}\, e^{-K_3(t - T_c)}\right]$$

where

$\Delta\dot{r} = \dot{r}$ = radial velocity of vehicle

$\Delta r = r - r_c$

r_c = desired constant altitude of vehicle

K_1 and K_2 are gains whose value is either input as constant or calculated as a function of time (optimum gains)

K_3 is an input constant

T_c = time at the beginning of the constant altitude phase

$sign_i$ is chosen in the same fashion as in the initial entry phases and provides out-of-plane control

This control law provides upward normal force ($|\varphi_c| < \pi/2$) as required to keep the vehicle at a constant altitude. The term $(\pi/2)e^{-K_3(t - T_c)}$ is used to make $|\varphi_c| = \pi$ at the beginning of the constant altitude. This is helpful in preventing an unintentional skipout.

5.1.1.4.3 Nominal Control in Pullout Phase. The roll angle is used as control variable and specified as

$$\varphi_c = sign_i \left[F_0 + F_1 (t - T'_c) + F_2 (t - T'_c)^2 \right]$$

F_0, F_1, F_2 are appropriate input quantities, T'_c the time at beginning of the pullout phase, and $sign_i$ is determined as in the initial entry phase and used for out-of-plane control.

5.1.1.4.4 Nominal Control in Final Descent Phase. The roll angle is used as control variable in the same way as in the initial entry phase.

5.1.2 LINEAR SYSTEM MATRICES

Two types of linear system matrices are discussed in this section. The first type arises from the form of the plant equation and the nature of the variables in the basic state vector, whereas the second derives from the particular formulation that is used to incorporate the IMU data.

5.1.2.1 Plant Matrices

The state vector contains a minimum of nine components. In addition to the position and velocity, the lift and drag coefficients, C_{D_o} and C_{N_α} are treated as unknown but constant parameters and provide two additional state variables. The atmospheric

density coefficient ρ_o is treated as the ninth variable. The density perturbation $\delta\rho_o$ is assumed to be described by a linear differential equation. It will be discussed below.

As can be seen from the preceding section, the equations of motion of a re-entry vehicle are described in general by

$$\ddot{\underline{r}} = \underline{g}(\underline{r}) + \underline{f}(\underline{r}, \dot{\underline{r}}, \underline{U}. \underline{A}^F, A^V)$$

where $\ddot{\underline{r}}$, $\dot{\underline{r}}$, and $\underline{r}$ represent the acceleration, velocity, and position, respectively, of the spacecraft. The term $\underline{g}(\underline{r})$ describes the gravitational acceleration. Atmospheric effects are described by the $\underline{f}$. The control vector $\underline{U}$ refers to the angle of attack and roll angle of the vehicle so it is two-dimensional. The $\underline{A}^F$ and A^V represent the lift and drag coefficients and the atmospheric density (i.e., the additional state variables). The superscripts denote the fact that the former two are constant whereas the density is assumed to vary.

It has been stated that the calculations relating to the linear system matrices are performed in a spherical coordinate system. Then, the equations of motion assume the form

$$\begin{bmatrix} \dot{\underline{X}}^p \\ \dot{\underline{X}}^v \end{bmatrix} = \begin{bmatrix} \underline{h}(\underline{X}^p, X^v) \\ \underline{g}(\underline{X}^p) + \underline{f}(\underline{X}^p, \underline{X}^v, \underline{U}, \underline{A}^F, A^V) \end{bmatrix}$$

where $\underline{X}^p$ and $\underline{X}^v$ are comprised of the r, θ, and ϕ and V, γ, β, respectively. The function $\underline{h}$ relates components of the $\underline{X}^p$ and $\underline{X}^v$ to the time derivatives of the $\underline{X}^p$.

The linear perturbation equations are formed from the equations of motion and can be written as

$$\dot{\underline{x}} = F_1(t)\,\underline{x} + F_2(t)\,\underline{x} + E_2(t)\,\underline{b} + E_3(t)\,c + E_4(t)\,\underline{u}$$

where

$$\underline{x} \overset{Df}{=} \underline{X}^p - \underline{X}^{p*}$$

$$\underline{u} \overset{Df}{=} \underline{U} - \underline{U}^* \overset{Df}{=} \begin{bmatrix} \delta\alpha \\ \delta_{rD} \end{bmatrix}$$

$$\underline{b} \overset{Df}{=} \underline{A}^F - \underline{A}^{F*} \overset{Df}{=} \begin{bmatrix} \delta C_{D_o} \\ \delta C_{N_\alpha} \end{bmatrix}$$

$$c = A^V - A^{V*} \overset{Df}{=} \delta\rho_o$$

Note that this has the form of Equation (A-4) since $\underline{b}$ and c are to be considered as state variables. The matrices appearing in this equation are defined to be

$$F_1(t) \stackrel{Df}{=} \begin{bmatrix} \dfrac{\partial \underline{h}}{\partial \underline{X}^p} & \dfrac{\partial \underline{h}}{\partial \underline{X}^v} \\ \dfrac{\partial \underline{g}}{\partial \underline{X}^p} & \dfrac{\partial \underline{g}}{\partial \underline{X}^v} \end{bmatrix}$$

$$F_2(t) \stackrel{Df}{=} \begin{bmatrix} 0 & 0 \\ \dfrac{\partial \underline{f}}{\partial \underline{X}^p} & \dfrac{\partial \underline{f}}{\partial \underline{X}^v} \end{bmatrix}$$

$$E_2(t) \stackrel{Df}{=} \begin{bmatrix} 0 \\ \dfrac{\partial \underline{f}}{\partial \underline{A}^F} \end{bmatrix}$$

$$E_3(t) \stackrel{Df}{=} \begin{bmatrix} 0 \\ \dfrac{\partial \underline{f}}{\partial A^V} \end{bmatrix}$$

$$E_4(t) \stackrel{Df}{=} \begin{bmatrix} 0 \\ \dfrac{\partial \underline{f}}{\partial \underline{U}} \end{bmatrix}$$

All of these matrices are evaluated with nominal values of the parameters.

The five matrices listed above must be evaluated in the program. Since a difference equation must be used to describe the plant, these matrices are used to obtain the solution of the differential equations.

First, the state transition matrix must be determined as the solution of

$$\dot{\Phi}(t, \tau) = (F_1 + F_2)\, \Phi(t, \tau)$$

where $\Phi(\tau, \tau) = I.$

Consider the augmenting variables $\underline{b}$ and c. The $\underline{b}$ has been defined as a constant vector so

$$\dot{\underline{b}} = 0$$

or, equivalently,

$$\underline{b}_k = \underline{b}_{k-1} \quad \text{for any k.}$$

The atmospheric density perturbation is described by a linear differential equation

$$\dot{c} = \delta\dot{\rho}_o = -\frac{|\dot{h}|}{h_\rho}\, \delta\rho_o + |\dot{h}|\, w_\rho(t)$$

where $\dot{h}$ represents the rate of change of altitude on the nominal trajectory. The h_ρ is an arbitrary constant. The forcing function w_ρ represents a white noise process with covariance given by

$$E\,[w_\rho(t)\, w_\rho(\tau)] = \frac{f_\rho(h(t))\, \delta(t - \tau)}{|\dot{h}|}$$

$$f_\rho(h) = k_0 + (k_1 + k_2\, h)\, e^{-k_3 [h - h(0)]}$$

where k_0, k_1, k_2 and k_3 are arbitrary constants. This equation must be solved. Thus

$$c_k = {}_c\Phi_{k,k-1}\; c_{k-1} + {}_cw_{k-1}$$

where

$${}_cw_{k-1} = \int_{t_{k-1}}^{t_k} {}_c\Phi(t_k, \tau)\, |\dot{h}(\tau)|\, w_\rho(\tau)\, d\tau$$

The ${}_cw_{k-1}$ represents a process with independent increments and has a variance given by

$$E\,[{}_cw_{k-1}^{\,2}] = \int_{t_{k-1}}^{t_k} {}_c\Phi^2(t_k, \tau)\, |\dot{h}(\tau)|\, f_\rho(\tau)\, d\tau.$$

Using these results, the solution of the linear perturbation differential equation can be written as

$$\underline{x}_k = \Phi_{k,k-1}\,\underline{x}_{k-1} + B_{k,k-1}\,\underline{b}_{k-1} + C_{k,k-1}\,\underline{c}_{k-1} + \Gamma_{k,k-1}\,\underline{u}_{k-1}$$

where

$$B_{k,k-1} \overset{Df}{=} \int_{t_{k-1}}^{t_k} \Phi(t_k, \tau)\, E_2(\tau)\, d\tau$$

$$C_{k,k-1} \overset{Df}{=} \int_{t_{k-1}}^{t_k} \Phi(t_k, \tau)\, E_3(\tau)\, {}_c\Phi(\tau, t_{k-1})\, dt$$

$$\Gamma_{k,k-1} \overset{Df}{=} \int_{t_{k-1}}^{t_k} \Phi(t_k, \tau)\, E_4(\tau)\, d\tau$$

These matrix calculations are accomplished in the spherical coordinate system and are then transformed into the non-rotating cartesian system.

This completes the general definition of the matrices that are involved in the description of the linear, plant equation.

5.1.2.2 IMU Matrices

In the performance assessment program the IMU data are treated as components of the measurement vector $\underline{z}$. The general formulation was described in Paragraph 2.4.2. Details that are relevant to the re-entry problem are discussed in this paragraph. The discussion rests upon several of the definitions introduced in the preceding section.

The linear model for the noise-free IMU data is given by

$$\underline{s}_k = {}_aJ_k\,\underline{x}_k + {}_2J_k\,\underline{b} + {}_3J_k\,c_k + \underline{n}_k + \underline{\sigma}_k$$

where

$${}_aJ_k = {}_aJ_{k-1}\,\Phi_{k-1,k} \int_{t_{k-1}}^{t_k} F_2(\tau)\,\Phi(\tau, t_k)\, d\tau$$

$$
{}_2J_k = {}_2J_{k-1} - {}_aJ_{k-1}\, \Phi_{k-1,k}\, B_{k,k-1} + \int_{t_{k-1}}^{t_k} F_2(t) \int_{t_k}^{t} \Phi(t,\tau)\, E_2(\tau)\, d\tau\, dt
$$

$$
+ \int_{t_{k-1}}^{t_k} E_2(t)\, dt
$$

$$
{}_3J_k = {}_3J_{k-1} - {}_aJ_{k-1}\, \Phi_{k-1,k}\, C_{k,k-1}\, {}_c\Phi_{k-1,k}
$$

$$
+ \int_{t_{k-1}}^{t_k} F_2(t) \int_{t_k}^{t} \Phi(t,\tau)\, E_3(\tau)\, {}_c\Phi(\tau, t_k)\, d\tau\, dt
$$

$$
+ \int_{t_{k-1}}^{t_k} E_3(t)\, {}_c\Phi(t, t_k)\, dt
$$

As indicated in Paragraph 2.4.2, the $\underline{\sigma}_k$ and $\underline{\eta}_k$ are described by linear difference equations

$$
\underline{\sigma}_k = \underline{\sigma}_{k-1} + \gamma_{k-1}\, \underline{u}_{k-1}
$$

$$
\gamma_{k-1} = -\, {}_aJ_{k-1}\, \Phi_{k-1,k}\, \Gamma_{k,k-1} + \int_{t_{k-1}}^{t_k} F_2(t) \int_{t_k}^{t} \Phi(t,\tau)\, E_4(\tau)\, d\tau\, dt
$$

$$
+ \int_{t_{k-1}}^{t_k} E_4(t)\, dt
$$

$$
\eta_k = \eta_{k-1} + \gamma_{k-1}\, \underline{w}_{k-1} \; .
$$

The $\underline{\eta}_{k-1}$ represents, essentially, the accumulative effect of control system noise.

It should be noted that, as written above, the $\underline{s}_k$ is a six-dimensional vector. However, the first three components are identically zero.

The matrices appearing in the IMU model are dependent upon the nominal trajectory and are computed prior to beginning the performance assessment. The calculations are accomplished in a spherical coordinate system and are then transformed into the non-rotating cartesian system.

5.1.3 ACTUAL TRAJECTORY

The actual trajectory is computed according to the same equations as the nominal and in basically the same manner. Initial conditions for the state can be either prespecified or obtained from a random number generator. The control that is used at every sampling time is determined as the sum of the nominal and perturbative control vectors.

$$\hat{\underline{U}}_k = \underline{U}_k^* + \underline{u}_k$$

The control $\underline{u}_k$ is not necessarily computed as frequently as the $\underline{U}_k^*$, but it is treated as a constant between control times used for the linear guidance calculations.

Control system errors prevent the commands $\hat{\underline{U}}_k$ from being implemented precisely. These errors are introduced as a random error $\underline{w}_k$. This vector is obtained from a noise generator having prespecified statistics. Thus, the control actually experienced by the vehicle in the calculation of the actual trajectory is

$$\underline{U}_k = \hat{\underline{U}}_k + \underline{w}_k$$

5.2 SENSORS

The Re-entry Performance Assessment Program has the capability of simulating several instruments. They are

1. Horizon sensor,
2. Radio altimeter,
3. Ground-based radar — three radar stations can be included simultaneously,
4. Inertial measurement unit.

These instruments are discussed in Paragraph 2.4. The IMU formulation causes the data to be treated as additional components of the measurement vector. This model is the first of the two discussed in Paragraph 2.4.2. It has also been considered in Paragraph 5.1.2.2.

5.2.1 MEASUREMENT ERRORS

The facility has been included in the program to consider bias errors in the measurement data. For the electromagnetic sensors, the introduction of the bias errors is optional. However, whenever the IMU is considered the bias errors constitute the principal source of error and are always included. Bias errors, when they are present, are treated as additional components of the state vector.

The bias errors are random quantities and are described as having mean zero and a known covariance matrix B_i. In the simulation the B_i is used in conjunction with a noise generator to obtain numerical values for the bias errors during a specific trajectory simulation.

The measurement data are also corrupted by white noise sequences (i.e., errors that are uncorrelated between sampling times). These random errors are also assumed to have a mean value of zero and known covariance matrices. At each sampling time, the covariance matrix of the noise is used with a noise generator to determine the realization of the noise.

5.2.2 IMU ERROR MODEL

The error model considered in the re-entry phase is considerably simpler than that discussed earlier for boost missions. The simplification was required in order to keep the dimension of the state vector to a reasonable value. A total of fifteen error sources are considered. Also, the option is available for simulating either a gimballed or strapdown system.

The 15 IMU bias errors are described by the following schedule.

$\epsilon_1, \epsilon_4, \epsilon_7$	Initial misalignments of gyros, 1, 2, 3
$\epsilon_2, \epsilon_5, \epsilon_8$	Constant drift of gyros 1, 2, 3
$\epsilon_3, \epsilon_6, \epsilon_9$	Acceleration-dependent drift of gyros 1, 2, 3
$\epsilon_{10}, \epsilon_{12}, \epsilon_{14}$	Bias errors of accelerometers 1, 2, 3
$\epsilon_{11}, \epsilon_{13}, \epsilon_{15}$	Scale factor errors of accelerometers 1, 2, 3

The gyros and accelerometers are assumed to be oriented with respect to each other according to Table A-1. The X, Y, Z define an orthogonal right-handed triad.

INERTIAL INSTRUMENTS	X	Y	Z
gyro 1	input	output	spin
gyro 2	spin	input	output
gyro 3	output	spin	input
accelerometer 1	sensitive		
accelerometer 2		sensitive	
accelerometer 3			sensitive

Table A-1. Gyro and Accelerometer Orientation

The X, Y, Z coordinate system is related to the initial pitch P_I, yaw Y_A, and roll R_o axes through an orthonormal transformation M. The orientation of the instrument axes to the basic non-rotating cartesian system is then established by an orthonormal transformation C.

For a gimballed system, the C is equal to a constant, prespecified matrix. For a strapdown configuration

$$C \overset{Df}{=} \begin{bmatrix} 1 & 0 & 0 \\ 0 & \cos\alpha_3 & \sin\alpha_3 \\ 0 & -\sin\alpha_3 & \cos\alpha_3 \end{bmatrix} \begin{bmatrix} \cos\alpha_2 & 1 & -\sin\alpha_2 \\ 0 & 1 & 0 \\ \sin\alpha_2 & 0 & \cos\alpha_2 \end{bmatrix} \begin{bmatrix} \cos\alpha_1 & \sin\alpha_1 & 0 \\ -\sin\alpha_1 & \cos\alpha_1 & 0 \\ 0 & 0 & 1 \end{bmatrix}$$

where $\alpha_1, \alpha_2, \alpha_3$ are the inner, middle, and outer gimbal angles, respectively.

The drift ω_i of the ith gyro about its input axis is described by

$$\omega_1 = \epsilon_1 K_1 + \epsilon_2 K_2 (t - t_o) + \epsilon_3 K_3 \int_o^t a_1 \, d\tau$$

$$\omega_2 = \epsilon_4 K_1 + \epsilon_5 K_2 (t - t_o) + \epsilon_6 K_3 \int_o^t a_2 \, d\tau$$

$$\omega_3 = \epsilon_7 K_1 + \epsilon_8 K_2 (t - t_o) + \epsilon_9 K_3 \int_o^t a_3 \, d\tau$$

The ϵ_i were defined above. The K_i are normalizing constants and the a_i are components of aerodynamic accelerations along the input axes of the gyros. This vector $\underline{a}$ may be computed from the acceleration $\underline{f}$ (relative to the basic non-rotating cartesian system $\underline{i}, \underline{j}, \underline{k}$ according to

$$\underline{a} = MC\underline{f}$$

The acceleration errors $\Delta\underline{a}$ resulting from the drifts are determined from

$$\Delta\underline{a} = \underline{\wp} \times \underline{f}$$

where in the $\underline{i}, \underline{j}, \underline{k}$ system $\underline{\wp} = \wp_1 \underline{x}_1 + \wp_2 \underline{x}_2 + \wp_3 \underline{x}_3$.

The acceleration errors $\Delta\underline{a}'$ caused by accelerometer errors are described by

$$\Delta\underline{a}' = \begin{bmatrix} \epsilon_{10} K_4 + \epsilon_{11} K_5 a_1 \\ \epsilon_{12} K_4 + \epsilon_{13} K_5 a_2 \\ \epsilon_{14} K_4 + \epsilon_{15} K_5 a_3 \end{bmatrix}$$

These errors are resolved along the axes of the basic $\underline{i}, \underline{j}, \underline{k}$ system by the transformation

$$\Delta\underline{a} = C^T M^T \Delta\underline{a}'$$

5.3 NAVIGATION

The Kalman filter equations that are utilized to estimate the state perturbations are almost identical with those stated in (A-10) of Paragraph 2.3. In the Reentry Performance Assessment Program the general form of the Kalman filter is

$$\hat{\underline{x}}_k = \hat{\underline{x}}_k' + K_k (\underline{z}_k - H_k \hat{\underline{x}}_k')$$

where

$$\hat{\underline{x}}_k' = \Phi_{k,k-1} \hat{\underline{x}}_{k-1} + \Gamma_{k,k-1} \underline{u}_{k-1}$$

$$K_k = P_k' H_k^T [H_k P_k' H_k^T + R_k]^{-1}$$

$$P_k' = \Phi_{k,k-1} P_{k-1} \Phi_{k,k-1}^T + \Gamma_{k,k-1} Q_{k-1} \Gamma_{k,k-1}^T$$

$$P_k = (I - K_k H_k) P_k' (I - K_k H_k)^T + K_k R_k K_k^T$$

The control perturbation $\underline{u}_{k-1}$ is computed by the guidance system and is discussed in Paragraph 5.4. The Q_{k-1} is included primarily to describe the control system noise.

The state vector $\underline{x}_k$ as considered by the navigation system has a variable dimension. The size of the state vector is determined by the instrument configuration. It is defined in Paragraph 5.3.1. Additional features of the navigation procedure are discussed in Paragraph 5.3.2.

5.3.1 THE STATE VECTOR

The state vector is at least nine-dimensional. In addition to the position and velocity, the basic state vector includes the lift and drag coefficients C_{D_0} and C_{N_α} and the atmospheric density coefficient ρ_0. The performance assessment program has the restriction that the maximum dimension that the state can assume is 34. Thus, the instruments must be selected so that this constraint is not violated.

Whenever the IMU is considered, the fifteen constant error sources are always included as state variables. In addition, the accumulative plant noise vector $\underline{\eta}_k$ (Paragraph 5.1.2.2 or Paragraph 2.4) is also added to the state. Thus, the presence of the IMU causes the state vector to have at least 27 components. Each of the three ground trackers can contribute seven additional bias errors. Five additional bias errors can be provided by the horizon sensor (i.e., three bias errors) and the radio altimeter (i.e., two bias errors).

<u>Basic State Vector</u>

X_1, X_2, X_3	position of the spacecraft
X_4, X_5, X_6	velocity of the spacecraft
X_7	drag coefficient
X_8	lift coefficient
X_9	atmospheric density coefficient

The maximum permissible dimension of the state vector in this program is 34. The remaining 25 components are made up of a judicious selection of instrument bias errors.

5.3.2 MISCELLANY

Very few of the navigation features included in the Free-Fall Performance Assessment Program can be utilized for the re-entry phase. For example, it is not possible to use an orbit rectification policy because of the trajectory constraints on the nominal. Also, the square-root formulation of the Kalman filter cannot be used because of the presence of plant noise. On the other hand, the presence of plant noise eliminates the problems caused by the vanishing of the error covariance matrix.

5.4 GUIDANCE

The Lambda Matrix Control Scheme described in Paragraph 4.2 is used to compute the control perturbations $\underline{u}_k$. Thus, at each time, the $\underline{u}_k$ is given by

$$\underline{u}_k = -\Lambda_{k+1} \Phi_{k+1,k} \hat{\underline{x}}_k$$

where

$$\Lambda_{k+1} = (\Gamma^T_{k+1,k} \pi'_{k+1} \Gamma_{k+1,k} + W^U_{k+1})^{-1} \Gamma^T_{k+1,k} \pi'_{k+1}$$

$$\pi'_{k+1} = \Phi^T_{k+2,k+1} \pi_{k+2} \Phi_{k+2,k+1} + W^X_{k+1}$$

$$\pi_{k+1} = \pi'_{k+1} - \pi'_{k+1} \Gamma_{k+1} \Lambda_{k-1}$$

and $\pi_{n+1} = 0$.

The matrices $\Gamma_{k+1,k}$ and $\Phi_{k+1,k}$ are defined in Paragraph 5.1.2.1. The W^U_{k-1} and W^X_k are arbitrary weighting matrices. The matrix π_k is computed prior to beginning the performance assessment for a specific trajectory. They have to be computed recursively starting at the terminal time t_N and then proceeding backwards to the initial time t_o.

SECTION VI

LOW-THRUST MISSIONS

6.2 TRAJECTORY

6.1.1 NOMINAL TRAJECTORY

6.1.1.1 General Assumptions

1. Thrust is constant and continuous. The only control is variable thrust direction.

2. The vehicle is a point with mass given by

$$m = m_o - \dot{m}t$$

$$\ddot{m} = 0$$

where $\dot{m}$ is the mass flow rate.

3. The low-thrust trajectory consists of three separate phases: escape, transfer, and capture.

4. In each phase, gravitational forces other than the appropriate central bodies are negligible. Furthermore, the central body is spherical having a homogeneous mass distribution.

6.1.1.2 Nominal Control

1. In heliocentric (transfer) phases, the nominal control is optimum in the sense of minimizing time of flight. Because of assumption 6.1.1(a), minimizing time of flight is equivalent to maximizing payload and minimizing fuel expenditure.

2. In planetocentric (escape and transfer) phases tangentially directed thrust is the nominal control. Such control is near-optimal.

6.1.1.3 Coordinate Systems

Coordinate system origins are located at the center of the central body.

1. In the heliocentric phase, the 1950 equatorial cartesian coordinate system is used.

2. In the planetocentric phases a three-dimensional cartesian coordinate system, such that the X_1, X_2 plane coincides with the nominal plane of motion,is used.

6.1.1.4 Differential Equations of Motion

The differential equations of motion for the vehicle are

$$\dot{X}_1 = X_4$$

$$\dot{X}_2 = X_5$$

$$\dot{X}_3 = X_6$$

$$\dot{X}_4 = -\frac{\mu X_1}{R^3} + \frac{a_o}{m} \cos\alpha \cos\beta$$

$$\dot{X}_5 = -\frac{\mu X_2}{R^3} + \frac{a_o}{m} \sin\alpha \cos\beta$$

$$\dot{X}_6 = -\frac{\mu X_3}{R^3} + \frac{a_o}{m} \sin\beta$$

$$R^2 = X_1^2 + X_2^2 + X_3^2$$

where X_1, X_2, X_3 are the cartesian components of position, X_4, X_5, X_6 are the respective velocity components and μ is the gravitational constant of the central body.

The angles α and β are the control variables which specify the thrust direction and are defined analogously to longitude and latitude.

For tangential thrust, α and β are given by

$$\alpha = \tan^{-1} (X_5/X_4), \qquad 0 \leq \alpha < 2\pi$$

$$\beta = \tan^{-1} (X_6/\sqrt{X_4^2 + X_5^2}) \qquad -\pi/2 < \beta \leq \pi/2$$

Let

$$\dot{\underline{X}} = \underline{f}(\underline{X}, \alpha, \beta, t)$$

denote the differential equations of motion. Then for optimum thrust, α and β are given by

$$\alpha = \tan^{-1} [\lambda_5/\lambda_4] \qquad 0 \leq \alpha < 2\pi$$

$$\beta = \tan^{-1} [\lambda_6/\sqrt{\lambda_4^2 + \lambda_5^2}] \qquad -\pi/2 < \beta \leq \pi/2$$

where $\lambda_1, \lambda_2, \ldots, \lambda_6$ are adjoint variables which satisfy the differential equations

$$\dot{\underline{\lambda}} = -\left(\frac{\partial \underline{f}}{\partial \underline{X}}\right)^T \underline{\lambda}$$

6.1.2 LINEAR SYSTEM MATRICES

It is evident from the preceding sections that the equations of motion for low thrust mission phases has the general form

$$\dot{\underline{X}} = \underline{g}\,(\underline{X}) + \underline{f}\,(\underline{A},\ \underline{U})$$

where $\underline{X}$ represents the six-dimensional state (i.e. position and velocity). The vector $\underline{A}$ is two-dimensional and its components represent the initial thrust-to-mass ratio and the mass flow rate. These two parameters are assumed to be constant and are treated as additional state variables. Thus, the minimum dimension of the state vector is eight for the Low Thrust Performance Assessment Program. As has been pointed out, the control vector $\underline{U}$ is two-dimensional and is comprised of two angles defining the direction of the control vector.

The linear perturbation equations follow from the general equations and are seen to be

$$\dot{\underline{x}} = F\,(t)\,\underline{x} + E_2\,(t)\,\underline{b} + E_4\,(t)\,\underline{u}$$

where

$$\underline{x} \overset{Df}{=} \underline{X} - \underline{X}$$

$$\underline{b} \overset{Df}{=} \underline{A} - \underline{A}^*$$

$$\underline{u} \overset{Df}{=} \underline{U} - \underline{U}^*$$

and

$$F(t) = \left(\frac{\partial \underline{g}}{\partial \underline{X}}\right)^*$$

$$E_2(t) = \left(\frac{\partial \underline{f}}{\partial \underline{A}}\right)^*$$

$$E_4(t) = \left(\frac{\partial \underline{f}}{\partial \underline{U}}\right)^*$$

To simplify notation, suppose that the basic state vector $\underline{x}_a$ is defined as

$$\underline{x}_a \overset{Df}{=} \begin{bmatrix} \underline{x} \\ \underline{b} \end{bmatrix}$$

so that

$$\dot{\underline{x}}_a = F_a(t)\,\underline{x}_a + {}_aE_4(t)\,\underline{u}$$

where

$$F_a(t) \stackrel{Df}{=} \begin{bmatrix} F(t) & E_2(t) \\ 0 & 0 \end{bmatrix}$$

and

$${}_aE_4(t) \stackrel{Df}{=} \begin{bmatrix} E_4(t) \\ 0 \end{bmatrix}$$

This linear differential equation must be solved in order to obtain the difference equations required for navigation. To this end, two transition matrices must be computed. First, it is necessary to solve

$$\frac{d}{dt}\,\Phi_a(t,\tau) = F_a(t)\,\Phi_a(t,\tau)$$

$$\Phi_a(\tau,\tau) = I \quad \text{for all } \tau.$$

Next, the matrix differential equation must be solved.

$$\frac{d}{dt}\,\Phi_G(t,\tau) = [(F_a(t) + {}_aE_4(t)\,\Lambda(t)]\,\Phi_G(t,\tau)$$

$$\Phi_G(\tau,\tau) = I \quad \text{for all } \tau.$$

The matrix Λ is computed in the guidance block and will be defined in Paragraph 6.4. The $\Phi_a(t_k, t_{k-1})$ and the $\Phi_G(t_k, t_{k-1})$ constitute the primary linear system matrix calculations. The solutions of the differential equations are obtained numerically.

6.1.3 ACTUAL TRAJECTORY

The actual trajectory is computed from the same equations as the nominal and in basically the same manner. Initial conditions for the state can either be prespecified or obtained from a random number generator. The control changes <u>continuously</u> according to

$$\hat{\underline{U}}(t) = \underline{U}(t) + \underline{u}(t)$$

The $\underline{u}(t)$ is determined from the particular linear guidance law that is used. (See Section 6.4). A control discontinuity occurs at those times at which data from the electromagnetic sensors are processed by the navigation system. (See Paragraph 6.3.) This occurs because of the change in the state estimate caused by the filtering of new data.

Control system errors prevent the guidance commands $\hat{\underline{U}}$ from being implemented precisely. These errors are introduced as the white noise $\underline{w}$. This vector is obtained from a random number generator according to prescribed statistics. Then, the control actually experienced in the trajectory is

$$\underline{U}(t) = \hat{\underline{U}}(t) + \underline{w}(t)$$

6.2 SENSORS

The Low-Thrust Performance Assessment Program has the capability of simulating several instruments. They are

(1) Horizon sensor

(2) Planet tracker

(3) Ground-based radar—three radar stations can be included simultaneously

(4) Inertial measurement unit.

These instruments are discussed in Paragraph 2.4. The IMU formulation used in this program corresponds with the second alternative discussed in Paragraph 2.4.2. In this model the IMU data enter into the plant rather than the measurement system so only electromagnetic sensor data are used in the filtering process. The IMU data influence the propagation of the statistics $\hat{\underline{x}}_k$ and P_k from the kth to the $(k+1)^{th}$ sampling times. This aspect is discussed in Paragraph 6.3.

6.2.1 ELECTROMAGNETIC SENSOR ERRORS

Two types of errors can corrupt the measurement data. The random (or white noise) sequences are assumed to have zero means and known covariance matrices. Using these statistics, values for the noise are determined at each sampling time using a gaussian random number generator.

As in the Free-fall and Reentry programs, it is reasonable to consider bias errors in the measurements. However, because this program is coded using double precision arithmetic, it was necessary to restrict the size of the state vector. Thus only the horizon sensor and planet tracker data are assumed to include bias errors. The radar measurements are corrupted <u>only</u> by additive white noise.

6.2.2 IMU ERROR MODEL

The error model for the IMU assumes its simplest form for low-thrust missions. The simplicity is made possible because the acceleration levels are sufficiently small to enable many of the acceleration - dependent errors to be neglected. In fact, for the Low Thrust Performance Assessment Program the IMU data are assumed to contain only constant bias errors for each of the orthogonally oriented accelerometers. These bias errors are treated as state variables when the IMU is included in a particular simulation run.

Two different IMU configurations can be considered: (i.e. a gimballed or a Carousel system). For the gimballed IMU it is assumed that the sensitive accelerometer axes, S_1, S_2, S_3, remain inertially stabilized throughout the flight. Three Euler angles, EA_1, EA_2, EA_3, define the orientation of these axes with respect to the basic cartesian nonrotating system defined in Paragraph 6.1.

For the Carousel configuration, the three Euler angles define the initial orientation of the sensitive axes. Then, a constant angular rotation ω about the third sensitive axis S_3 is introduced. Normally, the S_3 axis is oriented approximately normal to the nominal plane of motion.

For both IMU configurations, the orientation of the sensitive axes relative to the reference coordinate system is described by the rotation matrix G. This matrix is easily determined so a detailed description is omitted.

6.3 NAVIGATION

The form of the filter equations depends to a great extent upon the instrument configuration.

6.3.1 FORM OF THE FILTER EQUATIONS

IMU only.

Suppose that no electromagnetic sensor data are available. Then, it is not possible to filter in the sense of utilizing the Kalman equations. Instead, the estimate is propagated in the following manner.

First, recall from Paragraph 2.4.2 that the plant equation is assumed to have the form

$$\dot{\underline{x}}_a = F_a(t)\,\underline{x}_a + \underline{a}_m(t) - G(t)\,\underline{\epsilon} - \underline{\nu}$$

where $a_m(t)$ represents the difference between the measured acceleration and the nominal values. The G (t) and $\underline{\epsilon}$ are essentially defined in Paragraph 6.2 although the definitions have to be amended with appropriate rows of zeros to provide dimensional consistency. The $\underline{\nu}$ has been included to describe white noise in the accelerometer outputs.

First, consider the accelerometer errors $\underline{\epsilon}$ as additional state variables and define the augmented state vector $\underline{x}_A$ to be

$$\underline{x}_A \overset{Df}{=} \begin{bmatrix} \underline{x}_a \\ \\ \underline{\epsilon} \end{bmatrix}$$

$$\hat{\underline{x}}_A (t_k) = \Phi_A (t_k, t_{k-1}) \; \hat{\underline{x}}_A (t_{k-1}) + J \int_{t_{k-1}}^{t_k} \Phi (t_k, t) \; \underline{a}_m (t) \, dt$$

where

$$\Phi_A (t_k, t_{k-1}) \overset{Df}{=} \begin{bmatrix} \Phi (t_k, t_{k-1}) & \varphi_1 & \varphi_2 & 0 \\ 0 & I & 0 & 0 \\ 0 & 0 & I & 0 \\ 0 & 0 & 0 & I \end{bmatrix}$$

The Φ is the solution of

$$\frac{d}{dt} \Phi (t, \tau) = F (t) \; \Phi (t, \tau)$$

and

$$\varphi_1 = \int_{t_{k-1}}^{t_k} \Phi (t_k, t) \; E_2 (t) \, dt$$

$$\varphi_2 = - \int_{t_{k-1}}^{t_k} \Phi (t_k, t) \; G (t) \, dt$$

The matrix J has been included to ensure that the proper dimensionality is achieved and is composed of zeros and ones.

The error covariance matrix is described by

$$P'_A(t_k) = \Phi_A(t_k, t_{k-1})\, P_A(t_{k-1})\, \Phi_A^T(t_k, t_{k-1})$$

<u>Electromagnetic Sensors Only</u>:

Suppose that no IMU data are available. Then, the plant is described by

$$\dot{\underline{x}}_a = F_a(t)\, x_a + {}_aE_4(t)\, [\underline{u}(t) + \underline{w}(t)]$$

From the Separation Principle, it follows that

$$\frac{d}{dt}\, \Phi_G(t, \tau) = [F_a(t) + {}_aE_4(t)\, \Lambda(t)]\, \Phi_G(t, \tau)$$

where $\Lambda(t)$ is determined by the linear guidance law.

Based on this transition matrix, the filter equations are essentially the same as those described in Paragraph 2.3.

$$\hat{\underline{x}}_a(t_k) = \hat{\underline{x}}'_a(t_k) + K_k\, [z_k - H_k\, \underline{x}'(t_k)]$$

where

$$\hat{\underline{x}}'_a(t_k) = \Phi_G(t_k, t_{k-1})\, \hat{\underline{x}}_a(t_{k-1})$$

$$K_k = P'_a(t_k)\, H_k^T\, [H_k P'_a(t_k)\, H_k^T + R_k]^{-1}$$

also,

$$P'_a(t_k) = \Phi_a(t_k, t_{k-1})\, P_a(t_k, t_{k-1})\, \Phi_a^T(t_k, t_{k-1}) + Q^*_{k-1}$$

where

$$Q^*_{k-1} = \int_{t_{k-1}}^{t_k} \Phi_a(t_k, t)\, {}_aE_4(t)\, Q(t)\, {}_aE_4^T(t)\, \Phi_a^T(t_k, t)\, dt$$

and

$$P_a(t_k) = [I - K_k H_k]\, P'_a(t_k)\, [I - K_k H_k]^T + K_k R_k K_k^T$$

Electromagnetic Sensors and IMU:

In this case the extrapolated estimate and statistics $\hat{\underline{x}}'_a(t_k)$ and $P'_a(t_k)$ are computed in accordance with the equation for the IMU only configuration. Then, the electromagnetic sensor data are processed in the conventional manner.

To study the sensitivity of the model to errors in the a priori statistics, it was necessary to obtain a statistical measure of the degradation in performance due to the fact that the optimal filter equations are suboptimal with respect to the true statistics if these do not agree with the a priori statistics. The following procedure was used to obtain such a statistical measure in the form of sensitivity coefficients.

Let $\underline{K}(t_k)$ be the gain matrix computed using the a priori statistics. Let $\overline{P}(t_k)$, $\overline{Q}(t_k)$, and $\overline{R}(t_k)$ be the "true" statistics. Then

$$P^*(t_k) = [\, I - K(t_k)H(t_k)\,]\,P^{*\prime}(t_k)\,[\, I - K(t_k)H(t_k)\,]^T + K(t_k)\overline{R}(t_k)K^T(t_k)$$

where

$$P^{*\prime}(t_k) = \Phi(t_k, t_{k-1})P^*(t_{k-1})\Phi^T(t_k, t_{k-1}) + \overline{Q}(t_k) \quad , \qquad P^*(t_o) = \overline{P}(t_o)$$

This is merely the propagation of the "true" statistics using the a priori gain matrix $K(t_k)$. The sensitivity coefficient is then defined as

$$\eta_i(t_k) = \left[\frac{\overline{\lambda}_i(t_k)}{\lambda^*_i(t_k)}\right]$$

where $\overline{\lambda}_i$ and λ^*_i are the square roots of the corresponding position and velocity eigenvalues of $\overline{P}$ and P^*, and this is the statistical measure of degradation in performance.

6.3.2 THE STATE VECTOR

The state vector is at least eight dimensional. The first six represent the position and velocity of the spacecraft, whereas the seventh and eighth components relate to the initial thrust-to-mass ratio and the mass flow rate. The latter two are assumed to be constants.

The state vector can have at most fourteen components. This configuration occurs when the IMU is included and the horizon sensor serves as an aiding instrument. Then, the most general state vector has the following form.

X_1, X_2, X_3	position of the spacecraft
X_4, X_5, X_6	velocity of the spacecraft
X_7	initial thrust-to-mass ratio
X_8	mass flow rate
X_9, X_{10}, X_{11}	accelerometer bias errors
X_{12}, X_{13}, X_{14}	horizon sensor bias errors

6.4 GUIDANCE

Two different linear guidance laws can be utilized in the Low Thrust Performance Assessment Program. The Lambda Matrix control law described in Paragraph 2.3 in available as is the so-called Neighboring Optimal control law. (Reference 3)

6.4.1 LAMBDA MATRIX CONTROL

The version of Lambda Matrix Control differs from that described in Paragraph 2.3 because it is assumed that the control changes continuously rather than discretely. This assumption is made because of the relatively large intervals between sampling times. Even if the control perturbations were computed at discrete times, the computation should occur frequently enough that it can be approximated by a continuous control policy.

In the time-continuous model, the control is chosen to minimize

$$J = \underline{x}^T (t_f)\, \Pi (t_f)\, \underline{x} (t_f) + \int_{t_o}^{t_f} [\underline{x}^T (t)\, W_X (t)\, \underline{x} (t) + \underline{u}^T (t)\, W_U (t)\, \underline{u} (t)]\, dt$$

The W_X and W_U are arbitrary, nonnegative definite, symmetric weighting matrices as is the $\Pi (t_f)$. The control is determined by

$$\underline{u} (t) = \Lambda (t)\, \underline{x} (t)$$

where

$$\Lambda (t) = W_U^{-1} (t)\, E_4^T (t)\, \Pi (t).$$

The $\Pi (t)$ is found as the solution of the Matrix Ricatti equation

$$-\dot{\Pi} = F^T (t)\, \Pi + \Pi F (t) - \Pi E_4 (t)\, W_U\, E_4^T (t)\, \Pi + W_X$$

The terminal condition is defined to be $\Pi (t_f)$.

This control law can be used with any type of nominal trajectory.

6.4.2 NEIGHBORING OPTIMUM CONTROL

The Neighboring Optimum Control policy can be used only if the nominal is optimal in some sense. Then, the trajectories resulting from the application of this control law will be optimal in the same way as the nominal. In the Low Thrust Performance Assessment Program only the heliocentric phase is optimal so the use of this control law is restricted to this phase.

As described in Section 6.1, the nominal control policy in the heliocentric phase is determined so that the time of flight is minimized. Furthermore, prescribed values of position and velocity at the terminal time must be satisfied. Thus, the perturbed control using this guidance law is also selected to satisfy these constraints.

The Neighboring Optimum control law is based on the following computations. Let $\underline{\lambda}(t)$ represent the eight dimensional vector of Lagrange multipliers with the terminal conditions $\underline{\upsilon}$. The equations of motion have the general form

$$\dot{\underline{X}} = \underline{f}\ (\underline{X},\ \underline{U})$$

where the initial and terminal conditions are prescribed to be $\underline{X}_o$ and $\underline{X}_f$.

Denote the Hamiltonian for this problem by H.

$$H = \underline{\lambda}^T\ \underline{f}$$

Then, it is known that

$$\dot{\underline{\lambda}} = -\frac{\partial H}{\partial \underline{X}}$$

The equations of motion and the adjoint equations are linearized to yield a system of linear differential equations.

$$\frac{d}{dt}\begin{bmatrix} \underline{x} \\ \delta\underline{\lambda} \end{bmatrix} = \begin{bmatrix} C_1(t) & C_2(t) \\ C_3(t) & -C_1(t) \end{bmatrix}\begin{bmatrix} \underline{x} \\ \delta\underline{\lambda} \end{bmatrix}$$

It is also necessary to define perturbations in $\underline{X}_o$, $\underline{X}_f$, $\underline{\upsilon}$, and t_f. This procedure yields a total of 23 constraints on the 31 variables. Eight of these variables can be shown to be independent. Let them be defined as $d\underline{\mu}$. From the 23 constraints, form

$$\underline{x}_f = A d\underline{\mu}$$

and

$$\delta\underline{\lambda}_f = B d\underline{\mu}$$

Let $\Psi(t, t_f)$ be the state transition matrix associated with the linear differential equations. Then

$$\begin{bmatrix} \underline{x}(t) \\ \\ \delta\underline{\lambda}(t) \end{bmatrix} = \Psi(t, t_f)\begin{bmatrix} \underline{x}_f \\ \\ \delta\underline{\lambda}_f \end{bmatrix} = \Psi(t, t_f)\begin{bmatrix} A \\ \\ B \end{bmatrix} d\underline{\mu}$$

Partitioning $\Psi(t, t_f)$ into (8x8) submatrices allows the preceding to be written as

$$\delta\underline{\lambda} = [\Psi_{21} A + \Psi_{22} B] \; [\Psi_{11} A + \Psi_{12} B]^{-1} \underline{x}$$

The nominal control satisfies the condition that

$$\frac{\partial H}{\partial \underline{\upsilon}} = 0.$$

This can be linearized to obtain

$$\underline{u} = H_1 \underline{x} + H_2 \delta\underline{\lambda}$$

Substituting the relation between $\delta\underline{\lambda}$ and $\underline{x}$, the control is seen to be given by

$$\underline{u}(t) = \Lambda(t) \, \underline{x}(t)$$

where

$$\Lambda(t) = H_1 + H_2 \, [\Psi_{21} A + \Psi_{22} B] \; [\Psi_{11} A + \Psi_{12} B]^{-1}$$

REFERENCES

1. U.S. Standard Atmosphere 1962: United States Committee on Extension to the Standard Atmosphere (COSEA); . . . K.S.W. Champion, Editor

2. G. Knip, Jr. and C.L. Zola, "Three-dimensional Sphere-of-influence Analysis of Interplanetary trajectories to Mars", NASA TN D-1199, May, 1962.

3. Breakwell, J.V., J.L. Speyer, A.E. Bryson, "Optimization and Control of Nonlinear Systems Using the Second Variation, "SIAM J. on Control, Series A, Vol. 1, No. 2, 1963.

APPENDIX B

SUPPORT DATA FOR SECTION III

ABSTRACT

This appendix contains numerical data associated with the performance assessment studies reported in Section III of the report. Its organization parallels that of Section III; for example, Section I of the appendix contains data related to the studies described in Paragraph 3.1, and so on. In each section, the tables appear before the figures.

TABLE OF CONTENTS

SECTION	TITLE	PAGE
I	PERFORMANCE ASSESSMENT OF NAVIGATION AND GUIDANCE SYSTEMS FOR MIDCOURSE PHASES	B-1
II	PERFORMANCE ASSESSMENT OF NAVIGATION AND GUIDANCE SYSTEMS FOR ATMOSPHERIC ENTRY PHASES	B-111
III	POWERED FLIGHT PERFORMANCE RESULTS	B-185
IV	TRAJECTORIES AND SYSTEM CONFIGURATIONS	B-191

SECTION I

This section contains data pertinent to Section 3.1 of this volume. The data consists of initial conditions for the various trajectory segments (Tables 5-1, 5-2, 5-9, and 5-13 and Figures 5-1 through 5-4) instrument error budgets (Table 5-4), initial covariance matrices (Table 5-5), reference body schedules (Table 5-6), composite system configurations (Tables 5-3, 5-10, and 5-14), and computational bias (Table 5-7). This section also contains time history plots of the navigation process and plots of the effects of star selection techniques.

TRAJECTORY		BASIC MISSION DESCRIPTION	EARTH LAUNCH DATE	TARGET PLANET (Data in km, km/sec, degrees)						MISSION TIME (DAYS)
					Perifocal Passage		Re-entry Sphere			
Mission Categories	Mission Number			Planet and Date of Encounter*	Altitude	Velocity	Altitude	Velocity	Re-entry Angle	
MARTIAN LANDING	II	Martian Capture Mission	J.D. 2441100.5 May 29, 1971	Mars, arrive: J.D. 2441300.5 Dec. 15, 1971 Mars, depart: J.D. 2441400.5 Mar. 24, 1972 Earth J.D. 2442300.5 June 2, 1974	8300	3.78	125 122	8.69 12.30	-13.43° - 6.45°	1100
	III	Martian Flyby** (Long-short)	J.D. 2443121.5 Mar. 15, 1974	Mars J.D. 2443706.5 Earth J.D. 2442812.5			125 122	12.63 13.04	-13.68° - 6.75°	691
	VIII	Martian Capture Mission**	J.D. 2440960.5 Jan. 29, 1971	Mars, arrive: J.D. 2441240.5 Oct. 16, 1971 Mars, depart: J.D. 2441250.5 Oct. 26, 1971 Earth J.D. 2441530.5 July 22, 1972	386	7.77	125 122	15.66	- 7.30°	540
PLANETARY STOPOVER	II	Martian Capture Mission	J.D. 2441100.5 May 29, 1971	Mars, arrive: J.D. 2441300.5 Dec. 15, 1971 Mars, depart: J.D. 2441400.5 Mar. 24, 1972 Earth J.D. 2442300.5 June 2, 1974	8300 8300	3.93 3.78	122	12.30	- 6.45°	1100
	VIII	Martian Capture Mission	J.D. 2440960.5 Jan. 29, 1971	Mars, arrive: J.D. 2441240.5 Oct. 16, 1971 Mars, depart: J.D. 2441250.5 Oct. 26, 1971 Earth J.D. 2441530.5 July 22, 1972	386 386	7.77	122	15.66	- 7.30°	540
	IX	Martian Parking Orbit (Low alt.)		Mars	160	3.46				.23 (3 rev.)
	X	Martian Parking Orbit (Intermediate alt.)		Mars	1000	3.13				.31 (3 rev.)
	XI	Earth Parking Orbit (Low alt.)		Earth	186	7.79				.31 (3 rev.)
	XII	Martian Parking Orbit (High alt.)		Mars	8300	1.92				.87 (3 rev.)
SINGLE PLANETARY FLYBY	III	Martian Flyby (Long-short)	J.D. 2443121.5 Mar. 15, 1974	Mars J.D. 2443706.5 Earth J.D. 2442812.5	5665	10.94	122	13.04	- 6.75°	691
	IV	Venus Flyby	J.D. 2441430.5 April 23, 1972	Venus J.D. 2441522.5 July 24, 1972 Earth J.D. 2441780.0 April 8, 1973	1509	10.50	122	13.72	- 6.90°	349.5
	V	Martian Flyby (Long-short)	J.D. 2442889.5 April 21, 1976	Mars J.D. 2443470.5 Nov. 23, 1977 Earth J.D. 2443580.5 Mar. 13, 1978	5665	11.13	122		- 6.90°	691
	VII	Martian Flyby (Short-long)	J.D. 2441900.5 Aug. 14, 1973	Mars J.D. 2442002.5 Nov. 10, 1973 Earth J.D. 2442549.5 May 17, 1975	271	10.53	122	15.67	- 7.30°	641
MULTIPLE PLANETARY FLYBY (GRAND TOUR)	I	3-Planet Flyby (Grand tour)	J.D. 2440835.5 Sept. 6, 1970	Venus J.D. 2440910.5 Nov. 20, 1970 Mars J.D. 2441080.5 May 9, 1971 Venus J.D. 2441380.5 Mar. 4, 1972 Earth J.D. 2441519.5 July 21, 1972	1009 1300 5800	13.99 10.53 10.08	122	13.02	- 6.40°	684
	VI	Venus-Mars Swingby	J.D. 2440839.5 Sept. 10, 1970	Venus J.D. 2440925.5 Dec. 5, 1970 Mars J.D. 2441145.5 July 13, 1971 Earth J.D. 2441439.0 May 3, 1972	13,300 2100	8.90 6.87	122	13.98	- 6.95°	598.5

* "Encounter" is either perifocal passage or the re-entry sphere, as appropriate.

\+ All Martian entry trajectories are based on the "mean atmosphere.

** Martian Approach Conic redesigned for approach prior to entry or atmospheric braking.

4641

Table B-1. Mission Categories Investigated

MISSION CLASS		MARTIAN LANDING								
Trajectory Number, Leg, and Conic		II. 1. 1	II. 1. 2	II. 1. 3	III. 1. 1	III. 1. 2	III. 1. 3	VIII. 1. 1	VIII. 1. 2	VIII. 1. 3
Julian Date at Start of Conic		2441100.0 +.50	2441103.0 +.73236931	2441298.0 +.20827791	2442121.0 +.50	2442123.0 +.40337742	2442707.0 +.40337742	2440980.0 +.50	2440982.0 +.30347198	2441238.0 +.86823114
Flight Time in Conic	(days)	3.2	194.4	2.3	1.9	584.	.57	2.3	256	1.6
	(sec)	279276.71	16802719.	196585.01	164451.81	50502760.	49499.545	155819.98	22167195.	140765.28
Initial Position Vector (km)+	X_1	-6180.1350	-51655053.	-307361.24	-1890.0056	-14886620.	276675.85	-6229.6817	-94317157.	31057.111
	X_2	-13.465741	-131068620.	399483.85	6065.4221	9792838.3	448419.60	1888.8559	102794540.	458708.08
	X_3	2208.7816	-56992777.	282888.09	1646.6632	4220781.5	237601.13	834.41340	44758398.	350294.61
Initial Velocity Vector (km/sec)	$\dot{X}_1$	-.71323275	29.760775	1.4929547	-11.477196	-5.3886779	-5.6353044	-3.7750266	-21.108631	-.24061312
	$\dot{X}_2$	-11.175871	-10.825092	-1.9791621	-2.6794747	-31.539627	-8.9984836	-11.650333	-22.741253	-3.1861687
	$\dot{X}_3$	-2.0526197	-5.2153730	-1.4159805	-3.2906631	-13.809775	-4.7609426	-1.8108970	-8.7591149	-2.4702023
Initial Radius (km)		6563.		578000.	6563.		578000.	6563.		578000.
Initial Speed (km/sec)		11.385		2.8564842	12.236587		11.635976	12.330754		4.0387455
ΔV Vector at Perifocal Passage	(km/sec)									
ΔV at Perifocal Passage (km/sec)										
Comments		100-day Stopover at Mars. For return, see under Planetary Stopover.			One-way Martian Landing (no return flight designed). Also used for atmospheric braking.			10-day Stopover at Mars. For return, see under Planetary Stopover.		

The values of μ, the gravitational constant, used in the generation of the nominal trajectories are the following, in km^2/sec^3.

Earth	Sun	Venus	Mars	Saturn	Jupiter
$0.39860320E\,10^6$	$0.13271544E\,10^{12}$	$0.32485340E\,10^6$	$0.42977799E\,10^5$	$0.37918700E\,10^8$	$0.12671060E\,10^9$

4657

Table B-2. Trajectory Data for Martian Landing Mission Profile

MISSION CLASS		PLANETARY STOPOVER															
Trajectory Number, Leg, and Conic		II.1.1	II.1.2	II.1.3	II.2.1	II.2.2	II.2.3	VIII.1.1	VIII.1.2	VIII.1.3	VIII.2.1	VIII.2.2	VIII.2.3	IX	X	XI	XII
Julian Date at Start of Conic		(Same as above)	(Same as above)	2441298.0 +.20827791	2441400.0 +.50	2441402.0 +.97340749	2442198.0 +.53098000	(Same as above)	(Same as above)	2441238.0 +.88823114	2441250.0 +.50	2441251.0 +.57948142	2441519.0 +.54912840				
Flight Time in Conic	(days)			2.3	2.5	796	2.0			1.6	1.1	268.	.95	.22	.31	.31	
	(sec)			198004.79	213702.41	68736174	170328.59			140984.83	93267.195	23152578.	82106.067	19150.0	26537.381	26453.587	75682.874
Initial Position Vector	X_1			-314349.29	-6596.5354	643465.03	-706346.07			30803.155	-2227.7748	208045980.	327407.20	3540.0000	4400.0000	0.0	11595.066
	X_2			398066.28	-4094.4329	213498540.	-561030.37			458911.16	506.57761	20700178.	765061.40	0.0	0.0	6540.1690	0.0
	X_3			277149.26	-8612.0194	98170335.	200239.94			350050.94	-2981.8936	3845674	401573.72	0.0	0.0	0.0	0.0
Initial Velocity Vector	$\dot{X}_1$			1.4931149	3.0845601	-20.850692	4.0069798			-.24060944	-.46084315	-.1260689	3.8825385	0.0	0.0	-7.7925688	0.0
	$\dot{X}_2$			-1.9791331	-2.0903325	.76981429	3.1328750			-3.1861720	-6.1329011	18.518560	-9.2633180	2.46380002	-3.12532902	0.0	1.3613521
	$\dot{X}_3$			-1.4188527	-.61522361	1.6157545	-1.0513766			-2.4701983	-4.7613438	7.7982221	-4.7584814	2.46380002	0.0	0.0	0.0
Initial Radius				578000.	11595.066		924000.			578000.	3756.5			3540.0000	4400.0000	6564.1650	11595.066
Initial Speed				2.8564843	3.7766833		5.1938602			4.0387454	7.7717513			3.4843394	3.12532902	7.7925688	1.3613521
ΔV Vector at Perifocal Passage					.17612740 .31567820 .46900839						1.7390901 -.03326178 -2.8103703						
ΔV at Perifocal Passage											3.3051054						
Comments								Used for study of "fast" re-entry at Earth.						Three Revolutions around Mars	Three Revolutions around Mars	Five Revolutions around Earth	Two Revolutions around Mars

4662

Table B-3. Trajectory Data for Planetary Stopover Mission Profile

MISSION CLASS		SINGLE PLANETARY FLYBY											
Trajectory Number, Leg, and Conic		III.1.1	III.1.2	III.1.3	III.2.1	III.2.2	III.2.3	IV.1.1	IV.1.2	IV.1.3	IV.2.1	IV.2.2	IV.2.3
Julian Date at Start of Conic		(Same as above)	(Same as above)	2442707.0 +.92606137	2442708.0 +.50	2442709.0 +.13904524	2442811.0 +.0042955	2441430.0 +.50	2441432.0 +.69283031	2441521.0 +.18955325	2441522.0 +.50	2441523.0 +.80850277	2441778.0 +.71517096
Flight Time in Conic	(days)			.57	.64	101.9	1.5	2.2	89	1.3	1.3	255	1.3
	(sec)			49588.298	55213.509	8801153.7	129294.89	189460.54	7646116.9	113222.60	113054.64	22023936.	110915.79
Initial Position Vector	X_1 X_2 X_3			272595.50 450185.89 238973.46	-7173.0971 2909.3586 2264.4173	127736960. 165899150. 72680737.	-219512.46 812797.32 380723.93	2630.9145 -6010.6907 -151.17402	-123349170. -77876141. -34118221.	196651.15 -407264.25 -419706.00	-7123.6562 2873.9058 650.28005	90421535. -53555460. -29515917	-785068.07 -485868.44 37092.726
Initial Velocity Vector	$\dot{X}_{1\Sigma}$ $\dot{X}_2$ $\dot{X}_3$			-5.6352828 -8.9984928 -4.7609507	-4.7392402 -8.6906974 -4.6597181	-22.922876 5.9053708 2.5215809	1.6290769 -6.1590492 -2.7877564	10.920480 4.7706936 .24474214	17.908666 -18.238216 -9.6428925	-1.7779937 3.4299678 3.4856688	3.0526338 5.7347635 8.2559353	23.544757 27.759029 13.703825	6.9742063 4.2232045 -.27340947
Initial Radius				578000.	8065.0655		924000.	6563.		617000.	7709.		924000.
Initial Speed				11.635976	10.940822		6.9540897	11.919577		5.2034439	10.505549		8.1578037
ΔV Vector at Perifocal Passage					.7174181 ..8164961 .4145992						-.0095825 .0065824 .0042028		
ΔV at Perifocal Passage											.0123619		
Comments													

Table B-4 (Sheet 1 of 2). Trajectory Data for Single Planetary Flyby Mission Profile

MISSION CLASS		SINGLE PLANETARY FLYBY (cont)											
Trajectory Number, Leg, and Conic		V.1.1	V.1.2	V.1.3	V.2.1	V.2.2	V.2.3	VII.1.1	VII.1.2	VII.1.3	VII.2.1	VII.2.2	VII.2.3
Julian Date at Start of Conic		2442889.0 +.50	2442891.0 +.46126596	2443469.0 +.87693753	2443470.0 +.50	2443471.0 +.12666737	2443579.0 +.23620985	2441908.0 +.50	2441910.0 +.05160346	2442001.0 +.79740573	2442002.0 +.50	2442003.0 +.20993107	2442548.0 +.55020839
Flight Time in Conic	(days)	1.9	578	.62	.62	108	1.3	1.5	91	.70	.71	545	.95
	(sec)	169453.38	49975114.	53832.598	54144.061	9340664.5	109213.30	134058.54	7926837.4	60704.145	61338.045	47117400.	82049.948
Initial Position Vector	X_1	-6020.9218	-126415740.	-98961.044	-7288.7520	-14245741.	-751894.66	435.95227	120455040.	-423758.92	-2257.2406	157074620.	-729061.04
	X_2	1157.5844	-74984342	509297.95	-2740.9369	213809180.	446044.85	-6482.3107	-84587704.	-377794.47	2946.6683	140538480.	-537732.41
	X_3	2341.2530	-32682762	254767.10	-2099.1981	98492590.	299122.54	-928.74152	-36691899.	-108552.63	667.49903	60268006.	-181405.79
Initial Velocity Vector	$\dot{X}_1$	-3.7892042	17.675181	1.6923952	2.2031267	-20.703720	6.7327761	12.598543	22.785127	6.9124454	8.4878704	-7.8029040	8.8255457
	$\dot{X}_2$	-10.657474	-26.99312	-9.4898087	-9.7054391	-8.8213969	-4.0680590	.47777418	24.497559	6.2542770	5.9759376	21.920329	6.3878006
	$\dot{X}_3$	-4.4703584	-12.662665	-4.6798598	-4.9957445	-4.1396099	2.6148610	2.5604613	10.941695	1.7937562	1.7744139	9.8239632	2.2372312
Initial Radius		6563.		578000.	8065.0654		924000.	6563.		578000.	3771.5		924000.
Initial Speed		12.162398		10.715491	11.135833		8.2895642	12.864973		9.4929154	10.531112		11.123406
ΔV Vector at Perifocal Passage					-.0163719 -.0499321 -.0279370						-.0125786 -.1262211 -.0321239		
ΔV at Perifocal Passage					.0595124						.1308508		
Comments								Used to study total missions.					

Table B-4 (Sheet 2 of 2). Trajectory Data for Single Planetary Flyby Mission Profile

MISSION CLASS		MULTIPLE PLANETARY FLYBY											
Trajectory Number, Leg, and Conic		I.1.1	I.1.2	I.1.3	I.2.1	I.2.2	I.2.3	I.3.1	I.3.2	I.3.3	I.4.1	I.4.2	I.4.3
Julian Date at Start of Conic		2440835.0 +.50	2440837.0 +.63524825	2440909.0 +.81631453	2440910.0 +.50	2440911.0 +.18155214	2441079.0 +.82433409	2441080.0 +.50	2441081.0 +.19434007	2441379.0 +.51210399	2441379.0 +.50	2441381.0 +.49186718	2441517.0 +.36300684
Flight Time in Conic	(days)	2.1	72.	.68	.69	168	.65	.69	298.	.93	.95	136.	2.0
	(sec)	184485.45	6236444.1	59070.425	58886.105	14570736.	58377.535	59990.982	25774655	85354.216	85697.325	11739266.	184787.14
Initial Position Vector	X_1	-1128.6473	144930920.	280762.02	4252.5296	47117871.	388233.38	-1235.8010	-33720622.	486033.58	-9853.1080	-14324565.	155163.32
	X_2	6160.9575	-36983833.	448535.86	-1511.3690	89016034.	358185.26	2929.6927	-198630880.	255756.56	1502.2602	96597366.	905251.97
	X_3	1960.0315	-16117048.	317296.75	-5622.6564	37233032.	234653.22	-3321.7782	-90247133	281156.38	6926.0285	44054844.	101089.59
Initial Velocity Vector	$\dot{X}_1$	-11.461691	4.8833100	-4.5622228	-9.1052754	-39.742681	-6.6509611	-6.8814427	18.884079	-5.6683298	-5.7238455	-36.576880	-.84774909
	$\dot{X}_2$	-1.0470096	22.793956	-7.4845783	-9.7353818	7.0397084	-6.0601047	-7.0482277	-8.1763529	-2.8667659	-4.8343444	-8.6291883	-4.6592291
	$\dot{X}_3$	-3.2992983	9.5030324	-5.4021643	-4.2491381	7.3780585	-4.0680665	-3.7167544	-3.9773034	-3.0599934	-6.7518826	-5.8959274	-.45215206
Initial Radius		6563.		617000.	7209.8901		578000.	4598.3166		617000.	12137.150		924000.
Initial Speed		11.972968		10.296415	13.990671		9.8746805	10.528344		7.0506644	10.085722		4.7572613
ΔV Vector at Perifocal Passage					-.0253685 -.0137082 .0050094			.1479551 .1919125 .0543709			-.1445106 .0358270 .1276247		
ΔV at Perifocal Passage					.0292672			.2483492			.1960993		
Comments		Used to investigate influence of Venusian Swingby for low speed Earth re-entry.											

Table B-5 (Sheet 1 of 2). Trajectory Data for Multiple Planetary Flyby Mission Profile

MISSION CLASS		MULTIPLE PLANETARY FLYBY (cont)								
Trajectory, Number, Leg and Conic		VI.1.1	VI.1.2	VI.1.3	VI.2.1	VI.2.2	VI.2.3	VI.3.1	VI.3.2	VI.3.3
Julian Date at Start of Conic		2440839.0 +.50	2440842.0 +.09431315	2440924.0 +.48105894	2440925.0 +.50	2440926.0 +.51842028	2441144. +.32247154	2441145.0 +.50	2441146.0 +.67720809	2441437.0 +.76863276
Flight Time in Conic	(days)	2.5	82	.97	.97	2.1	1.1	1.1	291.	1.2
	(sec)	224149.09	7118214.4	88036.508	87991.513	18818270.	101738.46	101710.78	25150299.	106259.56
Initial Position Vector	X_1	1247.7705	147148430.	222107.99	15331.199	2289290.9	466608.68	-3963.2598	104056050.	695387.88
	X_2	6353.5576	-26682636.	423224.75	-3986.1036	97826982.	300281.36	3822.1899	-164973430.	508103.08
	X_3	1071.6080	-11496993.	390176.65	-11382.660	43851872.	161837.58	667.82160	-78508242	334728.01
Initial Velocity Vector	$\dot{X}_1$	-11.295240	2.4572057	-2.2133638	-4.9575295	-40.193733	-4.5898327	-4.7107128	18.979162	-6.4761580
	$\dot{X}_2$	2.4510309	24.267130	-4.7090659	-5.8348372	-4.0689601	-2.8767046	-4.5284780	8.6362485	-4.6552528
	$\dot{X}_3$	-1.3621024	10.846711	-4.4554664	-4.5407018	-.11188047	-1.5672381	-2.11366197	3.5622092	-3.0191083
Initial Radius		6563.		617000.	19506.4		578000.	5546.4		
Initial Speed		11.638098		6.8502161	8.9017073		5.6389918	6.8677009		
ΔV Vector at Perifocal Passage					-0.450983 .0087597 .0300613			.0054880 -.0070403 -.0014848		
ΔV at Perifocal Passage					.0549024			.0090492		
Comments		Used to study total missions and medium speed Earth re-entry.								

Table B-5 (Sheet 2 of 2). Trajectory Data for Multiple Planetary Flyby Mission Profile

Mission Category 1 Total Mission		Multiple Planetary Flyby Earth-Venus-Mars-Earth									Single Planetary Flyby Earth-Mars-Earth					
		Earth Departure Conic	Heliocentric Conic	Venus Approach Conic	Venus Departure Conic	Heliocentric Conic	Mars Approach Conic	Mars Departure Conic	Heliocentric Conic	Earth Approach Conic	Earth Departure Conic	Heliocentric Conic	Mars Approach Conic	Mars Departure Conic	Heliocentric Conic	Earth Approach Conic
Trajectory, Number, Leg and Conic*		VI. 1. 1	VI. 1. 2	VI. 1. 3	VI. 2. 1	VI. 2. 2	VI. 2. 3	VI. 3. 1	VI. 3. 2	VI. 3. 3	VII. 1. 1	VII. 1. 2	VII. 1. 3	VII. 2. 1	VII. 2. 2	VII. 2. 3
Julian Date at Start of Conic		2440839.0	2440842.0	2440924.0	2440925.0	2440926.0	2441144.	2441145.0	2441146.0	2441437.0	2441908.0	2441910.0	2442001.0	2442002.0	2442003.0	2442543.0
		+.50	+.09431315	+.48105994	+.50	+.51542028	+.32247154	+.50	+.37720809	+.75863276	+.50	+.05160346	+.79740573	+.50	+.20993107	+.53020839
Flight Time in Conic	(days)	2.5	82	.97	.97	2.1	1.1	1.1	291.	1.2	1.5	91	.70	.71	545	.95
	(sec)	224149.09	7118214.4	83836.508	87991.513	181818270.	101738.46	101710.78	25150299.	106259.56	134058.54	7926837.4	60704.145	61338.045	47117400.	82049.948
Initial Position Vector (km)	X_1	1247.7705	147148430.	222107.99	15331.199	2249290.9	466608.66	-3963.2594	104056050	695457.88	435.95227	12055040.	-423758.92	-2257.2406	157074620	-729061.04
	X_2	6353.5376	-26682636.	423224.75	-3986.1036	978269.2.	300281.36	3822.1899	-164973430	508103.08	-6482.3107	-84587704.	-377794.47	2946.6683	140538480	-537732.41
	X_3	1071.6050	-11496993.	390175.65	-11382.660	43851572.	161837.58	667.52160	-75508242	334728.01	-928.74152	-36691899.	-108552.63	667.49903	50268006.	-181405.79
Initial Velocity Vector (km/sec)	X_1	-11.295240	2.4572057	-2.2133638	-4.9375295	-40.193733	-4.5895327	-4.7107128	18.979162	-6.4761580	12.598543	22.785127	9.9124454	8.4878704	-7.8029040	8.8255457
	X_2	2.4510309	24.267130	-4.7090659	-5.8348572	-4.0689601	-2.8767046	-4.5284780	8.6362485	-4.6552527	.47777418	24.497559	8.2542770	5.9759076	21.920329	6.3875006
	X_3	-1.3621024	10.846711	-4.4554664	-4.7407018	-.1118047	-1.5672381	-2.1156197	3.5622092	-3.0191083	2.3604613	10.941695	1.7937562	1.7744139	9.8239632	2.2372312
Initial Radius (km)		6563.		617000.	19506.4		578000.	5546.4			6563.		578000.	3771.3		924000.
Initial Speed (km/sec)		11.638098		6.5502161	8.9017073		5.6389918	6.5677009			12.864973		9.4929154	10.531112		11.123406
ΔV Vector at Perifocal (km/sec) Passage**					-0.450983			.0054850						-.0125786		
					.0087597			-.0070403						-.1262211		
					.0300613			-.0014848						-.0321239		
ΔV at Perifocal Passage (km/sec)					.0549024			.0090492						.1308508		
Comments		* For values of μ, see Table B-2 in Appendix B.														

670315

Table B-6. Nominal Trajectory Data

	System Designation	Navigation				Data Processing			Guidance Information				Comments
		Type of Instrument	Error Budget	Initial Covariance Matrix	Ref. Body Schedule	Square Root Filter	Regular Kalman Filter	Q Schedule	Guidance Law	R_V	V_{min} (m/sec)	$(1-\kappa)t_A$ (hr)	
Ground-based	TM1	GT	G11	M1			X	Q6	1	.3	2	1.5	
	TM2	GT	G11	M2			X	Q7	1	.1	2	1.5	
	TM3	GT	G11	M3			X	Q8	3	.2	2	1.5	
Self-contained	TM4	HS	H11	M1	R1		X	Q0	1	.3	2	1.5	
	TM5	HS	H11	M2	R1		X	Q0	1	.1	2	1.5	
	TM6	HS	H11	M3	R1		X	Q10	3	.3	2	1.5	
	TM7	HS	H32	M1	R1		X	Q9	1	.1	2	1.5	
	TM8	HS	H32	M4	R1		X	Q9	1	.1	2	1.5	
	TM9	HS	H32	M5	R1		X	Q11	3	.21	2	1.5	
	TM10	SS	S11	M1	R1		X	Q0	1	.3	2	1.5	
	TM11	SS	S11	M2	R1		X	Q0	1	.2	2	1.5	
	TM12	SS	S11	M6	R1		X	Q0	3	.3	2	1.5	
	TM13	SS	S31	M1	R1		X	Q9	1	.1	2	1.5	
	TM14	SS	S31	M7	R1		X	Q9	1	.2	2	1.5	
	TM15	SS	S31	M8	R1		X	Q9	3	.3	2	1.5	
Ground-based	TM16	GT	G11	M1			X	Q4	1	.15	2.0	1.13	For typical behavior of the errors, see Figures B-5 through B-12.
	TM17	GT	G11	M9			X	Q1	3	.075	2.0	1.05	
	TM18	GT	G10	M1			X	Q3	1	.15	2.0	1.13	For the behavior of the errors, see Figures B-66 through B-69.
	TM19	GT	G10	M10			X	Q0	3	.075	2.0	1.05	
Self-contained	TM20	HS	H11	M9	R4		X	Q0	3	.15	2.0	1.05	
	TM21	HS	H10	M1	R3		X	Q2	1	.15	2.0	1.13	For the behavior of the errors, see Figures B-13 through B-16.
	TM22	HS	H10	M9	R4		X	Q0	3	.15	2.0	1.05	
	TM23	HS	H41	M1	R2		X	Q2	1	.075	2.0	1.13	
	TM24	HS	H41	M9	R4		X	Q0	3	.075	2.0	1.05	
	TM25	HS	H40	M1	R3		X	Q2	1	.075	2.0	1.13	For the behavior of the errors, see Figures B-17 through B-20.
	TM26	HS	H40	M1	R2		X	Q2	1	.075	2.0	1.13	
	TM27	HS	H40	M9	R4		X	Q0	3	.075	2.0	1.05	
	TM28	SS	S11	M1	R1		X	Q5	1	.075	2.0	1.13	
	TM29	SS	S10	M1	R1		X	Q5	1	.075	2.0	1.13	
	TM30	SS	S41	M9	R4		X	Q0	3	.075	2.0	1.05	
	TM31	SS	S40	M9	R4		X	Q0	3	.075	2.0	1.05	
Combinations	TM32	GT + HS	G11 + H41	M1	R2		X	Q1	1	.075	2.0	1.13	
	TM33	GT + HS	G10 + H40	M1	R2		X	Q3	1	.15	2.0	1.13	
	TM34	GT + HS	G10 + H40	M9	R4		X	Q1	3	.075	2.0	1.05	

4648

Table B-7. System Configurations, Mission Category 1

Budget Designation	Instrument	Quantity Measured	1σ Error Random	1σ Error Bias	Corr. Time	Comments
G10	Ground Tracking	Range	15 m	0	1 min	Range measurements available only when range < 800,000 km.
		Range Rate	3 cm/sec	0		
		Azimuth	.05°	0		Angular measurements available only when range < 400,000 km.
		Elevation	.05°	0		The comments above apply to all ground tracking systems unless otherwise specified.*
G11	Ground Tracking	Range	15 m	30 m	1 min	Each coordinate of the tracking station location is assumed to have a bias error of 100 m.
		Range Rate	3 cm/sec	5 cm/sec		
		Azimuth	.05°	.10°		State-of-the-art
		Elevation	.05°	.10°		
H10	Horizon Sensor (HS)	α	.05°	0	10 min	The two local vertical angles which define the l.o.s. from the probe to the reference body are hereafter referred to as α, δ.
		δ	.05°	0		The half-angle subtended by the reference body is hereafter referred to as β^H.
		β^H	.05°	0		The subtended angle measurement is available only when $3° < \beta^H < 85°$ unless otherwise specified.
H11	HS	α, δ, β^H	.05°	.1°	10 min	State-of-the-art
H20	HS	α, δ, β^H	.01°	0°	10 min	
H21	HS	α, δ, β^H	.01°	.01°	10 min	
H22	HS	α, δ, β^H	.01°	.02°	10 min	
H23	HS	α, δ, β^H	.01°	.10°	10 min	
H30	HS	α, δ, β^H	.005°	0°	10 min	
H31	HS	α, δ, β^H	.005°	.01°	10 min	
H32	HS	α, δ, β^H	.005°	.10°	10 min	
H40	HS	α, δ, β^H	10"	0°	10 min	10" ~ 0.0028°
H41	HS	α, δ, β^H	10"	.01°	10 min	
H50	HS	α, δ, β^H	.001°	0°	10 min	
H51	HS	α, δ, β^H	.001°	.01°	10 min	
S10	Space Sextant (SS)	α	.05°	0	10 min	α is the angle between a star and the near limb of a reference body.
S11	SS	α	.05°	.10°	10 min	State-of-the-art
S20	SS	α	.01°	0°	10 min	For all studies (unless otherwise specified), a realistic star catalog of 15 stars was used; and the stars were selected in an "optimum" manner. (See Appendix A)
S21	SS	α	.01°	.10°	10 min	
S30	SS	α	.005°	0°	10 min	
S31	SS	α	.005°	.10°	10 min	
S40	SS	α	10"	0°	10 min	
S41	SS	α	10"	.01°	10 min	
S50	SS	α	.001°	0°	10 min	
S51	SS	α	.001°	.01°	10 min	

* Throughout the entire midcourse guidance study, the following three trackers were used, unless otherwise specified. 4639

1. Goldstone, California
   Latitude 35.06662
   Longitude 243.20505
2. Johannesburg, South Africa
   Latitude -25.73876
   Longitude 27.68558
3. Woomera, Australia
   Latitude -31.212360
   Longitude 136.88614

Table B-8. Instrument Error Budgets

DESIGNATION	6 × 6 P_0 AND 6 × 6 M_0 (Units are $(km)^2$, $(km)^2/sec$, and $(km/sec)^2$ as appropriate.)						COMMENTS
M1	0.543	-0.174	-0.140	0.278×10^{-2}	-0.460×10^{-3}	-0.594×10^{-3}	Upper triangle portion of injection covariance matrix used in all Earth departure trajectories.
		0.217	0.433×10^{-1}	0.885×10^{-3}	0.700×10^{-2}	0.231×10^{-3}	
			0.783	0.507×10^{-3}	0.455×10^{-3}	0.368×10^{-2}	
				0.150×10^{-4}	0.229×10^{-5}	-0.239×10^{-5}	
					0.201×10^{-3}	0.247×10^{-5}	
	[Symmetric]					0.184×10^{-4}	
M2	$\begin{bmatrix} (400.0)I & 0 \\ 0 & (0.81 \times 10^{-4})I \end{bmatrix}$						Diagonal Matrix
M3	0.111×10^{2}	0.513×10^{1}	0.216×10^{1}	-0.830×10^{-3}	0.100×10^{-2}	0.467×10^{-2}	
		0.341×10^{2}	0.922×10^{1}	-0.394×10^{-2}	0.926×10^{-2}	0.300×10^{-2}	
			0.113×10^{2}	-0.107×10^{-2}	0.377×10^{-2}	-0.835×10^{-3}	
				0.165×10^{-5}	-0.398×10^{-6}	0.516×10^{-7}	
					0.312×10^{-5}	0.779×10^{-6}	
	[Symmetric]					0.777×10^{-6}	
M4	0.293×10^{1}	0.766	-0.237	0.437×10^{-3}	0.320×10^{-4}	-0.165×10^{-3}	
		0.694	0.351×10^{-1}	0.142×10^{-3}	0.183×10^{-4}	-0.993×10^{-5}	
			0.540	-0.436×10^{-4}	0.352×10^{-4}	0.268×10^{-4}	
				0.746×10^{-7}	0.131×10^{-7}	-0.150×10^{-7}	
					0.270×10^{-7}	0.176×10^{-7}	
	[Symmetric]					0.333×10^{-7}	
M5	0.192	0.101×10^{-1}	0.178×10^{-1}	0.805×10^{-4}	0.294×10^{-4}	0.224×10^{-4}	
		0.399	0.996×10^{-1}	-0.784×10^{-4}	0.168×10^{-3}	0.276×10^{-4}	
			0.133	-0.113×10^{-4}	0.438×10^{-4}	-0.778×10^{-6}	
				0.114×10^{-6}	0.217×10^{-7}	0.220×10^{-7}	
					0.542×10^{-7}	0.182×10^{-7}	
	[Symmetric]					0.159×10^{-7}	
M6	0.360×10^{2}	0	0	0	0	0	Diagonal Matrix
		0.250×10^{7}	0	0	0	0	
			0.225×10^{3}	0	0	0	
				0.400×10^{-6}	0	0	
					0.360×10^{-4}	0	
						0.900×10^{-5}	
M7	0.232×10^{1}	0.486×10^{-1}	0.191	0.282×10^{-3}	0.946×10^{-4}	-0.149×10^{-3}	
		0.149×10^{1}	-0.707	0.119×10^{-2}	-0.114×10^{-3}	0.930×10^{-4}	
			0.118×10^{1}	-0.658×10^{-4}	0.106×10^{-2}	-0.955×10^{-4}	
				0.471×10^{-7}	0.272×10^{-8}	-0.615×10^{-8}	
					0.296×10^{-7}	-0.121×10^{-7}	
	[Symmetric]					0.274×10^{-7}	
M8	0.278	0.835×10^{-1}	0.209	0.606×10^{-5}	0.446×10^{-4}	-0.196×10^{-4}	
		0.657	0.605	-0.967×10^{-4}	0.238×10^{-3}	-0.132×10^{-4}	
			0.993	-0.106×10^{-3}	0.266×10^{-3}	-0.842×10^{-4}	
				0.435×10^{-7}	-0.253×10^{-7}	0.142×10^{-7}	
					0.101×10^{-6}	-0.130×10^{-7}	
	[Symmetric]					0.280×10^{-7}	
M9	$\begin{bmatrix} (0.0625)I & 0 \\ 0 & (0.5 \times 10^{-6})I \end{bmatrix}$						Spherically distributed with each position component 250 m and each velocity component 0.7 m/sec
M10	$\begin{bmatrix} (17.2)I & 0 \\ 0 & (2.76 \times 10^{-6})I \end{bmatrix}$						Spherically distributed with each position component 4.2 km and each velocity component 1.6 m/sec
M11	$\begin{bmatrix} (100.0)I & 0 \\ 0 & (0.1 \times 10^{-6})I \end{bmatrix}$						Spherically distributed with each position component 10 km and each velocity component 3.2 m/sec
M15	$\begin{bmatrix} (1.0 \times 10^{6})I & 0 \\ 0 & (0.25 \times 10^{-6})I \end{bmatrix}$						Spherically distributed with each position component 100 km and each velocity component 5 m/sec
M16	9.0	0	0	0	0	0	Diagonal Matrix
		4.0	0	0	0	0	
			1.44	0	0	0	
				1.56×10^{-6}	0	0	
					1.0×10^{-6}	0	
	[Symmetric]					0.16×10^{-4}	
M17	4.6×10^{4}	0	0	0	0	0	Diagonal Matrix
		22.1×10^{4}	0	0	0	0	
			17.6×10^{4}	0	0	0	
				4.4×10^{-6}	0	0	
					7.0×10^{-6}	0	
						9.3×10^{-6}	
M18	$\begin{bmatrix} (0.360 \times 10^{6})I & 0 \\ 0 & (1.0 \times 10^{-6})I \end{bmatrix}$						Spherically distributed with each position component 60 km and each velocity component 10 m/sec
M19	$\begin{bmatrix} (33.3)I & 0 \\ 0 & (33.3 \times 10^{-6})I \end{bmatrix}$						

NOTE: I is a 3 × 3 identity matrix.

4640

Table B-9. Initial Covariance Matrices

Designation	Bodies Used	Comments
R1	Departure and target planets	Departure planet is used for approximately the first half of the mission and the target planet for the other half.
R2	Departure and target planets	Departure and target planets used in their respective spheres of influences. In the heliocentric phase, the two planets are switched.
R3	Earth-Mars-Sun-Venus	Departure and target planets used in their respective spheres of influence. In the heliocentric phase, the other planets and Sun are switched.
R4	Mars-Earth-Sun-Venus	Departure and target planets used in their respective spheres of influence. In the heliocentric phase, the other planets and Sun are switched,
R5	Earth-Moon-Earth	In the Earth approach conic, the reference body was switched every .7 hour until it was possible to use subtended angle information, after which time the Earth only was used.
R6	Mars-Sun-Mars	In the Martian approach conic, the reference body was switched every half hour until it was possible to use subtended angle information, after which Mars only was used.

Table B-10 (Sheet 1 of 2). Reference Body Schedules

MISSION PROFILE VII. 1
(OUTGOING LEG FROM EARTH TO MARS)

TIME SEC	REFERENCE BODY R2	REFERENCE BODY R3	
0.0 +	Earth	Earth	Earth Departure Conic (VII. 1. 1)
0.6×10^3	Earth	Earth	
0.12×10^4	Earth	Earth	
0.18×10^4	Earth	Earth	
0.24×10^4	Earth	Earth	
0.30×10^4 +	Earth	Earth	
0.36×10^4	Earth	Earth	
0.54×10^4	Earth	Earth	
0.72×10^4	Earth	Earth	
0.90×10^4	Earth	Earth	
0.108×10^5 +	Earth	Earth	
0.126×10^5	Earth	Earth	
0.144×10^5	Earth	Earth	
0.180×10^5	Earth	Earth	
0.216×10^5	Earth	Earth	
0.252×10^5 +	Earth	Earth	
0.288×10^5	Earth	Earth	
0.324×10^5	Earth	Earth	
0.360×10^5	Earth	Earth	
0.47658537×10^5	Earth	Earth	
0.69258535×10^5 +	Earth	Earth	
0.90858534×10^5	Earth	Earth	
0.11245853×10^6	Earth	Earth	
0.13405853×10^6	Earth	Earth	Conic Break
0.22045853×10^6	Mars	Sun	Heliocentric Conic (VII. 1. 2)
0.30685852×10^6 +	Mars	Sun	
0.39325852×10^6	Earth	Earth	
0.47965852×10^6	Earth	Earth	
0.56605850×10^6	Earth	Earth	
0.65245850×10^6	Earth	Earth	
0.73885849×10^6 +	Mars	Sun	
0.82525848×10^6	Mars	Sun	
0.91165848×10^6	Earth	Earth	
0.99805846×10^6	Earth	Earth	
0.10844584×10^7	Earth	Earth	
0.11708584×10^7 +	Earth	Earth	
0.12572584×10^7	Mars	Sun	
0.13436584×10^7	Mars	Sun	
0.14300584×10^7	Earth	Earth	
0.15164584×10^7	Earth	Earth	
0.16028584×10^7 +	Earth	Earth	
0.16892584×10^7	Earth	Earth	
0.17756584×10^7	Mars	Sun	
0.18620583×10^7	Mars	Sun	
0.19484583×10^7	Earth	Earth	
0.20348583×10^7 +	Earth	Earth	
0.21212582×10^7	Earth	Earth	
0.22076582×10^7	Earth	Earth	
0.22940582×10^7	Mars	Sun	
0.23804582×10^7	Mars	Sun	
0.24668581×10^7 +	Mars	Sun	
0.25532581×10^7	Mars	Sun	
0.26396580×10^7	Earth	Earth	
0.27260580×10^7	Earth	Earth	
0.28988580×10^7	Mars	Mars	
0.30716580×10^7 +	Earth	Earth	
0.32444580×10^7	Mars	Mars	
0.34172579×10^7	Mars	Mars	
0.35900579×10^7	Mars	Mars	
0.37628578×10^7	Earth	Earth	
0.39356578×10^7 +	Mars	Mars	
0.41084577×10^7	Earth	Earth	
0.42812577×10^7	Mars	Mars	
0.44540576×10^7	Earth	Earth	
0.46268575×10^7	Mars	Mars	
0.47996575×10^7 +	Earth	Earth	
0.49724574×10^7	Mars	Mars	
0.51452573×10^7	Earth	Earth	
0.53180572×10^7	Mars	Mars	
0.54908573×10^7	Earth	Earth	
0.55772572×10^7 +	Mars	Venus	
0.56636571×10^7	Mars	Venus	
0.57500571×10^7	Mars	Venus	
0.58364570×10^7	Mars	Venus	
0.59224569×10^7	Earth	Earth	
0.60092568×10^7 +	Earth	Earth	
0.60956568×10^7	Mars	Venus	
0.61820568×10^7	Mars	Venus	
0.62684568×10^7	Mars	Venus	
0.63548567×10^7	Mars	Venus	
0.64412566×10^7 +	Earth	Earth	
0.65276566×10^7	Earth	Earth	
0.66140565×10^7	Mars	Venus	
0.67004564×10^7	Mars	Venus	
0.67868564×10^7	Mars	Venus	
0.68732564×10^7 +	Mars	Venus	
0.69596563×10^7	Earth	Earth	
0.70460562×10^7	Earth	Earth	
0.71324562×10^7	Mars	Venus	
0.72188561×10^7	Mars	Venus	
0.73052560×10^7 +	Mars	Venus	
0.73916559×10^7	Mars	Venus	
0.74780558×10^7	Earth	Earth	
0.75644558×10^7	Earth	Earth	
0.76508558×10^7	Mars	Venus	
0.77372555×10^7 +	Mars	Venus	
0.78236554×10^7	Mars	Venus	
0.79100553×10^7	Mars	Venus	
0.79964552×10^7	Earth	Earth	
0.80180551×10^7	Mars	Mars	
0.80396550×10^7 +	Mars	Mars	Conic Break
0.80609922×10^7	Mars	Mars	Martian Approach Conic (VII. 1. 3)
0.80824921×10^7	Mars	Mars	
0.80860920×10^7	Mars	Mars	
0.80896919×10^7	Mars	Mars	
0.80932917×10^7 +	Mars	Mars	
0.80968916×10^7	Mars	Mars	
0.81004916×10^7	Mars	Mars	
0.81040914×10^7	Mars	Mars	
0.81058913×10^7	Mars	Mars	
0.81076911×10^7 +	Mars	Mars	
0.81094911×10^7	Mars	Mars	
0.81112911×10^7	Mars	Mars	
0.81130909×10^7	Mars	Mars	
0.81148907×10^7	Mars	Mars	
0.81166907×10^7 +	Mars	Mars	
0.81172906×10^7	Mars	Mars	
0.81178905×10^7	Mars	Mars	
0.81184905×10^7	Mars	Mars	
0.81190904×10^7	Mars	Mars	
0.81196904×10^7 +	Mars	Mars	
0.81202904×10^7	Mars	Mars	
0.81208904×10^7	Mars	Mars	
0.81214904×10^7	Mars	Mars	
0.81216000×10^7 +	Mars	Mars	

Note: + indicates a number that appears as a division of the time scales in Appendix B.

MISSION PROFILE VII. 2
(RETURN LEG FROM MARS TO EARTH)

TIME SEC	REFERENCE BODY R4	
0.0 +	Mars	Martian Departure Conic (VII. 2. 1)
0.12×10^4	Mars	
0.24×10^4	Mars	
0.36×10^4	Mars	
0.72×10^4	Mars	
0.108×10^5 +	Mars	
0.144×10^5	Mars	
0.216×10^5	Mars	
0.288×10^5	Mars	
0.360×10^5	Mars	
0.46937996×10^5 +	Mars	
0.61337996×10^5	Mars	Conic Break
0.16133799×10^6	Earth	Heliocentric Conic (VII. 2. 2)
0.26133799×10^6	Mars	
0.46133799×10^6	Earth	
0.66133794×10^6 +	Mars	
0.96133796×10^6	Earth	
0.13613379×10^7	Earth	
0.17613379×10^7	Mars	
0.21613379×10^7	Mars	
0.25613379×10^7 +	Sun	
0.29613378×10^7	Sun	
0.33613378×10^7	Mars	
0.37613377×10^7	Mars	
0.41613376×10^7	Sun	
0.45613375×10^7 +	Sun	
0.50613374×10^7	Mars	
0.56613374×10^7	Mars	
0.62613373×10^7	Mars	
0.68613372×10^7	Sun	
0.74613372×10^7 +	Sun	
0.80613370×10^7	Mars	
0.86613368×10^7	Mars	
0.92613366×10^7	Mars	
0.98613365×10^7	Sun	
0.10461336×10^8 +	Sun	
0.11061336×10^8	Mars	
0.11661336×10^8	Mars	
0.12261336×10^8	Mars	
0.12861336×10^8	Sun	
0.13461336×10^8 +	Sun	
0.14161336×10^8	Mars	
0.14961335×10^8	Mars	
0.15761335×10^8	Mars	
0.16561335×10^8	Venus	
0.17361335×10^8 +	Venus	
0.18161334×10^8	Mars	
0.18961334×10^8	Mars	
0.19761334×10^8	Mars	
0.20561334×10^8	Venus	
0.21361334×10^8 +	Venus	
0.22161333×10^8	Mars	
0.22961333×10^8	Mars	
0.23761333×10^8	Mars	
0.24561333×10^8	Venus	
0.25361333×10^8 +	Venus	
0.26161332×10^8	Mars	
0.26961332×10^8	Mars	
0.27761332×10^8	Earth	
0.28561332×10^8	Earth	
0.29361331×10^8 +	Earth	
0.30161331×10^8	Mars	
0.30961331×10^8	Mars	
0.31761331×10^8	Mars	
0.32561331×10^8	Earth	
0.33361331×10^8 +	Earth	
0.34061331×10^8	Mars	
0.34661329×10^8	Mars	
0.35261329×10^8	Mars	
0.35861328×10^8	Earth	
0.36461328×10^8 +	Earth	
0.37061327×10^8	Mars	
0.37661327×10^8	Mars	
0.38261326×10^8	Mars	
0.38861325×10^8	Earth	
0.39461325×10^8 +	Earth	
0.40061325×10^8	Mars	
0.40661324×10^8	Mars	
0.41261323×10^8	Mars	
0.41861322×10^8	Earth	
0.42461322×10^8 +	Earth	
0.42961322×10^8	Mars	
0.43361321×10^8	Mars	
0.43761321×10^8	Earth	
0.44161321×10^8	Earth	
0.44561321×10^8 +	Mars	
0.44961321×10^8	Mars	
0.45361321×10^8	Earth	
0.45761321×10^8	Earth	
0.46161321×10^8	Mars	
0.46561321×10^8 +	Mars	
0.46861320×10^8	Earth	
0.47061320×10^8	Mars	
0.47178719×10^8	Earth	Conic Break
0.47193118×10^8	Earth	Earth Approach Conic (VII. 2. 3)
0.47207518×10^8 +	Earth	
0.47218317×10^8	Earth	
0.47225516×10^8	Earth	
0.47232715×10^8	Earth	
0.47238914×10^8	Earth	
0.47245313×10^8 +	Earth	
0.47248912×10^8	Earth	
0.47252511×10^8	Earth	
0.47254911×10^8	Earth	
0.47256111×10^8	Earth	
0.47257310×10^8 +	Earth	
0.47258510×10^8	Earth	
0.47258710×10^8	Earth	
0.47260787×10^8	Earth	

4642

Table B-10 (Sheet 2 of 2). Reference Body Schedules

Designation	Up to Time (sec)	Position			Velocity			Comments
Q0	$.5x10^8$	0	0	0	0	0	0	All Q matrices are diagonal 6 x 6 matrices. The units are $(km)^2$ and $(km/sec)^2$
Q1	$.12x10^5$	0	0	0	0	0	0	
	$.15x10^5$	.2	.2	.2	$.2x10^{-6}$	$.2x10^{-6}$	$.2x10^{-6}$	
	$.5x10^8$	$.1x10^{-1}$	$.1x10^{-1}$	$.1x10^{-1}$	$.1x10^{-7}$	$.1x10^{-7}$	$.1x10^{-7}$	
Q2	$.12x10^4$	0	0	0	0			
	$.12x10^5$	0	0	0	$.2x10^{-6}$	$.2x10^{-6}$	$.2x10^{-6}$	
	$.22x10^6$	.2	.2	.2	$.2x10^{-6}$	$.2x10^{-6}$	$.2x10^{-6}$	
	$.117x10^7$	2.0	2.0	2.0	$.1x10^{-7}$	$.1x10^{-7}$	$.1x10^{-7}$	
	$.5x10^8$	$.1x10^{-1}$	$.1x10^{-1}$	$.1x10^{-1}$	$.1x10^{-7}$	$.1x10^{-7}$	$.1x10^{-7}$	
Q3	$.12x10^4$	0	0	0	0	0	0	
	$.16x10^7$	.2	0	0	0	0	0	
	$.80x10^7$	.5	0	0	0	0	0	
Q4	$.12x10^4$	0	0	0	0	0	0	
	$.47x10^6$	.2	.2	0	$.1x10^{-8}$	$.1x10^{-8}$	0	
	$.21x10^7$	.2	.2	.2	0	$.1x10^{-8}$	$.1x10^{-8}$	
	$.61x10^7$	.3	.4	.4	0	$.1x10^{-9}$	$.1x10^{-8}$	
	$.808x10^7$	.2	.4	.4	0	0	0	
	$.812x10^7$	.2	.1	.3	0	0	0	
Q5	$.12x10^5$	0	0	0	0	0	0	
	$.15x10^5$	.2	.2	.2	$.2x10^{-6}$	$.2x10^{-6}$	$.2x10^{-6}$	
	$.5x10^8$	$.1x10^{-3}$	$.1x10^{-3}$	$.1x10^{-3}$	$.1x10^{-9}$	$.1x10^{-9}$	$.1x10^{-9}$	
Q6	$.50x10^8$	$.1x10^{-3}$	$.1x10^{-3}$	$.1x10^{-3}$	$.1x10^{-9}$	$.1x10^{-9}$	$.1x10^{-9}$	
Q7	$.15x10^5$	$.1x10^{-1}$	$.1x10^{-1}$	$.1x10^{-1}$	$.1x10^{-6}$	$.1x10^{-6}$	$.1x10^{-6}$	
	$.50x10^8$	$.1x10^{-2}$	$.1x10^{-2}$	$.1x10^{-2}$	$.1x10^{-7}$	$.1x10^{-7}$	$.1x10^{-7}$	
Q8	$.2526201x10^8$	0	0	0	0	0	0	
	$.8x10^8$	.1	.1	.1	$.1x10^{-6}$	$.1x10^{-6}$	$.1x10^{-6}$	
Q9	$.50x10^8$	$.1x10^{-6}$	$.1x10^{-6}$	$.1x10^{-6}$	$.1x10^{-9}$	$.1x10^{-9}$	$.1x10^{-9}$	
Q10	$.10x10^6$	0	0	0	0	0	0	
	$.252x10^8$	.2	.2	.2	$.2x10^{-6}$	$.2x10^{-6}$	$.2x10^{-6}$	
	$.50x10^8$	.8	.8	.8	$.8x10^{-6}$	$.8x10^{-6}$	$.8x10^{-6}$	
Q11	$.10x10^6$	0	0	0	0	0	0	
	$.252x10^8$	.2	.2	.2	$.2x10^{-6}$	$.2x10^{-6}$	$.2x10^{-6}$	
	$.50x10^8$	.4	.3	.3	$.3x10^{-6}$	$.3x10^{-6}$	$.3x10^{-6}$	
Q12	$.2527x10^8$	0	0	0	0	0	0	
	$.26x10^8$	$.1x10^{-1}$	$.1x10^{-1}$	$.1x10^{-1}$	$.1x10^{-8}$	$.1x10^{-8}$	$.1x10^{-8}$	
Q13	$.253x10^8$	0	0	0	0	0	0	
	$.26x10^8$	.1	.1	.1	$.1x10^{-7}$	$.1x10^{-7}$	$.1x10^{-7}$	
Q14	$.15x10^5$	.2	.2	.2	$.2x10^{-6}$	$.2x10^{-6}$	$.2x10^{-6}$	
	$.50x10^8$	$.1x10^{-3}$	$.1x10^{-3}$	$.1x10^{-3}$	$.1x10^{-9}$	$.1x10^{-9}$	$.1x10^{-9}$	
Q15	$.20x10^5$	$.33x10^{-2}$	$.33x10^{-2}$	$.33x10^{-2}$	$.33x10^{-8}$	$.33x10^{-8}$	$.33x10^{-8}$	
Q16	$.5580x10^4$	0	0	0	0	0	0	
	$.7180x10^4$	$1.33x10^{-2}$	$1.33x10^{-2}$	$1.33x10^{-2}$	$1.33x10^{-8}$	$1.33x10^{-8}$	$1.33x10^{-8}$	
	$.11966x10^5$	0	0	0	0	0	0	
	$.13566x10^5$	$1.33x10^{-2}$	$1.33x10^{-2}$	$1.33x10^{-2}$	$1.33x10^{-8}$	$1.33x10^{-8}$	$1.33x10^{-8}$	
	$.17350x10^5$	0	0	0	0	0	0	
	$.20x10^5$	$1.33x10^{-2}$	$1.33x10^{-2}$	$1.33x10^{-2}$	$1.33x10^{-8}$	$1.33x10^{-8}$	$1.33x10^{-8}$	
Q17	$.20x10^5$	$1.3x10^{-6}$	$1.3x10^{-6}$	$1.3x10^{-6}$	0	0	0	
Q18	$.5580x10^4$	0	0	0	0	0	0	
	$.7180x10^4$	$5.1x10^{-6}$	$5.1x10^{-6}$	$5.1x10^{-6}$	0	0	0	
	$.11966x10^5$	0	0	0	0	0	0	
	$.13566x10^5$	$5.1x10^{-6}$	$5.1x10^{-6}$	$5.1x10^{-6}$	0	0	0	
	$.17350x10^5$	0	0	0	0	0	0	
	$.20x10^5$	$5.1x10^{-6}$	$5.1x10^{-6}$	$5.1x10^{-6}$	0	0	0	

4639

Table B-11. Q Schedules

Mission Category 2, Approach Phase						
		Earth Approach			Martian Approach	
		Slow	Medium	Fast	Slow	Fast
Trajectory, Number, Leg, and Conic		I. 4. 3	VI. 3. 3	VIII. 2. 3	II. 1. 3	III. 1. 3
Julian Date at Start of Conic		2441517.0 +.36300684	2441437.0 +.76863276	2441519.0 +.54912840	2441298.0 +.20827791	2442707.0 +.40337742
Flight Time in Conic	(days)	2.0	1.2	.95	2.3	.57
	(sec)	184787.14	106259.56	82106.067	196585.01	49499.545
Initial Position Vector (km)	X_1	155163.32	695387.88	327407.20	-307361.24	276675.85
	X_2	905251.97	508103.08	765061.40	399483.85	448419.60
	X_3	101089.59	334728.01	401573.72	282888.09	237601.13
Initial Velocity Vector (km/sec)	$\dot{X}_1$	-.84774909	-6.4761580	3.8825985	1.4929547	-5.6353044
	$\dot{X}_2$	-4.6592291	-4.6552528	-9.2633180	-1.9791621	-8.9984836
	$\dot{X}_3$	-.45215206	-3.0191083	-4.7584814	-1.4189805	-4.7609426
Initial Radius (km)		924000.			578000.	578000.
Initial Speed (km/sec)		4.7572613			2.8564842	11.635976
Speed at Re-entry (km/sec)		12.02	13.95	15.66	5.69	12.63
Comments						

4658

Table B-12. Nominal Trajectory Data for Mission Category 2, Planetary Approach Phase

	System Designation	Navigation				Data Processing			Guidance				Comments
		Type of Instrument	Error Budget	Initial Covariance Matrix	Ref. Body Schedule	Square Root Filter	Regular Kalman Filter	Q Schedule	Guidance Law	R_V	V_{min} (m/sec)	$(1-\kappa)t_A$ (hr)	
Ground-based	A1	GT	G11	M15			X	Q7	3	.1	2	1.0	
Self-contained	A2	HS	H11	M15	R1		X	Q0	3	.3	2	1.0	Slow Earth Approach
	A3	HS	H31	M15	R1		X	Q9	3	.1	2	1.0	
Self-contained	A4	HS	H11	M16	R5		X	Q13	3	.21	2	1.5	
	A5	HS	H21	M16	R1		X	Q12	3	.5	2	1.5	
	A6	HS	H21	M16	R5		X	Q0	3	.21	2	1.5	
	A7	HS	H40	M16	R1		X	Q0	3	.35	2	1.5	Medium Earth Approach
	A8	HS	H40	M16	R5		X	Q0	3	.08	2	1.5	
Combination	A9	GT + HS	GT10 + H40	M16	R5		X	Q12	3	.04	2	1.5	
Ground-based	A10	GT	G11	M15			X	Q14	3	.05	2	1.0	
Self-contained	A11	HS	H11	M15	R1		X	Q0	3	.4	2	1.0	Fast Earth Approach
	A12	HS	H31	M15	R1		X	Q0	3	.1	2	1.0	
Self-contained	A13	HS	H11	M17	R1		X	Q0	3	.25	2	1.0	
	A14	HS	H20	M17	R1		X	Q0	3	.05	0	1.0	
	A15	SS	S11	M17	R1		X	Q0	3	.25	2	1.0	
	A16	SS	S20	M17	R1		X	Q0	3	.15	0	1.0	Slow Martian Approach
Combination	A17	HS + SS	H20 + S20	M17	R1		X	Q0	3	.05	0	1.0	
	A18	GT + HS	G11 + H11	M17	R1		X	Q0	3	.15	2	1.0	
Self-contained	A19	HS	H11	M17	R1		X	Q0	3	.4	2	1.3	
	A20	SS	S11	M17	R1		X	Q0	3	.6	2	1.3	
Combination	A21	HS + GT	H11 + G11	M17	R1		X	Q0	3	.2	2	1.3	Fast Martian Approach
	A22	HS + GT	H40 + G10	M17	R1		X	Q0	3	.1	2	1.3	
	A23	HS + GT	H40 + G10	M17	R6		X	Q0	3	.1	2	1.3	

4660

Table B-13. System Configurations, Mission Category 2

Mission Category 3, Planetary Reconnaissance			
		Martian Parking Orbits	
Trajectory Number, Leg, and Conic		IX Low Altitude (140 km)	XII High Altitude (8, 200 km)
Julian Date at Start of Conic		NA	NA
Flight Time in Conic	(days)	.22	.90
	(sec)	19150.0	75682.874
Initial Position Vector (km)	X_1	3540.0000	11595.066
	X_2	0.0	0.0
	X_3	0.0	0.0
Initial Velocity Vector (km/sec)	$\dot{X}_1$	0.0	0.0
	$\dot{X}_2$	2.46370002	1.3613521
	$\dot{X}_3$	2.46380002	0.0
Initial Radius (km)		3540.0000	11595.066
Initial Speed (km/sec)		3.4843394	1.3613521
Comments		Three Revolutions around Mars	Two Revolutions around Mars

Table B-14. Nominal Trajectory Data—
Planetary Reconnaissance

System Designation	Navigation				Data Processing			Guidance			
	Type of Instrument	Error Budget	Initial Covariance Matrix	Ref. Body Schedule	Square Root Filter	Regular Kalman Filter	Q Schedule	Guidance Law	R_V	V_{min} (m/sec)	$(1-\kappa)t_A$ (hr)
P1	HS	H11	M18	R1		X	Q0	0			
P2	HS	H10	M18	R1		X	Q0	0			
P3	HS	H51	M18	R1		X	Q0	0			
P4	HS	H50	M18	R1		X	Q0	0			
P5	HS	H11	M19	R1		X	Q0	0			
P6	HS	H11	M19	R1		X	Q15	0			
P7	HS	H11	M19	R1		X	Q0	3	.05	0	.5
P8	HS	H11	M19	R1	X			0			
P9	HS	H10	M19	R1		X	Q0	0			
P10	HS	H10	M19	R1		X	Q15	0			
P11	HS	H10	M19	R1		X	Q16	0			
P12	HS	H10	M19	R1	X			0			
P13	HS	H20	M19	R1		X	Q0	0			
P14	HS	H20	M19	R1	X			0			
P15	HS	H20	M19	R1		X	Q0	3	$.5 \times 10^{-2}$	0	.5
P16	HS	H21	M19	R1		X	Q0	0			
P17	HS	H21	M19	R1	X			0			
P18	HS	H21	M19	R1		X	Q15	0			
P19	HS	H50	M19	R1		X	Q0	0			
P20	HS	H50	M19	R1		X	Q17	0			
P21	HS	H50	M19	R1		X	Q18	0			
P22	HS	H50	M19	R1	X			0			

4656

Table B-15. System Configurations, Mission Category 3, Planetary Reconnaissance

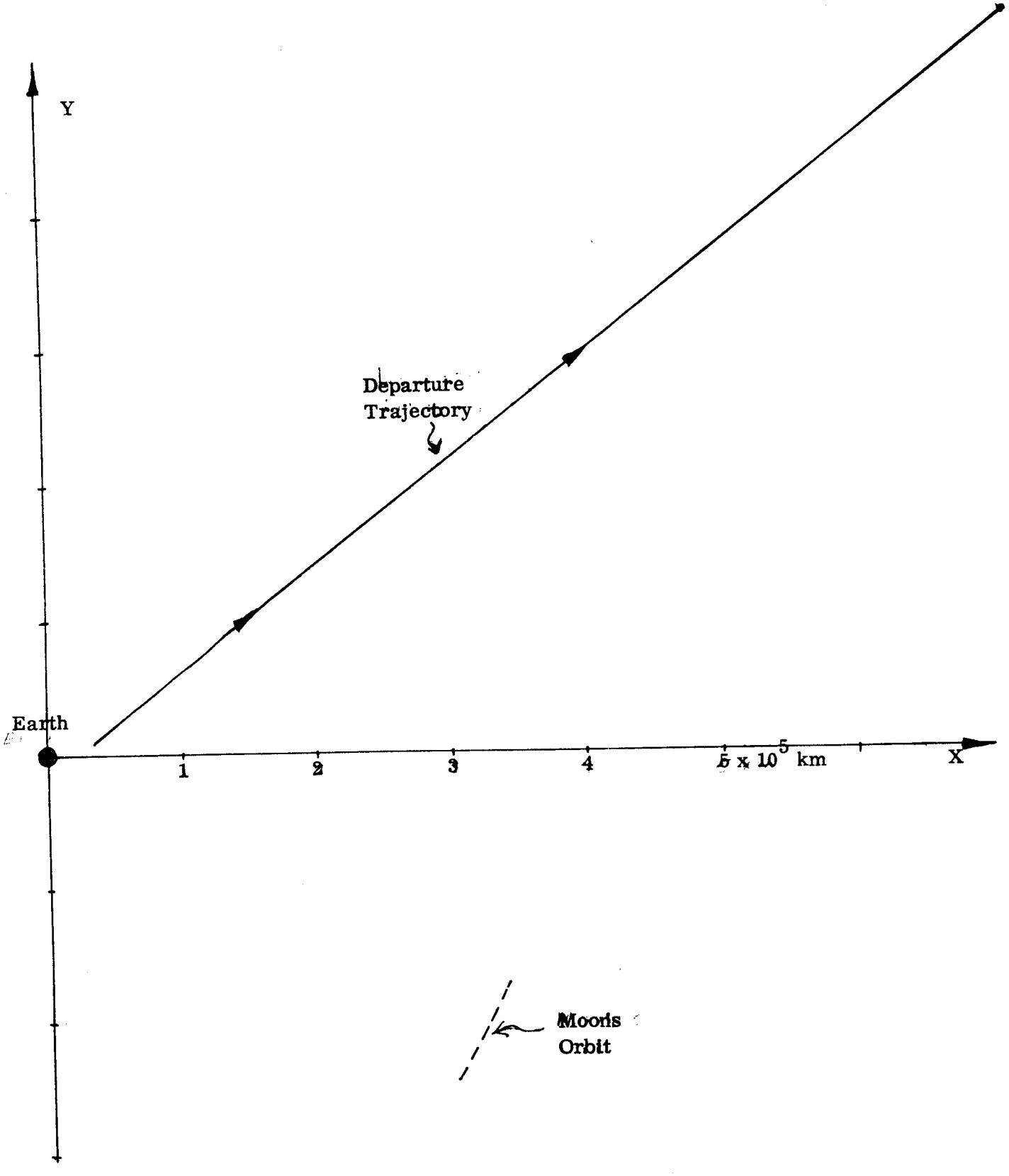

Figure B-1. Earth Departure Phase Conic-VII. 1. 1 Trajectory Projection on Ecliptic Plane

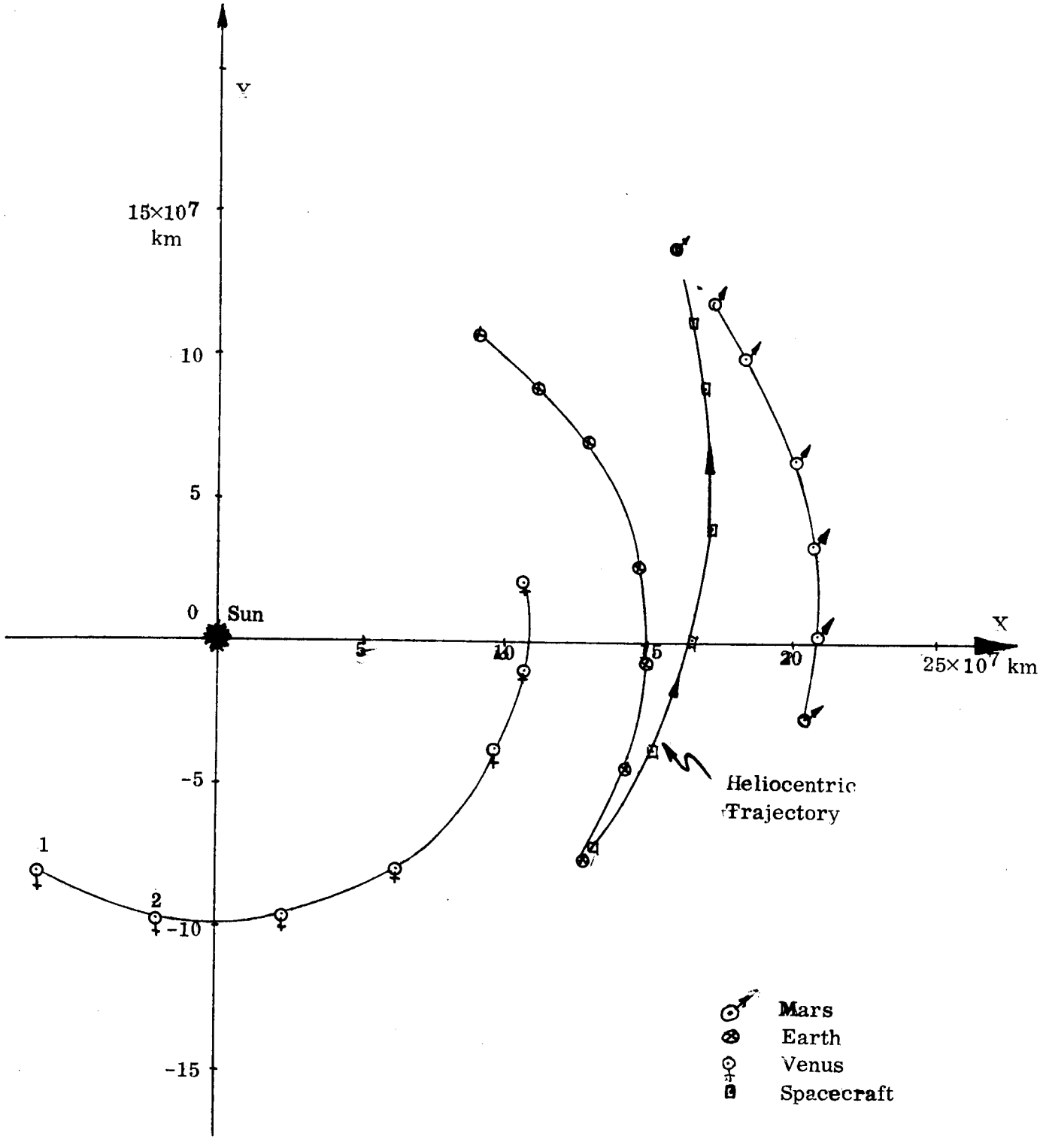

Figure B-2. Heliocentric Phase-VII. 1. 2 Trajectory Projection on Ecliptic Plane

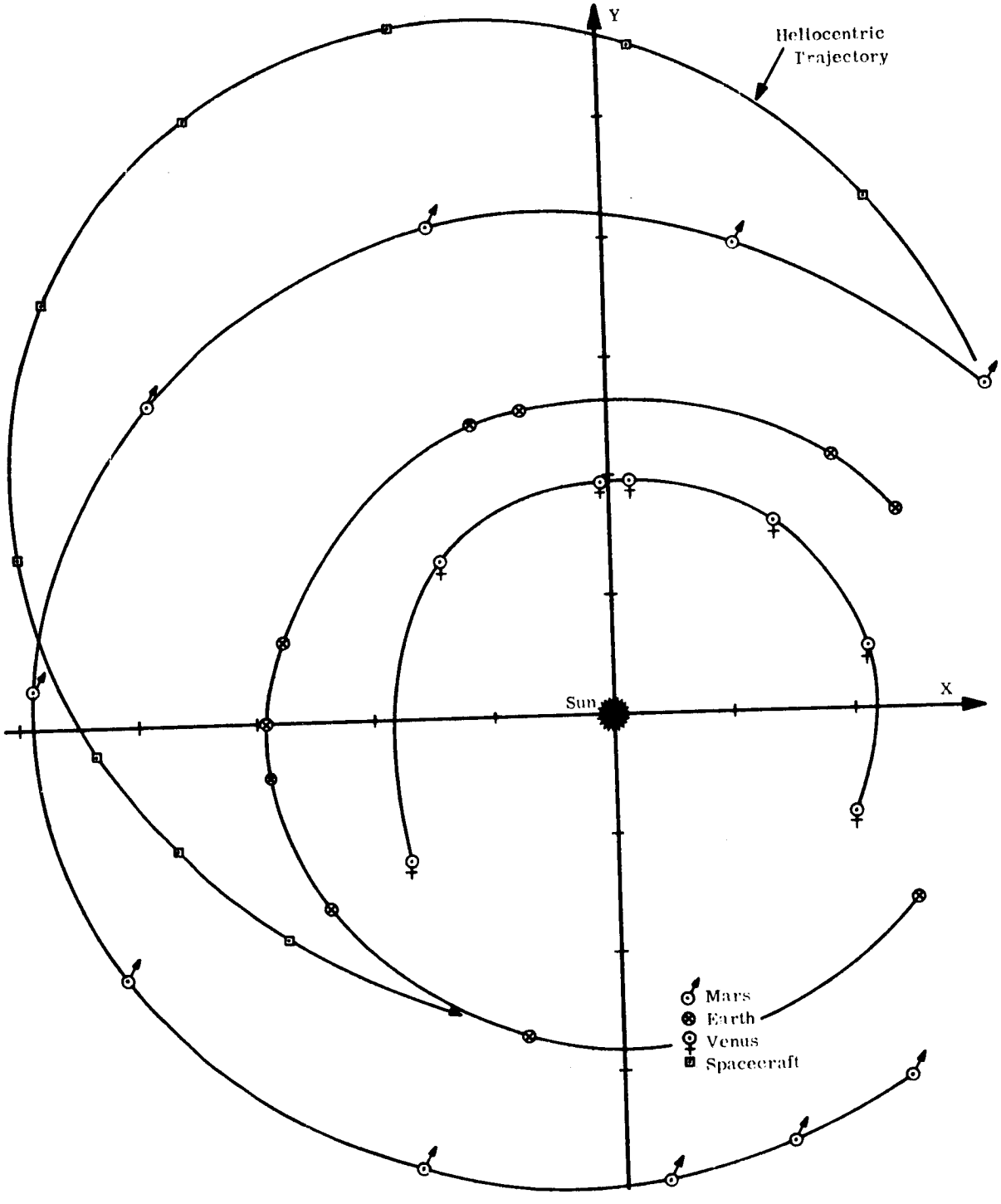

Figure B-3. Heliocentric Phase-VII. 2. 2 Trajectory Projection on Ecliptic Plane

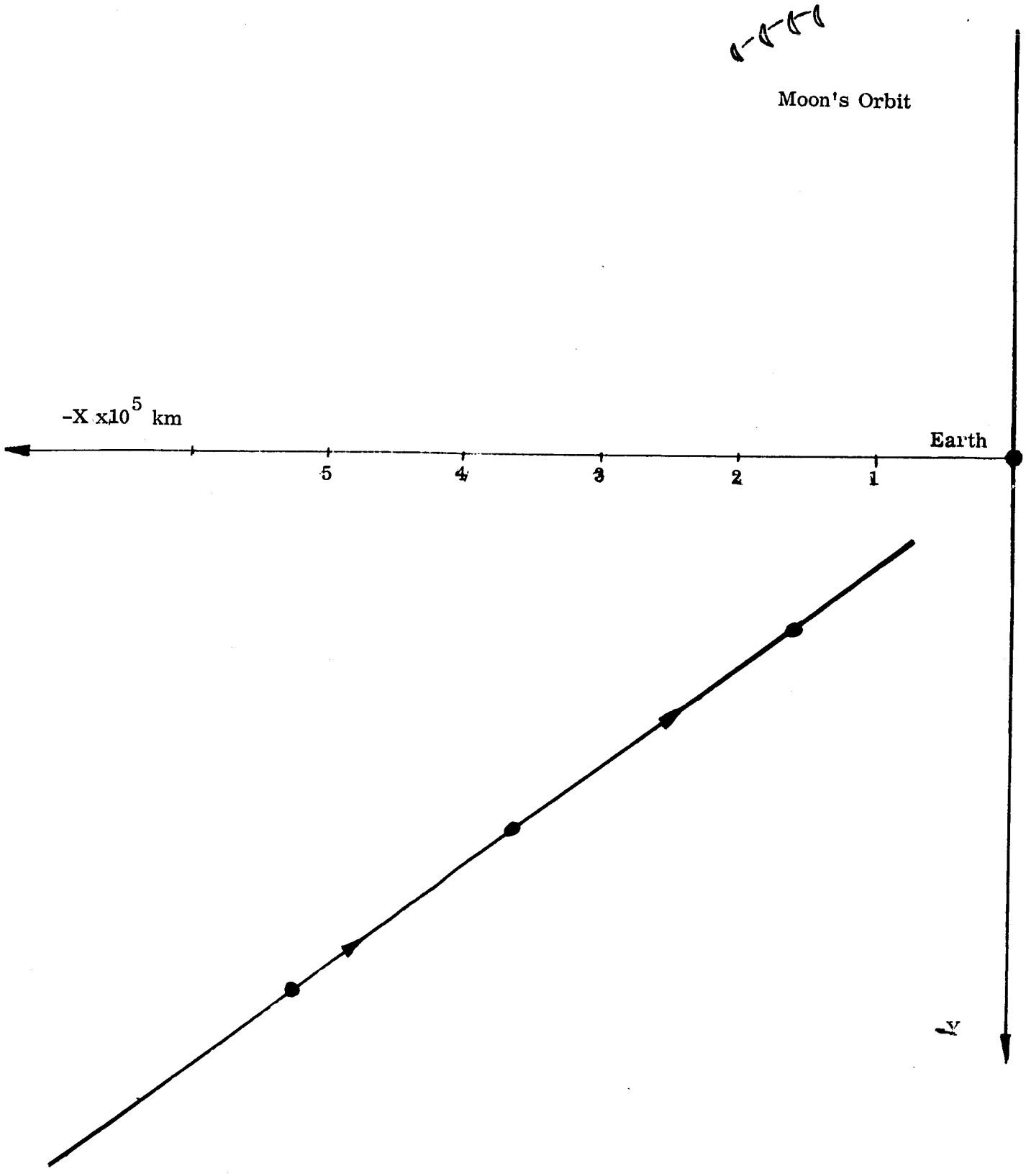

Figure B-4. Earth Approach Phase-Trajectory Projection on Ecliptic, VII. 2. 3

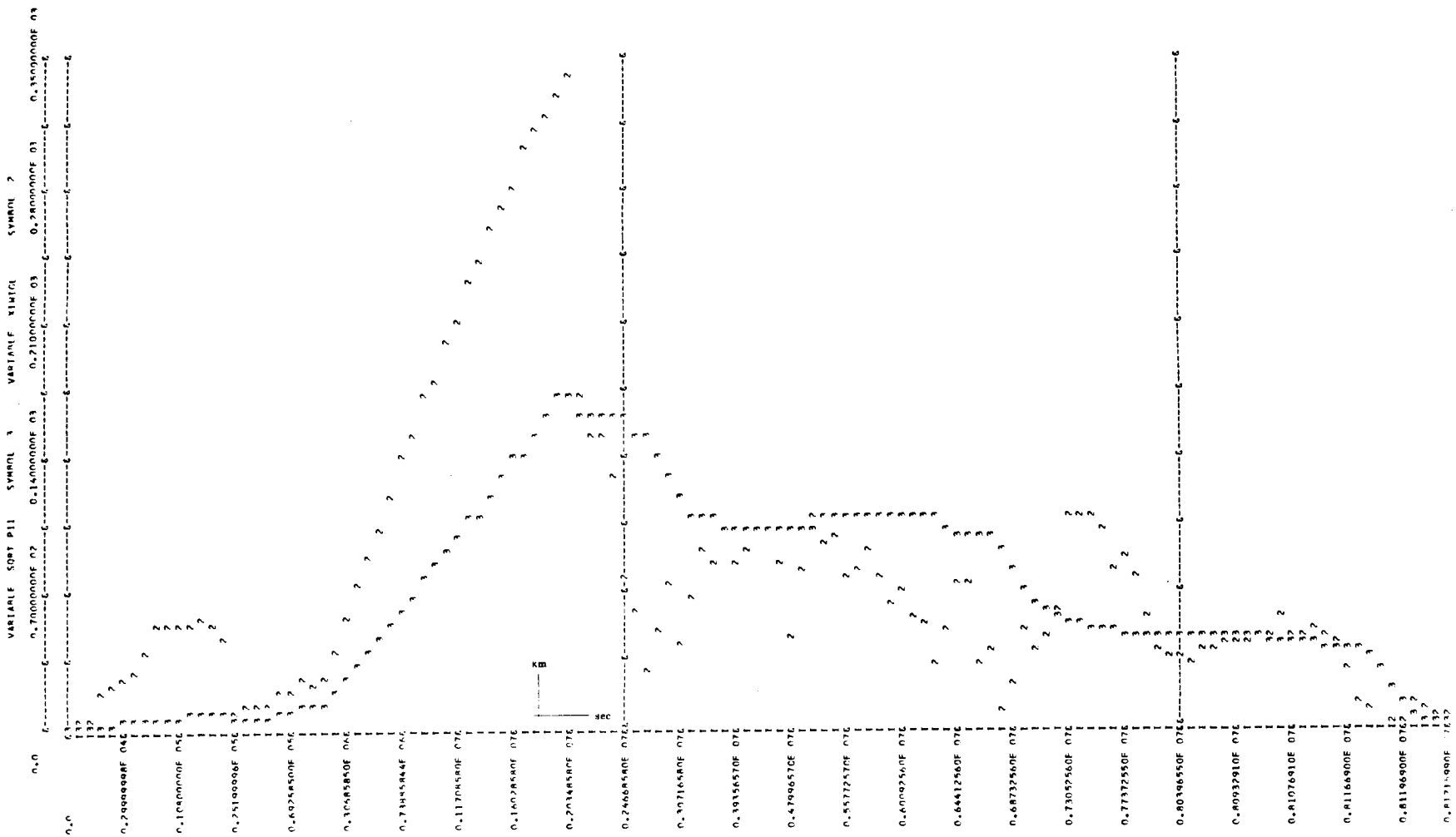

Figure B-5. $|\tilde{x}_1|$ and $\sqrt{P11}$ vs. Time - System Configuration TM16
(Ground Tracking)

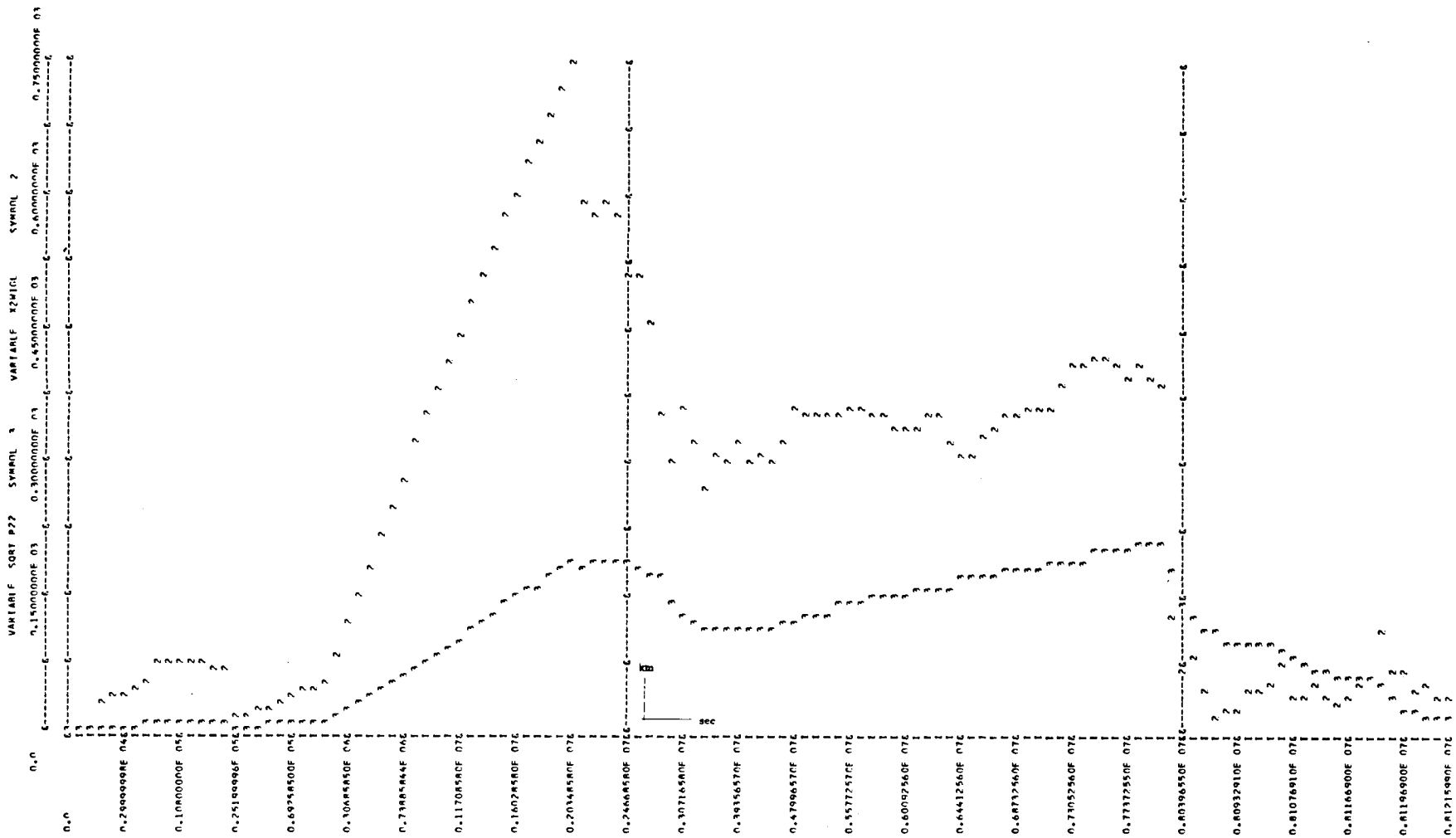

Figure B-6. $|\tilde{x}_2|$ and $\sqrt{P22}$ vs. Time - System Configuration TM16 Ground Tracking

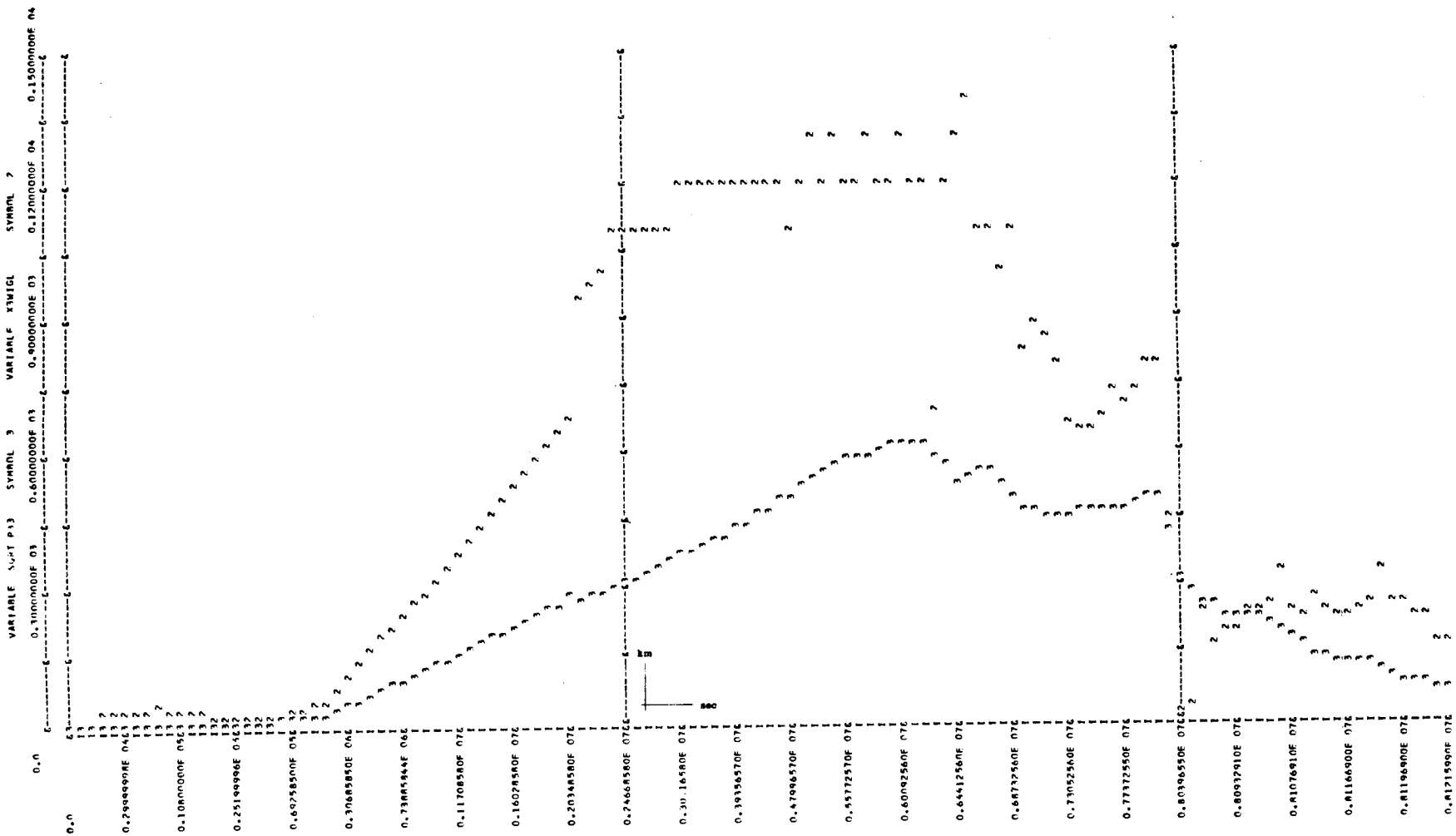

Figure B-7. $|\tilde{x}_3|$ and $\sqrt{P33}$ vs. Time - System Configuration TM16 (Ground Tracking)

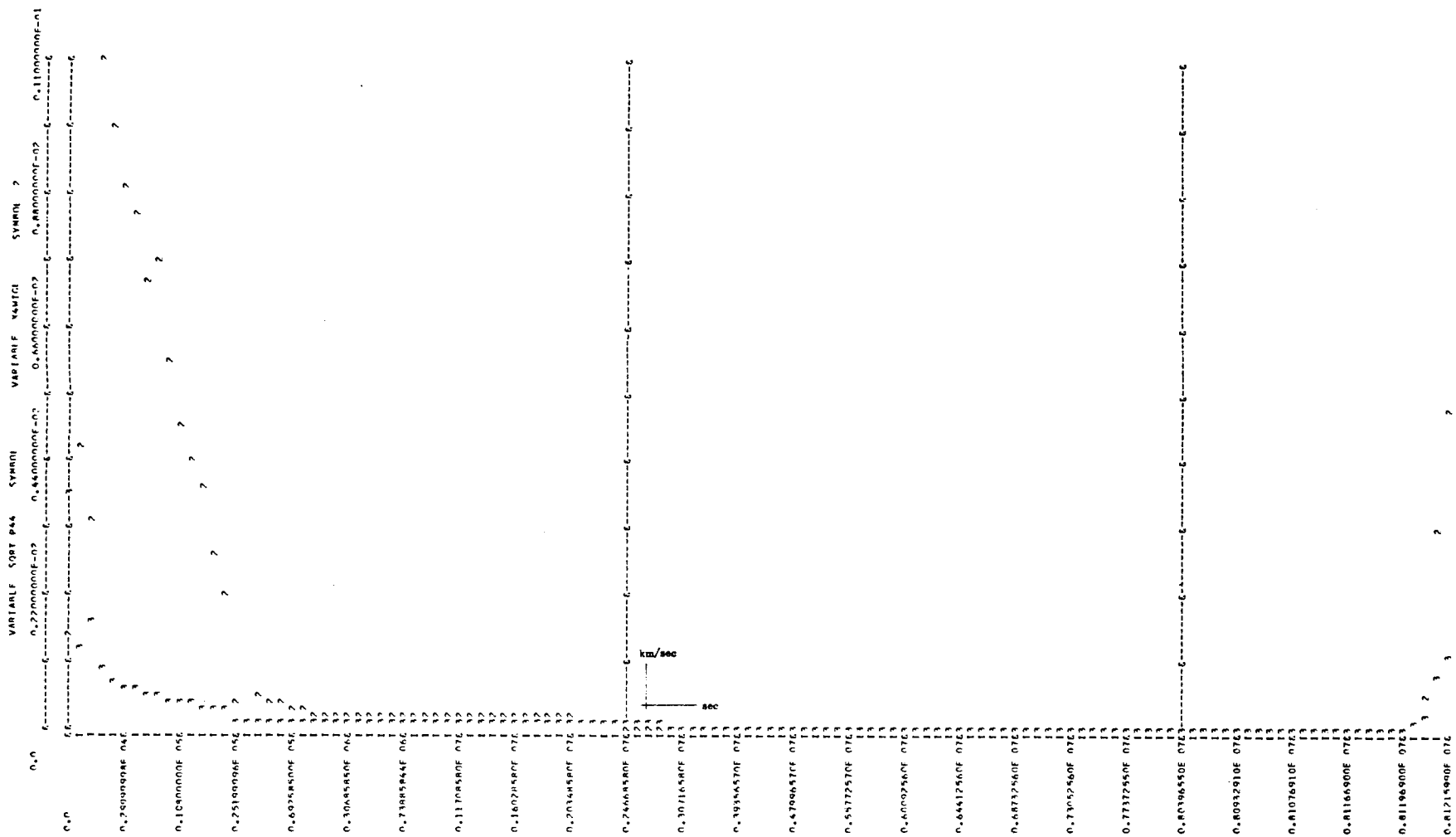

Figure B-8. $|\tilde{x}_4|$ and $\sqrt{P44}$ vs. Time - System Configuration TM16
(Similar Behavior for $|\tilde{x}_5|$, $|\tilde{x}_6|$, $\sqrt{P55}$, $\sqrt{P66}$)
(Ground Tracking)

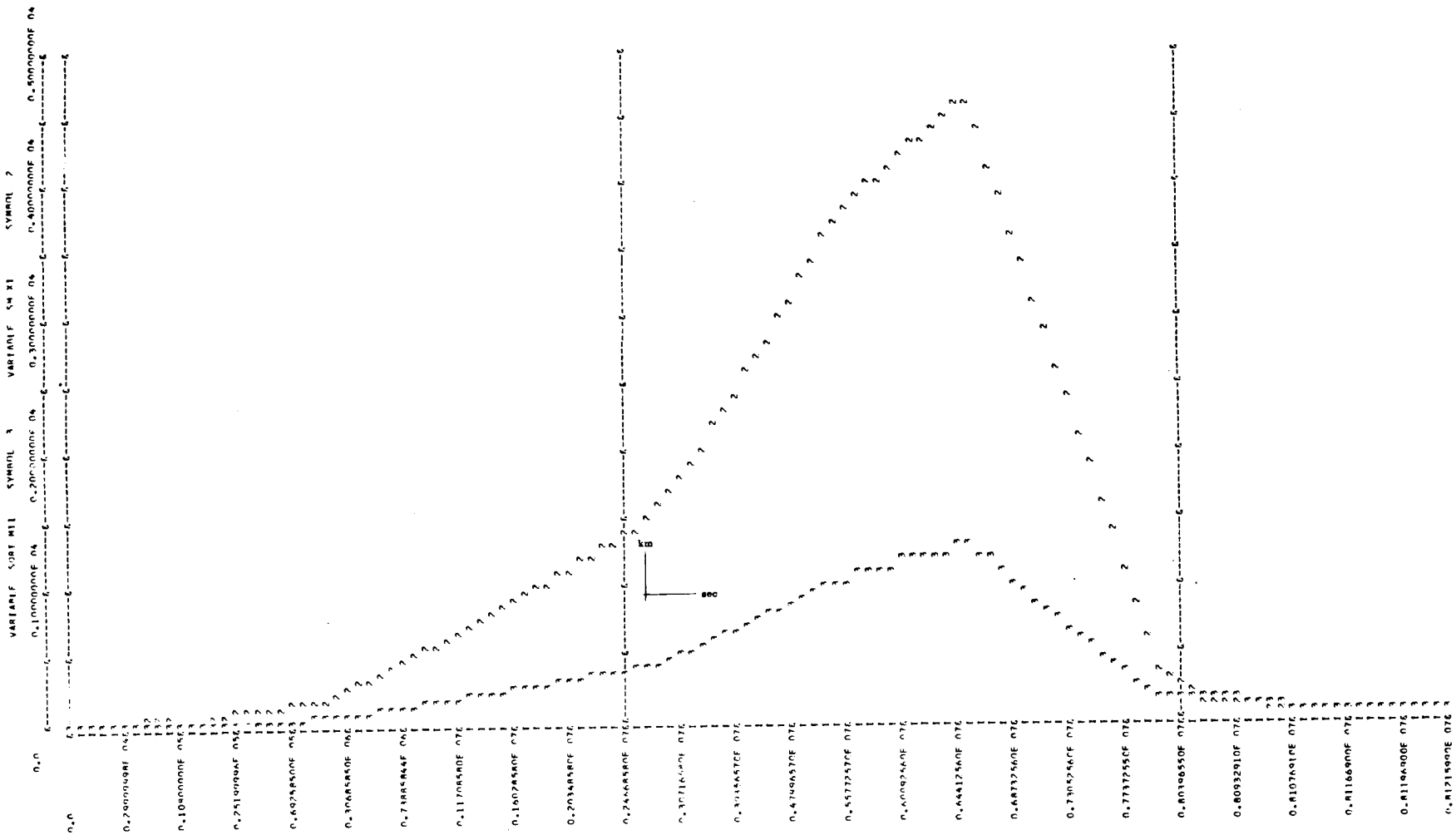

Figure B-9. $|x_1|$ and $\sqrt{M11}$ vs. Time - System Configuration TM16
(Ground Tracking)

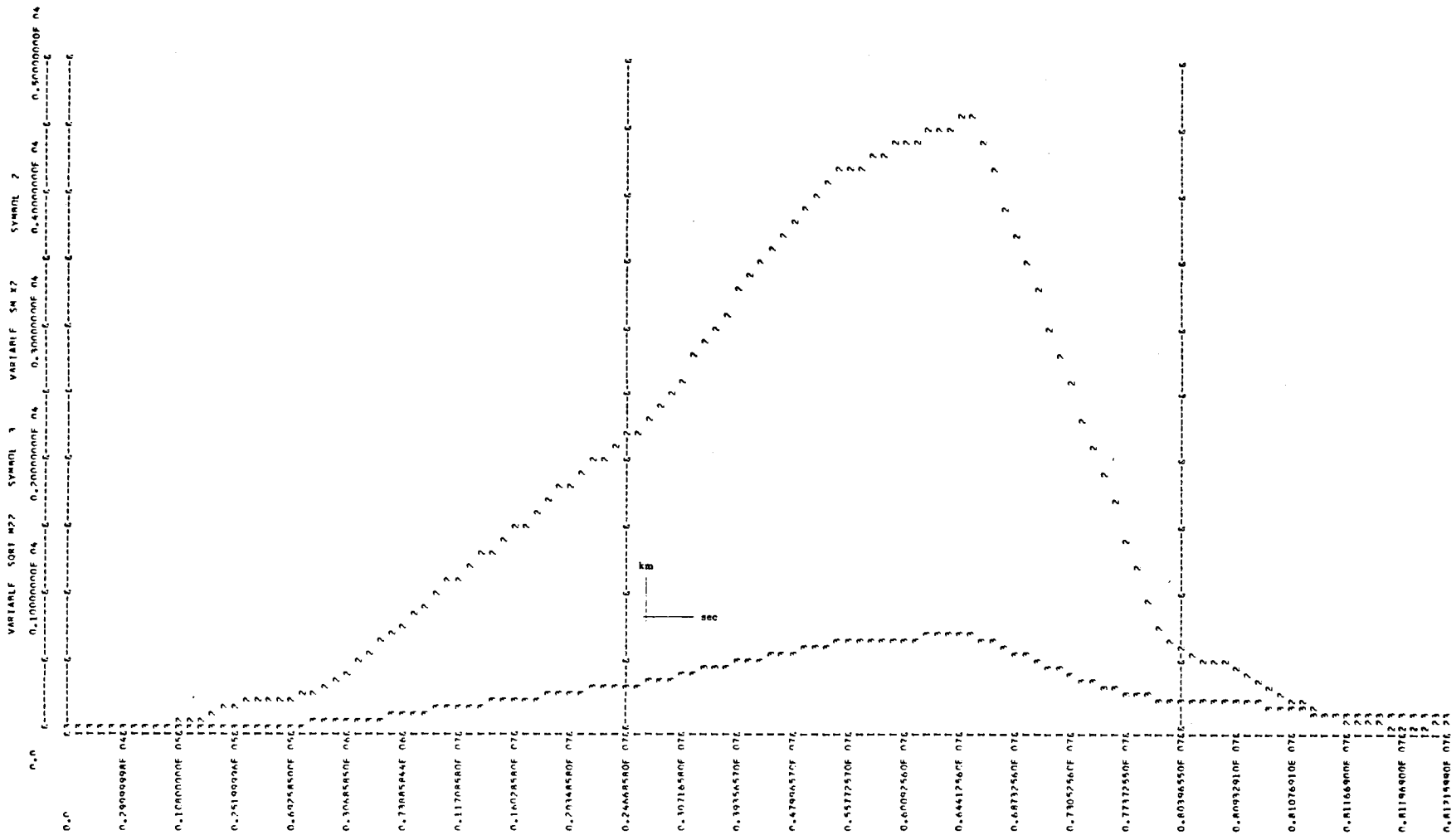

Figure B-10. $|x_2|$ and $\sqrt{M22}$ vs. Time - System Configuration TM16 (Ground Tracking)

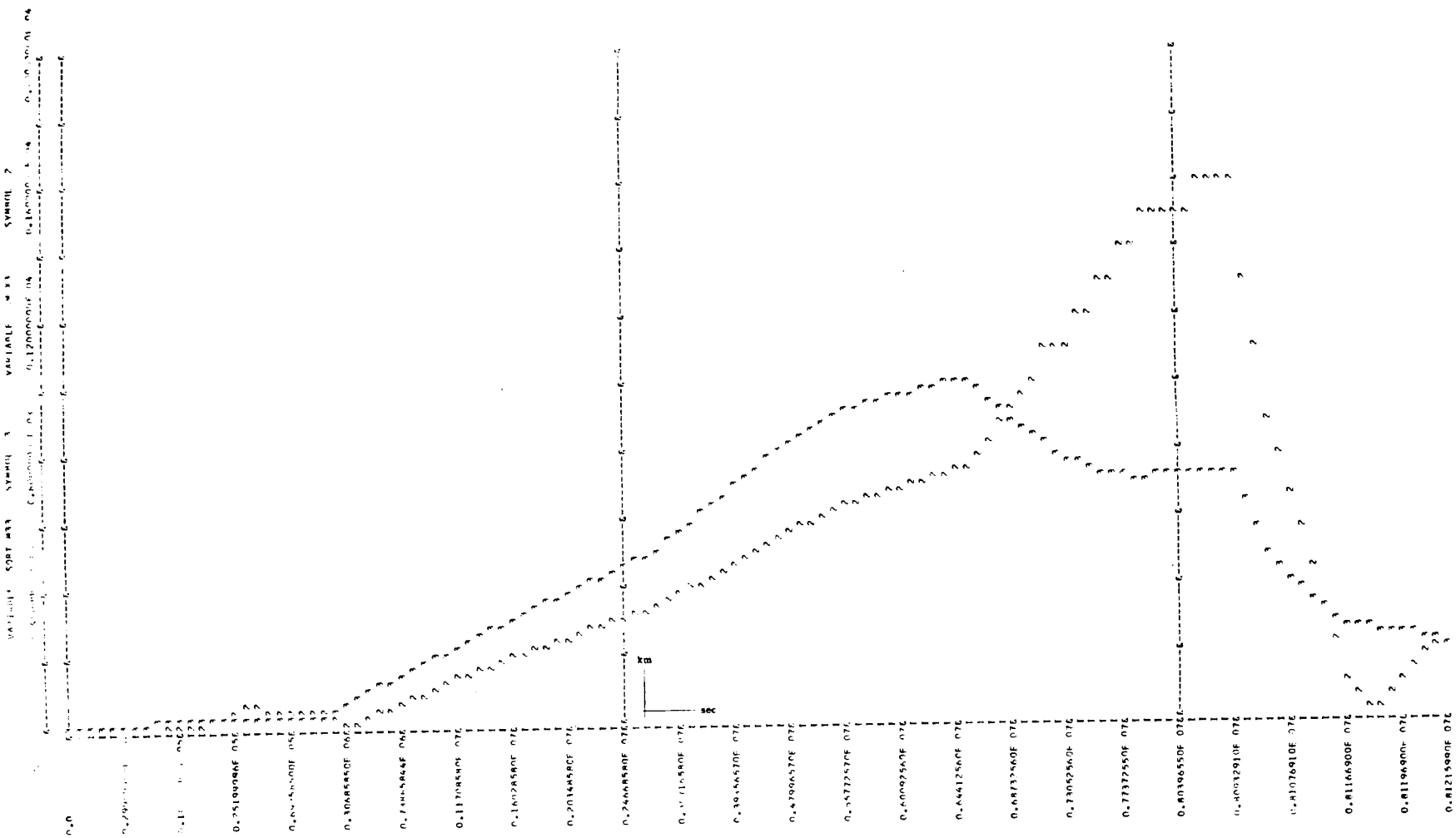

Figure B-11. $|x_3|$ and $\sqrt{M33}$ vs. Time - System Configuration TM16
(Ground Tracking)

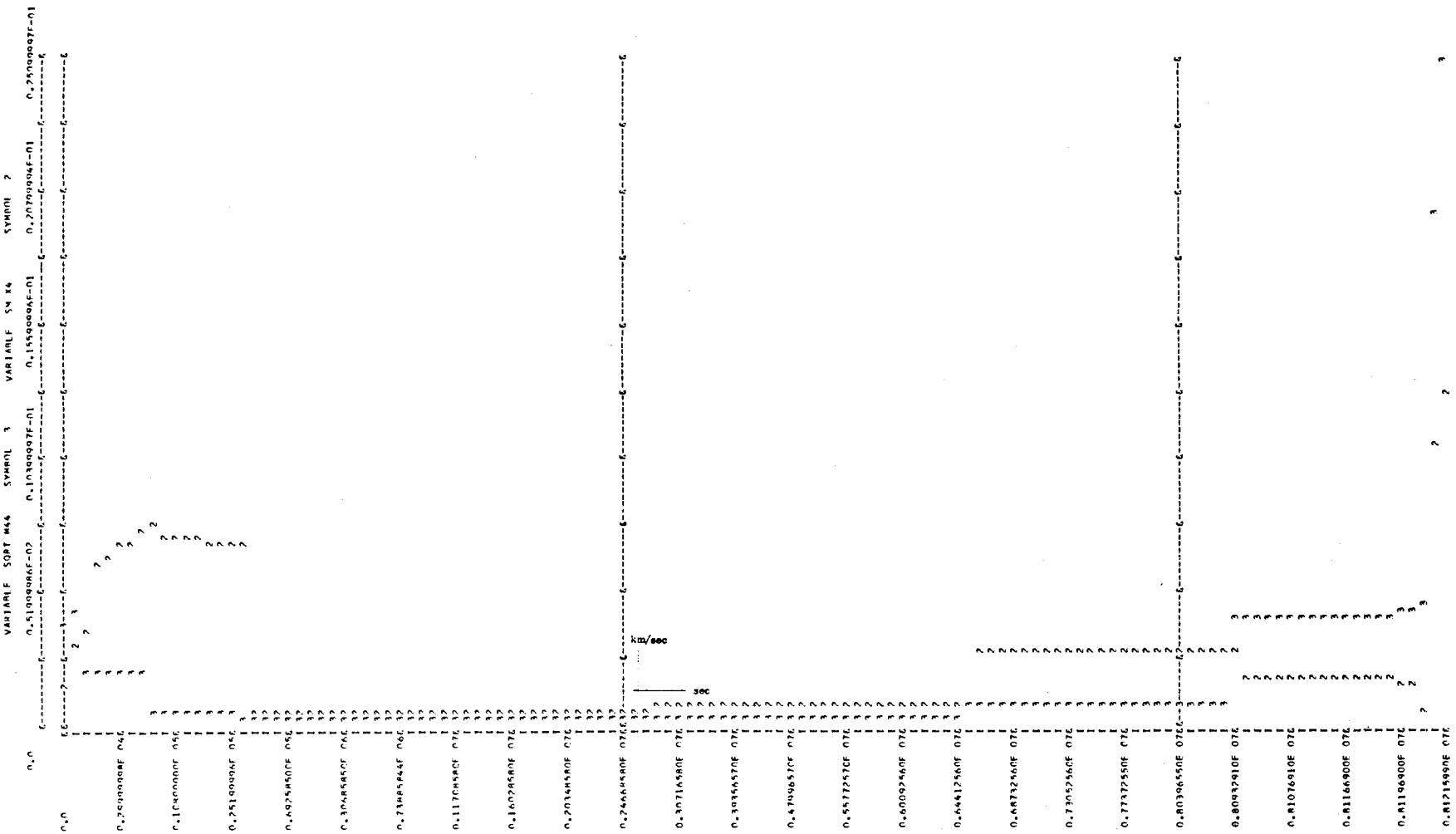

Figure B-12. $|x_4|$ and $\sqrt{M44}$ vs. Time - System Configuration TM16
(Similar Behavior for $|x_5|$, $|x_6|$, $\sqrt{M55}$, $\sqrt{M66}$)
(Ground Tracking)

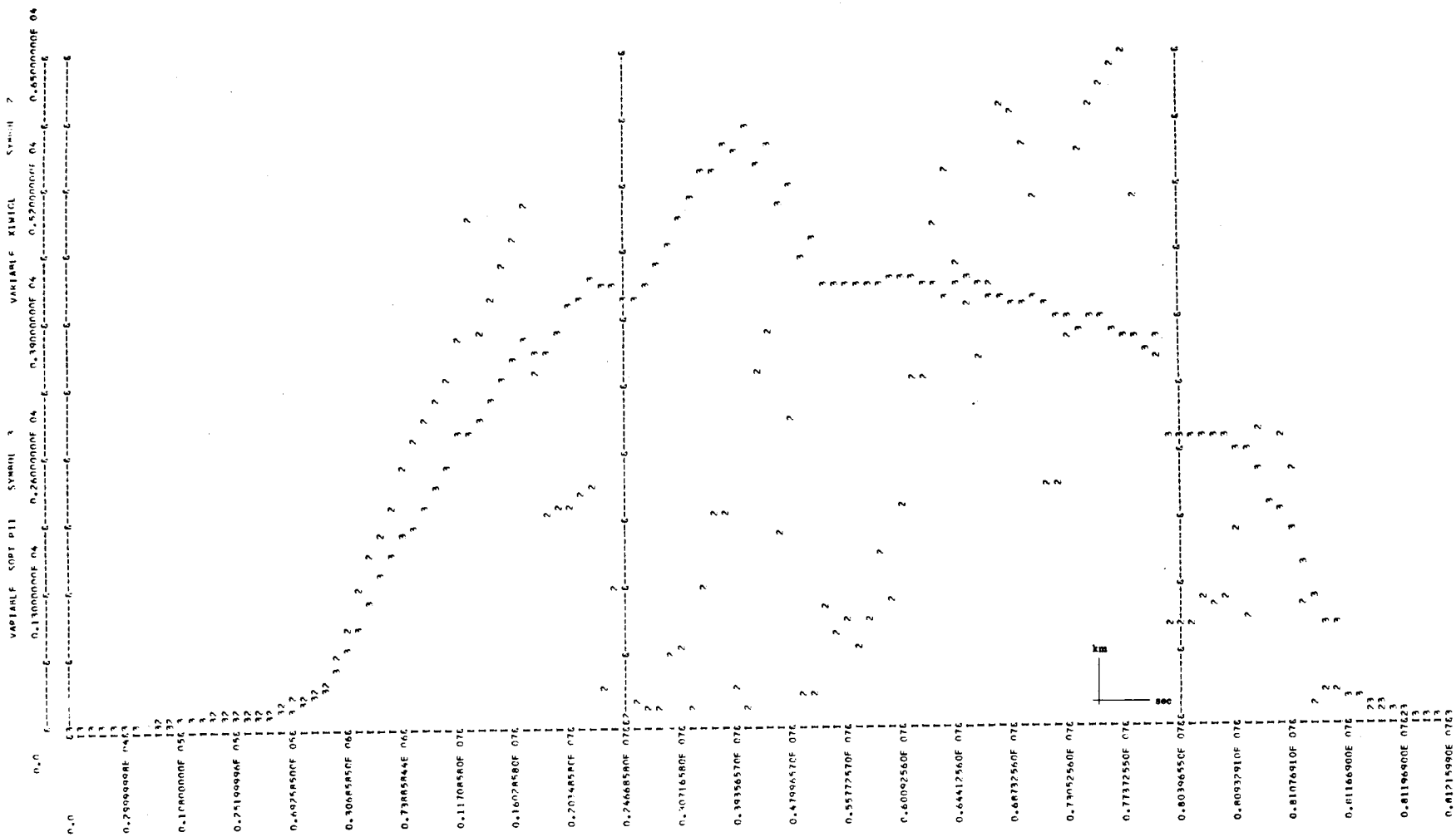

Figure B-13. $|\tilde{x}_1|$ and $\sqrt{P11}$ vs. Time—System Configuration TM21
(Similar Behavior for $|x_2|$, $|\tilde{x}_3|$, $\sqrt{P22}$, $\sqrt{P33}$)
(On-Board Instrument)

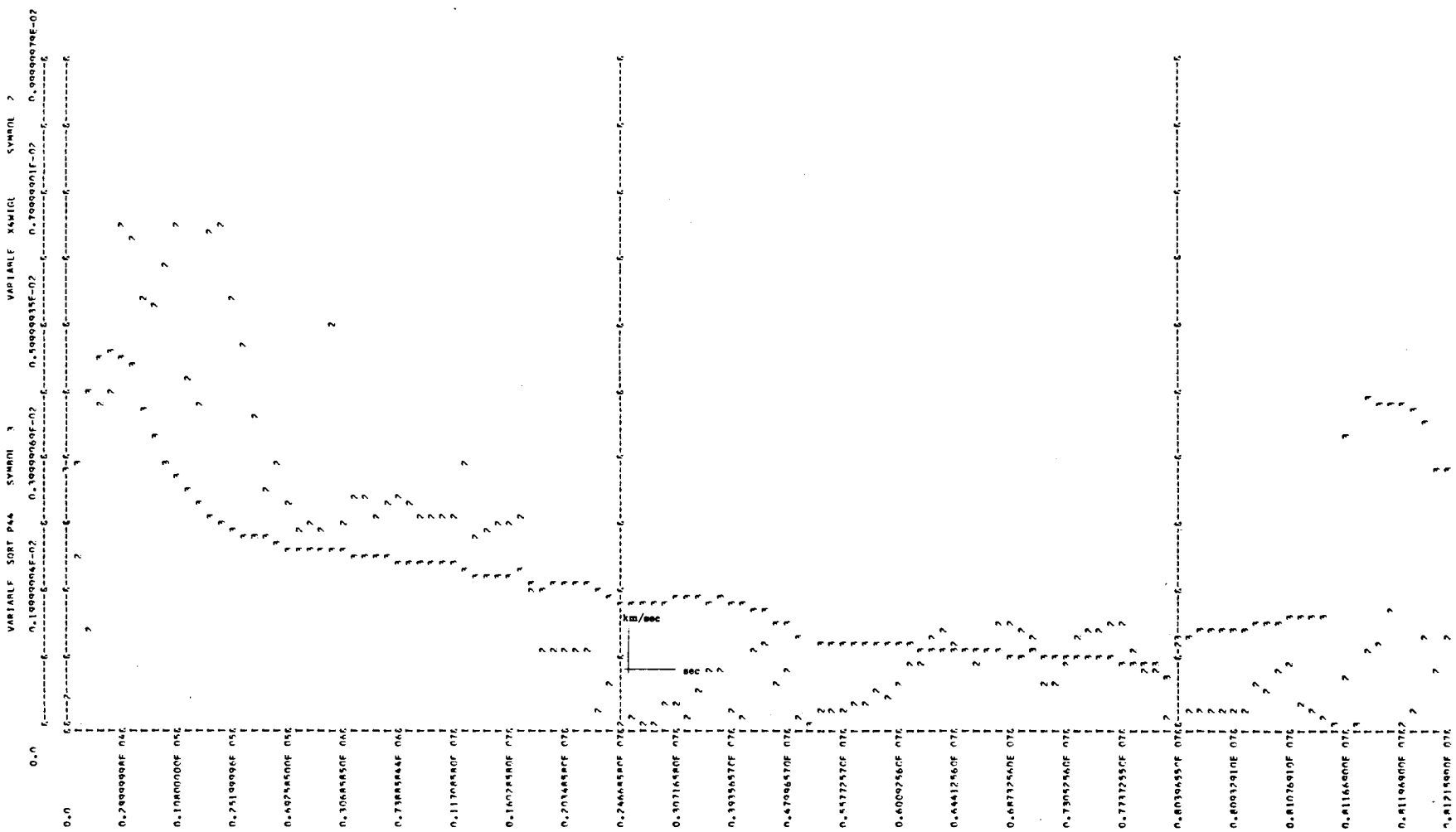

Figure B-14. $|\tilde{x}_4|$ and $\sqrt{P44}$ vs. Time—System Configuration TM21
(Similar Behavior for $|\tilde{x}_5|$, $|\tilde{x}_6|$, $\sqrt{P55}$, $\sqrt{P66}$)
(On-Board Instrument)

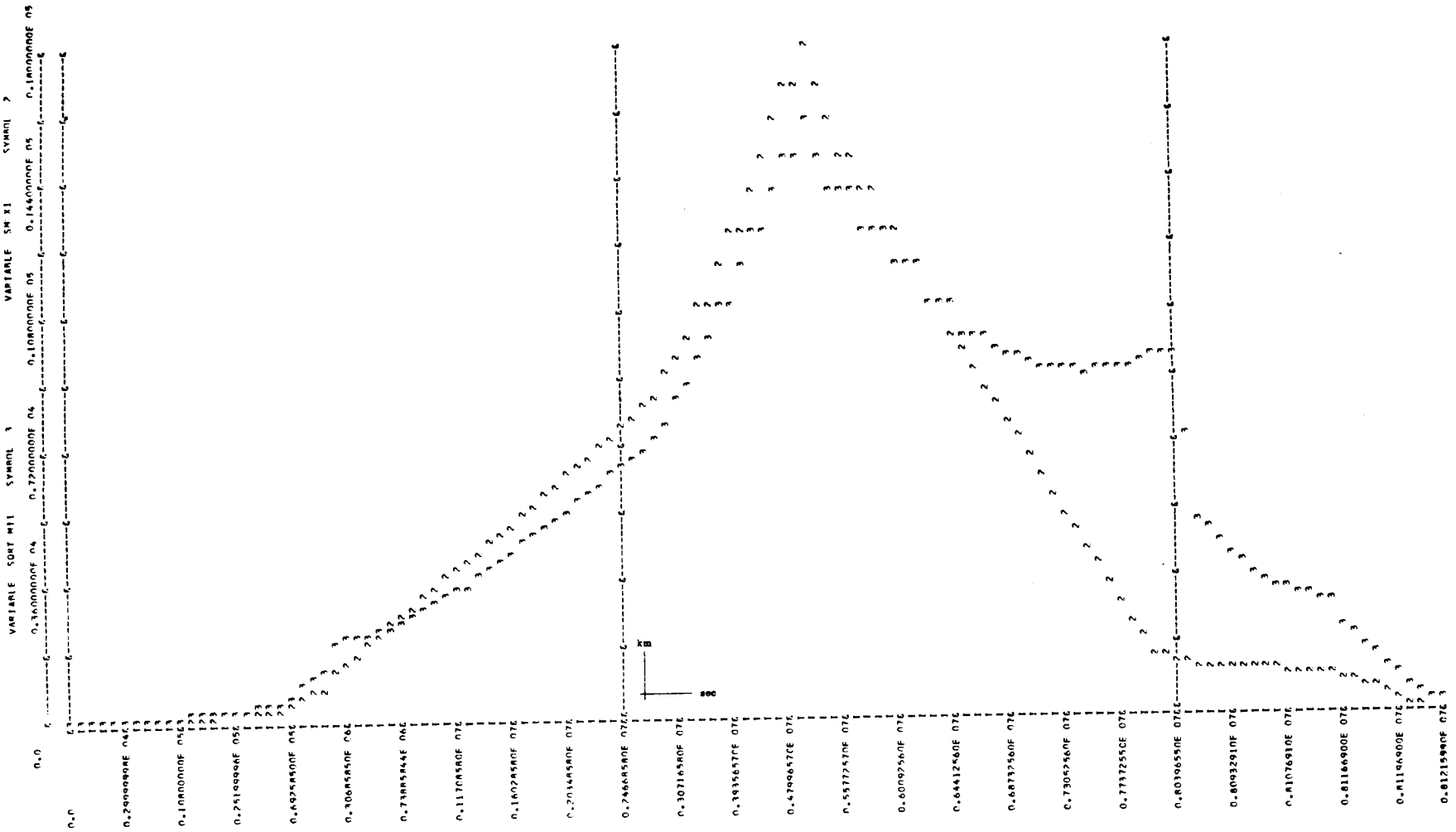

Figure B-15. $|x_1|$ and $\sqrt{M11}$ vs. Time - System Configuration TM21
(Similar Behavior for $|x_2|$, $|x_3|$, $\sqrt{M22}$, $\sqrt{M33}$)
(On-Board Instrument)

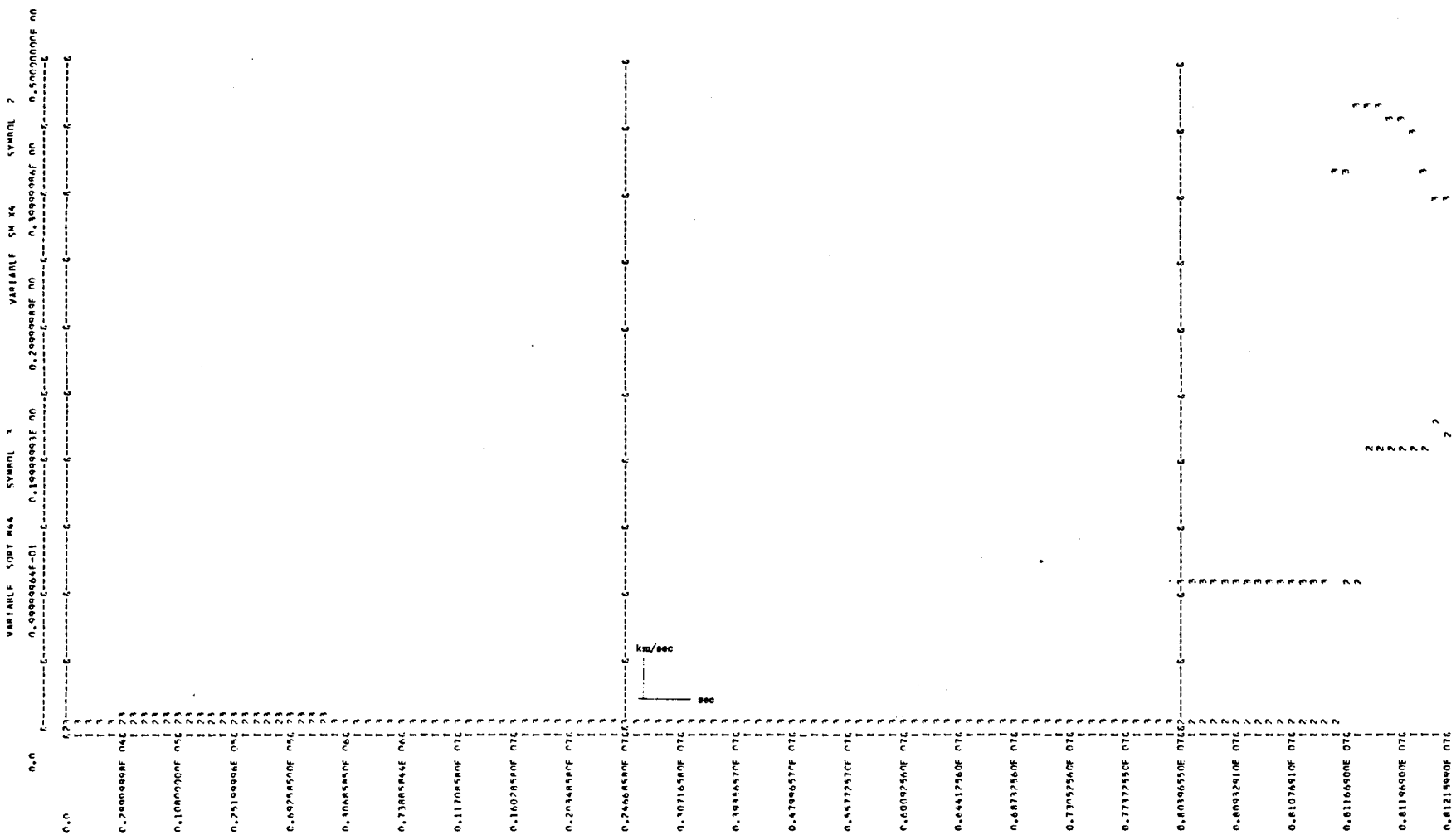

Figure B-16. $|x_4|$ and $\sqrt{M44}$ vs. Time—System Configuration TM21
(Similar Behavior for $|x_5|$, $|x_6|$, $\sqrt{M55}$, $\sqrt{M66}$)
(On-Board Instrument)

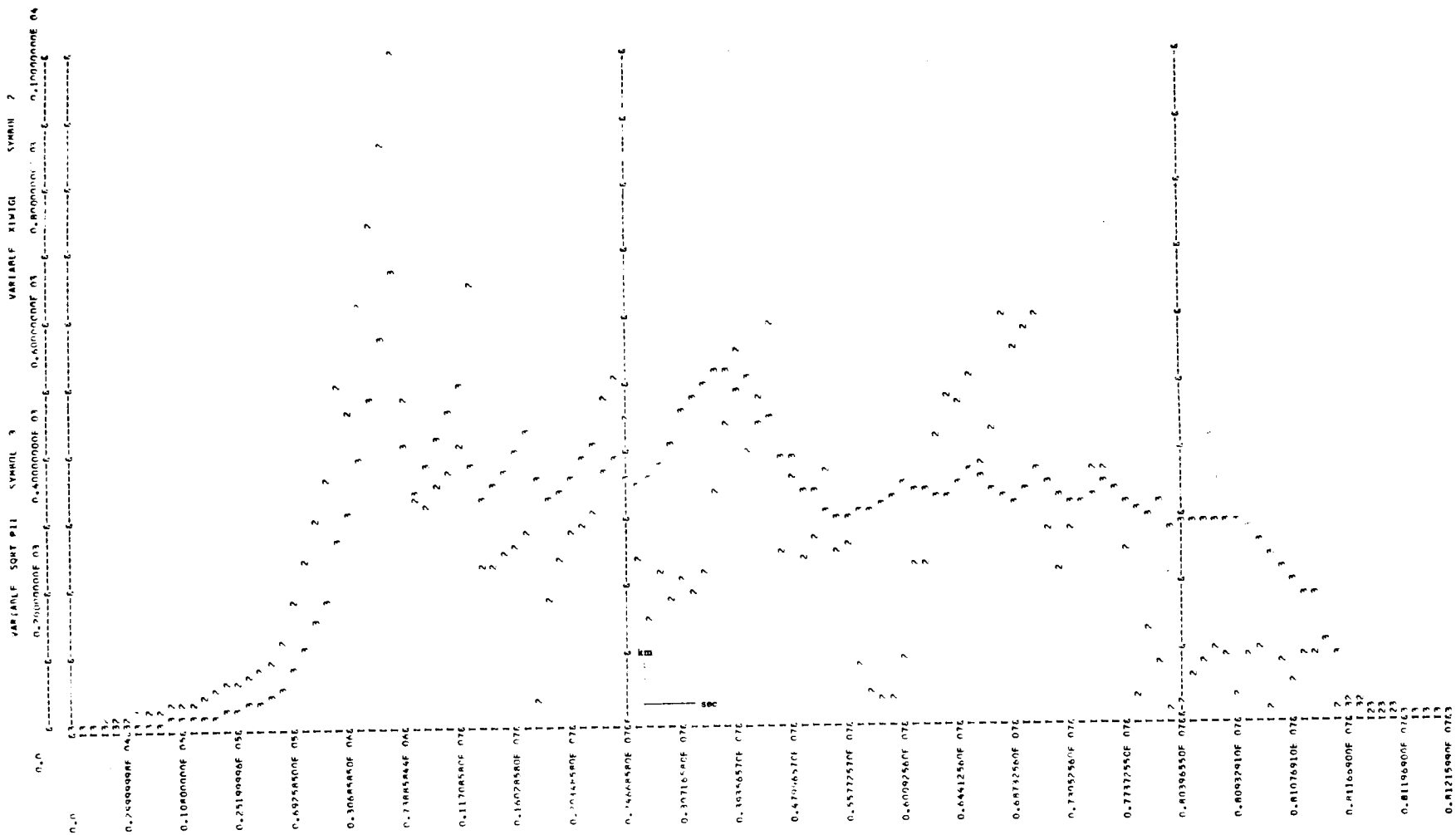

Figure B-17. $|\tilde{x}_1|$ and $\sqrt{P11}$ vs. Time—System Configuration TM25
(Similar Behavior for $|\tilde{x}_2|$, $|\tilde{x}_3|$, $\sqrt{P22}$, $\sqrt{P33}$)
(On-Board Instrument)

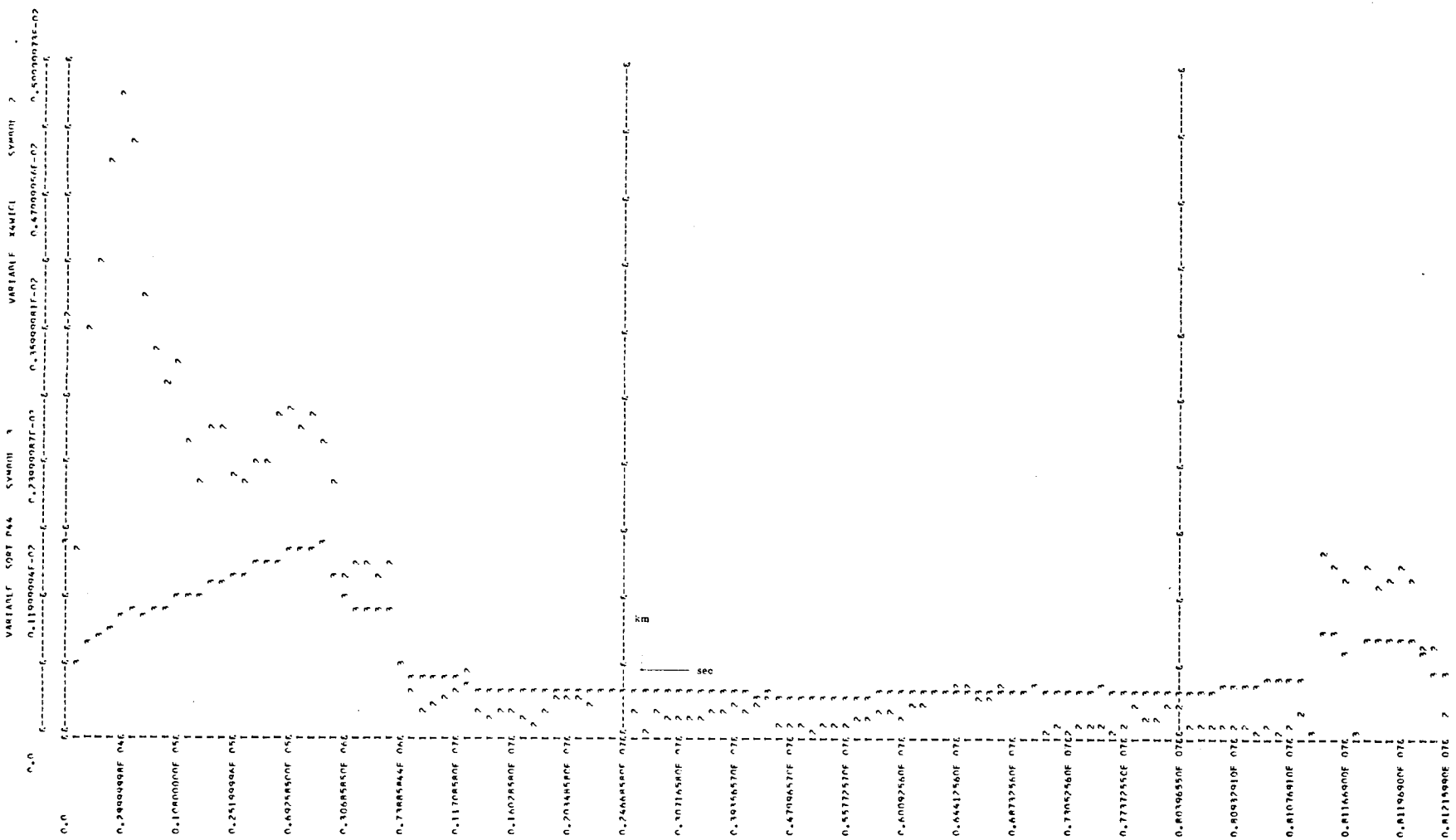

Figure B-18. $|\tilde{x}_4|$ and $\sqrt{P44}$ vs. Time—System Configuration TM25
(Similar Behavior for $|\tilde{x}_5|$, $|\tilde{x}_6|$, $\sqrt{P55}$, $\sqrt{P66}$)
(On-Board Instrument)

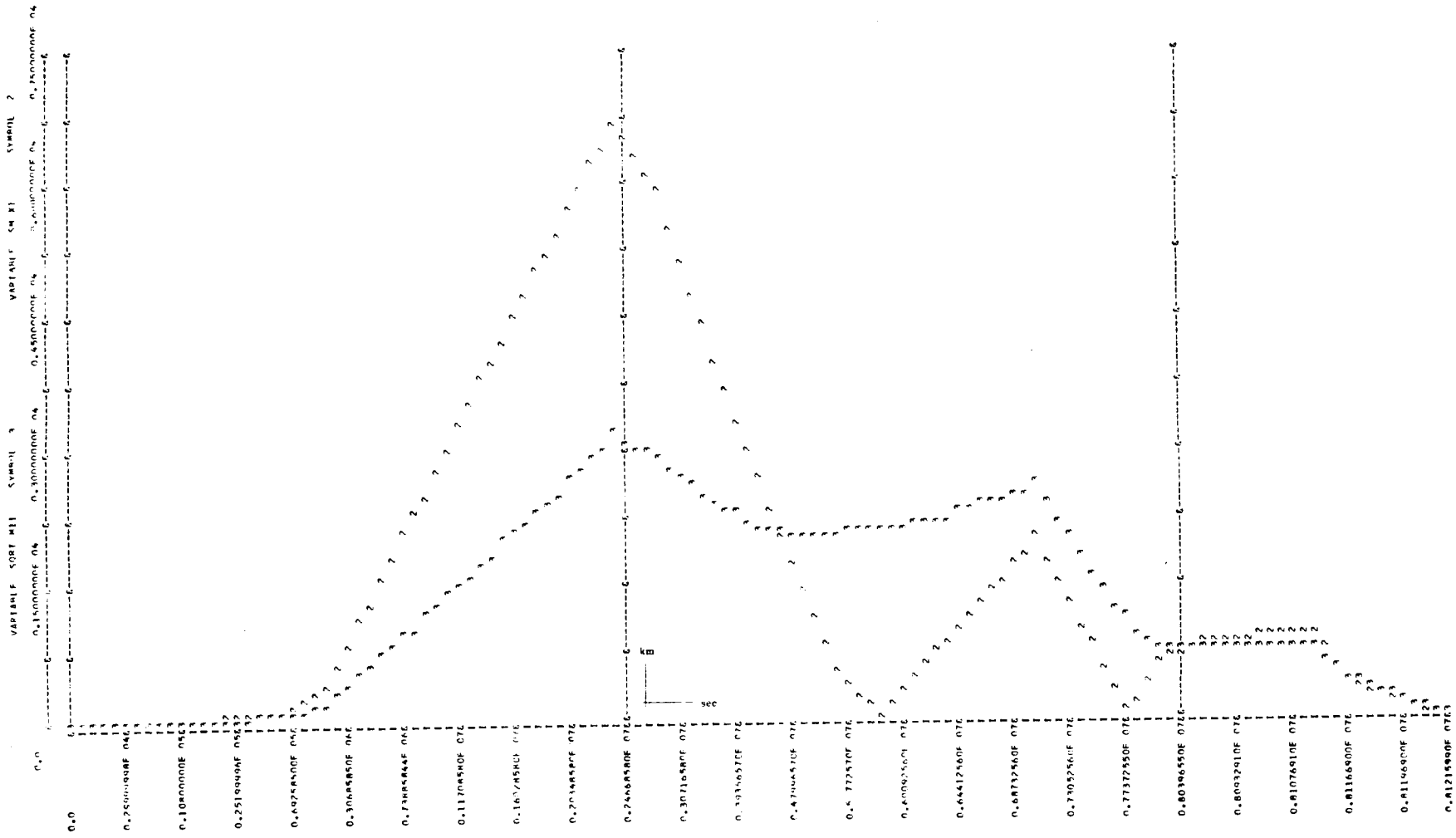

Figure B-19. . $|x_1|$ and $\sqrt{M11}$ vs. Time - System Configuration TM25
(Similar Behavior for $|x_2|$, $|x_3|$, $\sqrt{M22}$, $\sqrt{M33}$)
(On-Board Instrument)

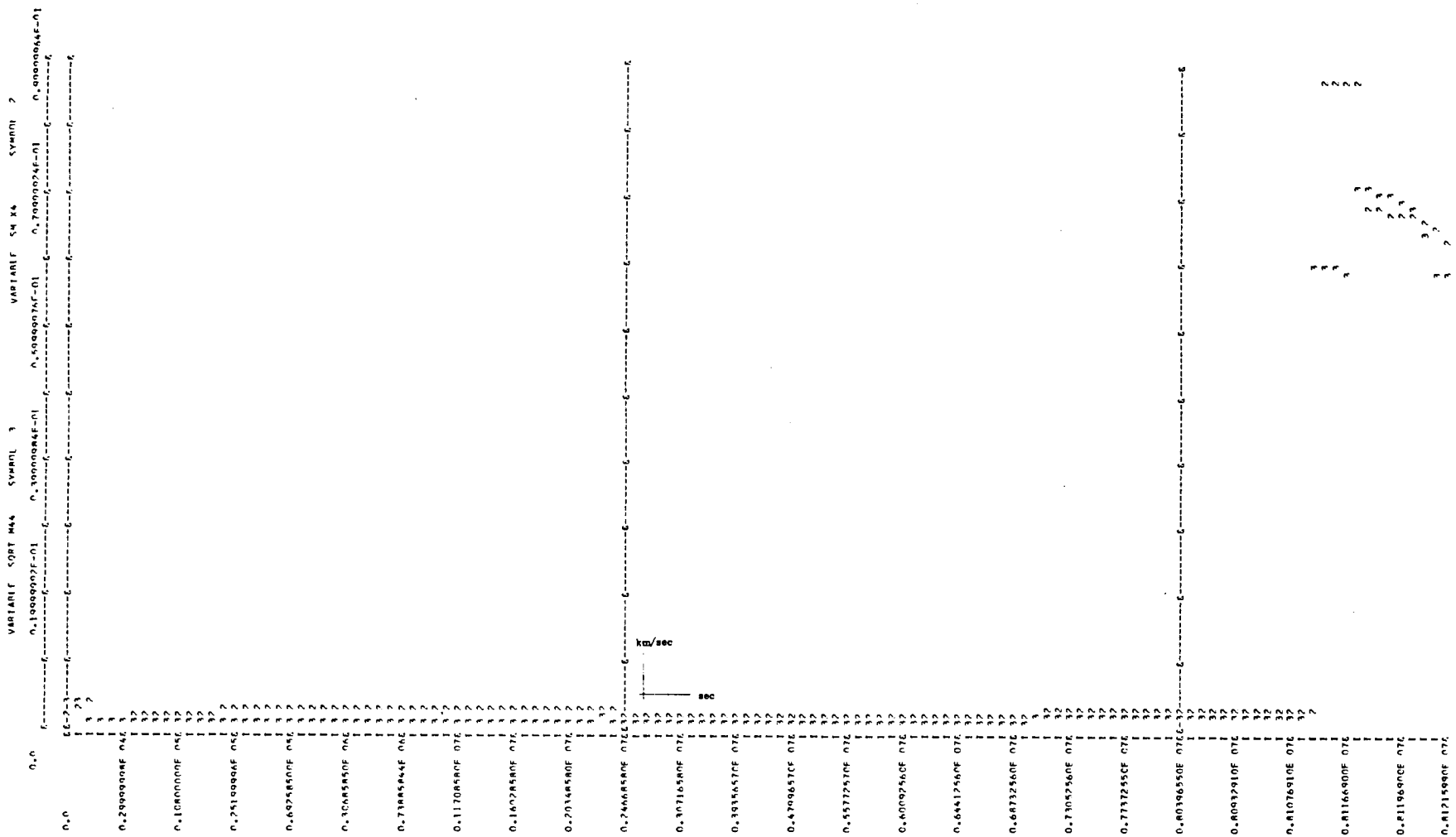

Figure B-20. $|x_4|$ and $\sqrt{M44}$ vs. Time—System Configuration TM25
(Similar Behavior for $|x_5|$, $|x_6|$, $\sqrt{M55}$, $\sqrt{M66}$)
(On-Board Instrument)

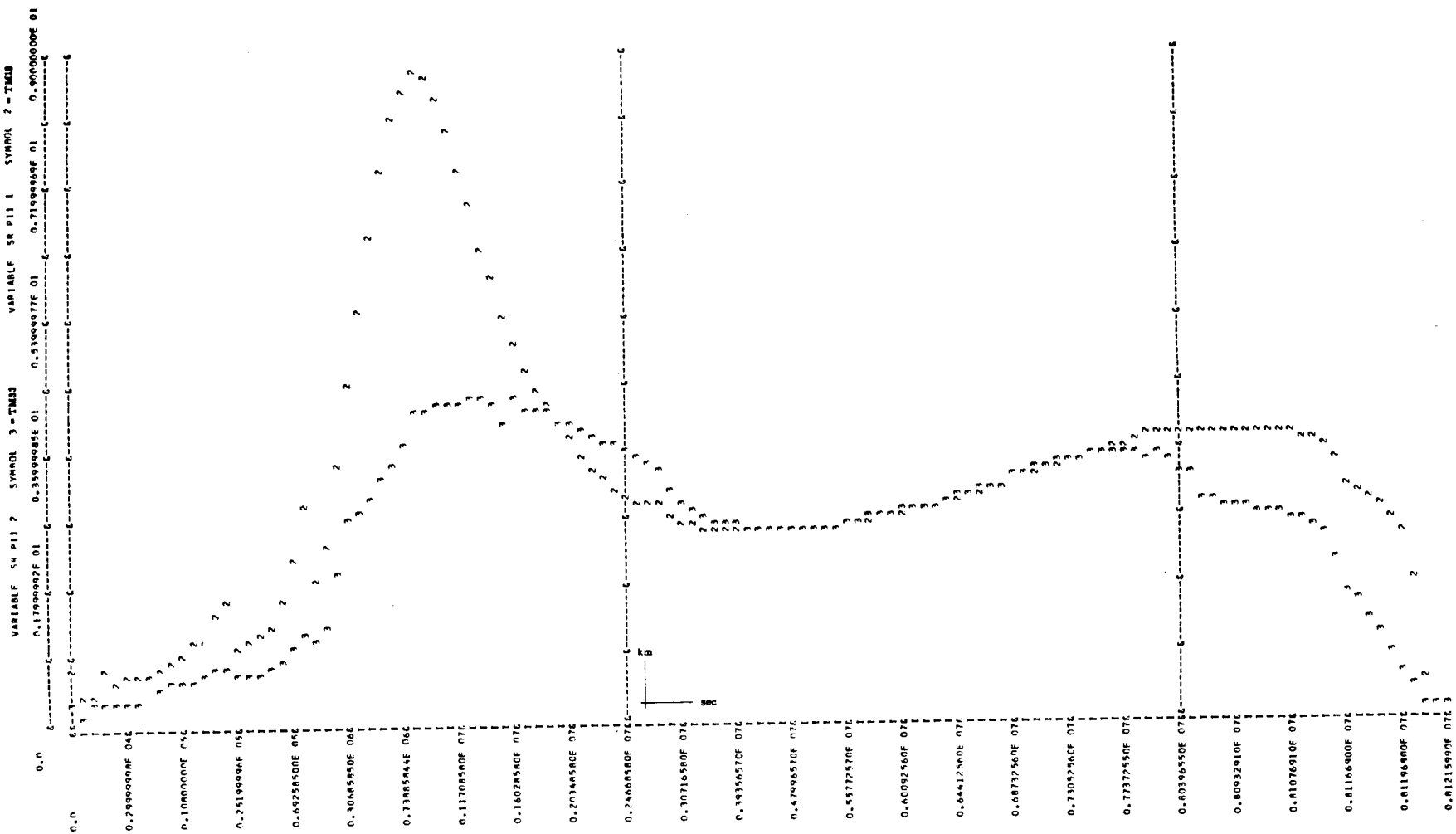

Figure B-21. Instrument Combination Effects
Upon the Statistics of the Error in the Position Estimate ($\sqrt{P11}$)

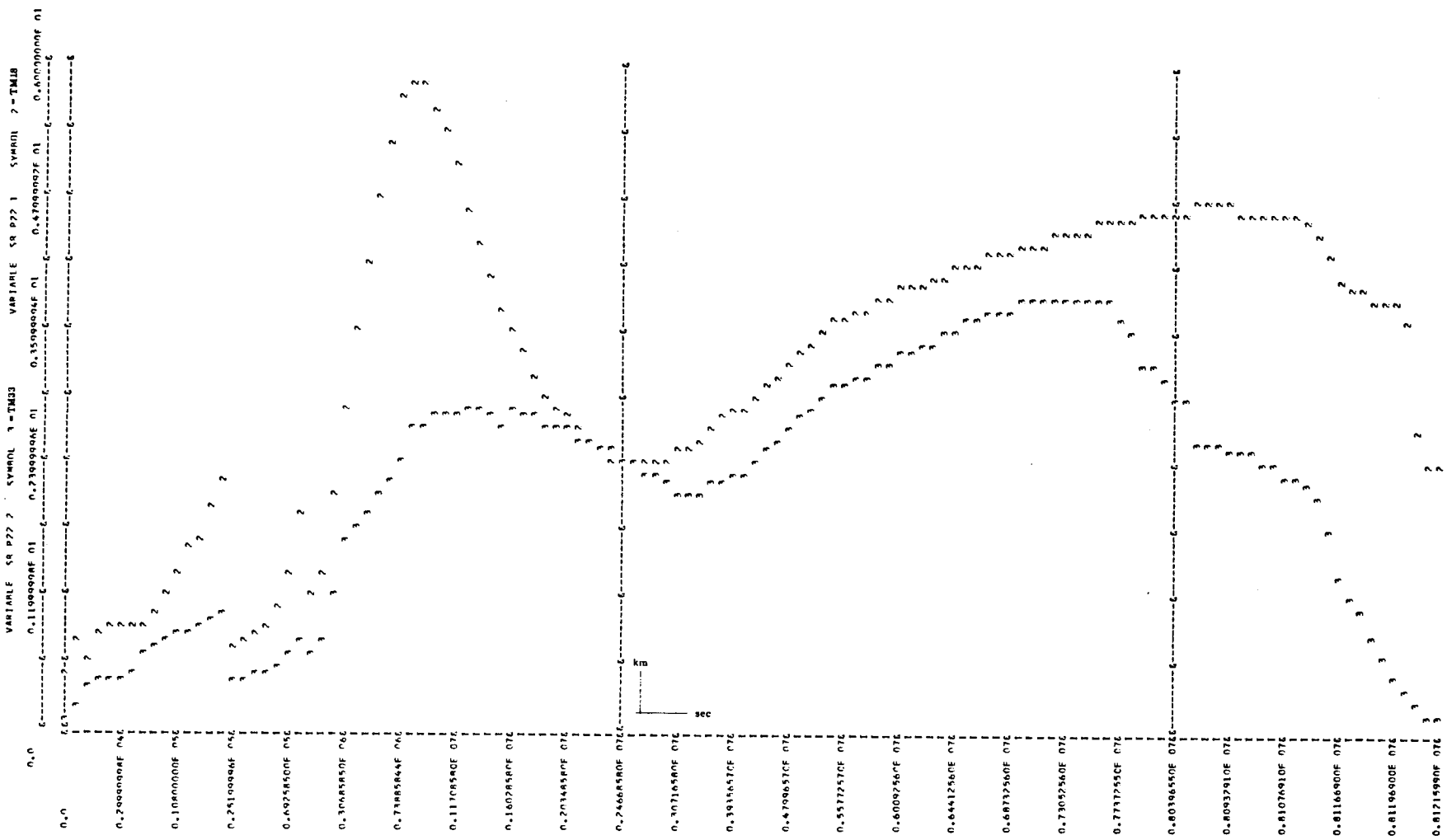

Figure B-22. Instrument Combination Effects
Upon the Statistics of the Error in the Position Estimate ($\sqrt{P22}$)

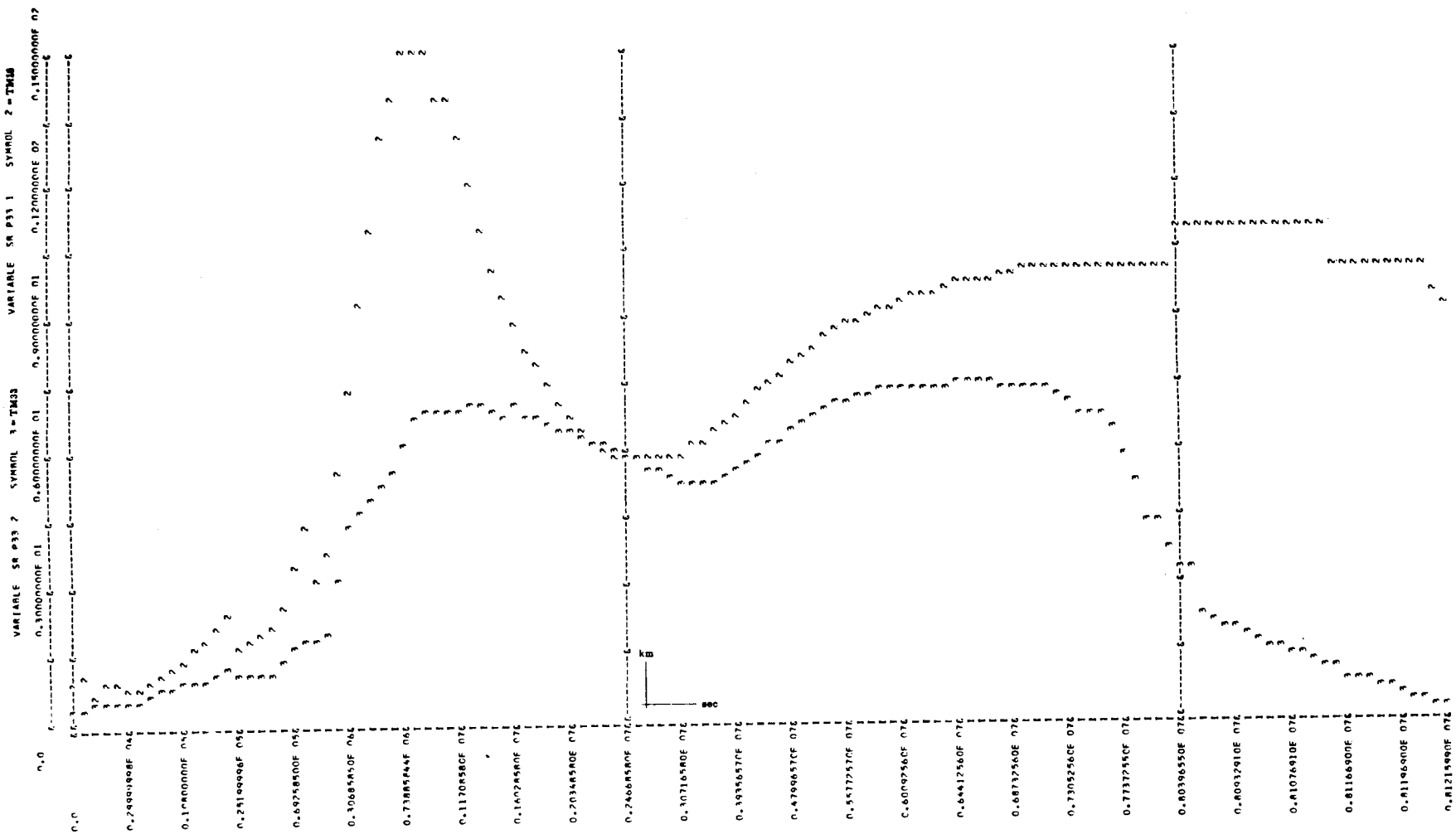

Figure B-23. Instrument Combination Effects
Upon the Statistics of the Error in the Position Estimate ($\sqrt{P33}$)

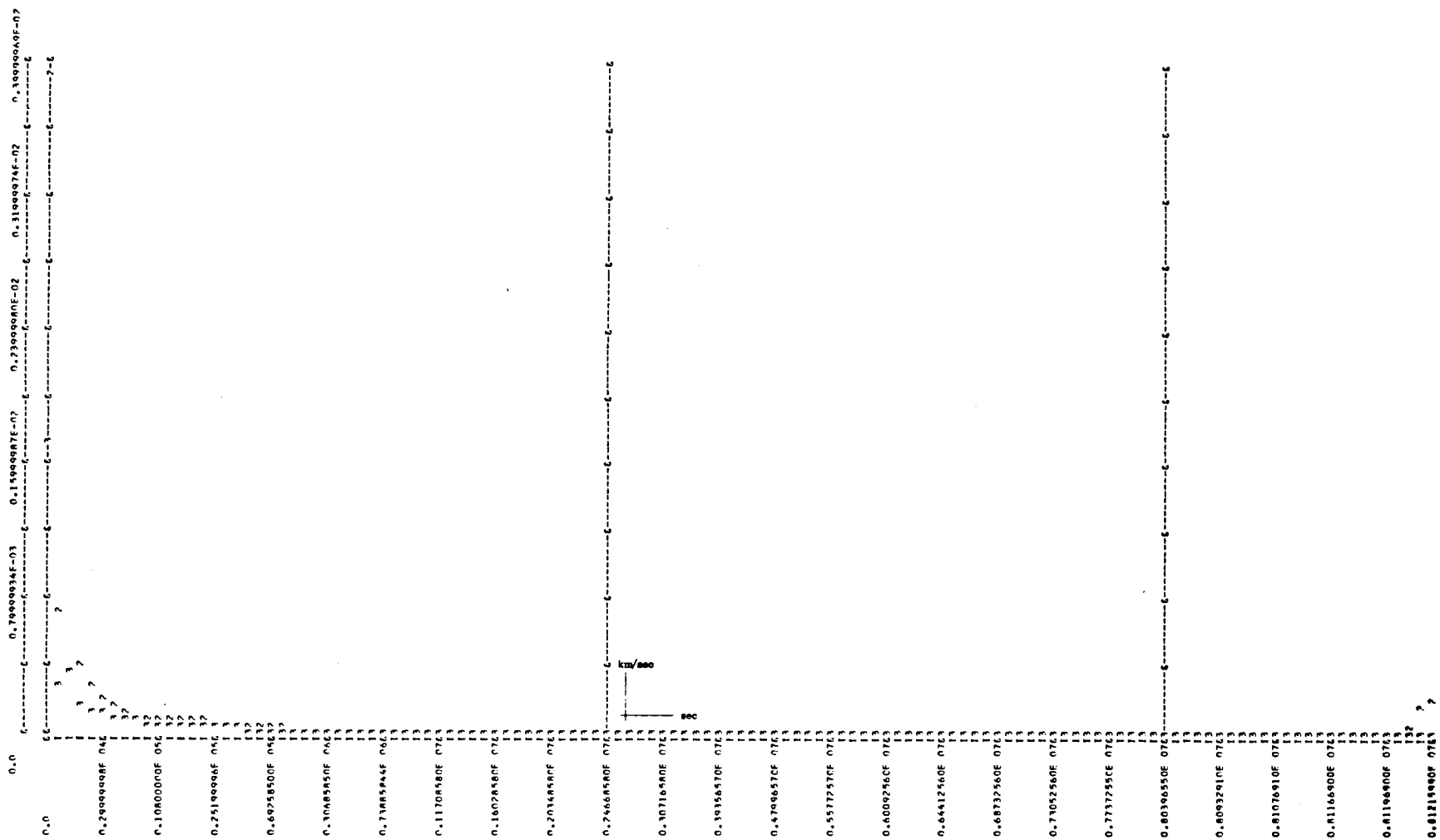

Figure B-24. Instrument Combination Effects
Upon the Statistics of the Error in the Velocity Estimate ($\sqrt{P44}$)
(Similar Behavior for $\sqrt{P55}$, $\sqrt{P66}$)

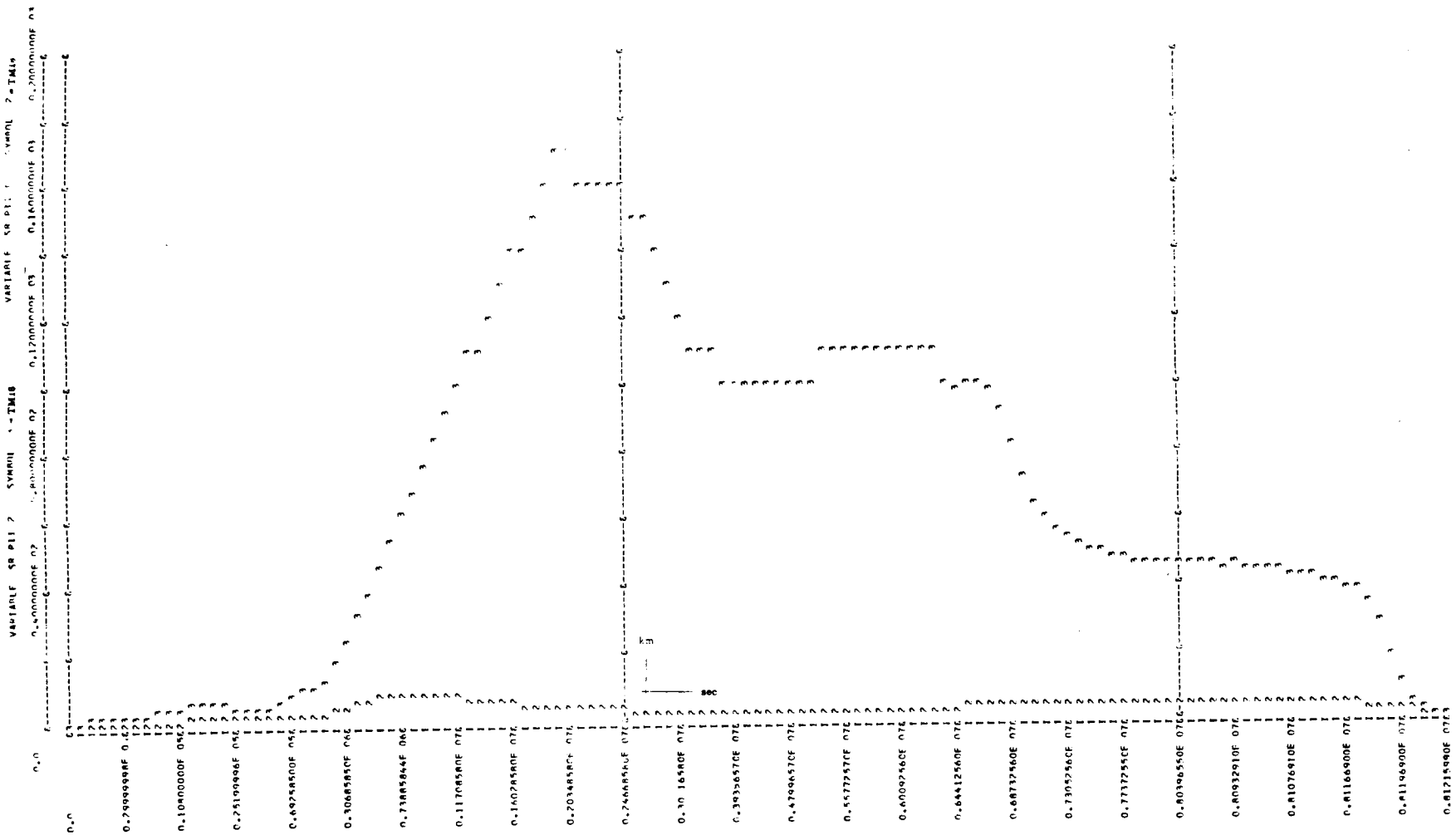

Figure B-25. Typical Ground Tracker Bias Influence
Upon the Statistics of the Error in Position Best Estimate ($\sqrt{P11}$)
(Similar Behavior for $\sqrt{P22}$, $\sqrt{P33}$)

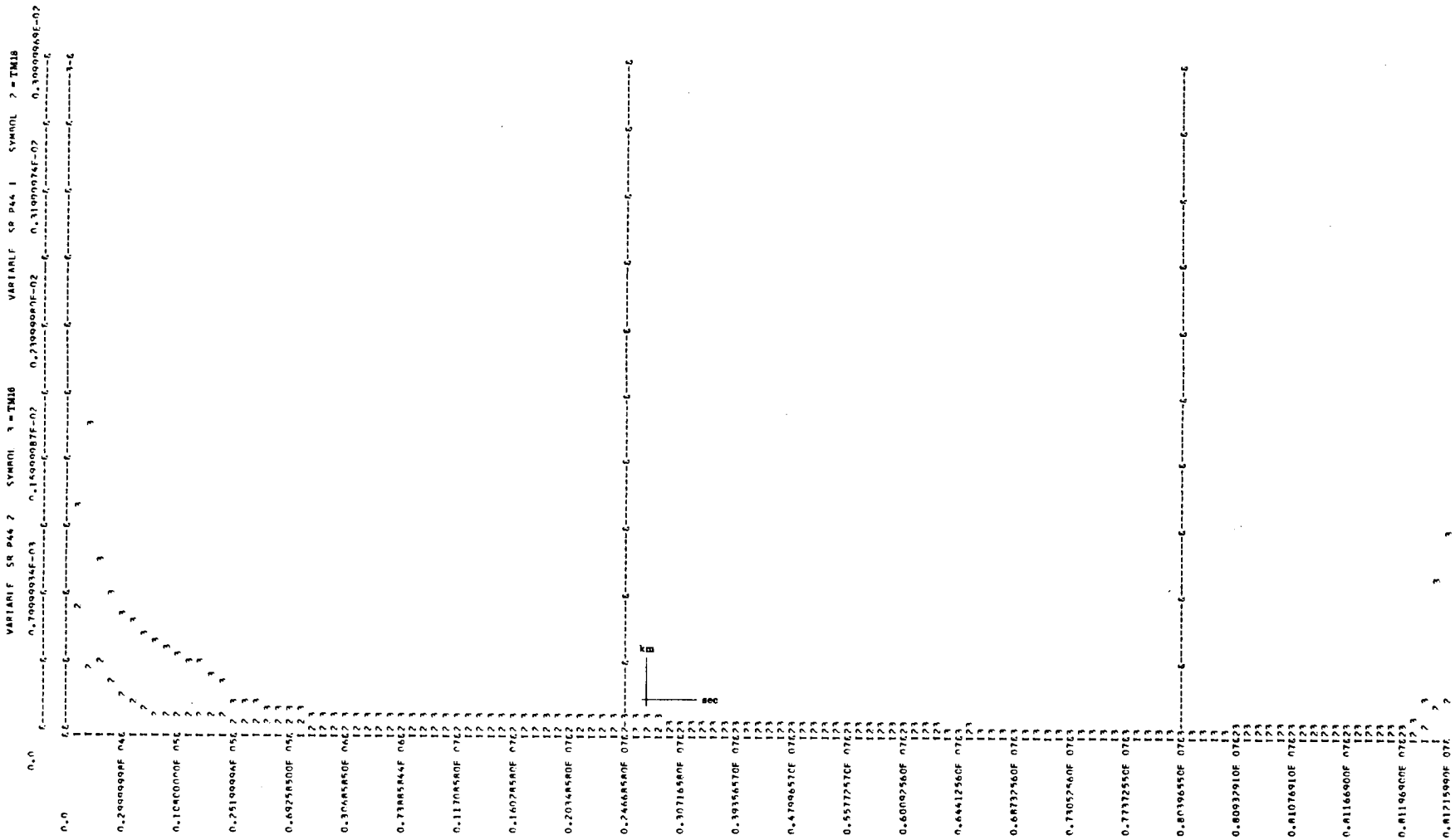

Figure B-26. Typical Ground Tracker Bias Influence
Upon the Statistics of the Error in Velocity Best Estimate ($\sqrt{P44}$)
(Similar Behavior for $\sqrt{P55}$, $\sqrt{P66}$)

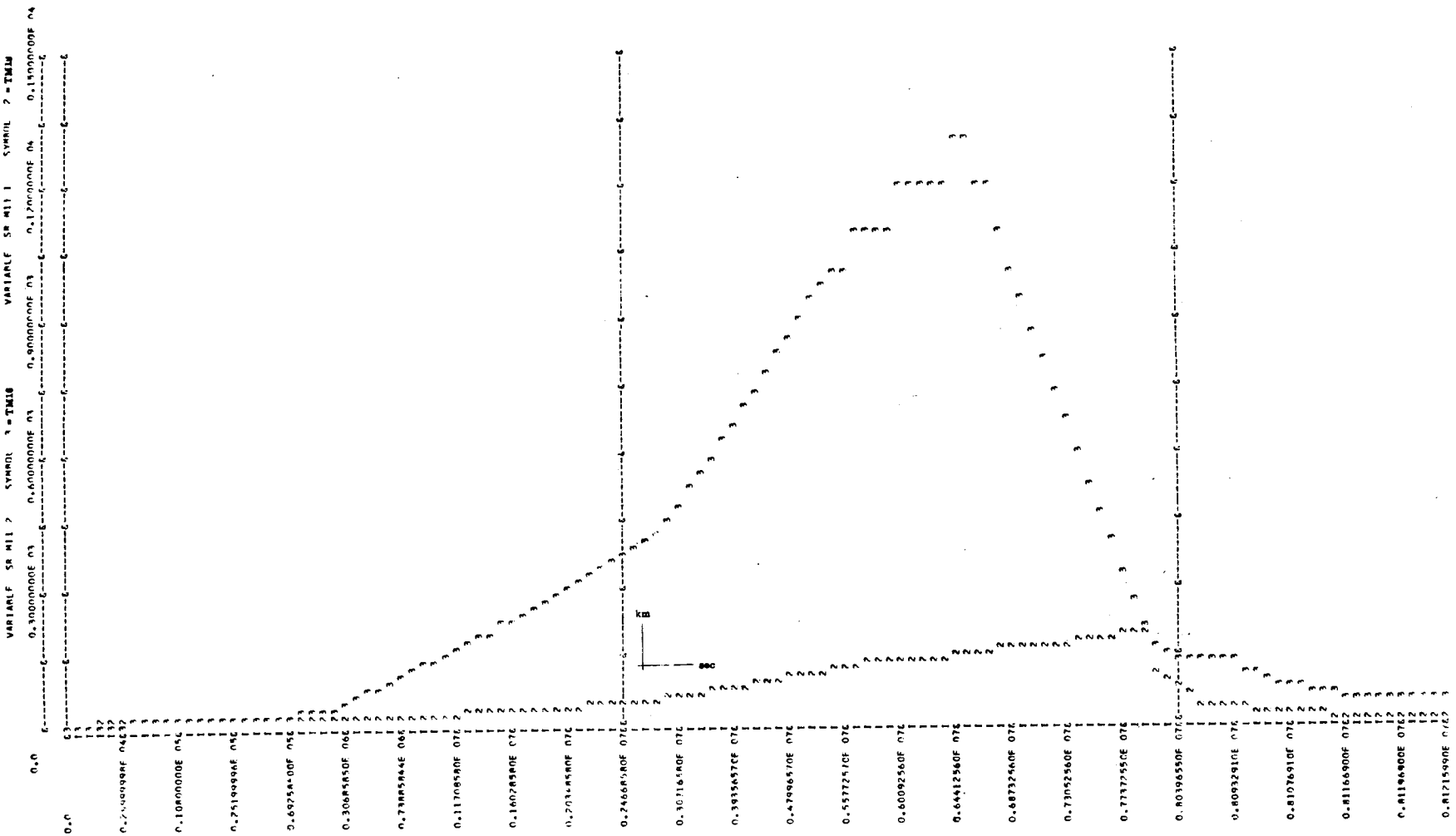

Figure B-27. Typical Ground Tracker Bias Influence
Upon the Statistics of the Actual Position Deviation ($\sqrt{M11}$)
(Similar Behavior for $\sqrt{M22}$, $\sqrt{M33}$)

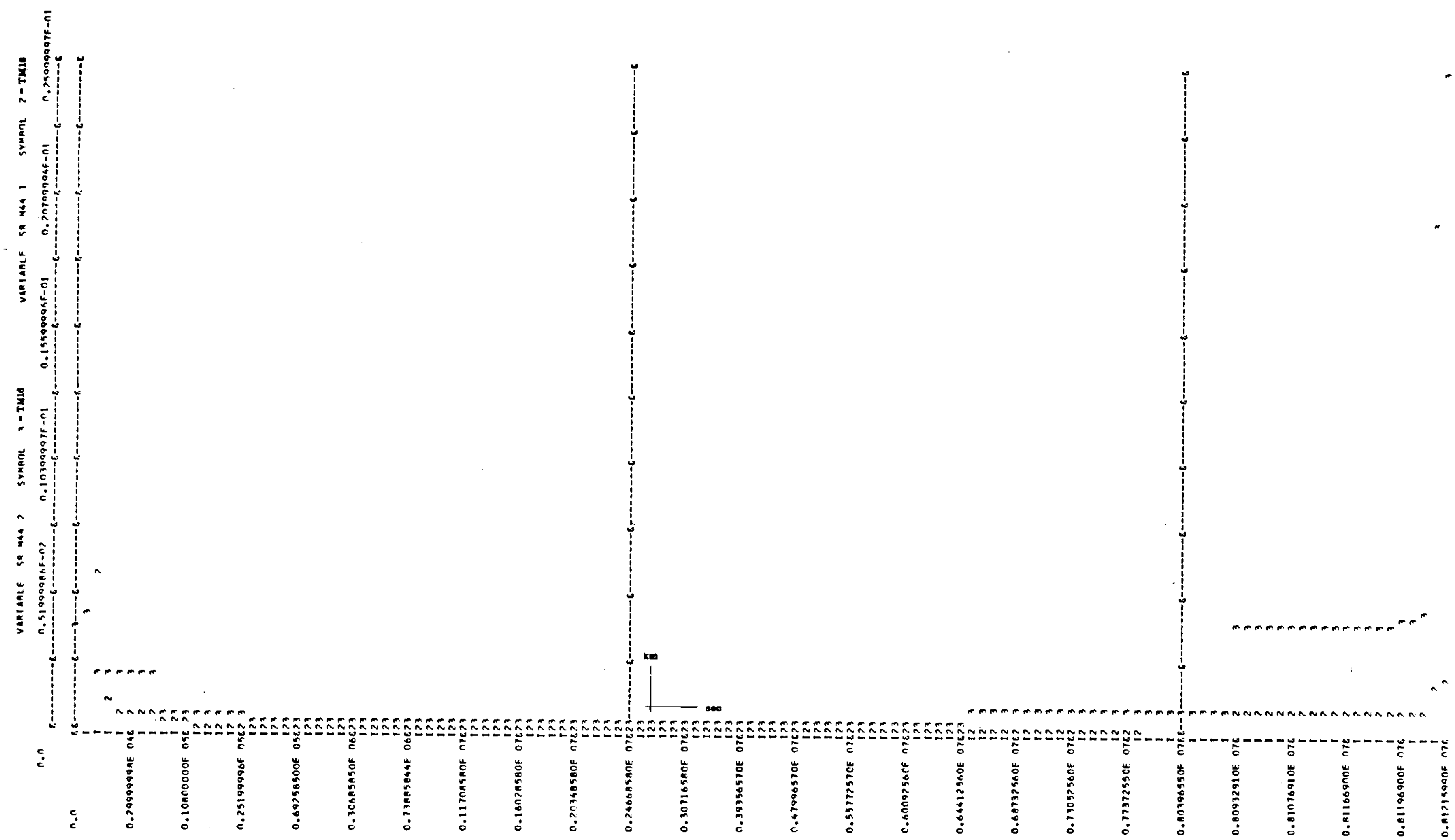

Figure B-28. Typical Ground Tracker Bias Influence Upon the Statistics of the Actual Velocity Deviation ($\sqrt{M44}$) (Similar Behavior for $\sqrt{M55}$, $\sqrt{M66}$)

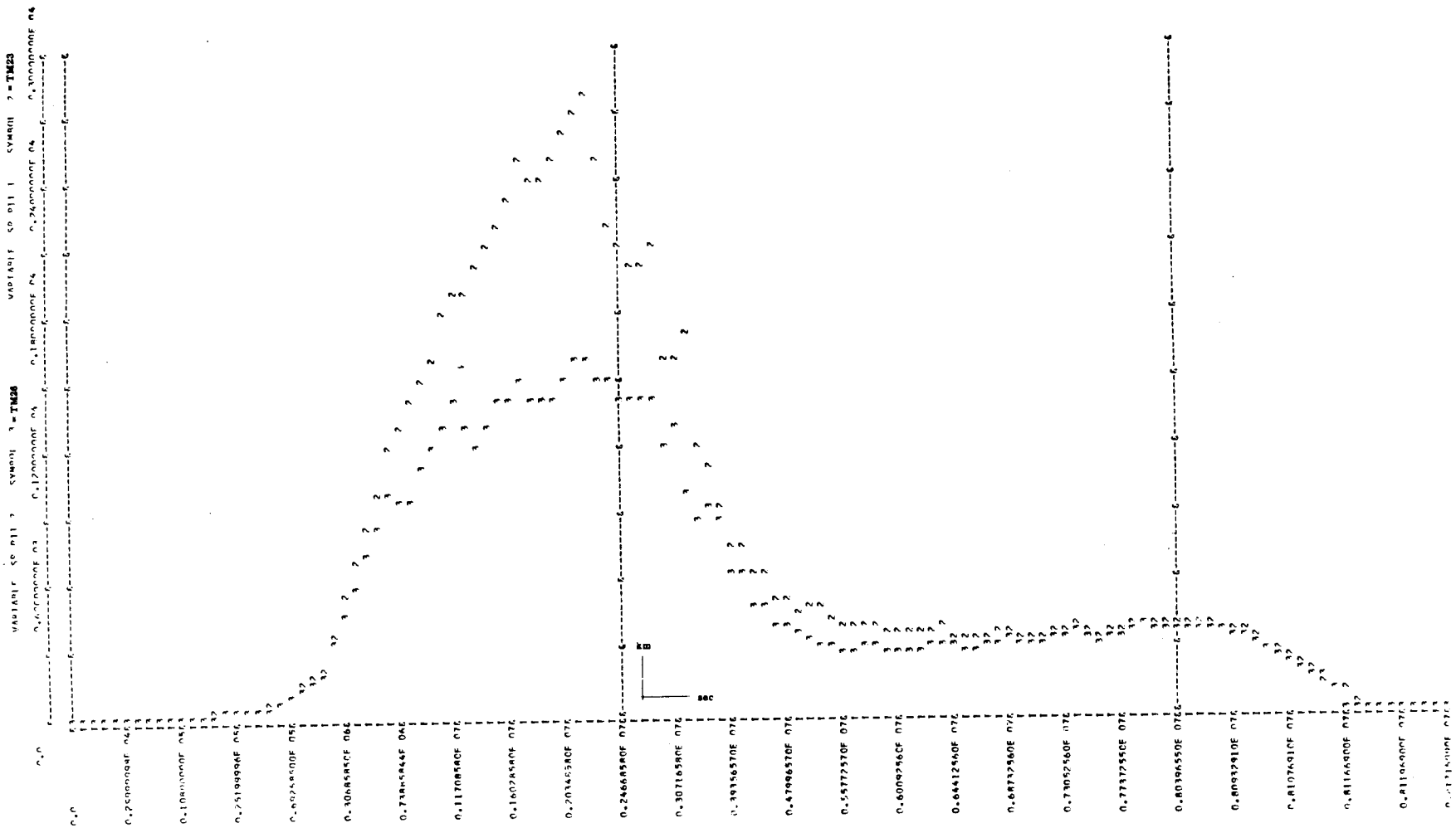

Figure B-29. Typical Horizon Sensor Bias Influence Upon the Statistics of the Error in Position Best Estimate ($\sqrt{P11}$)
(Similar Behavior for $\sqrt{P22}$, $\sqrt{P33}$)

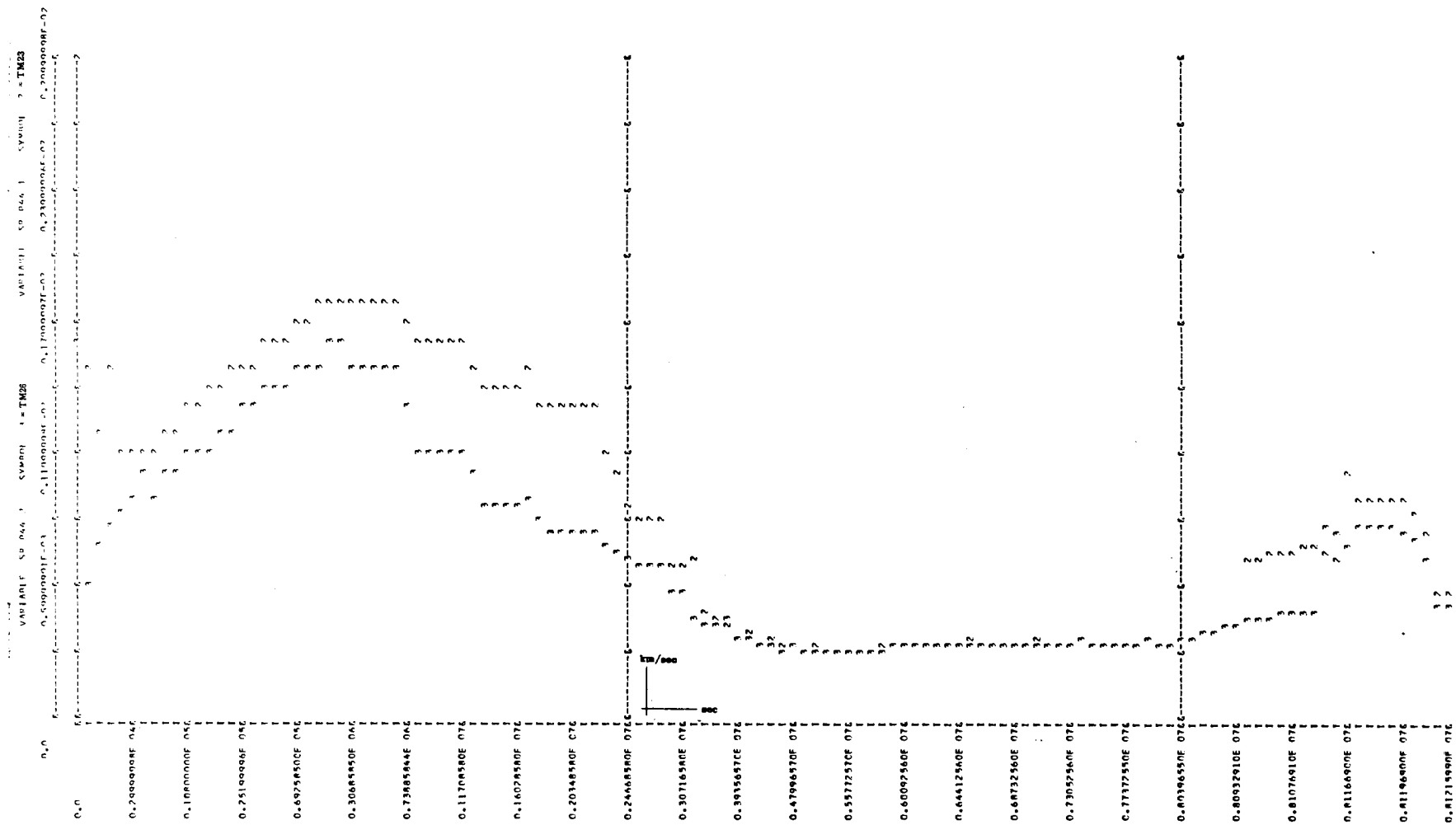

Figure B-30. Typical Horizon Sensor Bias Influence
Upon the Statistics of the Error in Velocity Best Estimate ($\sqrt{P44}$)
(Similar Behavior for $\sqrt{P55}$, $\sqrt{P66}$)

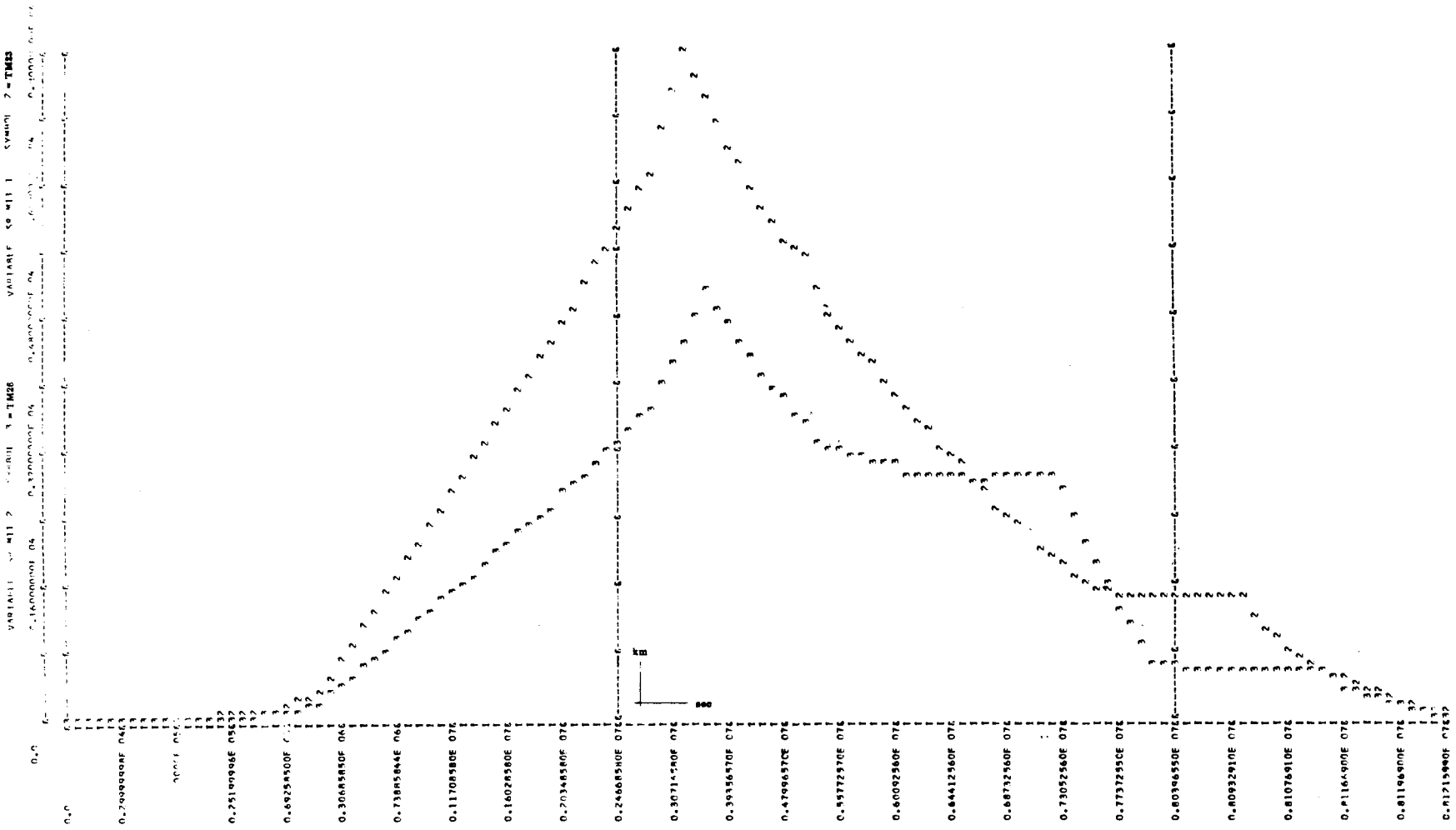

Figure B-31. Typical Horizon Sensor Bias Influence Upon the Statistics of the Actual Position Deviation ($\sqrt{M11}$) (Similar Behavior for $\sqrt{M22}$, $\sqrt{M33}$)

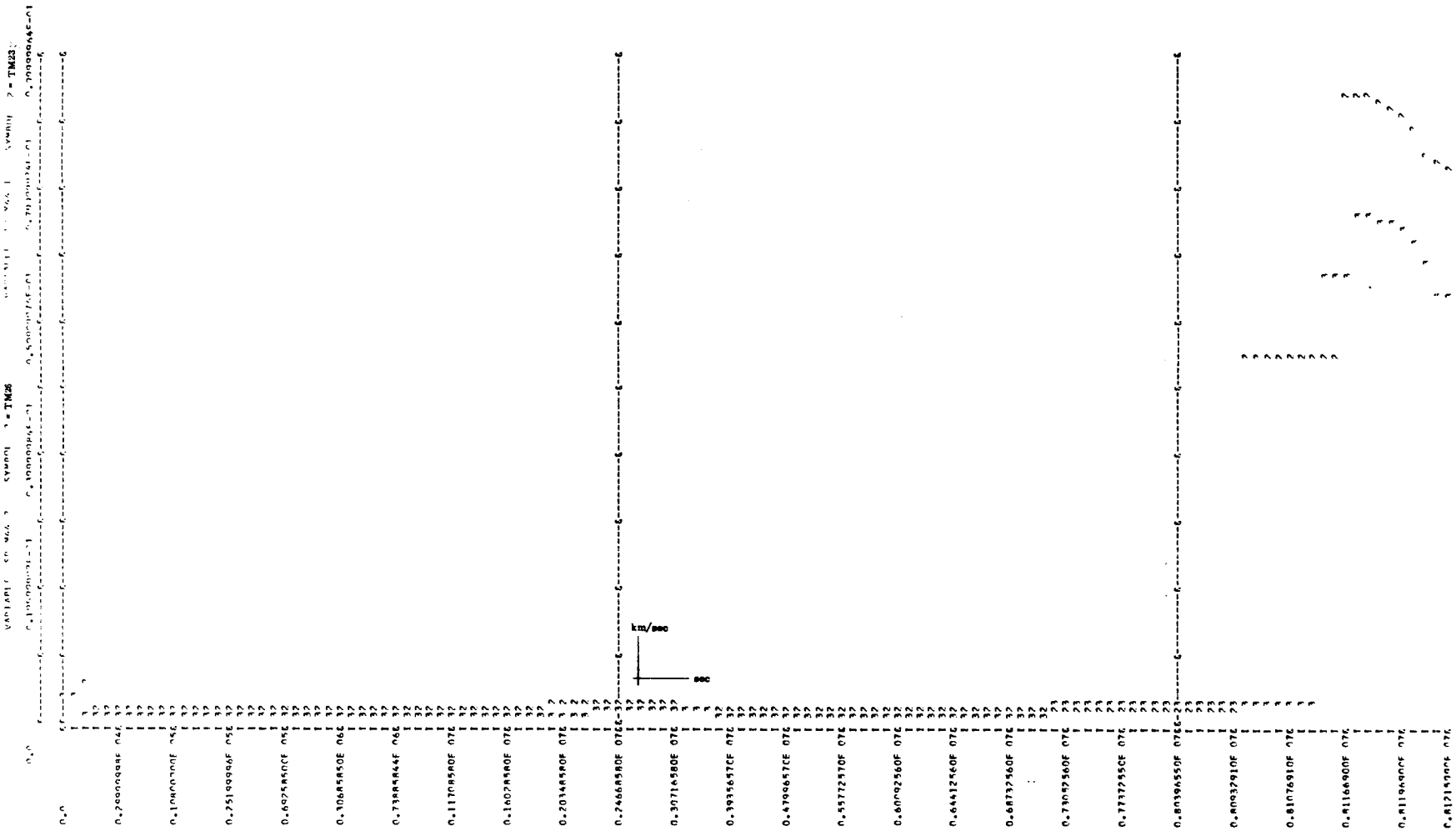

Figure B-32. Typical Horizon Sensor Bias Influence Upon the Statistics of the Actual Velocity Deviation ($\sqrt{M44}$) (Similar Behavior for $\sqrt{M55}$, $\sqrt{M66}$)

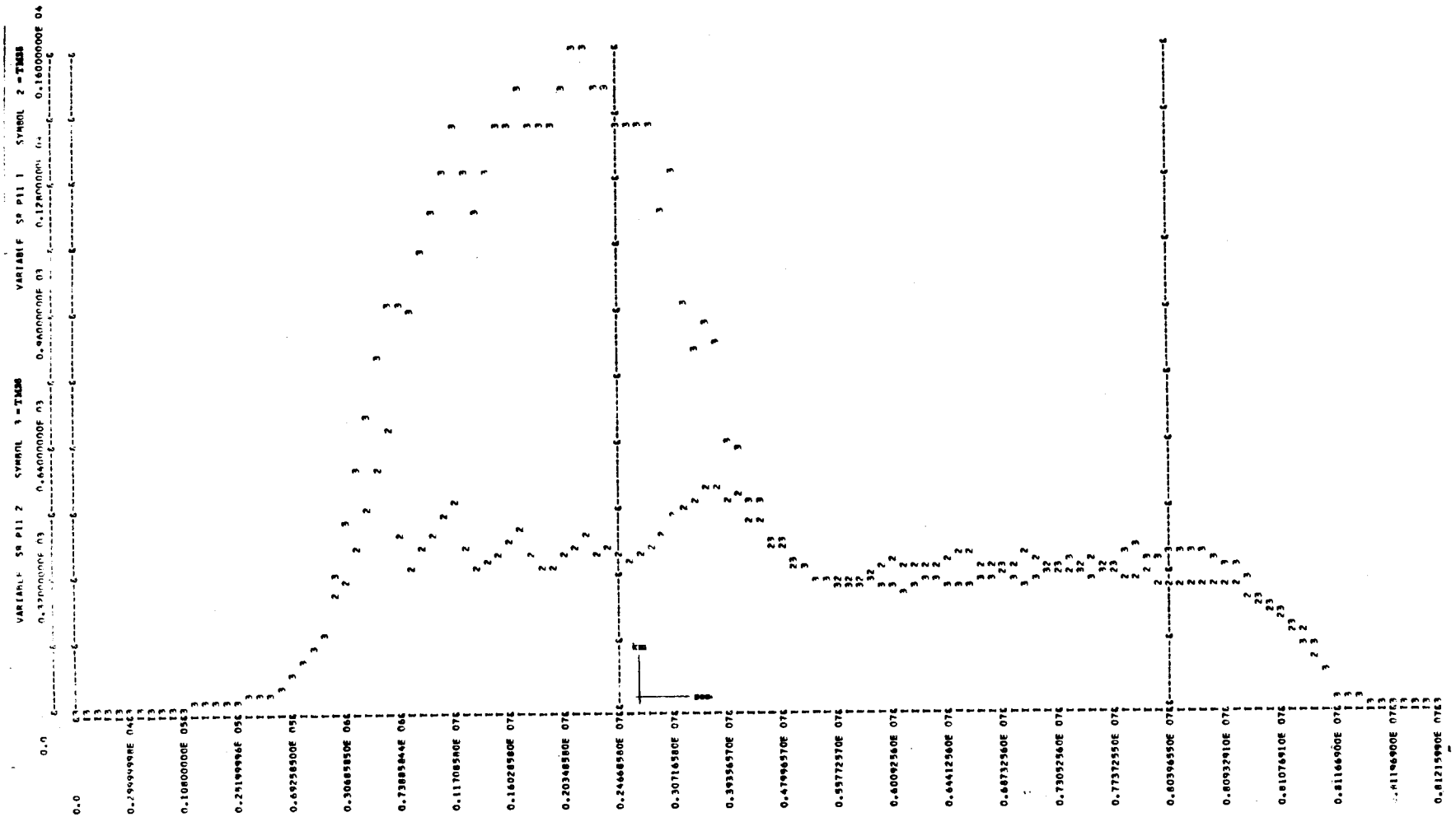

Figure B-33. Typical Reference Body Influence
Upon the Statistics of the Error in the Position Estimate ($\sqrt{P11}$)
(Similar Behavior for $\sqrt{P22}$, $\sqrt{P33}$)

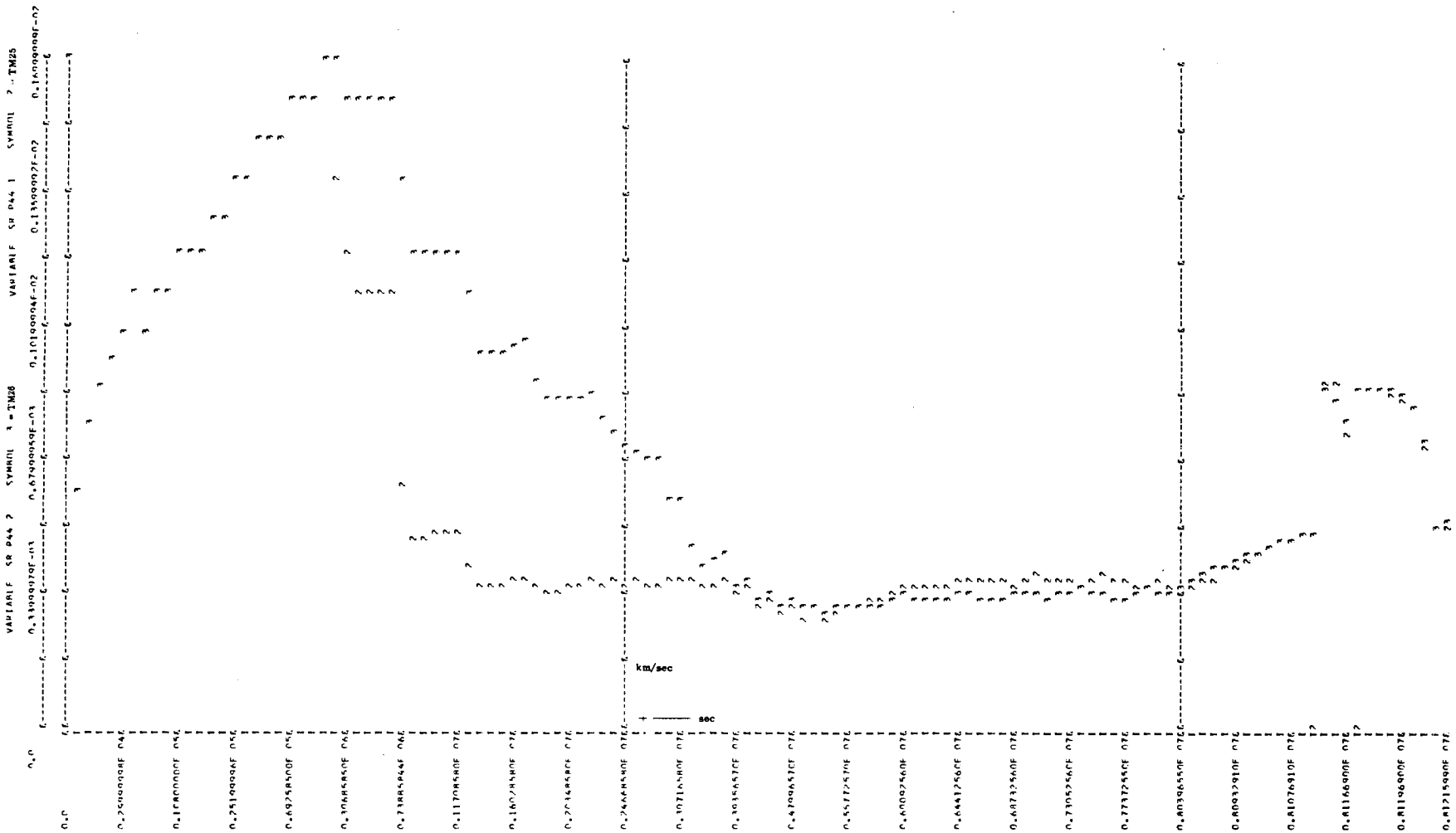

Figure B-34. Typical Reference Body Influence
Upon the Statistics of the Error in the Velocity Estimate ($\sqrt{P44}$)
(Similar Behavior for $\sqrt{P55}$, $\sqrt{P66}$)

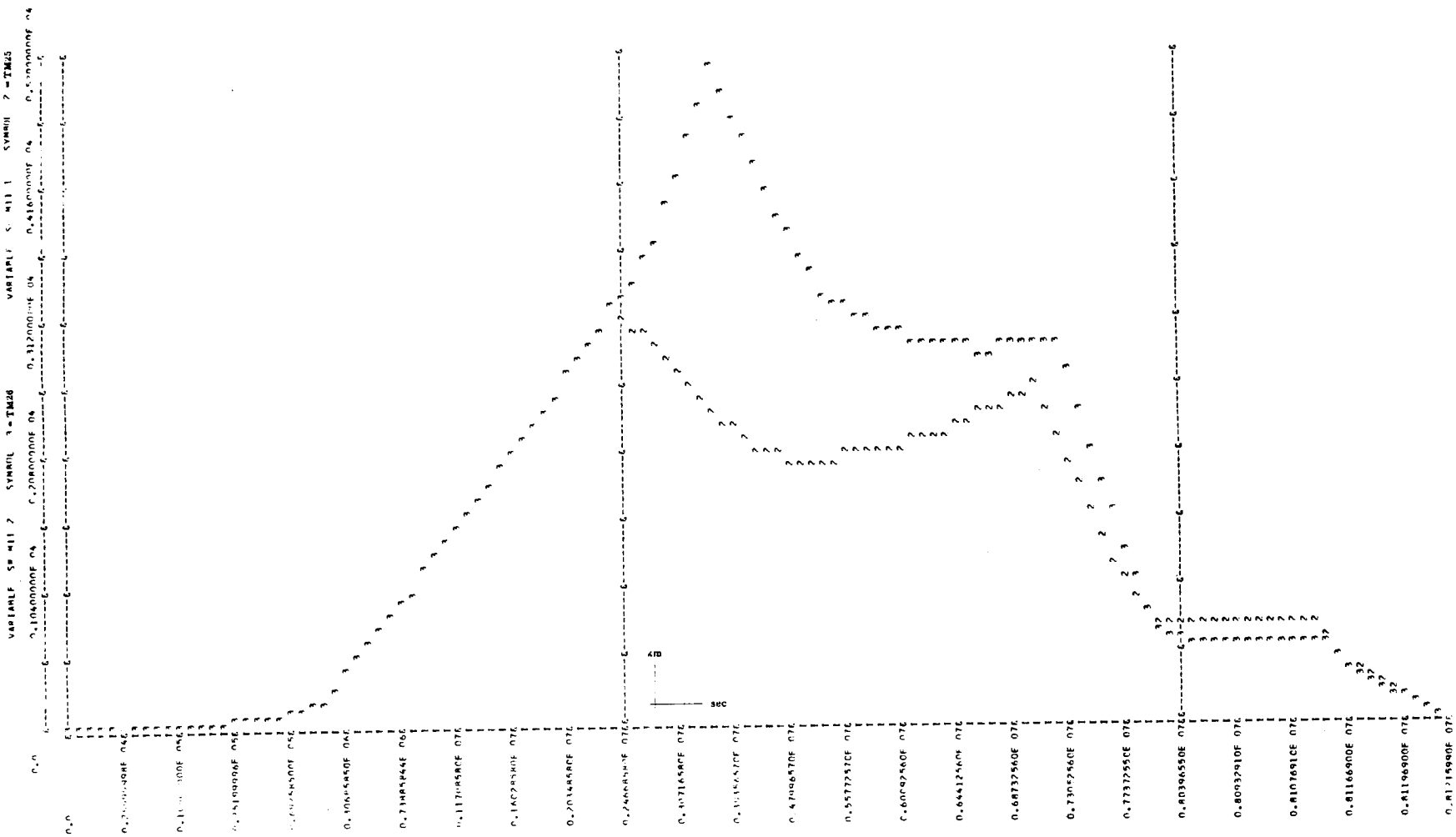

Figure B-35. Typical Reference Body Influence
Upon the Statistics of the Actual Position Deviation ($\sqrt{M11}$)
(Similar Behavior for $\sqrt{M22}$, $\sqrt{M33}$)

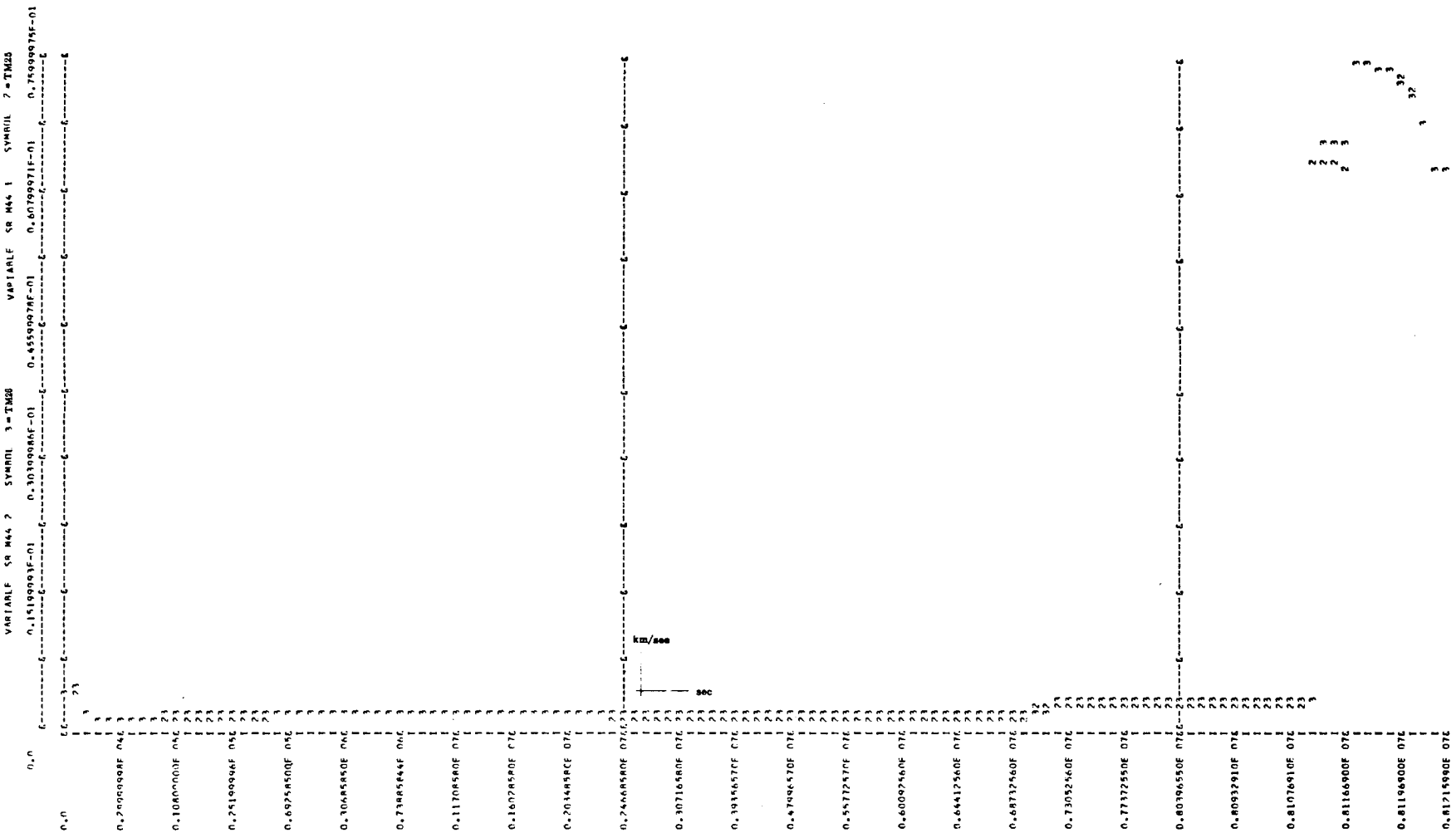

Figure B-36. Typical Reference Body Influence
Upon the Statistics of the Actual Velocity Deviation ($\sqrt{M44}$)
(Similar Behavior for $\sqrt{M55}$, $\sqrt{M66}$)

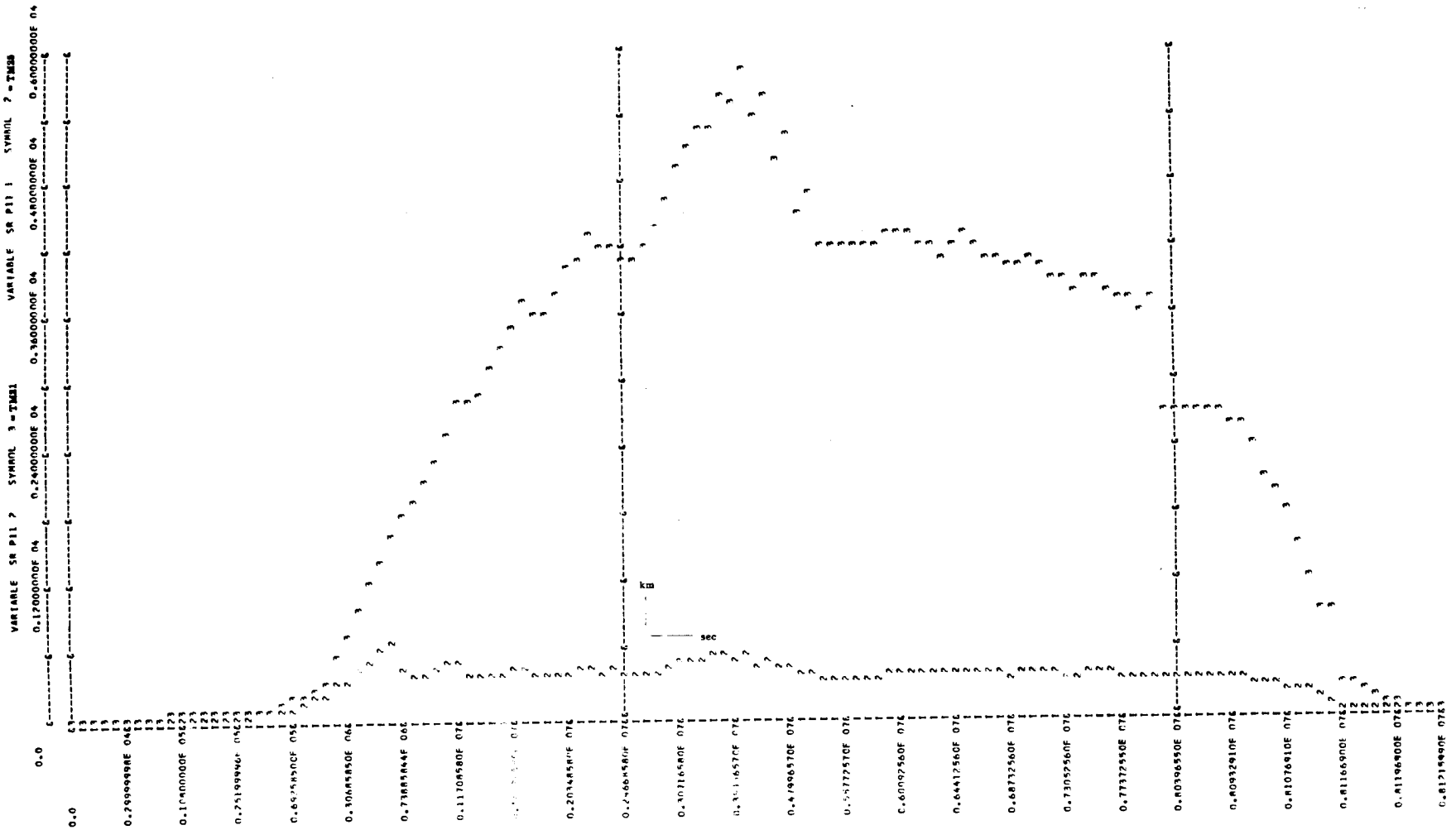

Figure B-37. Horizon Sensor Instrument Accuracy Effects Upon the Statistics of the Error in Position Estimate ($\sqrt{P11}$) (Similar Behavior for $\sqrt{P22}$, $\sqrt{P33}$)

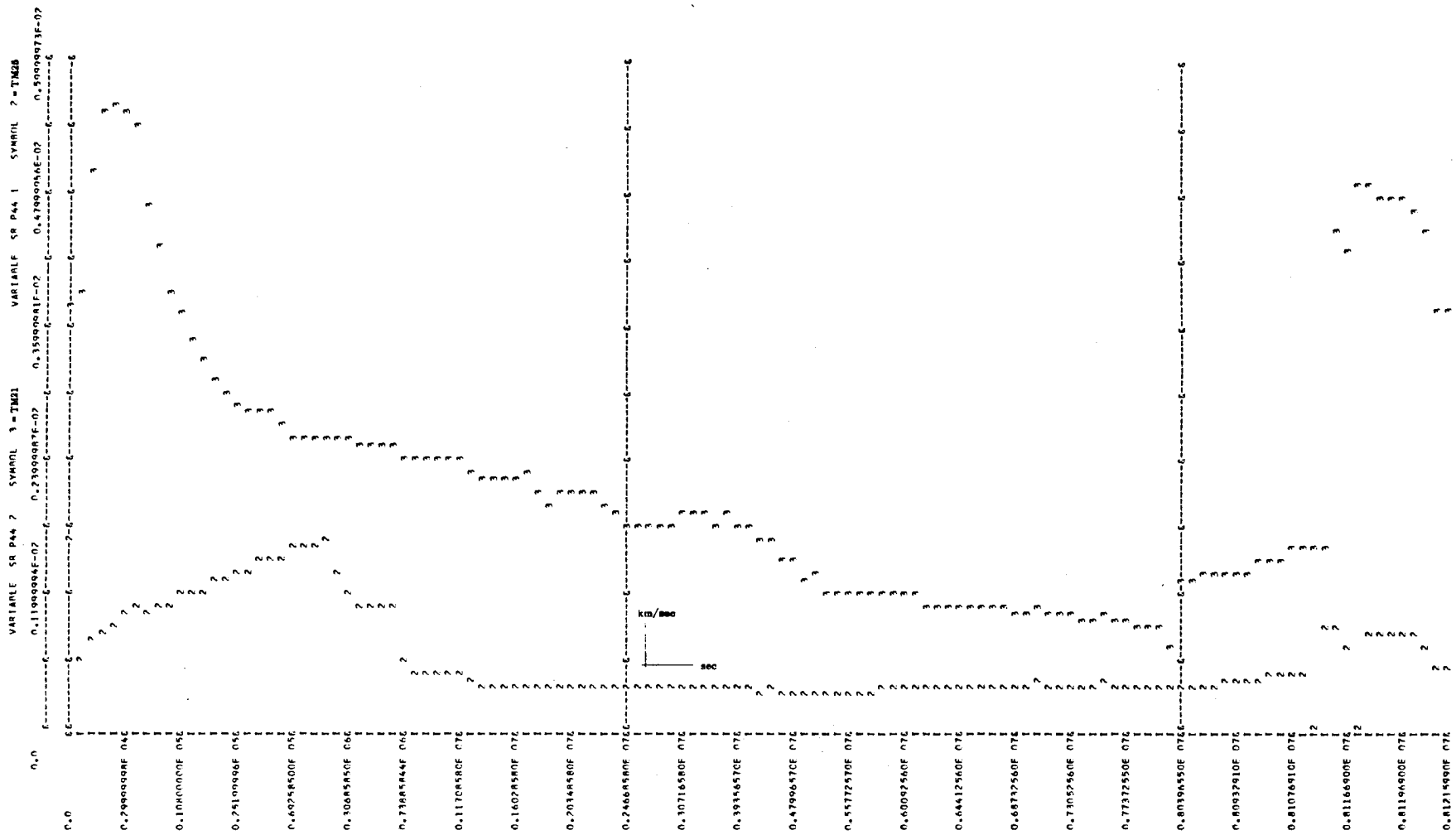

Figure B-38. Horizon Sensor Instrument Accuracy Effects Upon the Statistics of the Error in Velocity Estimate ($\sqrt{P44}$) (Similar Behavior for $\sqrt{P55}$, $\sqrt{P66}$)

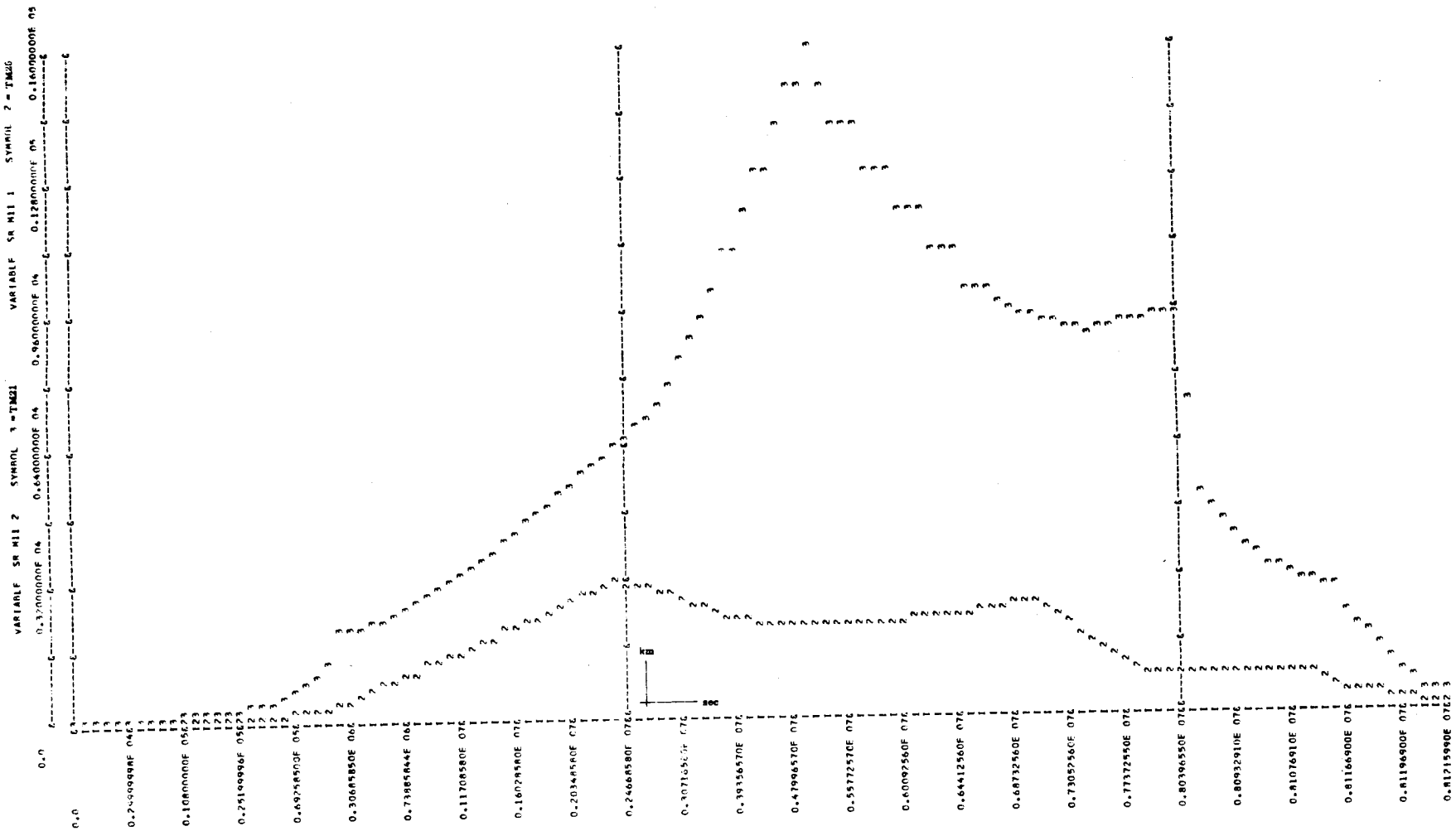

Figure B-39. Horizon Sensor Instrument Accuracy Effects Upon the Statistics of the Actual Position Deviation ($\sqrt{M11}$)
(Similar Behavior for $\sqrt{M22}$, $\sqrt{M33}$)

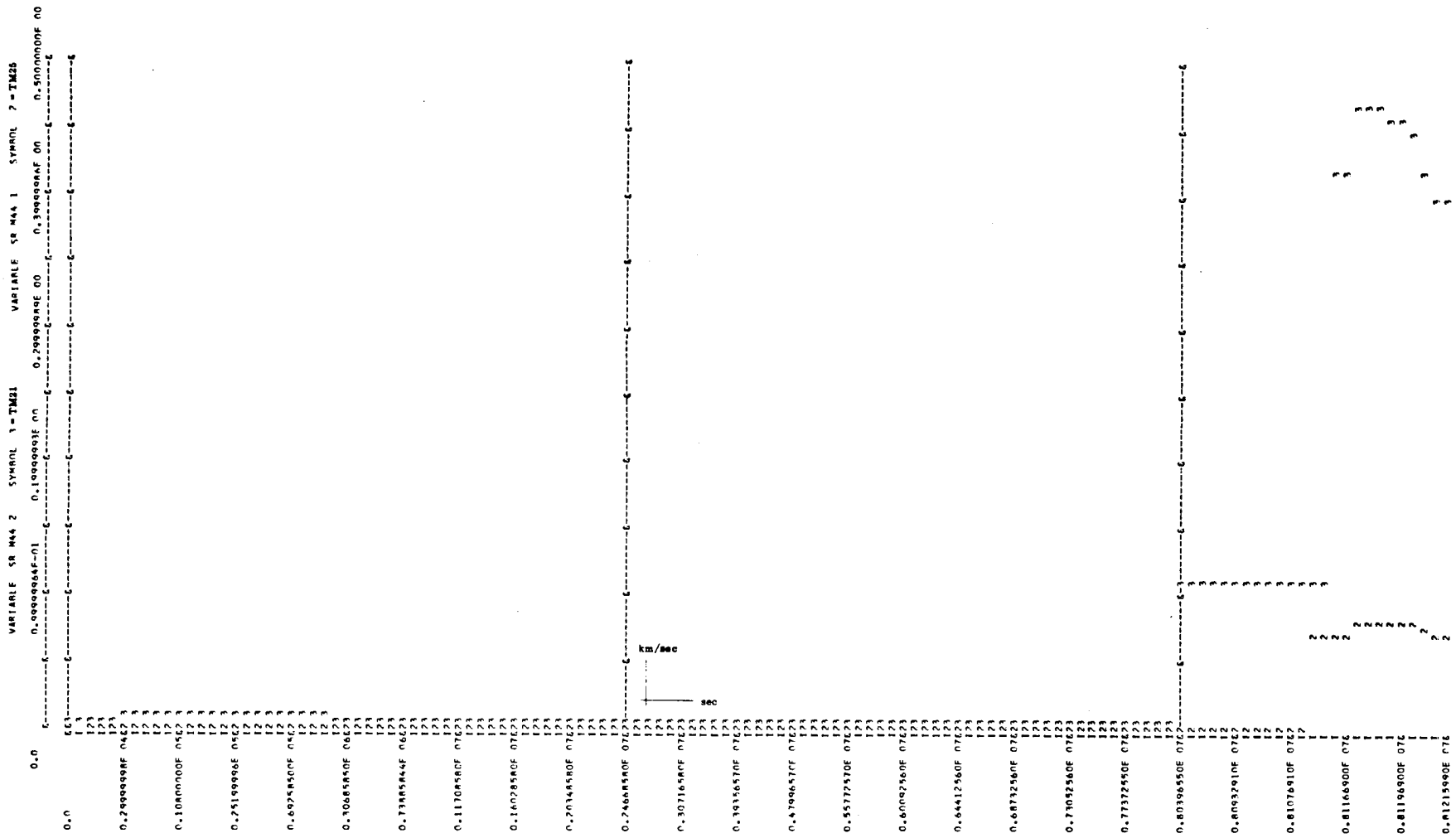

Figure B-40. Horizon Sensor Instrument Accuracy Effects Upon the Statistics of the Actual Velocity Deviation ($\sqrt{M44}$)
(Similar Behavior for $\sqrt{M55}$, $\sqrt{M66}$)

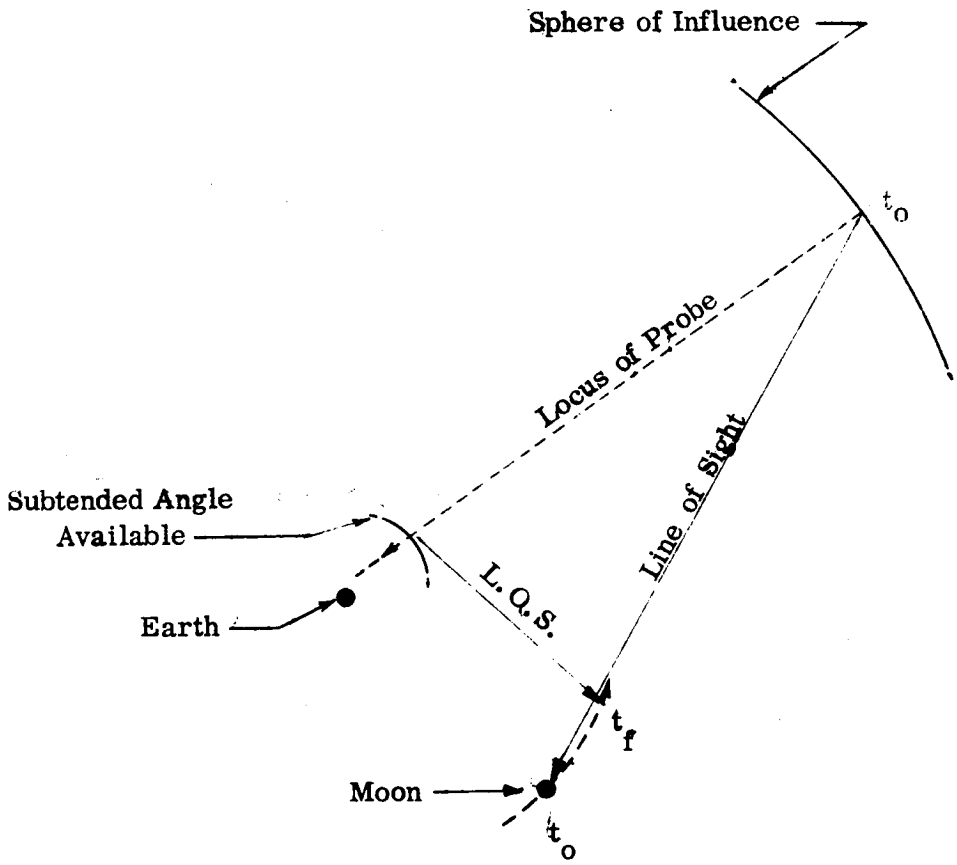

Figure B-41. Locus of Moon, Earth, and Probe for VI. 3. 3

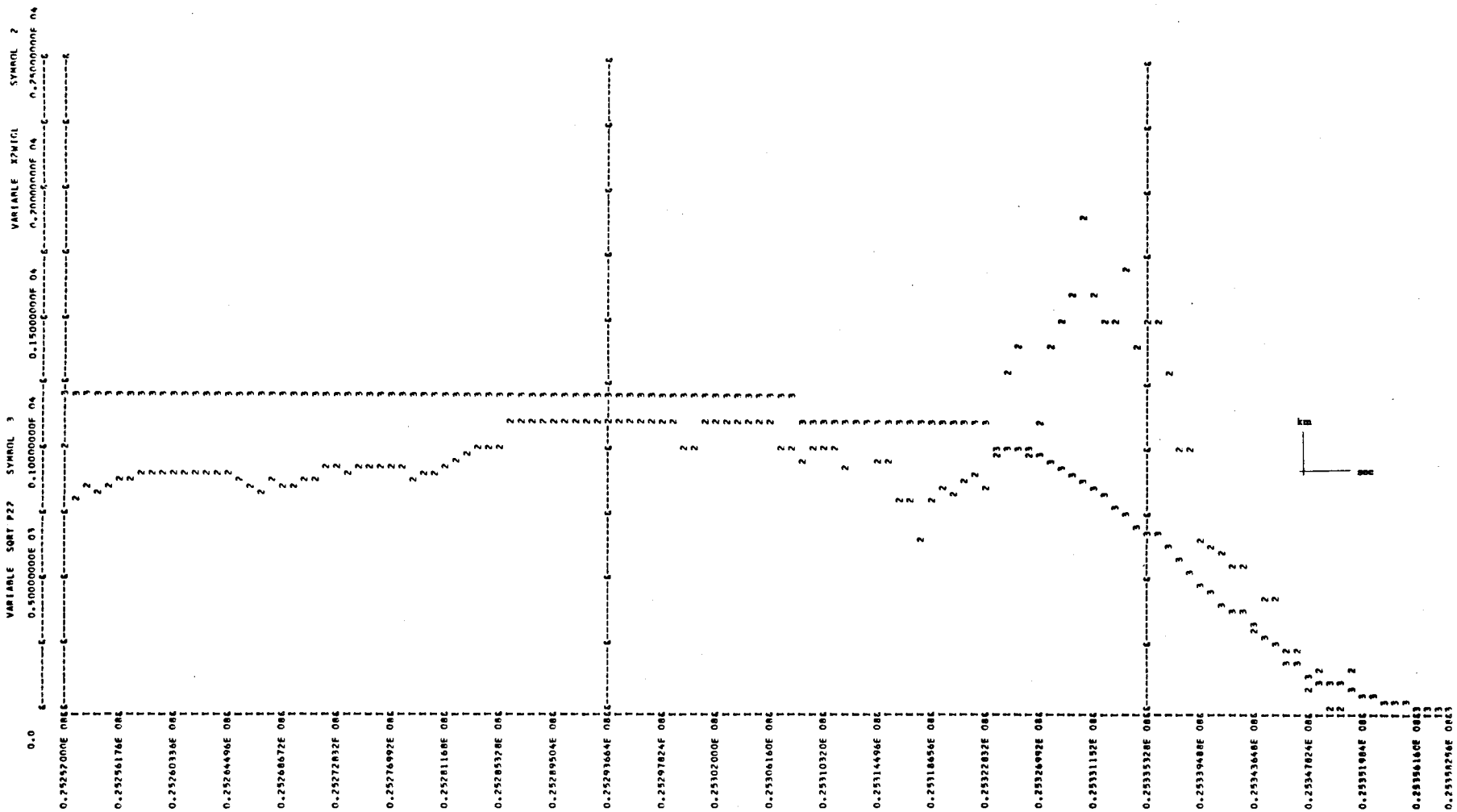

Figure B-42. Statistics from VI. 3. 3 When Moon Not Used

(Instrument H21)

Figure B-43. Statistics When Moon is Used (Instrument H21)

Figure B-44. Statistics When Moon is Not Used (Instrument H40)

Figure B-45. Statistics When Moon is Used (Instrument H40)

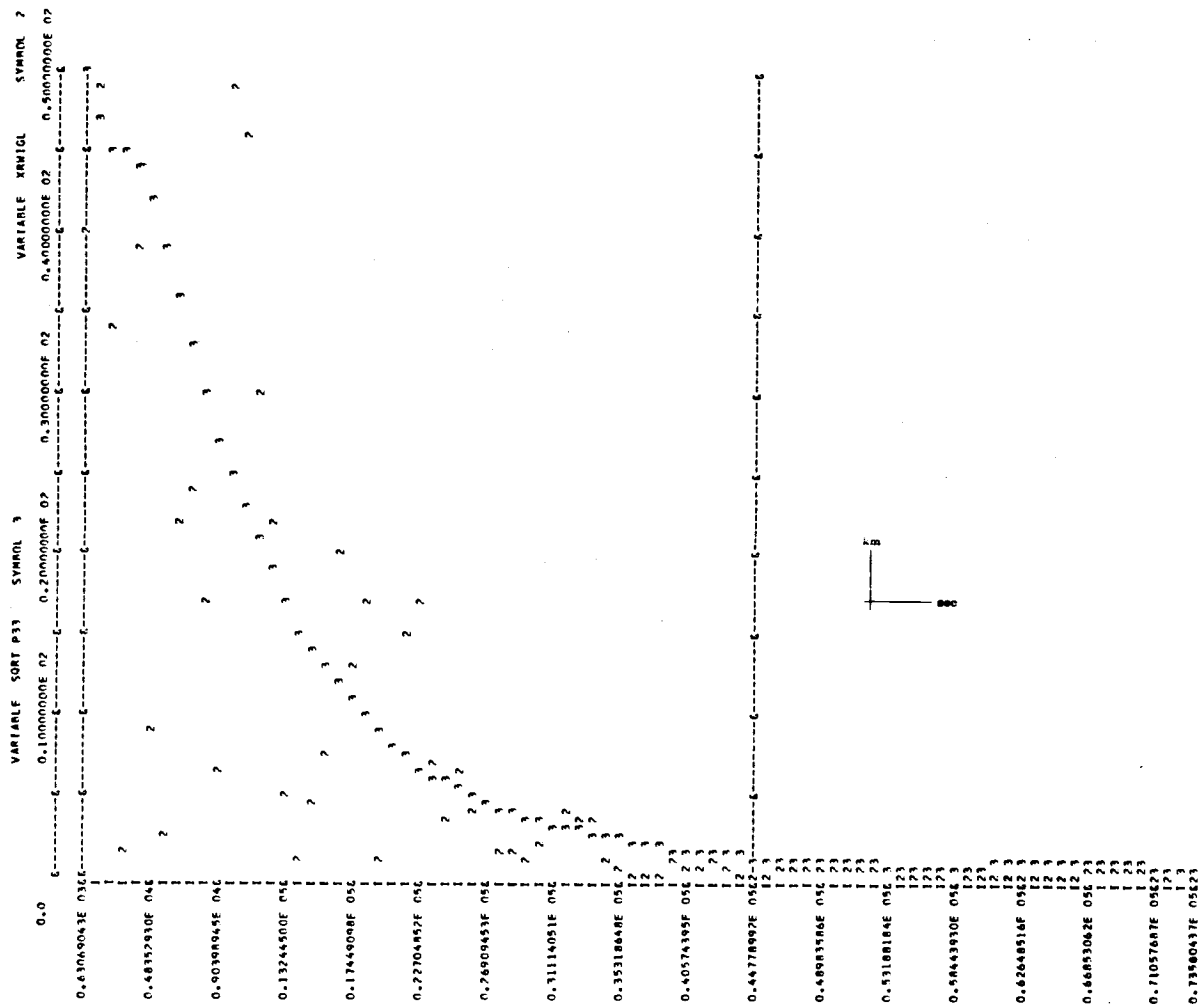

Figure B-46. $\left|\tilde{x}_R\right|$ and $\sqrt{P33}$ vs Time for Trajectory XII (1 Revolution ≅ 37,841 seconds), S.O.A. Horizon Sensor (Bias, System P1)

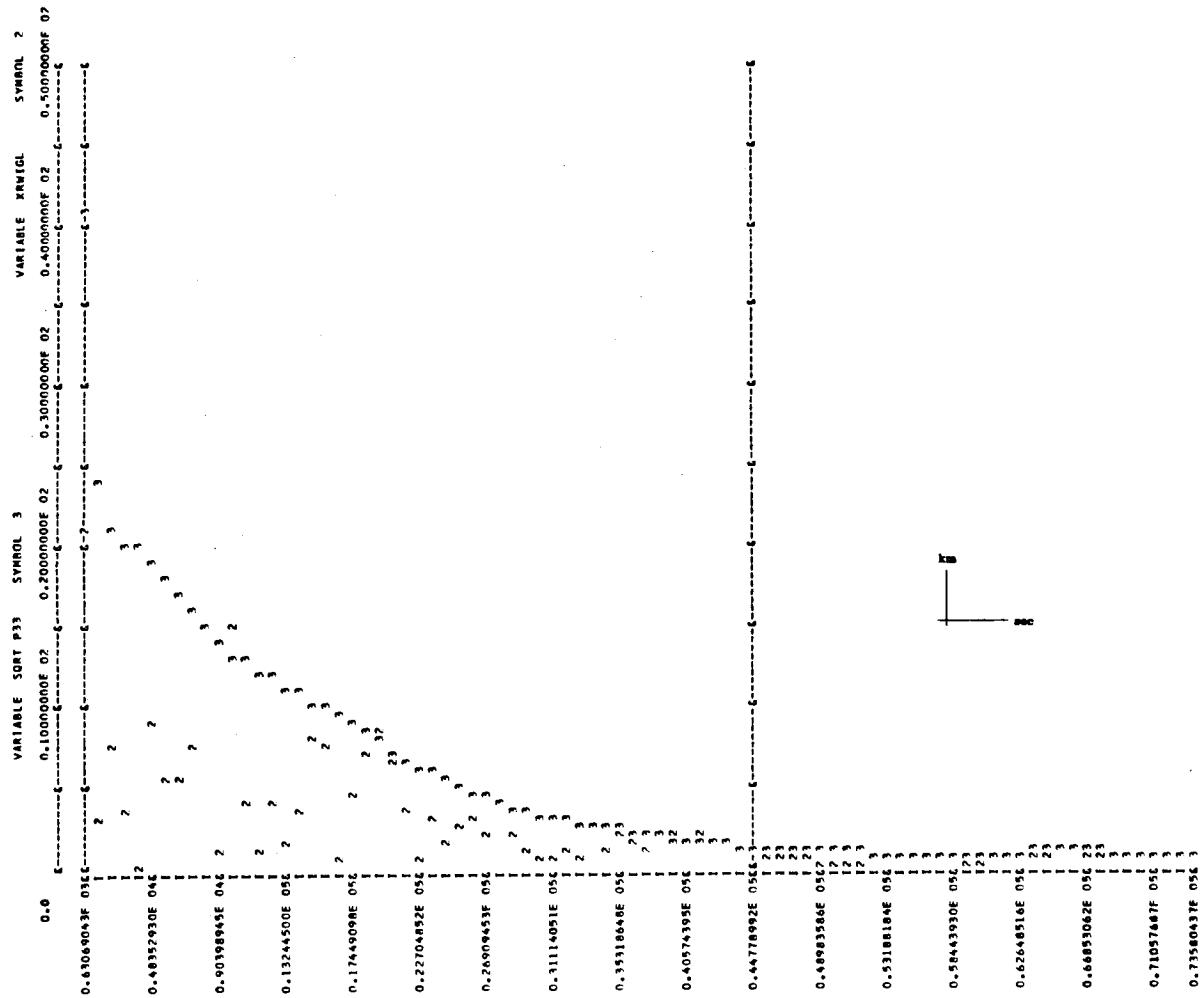

Figure B-47. $\left|\tilde{x}_R\right|$ and $\sqrt{P33}$ vs. Time for Trajectory XII (1 Revolution ≅ 37,841 seconds), S. O. A. Horizon Sensor (Without Bias, System P2)

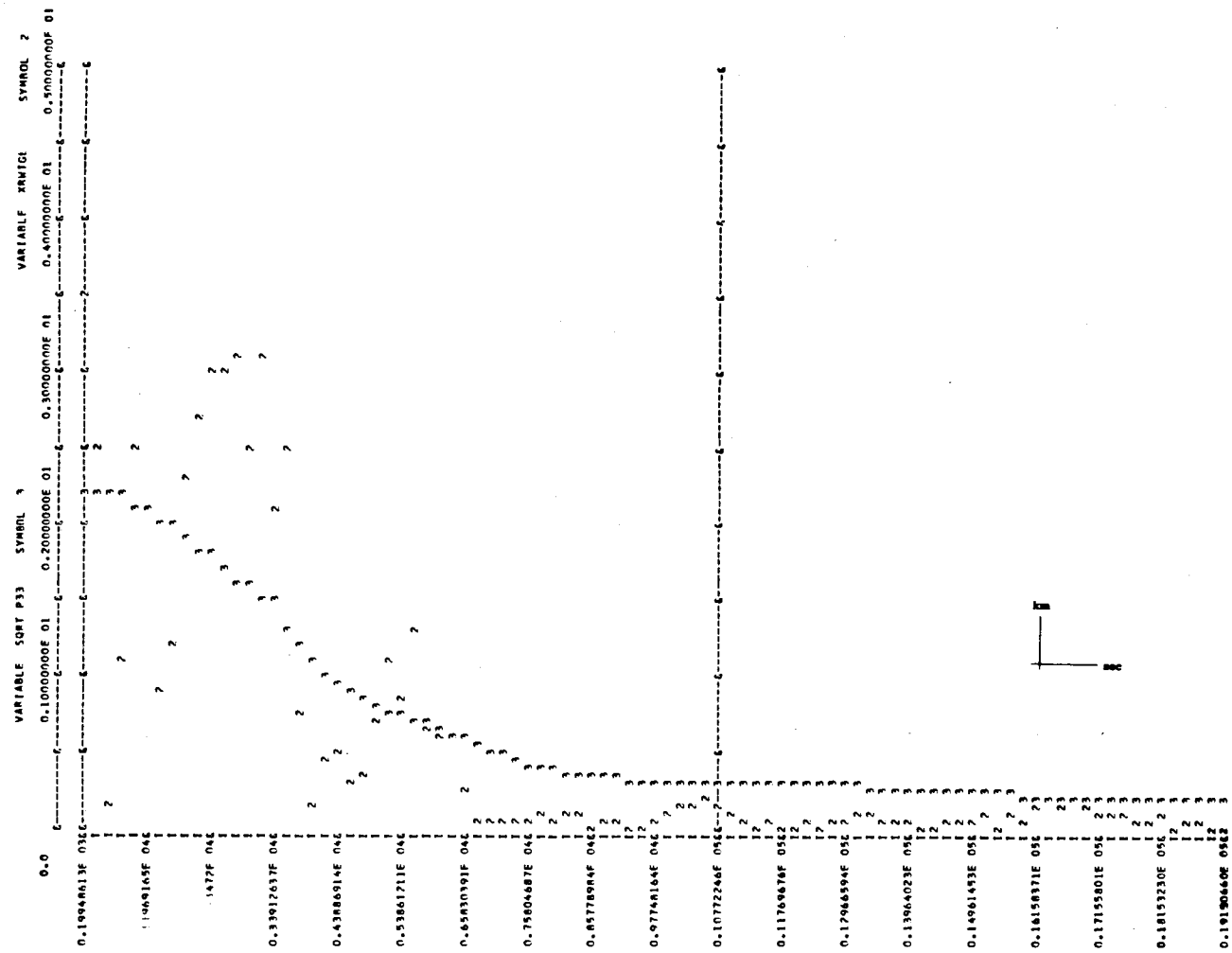

Figure B-48. $\left|\tilde{x}_R\right|$ and $\sqrt{P33}$ vs. Time for Trajectory IX (1 Revolution ≅ 6,333 seconds), S.O.A. Horizon Sensor (Bias, System P5)

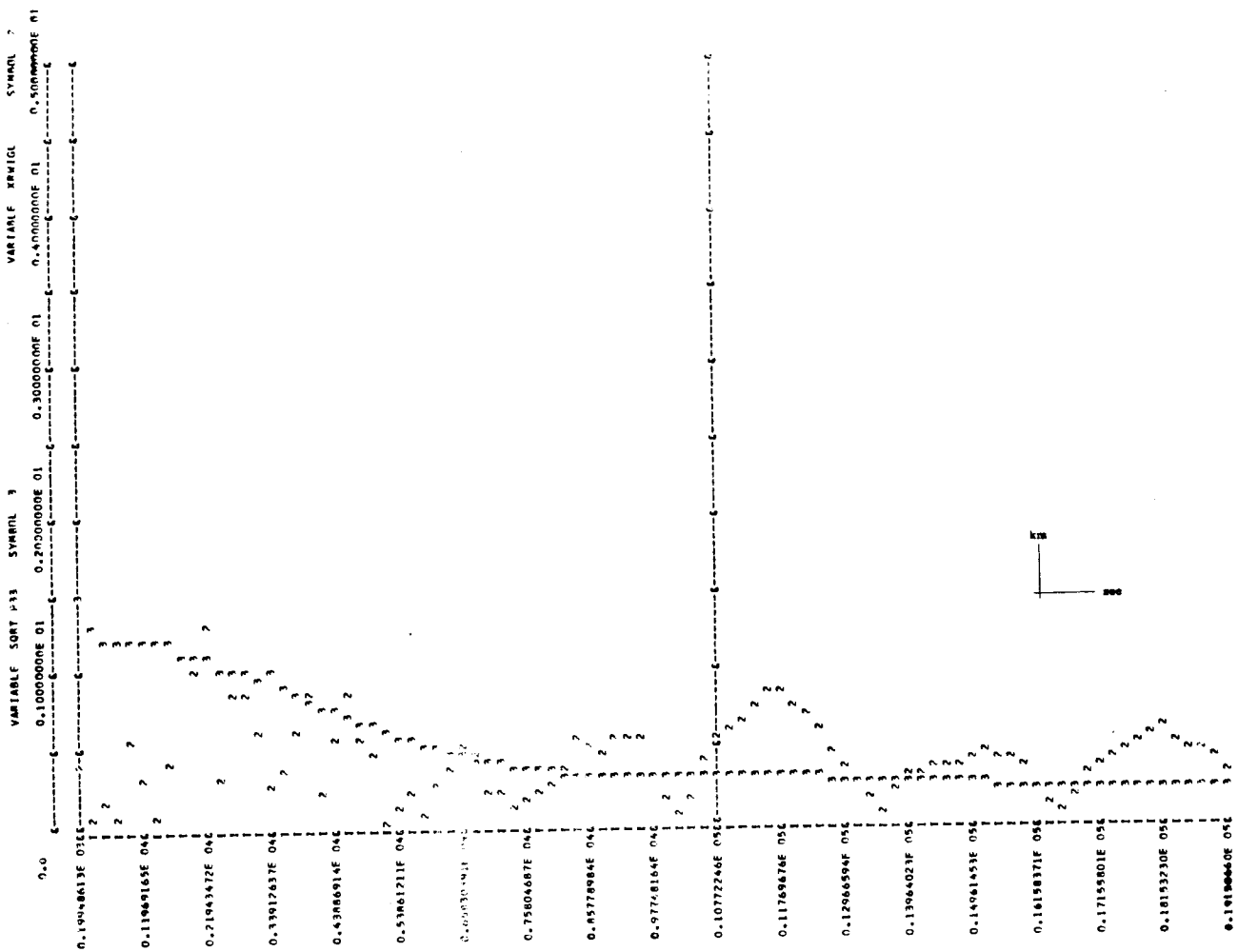

Figure B-49. $\left|\tilde{x}_R\right|$ and $\sqrt{P33}$ vs. Time for Trajectory IX (1 Revolution $\cong$ 6,333 seconds), S.O.A. Horizon Sensor (Without Bias, System P12)

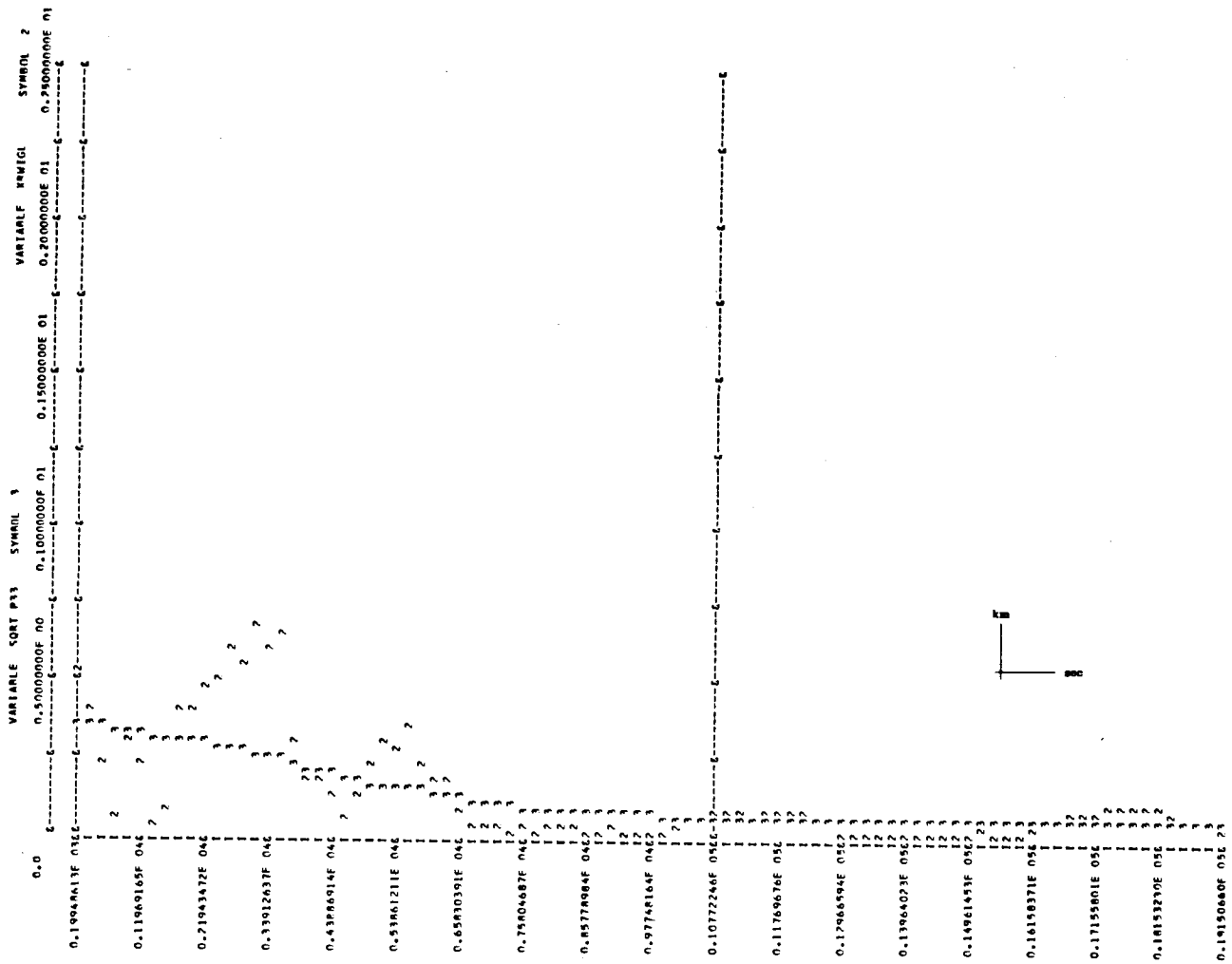

Figure B-50. $\left|\tilde{x}_R\right|$ and $\sqrt{P33}$ vs Time for Trajectory IX (1 Revolution ≅ 6,333 seconds), B.S.O.A. Horizon Sensor (Bias, System P16)

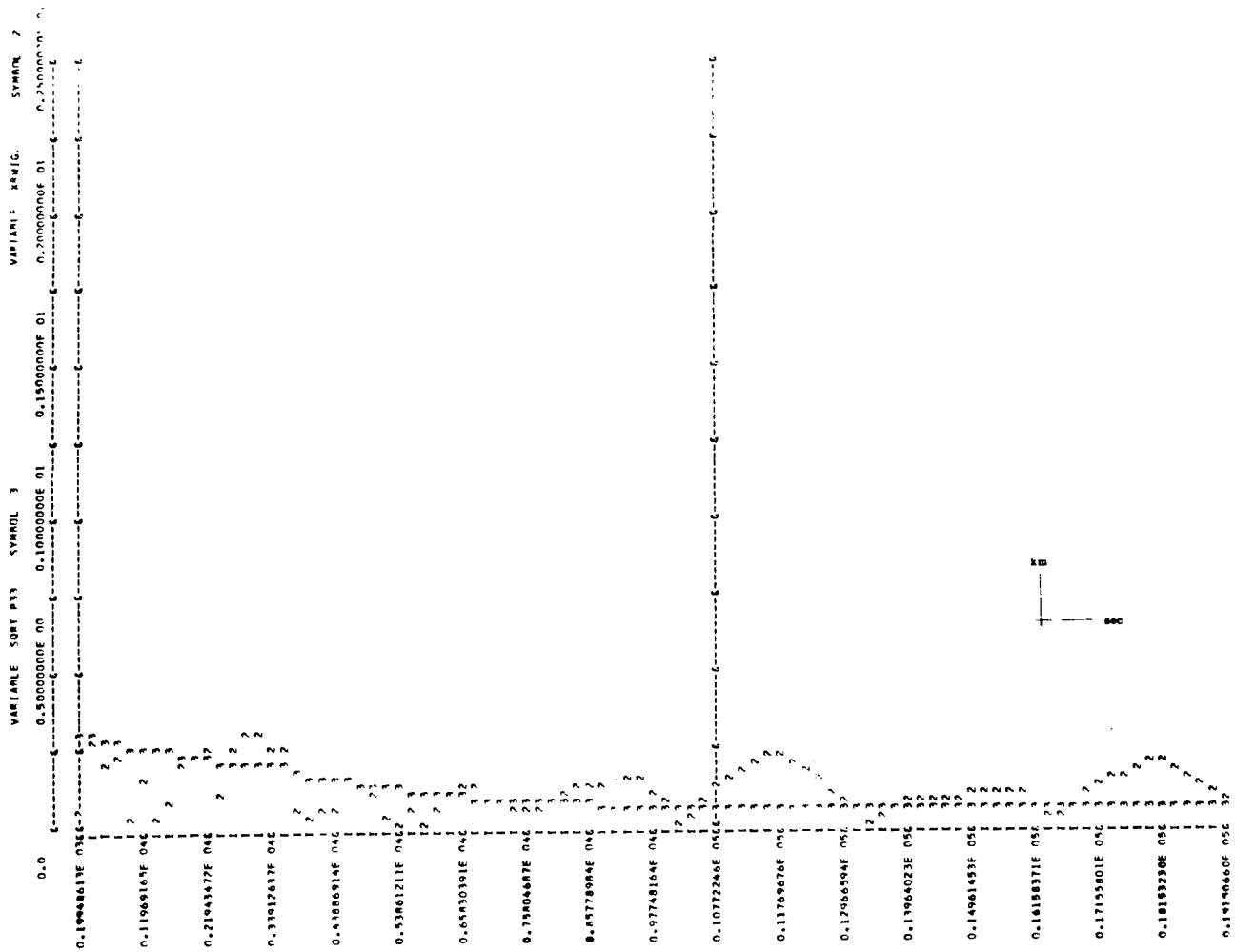

Figure B-51. $\left|\tilde{x}_R\right|$ and $\sqrt{P33}$ vs. Time for Trajectory IX (2 Revolution ≅ 6,333 seconds), B. S. O. A. Horizon Sensor (Without Bias, System P13)

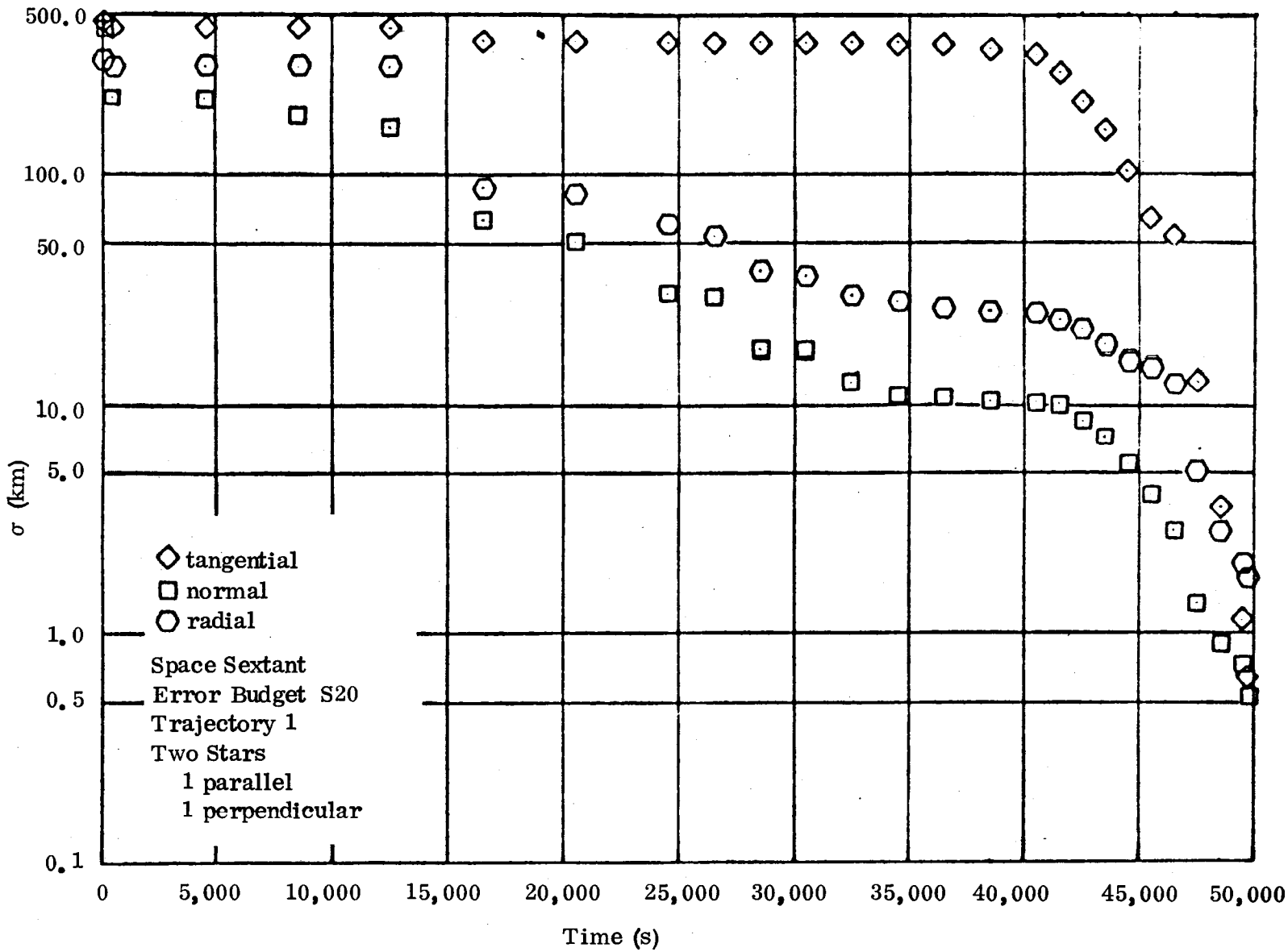

Figure B-52. 1σ Terminal Error in Estimate vs Time — Martian Approach

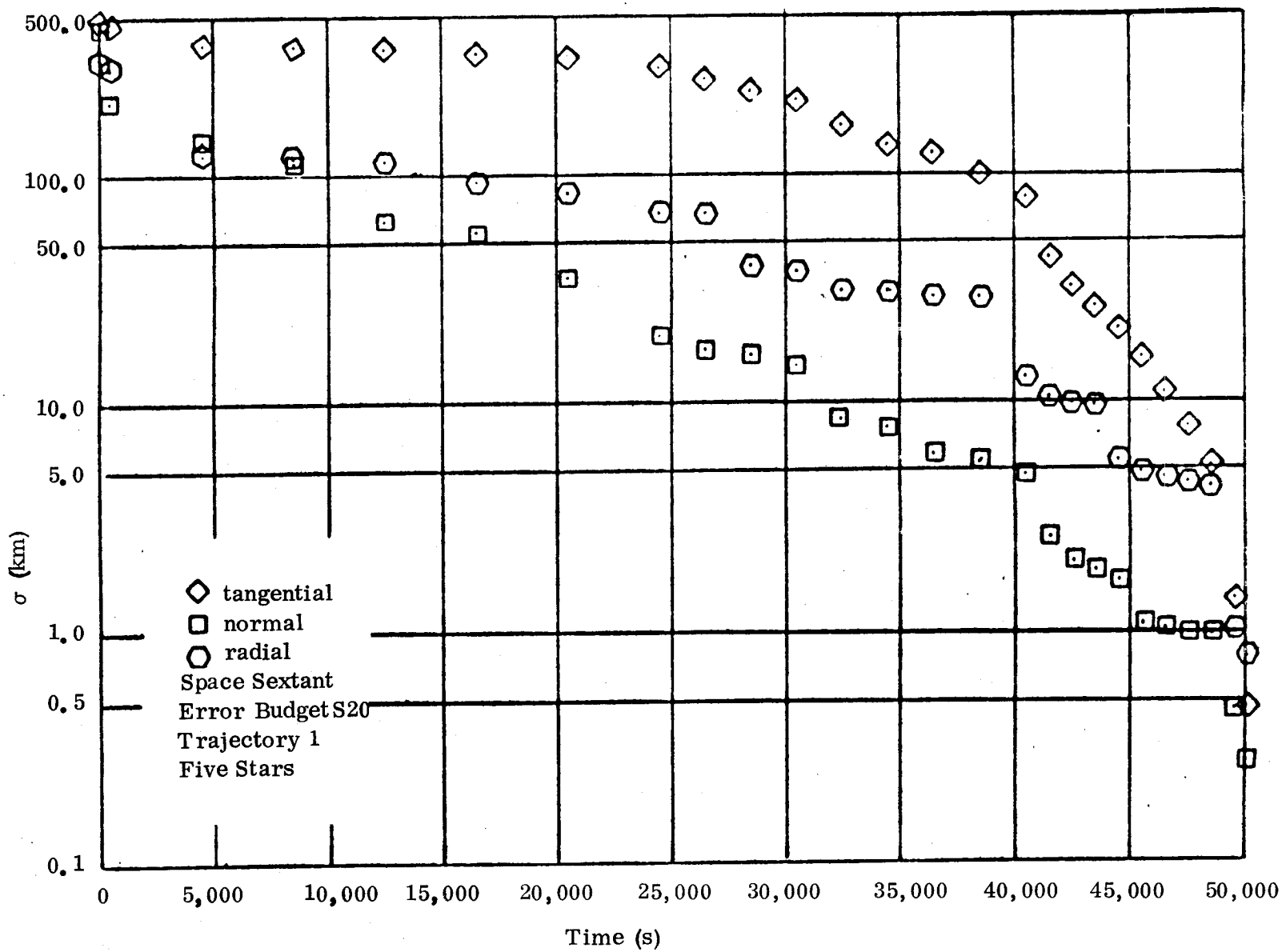

Figure B-53. 1σ Terminal Error in Estimate vs Time — Martian Approach

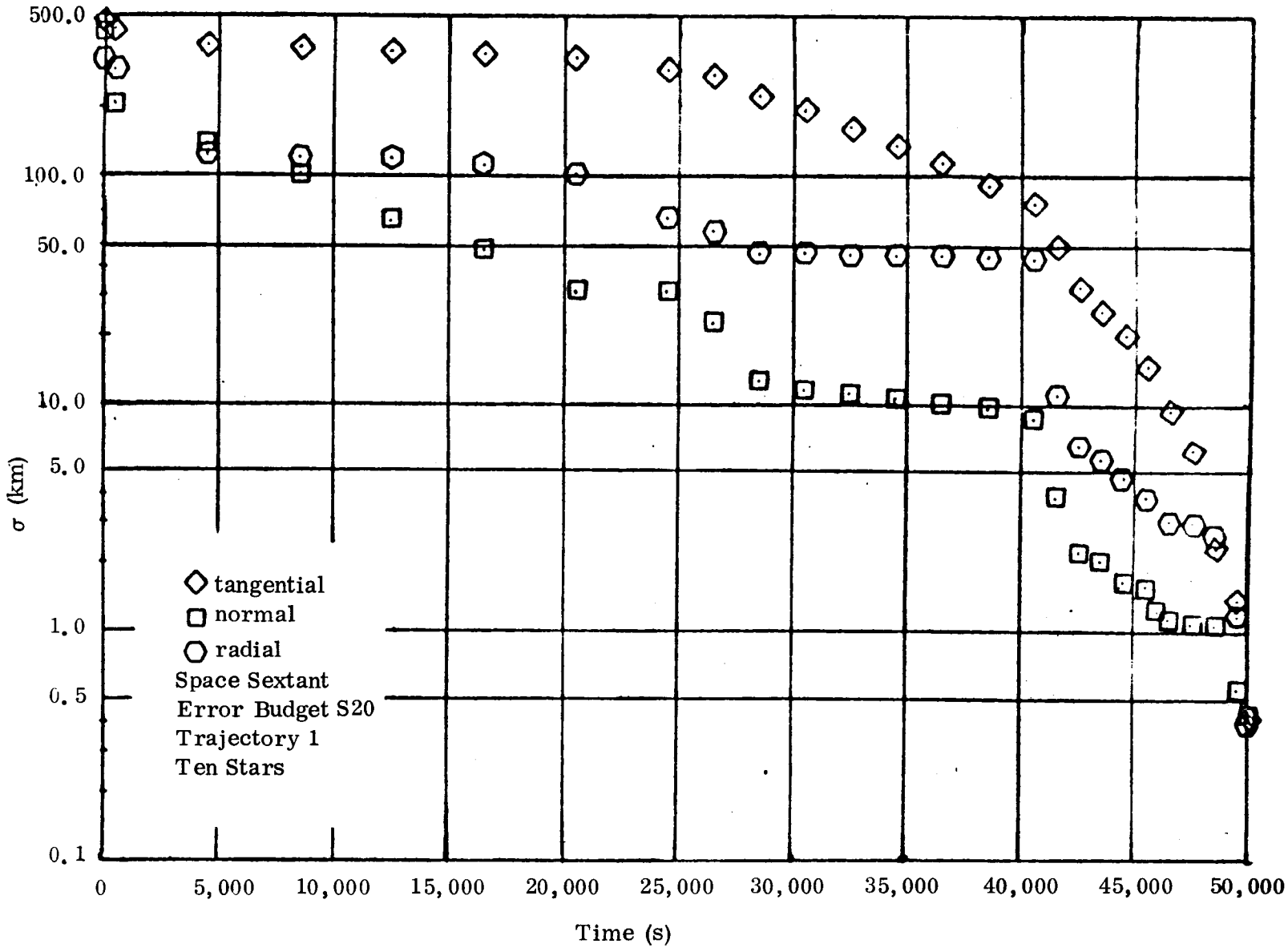

Figure B-54. 1σ Terminal Error in Estimate vs Time — Martin Approach

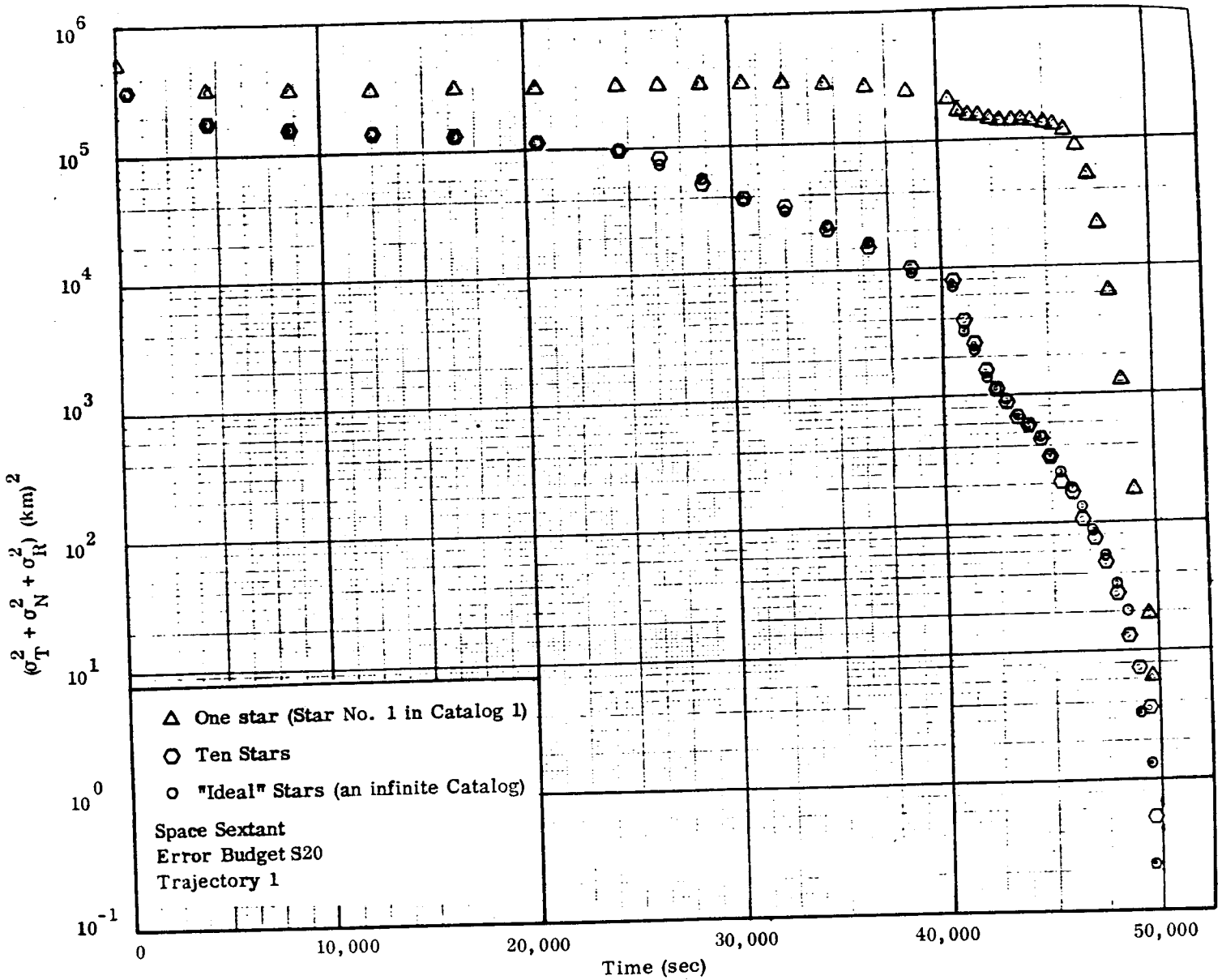

Figure B-55. Trace of Covariance Matrix of Terminal Error vs Time—Martian Approach

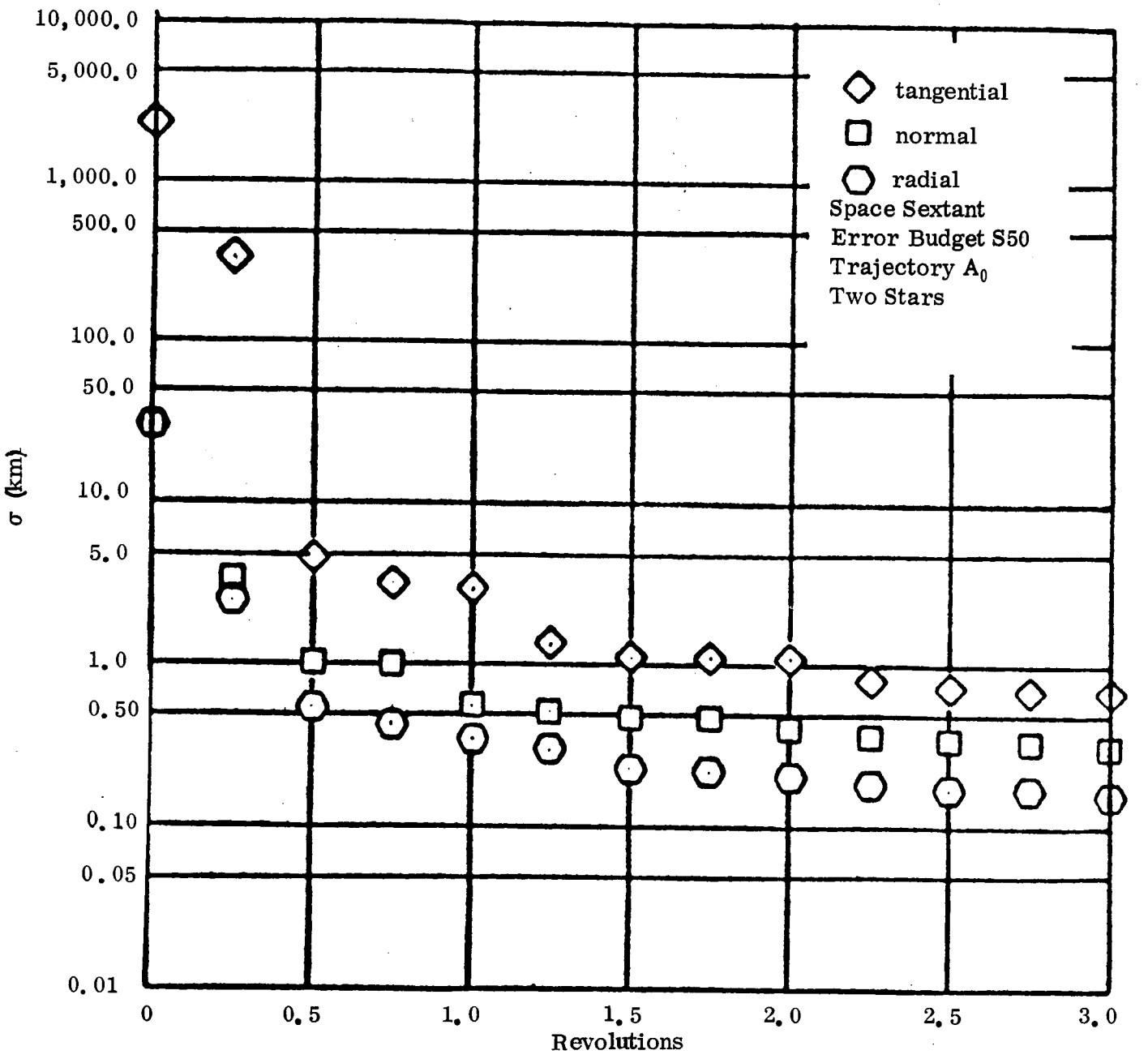

Figure B-56. 1σ Terminal Error in Estimate vs Number of Revolutions
Low-Altitude Martian Circular Orbit

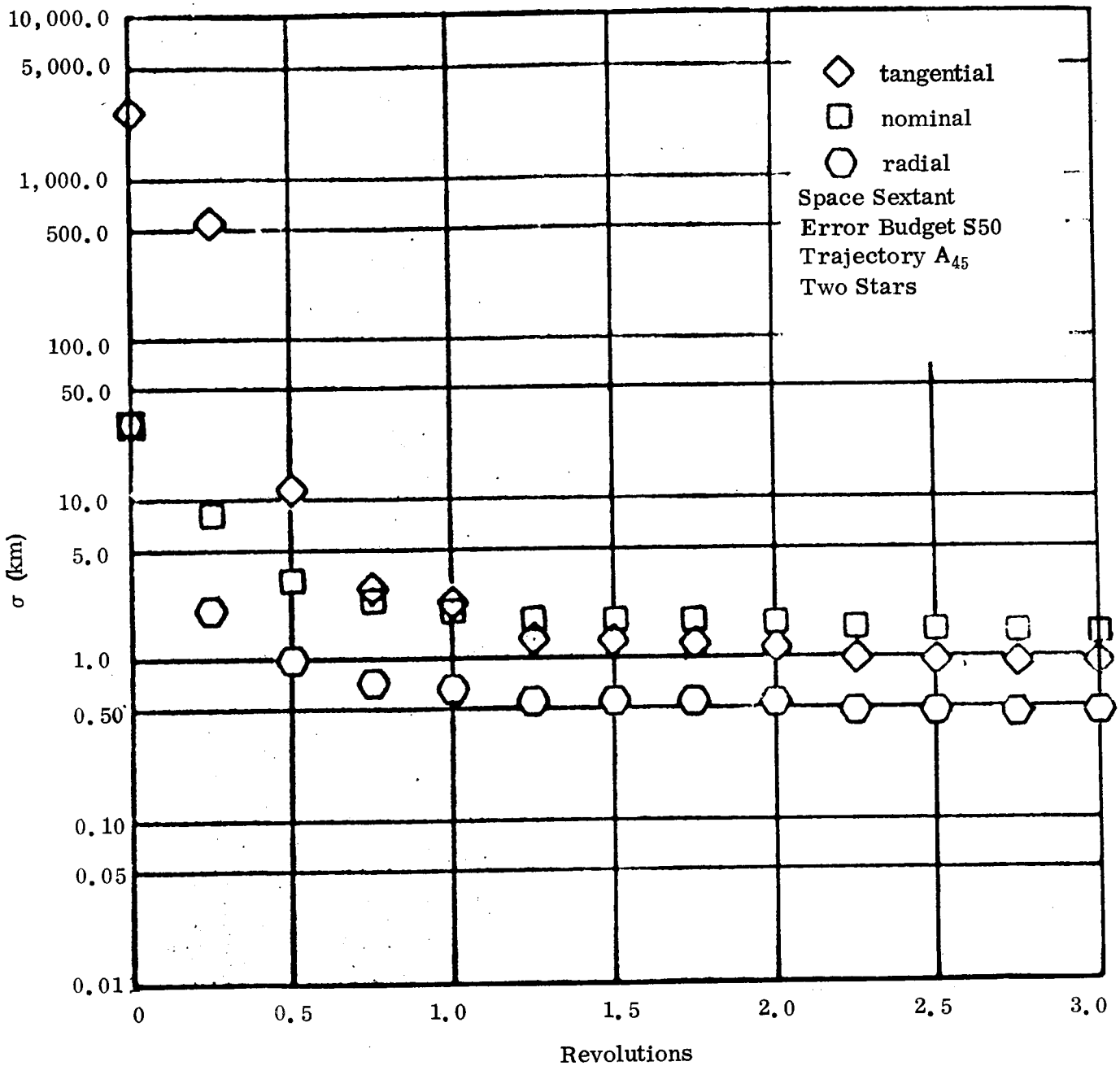

Figure B-57. 1σ Terminal Error Estimate vs Number of Revolutions
Low-Altitude Martian Circular Orbit

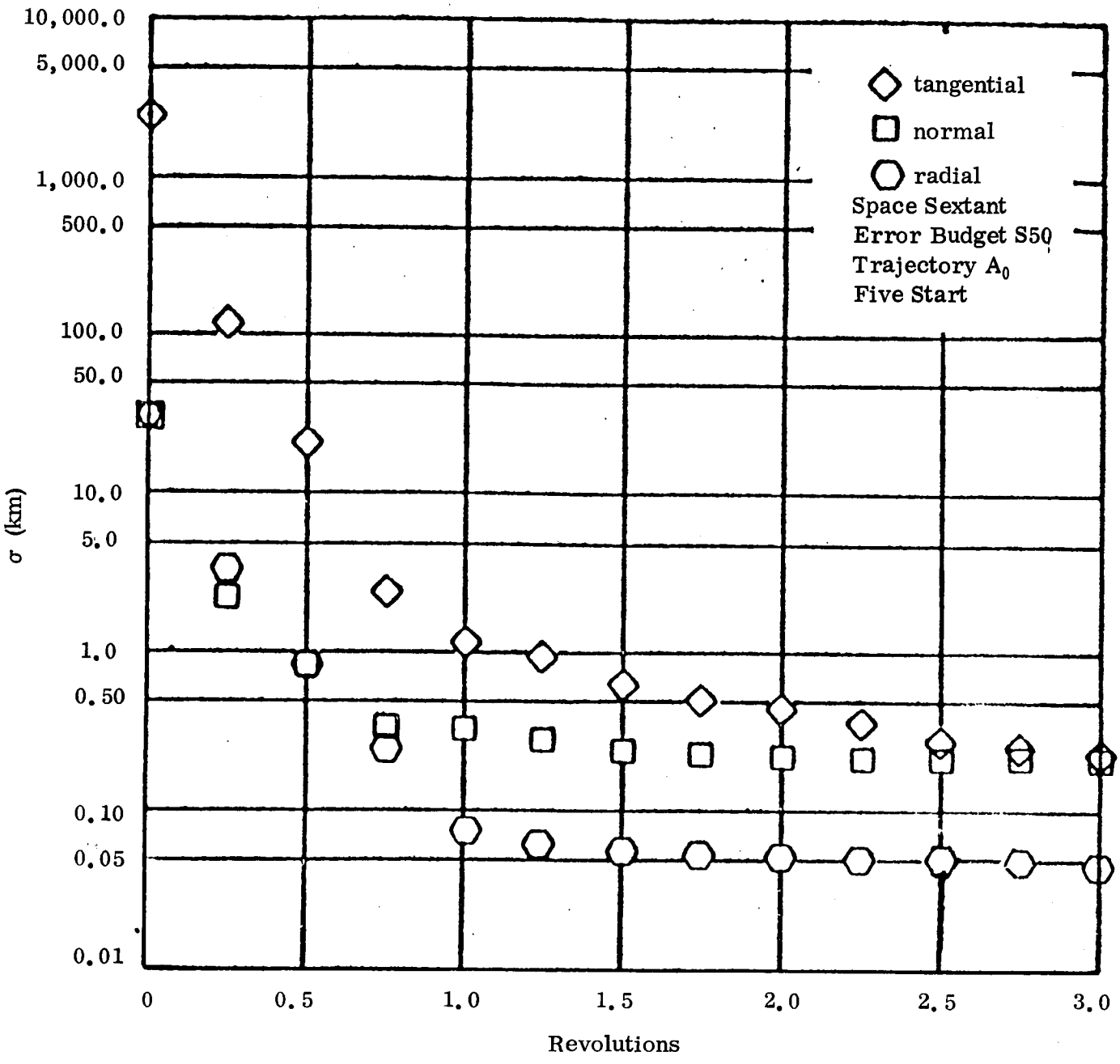

Figure B-58. 1σ Terminal Error in Estimate vs Number of Revolutions
Low-Altitude Martian Circular Orbit

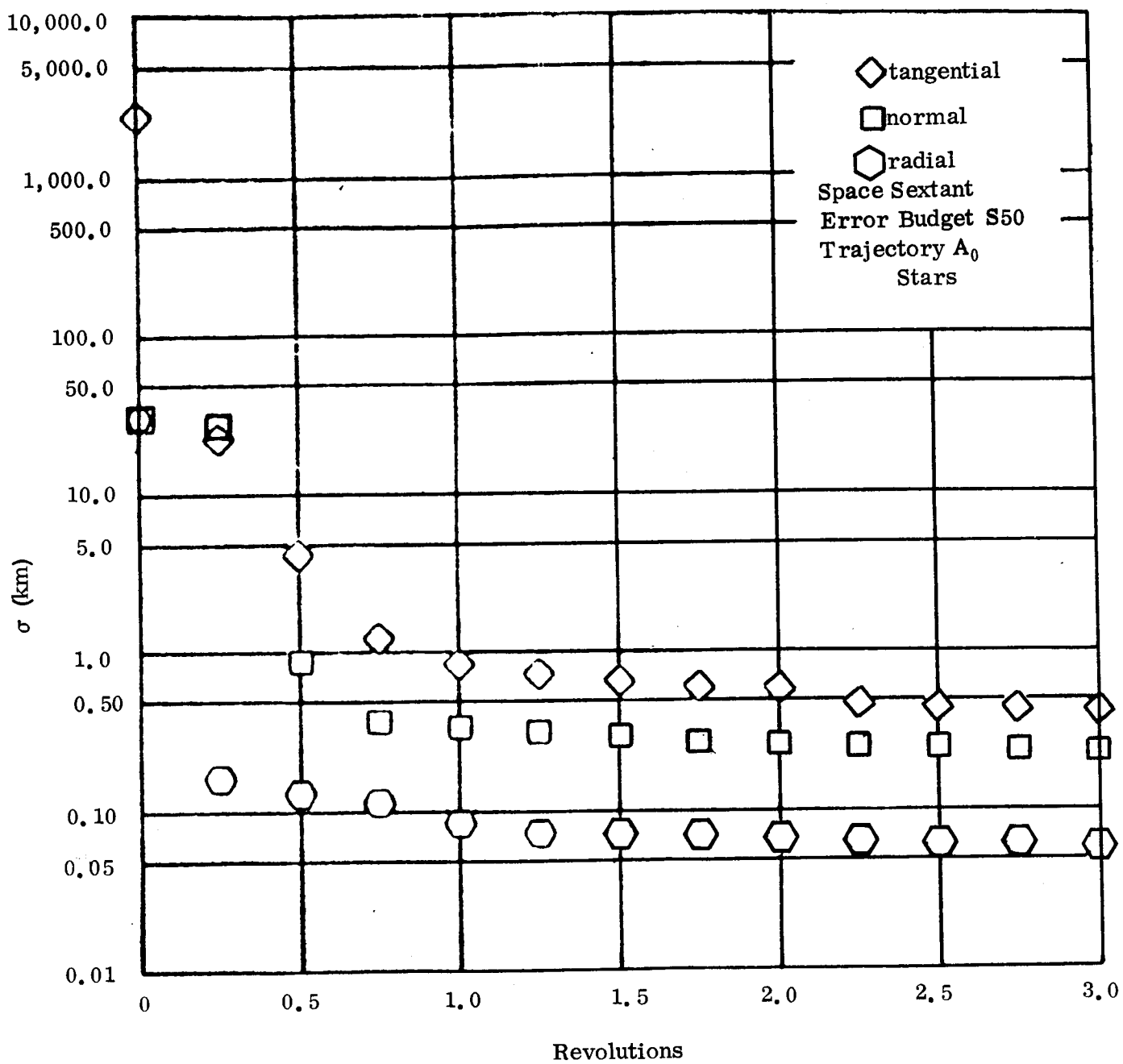

Figure B-59. 1σ Terminal Error in Estimate vs Number of Revolutions
Low-Altitude Martian Circular Orbit

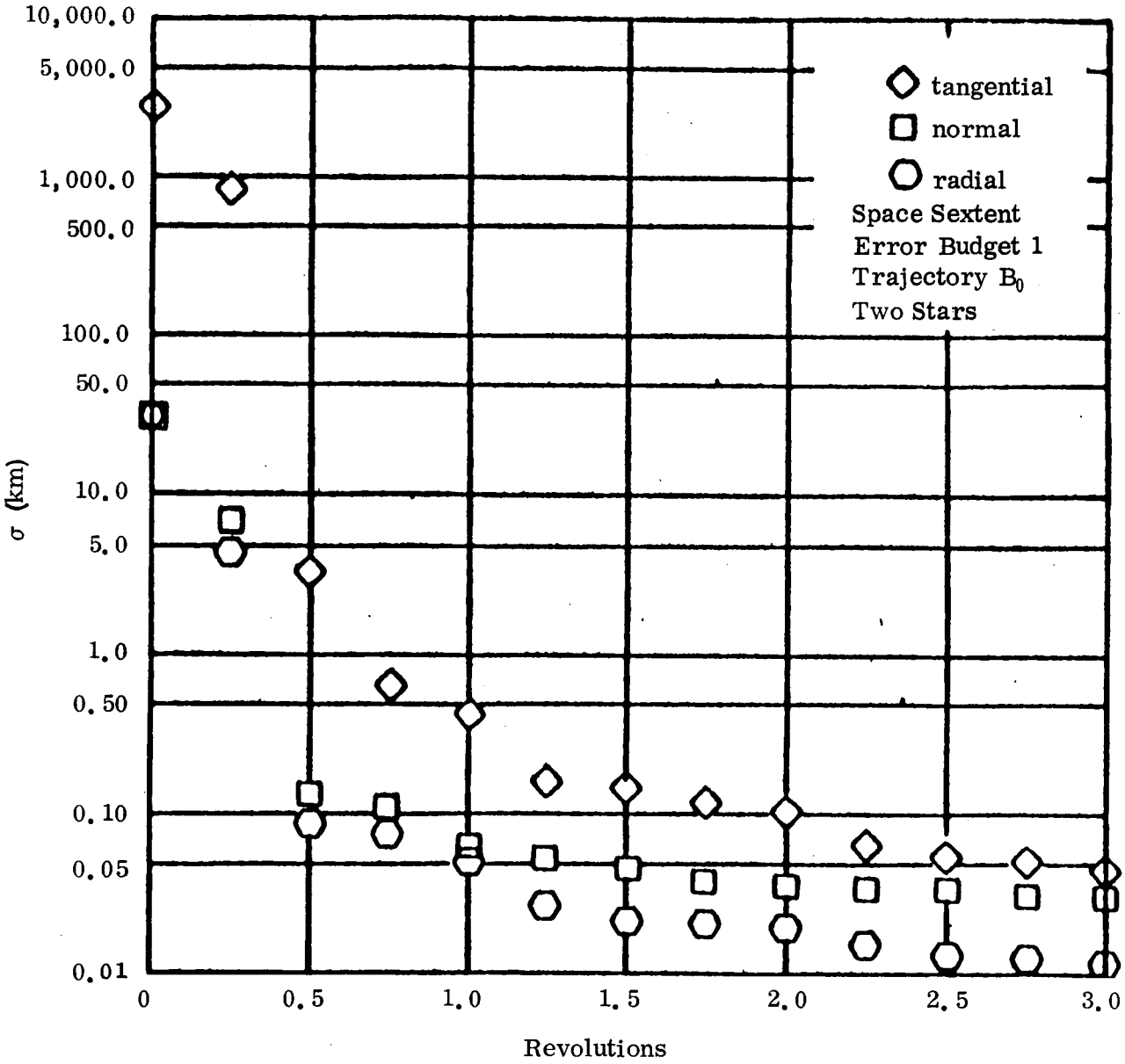

Figure B-60. 1σ Error in the Estimate

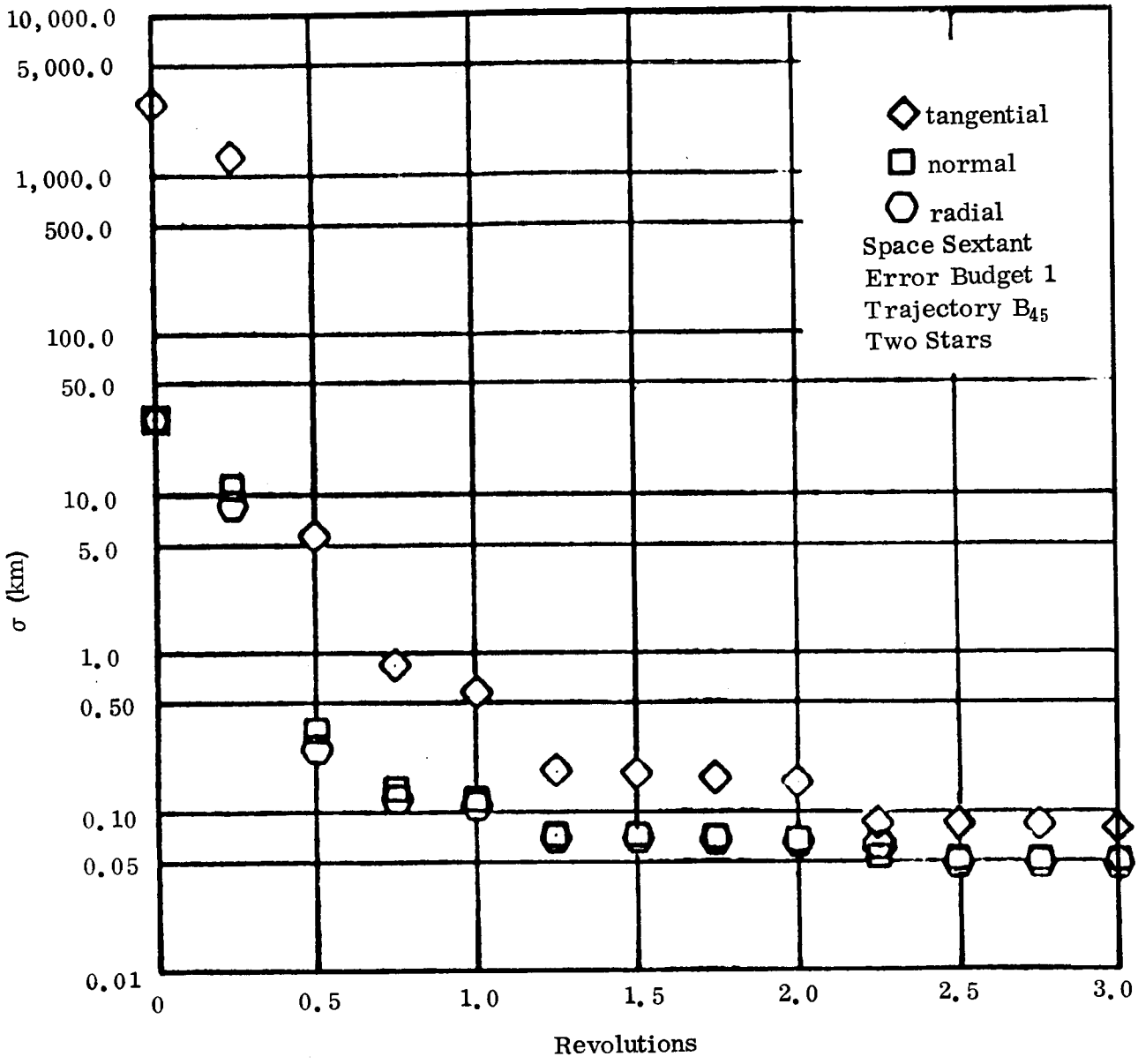

Figure B-61. 1σ Error in the Estimate

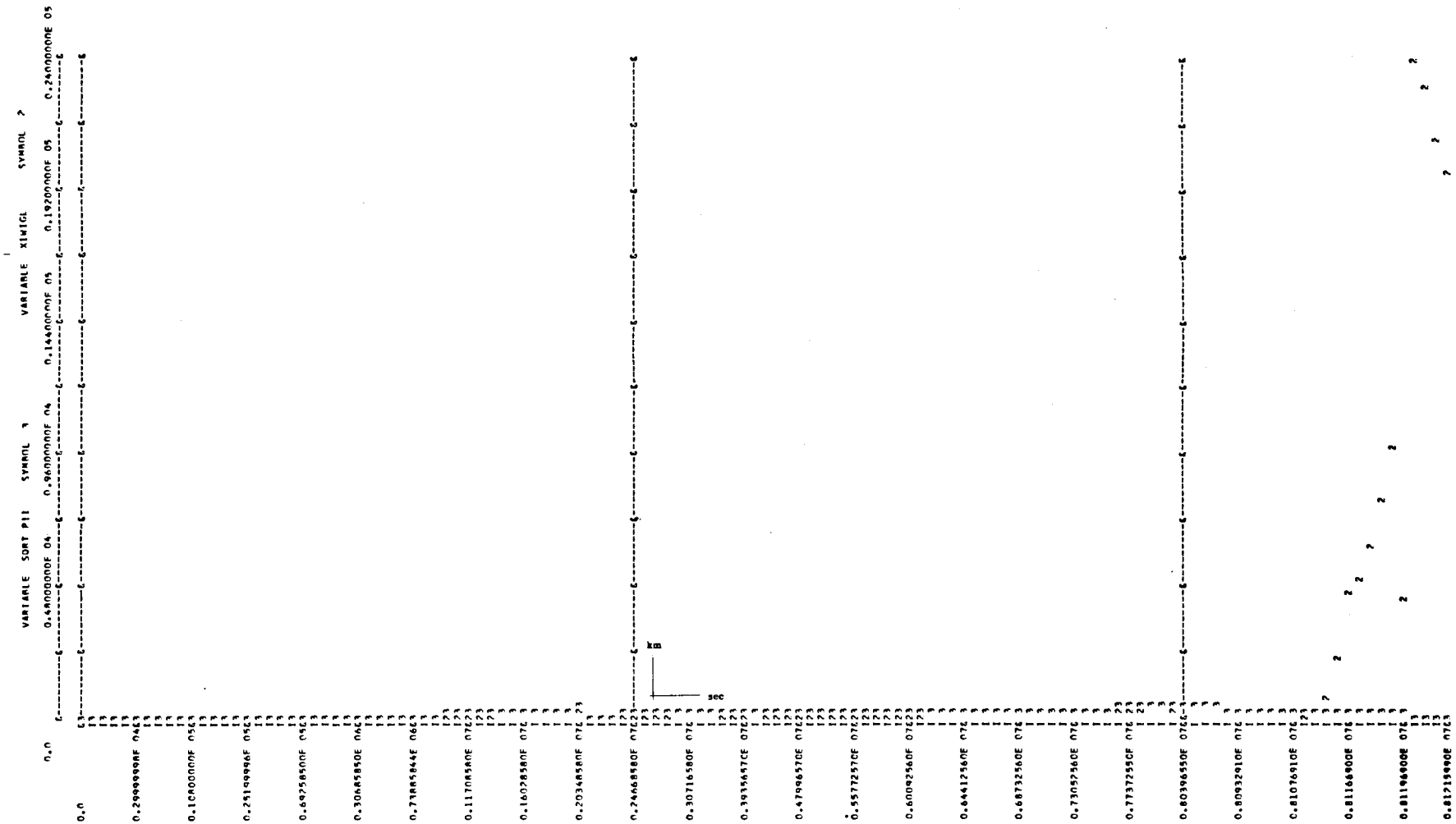

Figure B-62. $|\tilde{x}_1|$ and $\sqrt{P11}$ vs. Time - System Configuration TM18(Q1)
(Similar Behavior for $|\tilde{x}_2|$, $|\tilde{x}_3|$, $\sqrt{P22}$, $\sqrt{P33}$)

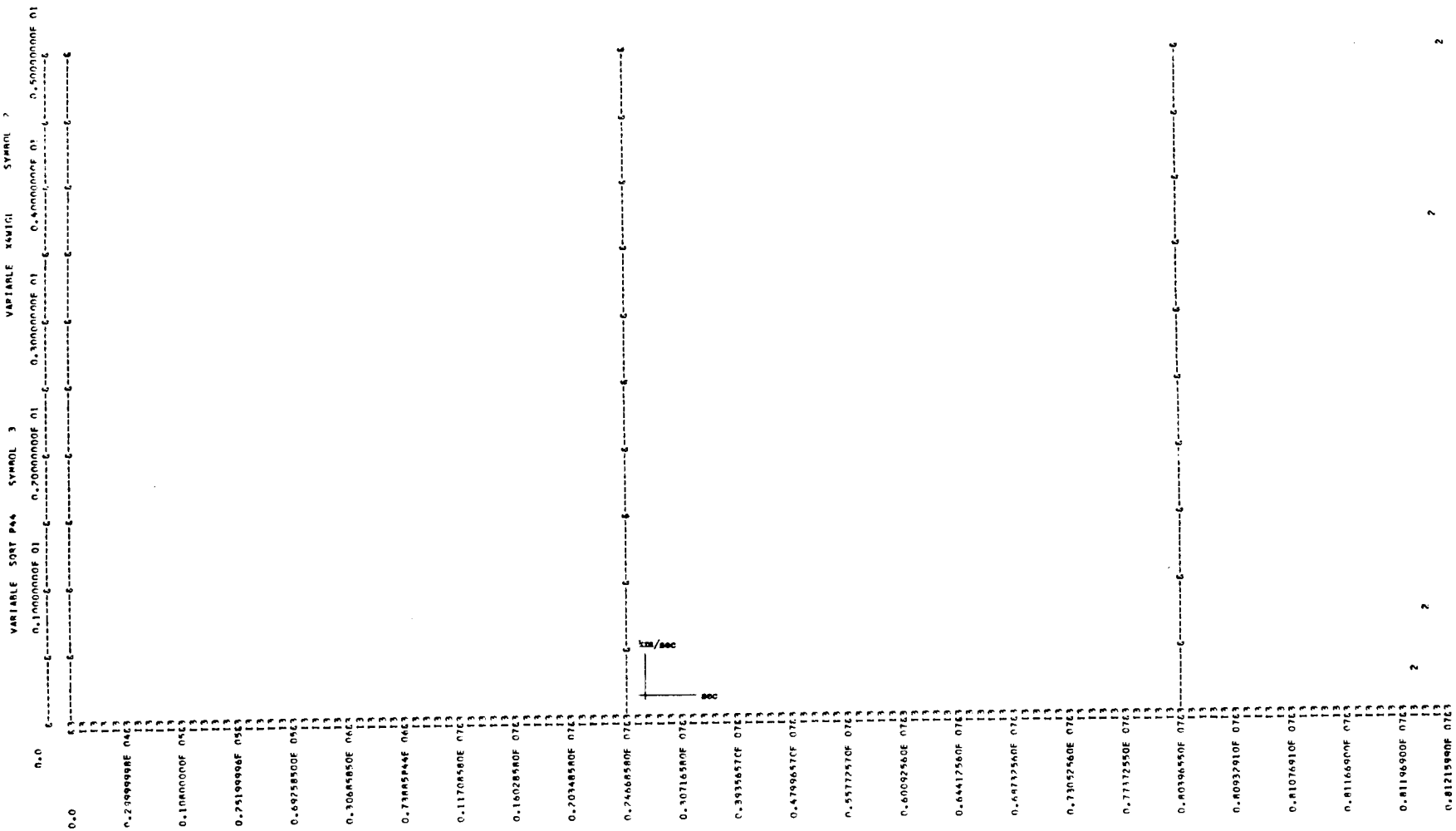

Figure B-63. $|\tilde{x}_4|$ and $\sqrt{P44}$ vs. Time - System Configuration TM18(Q1)
(Similar Behavior for $|\tilde{x}_5|$, $|\tilde{x}_6|$, $\sqrt{P55}$, $\sqrt{P66}$)

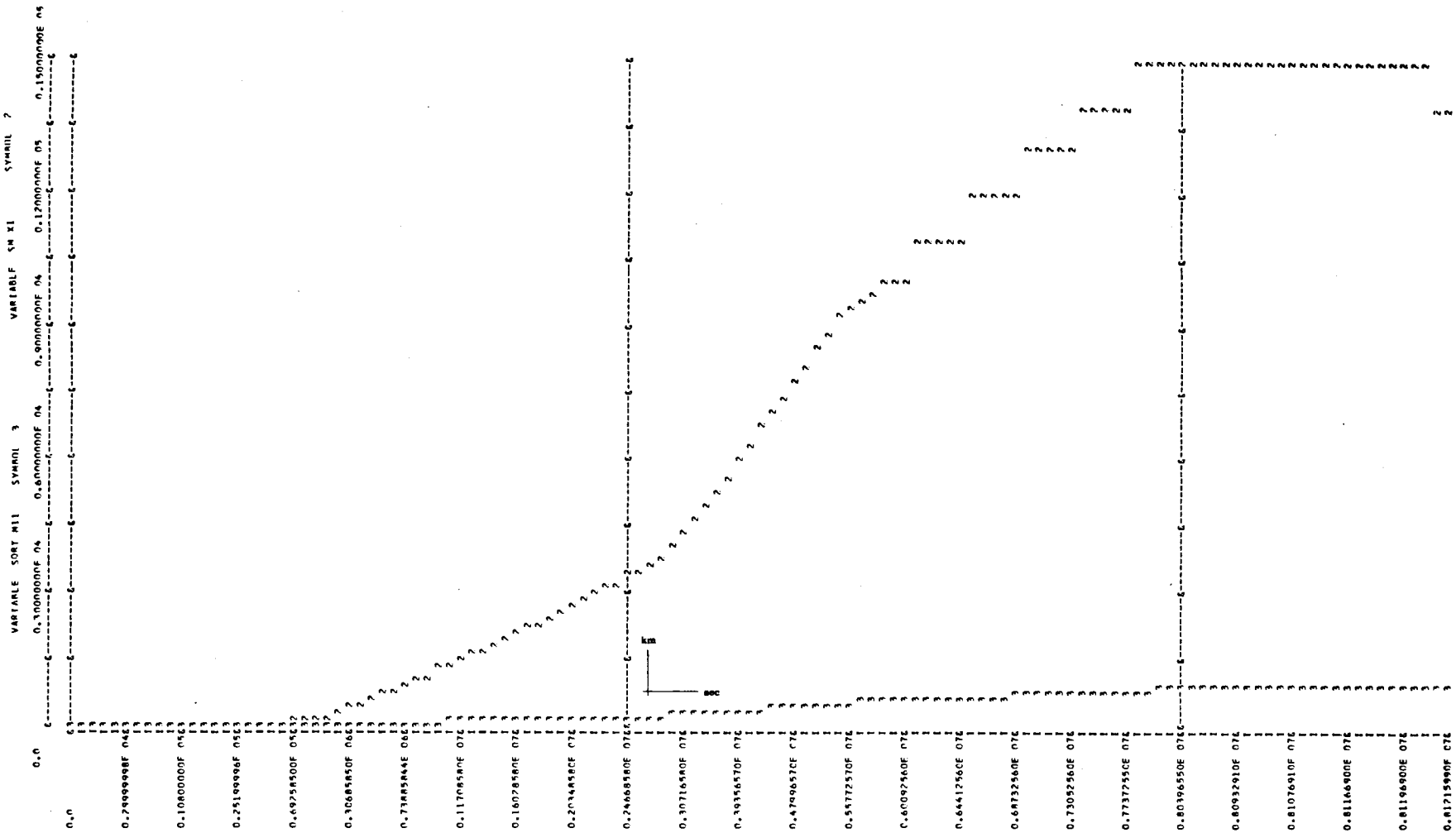

Figure B-64. $|x_1|$ and $\sqrt{M11}$ vs. Time - System Configuration TM18(Q1)
(Similar Behavior for $|x_2|$, $|x_3|$, $\sqrt{M22}$, $\sqrt{M33}$)

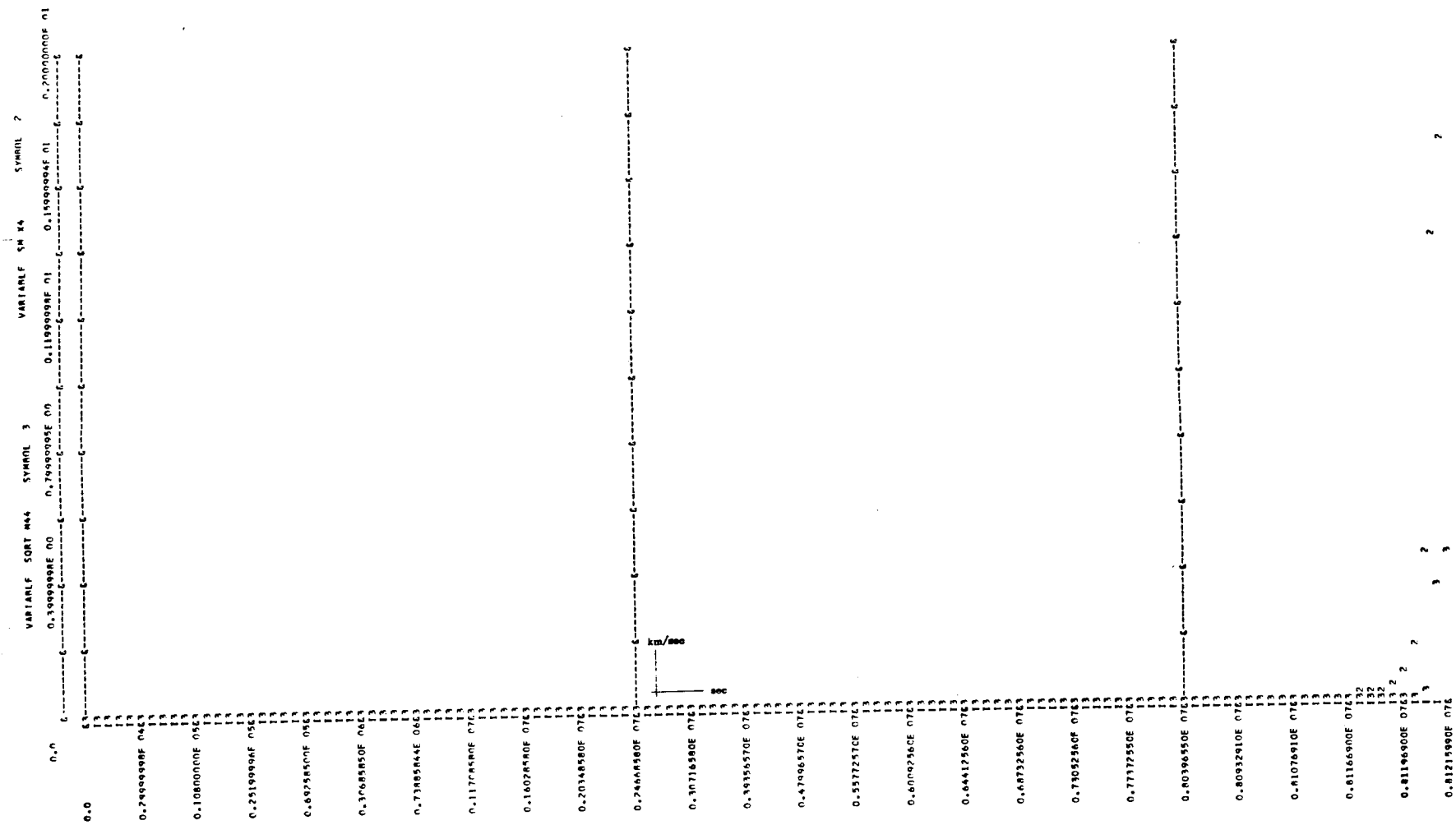

Figure B-65. $|x_4|$ and $\sqrt{M44}$ vs. Time - System Configuration TM18(Q1)
(Similar Behavior for $|x_5|$, $|x_6|$, $\sqrt{M55}$, $\sqrt{M66}$)

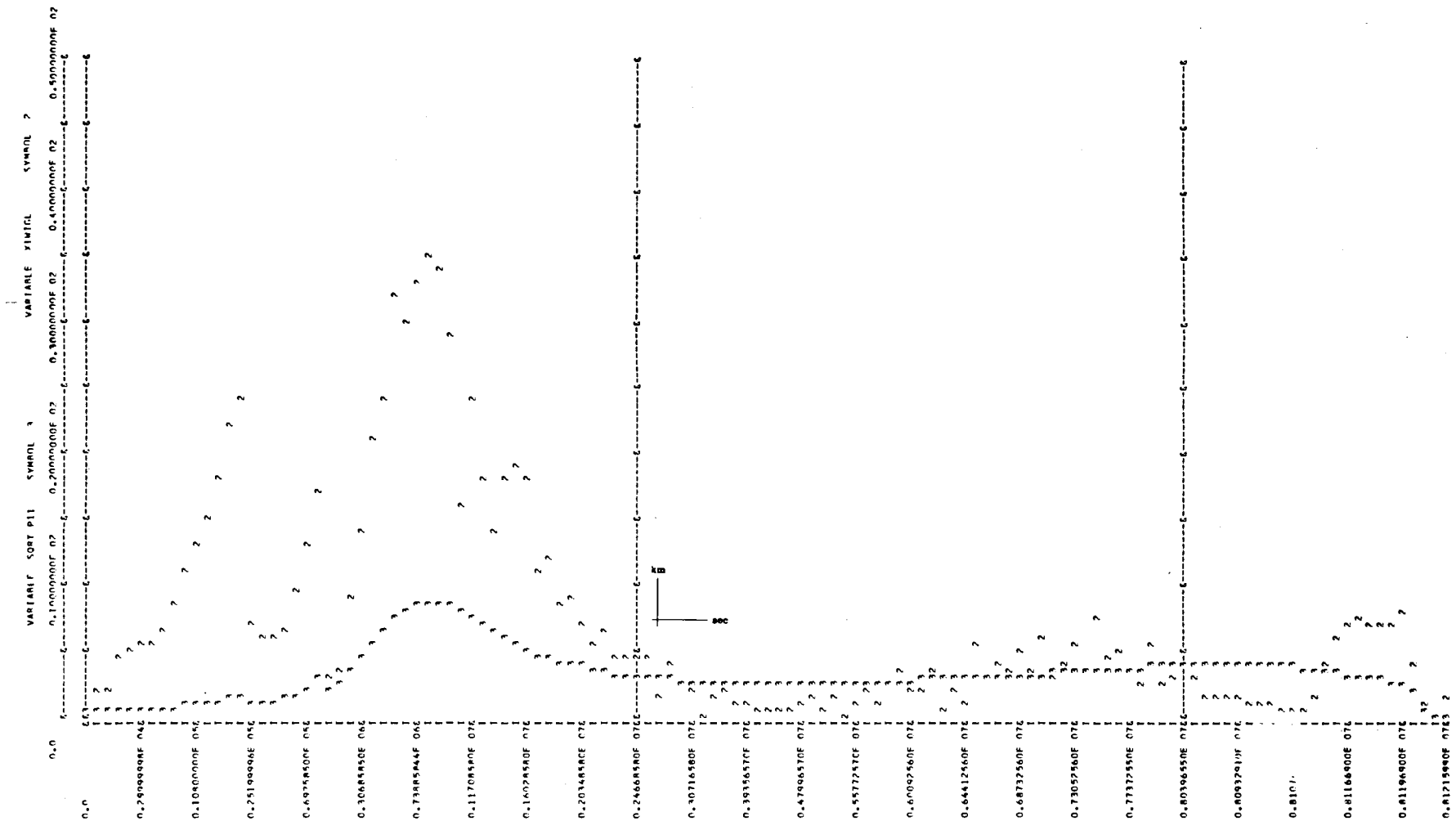

Figure B-66. $|\tilde{x}_1|$ and $\sqrt{P11}$ vs. Time - System Configuration TM18
(Similar Behavior for $|\tilde{x}_2|$, $|\tilde{x}_3|$, $\sqrt{P22}$, $\sqrt{P33}$)

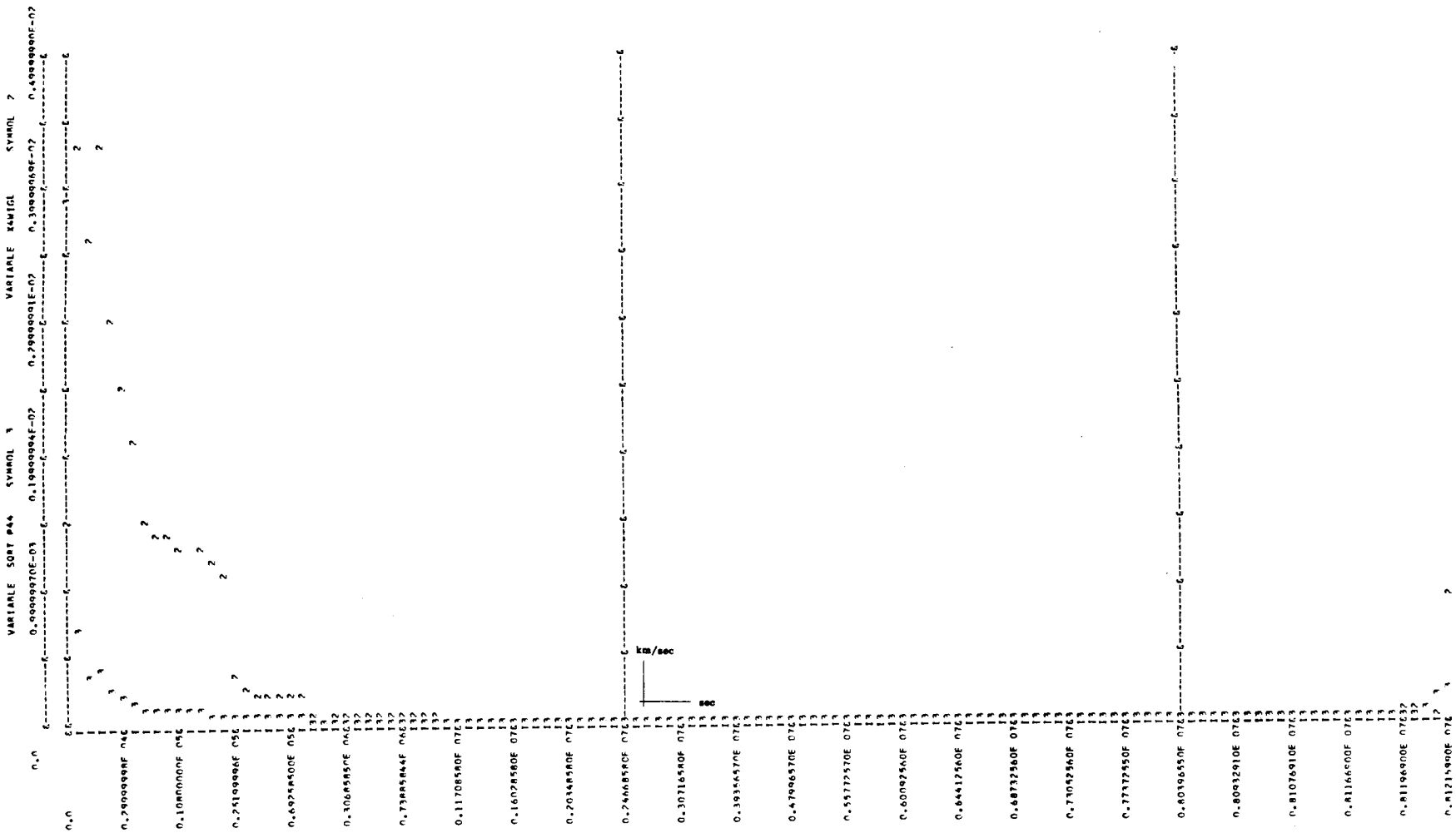

Figure B-67. $|\tilde{x}_4|$ and $\sqrt{P44}$ vs. Time - System Configuration TM18
(Similar Behavior for $|\tilde{x}_5|$, $|\tilde{x}_6|$, $\sqrt{P55}$, $\sqrt{P66}$)

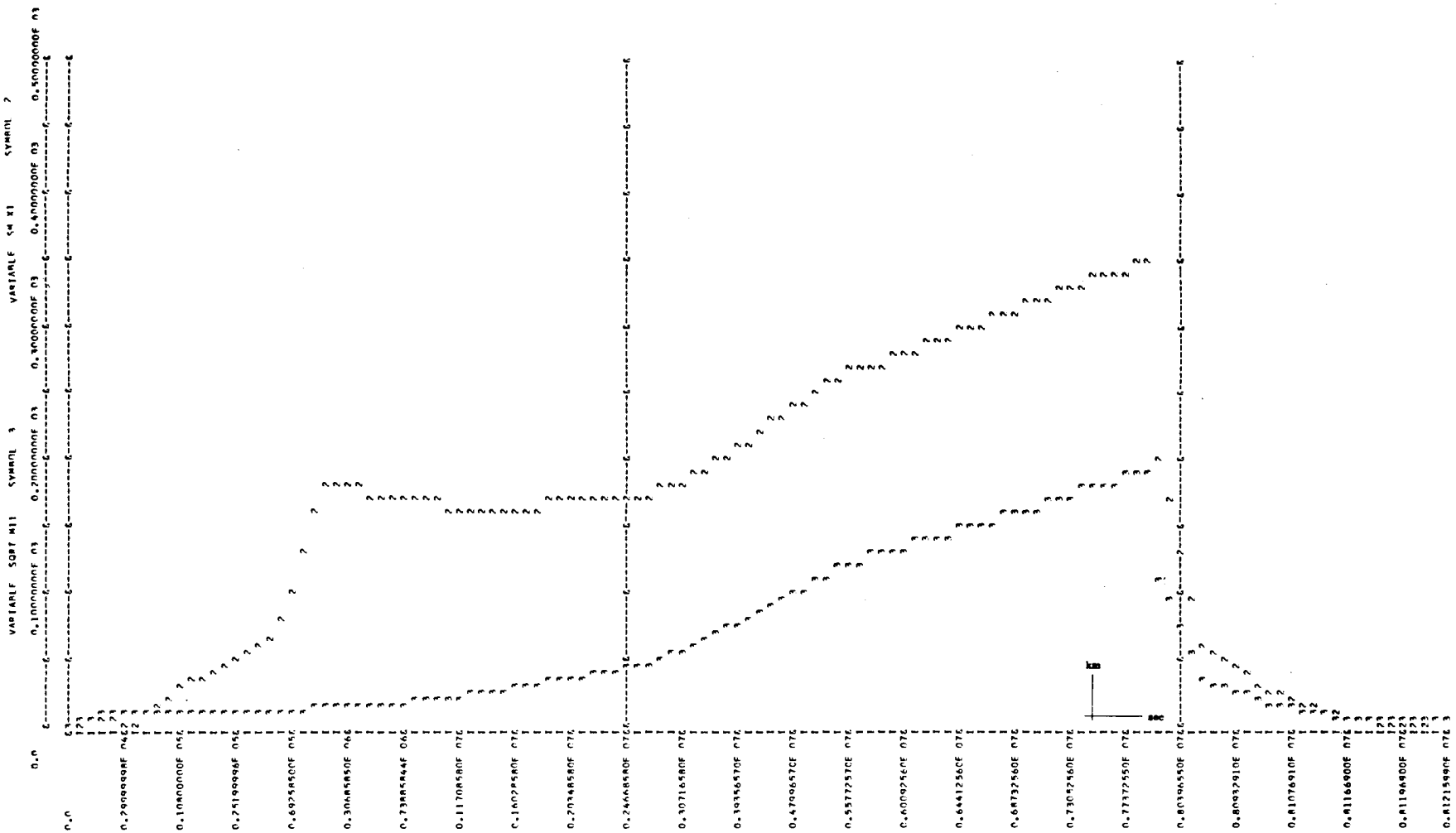

Figure B-68. $|x_1|$ and $\sqrt{M11}$ vs. Time - System Configuration TM18
(Similar Behavior for $|x_2|$, $|x_3|$, $\sqrt{M22}$, $\sqrt{M33}$)

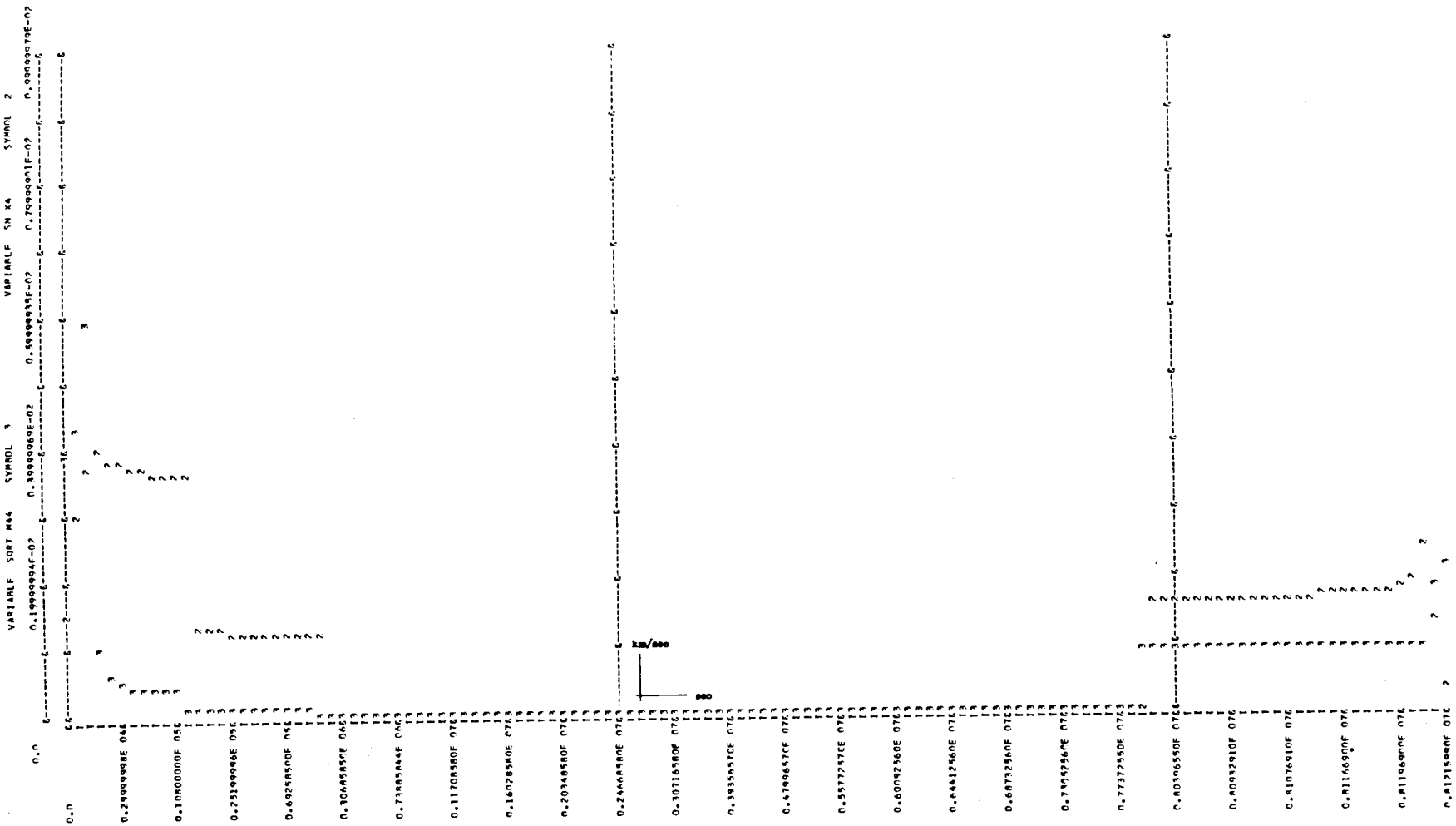

Figure B-69. $|x_4|$ and $\sqrt{M44}$ vs. Time - System Configuration TM18
(Similar Behavior for $|x_5|$, $|x_6|$, $\sqrt{M55}$, $\sqrt{M66}$)

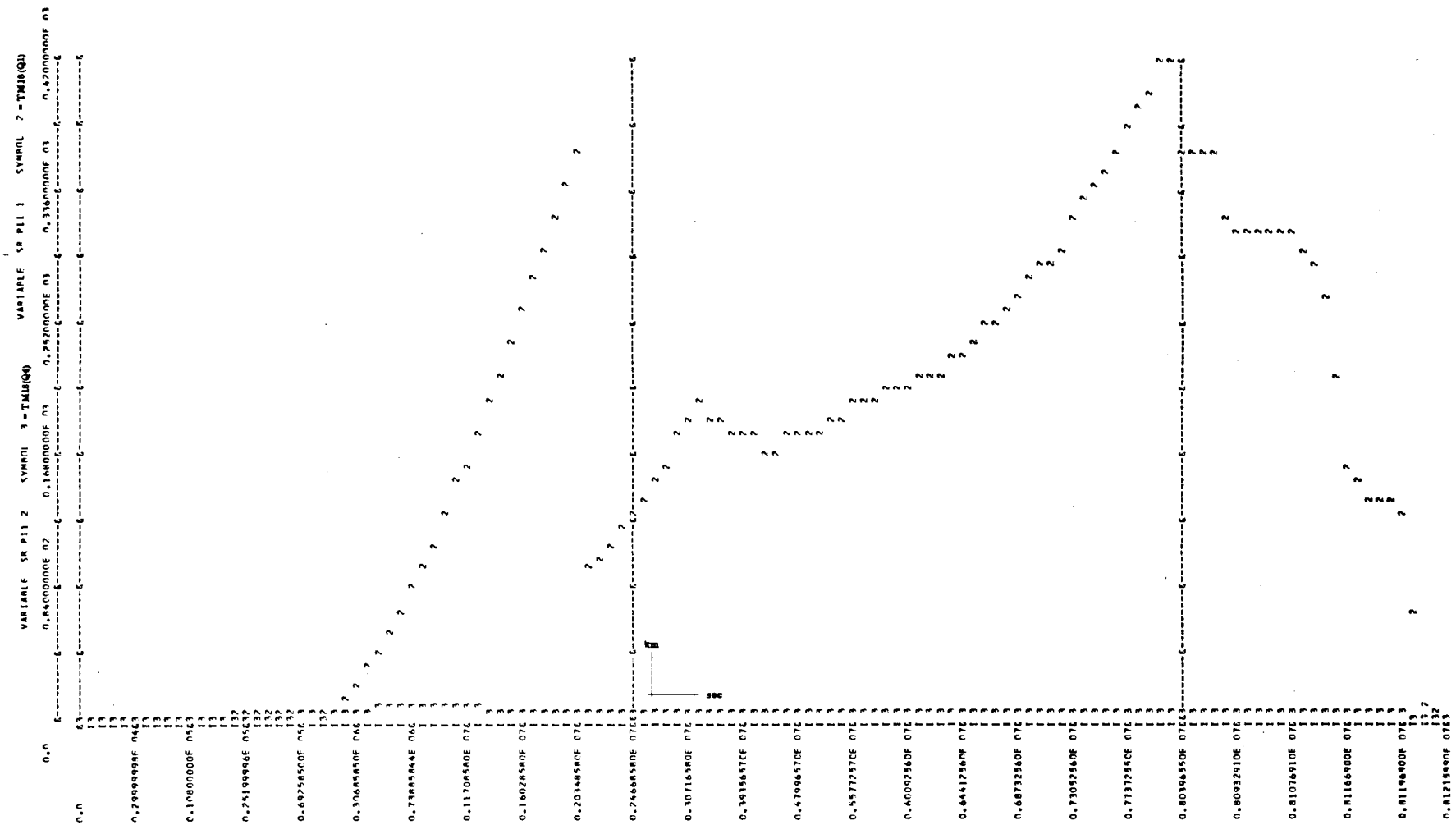

Figure B-70. Behavior of $\sqrt{P11}$ as a Function of Q - System Configuration TM18 (Similar Behavior for $\sqrt{P22}$, $\sqrt{P33}$)

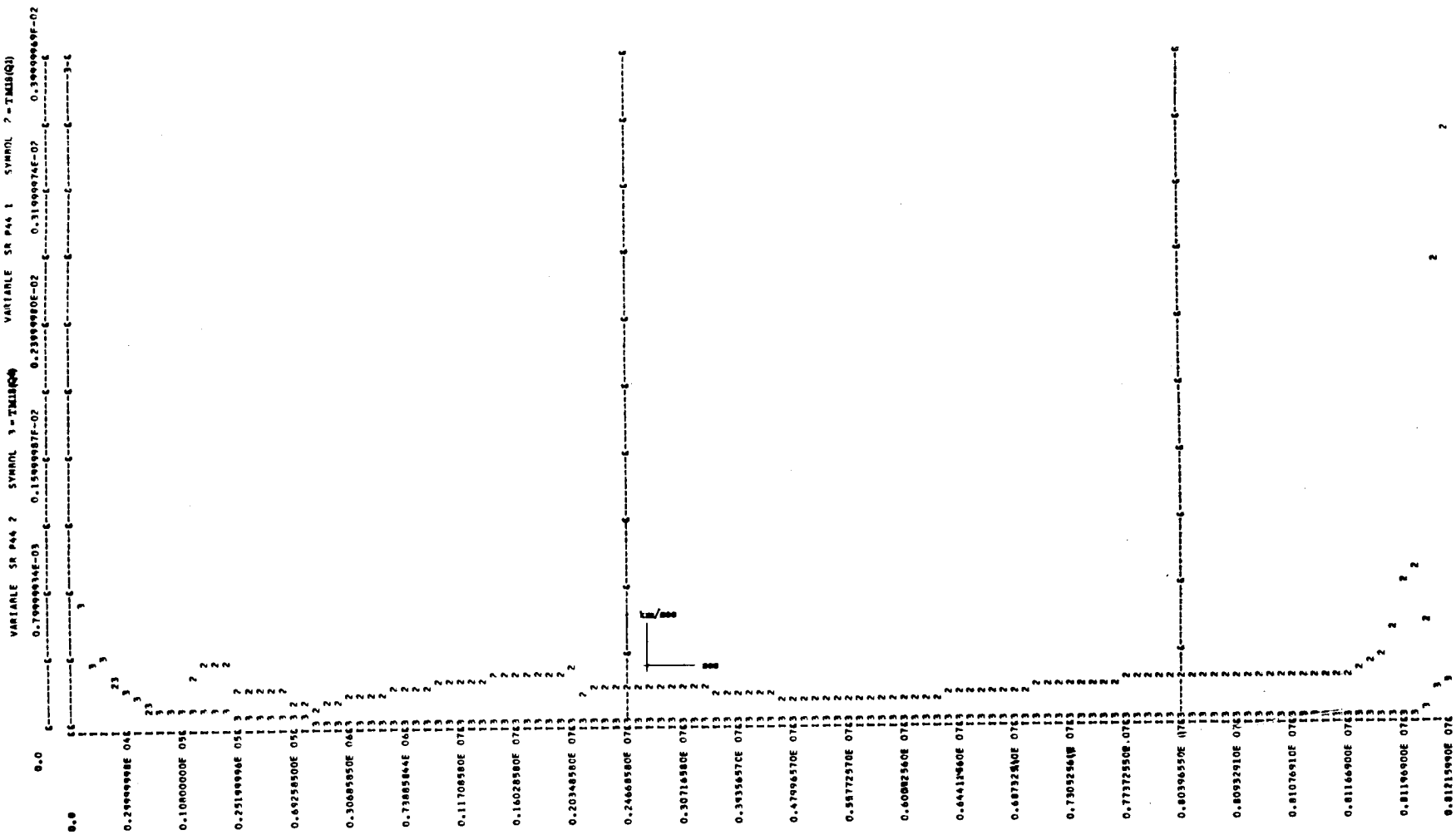

Figure B-71 Behavior of $\sqrt{P44}$ as a Function of Q - System Configuration TM18
(Similar Behavior for $\sqrt{P55}$, $\sqrt{P66}$)

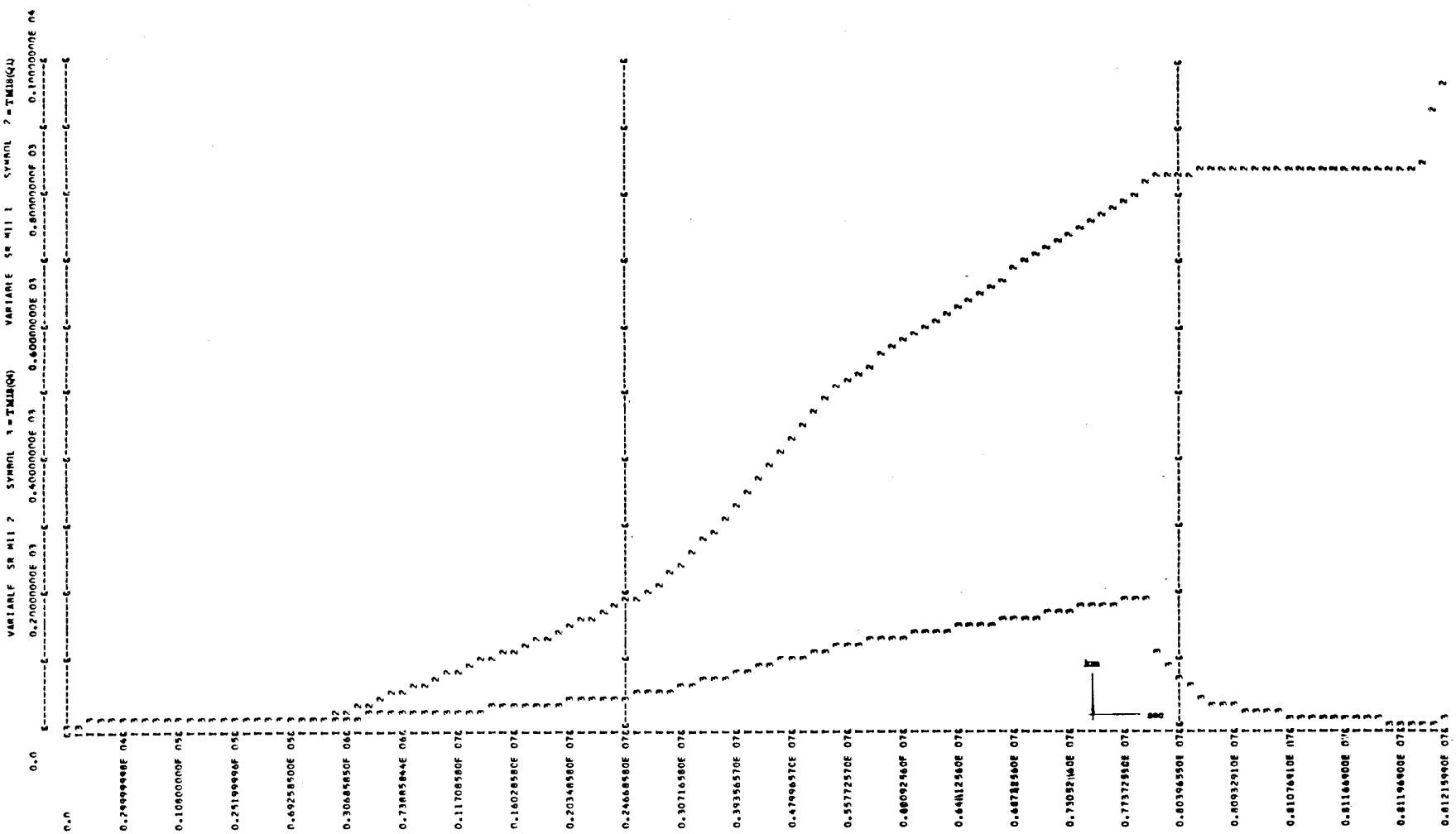

Figure B-72. Behavior of $\sqrt{M11}$ as a Function of Q - System Configuration TM18 (Similar Behavior for $\sqrt{M22}$, $\sqrt{M33}$)

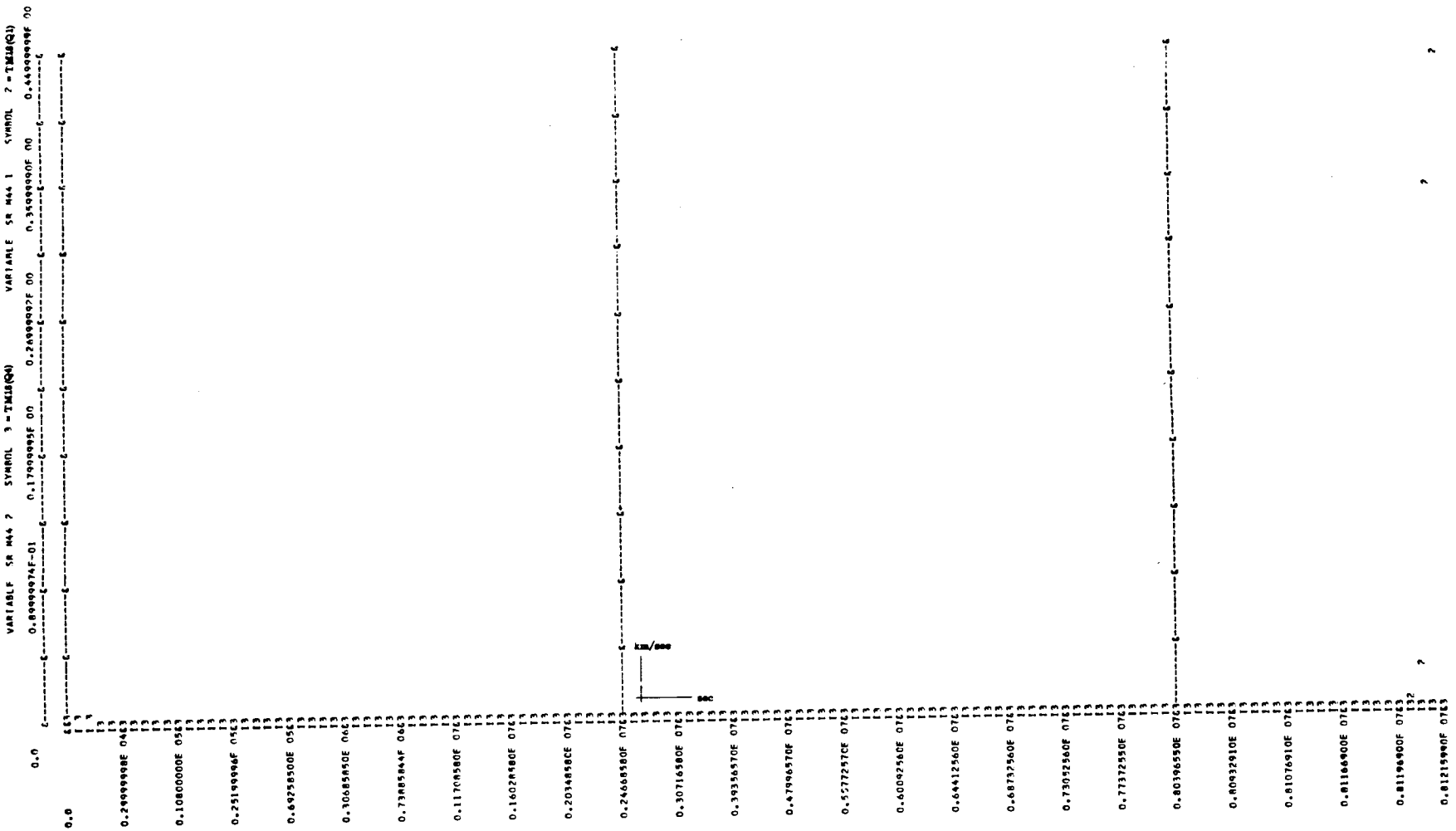

Figure B-73, Behavior of $\sqrt{M44}$ as a Function of Q - System Configuration TM18
(Similar Behavior for $\sqrt{M55}$, $\sqrt{M66}$)

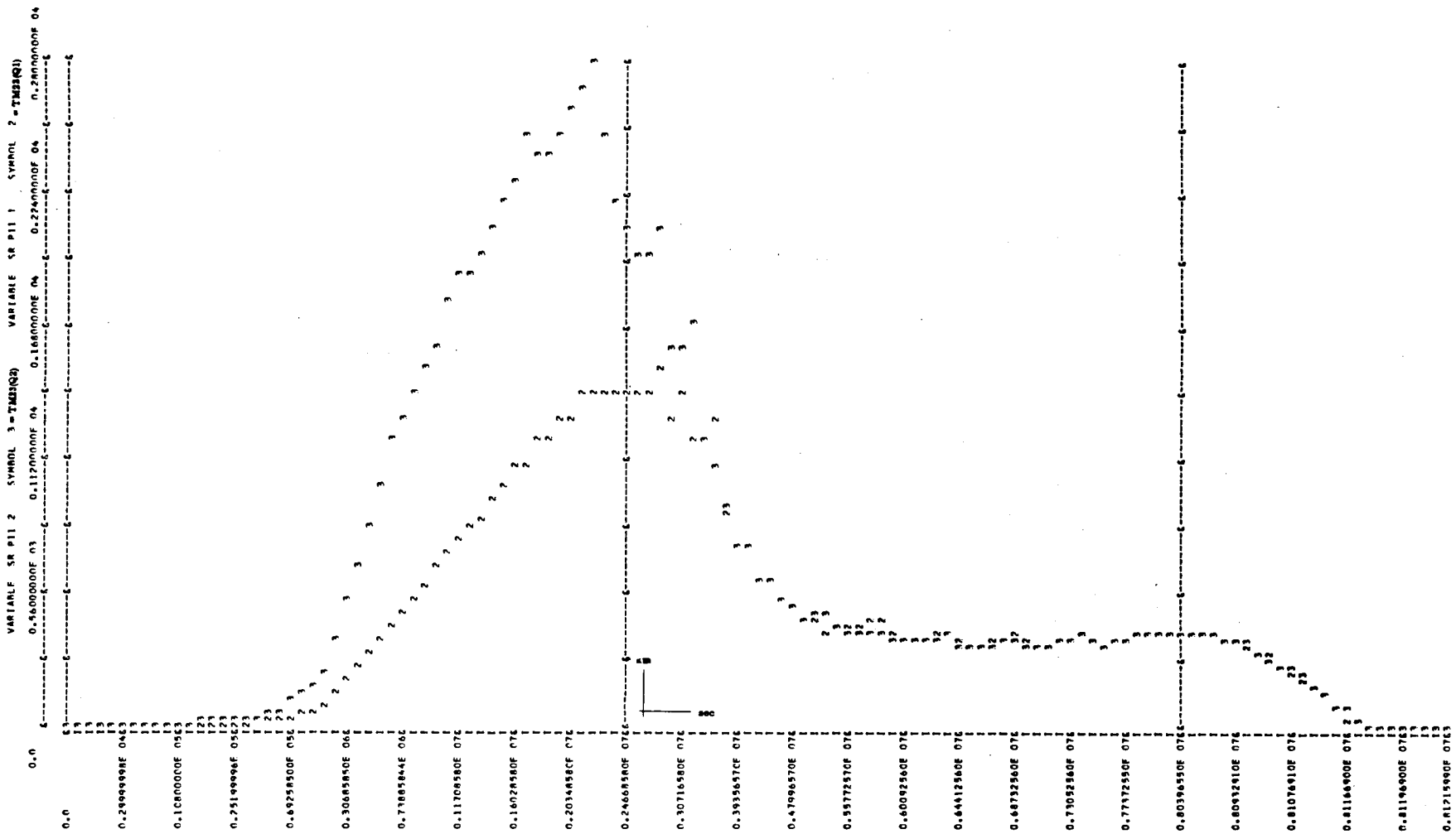

Figure B-74. Behavior of $\sqrt{P11}$ as a Function of Q - System Configuration TM23
(Similar Behavior for $\sqrt{P22}$, $\sqrt{P33}$)

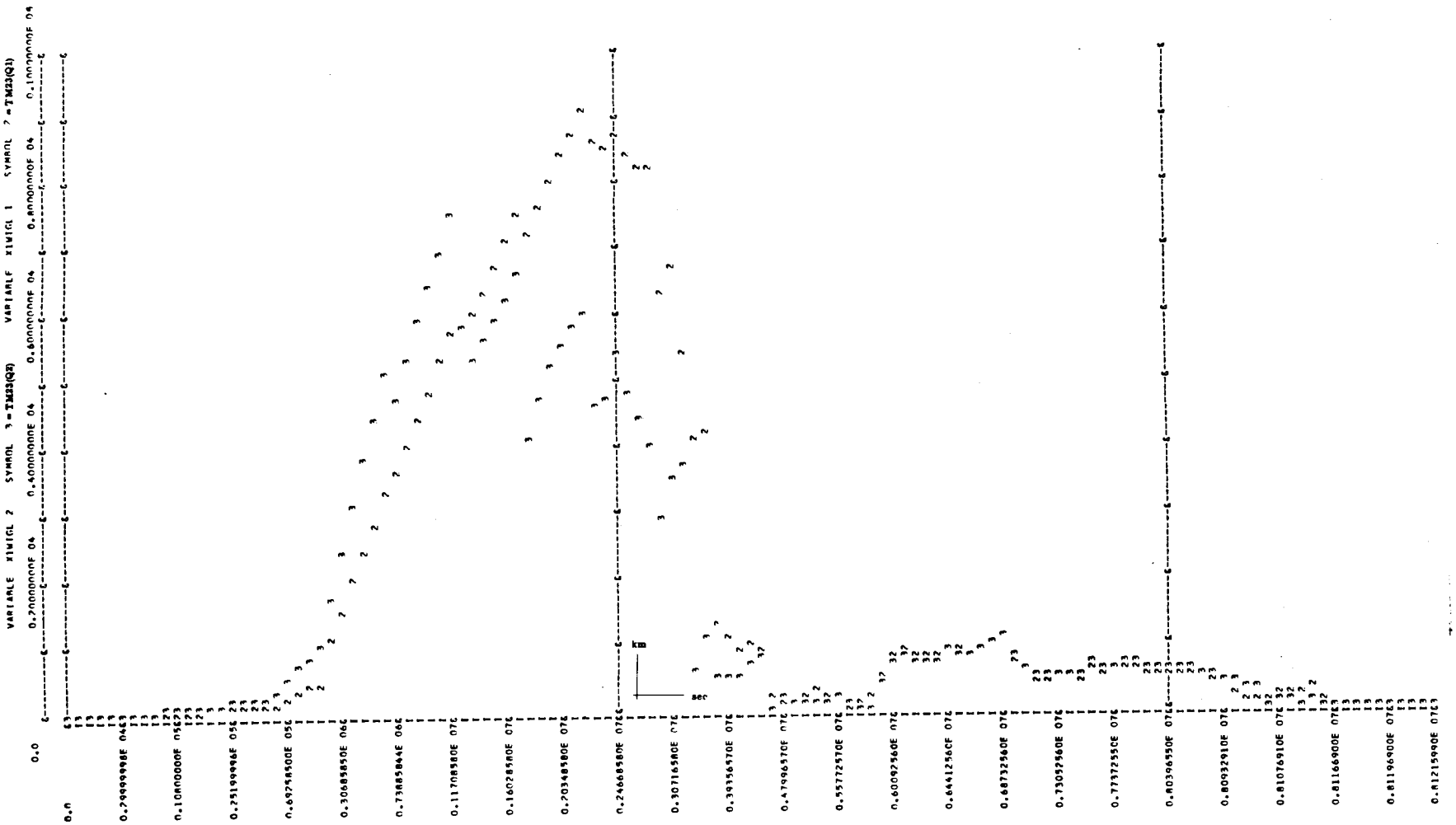

Figure B-75. Behavior of $|\tilde{x}_1|$ as a Function of Q - System Configuration TM23 (Similar Behavior for $|\tilde{x}_2|$, $|\tilde{x}_3|$)

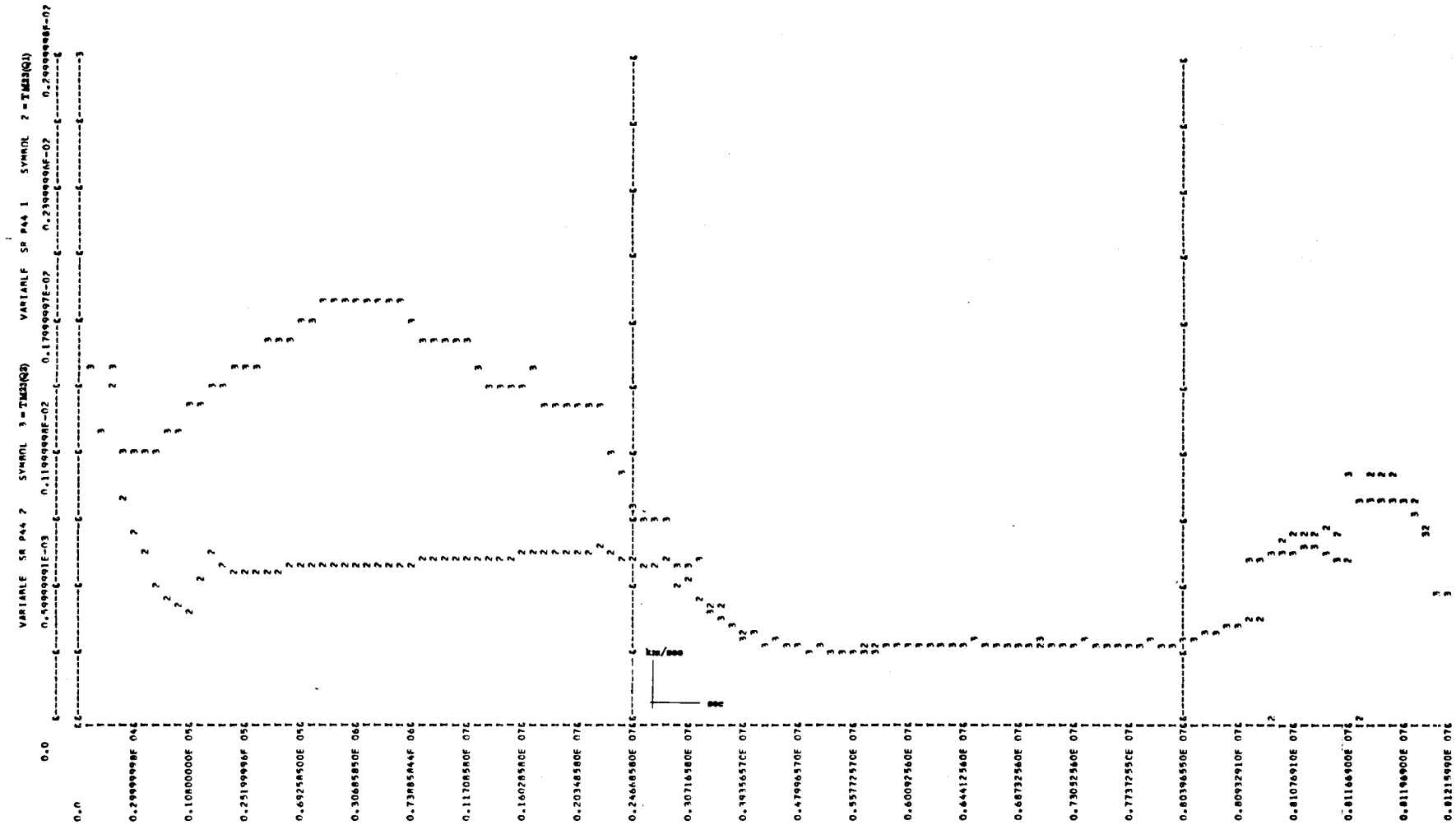

Figure B-76. Behavior of $\sqrt{P44}$ as a Function of Q - System Configuration TM23
(Similar Behavior for $\sqrt{P55}$, $\sqrt{P66}$)

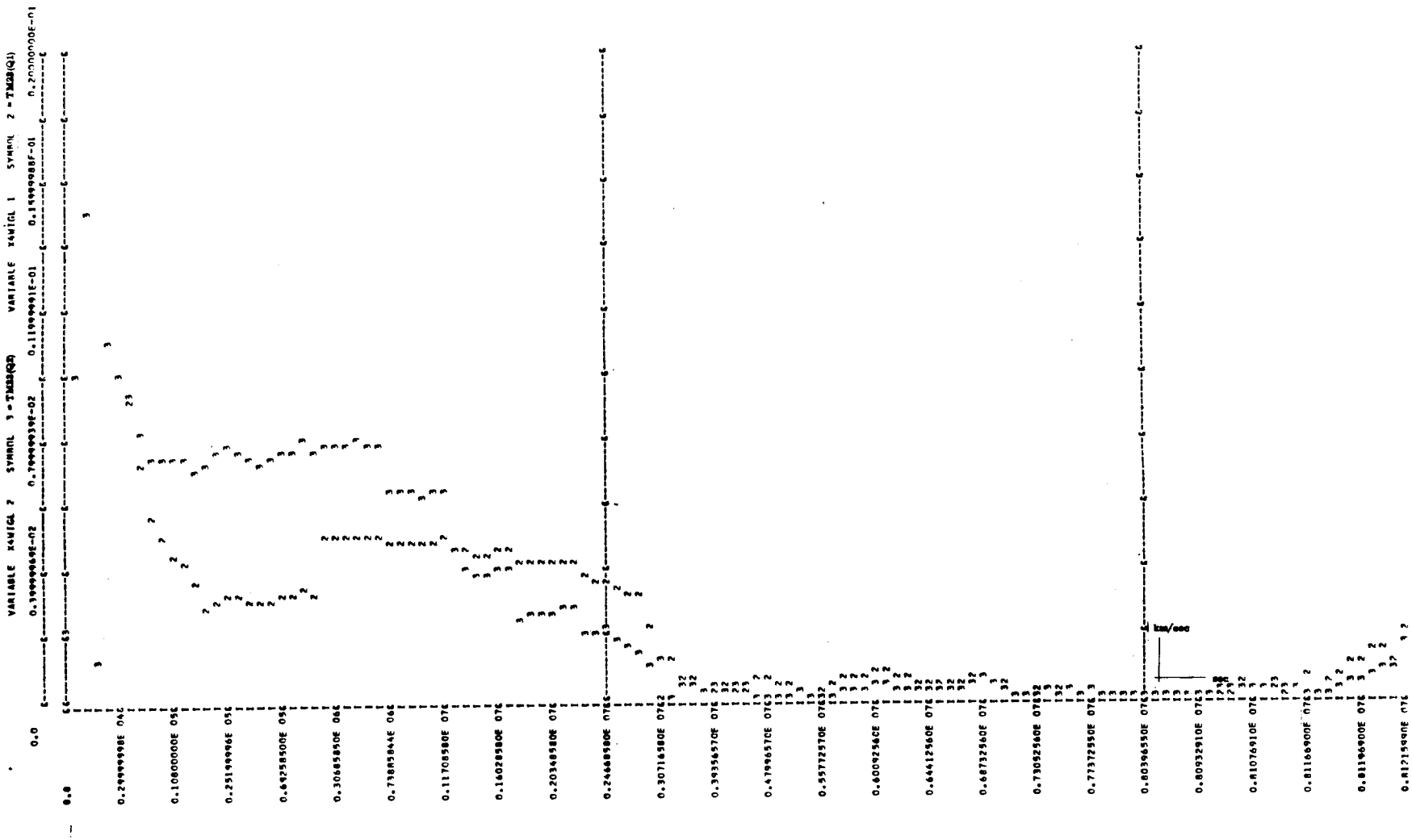

Figure B-77. Behavior of $|\tilde{x}_4|$ as a Function of Q - System Configuration TM23 (Similar Behavior for $|\tilde{x}_5|$, $|\tilde{x}_6|$)

Figure B-78. Behavior of $\sqrt{P11}$ as a Function of Initial Covariance (M) - System Configuration TM19

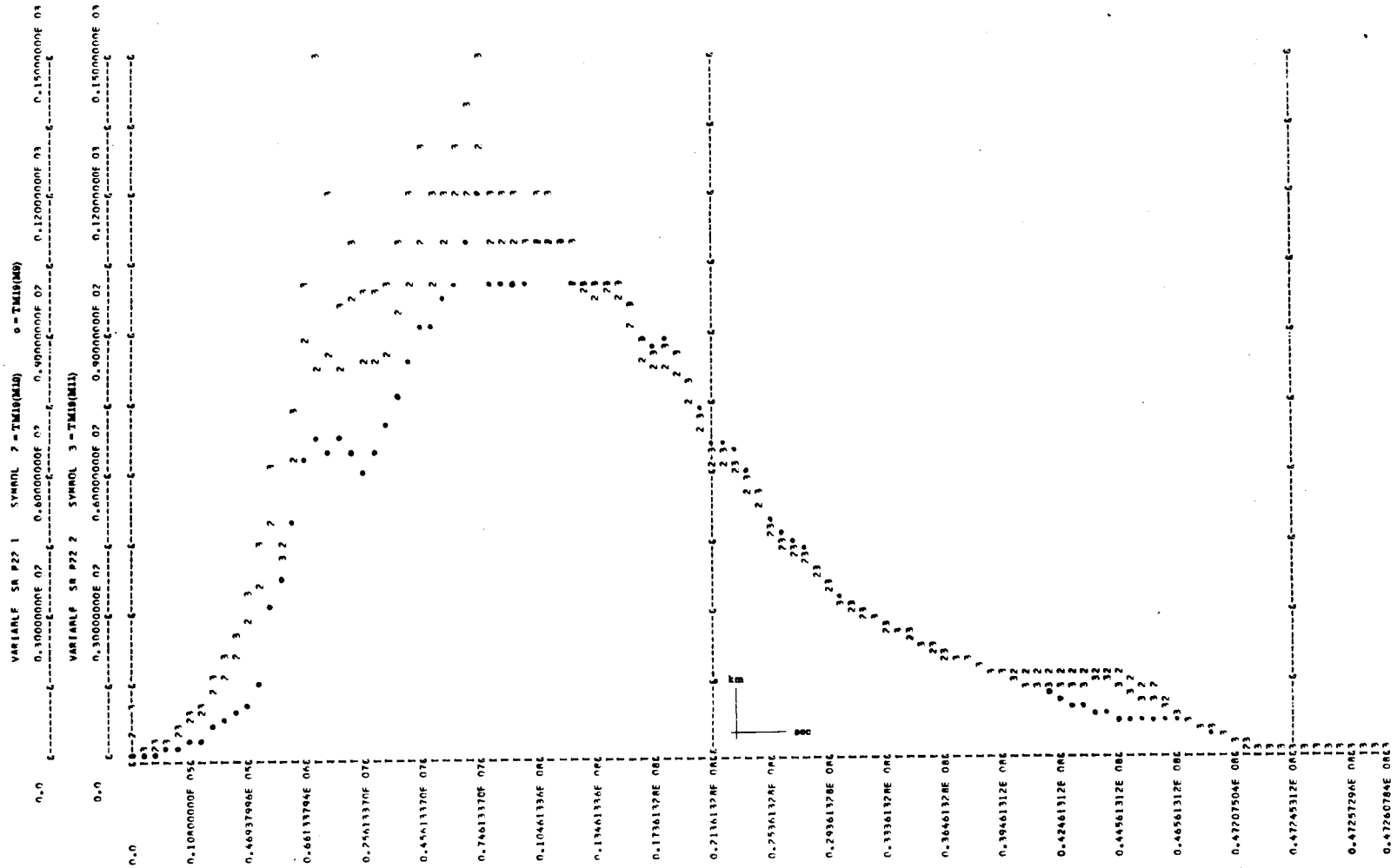

Figure B-78. Behavior of $\sqrt{P22}$ as a Function of Initial Covariance (M) - System Configuration TM19

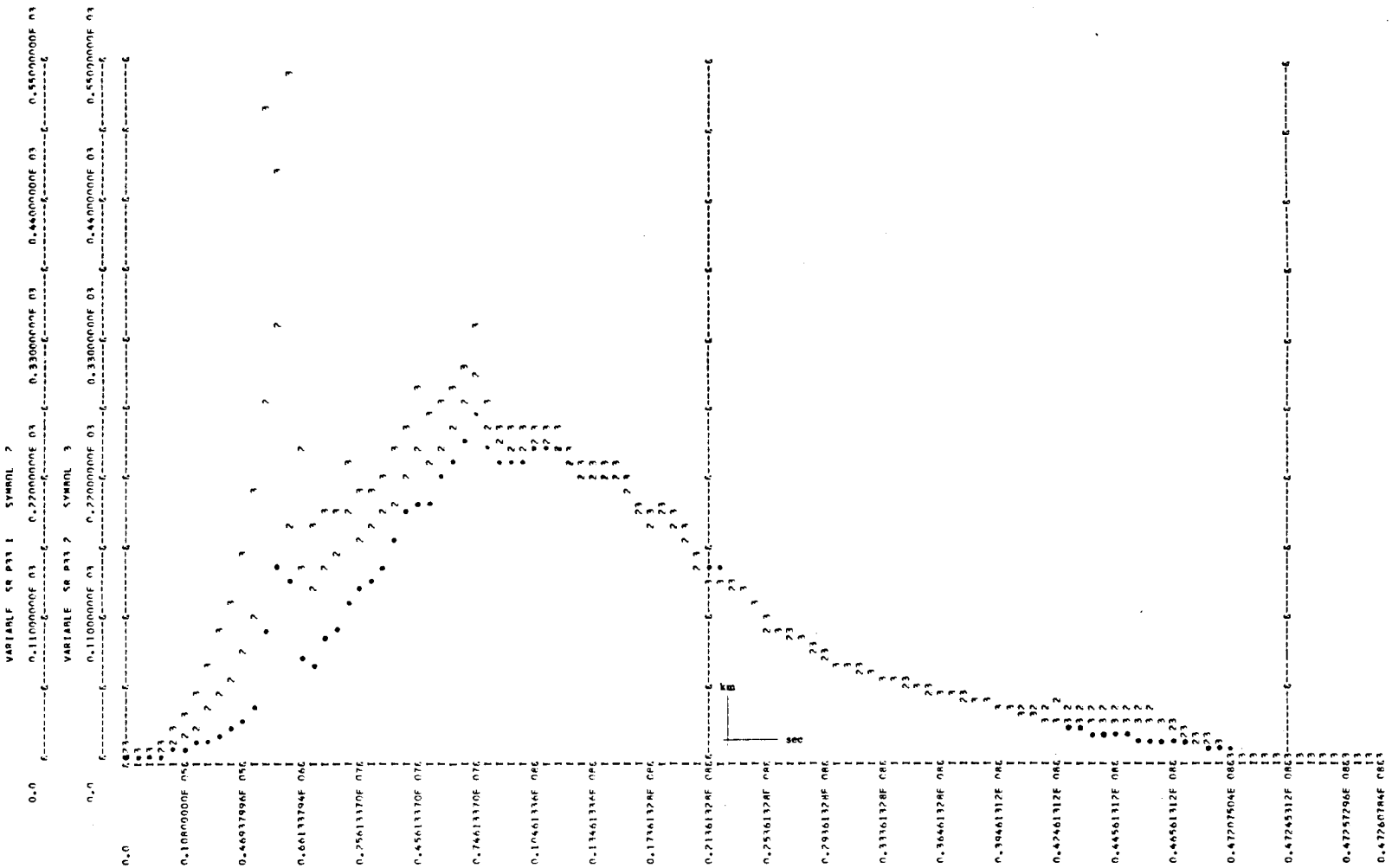

Figure B-80. Behavior of $\sqrt{P33}$ as a Function of Initial Covariance (M) - System Configuration TM19

Figure B-81. Behavior of $\sqrt{P44}$ as a Function of Initial Covariance (M) - System Configuration TM19

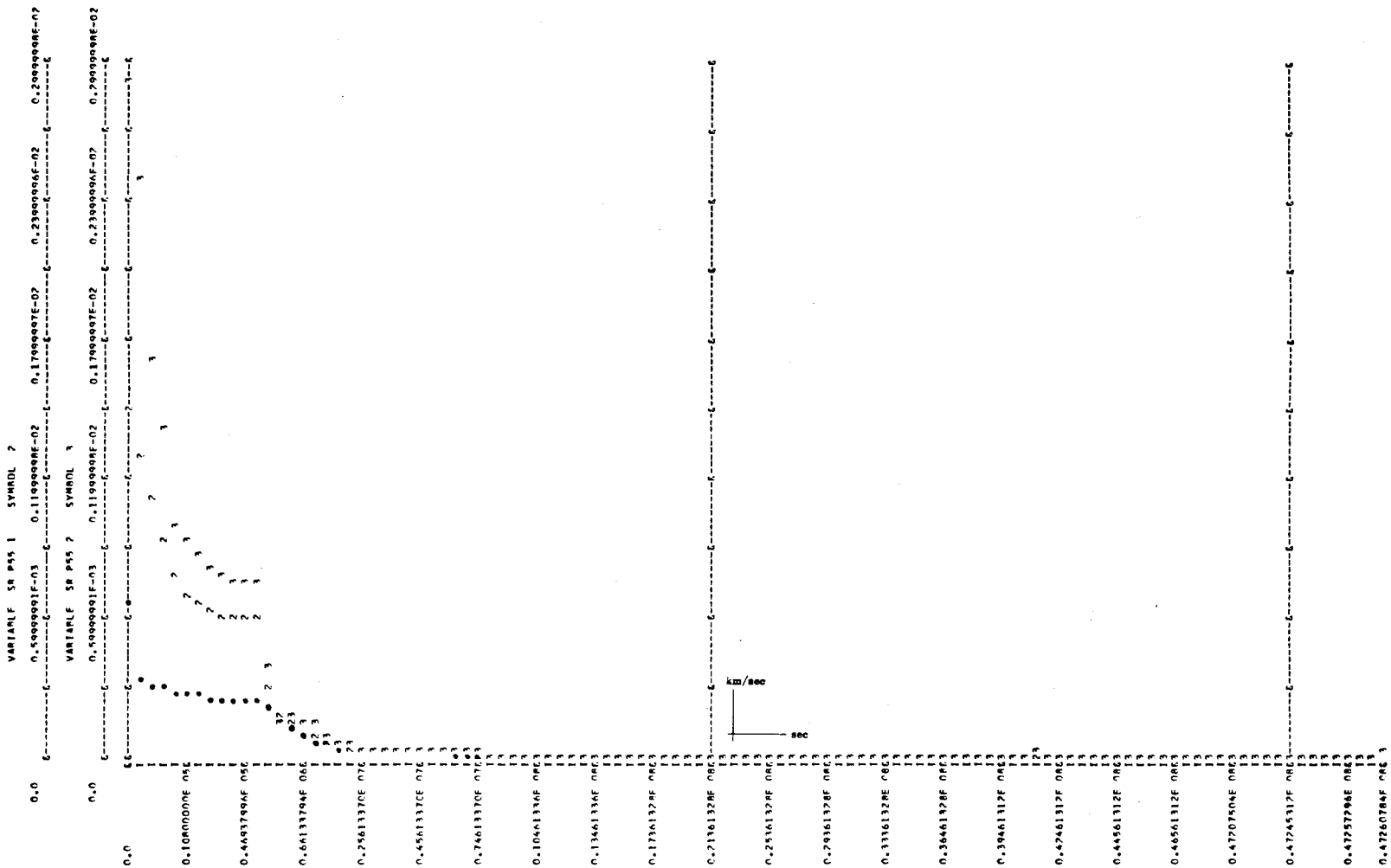

Figure B-82. Behavior of $\sqrt{P55}$ as a Function of Initial Covariance (M) - System Configuration TM19

Figure B-83. Behavior of $\sqrt{P66}$ as a Function of Initial Covariance (M) – System Configuration TM19

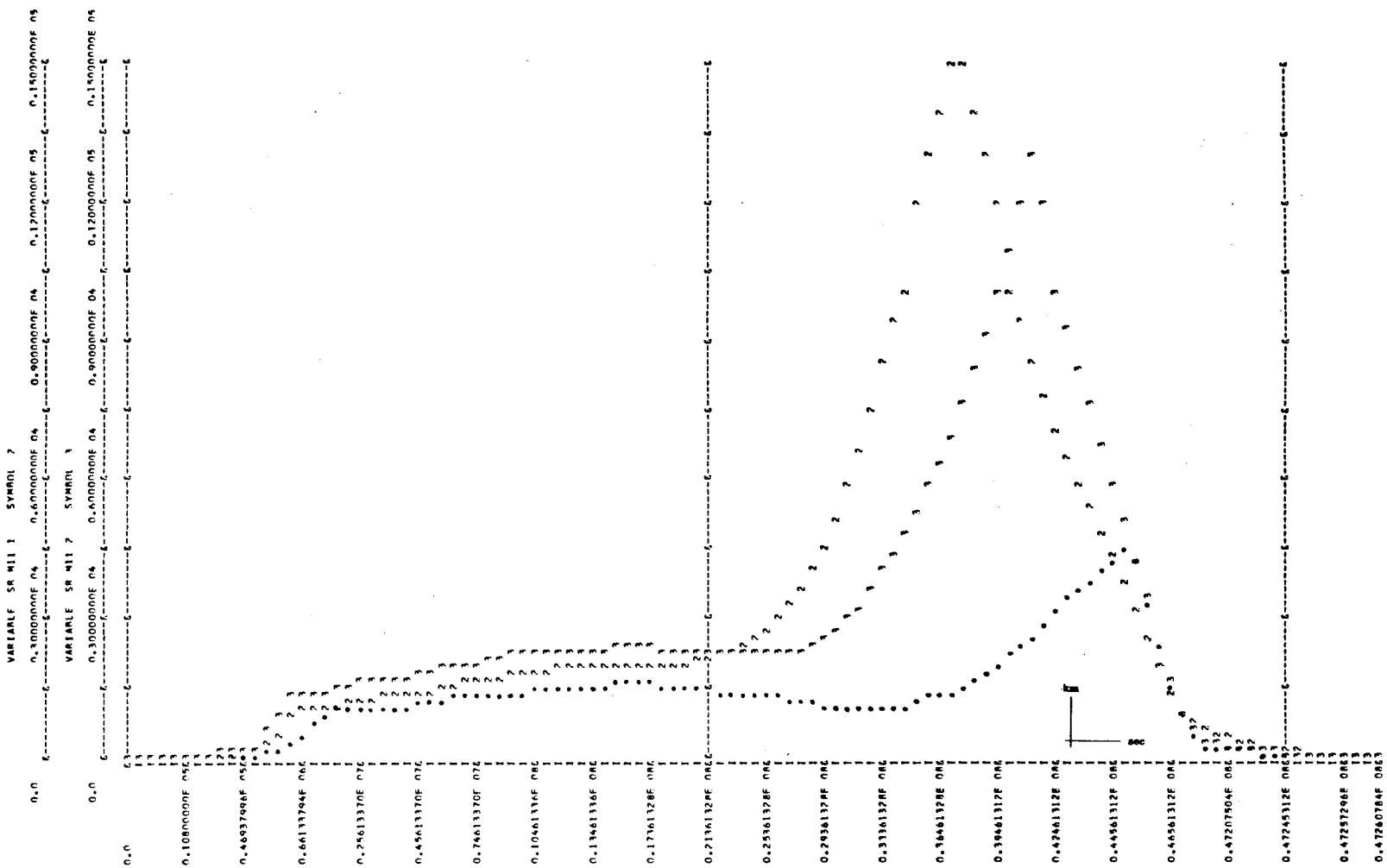

Figure B-84. Behavior of $\sqrt{M11}$ as a Function of Initial Covariance (M) - System Configuration TM19

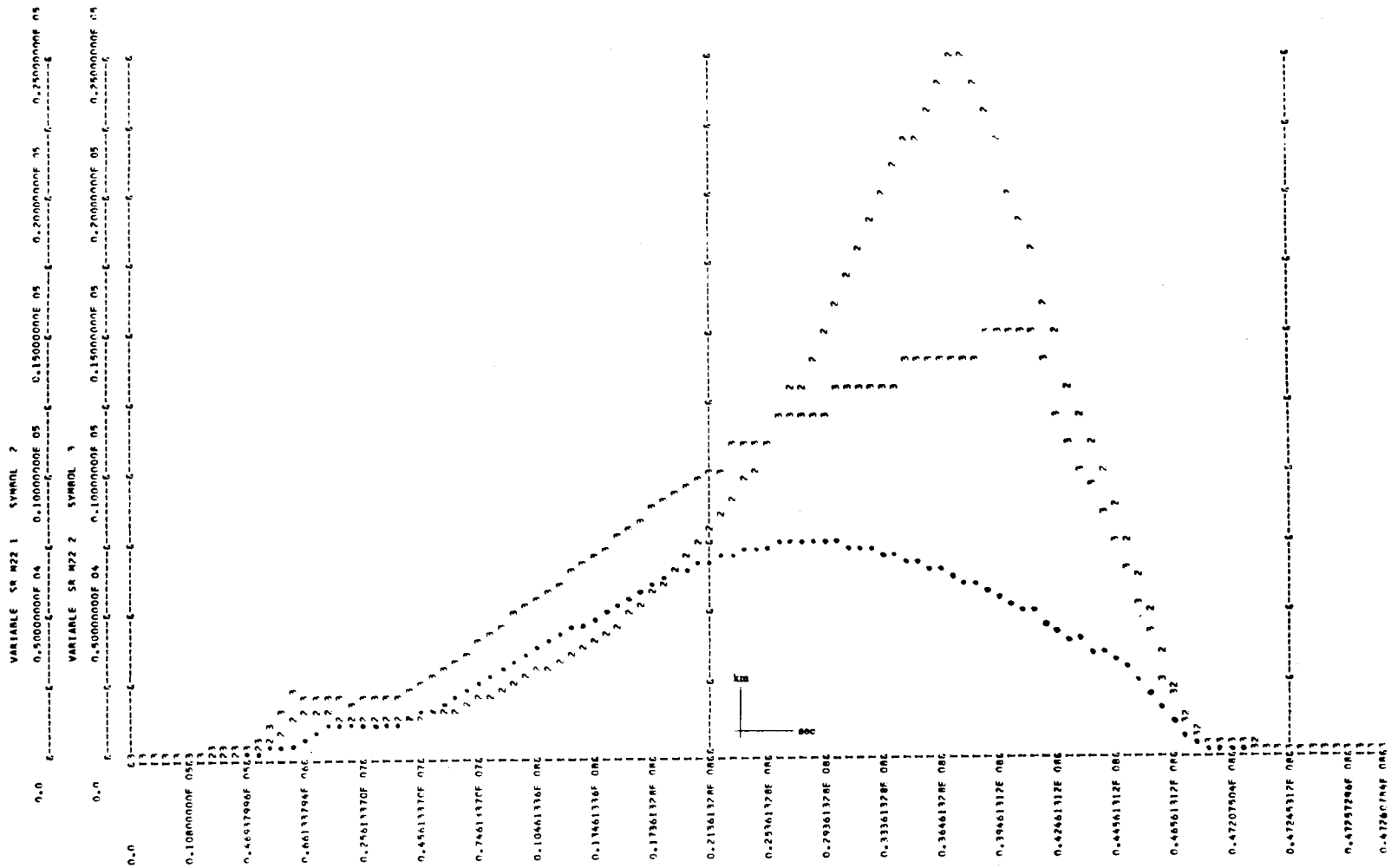

Figure B-85. Behavior of $\sqrt{M22}$ as a Function of Initial Covariance (M) - System Configuration TM19

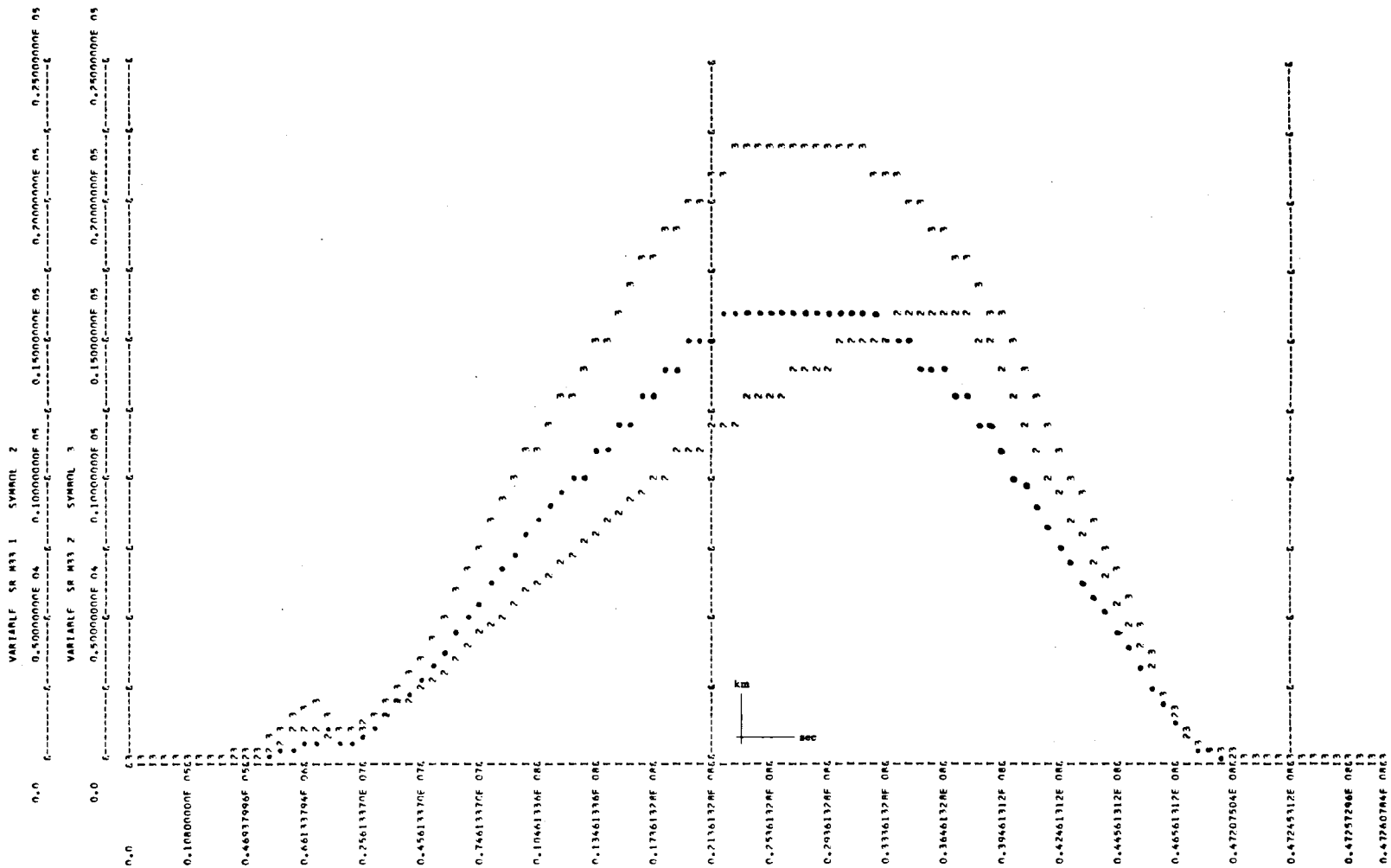

Figure B-86. Behavior of $\sqrt{M33}$ as a Function of Initial Covariance (M) - System Configuration TM19

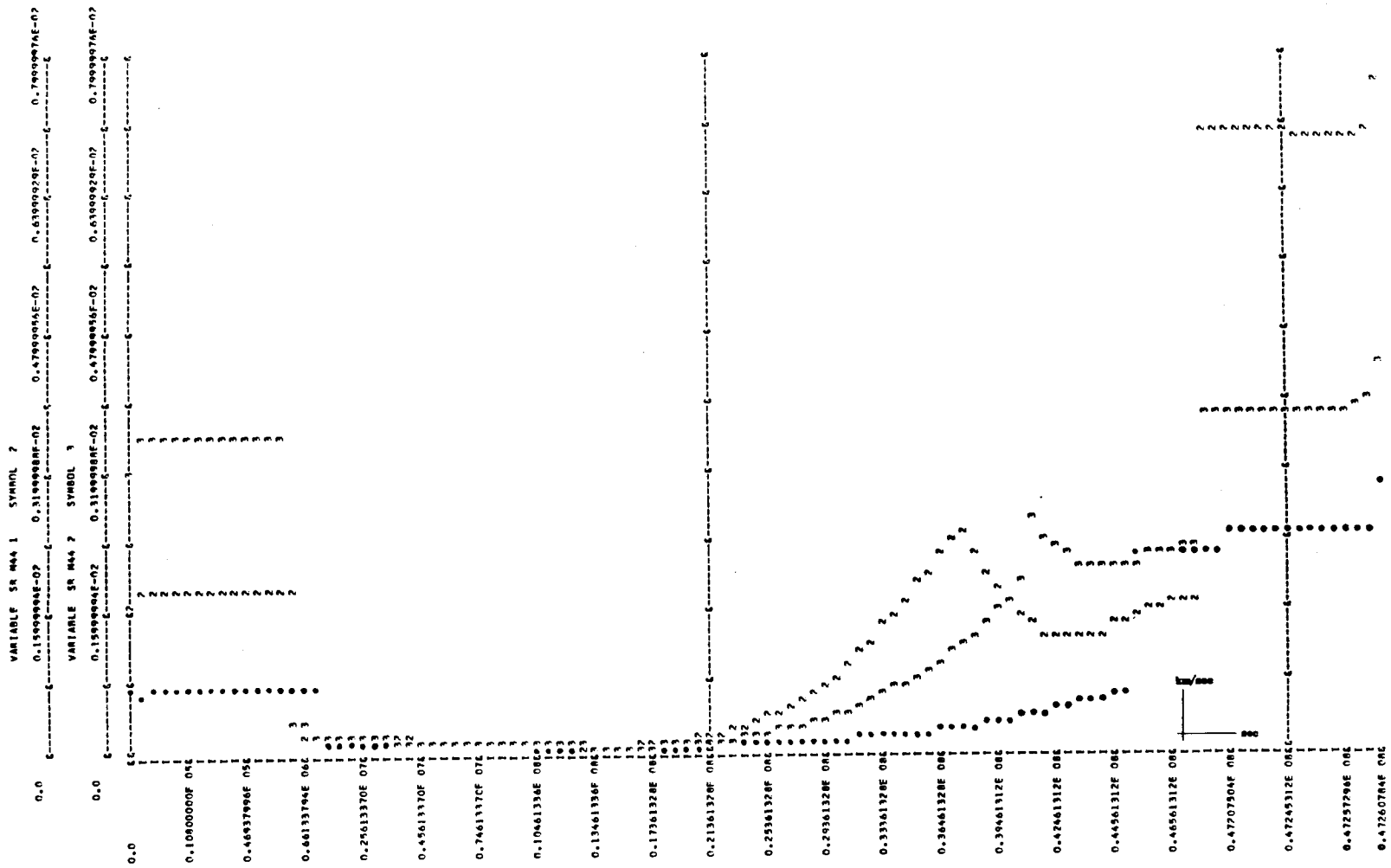

Figure B-87. Behavior of $\sqrt{M44}$ as a Function of Initial Covariance (M) - System Configuration TM19

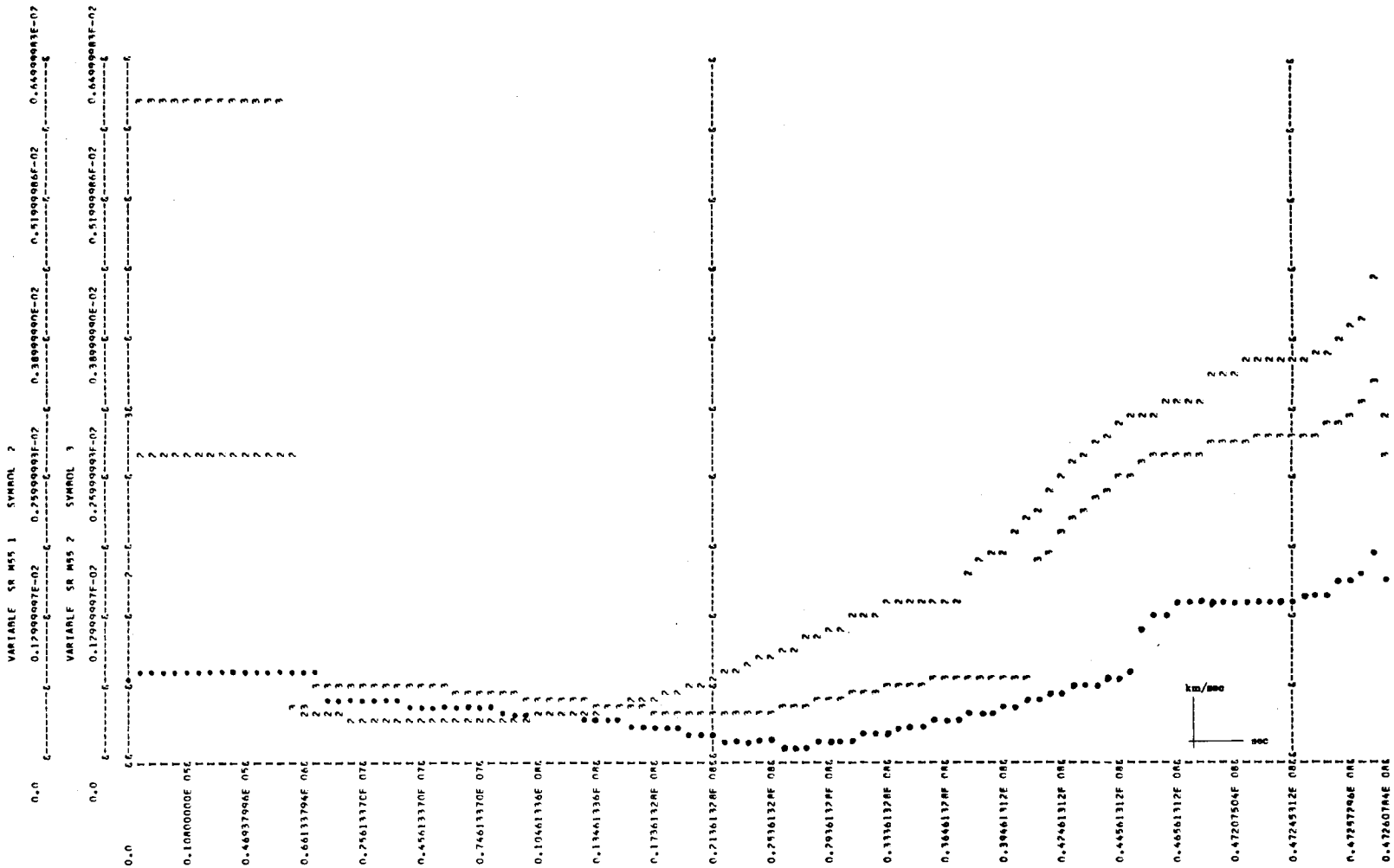

Figure B-88. Behavior of $\sqrt{M55}$ as a Function of Initial Covariance (M) - System Configuration TM19

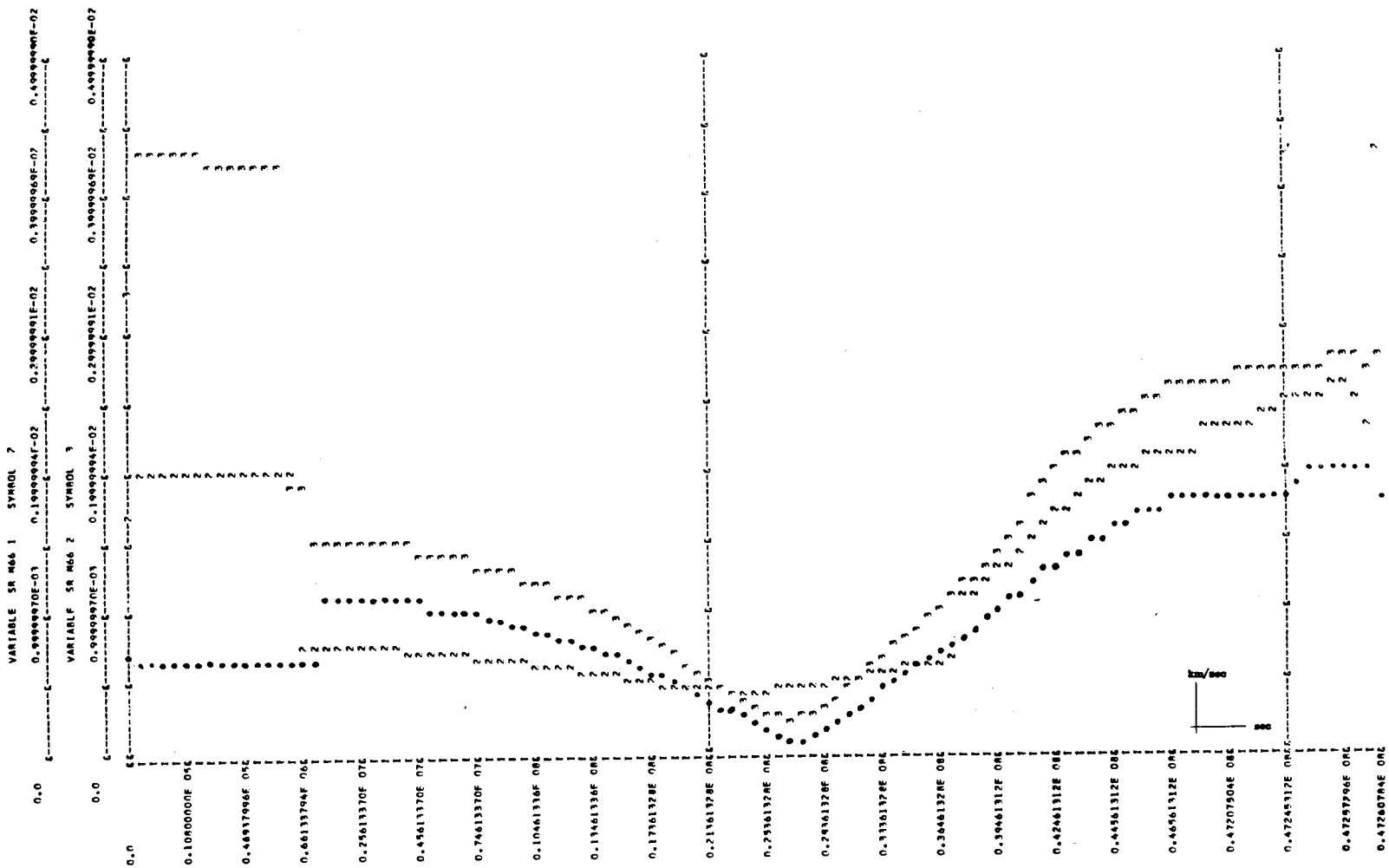

Figure B-89. Behavior of $\sqrt{M66}$ as a Function of Initial Covariance (M) - System Configuration TM19

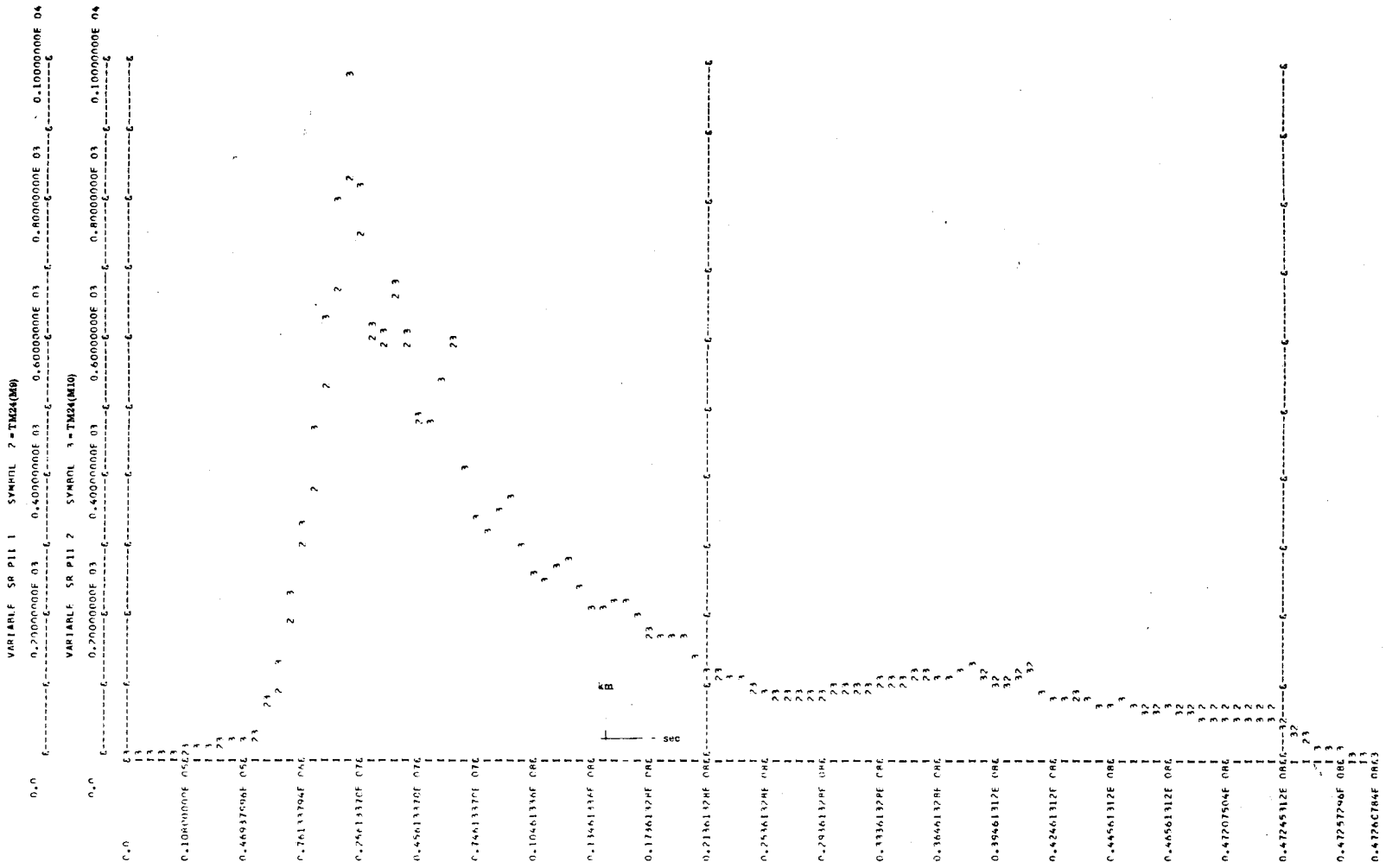

Figure B-90. Behavior of $\sqrt{P11}$ as a Function of Initial Covariance - System Configuration TM24)
(Similar Behavior for $\sqrt{P22}$, $\sqrt{P33}$)

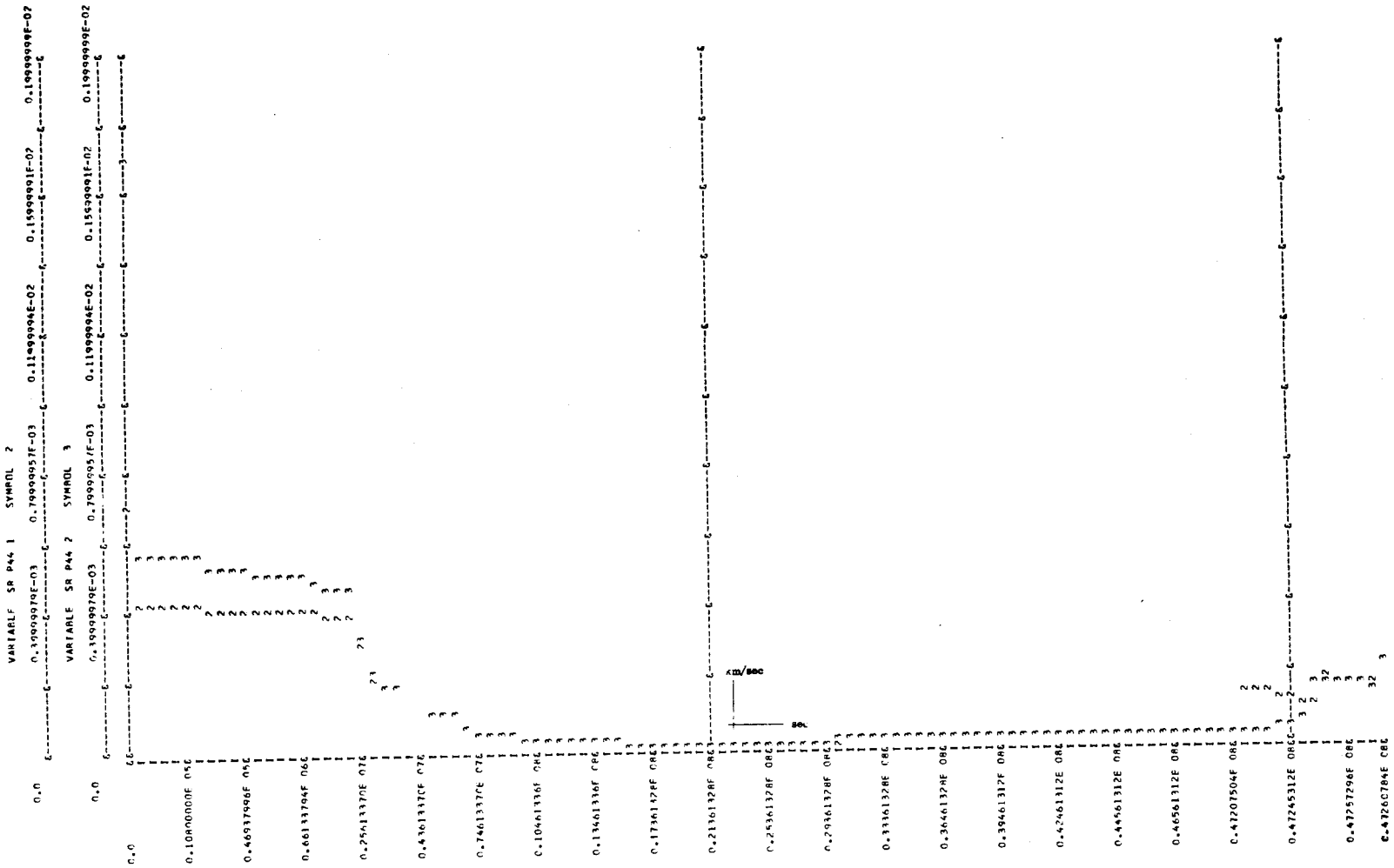

Figure B-91. Behavior of $\sqrt{P44}$ as a Function of Initial Covariance - System Configuration TM24 (Similar Behavior for $\sqrt{P55}$, $\sqrt{P66}$)

SECTION II

PERFORMANCE ASSESSMENT OF NAVIGATION AND GUIDANCE SYSTEMS FOR ATMOSPHERIC ENTRY PHASES

Atmospheric entry trajectories for landing at a planet, for changing the direction of a free-fall trajectory by passing through a planet's atmosphere, or for determining a planet's atmospheric density by measuring the atmosphere's effect on the trajectory—these are the interplanetary mission phases considered in this study. This portion of the appendix contains the trajectory information, parameter definition for the navigation and guidance systems, and time histories of navigation variables from selected simulation runs for the studies reported in Paragraph 3.2 of Volume I. In addition, studies of entry corridors at Earth and at Mars for different vehicles, control modes, and Martian atmosphere models are reported here.

2.1 ATMOSPHERIC ENTRY GUIDANCE AND NAVIGATION PRIOR TO LANDING

2.1.1 ALL-INERTIAL NAVIGATION FOR EARTH-ENTRY PERFORMANCE STUDIES

Earth-entry trajectories, both direct and skipout, were used to perform statistical performance assessment studies of four inertial navigation systems. These four systems, two gimballed and two strapdown, are defined in Tables B-16 and B-17. The four reference entry trajectories are defined in Table B-18. The study results are reported in Paragraph 3.2.2.1.1.3 of Volume I.

2.1.2 EMS NAVIGATION FOR EARTH ENTRY PERFORMANCE ASSESSMENT STUDIES

Electromagnetic sensors, such as horizon scanners, radio altimeters, and ground trackers (DSIF) can provide navigation capability on atmospheric entry trajectories if near-future technology provides the capability for electromagnetic propagation through the ionized atmosphere about the entry vehicle. Navigation system assessment studies of such systems are reported in Paragraph 3.2.2.1.3 of Volume I. The nominal trajectory parameters, Table B-19, and the navigation and guidance system parameters, Tables B-20 through B-24 are presented here.

A set of graphs showing the time history of the following navigation parameters is presented in Figures B-94 through B-102.

DELR	(km)	The position deviation from nominal
ACCEL*	(km/s^2)	The nominal acceleration profile
ACCEL	(g)	The actual acceleration profile
ALPHCON	(rad)	Control perturbation in pitch
PHICON	(rad)	Control perturbation in roll
XTIL	(km)	Error in best estimate of the X-component of position deviation
YTIL	(km)	Error in best estimate of the Y-component of position deviation
ZTIL	(km)	Error in best estimate of the Z-component of position deviation
XDOTIL	(km/s)	Error in best estimate of X-component of velocity deviation
YDOTIL	(km/s)	Error in best estimate of Y-component of velocity deviation
ZDOTIL	(km/s)	Error in best estimate of Z-component of velocity deviation
ZDOTSIG	(km/s)	Standard deviation of best estimate of X-component of velocity
YDOTSIG	(km/s)	Standard deviation of best estimate of Y-component of velocity
ZDOTSIG	(km/s)	Standard deviation of best estimate of Z-component of velocity

These graphs were made by using an option of the performance assessment for run number 3003, whose defining parameters are given in Table B-20.

Studies were also made to determine the effectiveness of estimating the aerodynamic coefficients of the entry vehicle when noise is superimposed upon the perturbative control. Run 3005 (Table B-20) is an example from this study. Figures B-101 through B-111 show the time history of navigation parameters, including the error in the best estimate for the drag coefficient C_D and the lift coefficient C_N.

2.2 GUIDANCE AND NAVIGATION PERFORMANCE ASSESSMENT STUDIES FOR ATMOSPHERIC BRAKING MANEUVER AT MARS

Atmospheric braking maneuver at Mars, as a means of changing a free-fall trajectory by passing through the Martian atmosphere, was a mission phase used for performance assessment studies of navigation and guidance systems that use electromagnetic sensors. The study results are reported in Paragraph 3.2.3 of Volume I. The nominal trajectory parameters are shown in Table B-25. The guidance and navigation parameters are given in Table B-26. Figure B-114 through Figure B-122 are computer plots of navigational parameter time histories of run 601.

WEIGHTING MATRICES FOR Λ MATRIX GUIDANCE DURING ATMOSPHERIC ENTRY

This section describes a procedure for choosing the weighting matrices used by Λ-matrix guidance, based on the experience gained in the use of the reentry performance assessment program in the atmospheric braking mission phase. The weighting matrices consist of control matrices, W_c^U, and state matrices, W_c^X. Both types are positive definite, symmetric matrices and have dimensions of 2×2 and 6×6, respectively.

As described in the guidance section of the mathematical model of the program description Performance Assessment of Atmospheric Entry Guidance Systems, Volume II, Part 7, it is the function of the guidance system to minimize the quadratic performance index

$$V_N = \sum_{i=1}^{N} (\underline{u}_{i-1}^T W_{i-1}^U \underline{u}_{i-1} + \underline{x}_i^T W_i^X \underline{x}_i)$$

where

$\underline{u}$ is the perturbative control vector with components $\delta\alpha$ and $\delta\varphi$, and

$\underline{x}$ is the six-dimensional state vector of perturbative position and velocity.

It is intuitively clear, and has been verified by simulations, that it is the relative size of the elements of the weighting matrices that is important; i.e., if all the elements were magnified by a constant, the guidance law matrices would be unchanged. To date, only diagonal elements of the weighting matrices have been nonzero which means that the summation has terms like

$$W(11)_o^U \, \delta\alpha_o^2$$

for control,

$$W(11)_1^X \, x_1^2$$

for position component deviations, and

$$W(44)_1^W \, \dot{x}_1^2$$

for velocity component deviations. Since the summation of terms of this type are minimized, it can be seen that the larger the element of the weighting matrix is, the smaller must be the quantity it multiplies. Assignment of the relative weights to control, position, and velocity deviations is described by means of the following example.

It is desired to weight 1 degree perturbative control equally with 1 km in position deviation and 1 m/sec deviation in velocity when calculations are done in units of rad, km, and km/sec, respectively. If the elements of the weighting matrices corresponding to position are arbitrarily chosen as 1, then the product of these elements and 1 km is equal to 1. The other types of elements of the weighting matrix must be chosen so that

$$W(11)_o^U \, \delta\alpha_o^2 = 1 \quad \text{or} \quad (.01745)^{-2} (.01745)^2 = 1$$

$$W(11)_o^U = .01745^{-2}$$

and

$$W(44)_1^X \, \dot{x}^2 = 1 \quad \text{or} \quad (1 \times 10^6)(1 \times 10^{-3})^2 = 1$$

therefore

$$W(44)_1^X = 1 \times 10^6$$

In many cases it is desirable that the terminal deviations in position be small as compared to values at other times. This can be accomplished by weighting the position elements of the weighting matrices at that time higher than at other times.

The choice of weighting matrices is further complicated by the fact that a given amount of control effort has different amounts of effectiveness throughout the trajectory as a function of dynamic pressure and location in the trajectory. That is, a 1-degree change in roll angle is more effective near the peak g portion of the trajectory than later in the mission. Similarly, a small correction near the beginning of the entry trajectory may be more effective than a large one near the terminal point. As a consequence of the minimization of the performance index, the control effort during the higher aerodynamic loading portions of the trajectory would be larger than at other times (even if the weighting matrices were constant throughout the trajectory). In practice, however, it may be desirable to expend more control effort toward the end of the trajectory when the navigation has reduced state uncertainties. In addition, if aerodynamic surfaces were used to change the attitude of the vehicle, the amount of control effort may not be important and the weighting matrices would be used to assure that the control both lies within the linear range and has sufficient magnitude during the late stages of the entry to correct the trajectory terminal conditions.

Reference to Figure B-115 will indicate that the aerodynamic deceleration for this atmospheric braking trajectory reaches a peak about halfway through the trajectory and that its profile is nearly symmetric. The weighting matrices that were used to generate the guidance law matrices are shown in Table B-26 as WXII and WUIII. Note that the state terminal conditions during the interval $80 < t \leq 120$ are weighted

100 times as high as the state before this time and that the control is weighted much lower. The latter condition is an attempt to generate guidance during latter stages of the trajectory. Notice that the ratio of control weighting matrix elements to the position element changes from 100,000:1 to 100:100 or a factor of 10^5. Figure B-116 shows the resultant large perturbative control that is commanded as a result of this change in ratio.

The 500-series of runs that were made show the terminal position and velocity deviations for different weighting matrices. A not entirely successful attempt was made to keep the navigation errors out of this weighting matrices evaluation by making frequent observations with three ground trackers which always had the vehicle in sight; that is, "transparent earth." Difficulties arose because the variances in the state decreased rapidly due to the use of three accurate aiding instruments. This resulted in a low weighting of the observations made by the aiding instruments. If the best estimate of the state were degraded after this point by a violation of the linear theory (for example, a large perturbative control was commanded), the statistics describing the uncertainty in the state would not recognize this and the observations by the aiding instruments would continue to hold little weight. A much more effective means of separating the guidance and navigation modes, requiring a change to the program, consists of replacing the best estimate of the state as computed in the navigation block with the deviation from the nominal trajectory. This could be done on an optional basis and used only to evaluate the weighting matrices.

The choice of weighting matrices is dictated to a certain extent by the magnitude of the initial deviations from the nominal trajectory. The evaluation of the weighting matrices must be accomplished using a number of different initial state deviations and, in particular, these deviations should be as large as can reasonably be expected. This is necessary since the guidance is based on linear theory and if we compare two runs in which the initial state of the second is perturbed by a factor of two over that of the first, the output of the guidance block is changed by this same amount. If the perturbative control in the first case had been marginal as far as remaining linear, the control used during the second run would be well outside the range. Unfortunately, however, if the weighting matrices are based on the larger perturbation, the amount of control effort used during the smaller perturbation is less and, indeed, may fall into the region of noise.

A practical solution is suggested. Choose the weighting matrices so that control is moderate during runs with moderate initial state perturbations and limit the control effort on the runs with large initial perturbations. In addition, introduce plant noise proportional to the magnitude of the control effort as a numerical device to degrade the statistics when larger perturbative controls are commanded resulting in greater weight on the observations made by the aiding instruments. Both of these devices will reduce the error in the estimate of the state at the expense of a minor change to the performance assessment program. The results which are published in this report were made with a program which did not have these modifications.

2.3 EXPLORATION OF PLANETARY ATMOSPHERES

Planetary atmospheric density and/or aerodynamic properties of the entry vehicle can be estimated by measuring the effect these parameters have upon the trajectory as the vehicle passes through the planetary atmosphere. Performance assessment studies of guidance and navigation systems, which have this capability, were performed for several navigation systems which used inertial and EMS sensors. Two reference trajectories were employed and are defined in Table B-27. The guidance and navigation system parameters are given in Table B-28. The study results are reported in Paragraph 3.2.4 of Volume I.

2.4 ENTRY CORRIDORS FOR ATMOSPHERIC ENTRY AT EARTH AND AT MARS

Several studies were performed using the program described in Volume II, Part 6 of the Interplanetary Guidance System Requirements Study. These studies were made to determine the entry corridor width for different vehicles, environments, nominal control philosophies, and control parameters. These corridors were used to help establish initial conditions for the nominal trajectories used in the entry guidance and navigation performance assessment studies and also to establish standards that the midcourse guidance and navigation system must meet during the interplanetary mission phase.

2.4.1 MATHEMATICAL MODEL

The mathematical model simulated in the program used in this study is presented in this section. It can describe the following major mission profiles:

1. Single-pass trajectories. This class encompasses those trajectories in which the vehicle does not leave the atmosphere after having entered it once.
2. Single-skipout trajectories. This class encompasses those trajectories for which two entrances into the atmosphere are linked by a free-fall orbit.

In addition to these two major classes, the model provides the possibility of describing other trajectories such as those encountered in atmospheric braking maneuvers. The latter can be simulated by starting the program in phase 3. The entry trajectory profile is divided into 7 phases, but the starting point of the simulation can start in any of these.

The different phases, as numbered in Figure B-123 are defined as follows.

Phase 1: Initial entry phase. A "constant" roll angle control policy is used during this phase. The sign of the roll angle is allowed to change so that the vehicle will remain sufficiently near to its initial trajectory plane.

Phase 2: Constant altitude phase. The roll angle is changed such that the vehicle maintains constant altitude.

Phase 3: Pullout phase. The roll angle is changed according to a prespecified time history. This is done by specifying the coefficients of two second-order polynomials in time. The length of time that the two curve fit control laws are used may be specified. If the vehicle has sufficient speed and if appropriate coefficients are specified, a path is generated such that phase 4 will be entered.

Phase 4: Skipout phase. No trajectory control because thrust is available only for vehicle attitude control.

Phase 5:
Phase 6: Entry and constant altitude phases. The control policies are equivalent to those in phases 1 and 2, respectively.

Phase 7: Final descent phase. The vehicle is kept at constant roll angle. The roll angle can change signs in order to provide out-of-plane control.

A number of basic assumptions were made in the simulation as listed below.

1. Physical Environment. Nonrotating planet with a spherically symmetric gravitational potential and an exponential nonrotating atmosphere constitutes the physical environment.
2. Vehicle Configuration. A rigid lifting vehicle without any thrusting capability outside that required for attitude changes is assumed.
3. Nominal Control. Aerodynamic control is achieved through changes of the roll angle, φ, and angle of attack, α. Control philosophy is dependent upon the scientific phase of the flight and is described in a phenomenological manner in the next paragraph.

2.4.2 NOMINAL CONTROL PHILOSOPHY

The nominal control philosophy, as described in detail in Volume II, Part 6, is summarized here because the re-entry corridor is very dependent on it and its associated parameters.

2.4.2.1 Roll Control

The roll angle of the vehicle is determined by computing a commanded roll angle, φ_c, and requiring the vehicle to rotate from its current to the commanded orientation at an angular rate, ω_φ, which is proportional to the angular difference between the commanded and current orientation. That is

$$\omega_\varphi = K_\varphi (\varphi_c - \varphi)$$

where K_φ is a preselected constant which represents the vehicle response to the control system. The angular rate is limited to another preselected constant, β_φ.

The in-plane control is phase-dependent and is described below.

1. Nominal Control During Phases 1 and 5. φ_c is set to a constant. These phases are terminated on one of two conditions selected by the user:

   a. $\dot{r} = 0$

   b. The earlier of (1) $\dot{r} = 0$

      (2) $\dot{r} \geq C_{vpc} \sqrt{g_o R}$ and $\ddot{r} \leq g_o C_{vpc}$ should be nonpositive

2. Nominal Control During Phases 2 and 6. The roll angle control is given by

$$\varphi_c = \left[\frac{\pi}{2} + \sin^{-1} (K_1 \Delta\dot{r} + K_2 \Delta r) + \frac{\pi}{2} \delta e^{-K_3 (t - T_c)} \right]$$

   This control law provides an in-plane component of normal force required to maintain constant altitude. The gains K_1 and K_2 may either be input, in which case they are constant through the constant altitude phase, or computed as time-varying functions of input values of damping, ζ, and period, τ. The term

$$\frac{\pi}{2} \delta e^{-K_3 (t - T_c)}$$

   can be used to make $|\varphi_c| = \pi$ at the beginning of the constant altitude. This can be helpful in preventing an unintentional skipout.

3. Nominal Control During Phase 3. The roll angle used a variable and is specified as

$$\varphi_c = [F_0 + F_1 (t - T'_c) + F_2 (t - T'_c)^2]$$

   F_0, F_1, and F_2 are appropriate input quantities; T'_c is the time at beginning of pullout phase.

4. Nominal Control During Phase 7. The roll angle is used as a control variable in the same way as in phases 1 and 5.

The out-of-plane control is accomplished by multiplying the commanded roll angle by ±1 where the appropriate value is chosen so as to direct the normal lift vector toward the trajectory plane determined by the initial position and velocity vectors. The sign ±1 is changed when the absolute magnitude of the sine of the angle between the nominal trajectory plane and the velocity vector is greater than ϵ_s, a preselected constant.

2.4.2.2 Angle of Attack Control

The angle of attack (α) may be either held constant or varied for all phases except Phase 4, during which no atmosphere is present. The variation of the angle of attack is referred to as pitch modulation control; α is varied between maximum and minimum values so as to try to make the magnitude of the aerodynamic acceleration (a') attain desired values, a'_{nom}. The aerodynamic acceleration, a', is input for each phase in which α is not constant.

2.4.3 RESULTS OF THE STUDIES

The inputs defining the various studies are presented in Table B-30. A detailed explanation of the symbols used in the headings is presented in Paragraph 3.1.3 of the Nominal Trajectory Program Description (Volume II, Part 6, Version II). A dash indicates that either no input is required or the quantity at the top of the column varies. The Time-Varying Gains refer to ζ_2 and τ_2 (damping ratio and period for Constant Altitude Control) as opposed to K_{21} and K_{22} (constant values of gain).

The environment consists of the sea-level gravitational acceleration of the entry planet (g_o;m/sec^2), the sea-level, atmospheric density (ρ_o;kg/km^3), and the exponential decay factor (β';1/km) of re-entry planet.

The vehicle characteristics consist of the ballistic coefficient (W/C_DA;kg/km^2), nominal angle of attack (α''; radians, not used when pitch modulation is employed). curve fit coefficients for the drag $[C_{Di}(\alpha)]$and lift $[C_{Ni}(\alpha)]$coefficients.

The Nominal Control parameters include the nominal control interval (Δt_G;sec), pseudo-autopilotgain (K_φ),maximum roll rate(β_φ; rad/sec), out-of-plane control (ϵ_s), constant altitude parameters (K_{21}, K_{22}; sec/km, 1/km constant gains, ζ_2, τ_2 (sec); damping ratio and period for calculation of time-varying gains). The parameters controlling pitch modulation are the desired values of aerodynamic deceleration in the first constant attitude phase and the constant altitude phase (a'_{nom}, 5, a'_{nom}, 6; earth g's), and the limits on the range of values the angle of attack (α) may have such that the $C_{Di}C_{Ni}$ curve fit parameters are valid (α_{min}, α_{max}; radians).

The Maximum Corridor Width is the range in λ from overshoot at $\varphi = \pi$ to undershoot at $\varphi = 0$).

The studies are divided into the 5 categories listed below.

2.4.3.1 Entry Corridor Widths As a Function of Entry Velocity ($V-\gamma$)

The corridors shown in the $V-\gamma$ studies (Figures B-124 through B-128 depict the maximum capability of a particular vehicle to enter the planetary atmosphere specified. The upper curve (large values of $|\gamma|$, undershoot boundary, is determined by holding the lift vector up ($\varphi = 0$) during the first constant altitude phase. The lower curve overshoot boundary is obtained by keeping the lift vector pointed down ($\varphi = \pi$) throughout the first phase. When the initial conditions of the vehicle place it above the curve representing the undershoot boundary an aerodynamic deceleration of 10 earth g's will be exceeded at some point on the trajectory.

If the initial flight path angle (γ) is below the overshoot boundary (at a particular entry speed), the vehicle will not remain within the atmosphere.

Employing pitch modulation in the control philosophy increases the corridor width by allowing the vehicle to enter with a larger $|\gamma|$ without undershooting. Since pitch modulation involves varying the angle of attack (which determines the lift over drag ratio) in an attempt to maintain a constant level of aerodynamic deceleration (e.g., 7 g), peaks of deceleration are reduced. This has the effect of raising the undershoot boundary and leaving the overshoot boundary essentially unchanged.

The low velocity Martian corridors (Figures B-126 to B-128) show a decreased corridor width for both pitch-modulated and nonpitch-modulated control philosophies. The Martian atmosphere is so tenuous that at low velocities the magnitude of the lift is insufficient to keep the vehicle from plunging into the surface of the planet. At velocities where this was a problem, an alternative criterion was used to specify the location of the undershoot boundary. This criterion stated that the vehicle must have entered its constant altitude phase before an altitude of 30,000 feet was reached or the trajectory was considered to have undershot.

2.4.3.2 Entry Corridor Widths as a Function of Vehicle Dynamics ($\varphi-\gamma$)

The actual entry corridor is more realistically represented by a graph of roll angle versus actual entry corridor is more realistically represented by a graph of roll angle versus flight path angle for a particular entry velocity than by the $V-\gamma$ graphs. A $\varphi-\gamma$ graph shows the effect of the roll angle control philosophy on the entry corridor. For example, the first constant attitude phase of the trajectory may have a roll angle of 0. This roll angle will have associated with it both an undershoot and an overshoot boundary. How-

ever, only the undershoot boundary is shown by the V-γ graph. The φ-γ graphs show the undershoot boundary on the right and the overshoot on the left. Figures B-129 and B-131 demonstrate the effect of initial velocity upon re-entry corridor.

The effects of various control philosophies is clearly shown in Figures B-131 through B-135. Figure B-131 was formed using the standard nonpitch-modulated change to the constant altitude control phase when the radial velocity equals zero ($\dot{r} = 0$) control philosophy. The discontinuity at $\varphi = \pi/2$ is caused by the control used to keep the vehicle near its initial trajectory plane. When the sine of the angle between the current velocity vector and the initial trajectory plane exceeds ϵ_S, the sign of the commanded roll angle (φ_c) changes. The maximum rate at which the roll angle changes to attain its commanded value is β_φ. The direction of roll is such that π radians is the greatest angle traversed. Thus at $|\varphi_c| > \pi/2$, the vehicle rolls through $\varphi = \pi$, and at $|\varphi_c| < \pi/2$ the vehicle rolls through $\varphi = 0$. The added upward or downward force provided by the lift vector during its roll shifts the satisfactory region of the φ-γ graph.

Figure B-132 was formed by changing to constant altitude control when either radial acceleration equals zero ($\ddot{r} = 0$) or radial velocity equals zero. A typical radial velocity time history for Mars II at $\varphi = \pi/2$ near the undershoot boundary is shown in Figure B-130. In the region R, the radial velocity is close to, but never reaches, zero. Thus, if the program was to switch to constant altitude control in this region (e.g., at $\ddot{r} = 0$), a satisfactory trajectory may result.

The use of pitch modulation in the first two phases of the trajectory (first constant attitude and constant altitude) gives the greatest increase in the usable corridor width as shown in Figure B-133, when compared to Figure B-131. This graph was formed by varying the pitch in an attempt to maintain an aerodynamic deceleration of 7 g in the first constant attitude phase and 6 g in the constant altitude phase. By adding the capability to switch to constant altitude control on $\dot{r} = 0$, the corridor is widened enough to overlap the regions of discontinuity (Figure B-134).

The discontinuity at $\varphi = \pi/2$ may be eliminated by either not attempting to keep the trajectory near the initial trajectory plane (Figures B-137 and B-141 where $\epsilon_S = 0.7$), or by modifying the control philosophy. One such modification is shown in Figure B-135 where the direction of roll depends upon the region of the φ-γ graph specified by the initial conditions of the trajectory. The undershoot boundary (right solid line) is obtained by always rolling upward (through $\varphi = 0$). The overshoot boundary is obtained by rolling downward. The dotted lines indicate the previous boundaries (Figure B-133) obtained by rolling through an angle less than or equal to π radians. This control policy certainly eliminates the discontinuity, but its implementation introduces the added requirement that the vehicle "know" its initial conditions accurately enough to locate its position in the φ-γ graph so that the proper initial roll angle can be selected.

Since the composition of the Martian atmosphere is uncertain (estimates designated as Mars I, II, III), the areas of successful entry on a φ-γ graph must overlap. Figure B-139 indicates that effectively no overlap exists at an entry speed equal to twice circular speed without pitch modulation. Even using pitch modulation provides overlap

only between adjacent estimates of the atmosphere (Figure B-140). An overlap of only 30 milliradians exists between the Mars I and III atmospheres if the entry speed is reduced to 13,000 ft/sec (slightly above circular), and the control philosophy includes pitch modulation (Figure B-138).

The overshoot boundary is strongly determined by the ability of the vehicle to roll in a manner such that it maintains a constant altitude. The gains used in this roll angle control (see math model) may be input as constants or may be computed by specifying the damping ratio and the period. The latter method is deisrable if there exists a significant uncertainty in the composition of the atmosphere because this results in an uncertainty in the aerodynamic deceleration which is used in determining the constant gains. (The same equations are used for computing the constant gains as are used for the time-varying set but the calculations occur only once in the former case.)

Figures B-129 and B-137 present entry corridors for Earth using the Apollo and HL10-type vehicles, respectively.

2.4.3.3 Effect of Out-of-Plane Control on Entry Corridor (ϵ_s-γ)

A study of the effect of the out-of-plane control parameter, ϵ_s (previously described), on the discontinuity in the φ-γ plots at $\varphi = \pi/2$ is shown in Figure B-142. The regions of satisfactory entry are R_2 and R_4. The region of overlap of the continuity is about $0.01 < \epsilon_s < 0.1$. If $\epsilon_s > \epsilon_s^*$, no discontinuity exists.

2.4.3.4 Effect of Maximum Roll Rate on Entry Corridor Widths (β_φ)

The rate at which the vehicle can roll has a strong influence on the entry corridor as shown in Figure B-143. It is important to note that a V-γ type graph would not reflect this dependence. At $\varphi = 0$, there is very little change in the undershoot boundary and at $\varphi = \pi$, there is only a small change in the overshoot boundary. The large changes occur in the overshoot boundary at $\varphi < \pi/2$ and in the undershoot boundary at $\varphi > \pi/2$. These changes are due to the inability of the vehicle to reorient its lift properly as the roll rate decreases when entering the constant altitude control phase (that is, down, near the overshoot boundary and up, near the undershoot boundary).

2.4.3.5 Effect of Ballistic Coefficient on Entry Corridor Width (W/C_DA)

The last study investigated the effect of varying the ballistic coefficient on the entry corridor (Figure B-144). Three extremely thin corridors (shown as a line) are shown representing three ranges (W/C_DA; C_D is a function of the pitch angle) of ballistic coefficient. It should be noted that a V-γ graph would indicate a corridor width of about 20 milliradians without indicating that the allowable uncertainty in the knowledge of the flight path angle must be accurate to less than 1 milliradian.

Error Source	Units	Budget A	Budget B
GYROS			
Random Drift			
X-gyro	meru	5	2.5
Y-gyro	meru	5	3
Z-gyro	meru	5	3
g-Dependent Drifts			
acceleration along input axes			
X-gyro	meru/g	15	10
Y-gyro	meru/g	10	3
Z-gyro	meru/g	15	3
acceleration along spin axes			
X-gyro	meru/g	15	5
Y-gyro	meru/g	10	8
Z-gyro	meru/g	15	8
g^2-Dependent Drift			
acceleration along input and spin axis			
X-gyro	meru/g^2	1	0.5
Y-gyro	meru/g^2	1	0.5
Z-gyro	meru/g^2	1	0.5
ACCELEROMETERS			
Bias			
X-accelerometer	μg	204	200
Y-accelerometer	μg	204	200
Z-accelerometer	μg	204	200
Scale Factor			
X-accelerometer	μg/g	100	50
Y-accelerometer	μg/g	100	50
Z-accelerometer	μg/g	100	50
Non-Linearity			
X-accelerometer	μg/g^2	10	10
Y-accelerometer	μg/g^2	10	10
Z-accelerometer	μg/g^2	10	10
Sensitive Axis Misalignments			
X → Y	arc-sec	41	35
X → Z	arc-sec	41	50
Y → Z	arc-sec	41	15
INITIAL ALIGNMENT			
φ_X	arc-sec	41	41
φ_Y	arc-sec	41	41
φ_Z	arc-sec	41	41

4685

Table B-16. Gimballed IMU Error Budgets Employed in Atmospheric Entry Studies

Error Source	Units	Rate Gyro System	RIG Gyro System
GYROS			
Random Drift			
X-gyro	meru	20	6
Y-gyro	meru	20	6
Z-gyro	meru	20	6
g-Dependent Drifts			
acceleration along input axes			
X-gyro	meru/g	50	10
Y-gyro	meru/g	50	10
Z-gyro	meru/g	50	10
acceleration along spin axes			
X-gyro	meru/g	30	10
Y-gyro	meru/g	30	10
Z-gyro	meru/g	30	10
g^2-Dependent Drifts			
acceleration along input and spin axes			
X-gyro	meru/g^2	20	5
Y-gyro	meru/g^2	20	5
Z-gyro	meru/g^2	20	5
Input Axes Misalignments			
X-gyro input → output	arcsec	20	10
X-gyro input → spin	arcsec	20	10
Y-gyro input → output	arcsec	20	10
Y-gyro input → spin	arcsec	20	10
Z-gyro input → output	arcsec	20	10
Z-gyro input → spin	arcsec	20	10
Scale Factor (rate gyro only)			
X-gyro	10^{-6}	16.6	
Y-gyro	10^{-6}	16.6	
Z-gyro	10^{-6}	16.6	
Non-linearity (rate gyro only)			
X-gyro	10^{-6}/(rad/sec)	2666.6	
Y-gyro	10^{-6}/(rad/sec)	2666.6	
Z-gyro	10^{-6}/(rad/sec)	2666.6	
ACCELEROMETERS			
Bias			
X-accelerometer	μg	300	200
Y-accelerometer	μg	300	200
Z-accelerometer	μg	300	200
Scale Factor			
X-accelerometer	μg/g	210	100
Y-accelerometer	μg/g	210	100
Z-accelerometer	μg/g	210	100
Non-Linearity			
X-accelerometer	μg/g^2	60	10
Y-accelerometer	μg/g^2	60	10
Z-accelerometer	μg/g^2	60	10
Input Axes Misalignment			
X → Y	arcsec	30	18
X → Z	arcsec	30	18
Y → Z	arcsec	30	18
Y → X	arcsec	30	18
Z → X	arcsec	30	18
Z → Y	arcsec	30	18
INITIAL ALIGNMENT			
Φ_X	arcsec	30	30
Φ_Y	arcsec	30	30
Φ_Z	arcsec	30	30

Table B-17. Strapdown System Error Budget Employed in Atmospheric Entry Studies

4689

Nominal Trajectory Description	Mission Phase			
	10A	10B	11A	11B
Reference Mission Class (Number)	4(VI)	4(VI)	4(VI)	4(VI)
Description	Single pass re-entry with pitch modulation control	Single pass re-entry without pitch modulation control	Single skipout with large (280°) central angle; pitch modulation control	Single skipout with small (80°) central angle; pitch modulation control
Environmental Data				
Central Body	Earth	Earth	Earth	Earth
Atmosphere Model	Exponential	Exponential	Exponential	Exponential
Gravity Model	Spherical	Spherical	Spherical	Spherical
Trajectory Data				
Initial Conditions				
Altitude (km)	122.	122.	122.	122.
R (km)	6500.6	6500.6	6500.6	6500.6
V (m/sec)	13946.2	13946.2	13946.2	13946.2
Re-entry angle, γ (radians)	-.122	-.122	-.122	-.122
X (km)	-5147.3	-5147.3	-5147.3	5147.3
Y (km)	1144.1	1144.1	1144.1	1144.1
Z (km)	3802.0	3802.0	3802.0	3802.0
$\dot{X}$ (m/sec)	-6242.6	-6242.6	-6242.6	-6242.6
$\dot{Y}$ (m/sec)	-8976.5	-8976.5	-8976.5	8976.5
$\dot{Z}$ (m/sec)	-8657.4	-8657.4	-8657.4	8657.4
Terminal Conditions				
Time of Flight (sec)	511	785.7	5957.	1814.8
Altitude (km)	20.6	20.1	20.0	20.5
R (km)	6398.8	6398.2	6398.1	6398.6
V (m/sec)	304.8	304.8	304.8	304.8
γ (rad)	-.8145	-.658	-.6572	-.8180
Central Angle (rad)	.520	.699	5.781	1.940
X (km)	-6140.2	-6135.9	-2758.3	-1464.9
Y (km)	-1014.9	-1716.7	2939.1	-4202.8
Z (km)	1487.3	584.0	4968.9	-4597.0
$\dot{X}$ (m/sec)	195.6	200.4	-127.7	245.7
$\dot{Y}$ (m/sec)	-97.1	-92.7	-197.8	158.2
$\dot{Z}$ (m/sec)	-212.7	-210.1	-193.6	86.7
Terminal Conditions for Skipout Trajectories				
Initial Atmospheric Portion				
Duration (sec)			284.9	222.5
Minimum Altitude (km)			59.7	50.3
Central Angle (rad)			.457	.357
Exit γ (rad)			.0710	.0987
Free-fall Portion				
Initial V (m/sec)			8213.9	7439.1
Duration (sec)			5053.1	1278.5
Maximum Altitude (km)			1731.1	362.3
Central Angle (rad)			4.906	1.388
Final Re-entry Portion				
Re-entry γ (rad)			-.0711	-.0986
Initial V (m/sec)			8213.4	7439.6
Duration (sec)			619.2	313.8
Central Angle (rad)			.418	.1945
Vehicle Parameters				
Type	Apollo	Apollo	Apollo	Apollo
L/D (nd)	0.5	0.5	0.5	0.5
Mass (kilograms)	4985.3	4985.3	4985.3	4985.3
Guidance and Control Parameters				
Initial Roll Angle (rad)	.7854	.7854	.7854	.7854
Maximum Roll Rate (rad/sec)	.698	.698	.698	.698
Trajectory Plane Constraint; ϵ_s (nd)	10^{-4}	10^{-4}	10^{-4}	10^{-4}
IMU Environmental Data				
Aerodynamic Acceleration (m/sec^2)	59.65	66.23	59.65	124.17
Maximum Body Angular Rates (rad/sec)	.69813	.69813	.69813	.69813

Table B-18. Reference Trajectory Parameters for Atmospheric Re-entry at Earth

Mission Class			Manned Earth Single Pass Entry
Trajectory Data	Vehicular Position and Velocity	X (km)	-5147.2705
		Y (km)	1144.0607
		Z (km)	3801.9823
		X (m/sec)	-6242.6251
		Y (m/sec)	-8976.4800
		Z (m/sec)	-8657.3749
		r (km)	6600.6413
		V (m/sec)	13946.246
		γ (rad)	-.12221453
	Max. Deceleration	G_{max} (g's)	6.7
	Time of Flight	TOF (sec)	720
Vehicle Data	Mass	M (kg)	4985.4931
	Cross Section Area	S (km^2)	1.2021652×10^{-5}
	Lift-drag Ratio	L/D	.5
Environment	Atmos. Surface Density	ρ_o (kg/km^3)	$.13915225 \times 10^{10}$
	Atmos. Decay Factor	β' (km^{-1})	.13961021
	Planet Radius	R (km)	6378.165
	Surface Gravity	g_o (km/sec^2)	$.97982665 \times 10^{-2}$
Nominal Guidance and Control Philosophy			Supercircular Roll Angle = $\pi/4$ Constant Altitude Subcircular Roll Angle = 0 Angle of Attack = .5411

Table B-19. Nominal Mission Data for Manned Earth Single Pass Entry Employed in Performance Assessment of Navigation with Electromagnetic Sensors Only

Mission Phase	Run Identification	NAVIGATION												CONTROL		
		Sensor			Error Budget						Observation Interval (sec)	Initial Statistics	Initial State Perturbation	Interval (sec)	Weighting Matrices	Variance of Noise $(rad)^2$ $\delta\alpha$, $\delta\varphi$
					Random			Bias								
		GT	RA	HS	GT	RA	HS	GT	RA	HS						
Manned Earth Single Pass Entry	3001	3	x	x	1	3	3	1	1	1	6	P5, B0	X5, C0	6	WXI, WUI	0, 0
	3002		x	x		4	3		1	1	6	P5, B0	X5, C0	6	WXI, WUI	0, 0
	3003		x	x		2	2		1	1	6	P5, B0	X5, C0	6	WXI, WUI	0, 0
	3004		x	x		4	3		1	1	6	P5, B1	X5, C1	6	WXI, WUI	0, 0
	3005		x	x		4	3		1	1	6	P5, B1	X5, C1	6	WXI, WUI	$.3\times10^{-5}, .27\times10^{-4}$
	3006		x	x		4	3		1	1	6	P5, B0	X5, C0	6	WXI, WUI	$.3\times10^{-5}, .27\times10^{-4}$

4688

Sensors:

GT ground trackers (entry indicates number of instruments used)
RA radio altimeter
HS horizon sensor

Note: The tabular data contained under Error Budget, Initial Statistics, Initial State Perturbation, and Weighting Matrices is defined in Tables B-21, B-22, B-23, and B-24, respectively.

Table B-20. Parameter Definition for Guidance and Navigation Performance Assessment of Navigation Electromagnetic Sensors Only on the Manned Earth Single Pass Entry Trajectory

INSTRUMENT	INSTRUMENT VARIANCES					
HORIZON SENSOR	1	2	3			
Random						
σ_α^2 (rad)^2	$.235\times10^{-8}$	$.3\times10^{-7}$	$.76\times10^{-6}$			
σ_δ^2 (rad)^2	$.235\times10^{-8}$	$.3\times10^{-7}$	$.76\times10^{-6}$			
σ_β^2 (rad)^2	$.235\times10^{-8}$	$.3\times10^{-7}$	$.76\times10^{-6}$			
Bias						
σ_α^2 (rad)^2	0	$.3\times10^{-5}$				
σ_δ^2 (rad)^2	0	$.3\times10^{-5}$				
σ_β^2 (rad)^2	0	$.3\times10^{-5}$				
RADIO ALTIMETER	1	2	3	4	5	6
Random						
σ_h^2 (km)^2	$.25\times10^{-4}$	$.4\times10^{-3}$	$.9\times10^{-3}$	$.1\times10^{-1}$	$t \le 1000$ $t > 1000$	$.1\times10^{-1}$
$\sigma_{\dot h}^2$ (m/sec)^2	.25	$.9\times10^{1}$	$.25\times10^{-2}$	$.9\times10^{1}$	$.2\times10^{-1}$ .1	
					$.18\times10^{2}$ $.9\times10^{2}$	$.1\times10^{4}$
Bias						
σ_h^2 (km)^2	0	$.25\times10^{-2}$				
$\sigma_{\dot h}^2$ (m/sec)^2	0	$.25\times10^{2}$				
GROUND TRACKER	1					
Random						
σ_ρ^2 (km)^2	$.225\times10^{-3}$					
$\sigma_{\dot\rho}^2$ (m/sec)^2	$.9\times10^{-3}$					
σ_ψ^2 (rad)^2	$.305\times10^{-5}$					
σ_η^2 (rad)^2	$.305\times10^{-5}$					
Bias	0					
IMU	1	2	3			
Random						
$\sigma_{\dot X}^2$ (m/sec)^2	$.9\times10^{-3}$	$.9\times10^{-1}$				
$\sigma_{\dot Y}^2$ (m/sec)^2	$.9\times10^{-3}$	$.9\times10^{-1}$				
$\sigma_{\dot Z}^2$ (m/sec)^2	$.9\times10^{-3}$	$.9\times10^{-1}$				
Bias						
$\sigma_{\varphi_o}^2$ (arcsec)^2	$.4\times10^{1}$	$.9\times10^{2}$	$.9\times10^{5}$			
σ_R^2 (meru)^2	$.4\times10^{1}$	$.9\times10^{1}$	$.9\times10^{3}$			
σ_K^2 (meru/g)^2	$.25\times10^{4}$	$.25\times10^{2}$	$.25\times10^{4}$			
σ_b^2 (10^{-6}g/g)^2	$.1\times10^{5}$	$.1\times10^{5}$	$.1\times10^{7}$			
σ_β^2 (10^{-6}g/g)^2	$.25\times10^{4}$	$.25\times10^{4}$	$.25\times10^{6}$			

4691

The horizon sensor measures two angles (α, δ) defining the local vertical and planet's subtended angle (β^H)

The radio altimeter measures altitude (h) and time rate of change of altitude ($\dot h$)

The ground tracker measures range (ρ), range rate ($\dot\rho$), azimuth (η) and elevation (ψ)

The IMU measures the integral of non-gravitational acceleration ($\dot X$, $\dot Y$, $\dot Z$). The bias errors consist of initial platform misalignment (φ_o), random drift (R), g dependent drift (K), accelerometer bias errors (b), and accelerometer scale factor (k).

In all runs for re-entry performance assessment, the instrument bias errors have been chosen as the positive square roots of the variances as tabulated on this page.

Table B-21. Instrument Error Variances Used for the Entry Guidance and Navigation Performance Assessment

Identification	Position and Velocity						Identification	Aerodynamic and Atmospheric Coefficients		
	$P_o(11)$ $(km)^2$	$P_o(22)$ $(km)^2$	$P_o(33)$ $(km)^2$	$P_o(44)$ $(m/sec)^2$	$P_o(55)$ $(m/sec)^2$	$P_o(66)$ $(m/sec)^2$		$P_o(77)$ (none)	$P_o(88)$ (none)	$P_o(99)$ $(kg/km^3)^2$
P0	0	0	0	0	0	0	B0	0	0	0
P1	.01	.01	.01	.01	.01	.01	B1	.01	.01	0
P2	1.	1.	1.	1.	1.	1.	B2	0	0	$.017\times 10^{14}$
P3	1.	1.	1.	9.	9.	9.	B3	.01	.01	$.017\times 10^{14}$
P4	9.	9.	9.	10.	10.	10.	B4	.01	0	$.017\times 10^{14}$
P5	10.	10.	10.	9.5	9.5	9.5	B5	0	0	1. *
P6	100.	100.	100.	90.	90.	90.	B6	0	0	$.014\times 10^{10}$*

* Used in the δ_ρ formulation, i.e., the state variable is current atmospheric density rather than sea level density.

Table B-22. Statistics of Initial State Perturbations

Identification	Position and Velocity						Identification	Aerodynamic and Atmospheric Coefficients		
	x (km)	y (km)	z (km)	$\dot{x}$ (m/sec)	$\dot{y}$ (m/sec)	$\dot{z}$ (m/sec)		δC_D (none)	δC_N (none)	$\delta \rho_o$ (kg/km^3)
X0	0	0	0	0	0	0	C0	0	0	0
X1	.1	.1	.1	.1	.1	.1	C1	.1	.05	0
X2	1.	1.	.805	-4.	-8.	-4.	C2	0	0	$.13\times 10^7$
X3	1.	1.	1.	1.	1.	1.	C3	.1	.05	$.13\times 10^7$
X4	3.	3.	2.4	-4.	-8.	-4.	C4	.1	0	$.13\times 10^7$
X5	5.1	7.33	7.1	19.3	-4.26	-14.2	C5	0	0	1. *
X6	10.	10.	10.	10.	10.	10.	C6	0	0	$.2\times 10^5$*

* Used in the δ_ρ formulation, i.e., the state variable is current atmospheric density rather than sea level density.

Table B-23. Initial State Perturbations

	Diagonal Elements	WXI				WXII		
		$t_o \le t \le 30$	$30 < t \le 70$	$70 < t \le 719$	$719 < t \le 720$	$t_o \le t \le 40$	$40 < t \le 80$	$80 < t \le 120$
State Matrices	W(11) $(km)^{-2}$	1.	10.	1.	10.	$1. \times 10^{-2}$	1.	$1. \times 10^{2}$
	W(22) $(km)^{-2}$	1.	10.	1.	10.	$1. \times 10^{-2}$	1.	$1. \times 10^{2}$
	W(33) $(km)^{-2}$	1.	10.	1.	10.	$1. \times 10^{-2}$	1.	$1. \times 10^{2}$
	W(44) $(m/sec)^{-2}$	$1. \times 10^{-2}$	1.	$1. \times 10^{-2}$	1.	$1. \times 10^{-4}$	$1. \times 10^{-2}$	1.
	W(55) $(m/sec)^{-2}$	$1. \times 10^{-2}$	1.	$1. \times 10^{-2}$	1.	$1. \times 10^{-4}$	$1. \times 10^{-2}$	1.
	W(66) $(m/sec)^{-2}$	$1. \times 10^{-2}$	1.	$1. \times 10^{-2}$	1.	$1. \times 10^{-4}$	$1. \times 10^{-2}$	1.

	Diagonal Elements	WUI	WUII	WUIII		WUIV		
		$t_o \le t \le 720$	$t_o \le t \le 120$	$t_o \le t \le 80$	$80 < t \le 120$	$t_o < t \le 40$	$40 < t \le 80$	$80 < t \le 120$
Control Matrices	W(11) $(rad)^{-2}$	$2. \times 10^{4}$	$1. \times 10^{5}$	$1. \times 10^{5}$	$1. \times 10^{2}$	$1. \times 10^{4}$	$1. \times 10^{5}$	$1. \times 10^{2}$
	W(22) $(rad)^{-2}$	$2. \times 10^{4}$	$1. \times 10^{5}$	$1. \times 10^{5}$	$1. \times 10^{2}$	$1. \times 10^{4}$	$1. \times 10^{5}$	$1. \times 10^{2}$

Table B-24. State and Control Weighting Matrices Used to Compute the Re-entry Guidance Law Matrices

Trajectory Data	Vehicular Position and Velocity	X (km)	-2781.3483
		Y (km)	1761.6086
		Z (km)	1259.9220
		X (m/sec)	-5373.4887
		Y (m/sec)	-10074.574
		Z (m/sec)	-5409.2494
		r (km)	3525.1335
		V (m/sec)	12634.510
		γ (rad)	-.21764267
	Max. Deceleration	G_{max} (g's)	3.8
	Time of Flight	TOF (sec)	120
Vehicle Data	Mass	M (kg)	4985.4931
	Cross Section Area	S $(km)^2$	1.2021653×10^{-5}
	Lift-drag Ratio	L/D	.5
Environment	Atmos. Surface Density	ρ_o (kg/km^3)	$.131937 \times 10^8$
	Atmos. Decay Factor	β' (km^{-1})	.1111056
	Planet Radius	R (km)	3400.1658
	Surface Gravity	g_o (km/sec^2)	$.37174404 \times 10^2$
Nominal Guidance and Control Philosophy			Roll Angle = 0 Angle of Attack = .5411

Table B-25. Nominal Mission Data for Martian Atmospheric Braking Trajectory

Mission	Identification	NAVIGATION												CONTROL		
		Sensor			Error Budget						Observation Interval (sec)	Initial Statistics	Initial State Perturbation	Interval (sec)	Weighting Matrices	Variance of Noise (rad)^2 $\delta\alpha$, $\delta\upsilon$
					Random			Bias								
		GT	RA	HS	GT	RA	HS	GT	RA	HS						
Manned Atmospheric Braking at Mars	511	No Observations Made											X3	No Guidance Used		
	540	3			1*			1*			5	P3, B0	X3, C0	15	WUII, WXII	0, 0
	546	3			1*			1*			1	P3, B0	X3, C0	1	WUIII, WXII	0, 0
	534	3			1*			1*			5	P3, B0	X3, C0	15	WUIII, WXII	0, 0
	550	3			1*			1*			1	P3, B0	X3, C0	1	WUIV, WXII	0, 0
	600		x	x		1	1		1	1	1	P3, B0	X3, C0	1	WUIII, WXII	0, 0
	601		x	x		1	1		1	1	1	P3, B0	X3, C0	1	WUIII, WXII	$.3\times10^{-5}$, $.27\times10^{-4}$
	602		x	x		1	1		1	1	1	P3, B0	X3, C0	1	WUIII, WXII	$.3\times10^{-3}$, $.27\times10^{-2}$
	603		x	x		1	1		1	1	1	P3, B0	X3, C0	1	WUIII, WXII	$.12\times10^{-2}$, $.108\times10^{-1}$
	604		x	x		4	3		2	2	1	P3, B0	X3, C0	1	WUIII, WXII	0, 0
	605		x	x		4	3		2	2	1	P3, B0	X3, C0	1	WUIII, WXII	$.3\times10^{-5}$, $.27\times10^{-4}$
	606		x	x		4	3		2	2	1	P3, B0	X3, C0	1	WUIII, WXII	$.3\times10^{-3}$, $.27\times10^{-2}$
	607		x	x		4	3		2	2	1	P3, B0	X3, C0	1	WUIII, WXII	$.12\times10^{-2}$, $.108\times10^{-1}$
	608		x	x		4	3		1	1	1	P3, B0	X3, C0	1	WUIII, WXII	0, 0

4687

Sensors:

GT ground tracker (entry indicates number of instruments used)
RA radio altimeter
HS horizon sensor

* This error budget is used in the statistics; however, the measurements are not contaminated by noise.

Note: The tabular data contained under Error Budget, Initial Statistics, Initial State Perturbation, and Weighting Matrices is defined in Tables B-21, B-22, B-23, and B-24, respectively.

Table B-26. Parameter Definition for Guidance and Navigation Performance Assessment Studies on Martian Atmospheric Braking Trajectory

Mission Class			10g Mars Unmanned Entry from Parking Orbit	Parameter Estimation during Atmospheric Braking
Trajectory Data	Vehicular Position and Velocity	X(km)	3538.9876	- 2781.3483
		Y(km)	0	1761.6086
		Z(km)	0	1259.9220
		$\dot{X}$(m/sec)	-1273.5815	- 5373.4888
		$\dot{Y}$(m/sec)	4117.1426	-10074.547
		$\dot{Z}$(m/sec)	0	- 5409.2494
		r(km)	3538.9875	3525.1335
		V(m/sec)	4309.6257	12634.510
		γ(rad)	-.3	- .21764267
	Max. Deceleration	G_{max} (g's)	10	3.8
	Time of Flight	TOF(sec)	160	Part I: 120 Part II: 1600
Vehicle Data	Mass	M(kg)	100	4985.4931
	Cross Section Area	S(km^2)	$.23\times10^{-5}$	1.2021635×10^{-5}
	Lift-drag Ratio	L/D	0	.5
Environment	Atmos. Surface Density	ρ_0(kg/km^3)	$.131937\times10^{8}$	$.131937\times10^{8}$
	Atmos. Decay Factor	β' (km^{-1})	.1111056	.1111056
	Planet Radius	R(km)	3400.	3400.
	Surface Gravity	g_0(km/sec^2)	$.37174404\times10^{-2}$	$.37174404\times10^{-2}$
Nominal Guidance and Control			Roll Angle = 0 Angle of Attack = 0	Roll Angle = 0 Angle of Attack = .5411

4690

Table B-27. Nominal Mission Data for Trajectories Used in the Exploration of Planetary Atmosphere Studies

Mission	Identification	NAVIGATION														CONTROL		
		Sensor				Error Budget								Observation Interval (sec)	Initial Statistics	Initial State Perturbation	Interval (sec)	Weighting Matrices	Variance of Noise (rad)^2 $\delta\alpha$, $\delta\varphi$
						Random				Bias									
		GT	RA	HS	IMU	GT	RA	HS	IMU	GT	RA	HS	IMU						
10g Mars II Unmanned Entry from Parking Orbit	481				x				1				3	4	P0, B4	X0, C4		No Guidance Used	
	482				x				1				3	4	P1, B4	X1, C4		No Guidance Used	
	483				x				1				3	4	P3, B4	X3, C4		No Guidance Used	
	484		x				4				2			4	P0, B4	X0, C4		No Guidance Used	
	485		x				4				2			4	P1, B4	X1, C4		No Guidance Used	
	486		x				4				2			4	P3, B4	X3, C4		No Guidance Used	
Parameter Estimation During Atmospheric Braking Part I	427				x				1				2	1	P1, B1	X1, C1		No Guidance Used	
	428				x				1				2	1	P1, B2	X1, C2		No Guidance Used	
	429				x				1				2	1	P1, B3	X1, C3		No Guidance Used	
	459				x				1				3	1	P4, B3	X4, C3	1	$\delta\alpha = \delta\varphi = 0$	$.3\times10^{-5}$, $.3\times10^{-5}$
	460				x				1				3	1	P4, B3	X4, C3	1	$\delta\alpha = \delta\varphi = 0$	$.3\times10^{-3}$, $.3\times10^{-3}$
	461				x				1				3	1	P4, B3	X4, C3	1	$\delta\alpha = \delta\varphi = 0$	0, 0
	424		x	x			4	3			2	2		1	P1, B1	X1, C1		No Guidance Used	
	425		x	x			4	3			2	2		1	P1, B2	X1, C2		No Guidance Used	
	439		x	x			4	3			2	2		5	P1, B1	X1, C1		No Guidance Used	
	440		x	x			4	3			2	2		5	P1, B2	X1, C2		No Guidance Used	
	433			x				3				2		5	P1, B1	X1, C1		No Guidance Used	
	434			x				3				2		5	P1, B2	X1, C2		No Guidance Used	
	435			x				3				2		5	P1, B3	X1, C3		No Guidance Used	
	436		x				4				2			5	P1, B1	X1, C1		No Guidance Used	
	437		x				4				2			5	P1, B2	X1, C2		No Guidance Used	
	438		x				4				2			5	P1, B3	X1, C3		No Guidance Used	
	451		x				4				2			5	P4, B1	X4, C1		No Guidance Used	
	452		x				4				2			5	P4, B2	X4, C2		No Guidance Used	
	454		x				6				2			5	P1, B1	X1, C1		No Guidance Used	
	455		x				6				2			5	P1, B2	X1, C2		No Guidance Used	
	445		x				4				2			10	P1, B1	X1, C1		No Guidance Used	
	446		x				4				2			10	P1, B2	X1, C2		No Guidance Used	
	448		x				4				2			10	P4, B1	X4, C1		No Guidance Used	
	449		x				4				2			10	P4, B2	X4, C2		No Guidance Used	
	430		x	x	x		4	3	1		2	2	2	1	P1, B1	X1, C1		No Guidance Used	
	431		x	x	x		4	3	1		2	2	2	1	P1, B2	X1, C2		No Guidance Used	
	432		x	x	x		4	3	1		2	2	2	1	P1, B3	X1, C3		No Guidance Used	
	442		x	x	x		4	3	1		2	2	2	1	P0, B3	X0, C3		No Guidance Used	
	444		x	x	x		4	3	1		2	2	2	1	P4, B3	X4, C3		No Guidance Used	
	416*		x	x	x		4	3	1		2	2	2	5	P3, B5	X0, C5		No Guidance Used	
	420*		x	x	x		4	3	1		2	2	2	5	P3, B6	X0, C6		No Guidance Used	
	423*		x	x	x		4	3	1		2	2	2	5	P3, B6	X0, C6		No Guidance Used	
Part II	475		x				4					2		20**	P0, B3	X0, C3		No Guidance Used	
	476		x				4					2		20**	P1, B3	X1, C3		No Guidance Used	

4692

Sensors:

GT ground tracker
RA radio altimeter
HS horizon sensor
IMU inertial measurement unit

* Estimation is on current atmospheric density rather than on sea level density.
** No observations are made while in the atmosphere (first 120 seconds). Observations are every 20 seconds after this.

Note: The tabular data contained under Error Budget, Initial Statistics, Initial State Perturbation, and Weighting Matrices is defined in Tables B-21, B-22, B-23, and B-24, respectively.

Table B-28. Guidance and Navigation System Parameter Definition for the Exploration of Planetary Atmosphere Studies

Mission	Identification	Error in Estimate ($\tilde{x}$) and Statistics (σ_x)										Maximum Control	
		Position		Velocity		Aerodynamic				Atmosphere		Pitch	Roll
		$\Delta\tilde{R}$ (km)	σ_R (km)	$\Delta\tilde{V}$ (m/sec)	σ_V (m/sec)	$\delta\tilde{C}_D$	σ_{CD}	$\delta\tilde{C}_N$	σ_{CN}	$\delta\tilde{\rho}$ (kg/km^3)	σ_ρ (kg/km^3)	$\delta\alpha$ (rad)	$\delta\rho$ (rad)
10g Mars II Unmanned Entry from Parking Orbit	481	.27	$.18\times10^{-2}$	$.15\times10^{1}$	$.50\times10^{-2}$	$.2\times10^{-2}$	$.70\times10^{-1}$			$.5\times10^{5}$	$.93\times10^{6}$	0	0
	482	$.26\times10^{1}$	.16	$.15\times10^{1}$	$.20\times10^{-1}$	$.9\times10^{-2}$	$.71\times10^{-1}$			$.2\times10^{6}$	$.93\times10^{6}$	0	0
	483	$.18\times10^{1}$	$.14\times10^{1}$	.42	.20	$.18\times10^{-2}$	$.83\times10^{-1}$			$.12\times10^{6}$	$.93\times10^{6}$	0	0
	484	$.24\times10^{-1}$	.13	.32	.25	$.5\times10^{-2}$	$.70\times10^{-1}$			$.1\times10^{6}$	$.93\times10^{6}$	0	0
	485	.14	.21	.34	.29	$.2\times10^{-2}$	$.70\times10^{-1}$			$.7\times10^{5}$	$.93\times10^{6}$	0	0
	486	$.11\times10^{1}$	$.12\times10^{1}$	.17	.43	$.4\times10^{-2}$	$.70\times10^{-1}$			$.8\times10^{5}$	$.93\times10^{6}$	0	0
Parameter Estimation During Atmospheric Braking Part I	427	.79	.14	$.12\times10^{1}$	.19	$.9\times10^{-1}$	$.11\times10^{-1}$	$.4\times10^{-1}$	$.11\times10^{-1}$			0	0
	428	.41	.14	.24	.16					$.1\times10^{6}$	$.14\times10^{6}$	0	0
	429	.96	.14	$.11\times10^{1}$	.19	$.2\times10^{-1}$	$.6\times10^{-1}$	$.2\times10^{-1}$	$.56\times10^{-1}$	$.3\times10^{6}$	$.76\times10^{6}$	0	0
	459	$.92\times10^{1}$	$.39\times10^{1}$	$.57\times10^{2}$	$.11\times10^{2}$	.10	$.72\times10^{-1}$	.10	$.67\times10^{-1}$	$.2\times10^{7}$	$.12\times10^{7}$	0	0
	460	$.21\times10^{3}$	$.39\times10^{1}$	$.22\times10^{3}$	$.88\times10^{1}$	.14	$.72\times10^{-1}$	$.58\times10^{-1}$	$.67\times10^{-1}$	$.23\times10^{7}$	$.12\times10^{7}$	0	0
	461	$.23\times10^{2}$	$.39\times10^{1}$	$.17\times10^{3}$	$.89\times10^{1}$	.16	$.71\times10^{-1}$	.20	$.66\times10^{-1}$	$.27\times10^{7}$	$.12\times10^{7}$	0	0
	424	.53	.25	$.73\times10^{1}$	$.29\times10^{1}$	$.6\times10^{-2}$	$.58\times10^{-2}$	$.2\times10^{-2}$	$.49\times10^{-2}$			0	0
	425	.32	.18	$.37\times10^{1}$	$.16\times10^{1}$					$.4\times10^{5}$	$.65\times10^{5}$	0	0
	439	.65	.42	$.67\times10^{1}$	$.60\times10^{1}$	$.5\times10^{-2}$	$.83\times10^{-2}$	$.2\times10^{-2}$	$.59\times10^{-2}$			0	0
	440	.49	.26	$.39\times10^{1}$	$.30\times10^{1}$					$.3\times10^{5}$	$.74\times10^{5}$	0	0
	433	$.21\times10^{1}$	$.15\times10^{1}$	$.31\times10^{2}$	$.24\times10^{2}$	$.41\times10^{-1}$	$.28\times10^{-1}$	$.18\times10^{-1}$	$.18\times10^{-1}$			0	0
	434	.97	.93	$.11\times10^{2}$	$.12\times10^{2}$					$.3\times10^{6}$	$.25\times10^{6}$	0	0
	435	$.21\times10^{1}$	$.15\times10^{1}$	$.31\times10^{2}$	$.24\times10^{2}$	$.37\times10^{-1}$	$.62\times10^{-1}$	$.17\times10^{-1}$	$.59\times10^{-1}$	$.6\times10^{5}$	$.77\times10^{6}$	0	0
	436	.35	.41	$.79\times10^{1}$	$.62\times10^{1}$	$.2\times10^{-1}$	$.87\times10^{-2}$	$.8\times10^{-2}$	$.61\times10^{-2}$			0	0
	437	.31	.27	$.22\times10^{1}$	$.30\times10^{1}$					$.5\times10^{5}$	$.77\times10^{5}$	0	0
	438	.43	.43	$.11\times10^{2}$	$.62\times10^{1}$	$.8\times10^{-2}$	$.6\times10^{-1}$	$.18\times10^{-1}$	$.56\times10^{-1}$	$.3\times10^{6}$	$.75\times10^{6}$	0	0
	451	$.15\times10^{1}$	$.39\times10^{1}$	$.13\times10^{2}$	$.13\times10^{2}$	$.3\times10^{-1}$	$.1\times10^{-1}$	$.19\times10^{-1}$	$.86\times10^{-2}$			0	0
	452	$.12\times10^{1}$	$.39\times10^{1}$	$.15\times10^{2}$	$.12\times10^{2}$					$.3\times10^{6}$	$.11\times10^{6}$	0	0
	454	.92	$.10\times10^{1}$	$.12\times10^{2}$	$.16\times10^{2}$		$.45\times10^{-1}$	$.2\times10^{-2}$	$.13\times10^{-1}$			0	0
	455	.47	.31	$.45\times10^{1}$	$.37\times10^{1}$					$.6\times10^{5}$	$.8\times10^{5}$	0	0
	445	.23	.55	$.57\times10^{1}$	$.81\times10^{1}$	$.2\times10^{-1}$	$.11\times10^{-1}$	$.11\times10^{-1}$	$.70\times10^{-2}$			0	0
	446	.29	.32	$.18\times10^{1}$	$.39\times10^{1}$					$.1\times10^{7}$	$.85\times10^{5}$	0	0
	448	$.16\times10^{1}$	$.39\times10^{1}$	$.11\times10^{2}$	$.15\times10^{2}$	$.3\times10^{-3}$	$.12\times10^{-1}$	$.23\times10^{-1}$	$.10\times10^{-1}$			0	0
	449	$.14\times10^{1}$	$.39\times10^{1}$	$.13\times10^{2}$	$.15\times10^{2}$					$.3\times10^{7}$	$.13\times10^{6}$	0	0
	430	.17	.11	$.11\times10^{1}$	.18	$.5\times10^{-2}$	$.49\times10^{-2}$	$.6\times10^{-2}$	$.46\times10^{-2}$			0	0
	431	.29	.11	.17	.18					$.9\times10^{5}$	$.61\times10^{5}$	0	0
	432	.15	.13	$.29\times10^{1}$	.33	$.16\times10^{-1}$	$.60\times10^{-1}$	$.19\times10^{-1}$	$.56\times10^{-1}$	$.1\times10^{6}$	$.75\times10^{6}$	0	0
	443	.47	.57	$.73\times10^{1}$	$.94\times10^{-1}$	$.22\times10^{-1}$	$.60\times10^{-1}$	$.9\times10^{-2}$	$.56\times10^{-1}$	$.3\times10^{6}$	$.75\times10^{6}$	0	0
	444	$.29\times10^{1}$	$.12\times10^{1}$	$.30\times10^{2}$	$.72\times10^{1}$	$.21\times10^{-1}$	$.60\times10^{-1}$	$.24\times10^{-1}$	$.56\times10^{-1}$	$.2\times10^{6}$	$.75\times10^{6}$	0	0
	416*	.66	.86	$.17\times10^{1}$	$.51\times10^{1}$					.65*	$.15\times10^{2}$	0	0
	420*	$.70\times10^{1}$	.86	$.70\times10^{2}$	$.33\times10^{1}$					$.51\times10^{-3}$*	$.85\times10^{-5}$	0	0
	423*	$.63\times10^{1}$	.86	$.58\times10^{2}$	$.33\times10^{1}$					$.21\times10^{2}$*	$.20\times10^{2}$	0	0
Part II	475	.27	.32	.18	.29	$.18\times10^{-1}$	$.60\times10^{-1}$	$.18\times10^{-1}$	$.56\times10^{-1}$	$.2\times10^{6}$	$.75\times10^{6}$	0	0
	476	.74	.48	.44	.46	$.16\times10^{-1}$	$.60\times10^{-1}$	$.17\times10^{-1}$	$.56\times10^{-1}$	$.3\times10^{6}$	$.75\times10^{6}$	0	0

* Estimation is on current atmospheric density rather than sea level density.

4693

Note: ΔR = magnitude of terminal position perturbation.
ΔV = magnitude of terminal velocity perturbation.

Table B-29. Trade-off Results of the Exploration of Planetary Atmosphere Studies

Type of Study	Planet	Vehicle	Entry Speed (m/sec)	Control Philosophy: Time Varying Gains	Control Philosophy: Change Phase on $\ddot{r}$ Criteria	Control Philosophy: Pitch Modulation	Environment: g_o (m/sec²)	Environment: ρ_o (kg/km³)	Environment: β' (1/km)	Vehicle Characteristics: * $W/C_D{}^A$ (kg/m²)	Vehicle Characteristics: α'' (rad)	Vehicle Characteristics: + C_{Di} (nd)	Vehicle Characteristics: + C_{Ni} (nd)	Nominal Control Parameters: Δt_G (sec)	K_φ (1/sec)	β_φ (rad/sec)	ϵ_a (nd)	K_{T1} (sec/km)	K_{T2} (1/km)	ζ_2 (nd)	τ_2 (sec)	K_{T3} (1/sec)	$a'_{nom,s}$ (g)	$a'_{nom,\epsilon}$ (g)	α_{min} (rad)	α_{max} (rad)	Maximum Corridor Width (rad)	Figure Number
V-γ	Earth	Apollo	—	Yes	—	Yes-No	9.81456	$.13915225\times10^{10}$	.13961021	B_4	.5411	A	A	1	3	.698	—	—	—	.8	20	.1	7	6	.4	1.05	—	B-124
	Earth	HL10	—	Yes	—	Yes-No	9.81456	$.13915225\times10^{10}$	.13961021	B_1	.785	C	C	1	3	.698	—	—	—	.7	20	11	7	6	.175	.9	—	B-125
	Mars	Apollo	—	Yes	—	Yes-No	3.71734	$.68030\times10^{7}$	.0704659	B_4	.5411	A	A	1	3	.698	—	—	—	.8	20	.1	7	6	.4	1.05	—	B-126
	Mars	Apollo	—	Yes	—	Yes-No	3.71734	$.131937\times10^{8}$	.1111056	B_4	.5411	A	A	1	3	.698	—	—	—	.8	20	.1	7	6	.4	1.05	—	B-127
	Mars	Apollo	—	Yes	—	Yes-No	3.71734	$.25666\times10^{8}$	.19300	B_4	.5411	A	A	1	3	.698	—	—	—	.8	20	.1	7	6	.4	1.05	—	B-128
σ-γ	Earth	Apollo	9,144	No	No	No	9.81456	$.13915225\times10^{10}$	.13961021	395	.5411	B	B	2	3	.698	10^{-4}	131	59	—	—	.1	—	—	—	—	70	B-129
	Earth	Apollo	15,240	Yes	No	No	9.81456	$.13915225\times10^{10}$	.13961021	395	.5411	A	A	1	3	.698	10^{-4}	—	—	.8	20	.1	—	—	—	—	25	B-131
	Earth	Apollo	15,240	Yes	Yes	No	9.81456	$.13915225\times10^{10}$	.13961021	395	.5411	A	A	1	3	.698	10^{-4}	—	—	.8	20	11	—	—	—	—	25	B-132
	Earth	Apollo	15,240	Yes	No	Yes	9.81456	$.13915225\times10^{10}$	.13961021	B_4	—	A	A	1	3	.698	10^{-4}	—	—	.8	20	.1	7	6	.4	1.05	36	B-133
	Earth	Apollo	15,240	Yes	Yes	Yes	9.81456	$.13915225\times10^{10}$	.13961021	B_4	—	A	A	1	3	.698	10^{-4}	—	—	.8	20	11	7	6	.4	1.05	38	B-134
	Earth	Apollo	15,240	Yes	Yes	Yes	9.81456	$.13915225\times10^{10}$	.13961021	B_4	—	A	A	1	3	.698	10^{-4}	—	—	.8	20	11	7	6	.4	1.05	38	B-135
	Earth	HL10	15,240	Yes	Yes	Yes	9.81456	$.13915225\times10^{10}$	.13961021	B_1	—	C	C	1	3	.698	10^{-4}	—	—	.7	20	11	7	6	.175	.9	45	B-136
	Earth	HL10	15,240	Yes	No	No	9.81456	$.13915225\times10^{10}$	.13961021	976	.1309	.057 0.0	.43545 0.0	1	3	.698	.7	—	—	.8	20	11	—	—	—	—	25	B-137
	Mars	Apollo	3,962	Yes	No	Yes	3.71734	$.68030\times10^{7}$	.0704659	B_4	—	A	A	1	3	.698	10^{-4}	—	—	.8	20	.1	7	6	.4	1.05	105	B-138
	Mars	Apollo	3,962	Yes	No	Yes	3.71734	$.131937\times10^{8}$	.1111056	B_4	—	A	A	1	3	.698	10^{-4}	—	—	.8	20	.1	7	6	.4	1.05	140	
	Mars	Apollo	3,962	Yes	No	Yes	3.71734	$.25666\times10^{8}$	.19300	B_4	—	A	A	1	3	.698	10^{-4}	—	—	.8	20	.1	7	6	.4	1.05	170	
	Mars	Apollo	7,132	Yes	No	No	3.71734	$.68030\times10^{7}$	.0704659	395	.5411	A	A	1	3	.698	10^{-4}	—	—	.8	20	11	—	—	—	—	60	B-139
	Mars	Apollo	7,132	Yes	No	No	3.71734	$.131937\times10^{8}$	.1111056	395	.5411	A	A	1	3	.698	10^{-4}	—	—	.8	20	11	—	—	—	—	80	
	Mars	Apollo	7,132	Yes	No	No	3.71734	$.25666\times10^{8}$	.19300	B_4	.5411	A	A	1	3	.698	10^{-4}	—	—	.8	20	11	—	—	—	—	105	
	Mars	Apollo	7,132	Yes	Yes	Yes	3.71734	$.68030\times10^{7}$	.0704659	B_4	—	A	A	1	3	.698	10^{-4}	—	—	.8	20	11	7	6	.4	1.05	70	B-140
	Mars	Apollo	7,132	Yes	Yes	Yes	3.71734	$.131937\times10^{8}$	.1111056	B_4	—	A	A	1	3	.698	10^{-4}	—	—	.8	20	11	7	6	.4	1.05	115	
	Mars	Apollo	7,132	Yes	Yes	Yes	3.71734	$.25666\times10^{8}$	.19300	B_4	—	A	A	1	3	.698	10^{-4}	—	—	.8	20	11	7	6	.4	1.05	150	
	Mars	Apollo	12,192	No	No	No	12.43	$.131937\times10^{8}$	.1111056	395	.5411	B	B	1	3	.698	.7	131	59	—	—	.1	—	—	—	—	29	B-141
$\sigma_{\bar{s}}$	Mars	Apollo	12,192	No	No	No	12.43	$.131937\times10^{8}$	.1111056	395	.5411	B	B	1	3	.698	—	131	59			.1					—	B-142
β_c	Earth	Apollo	15,240	Yes	Yes	Yes	9.81456	$.13915225\times10^{10}$	.13961021	B_4	—	A	A	1	3	.1743	10^{-4}	—	—	.8	20	11	7	6	.4	1.05		B-143
	Earth	Apollo	15,240	Yes	Yes	Yes	9.81456	$.13915225\times10^{10}$	.13961021	B_4	—	A	A	1	3	.4358	10^{-4}	—	—	.8	40							
	Earth	Apollo	15,240	Yes	Yes	Yes	9.81456	$.13915225\times10^{10}$	.13961021	B_4	—	A	A	1	3	.1743	10^{-4}	—	—	.8	60							
$W/C_D{}^A$	Earth	HL10	21,336	Yes	Yes	Yes	9.81456	$.13915225\times10^{10}$	.13961021	B_1	—	C	C	1	3	.698	10^{-4}	—	—	.7	20	11	7	6	.175	.9		B-144
		—	21,336	Yes	Yes	Yes	9.81456	$.13915225\times10^{10}$	.13961021	B_2	—	C	C	1	3	.698	10^{-4}	—	—	.7	20				.1	.55		
		—	21,336	Yes	Yes	Yes	9.81456	$.13915225\times10^{10}$	.13961021	B_3	—	C	C	1	3	.698	10^{-4}	—	—	.7	20				.1	.55		

*B_1 = 674 to 5,029
B_2 = 234 to 620
B_3 = 2,099 to 5,615
B_4 = 337 to 757

*A: C_{Di} = 1.48587, -1.65601, .726682, C_{Ni} = 1.36395, -1.40563, .322713;
B: C_{Di} = 1.50571, -1.81701, .926574, C_{Ni} = 1.36087, -1.3843, .29526;
C: C_{Di} = .0643179, .542678, .291818, C_{Ni} = .316628, .903799, -.577941

4694

Table B-30. Definition of Inputs for Special Studies

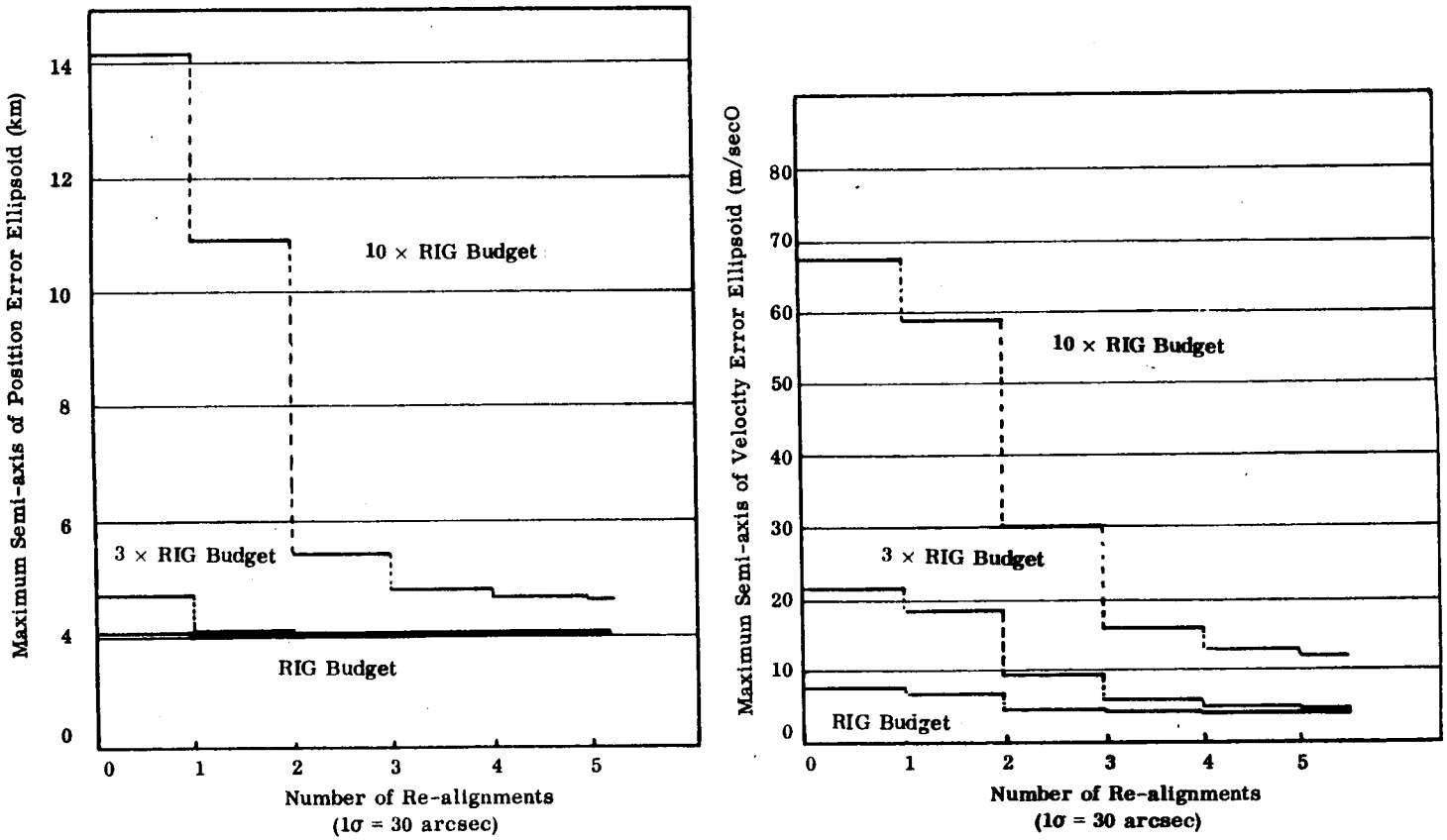

Figure B-92. Performance Improvement due to Repeated Alignment (Trajectory 10A) ($P_o = P_{nom}$)

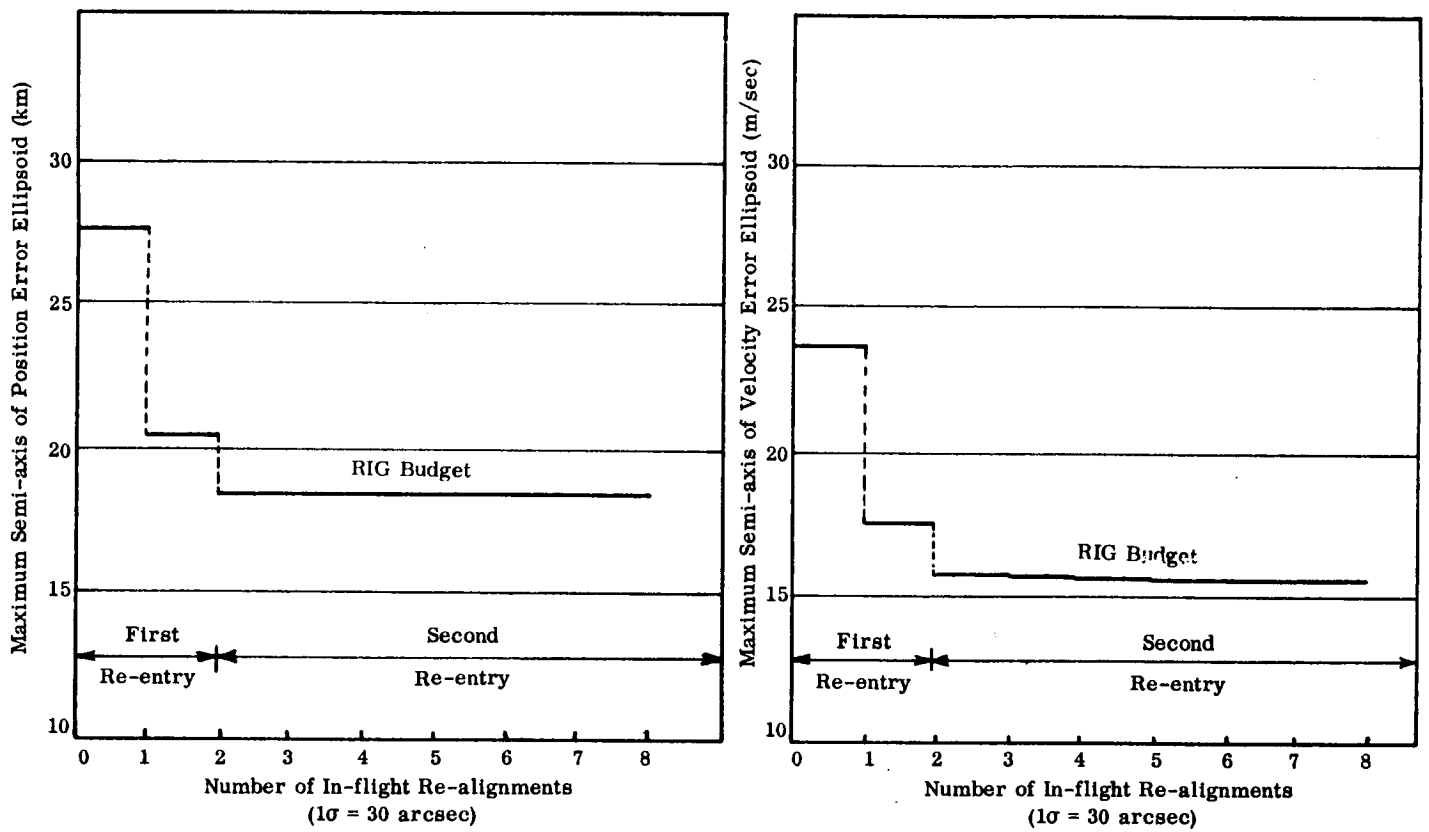

Figure B-93. Performance Improvement due to Repeated Platform Alignment (Trajectory 11A)($P_o = 0$)

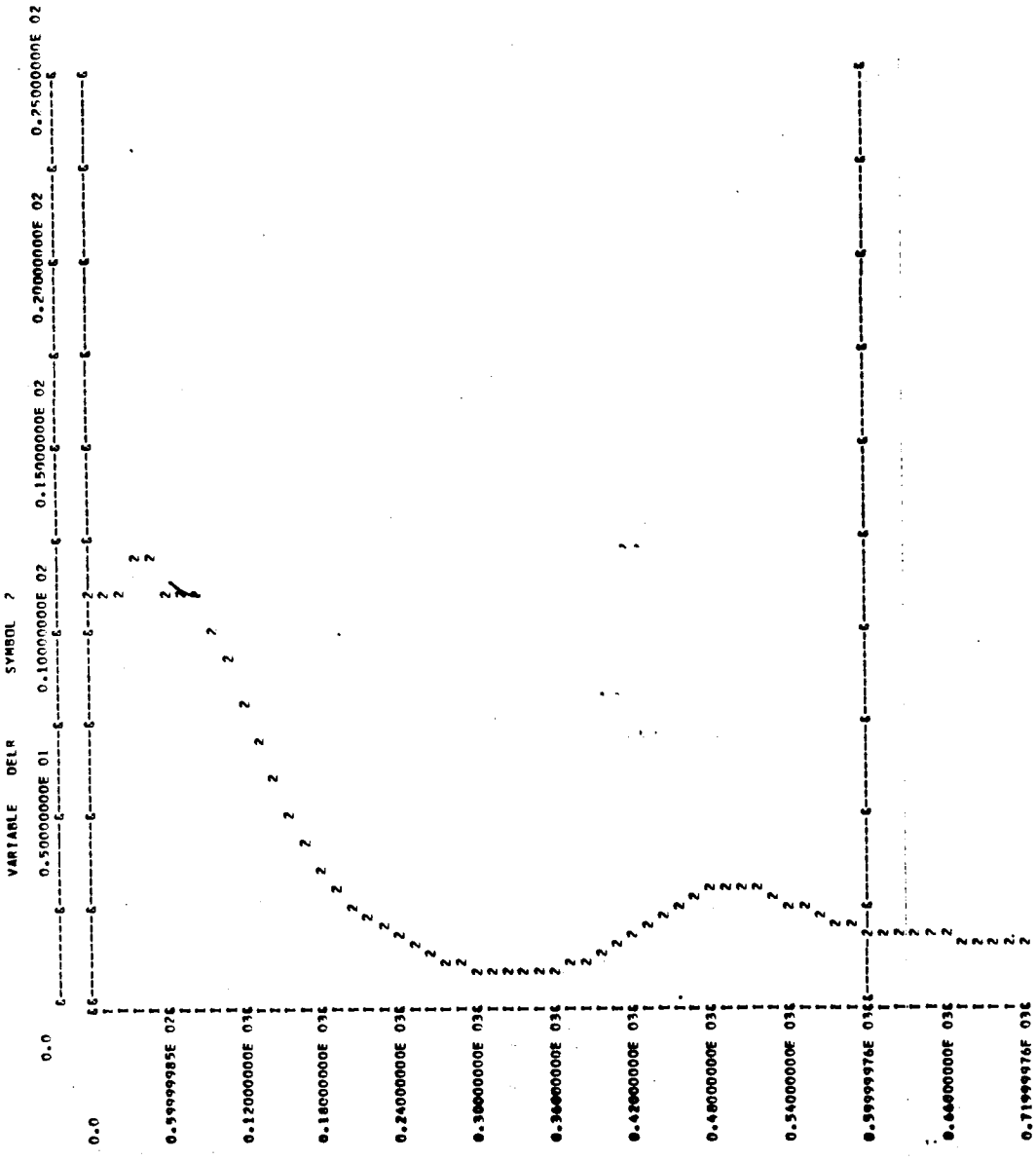

Figure B-94. Plot of the Magnitude of the Position Perturbation, $\Delta R \sim$ km, vs Time $\sim$ secs for Earth Single Pass Entry (Run 3003)

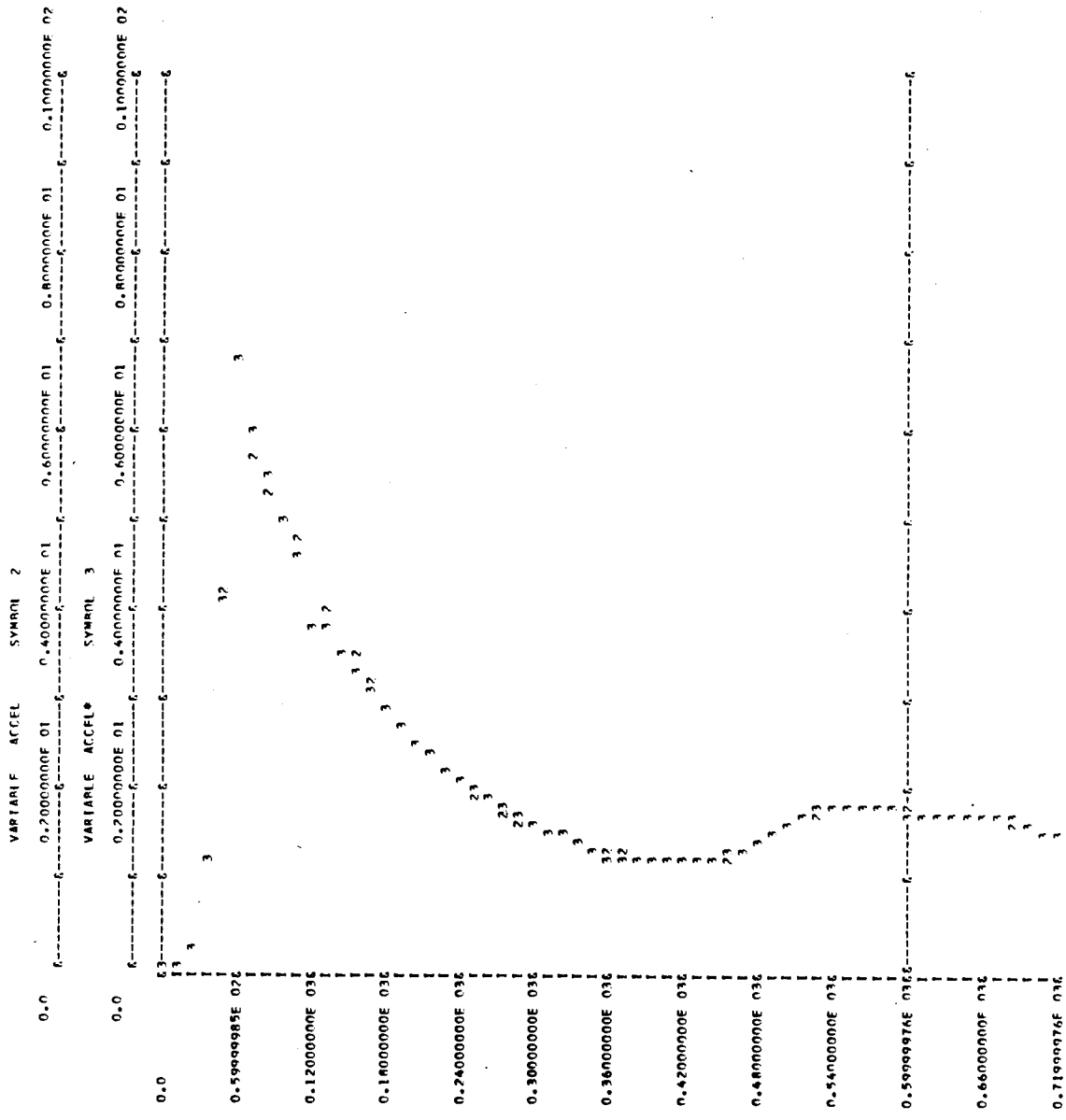

Figure B-95. Plot of the Aerodynamic Deceleration along the Actual, a ~ g's and Nominal, a* ~ g's, Trajectories vs Time ~ secs for Earth Single Pass Entry (Run 3003)

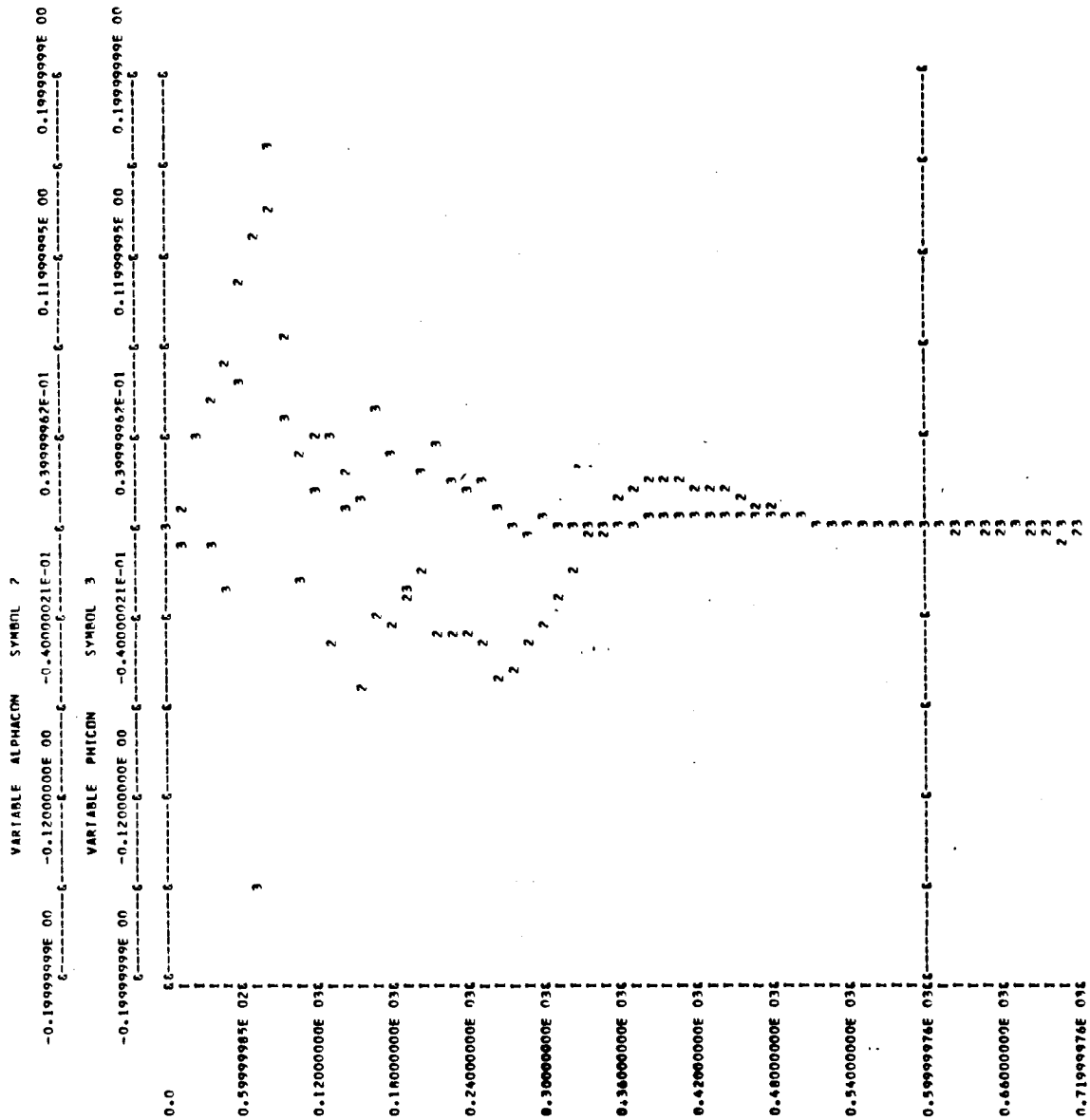

Figure B-96. Plot of the Perturbative Control in Pitch, $\delta\alpha \sim$ rad, and Roll, $\delta\varphi \sim$ rad, vs Time $\sim$ secs for Earth Single Pass Entry (Run 3003)

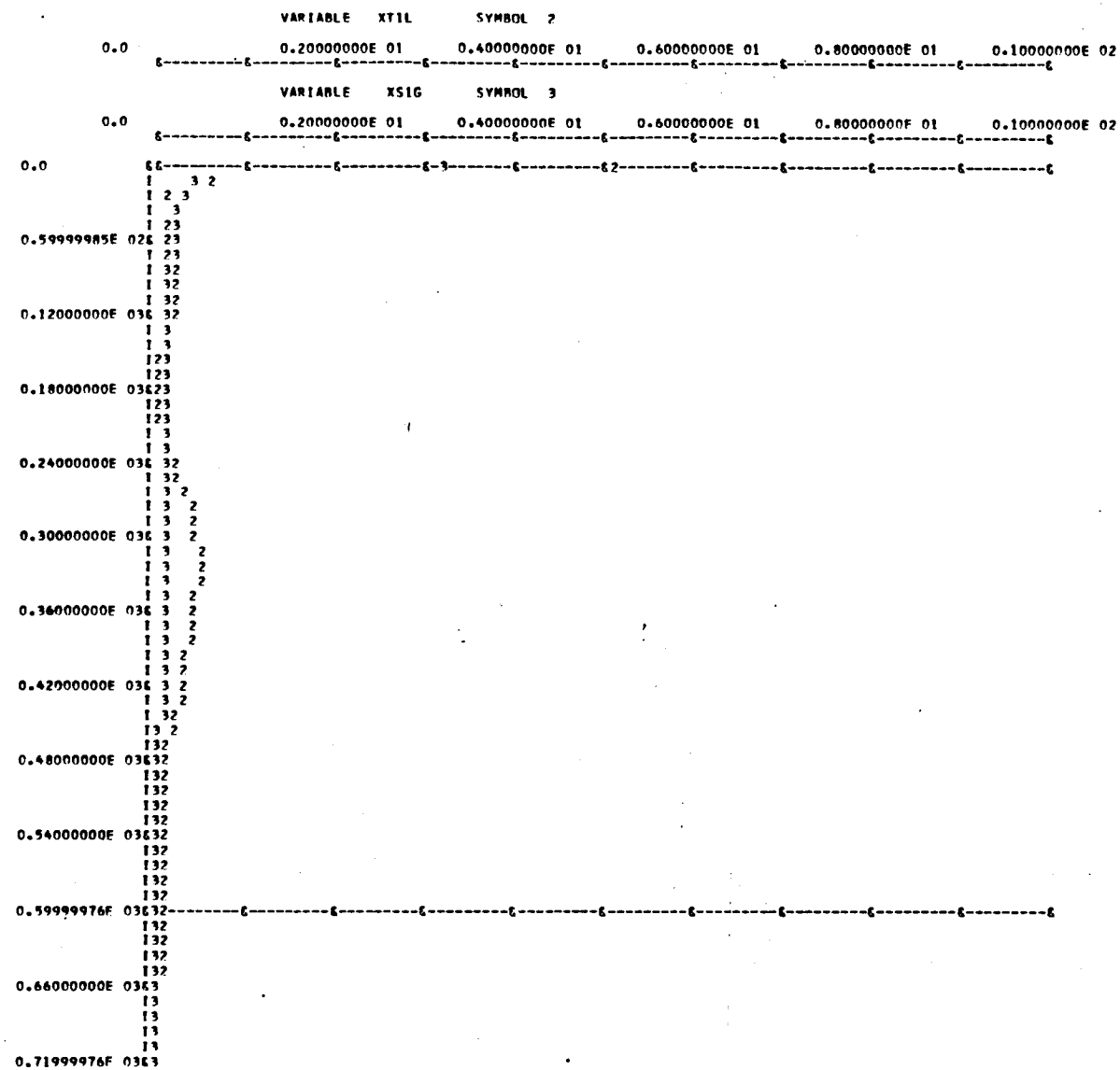

Figure B-97. Plot of the Error in Estimate, $\tilde{x} \sim$ km, and the Standard Deviation of the Error, $\sigma_x \sim$ km, vs Time $\sim$ secs for Earth Single Pass Entry (Run 3003)

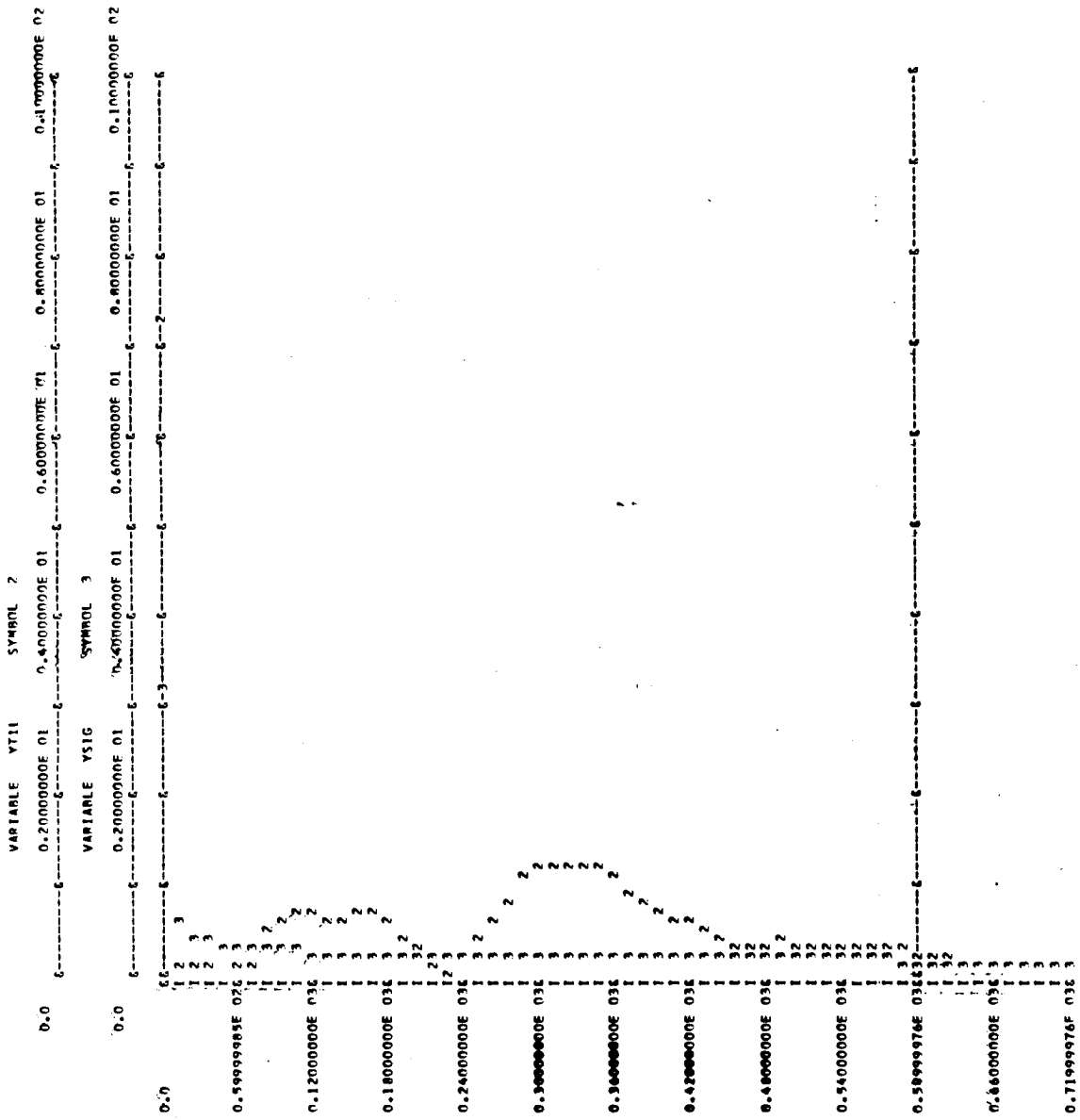

Figure B-98. Plot of the Error in Estimate, $\tilde{y} \sim$ km, and the Standard Deviation of the Error, $\sigma_y \sim$ km, vs Time $\sim$ secs for Earth Single Pass Entry (Run 3003)

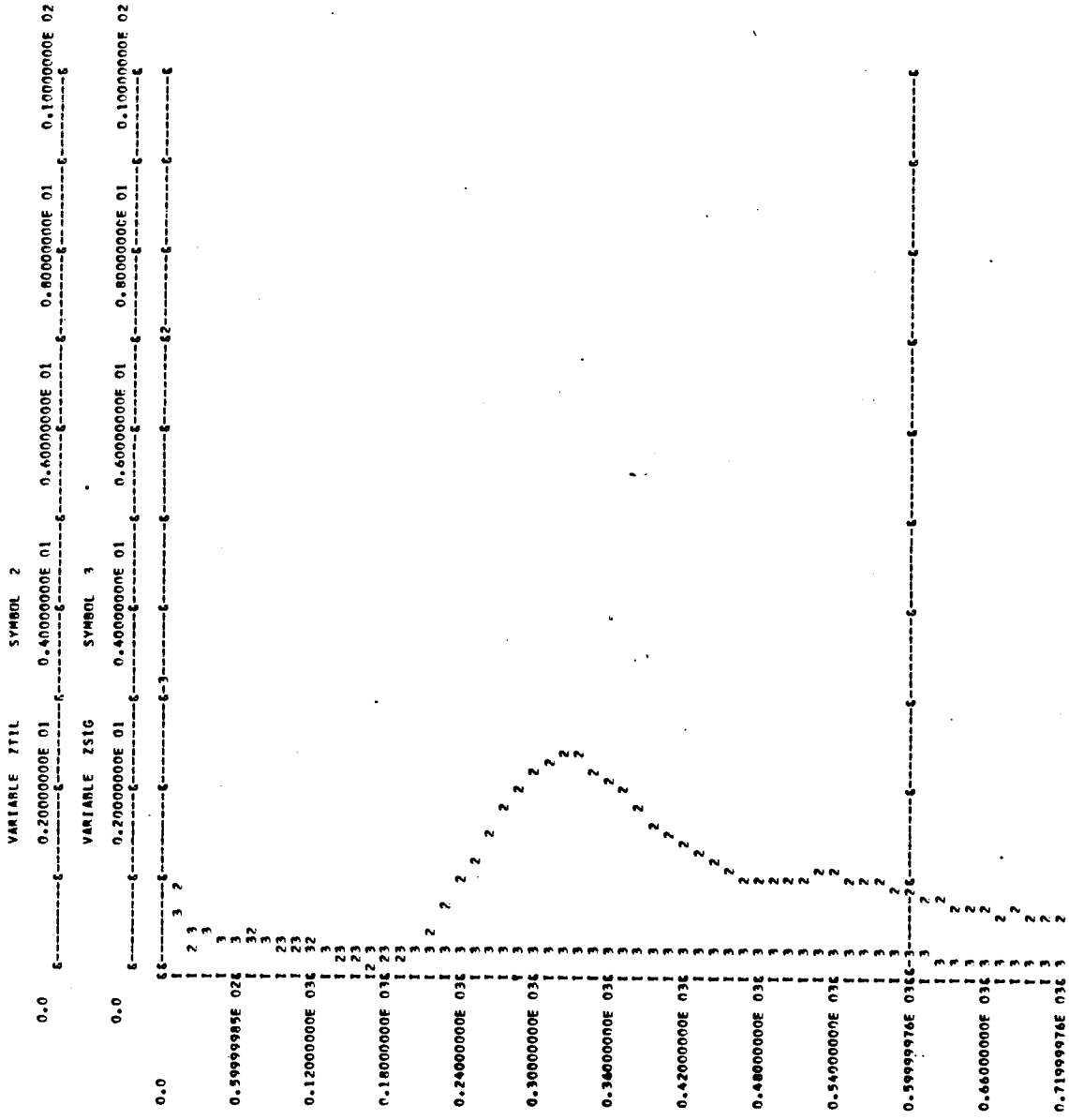

Figure B-99. Plot of the Error in Estimate, $\tilde{z} \sim$ km, and the Standard Deviation of the Error, $\sigma_z \sim$ km, vs Time $\sim$ secs for Earth Single Pass Entry (Run 3003)

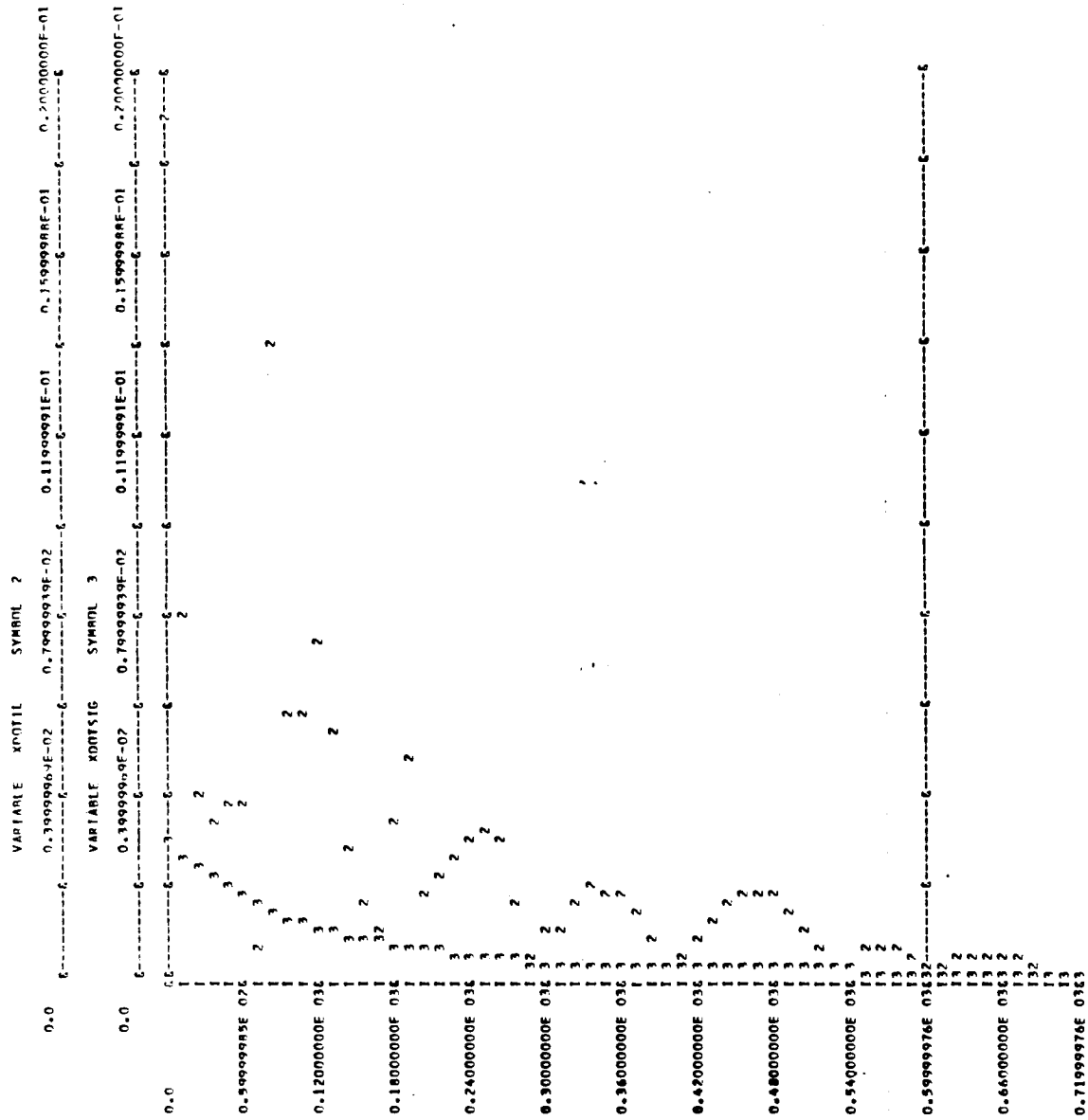

Figure B-100. Plot of the Error in Estimate $\tilde{\dot{x}} \sim$ km/sec, and the Standard Deviation of the Error, $\sigma_{\dot{x}} \sim$ km/sec, vs Time $\sim$ secs for Earth Single Pass Entry (Run 3003)

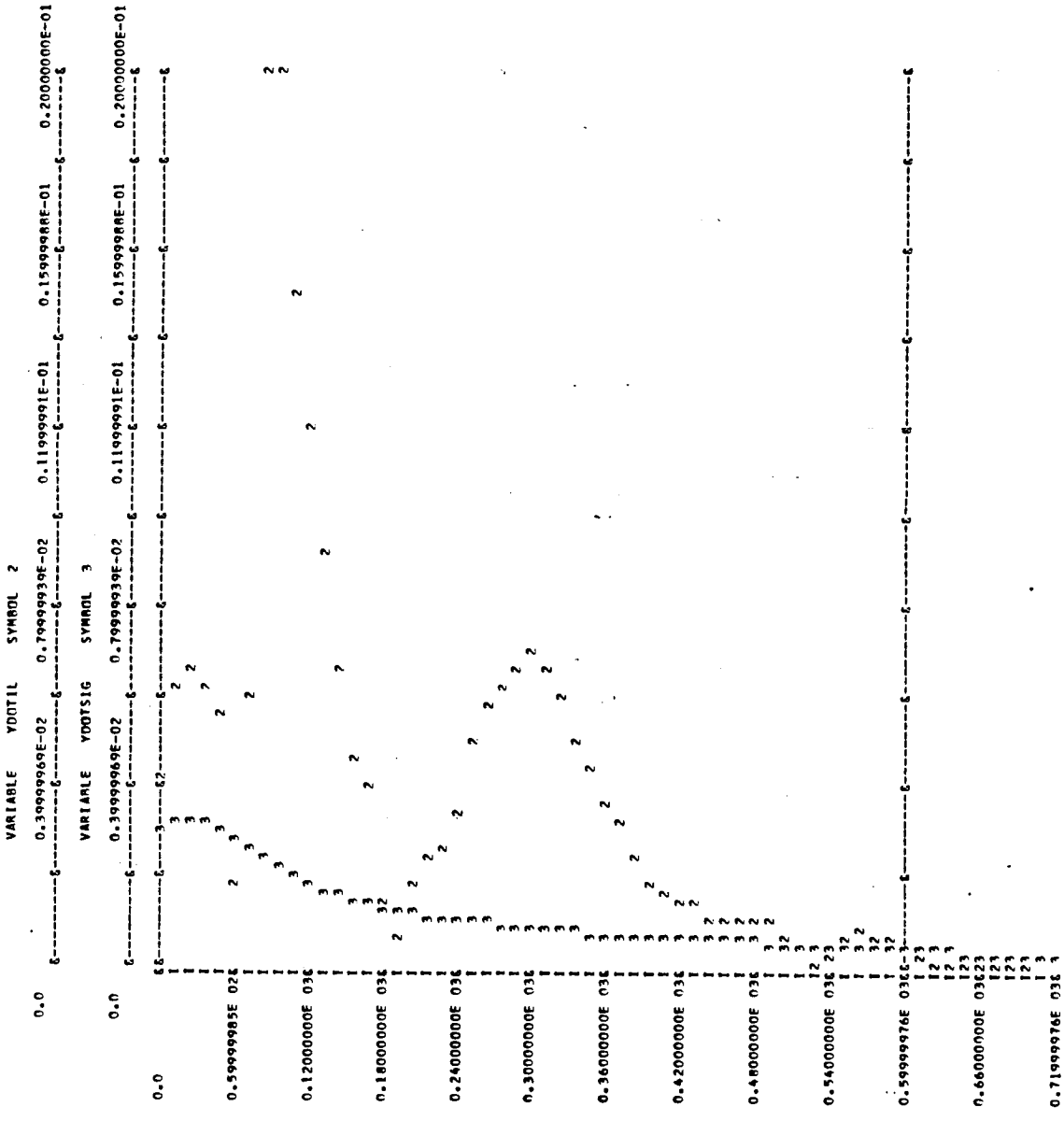

Figure B-101. Plot of the Error in Estimate, $\tilde{\dot{y}}$ ~ km/sec and the Standard Deviation of the Error $\sigma_{\dot{y}}$ ~ km/sec vs Time ~ secs for Earth Single Pass Entry (Run 3003)

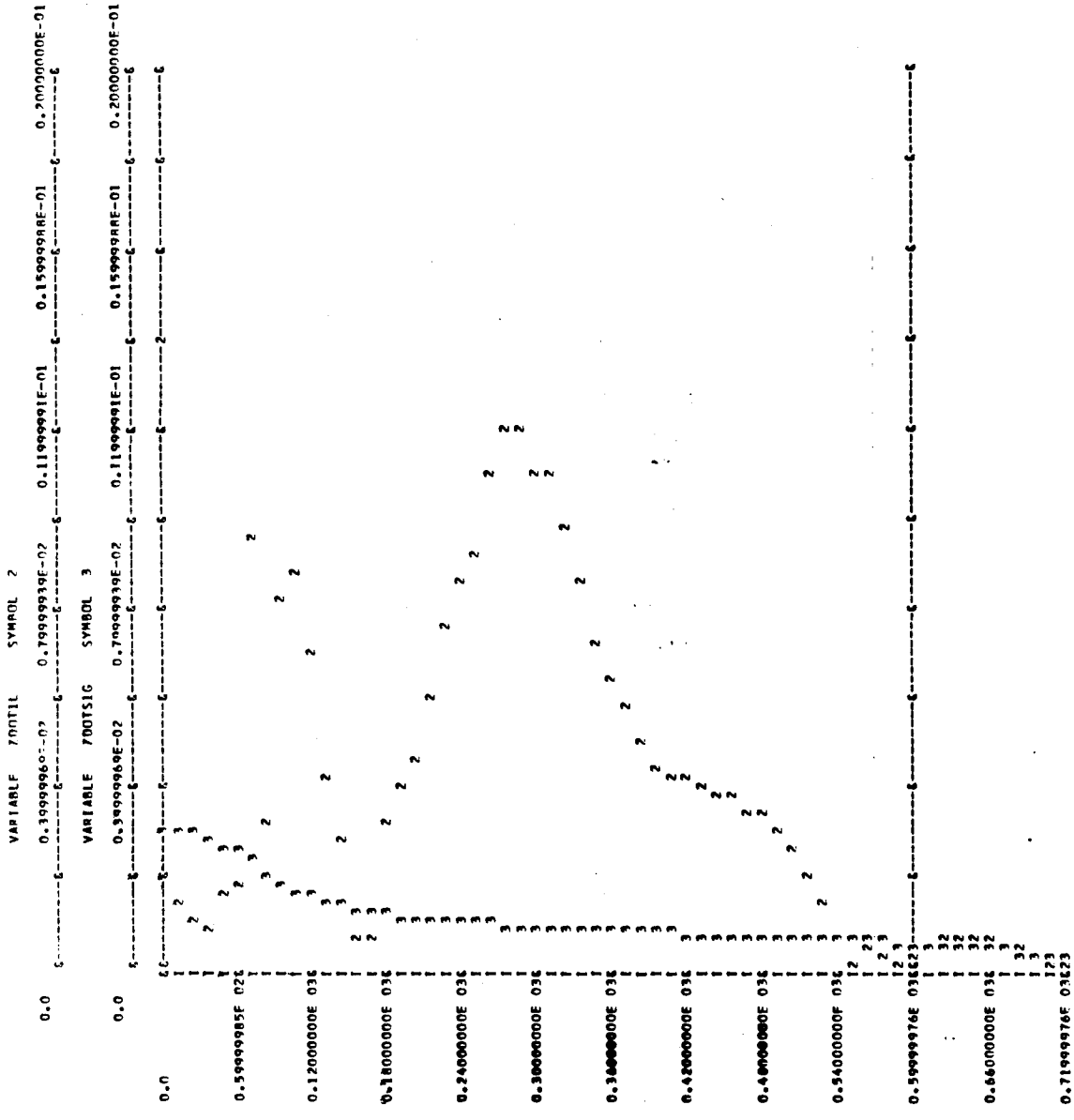

Figure B-102. Plot of the Error in Estimate $\tilde{\dot{z}}$ ~ km/sec and the Standard Deviation of the Error, $\sigma_{\dot{z}}$ ~ km/sec, vs Time ~ secs for Earth Single Pass Entry (Run 3003)

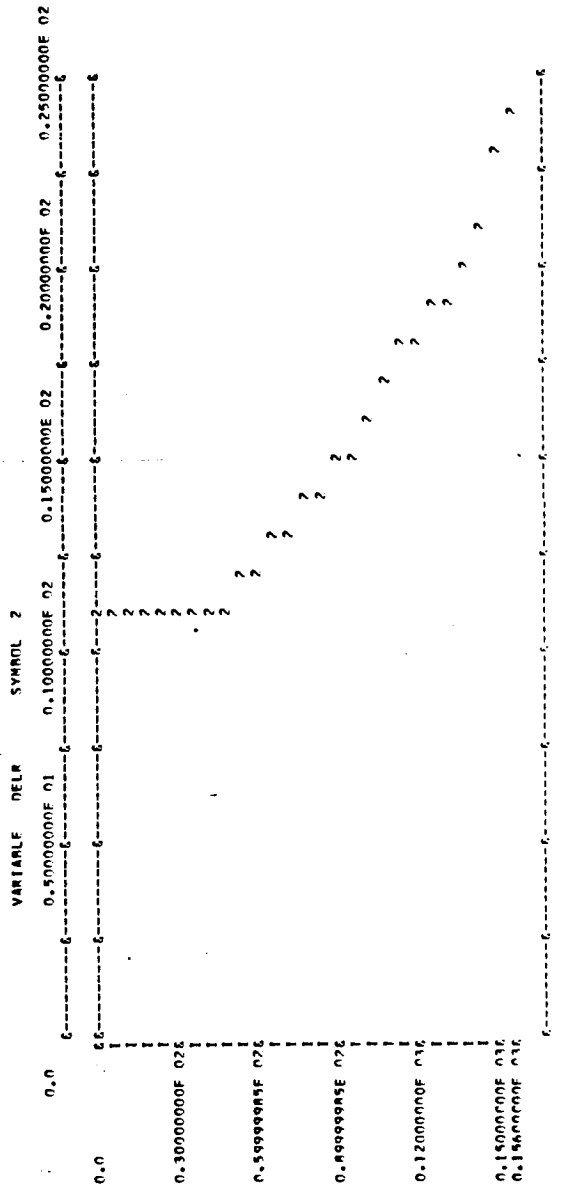

Figure B-103. Plot of the Magnitude of the Position Perturbation, $\Delta R \sim$ km, vs Time $\sim$ secs for Earth Single Pass Entry with Estimation on Aerodynamic Coefficients (Run 3005)

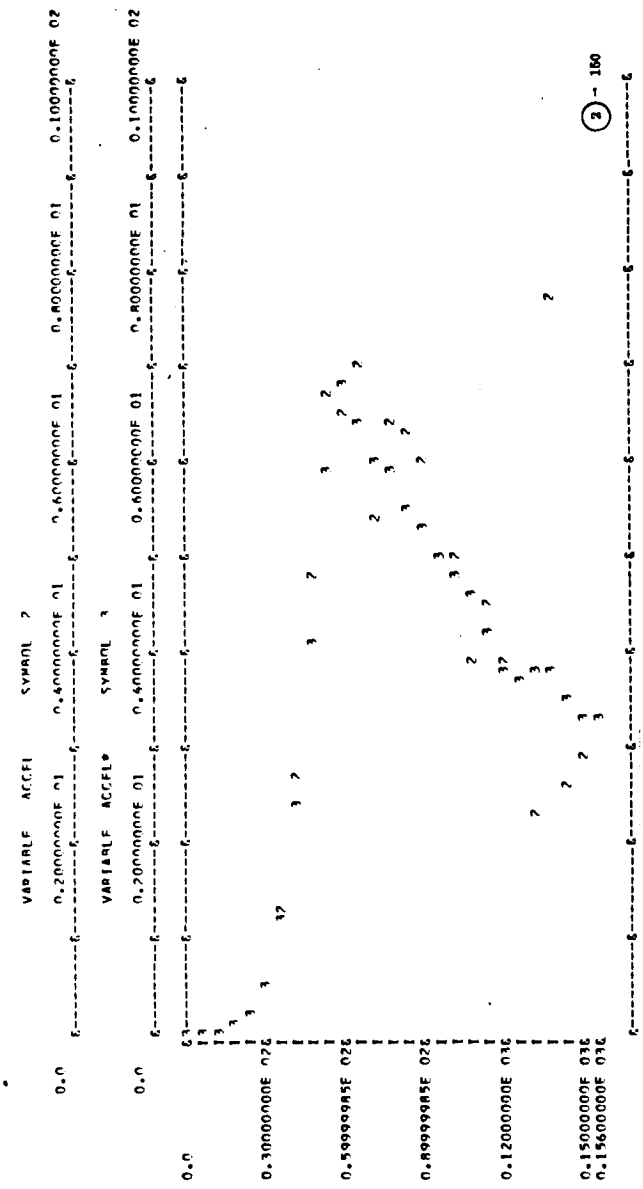

Figure B-104. Plot of the Aerodynamic Deceleration along the Actual, $a \sim$ g's and Nominal, $a^* \sim$ g's, Trajectories vs Time $\sim$ secs for Earth Single Pass Entry with Estimation on Aerodynamic Coefficients (Run 3005)

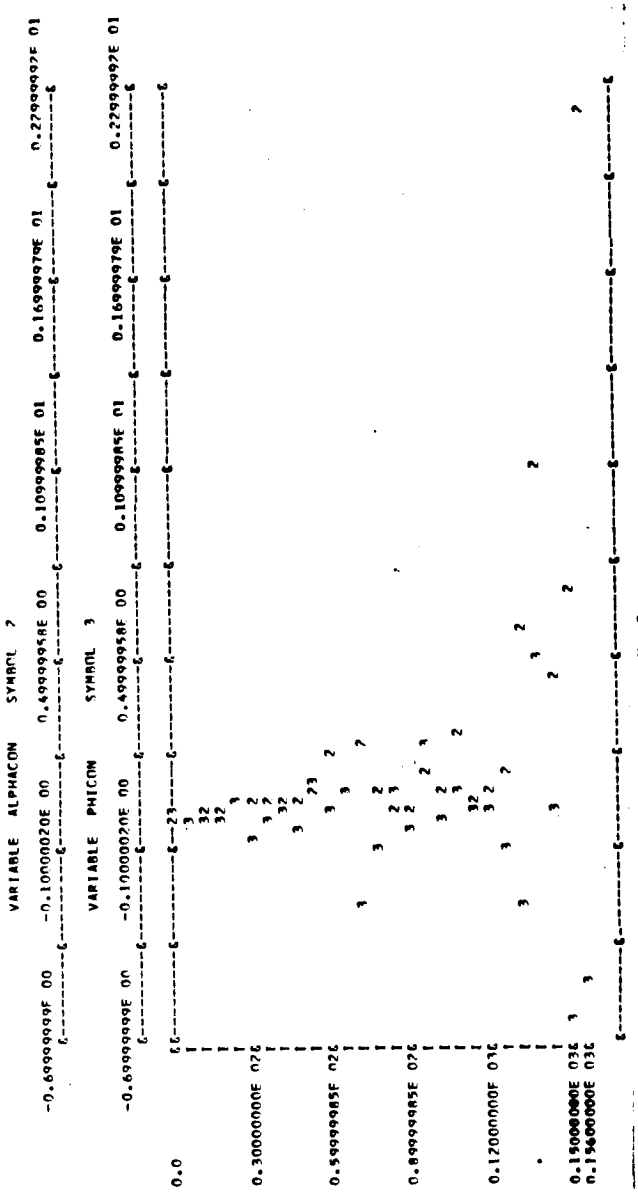

Figure B-105. Plot of the Perturbative Control in Pitch, $\delta\alpha \sim$ rad, and Roll, $\delta\varphi \sim$ rad, vs Time $\sim$ secs for Earth Single Pass Entry with Estimation on Aerodynamic Coefficients (Run 3005)

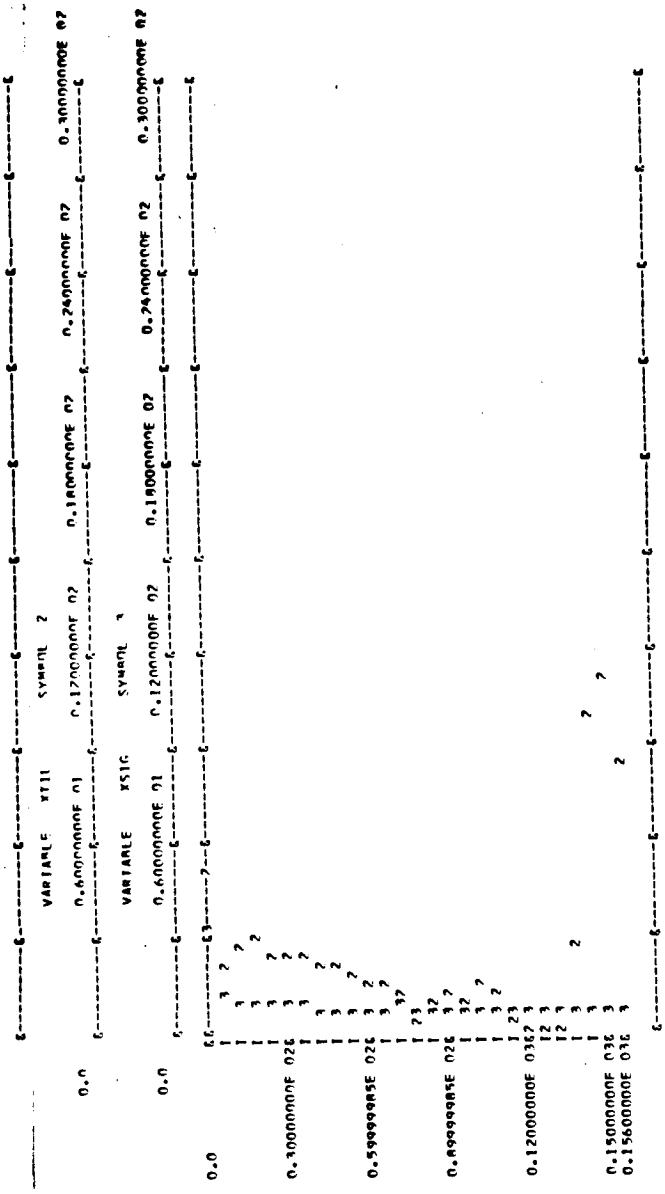

Figure B-106. Plot of the Error in Estimate, $\tilde{X} \sim$ km, and the Standard Deviation of the Error, $\sigma_X \sim$ km, vs Time $\sim$ secs for Earth Single Pass Entry with Estimation on Aerodynamic Coefficients (Run 3005)

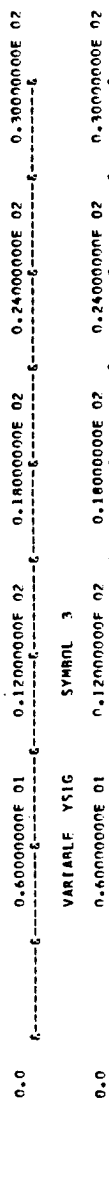

Figure B-107. Plot of the Error in Estimate, $\tilde{y} \sim$ km, and the Standard Deviation of the Error, $\sigma_y \sim$ km, vs Time $\sim$ secs for Earth Single Pass Entry with Estimation on Aerodynamic Coefficients (Run 3005)

Figure B-108. Plot of the Error in Estimate, $\tilde{z} \sim$ km, and the Standard Deviation of the Error, $\sigma_z \sim$ km, vs Time $\sim$ secs for Earth Single Pass Entry with Estimation on Aerodynamic Coefficients (Run 3005)

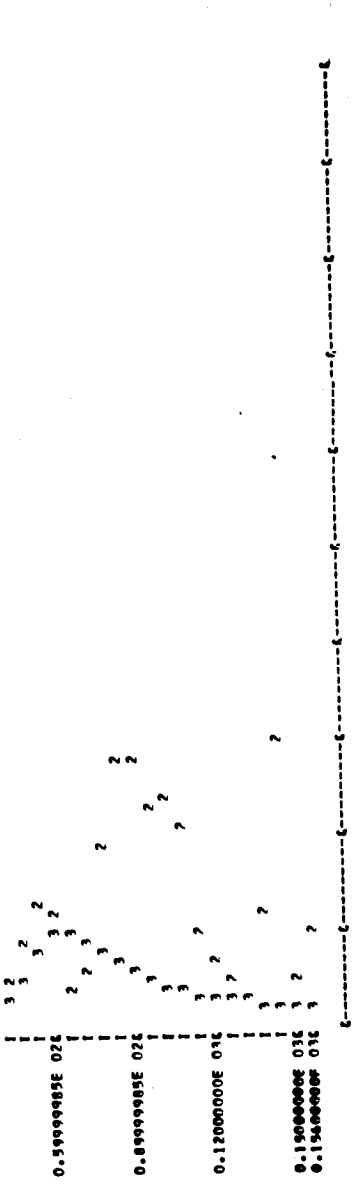

Figure B-109. Plot of the Error in Estimate, $\tilde{\dot{x}} \sim$ km/sec and the Standard Deviation of the Error, $\sigma_{\dot{x}} \sim$ km/sec vs Time $\sim$ secs for Earth Single Pass Entry with Estimation on Aerodynamic Coefficients (Run 3005)

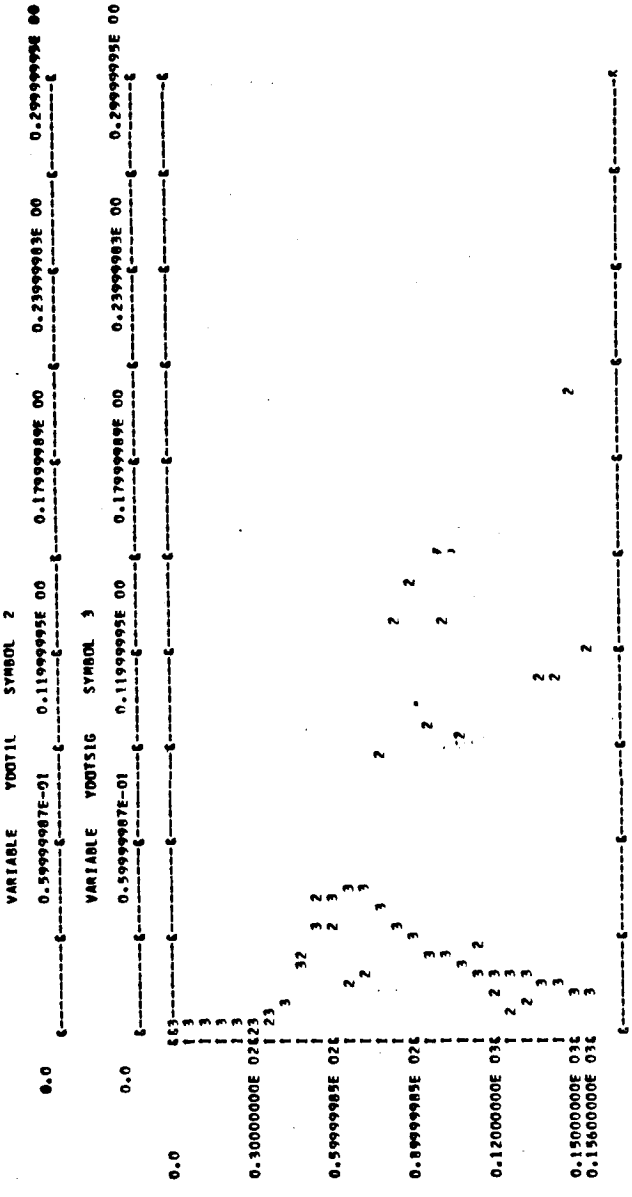

Figure B-110. Plot of the Error in Estimate, $\tilde{\dot{y}} \sim$ km/sec and the Standard Deviation of the Error, $\sigma_{\dot{y}} \sim$ km/sec vs Time $\sim$ secs for Earth Single Pass Entry with Estimation on Aerodynamic Coefficients (Run 3005)

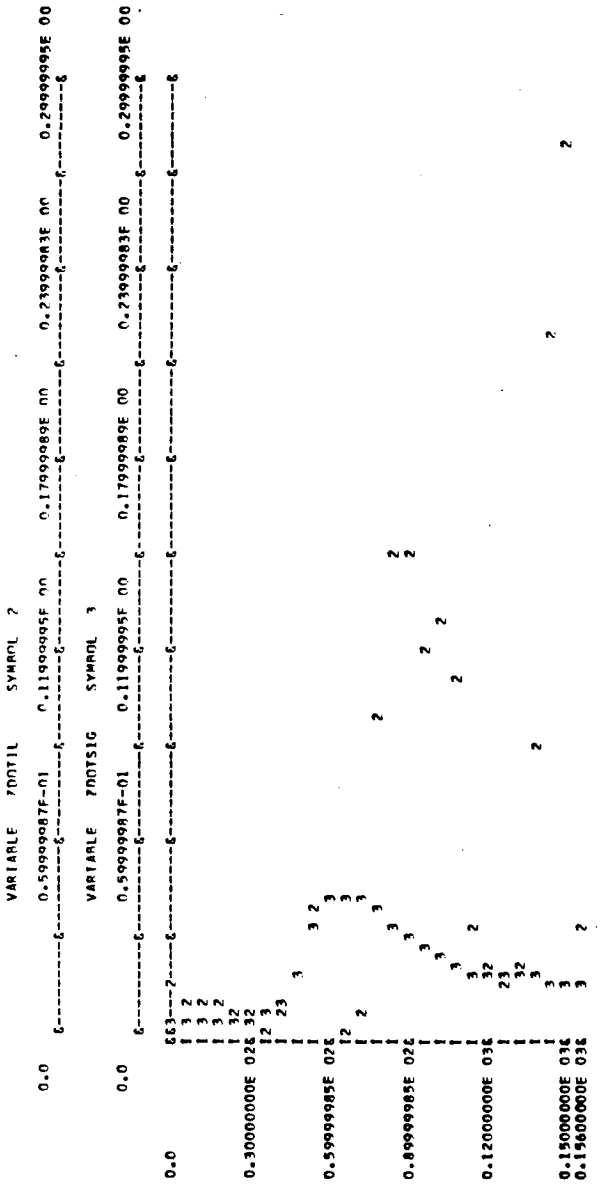

Figure B-111. Plot of the Error in Estimate $\tilde{z}$ ~ km/sec and the Standard Deviation of the Error, $\sigma_{\dot{z}}$ ~ km/sec, vs Time ~ secs for Earth Single Pass Entry with Estimation on Aerodynamic Coefficients (Run 3005)

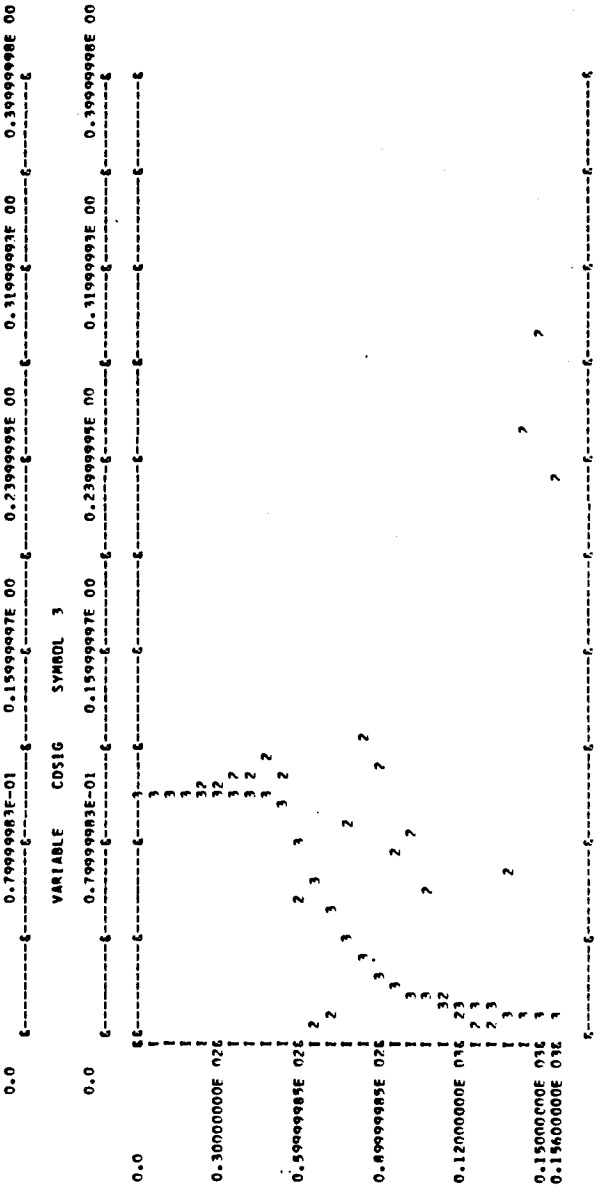

Figure B-112. Plot of the Error in Estimate, $\delta\tilde{C}_D$, and the Standard Deviation of the Error, σ_{CD}, vs Time ~ secs for Earth Single Pass Entry with Estimation on Aerodynamic Coefficients (Run 3005)

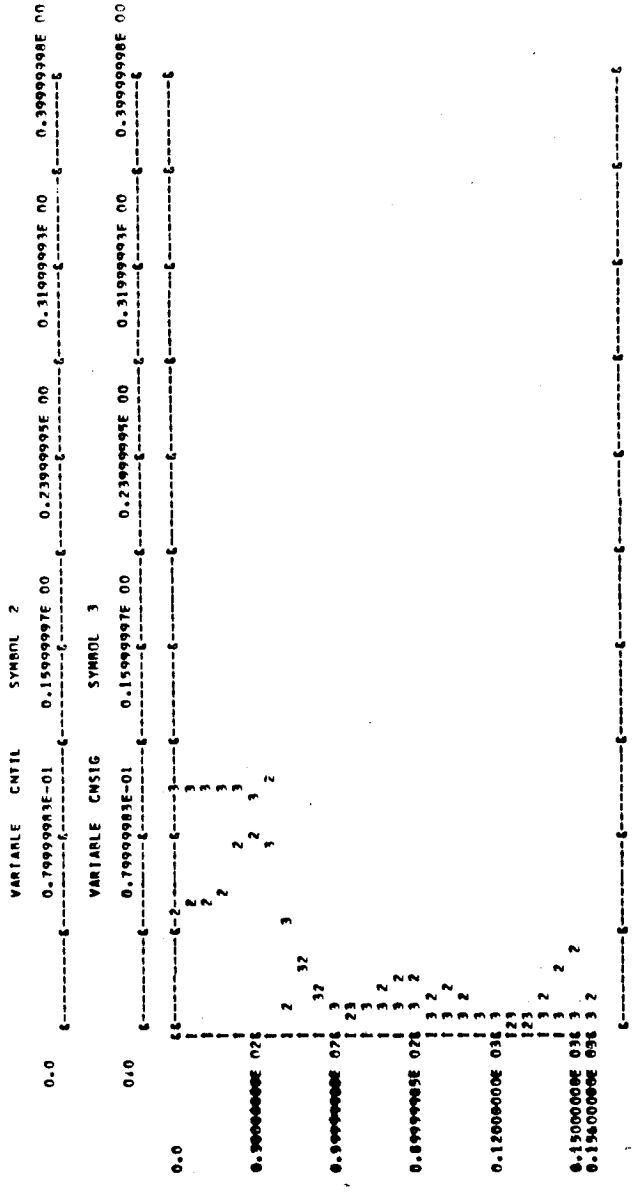

Figure B-113. Plot of the Error in Estimate, $\delta\tilde{C}_N$, and the Standard Deviation of the Error, σ_{C_N}, vs Time ~ secs for Earth Single Pass Entry with Estimation on Aerodynamic Coefficients (Run 3005)

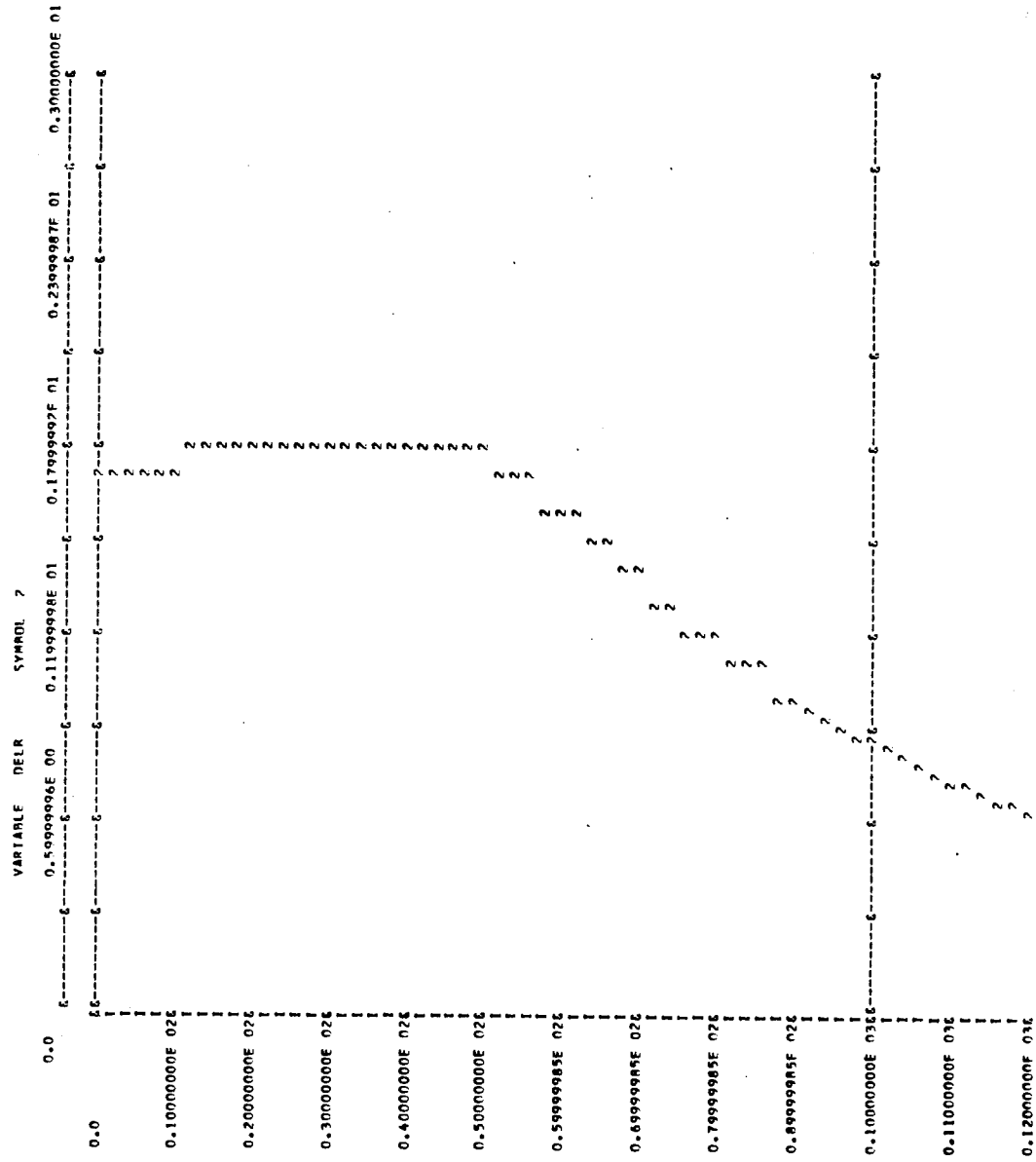

Figure B-114. Plot of the Magnitude of the Position Perturbation, $\Delta R \sim$ km, vs. Time $\sim$ secs for Guided Atmospheric Braking Trajectory (Run 601)

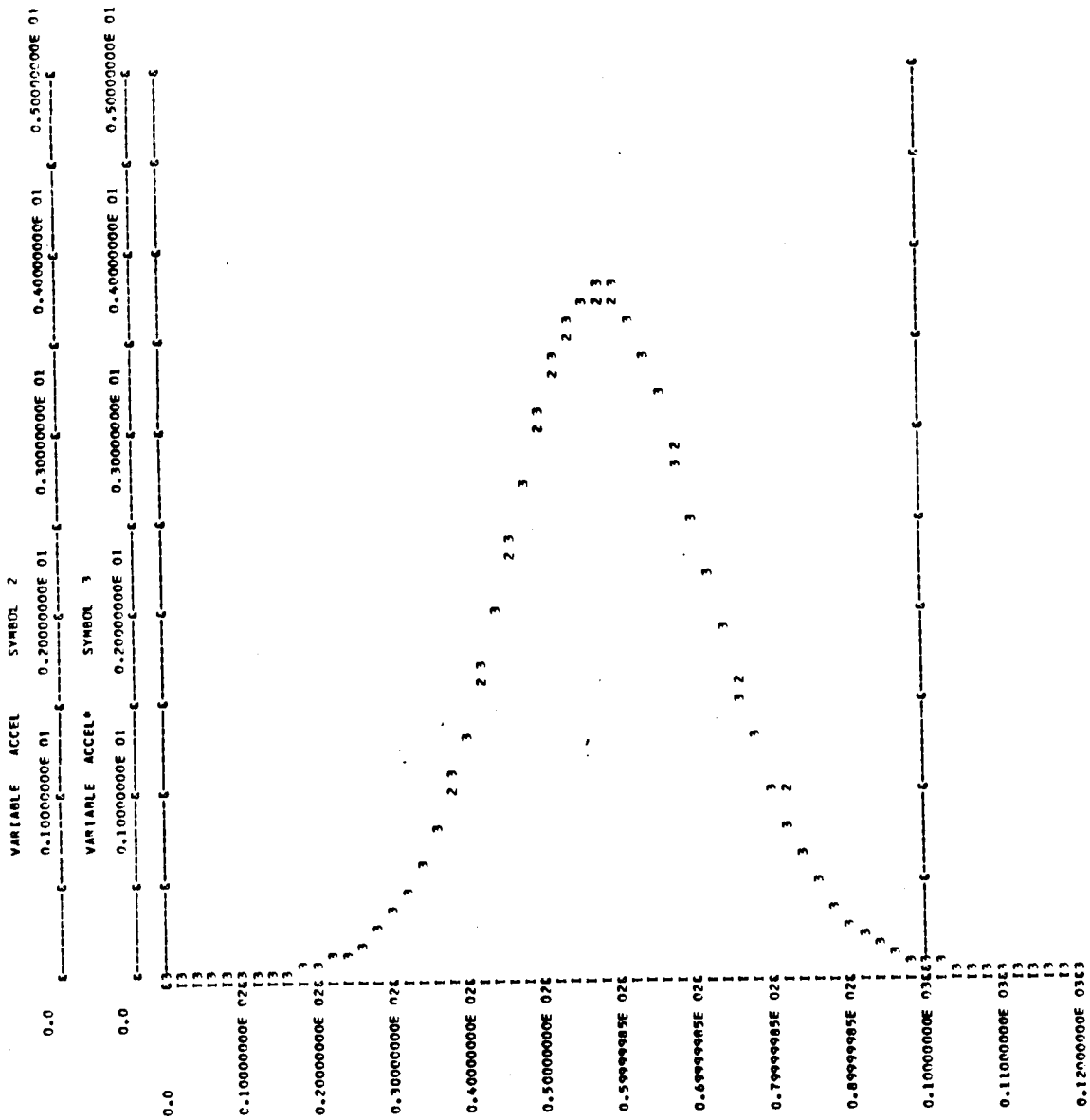

Figure B-115. Plot of the Aerodynamic Deceleration Along the Actual, a ~ g's, and Nominal, a* ~ g's Trajectories vs. Time ~ secs for Guided Atmospheric Braking Trajectory (Run 601)

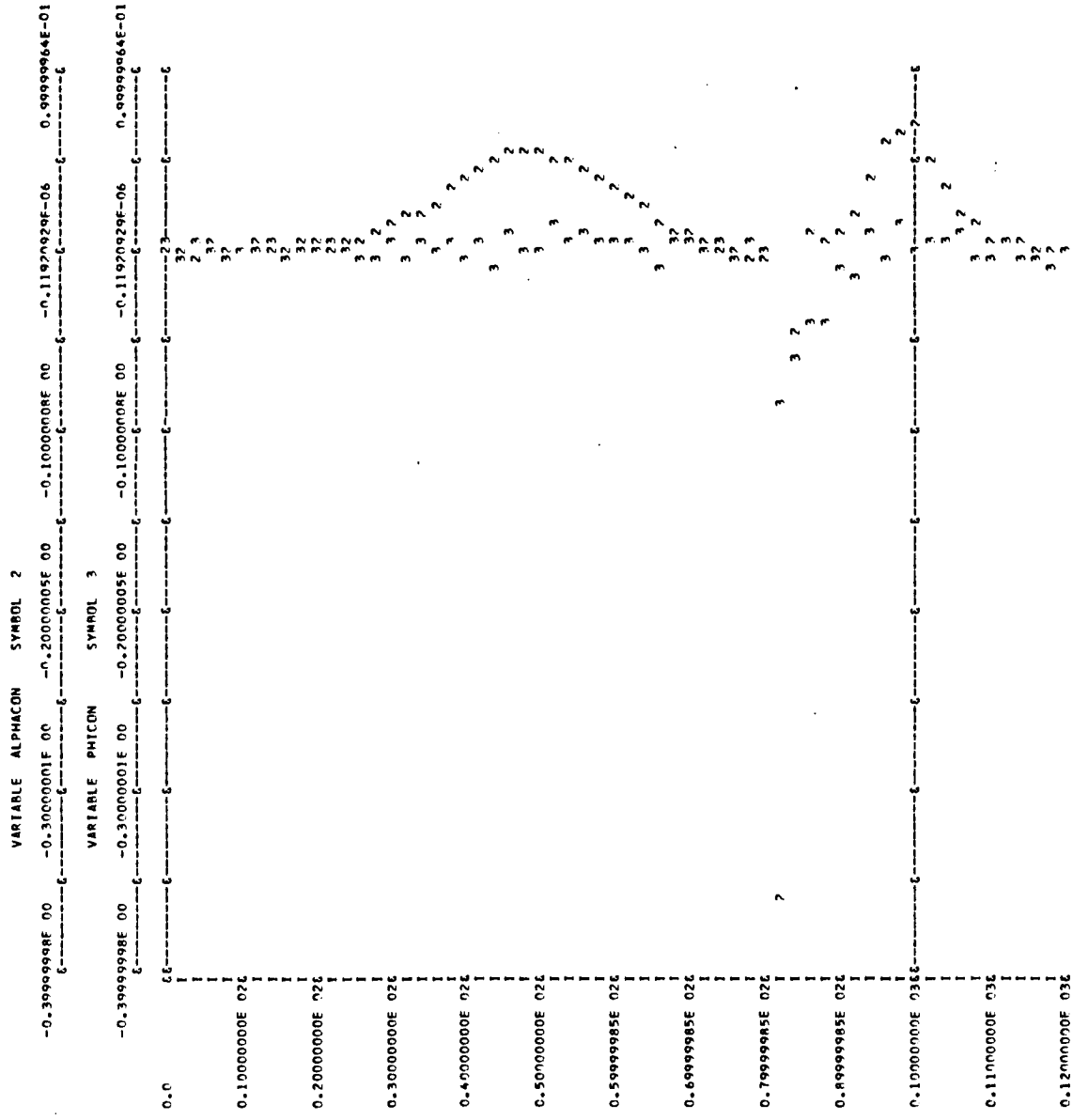

Figure B-116. Plot of the Perturbative Control in Pitch, $\delta\alpha \sim$ rad, and Roll, $\delta\varphi \sim$ rad, vs. Time $\sim$ secs for Guided Atmospheric Braking Trajectory (Run 601)

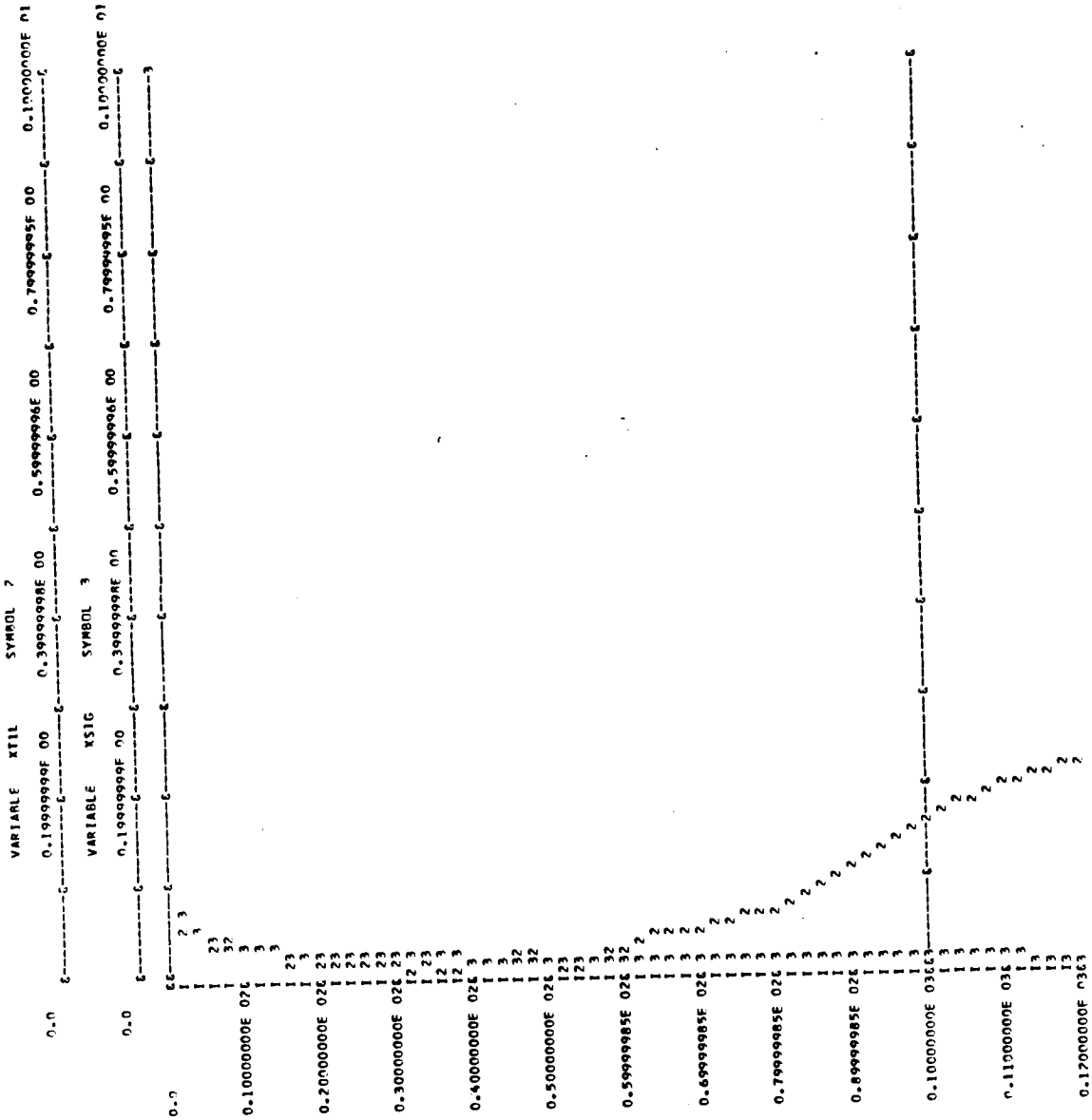

Figure B-117. Plot of the Error in Estimate, $\tilde{x} \sim$ km, and the Standard Deviation of the Error, $\sigma_x \sim$ km, vs. Time $\sim$ secs for Guided Atmospheric Braking Trajectory (Run 601)

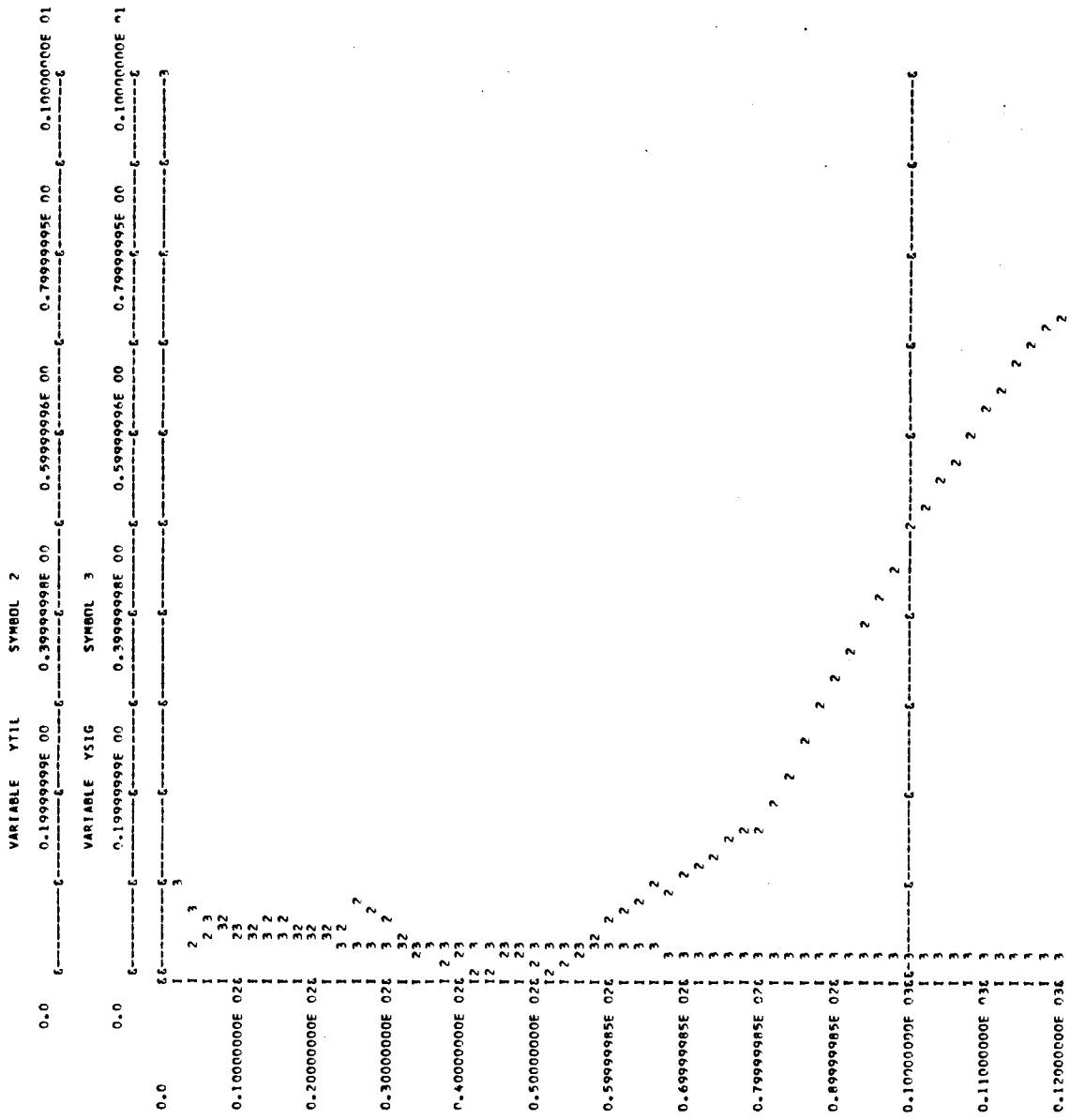

Figure B-118. Plot of the Error in Estimate, $\tilde{y} \sim$ km, and the Standard Deviation of the Error, $\sigma_y \sim$ km, vs. Time $\sim$ secs for Guided Atmospheric Braking Trajectory (Run 601)

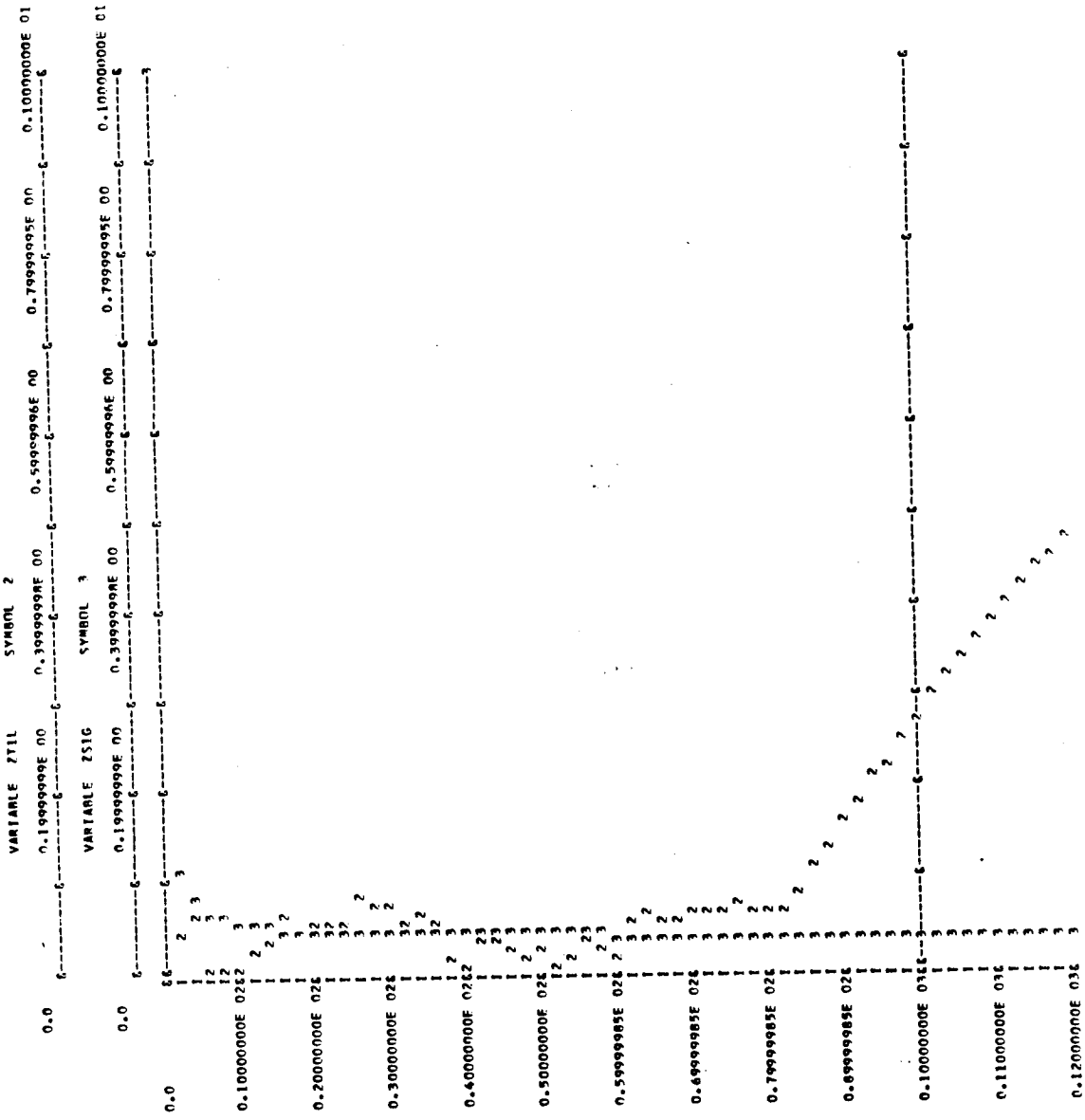

Figure B-119. Plot of the Error in Estimate, $\tilde{z}$ ~ km, and the Standard Deviation of the Error, σ_z ~ km, vs. Time ~ secs for Guided Atmospheric Braking Trajectory (Run 601)

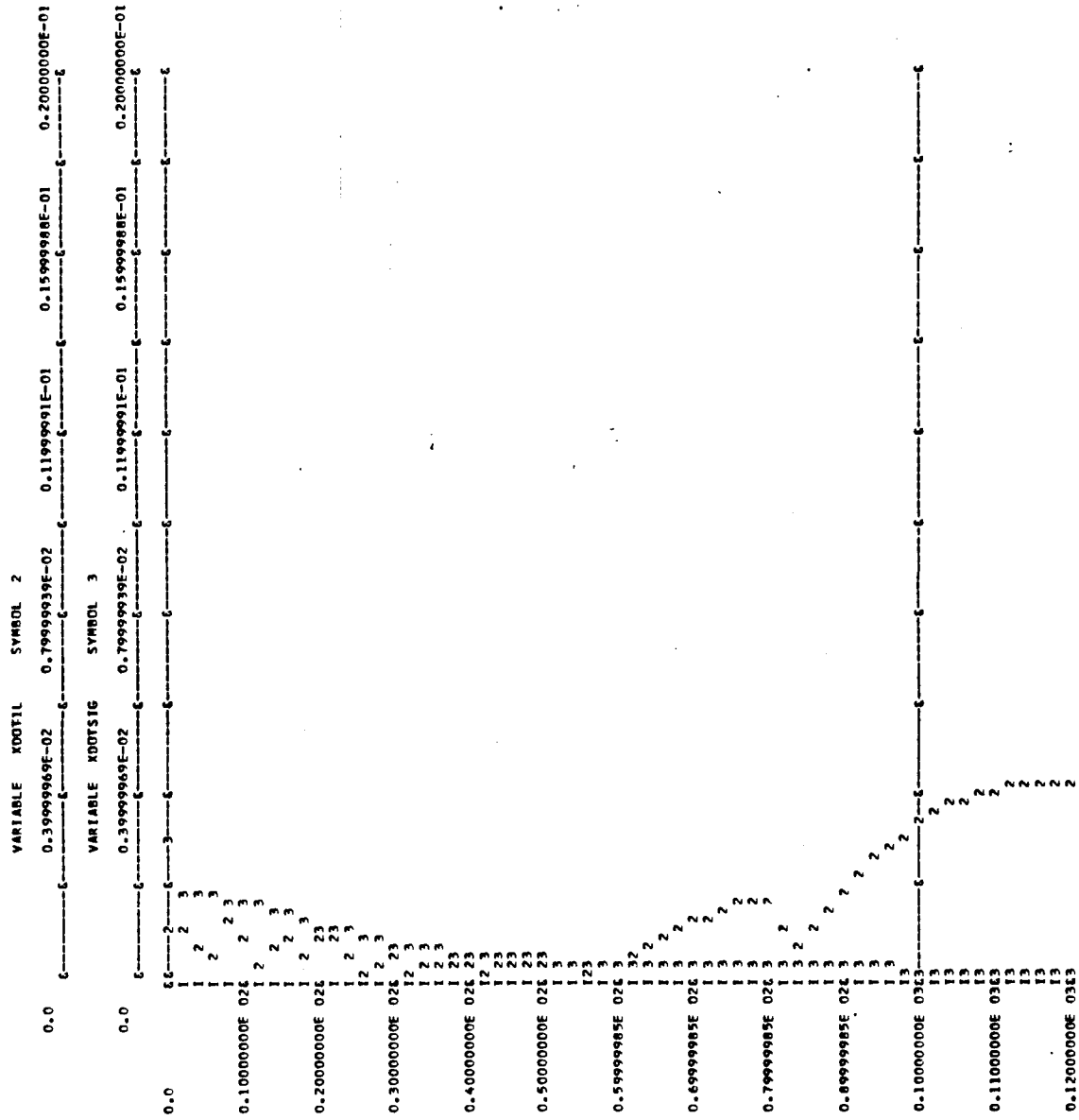

Figure B-120. Plot of the Error in Estimate $\tilde{\dot{x}}$ ~ km/sec, and the Standard Deviation of the Error, $\sigma_{\dot{x}}$ ~ km/sec, vs. Time ~ secs for Guided Atmospheric Braking Trajectory (Run 601)

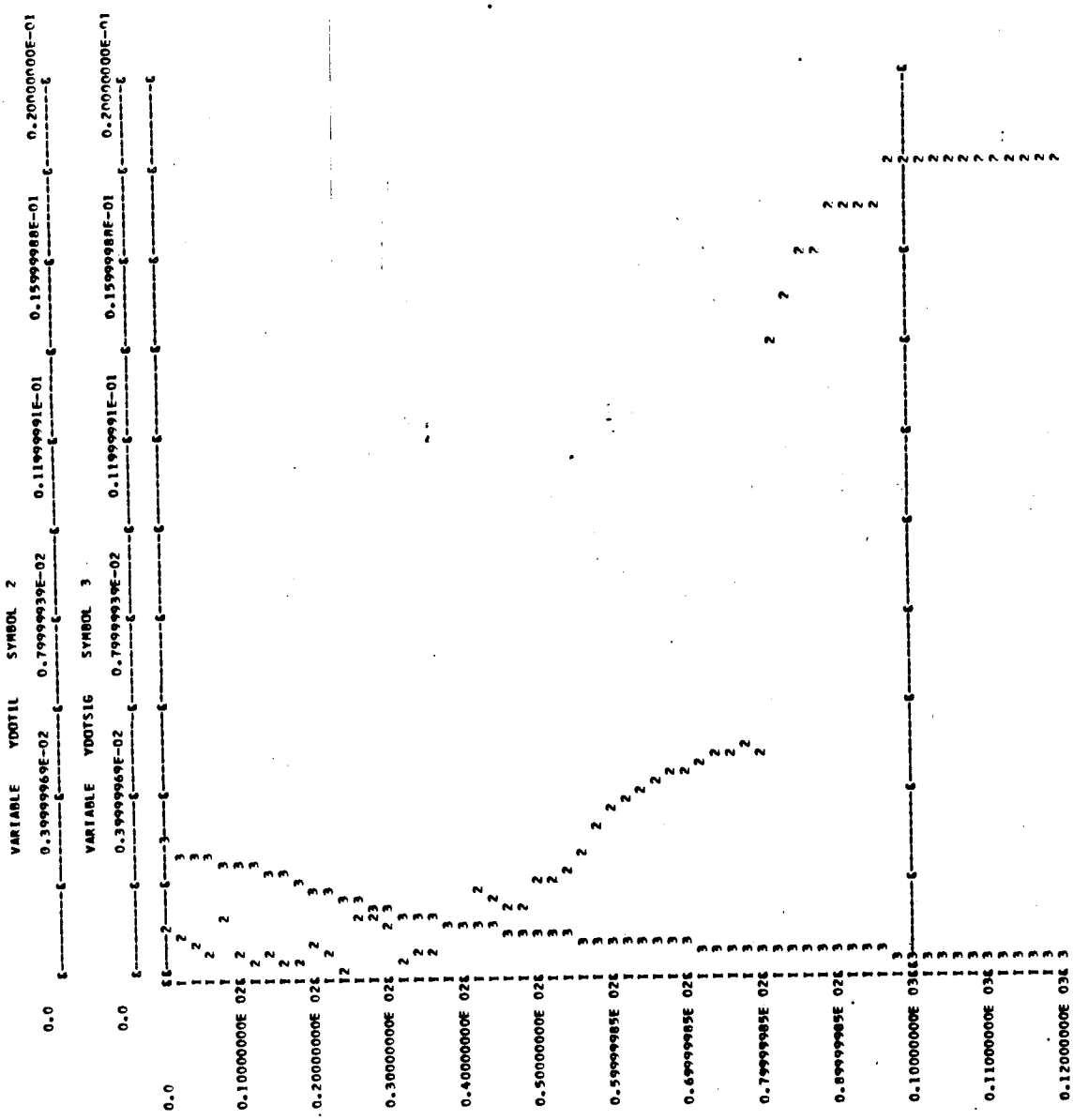

Figure B-121. Plot of the Error in Estimate $\tilde{\dot{y}}$ ~ km/sec and the Standard Deviation of the Error, $\sigma_{\dot{y}}$ ~ km vs. Time ~ secs for Guided Atmospheric Braking Trajectory (Run 601)

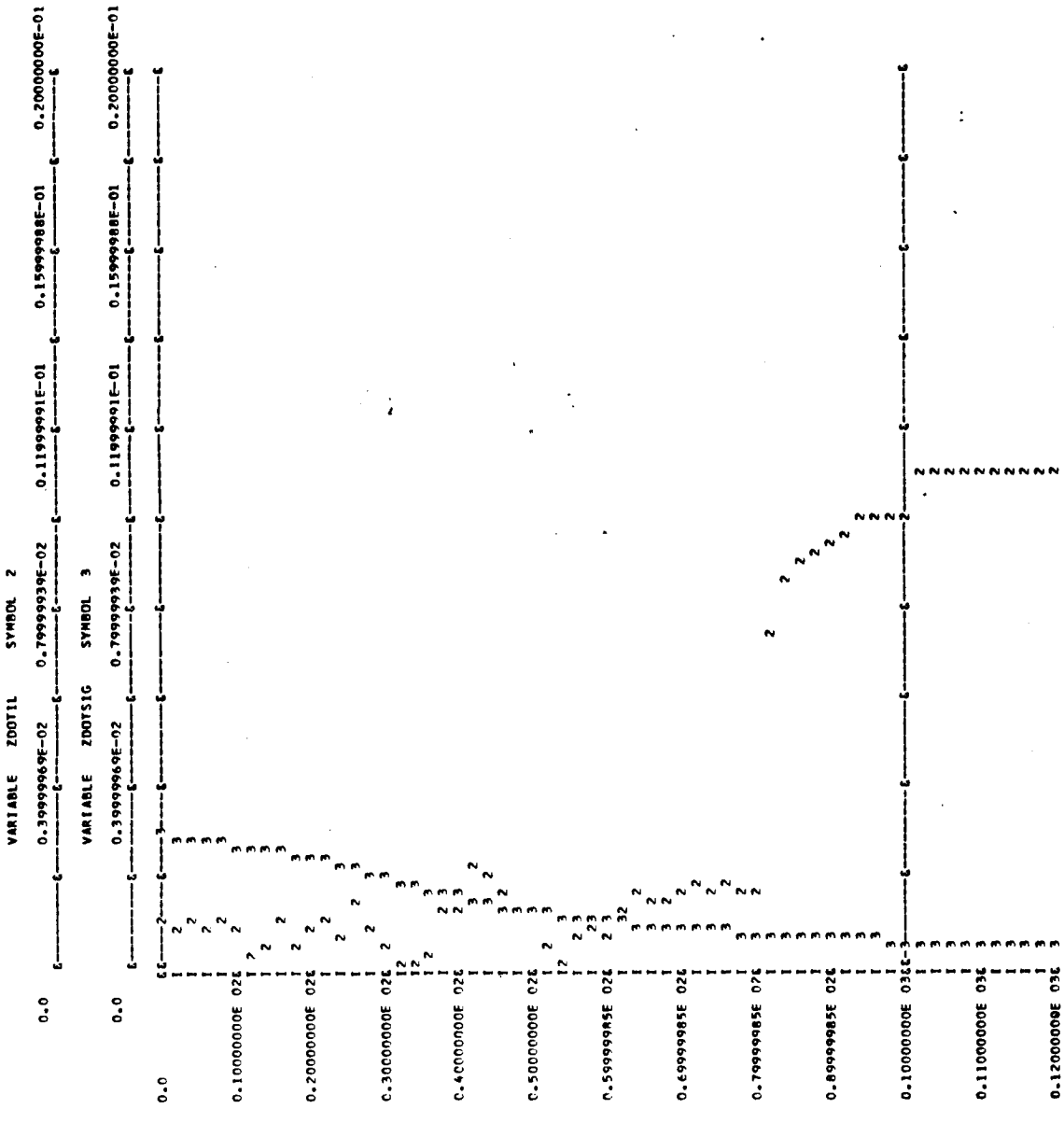

Figure B-122. Plot of the Error in Estimate $\tilde{\dot{z}}$ ~ km/sec and the Standard Deviation of the Error, $\sigma_{\dot{z}}$ ~ km/sec, vs. Time ~ secs for Guided Atmospheric Braking Trajectory (Run 601)

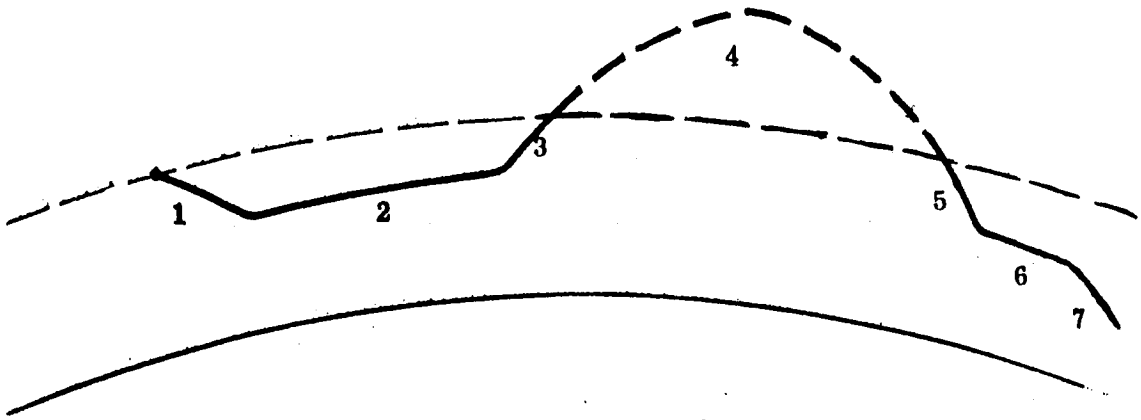

Figure B-123. Trajectory Profile (Schematic)

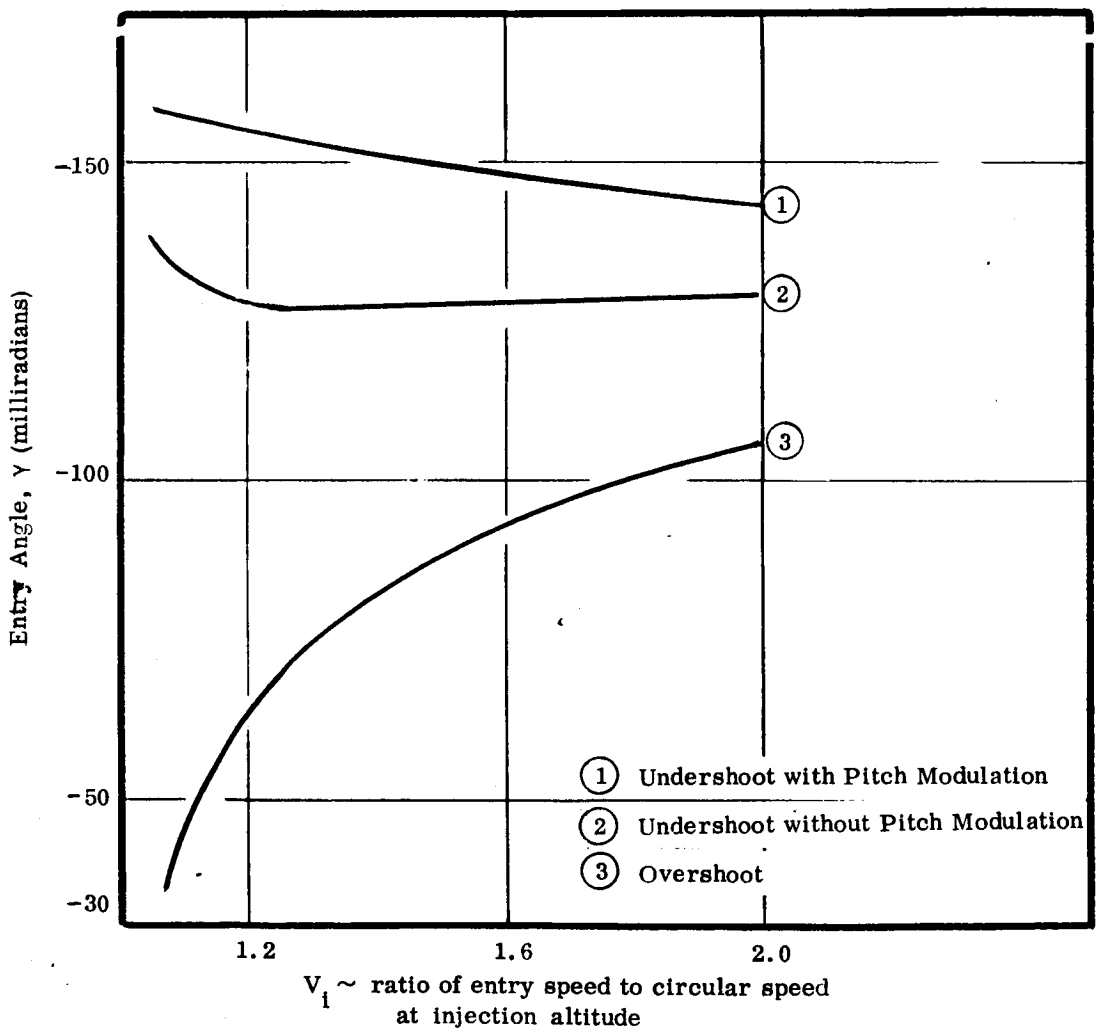

Figure B-124. Earth Entry Corridor for Apollo Type Vehicles, With and Without Pitch Modulation

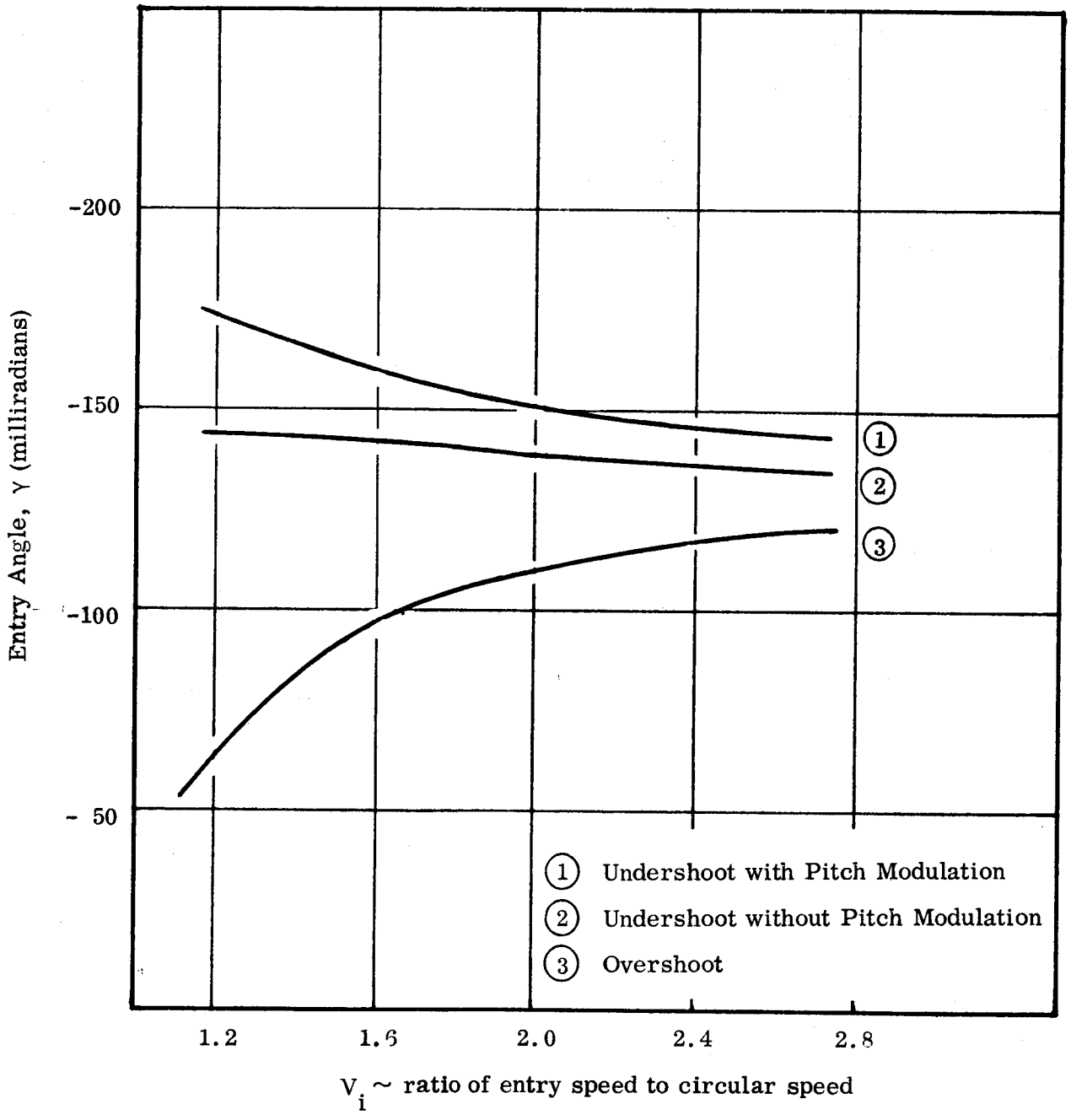

Figure B-125. Earth Entry Corridor for HL-10 Type Vehicle, With and Without Pitch Modulation

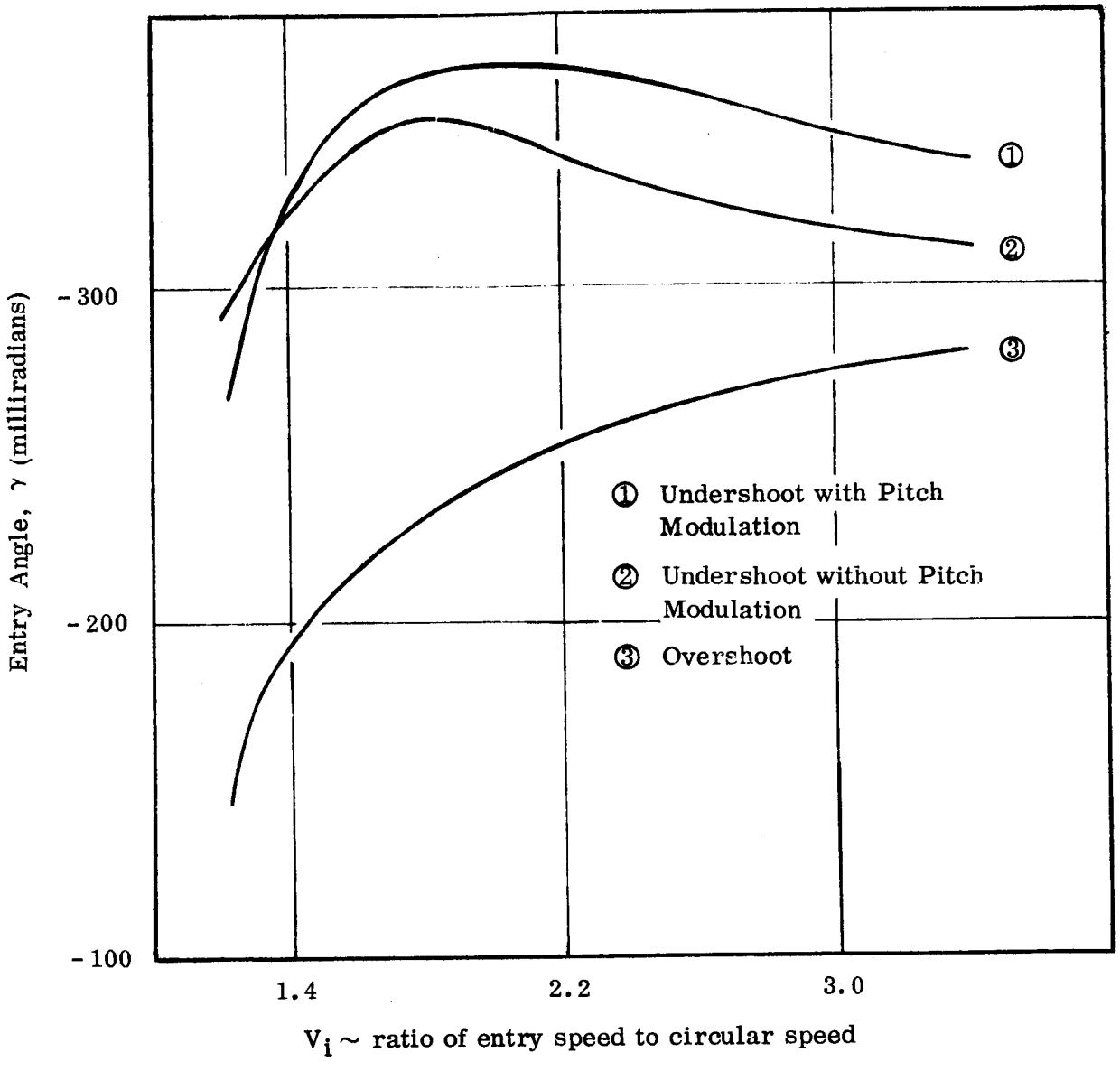

Figure B-126. Mars Entry Corridor for Apollo Type Vehicle With and Without Pitch Modulation, Mars I Atmosphere

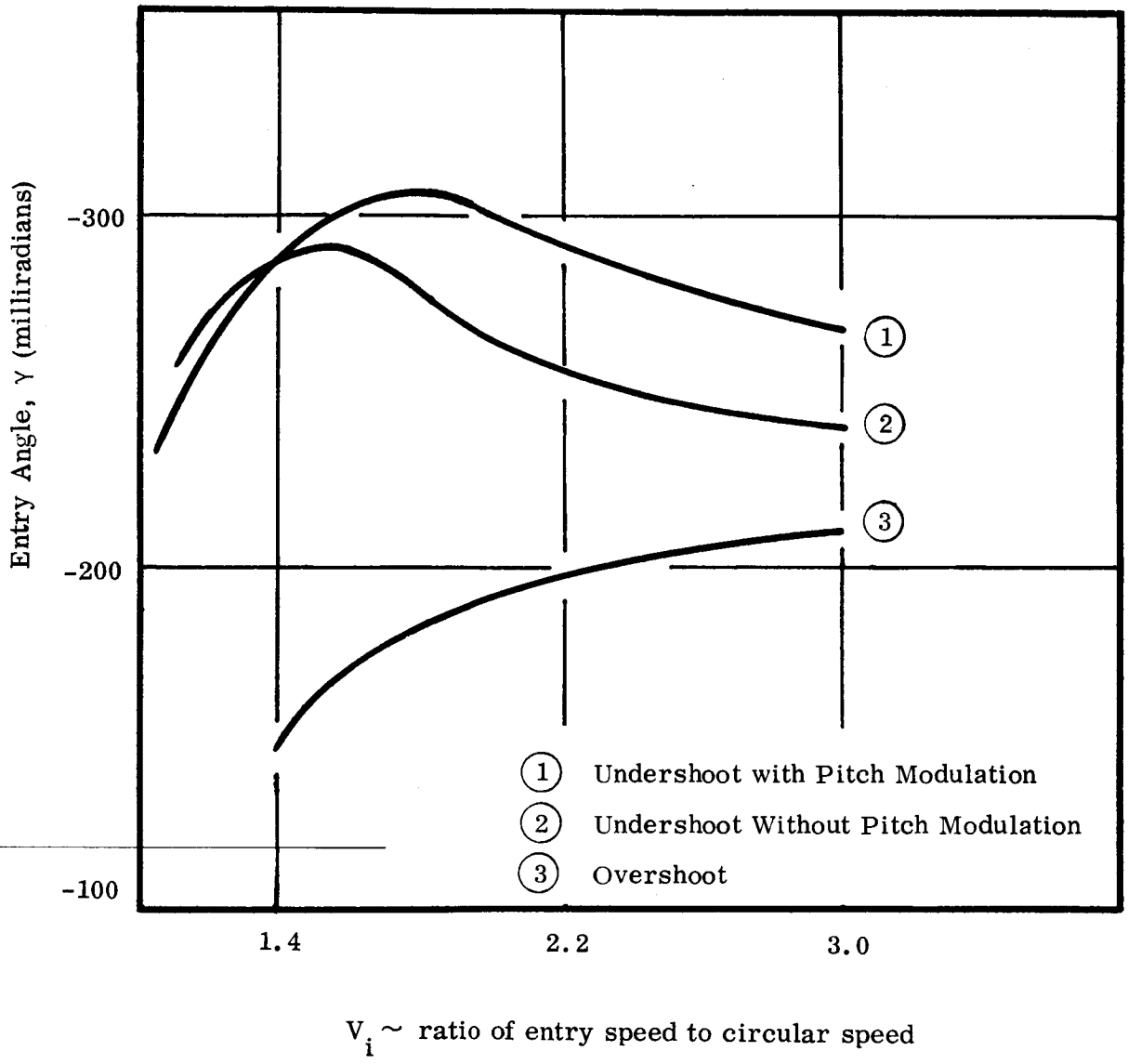

Figure B-127. Mars Entry Corridor for Apollo Type Vehicle, With and Without Pitch Modulation, Mars III Atmosphere

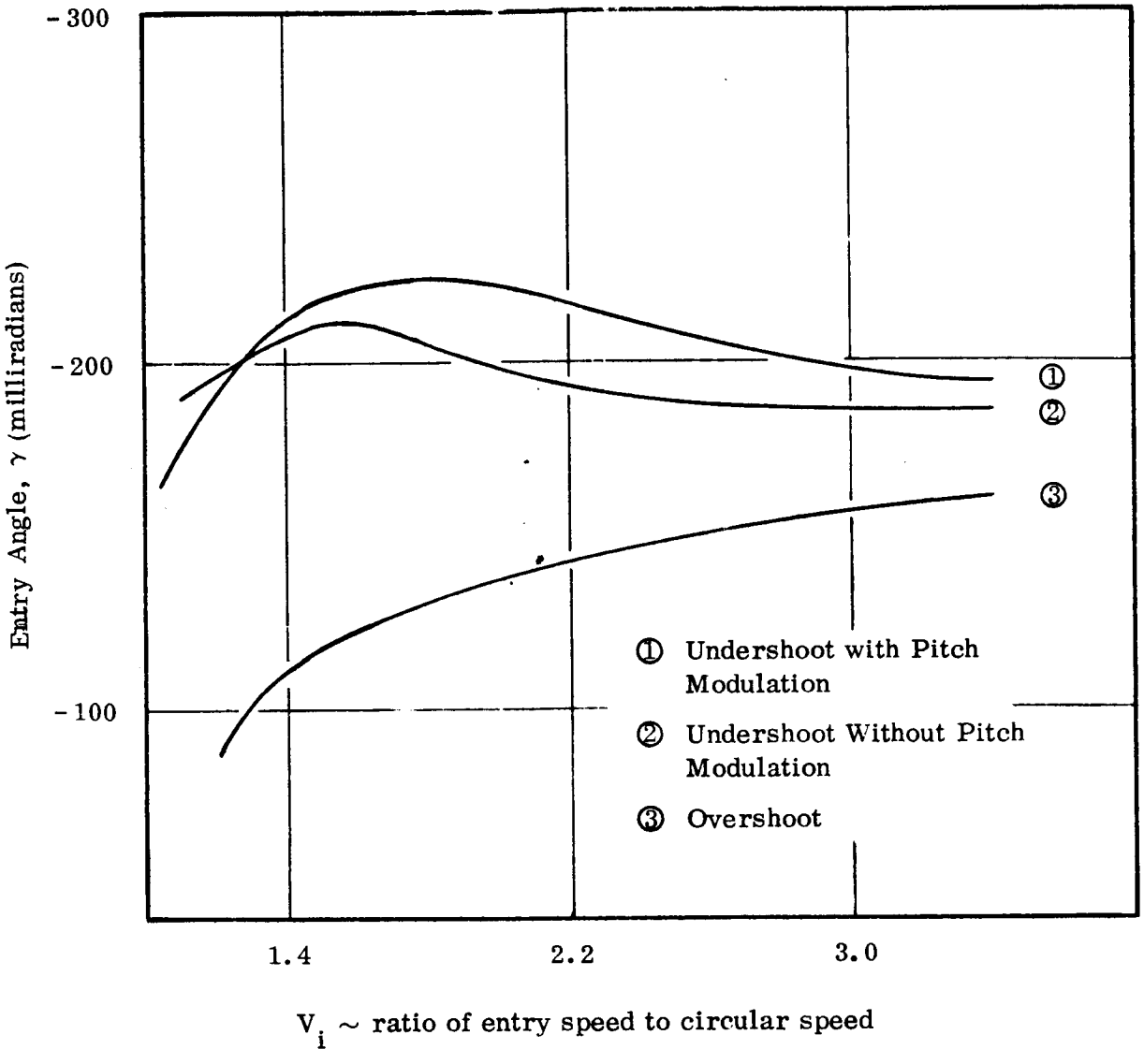

Figure B-128. Mars Entry Corridor for Apollo Type Vehicle, With and Without Pitch Modulation, Mars III Atmosphere

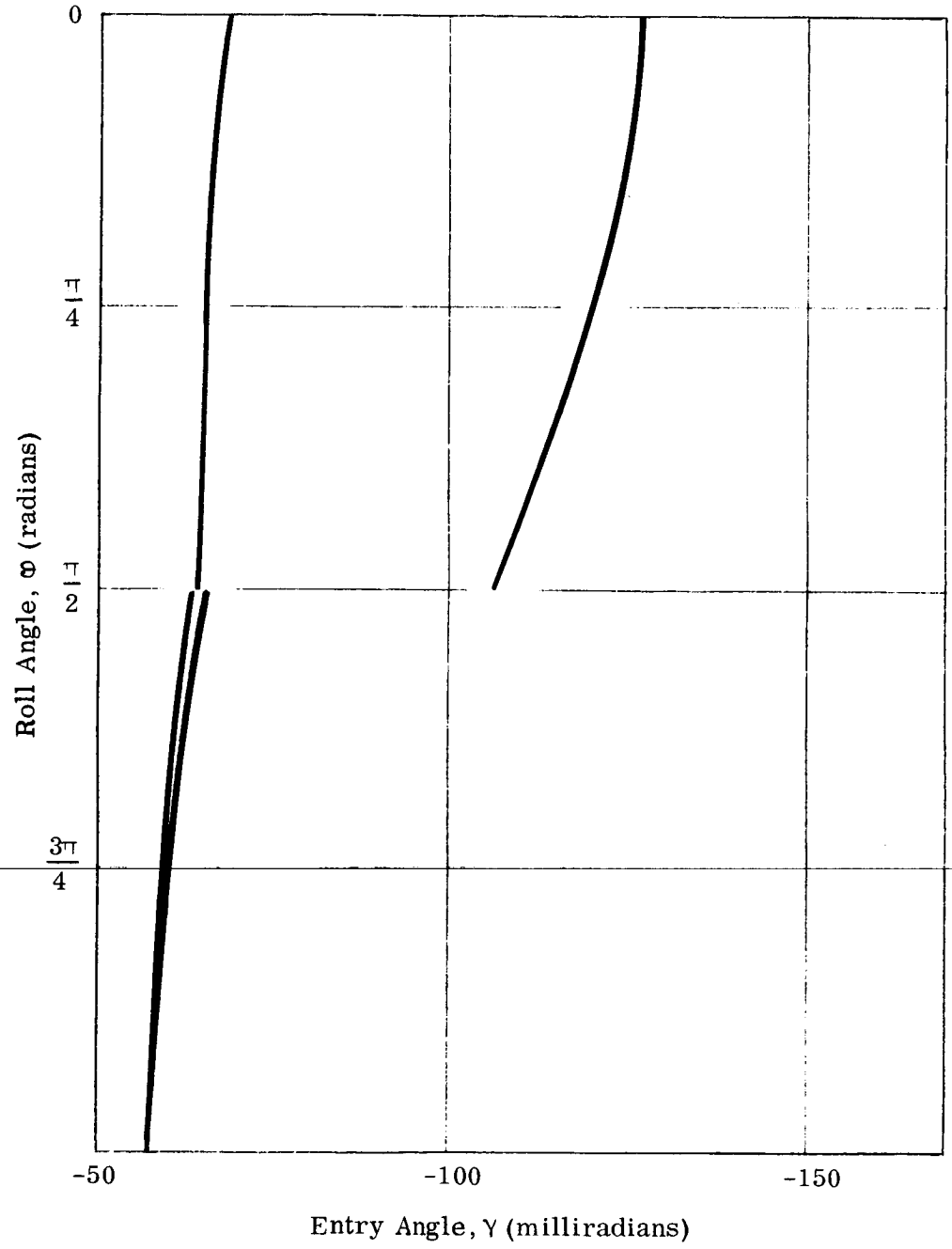

Figure B-129. Entry Corridor at Earth, Apollo Vehicle, Injection Speed=9,144 m/sec, No Pitch Modulation, Change Phase at $\dot{r}$=0

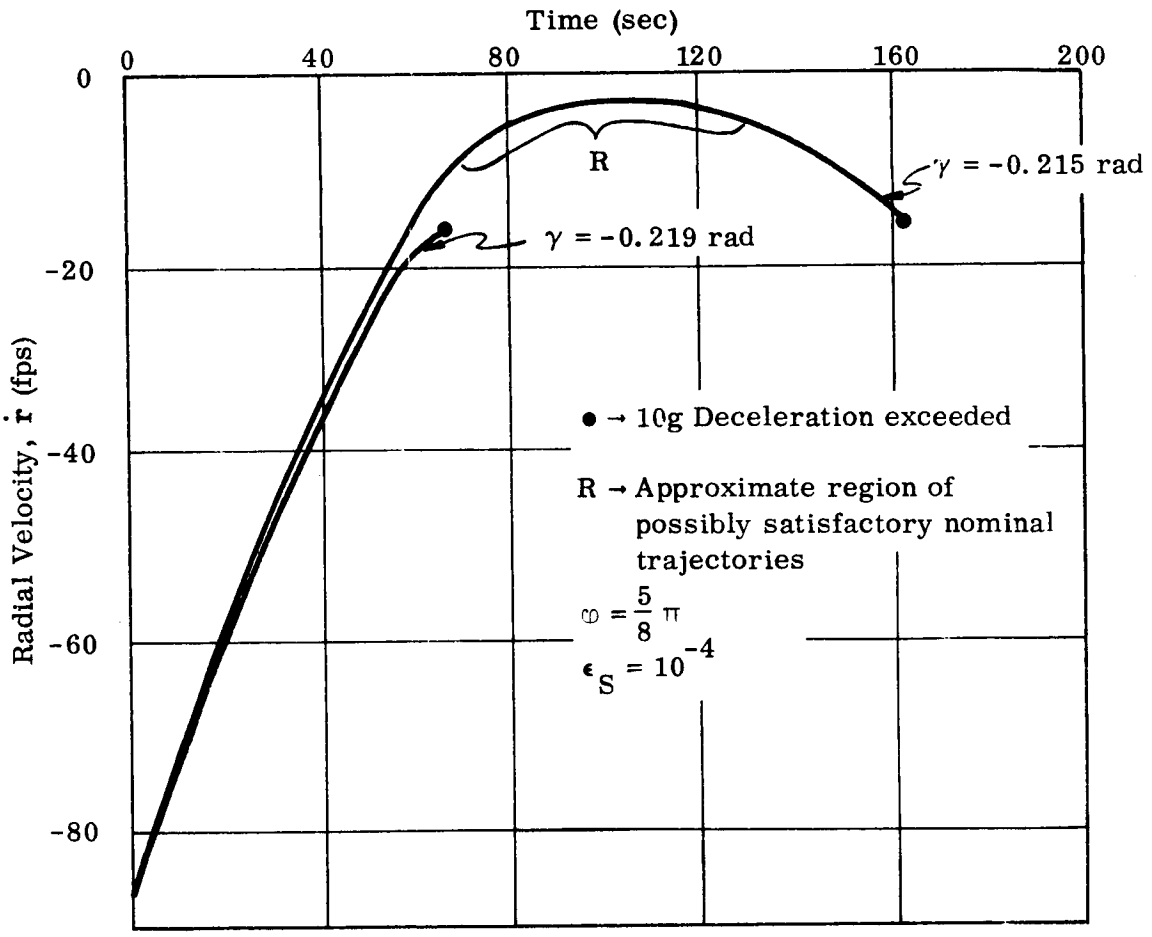

Figure B-130. Typical Radial Velocity Time Histories; Mars II Atmosphere $\varphi > \pi/2$, Injection Speed = 12,192 m/sec

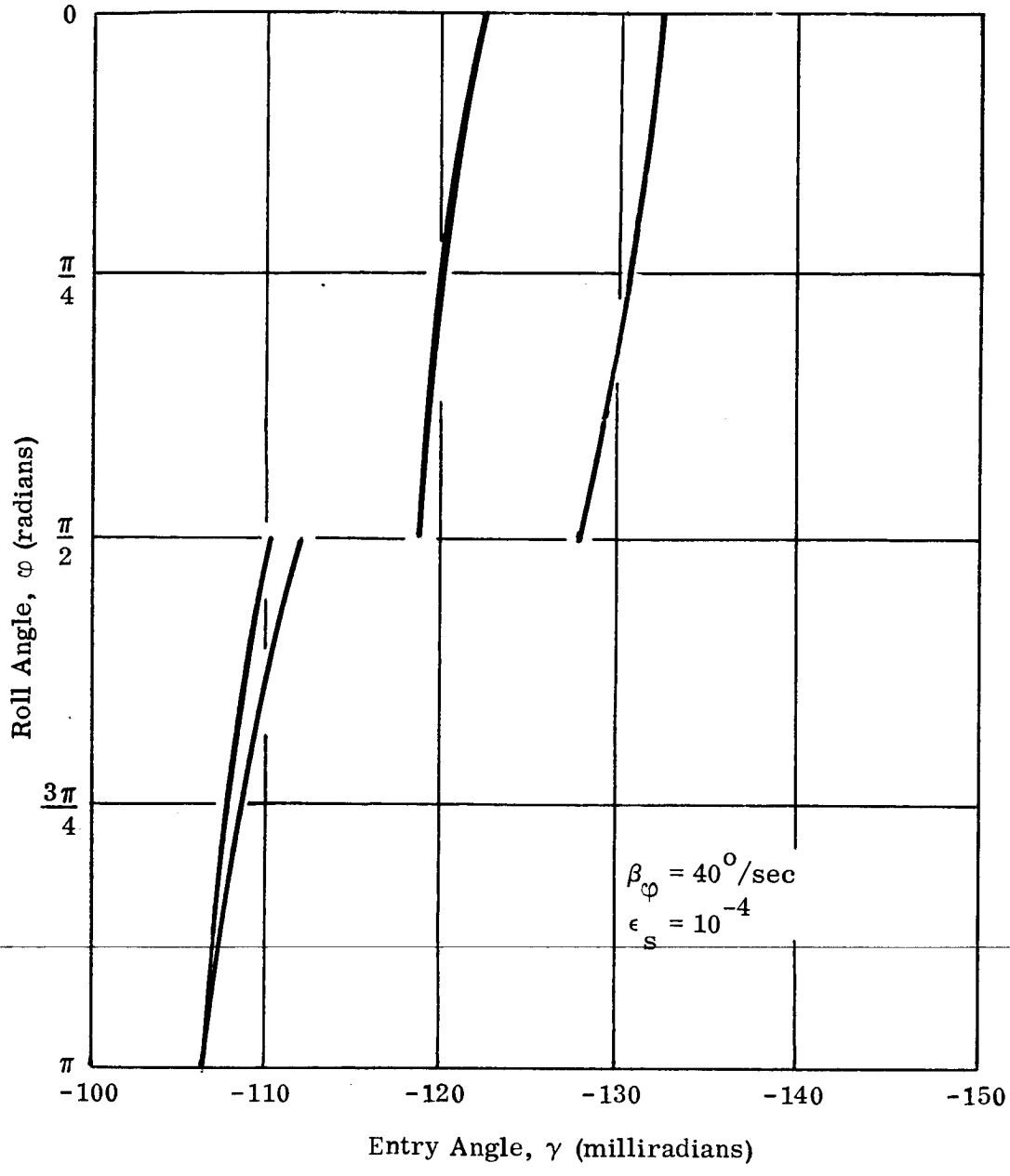

Figure B-131. Entry Corridor at Earth, Apollo Vehicle, Injection Speed=15, 240 m/sec, No Pitch Modulation, Change Phase at $\dot{r}=0$

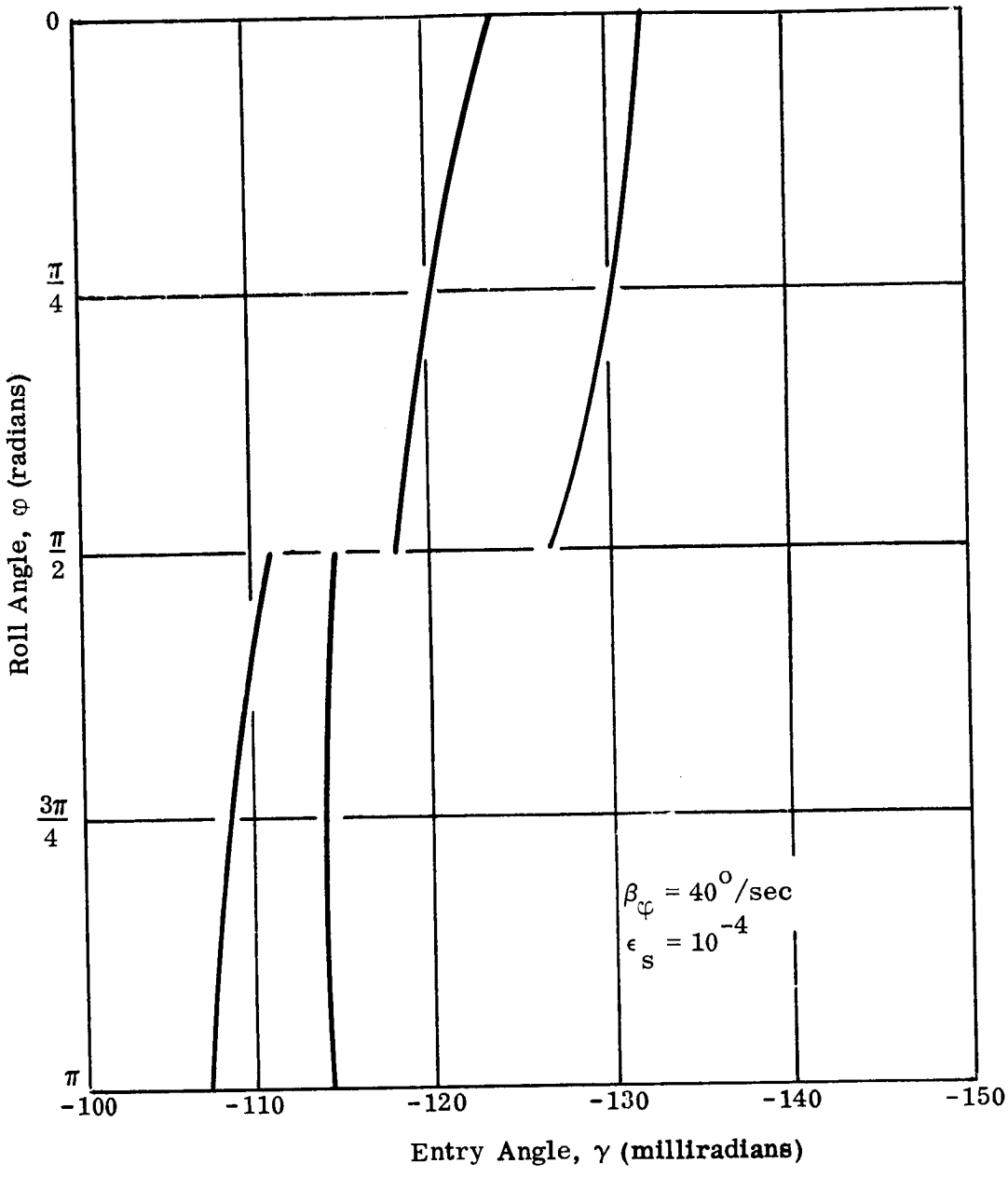

Figure B-132. Entry Corridor at Earth, Apollo Vehicle, Injection Speed=15, 240 m/sec, No Pitch Modulation, Change Phase at $\ddot{r}=0$

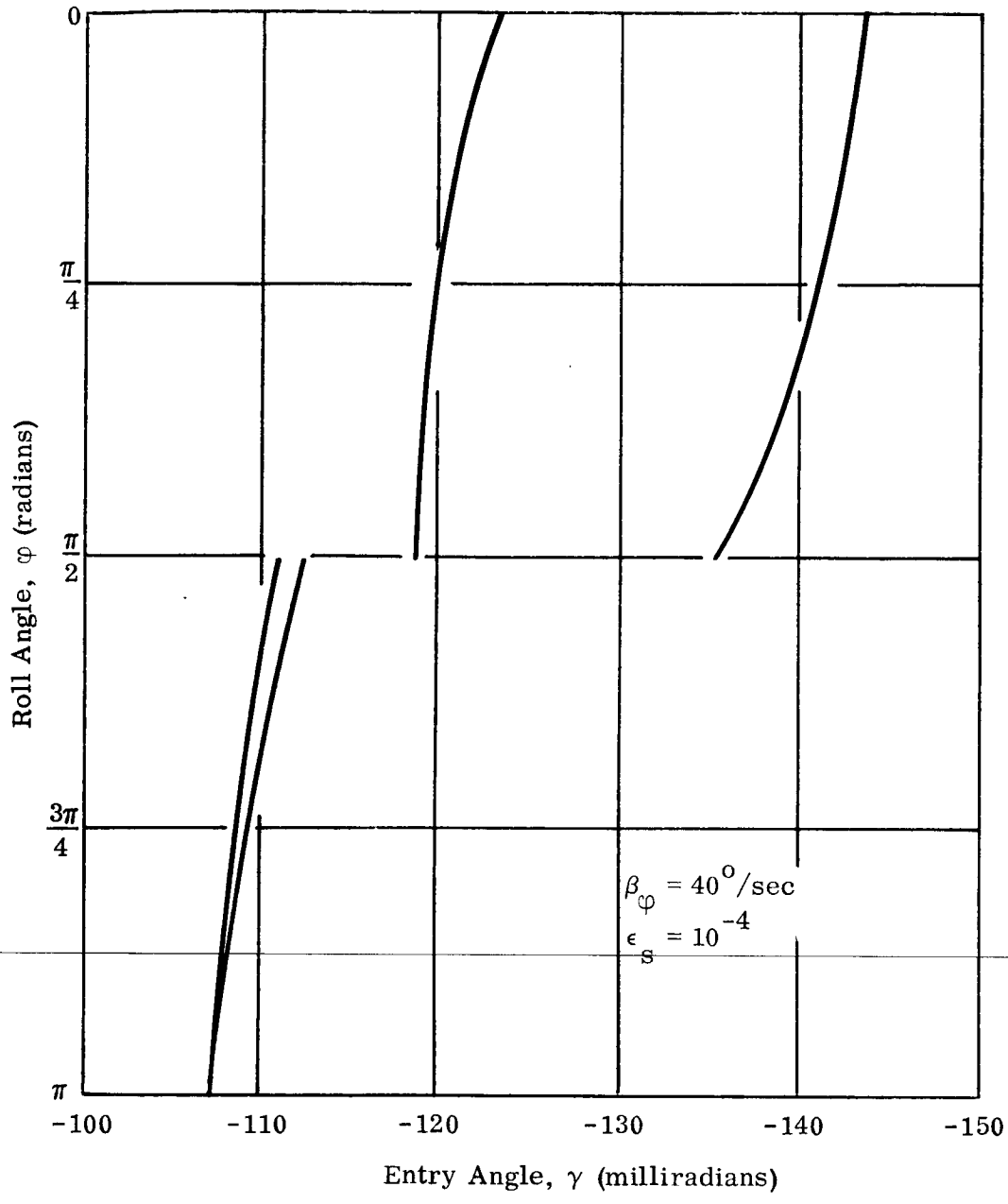

Figure B-133. Entry Corridor at Earth, Apollo Vehicle, Injection Speed=15, 240 m/sec, Pitch Modulation, Change Phase at $\dot{r}$=0

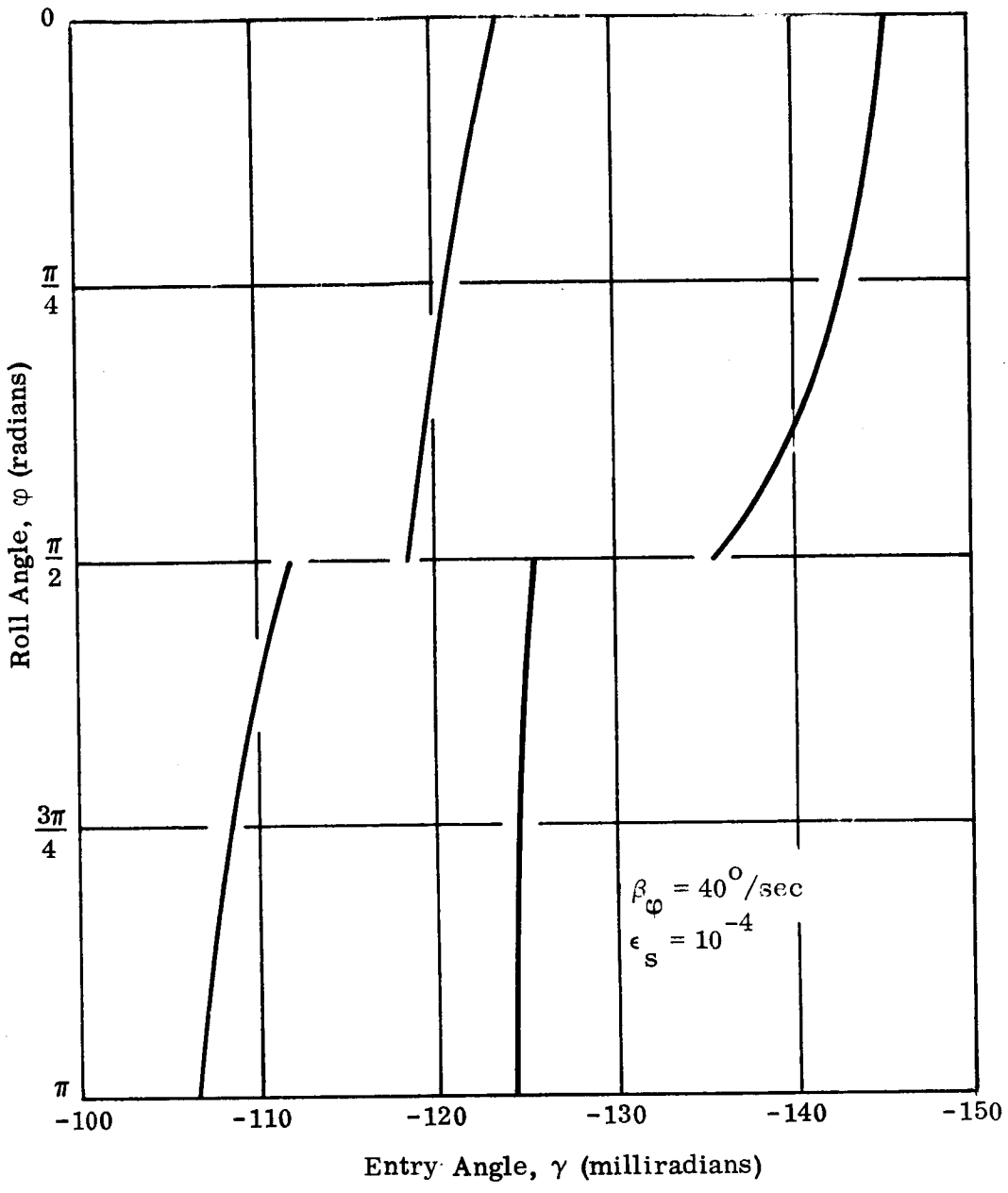

Figure B-134. Entry Corridor at Earth, Apollo Vehicle, Injection Speed=15, 240 m/sec, Pitch Modulation, Change Phase at $\ddot{r}=0$

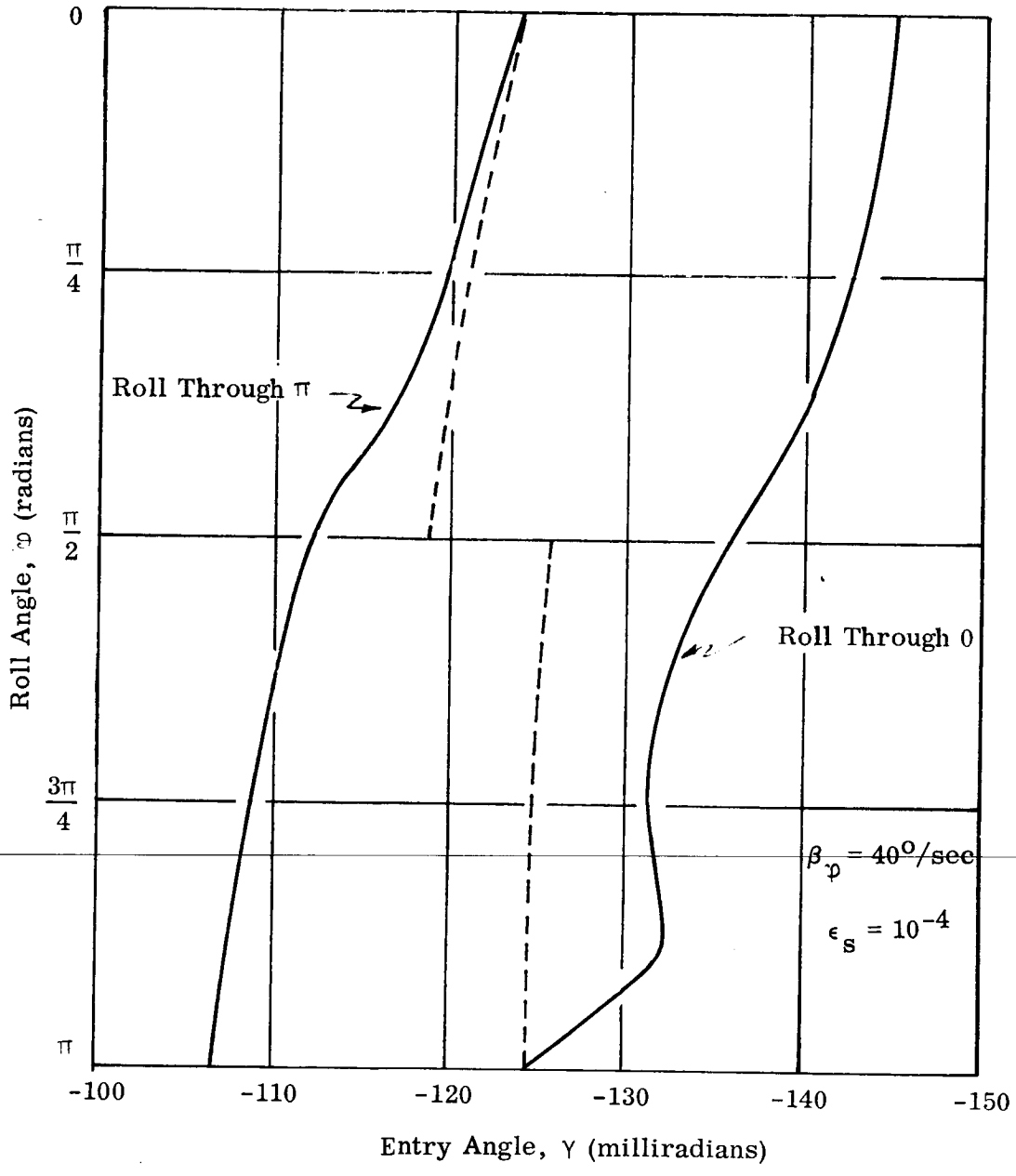

Figure B-135. Entry Corridor at Earth, Apollo Vehicle, Injection Speed=15, 240 m/sec, Pitch Modulation, Change Phase at $\ddot{r}$=0, Roll through 0 or π

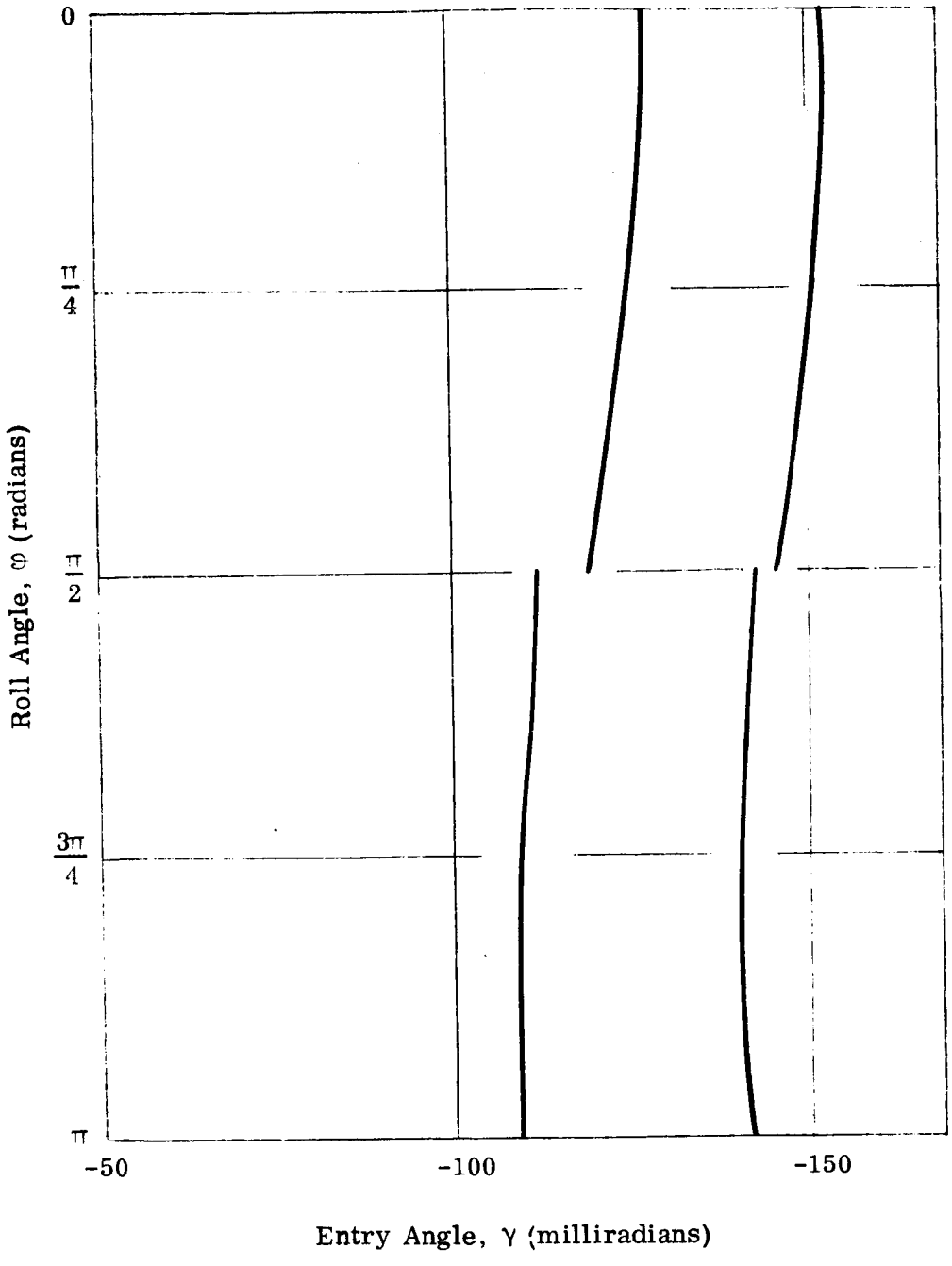

Figure B-136. Entry Corridor at Earth, HL10 Vehicle, Injection Speed=15,240 m/sec, No Pitch Modulation, Change Phase at $\ddot{r}=0$

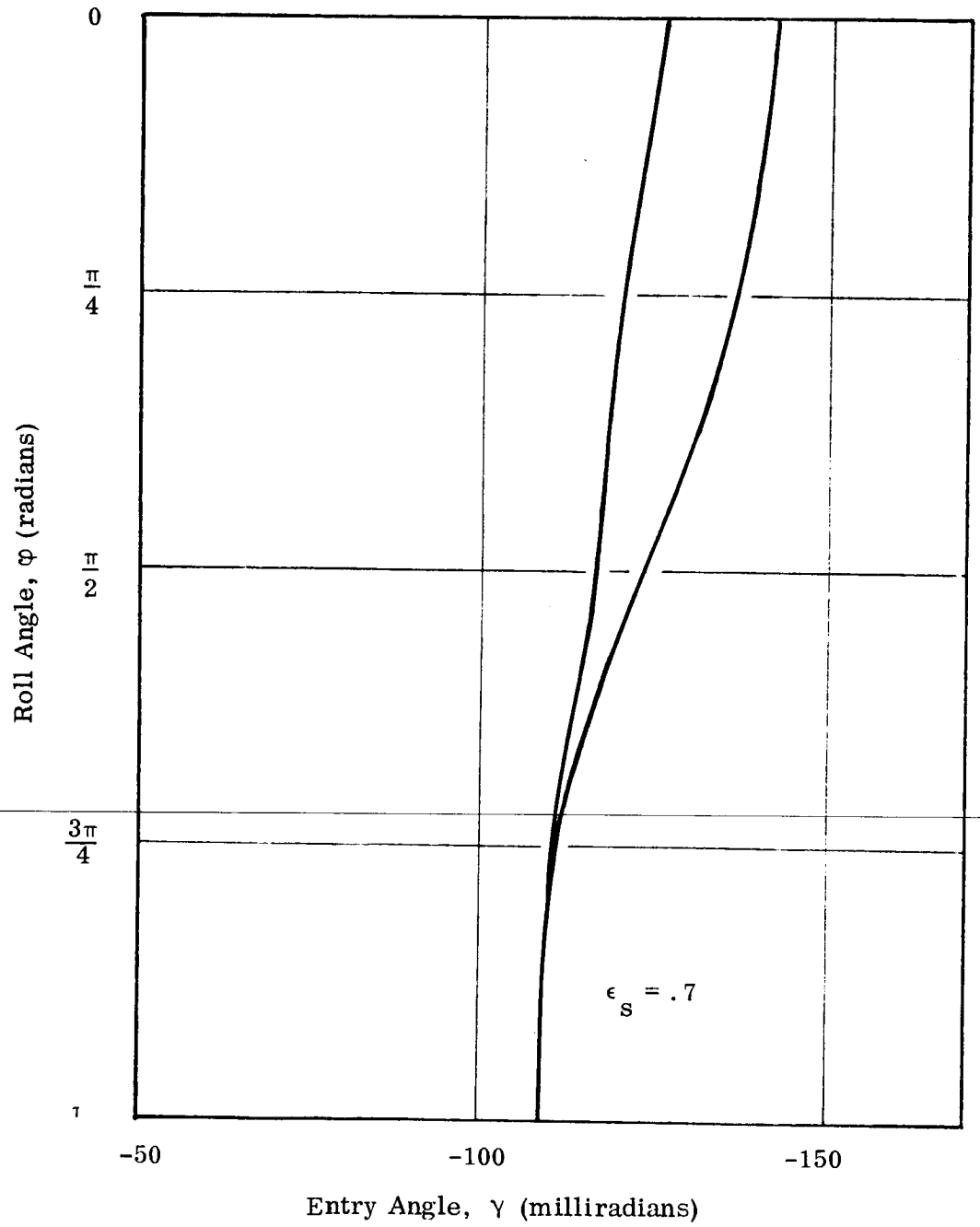

Figure B-137. Entry Corridor at Earth, HL10 Vehicle Injection Speed=15,240 m/sec, No Pitch Modulation, Change Phase at $\dot{r}$=0

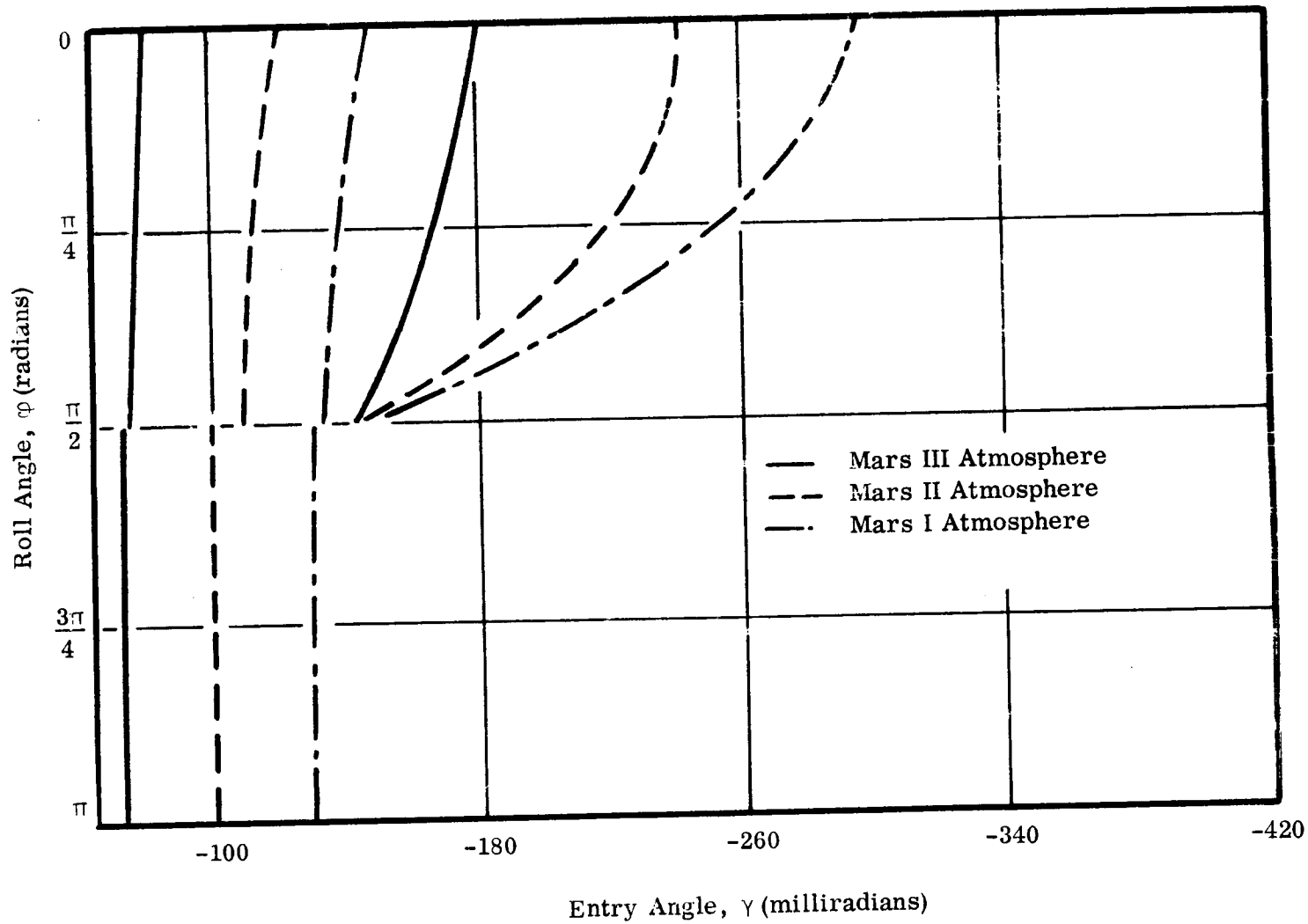

Figure B-138. Entry Corridor at Mars with Injection Speed = 3,962 m/sec for the Apollo Vehicle, Pitch Modulation, Change Phase at $\ddot{r} = 0$

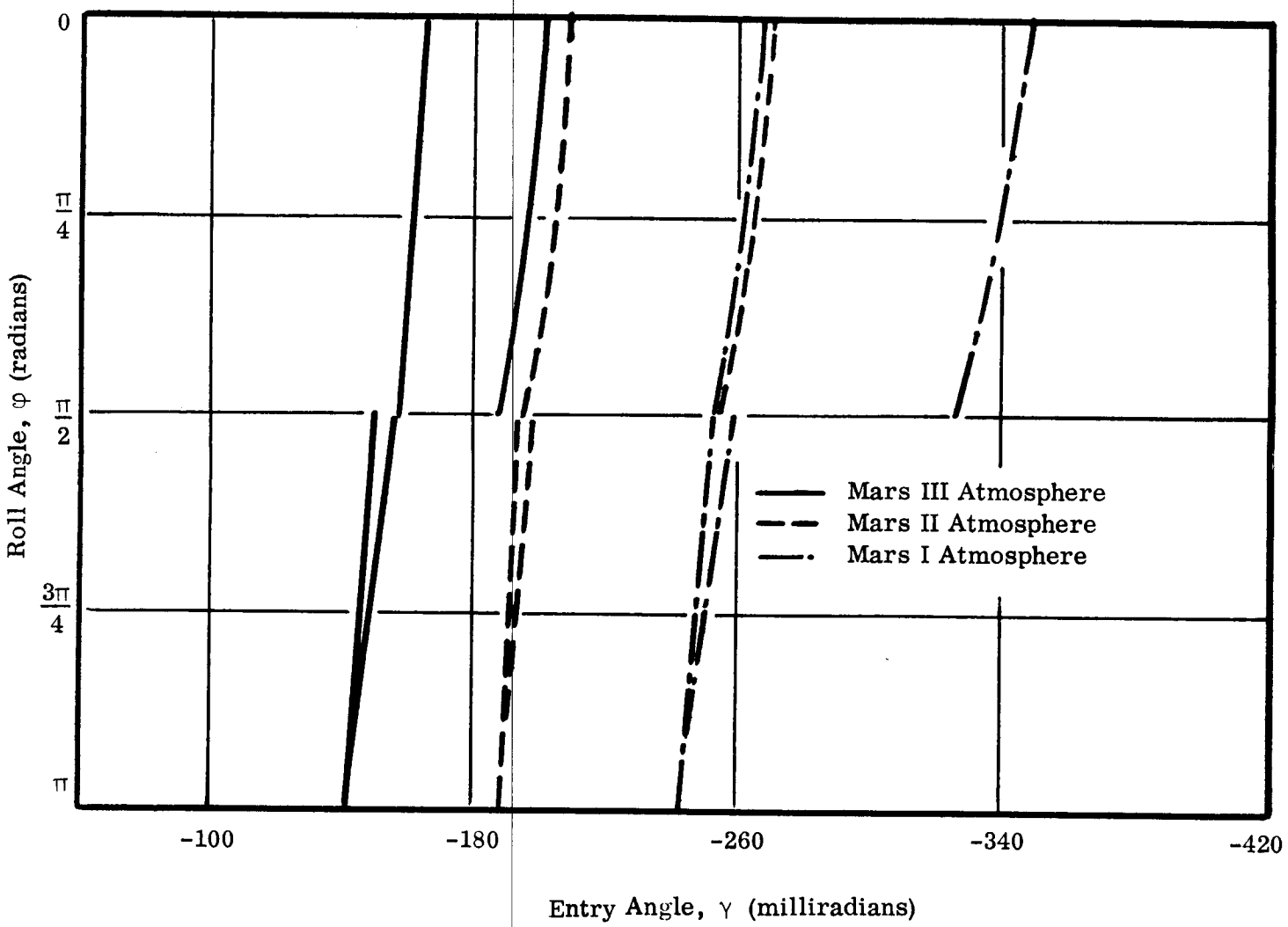

Figure B-139. Entry Corridor at Mars with Injection Speed = 7,132 m/sec for the Apollo Vehicle, No Pitch Modulation, Change Phase at $\dot{r} = 0$

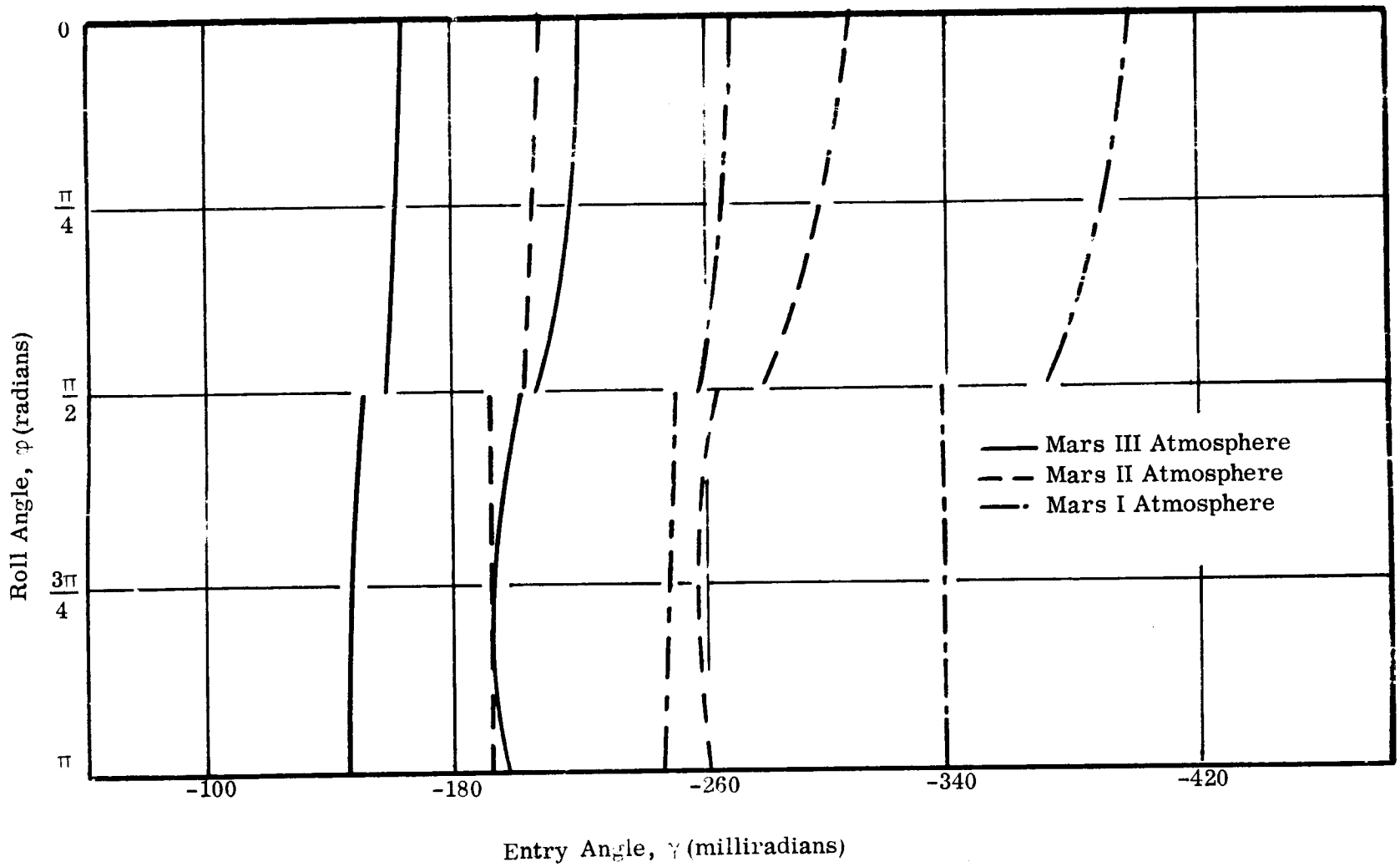

Figure B-140. Entry Corridor at Mars with Injection Speed = 7,132 m/sec for the Apollo Vehicle, Pitch Modulation, Change Phase at $\ddot{r} = 0$

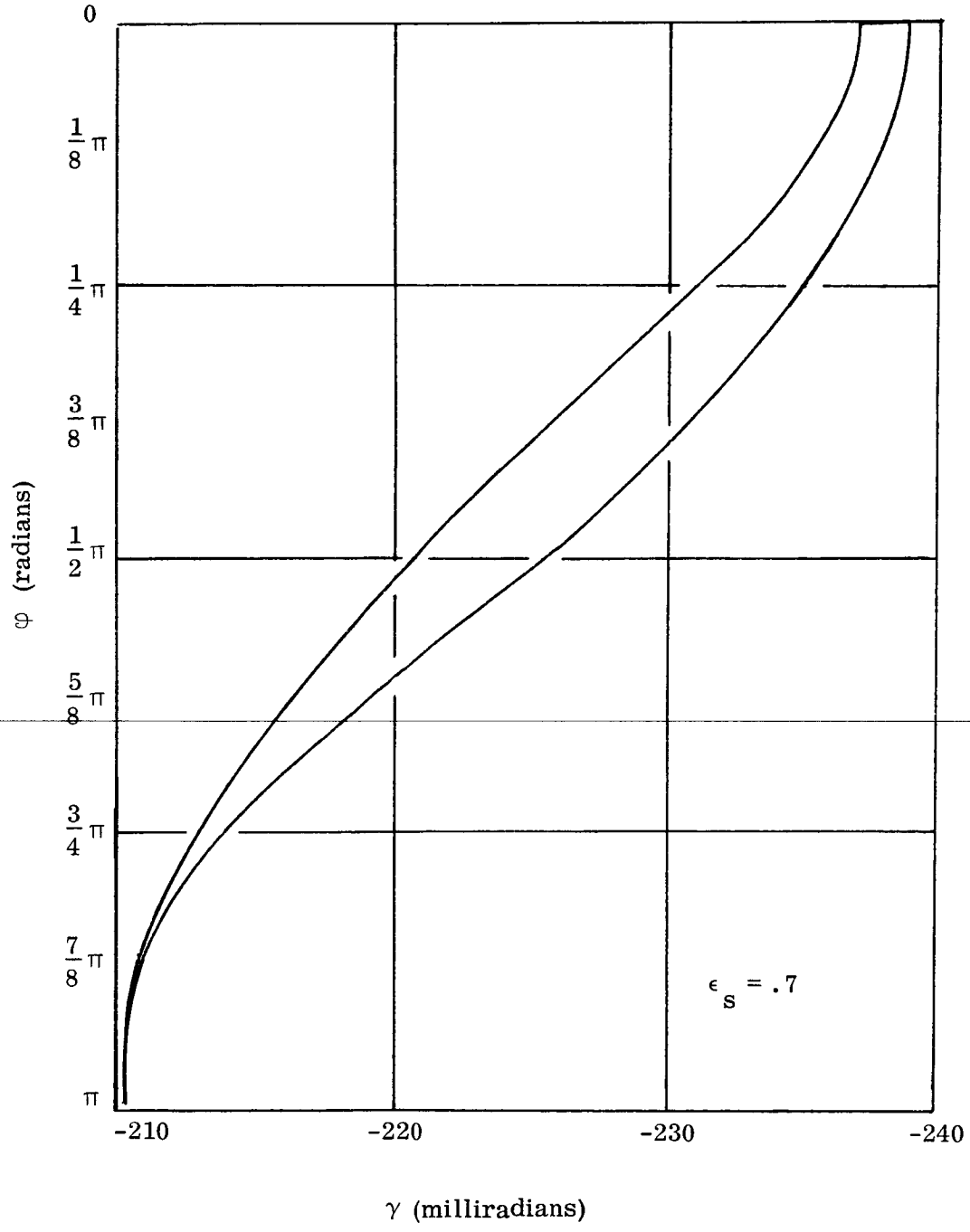

Figure B-141. Entry Corridor at Mars II, Apollo Vehicle Injection Speed= 12,192 m/sec, No Pitch Modulation. Change Phase at $\dot{r} = 0$

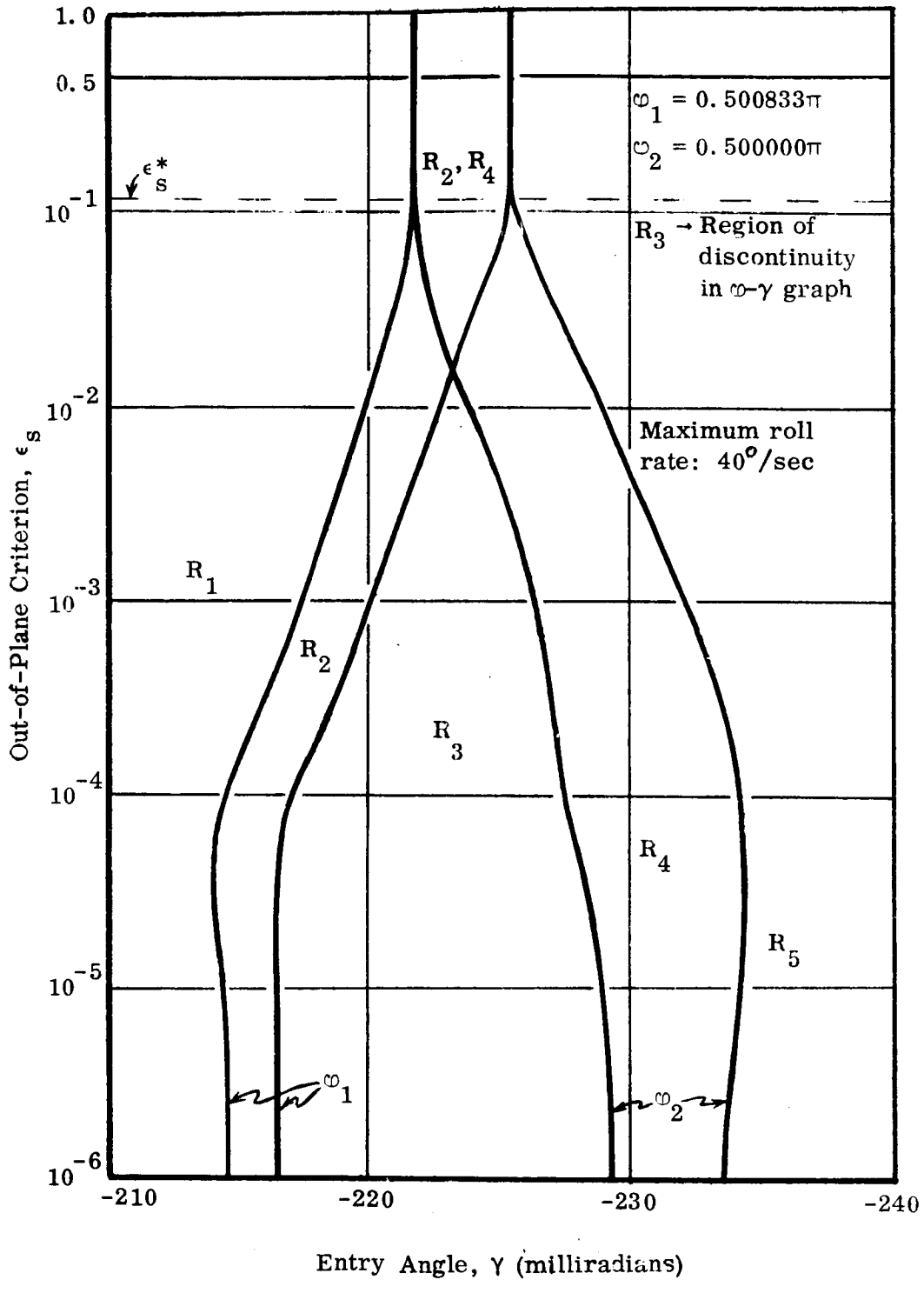

Figure B-142. Effect of Yaw Boundary Control on φ-γ Graph for Mars II Atmosphere Without Pitch Modulation and Change Phase at r = 0

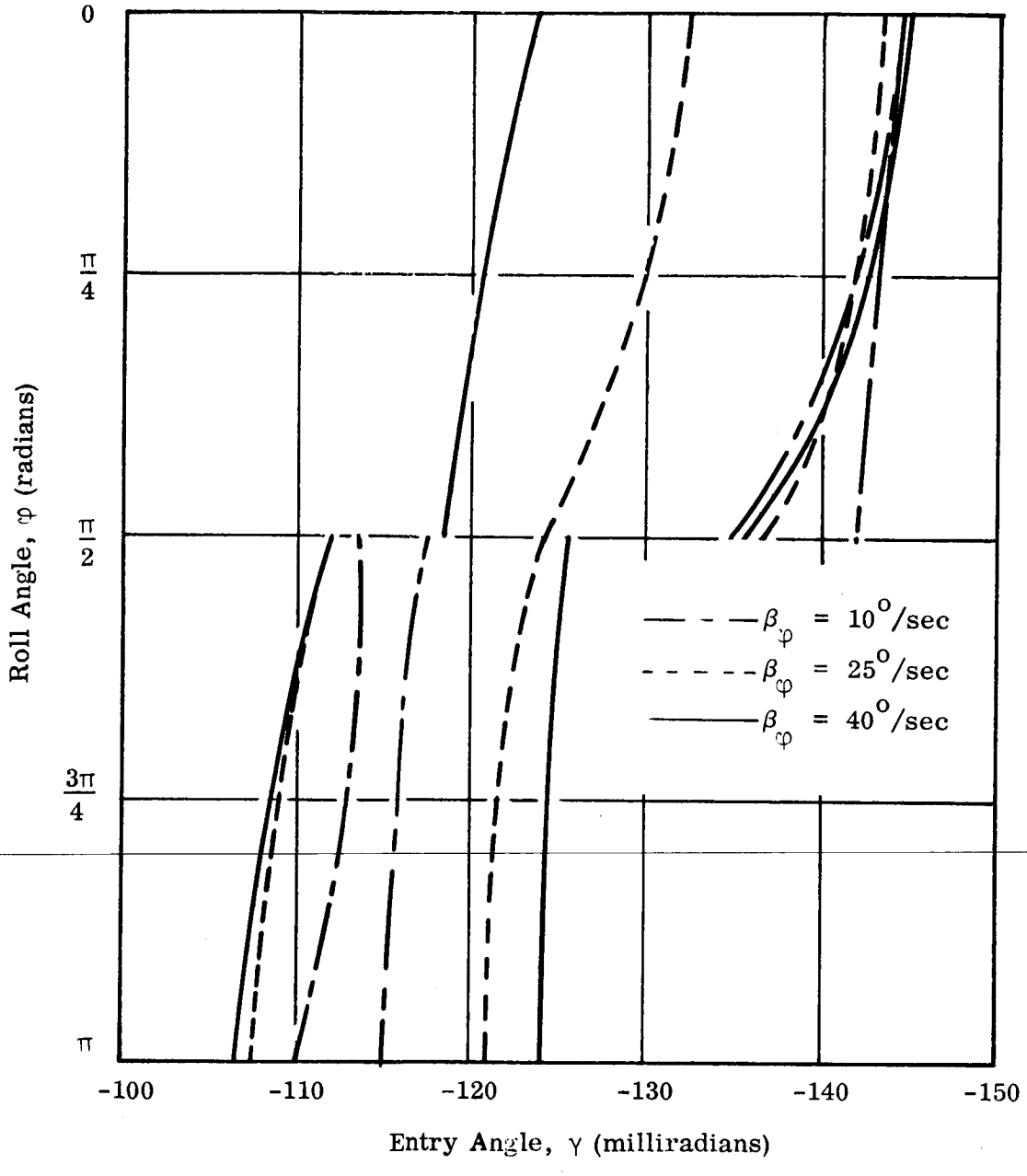

Figure B-143. Variation of the Earth-Entry Corridor for Different Maximum Vehicular Rates About the Velocity Vector, Apollo Vehicle, Injection Speed = 15,240 m/sec

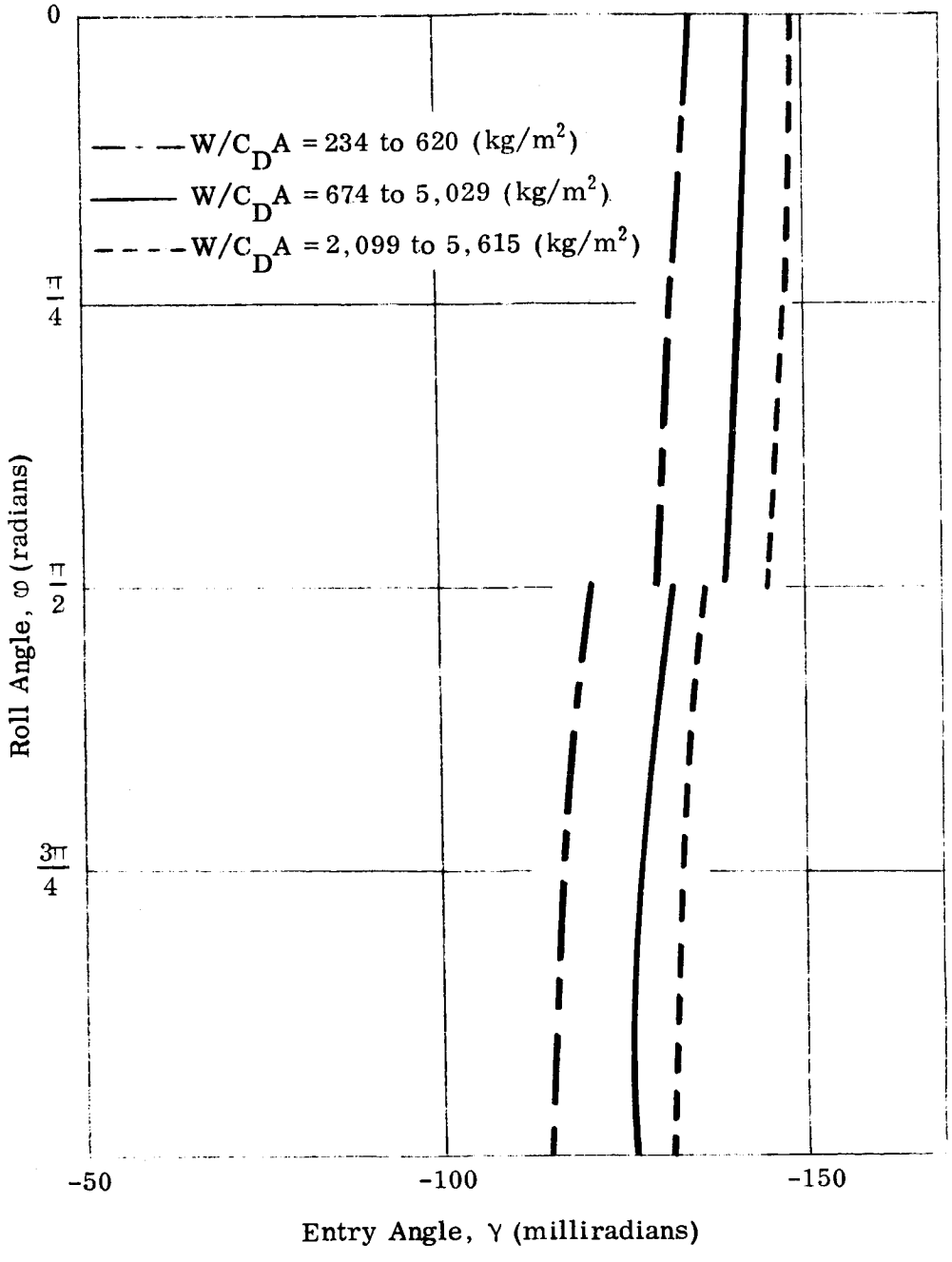

Figure B-144. Variation of the Earth-Entry Corridor with Different Ranges of Ballistic Coefficient, W/C_DA, Injection Speed = 70,000 ft/sec

SECTION III

POWERED FLIGHT PERFORMANCE RESULTS

The information in this section pertains to Paragraph 3.3. For the powered flight deboost maneuver prior to Earth reentry, a series of runs were made to determine the effect of reentry angle uncertainty resulting from a degradation in the acceleration-dependent error terms in an inertial measurement unit. The error budgets used are shown in Table B-31. Both strapdown and gimballed IMU configurations, based upon these budgets, were simulated.

All combinations of the degraded gyro and accelerometer error budgets of Table B-31 were evaluated using the 1σ value of reentry angle deviation as a performance index. The results are shown in Table B-32 and Figures B-145 and B-146 for the strapdown and gimballed systems, respectively.

Figures B-145 and B-146 show the effect of varying either the gyro or accelerometer budgets, holding the other (accelerometer or gyro) budget constant at any of the possible values. An ordered pair notion (i, j) is used to specify the guidance system composition, where i and j are the multipliers of the reference error budgets for the gyros (i) and accelerometers (j).

For strapdown systems, guidance system performance does not change when the gyro error budgets are varied. This phenomenon is due to the instrument orientation and the nature of the trajectory. Since the pitch and yaw gyros have their output axes along the roll axis, the only effective acceleration-dependent error sources are those of the roll gyro; but this affects only the resolution of accelerations in the pitch and yaw directions, which are very small. The angular rates are also very small ($\approx 10^{-4}$ rad/sec maximum); consequently, gyro scale factor and nonlinearity affects are also small.

When accelerometer error budgets are varied, an expected variation of the performance index occurs; but the magnitude of the entry-angle standard deviation reaches only 221 arc-seconds, which is still relatively small with respect to the entry corridor of the Apollo entry vehicle for this speed.

The gimballed system shows a variation of the reentry-angle standard deviation with both gyro and accelerometer degradation. Due to the nature of a gimballed system, the acceleration-dependent error sources of the pitch and yaw gyros do contribute drift error due to accelerations along their input and spin axes as the vehicle rotates about its initial orientation.

On this particular trajectory, the strapdown system performance is slightly better than that of the gimballed system. However, if the angular rate of the vehicle had been significantly higher, the opposite conclusion could be made. The reentry angle standard deviation had a maximum value of about 5 arc-minutes or a 3σ value of 0.25 degree. These values approach the maximum acceptable values, but are the results of extremely large error budgets for those error sources that are not easily calibrated.

Error Source	Units	Reference Budget	1σ Error Budget Values			
			i = 2	i = 4	i = 10	i = 20
Gyro (Rate)						
Constant Drift	meru	20	20	20	20	20
Mass Unbalance along Spin Axis	meru/g	50	100	200	500	1000
Mass Unbalance along Input Axis	meru/g	30	60	120	300	600
Anisoelasticity	meru/g^2	20	40	80	200	400
Input Axis Misalignment in Plane of Input Axis and Output Axis	arcsecond	20	40	80	200	400
Input Axis Misalignment in Plane of Input Axis and Spin Axis	arcsecond	20	40	80	200	400
Scale Factor	10^{-6} $\frac{\text{rad/sec}}{\text{rad/sec}}$	16.7	33.3	66.7	166.7	333.3
Nonlinearity	10^{-6} $\frac{\text{rad/sec}}{(\text{rad/sec})^2}$	2666.7	5333.3	10666.7	26666.7	53333.3
			j = 2	j = 4	j = 10	j = 20
Accelerometer (Proof Mass)						
Bias	10^{-6} g	300	300	300	300	300
Scale Factor	10^{-6} g/g	210	420	840	2100	4200
Nonlinearity	10^{-6} g/g^2	60	120	240	600	1200
Sensitive Axis Misalignment $\Delta\beta_1$	arcsecond	18	36	72	180	360
Sensitive Axis Misalignment $\Delta\beta_2$	arcsecond	18	36	72	180	360
Initial Misalignment	arcsecond	30	30	30	30	30

Table B-31. Gyro and Accelerometer Error Budgets for Degraded Inertial Systems

GYRO BUDGET MULTIPLYING FACTOR	ACCELEROMETER BUDGET MULTIPLYING FACTOR	σ_γ, STANDARD DEVIATION OF REENTRY ANGLE (arc-seconds)	
		Strapdown IMU	Gimballed IMU
2	2	59	63
	4	70	72
	10	120	140
	20	221	263
4	2	59	69
	4	70	80
	10	120	142
	20	221	265
10	2	59	100
	4	70	110
	10	120	160
	20	221	274
20	2	59	170
	4	70	174
	10	120	210
	20	221	308

Table B-32. Reentry Accuracies for Degraded IMU Systems

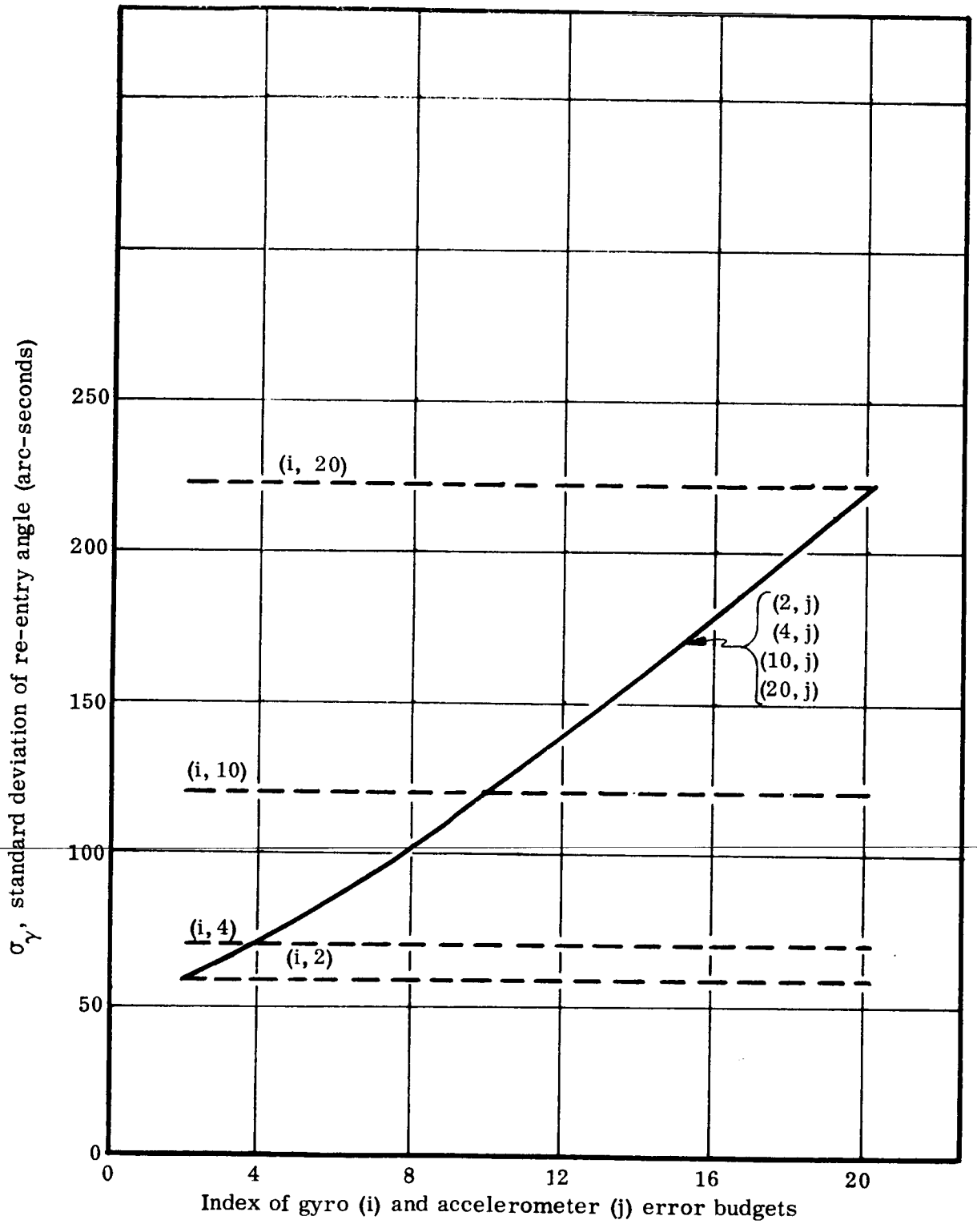

Figure B-145. Reentry Angle Standard Deviation as a Function of Gyro and Accelerometer Error Budgets for Strapdown Systems

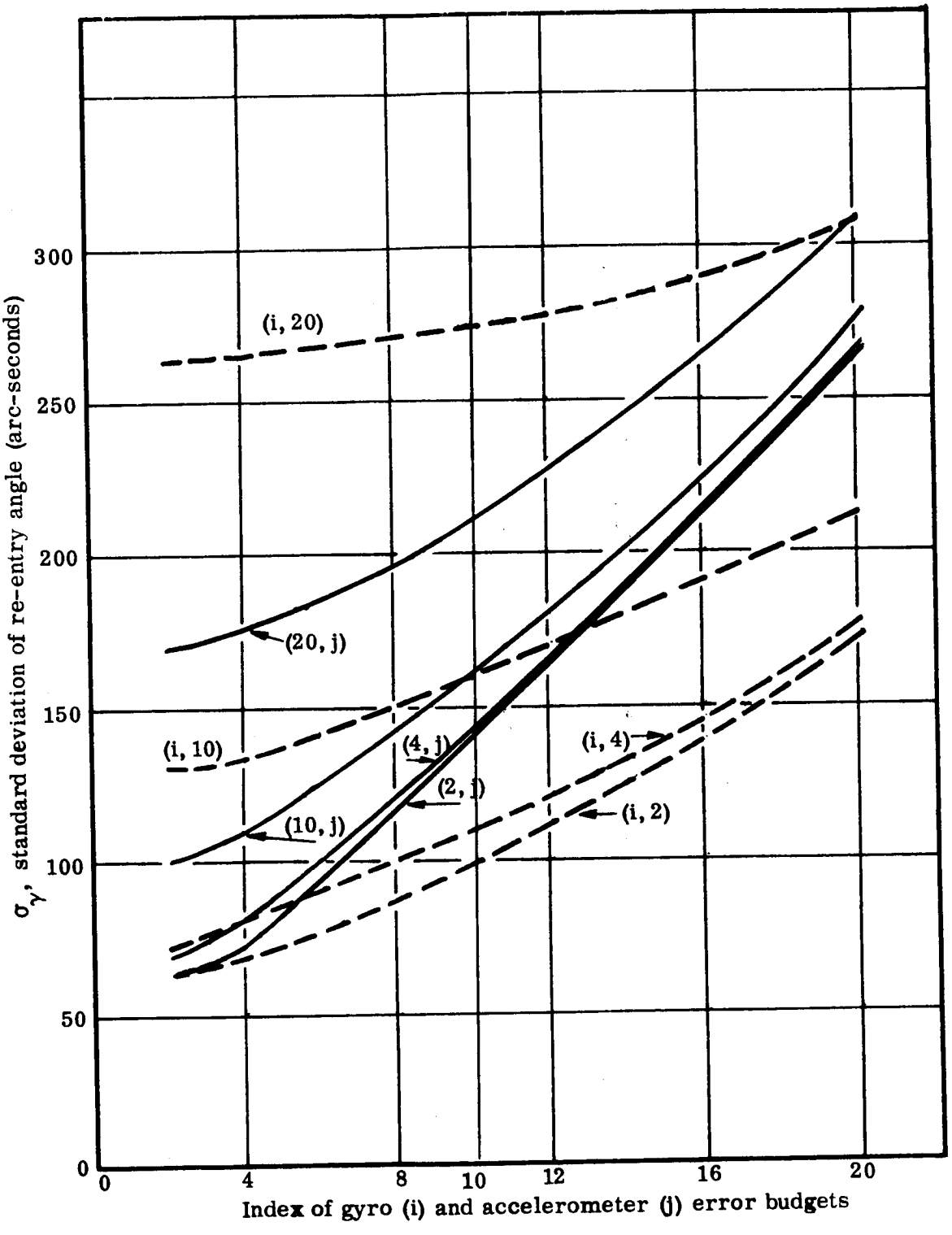

Figure B-146. Reentry Angle Standard Deviation as a Function of Gyro and Accelerometer Error Budgets for Gimballed Systems

SECTION IV

TRAJECTORIES AND SYSTEM CONFIGURATIONS

The tables and figures in this section give data defining the trajectories and system configurations employed in the low thrust guidance and navigation studies described in Paragraph 3.4, plus graphical results of the studies.

Tables B-33 through B-36 list trajectory data, and Table B-37 lists error budgets for the system configuration employed. Figures B-147 through B-163 show the results.

TRAJECTORY	POSITION		VELOCITY		PROPULSION	
	X_1 (km)	X_2 (km)	$X_3 = \dot{X}_1$ (km/ sec)	$X_4 = \dot{X}_2$ (km/ sec)	a_o (km/ sec^2)	$\dot{m}$ (/ sec^{-1})
HTR2	0.1407949×10^9	0.35684061×10^8	-0.11383675×10^2	0.4089204×10^2	0.1220741×10^{-1}	0.309278×10^{-7}
HTR4	0.14045825×10^9	0.59340851×10^8	-0.10813174×10^2	0.29123758×10^2	0.973×10^{-6}	0.10204×10^{-8}
LAGRANGE MULTIPLIERS						
	λ_1	λ_2	λ_3	λ_4	α	
HTR2	-0.467691×10^{-5}	$0.15009442 \times 10^{-4}$	-0.11678042×10^2	0.32858647×10^2	1.9489317	
HTR4	0.3516422×10^{-7}	$0.17116486 \times 10^{-6}$	$-0.32438167 \times 10^{-1}$	0.706558	1.6167	

Table B-33. Initial Conditions for Nominal Heliocentric Transfer Trajectories

TRAJECTORY	EARTH			MARS		
	R (km)	ω (rad/sec)	T_o (sec)	R km	ω rad/sec	T_o sec
HTR2	0.1471×10^{9}	0.2042×10^{-6}	-0.1×10^{7}	0.244×10^{9}	0.95579×10^{-7}	-0.11157×10^{8}
HTR4	0.15322×10^{9}	0.196331×10^{-6}	-0.1815×10^{7}	0.20749×10^{9}	0.12086×10^{-6}	-0.725×10^{7}

Table B-34. Planetary "Ephemerides" for Heliocentric Transfer Trajectories

TRAJECTORY	POSITION		VELOCITY		PROPULSION	
	X_1 (km)	X_2 (km)	$X_3 = \dot{X}_1$ (km/sec)	$X_4 = \dot{X}_2$ (km/sec)	a_o (km/sec^2)	$\dot{m}$ (/sec)
Mars Out (MO)	0.3540×10^{4}	0.0	0.0	0.3484394×10^{1}	0.130×10^{-4}	0.3×10^{-7}
Earth Out (EO)	0.6500×10^{4}	0.0	0.0	0.783×10^{1}	0.130×10^{-4}	0.3×10^{-7}

Table B-35. Nominal Initial Conditions for Planetocentric Escape Trajectories

TRAJECTORY	POSITION		VELOCITY		PROPULSION	
	X_1 (km)	X_2 (km)	$X_3 = \dot{X}_1$ (km/sec)	$X_4 = \dot{X}_2$ (km/sec)	a_o (km/sec^2)	$\dot{m}$ (/sec)
Mars In (MI)	-0.3676×10^{5}	-0.1545×10^{5}	-0.18646	0.12799×10^{1}	0.13×10^{-4}	0.3×10^{-7}
Earth In (EI)	0.8329×10^{4}	0.11897×10^{5}	-0.42571×10^{1}	0.30611×10^{1}	0.13×10^{-4}	0.3×10^{-7}

Table B-36. Nominal Initial Conditions for Planetocentric Capture Trajectories

GROUND TRACKER
G1: $\sigma_R^2 = 10^{12}$ (km)^2 for heliocentric, 0.000225 (km)^2 for planetocentric
$\sigma_{\dot{R}}^2 = 0.11 \times 10^{-10}$ (km/sec)^2
$\sigma_{\alpha_R}^2 = 0.3 \times 10^{-8}$ (rad)^2
$b_R^2 = b_{\dot{R}}^2 = b_{\alpha_R}^2 = 0$
PLANET TRACKERS
P1: $\sigma_\alpha^2 = 0.36 \times 10^{-11}$ (rad)^2, $b_\alpha^2 = 0.3\ 10^{-4}$ (rad)^2
P2: $\sigma_\alpha^2 = 0.235 \times 10^{-8}$ (rad)^2, $b_\alpha^2 = 0.3 \times 10^{-4}$ (rad)^2
P3: $\sigma_\alpha^2 = 0.36 \times 10^{-10}$ (rad)^2, $b_\alpha^2 = 0.3 \times 10^{-4}$ (rad)^2
P4: $\sigma_\alpha^2 = 0.1 \times 10^{-9}$ (rad)^2, $b_\alpha^2 = 0.3 \times 10^{-4}$ (rad)^2
P5: $\sigma_\alpha^2 = 0.9 \times 10^{-11}$ (rad)^2, $b_\alpha^2 = 0.3 \times 10^{-4}$ (rad)^2
P6: $\sigma_\alpha^2 = 0.36 \times 10^{-9}$ (rad)^2, $b_\alpha^2 = 0$
P7: $\sigma_\alpha^2 = 0.36 \times 10^{-7}$ (rad)^2, $b_\alpha^2 = 0$
P8: $\sigma_\alpha^2 = 0.36 \times 10^{-11}$ (rad)^2, $b_\alpha^2 = 0$
P9: $\sigma_\alpha^2 = 0.36 \times 10^{-11}$ (rad)^2, $b_\alpha^2 = 0.3 \times 10^{-2}$
P10: $\sigma_\alpha^2 = 0.36 \times 10^{-11}$ (rad)^2, $b_\alpha^2 = 0.3 \times 10^{-6}$

Table B-37 (Sheet 1 of 2). Instrument Error Budgets

Heliocentric Correlation Time	-	5,000 seconds for all instruments
Planetocentric Correlation Time	-	100 seconds for all instruments
For HTR2 - Measure Earth		$0 < T \leq 1.5 \times 10^6$ sec
Sun		$1.5 \times 10^6 < T \leq 3.5 \times 10^6$ sec
Mars		$3.5 \times 10^6 < T \leq 5 \times 10^6$ sec
HTR4 - Measure Earth		$0 < T \leq 3 \times 10^6$ sec
Sun		$3 \times 10^6 < T \leq 7 \times 10^6$ sec
Mars		$7 \times 10^6 < T \leq 10^7$ sec

For any of the EMS with no inertial instrument, values of noise on the dynamics of $Q_{a_o} = Q_{55} = 0.25 \times 10^{-16}$ $(km/sec^2)^2$, $Q_{\alpha *} = 0.306 \times 10^{-5}$ $(rad)^2$ are used.

GIMBALLED IMU's		
IG1:	$\epsilon^2 = 0.1 \times 10^{-11}$ $(km/sec^2)^2$	(10^{-4} g bias)
CAROUSEL IMU's:		
IC1:	$\epsilon^2 = 0.1 \times 10^{-11}$ $(km/sec^2)^2$	(10^{-4} g bias)
	$\omega = 0.125664 \times 10^{-4}$ rad/sec	(heliocentric)
	$\omega = 0.628 \times 10^{-3}$ rad/sec	(planetocentric)
IC2:	$\epsilon^2 = 0.1 \times 10^{-11}$ $(km/sec^2)^2$	
	$\omega = 0.62832 \times 10^{-4}$ rad/sec	
IC3:	$\epsilon^2 = 0.1 \times 10^{-11}$ $(km/sec^2)^2$	
	$\omega = 0.125664 \times 10^{-3}$ rad/sec	

Table B-37 (Sheet 2 of 2). Instrument Error Budgets

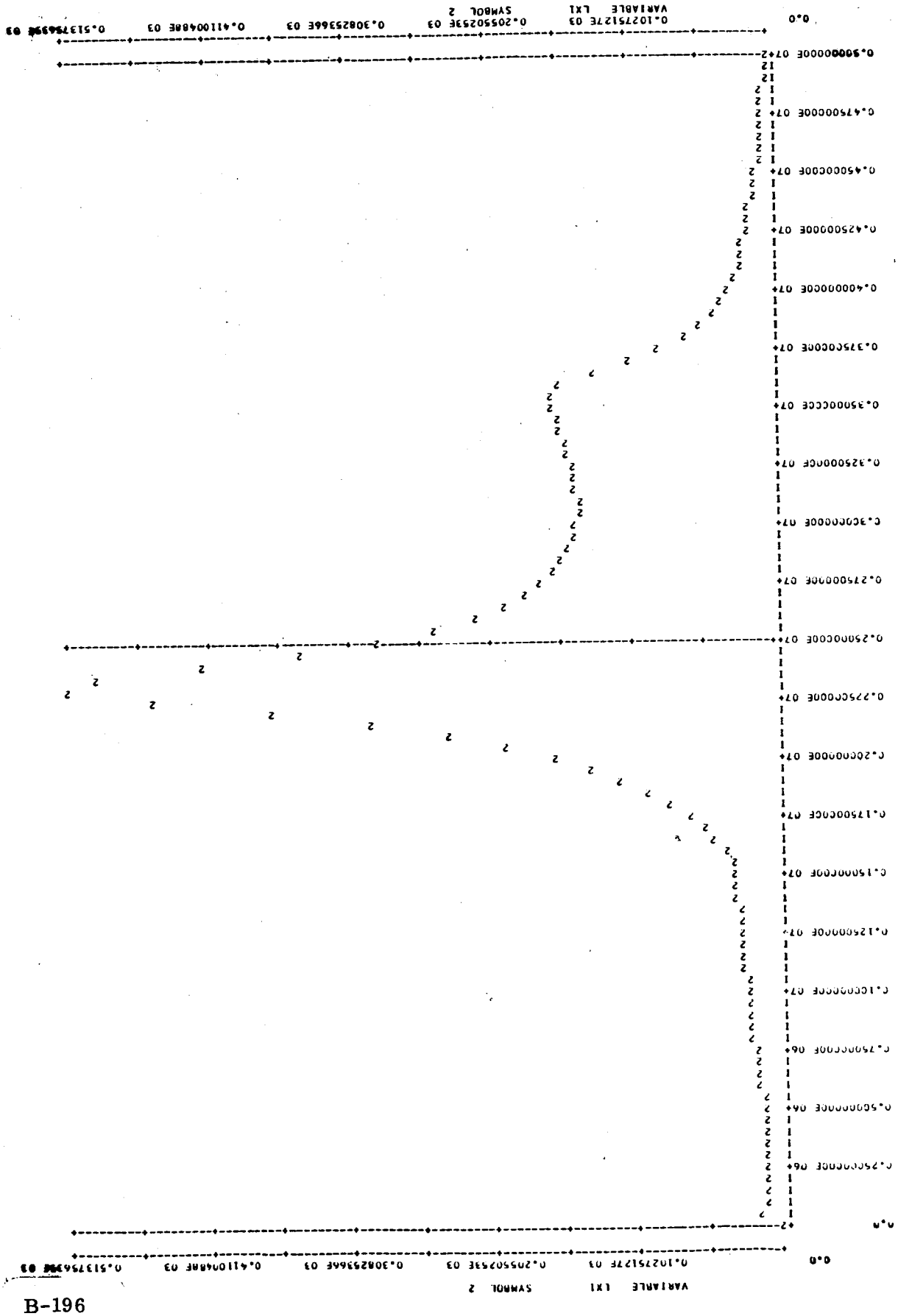

Figure B-147. System P1-IG1 on Trajectory HTR2

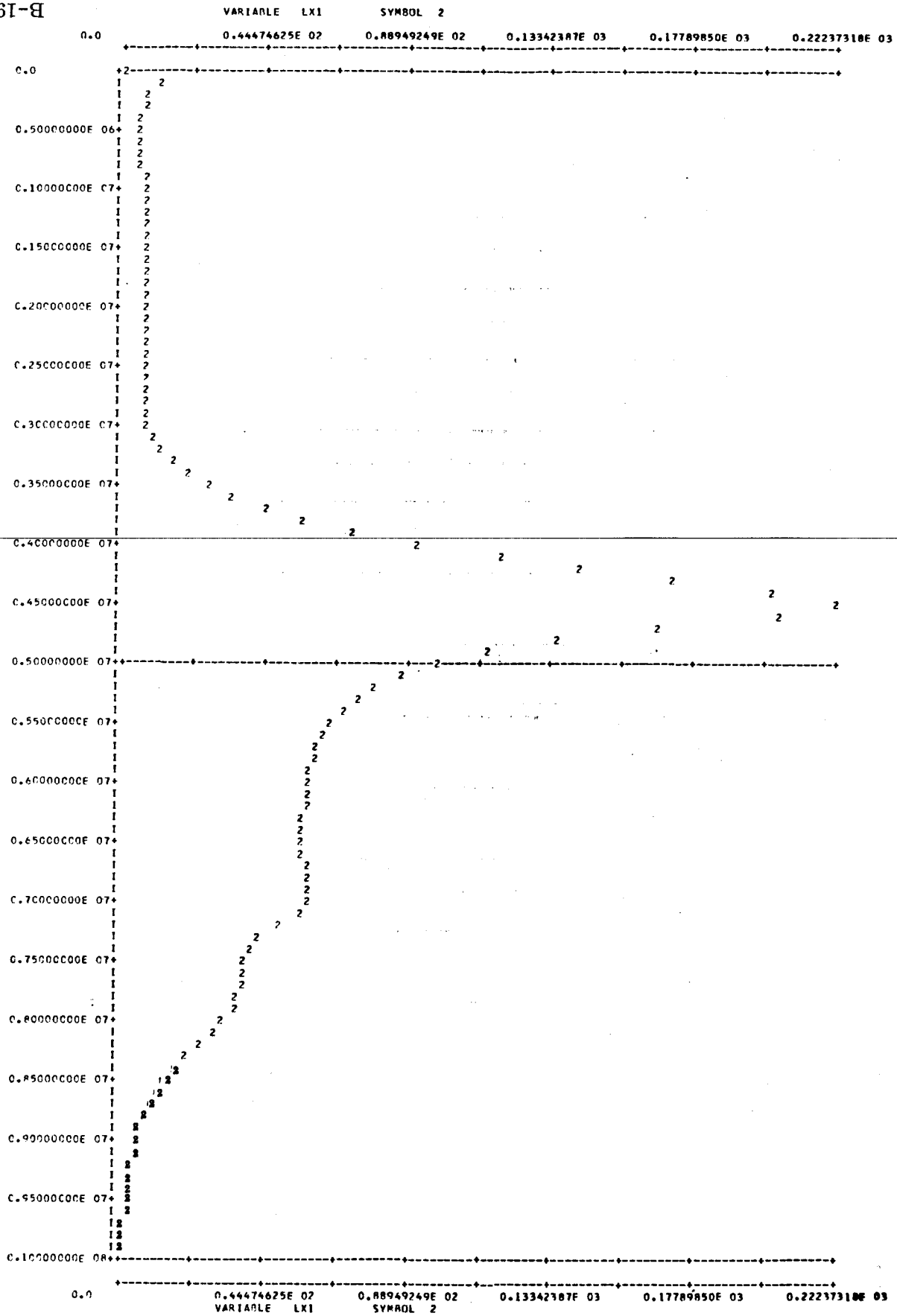

Figure B-148. System P1-IG1 on Trajectory HTR4

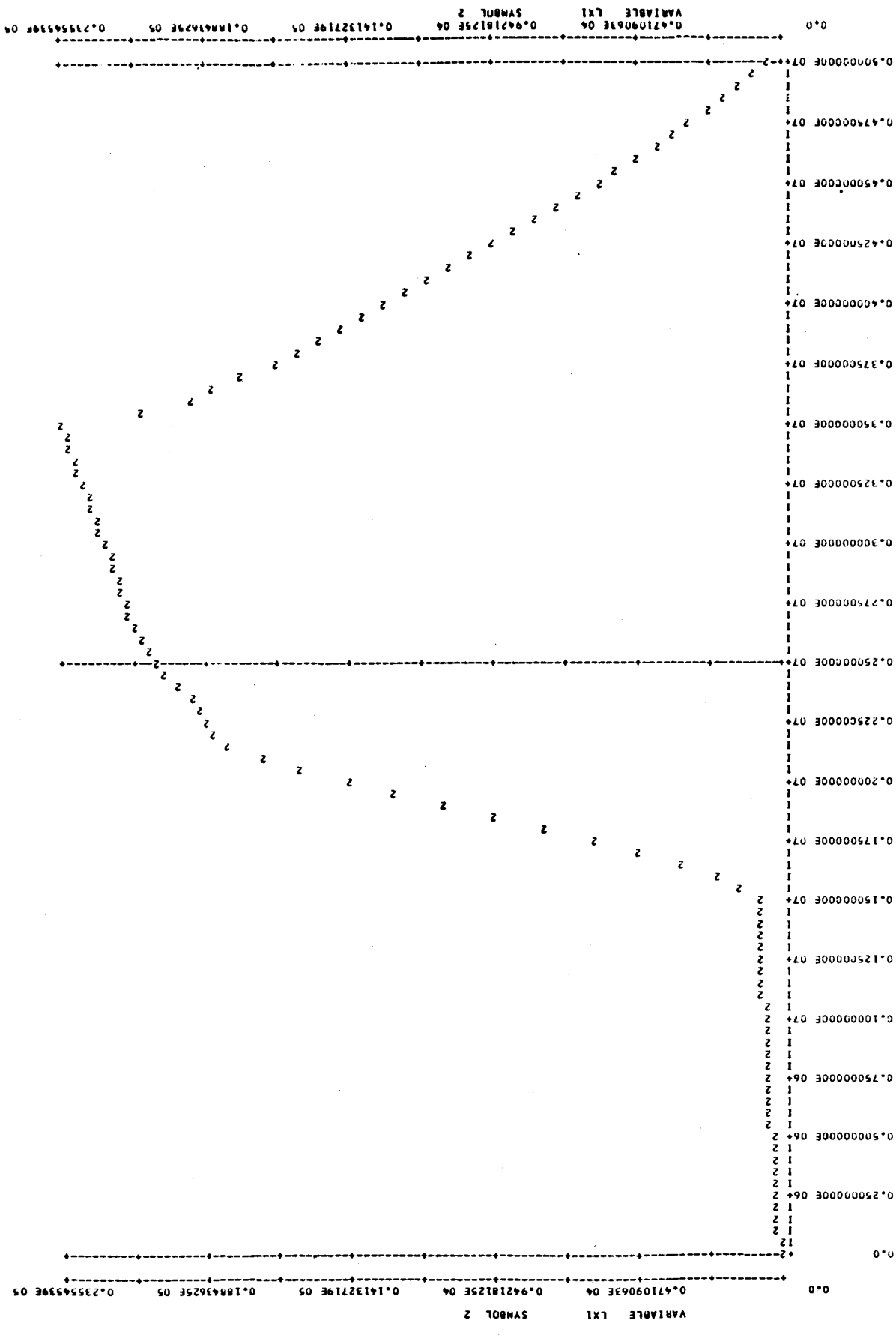

Figure B-149. Planet Tracker P2

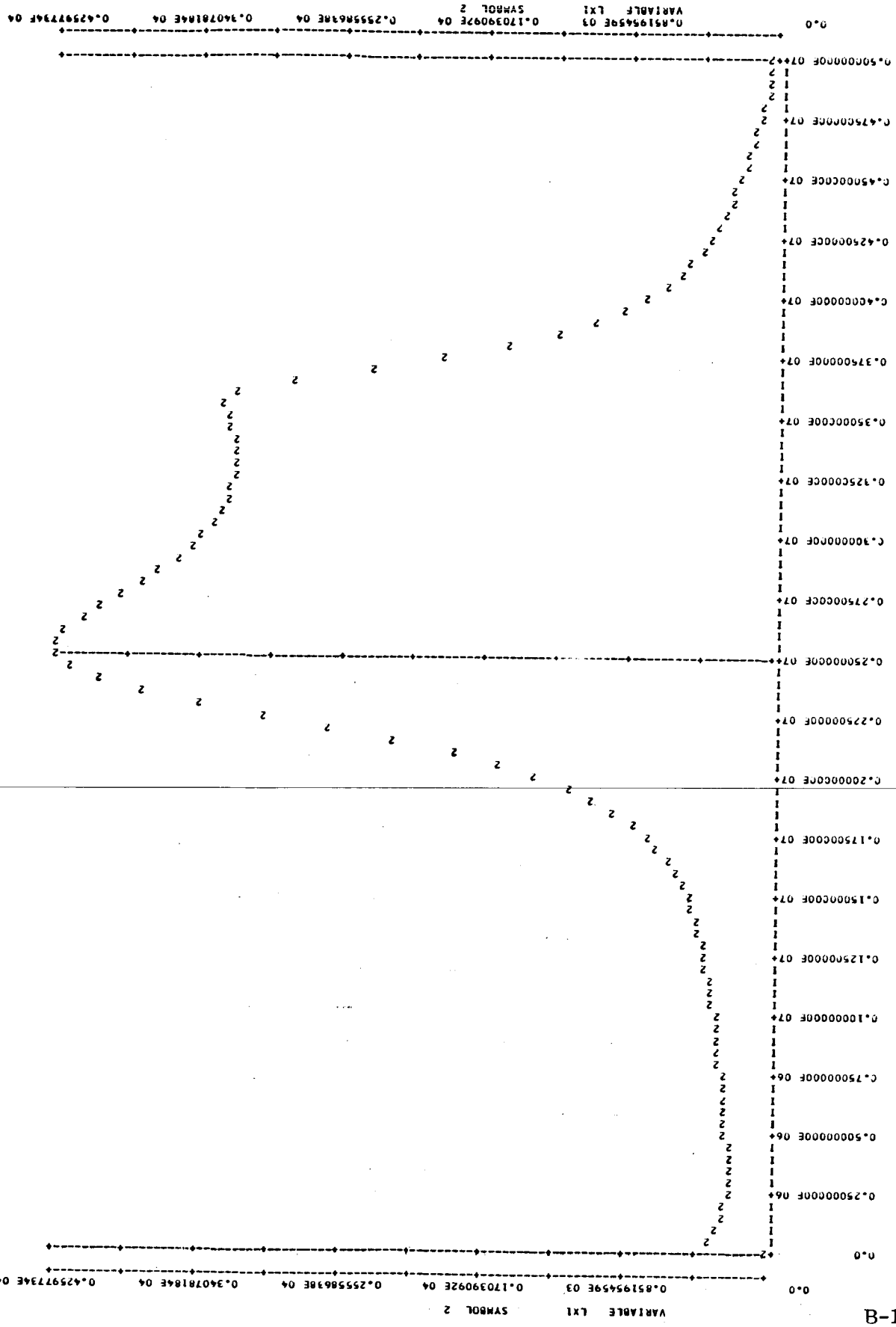

Figure B-150. Planet Tracker P2 with Gimballed IMU IG1

Figure B-151. Planet Tracker P2 with Carousel IMU IC1

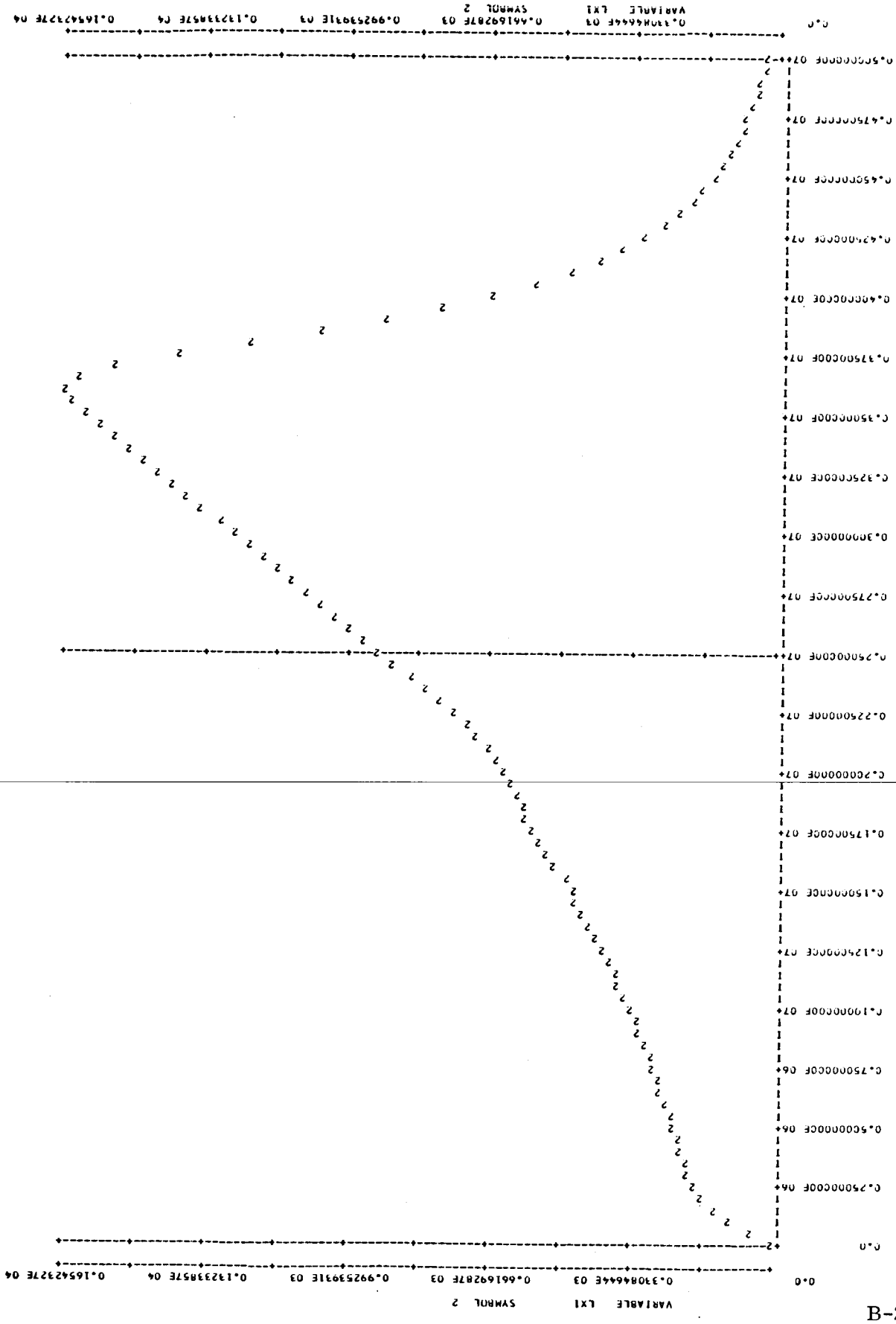

Figure B-152. Planet Tracker P2 with Faster Carousel IMU IC3

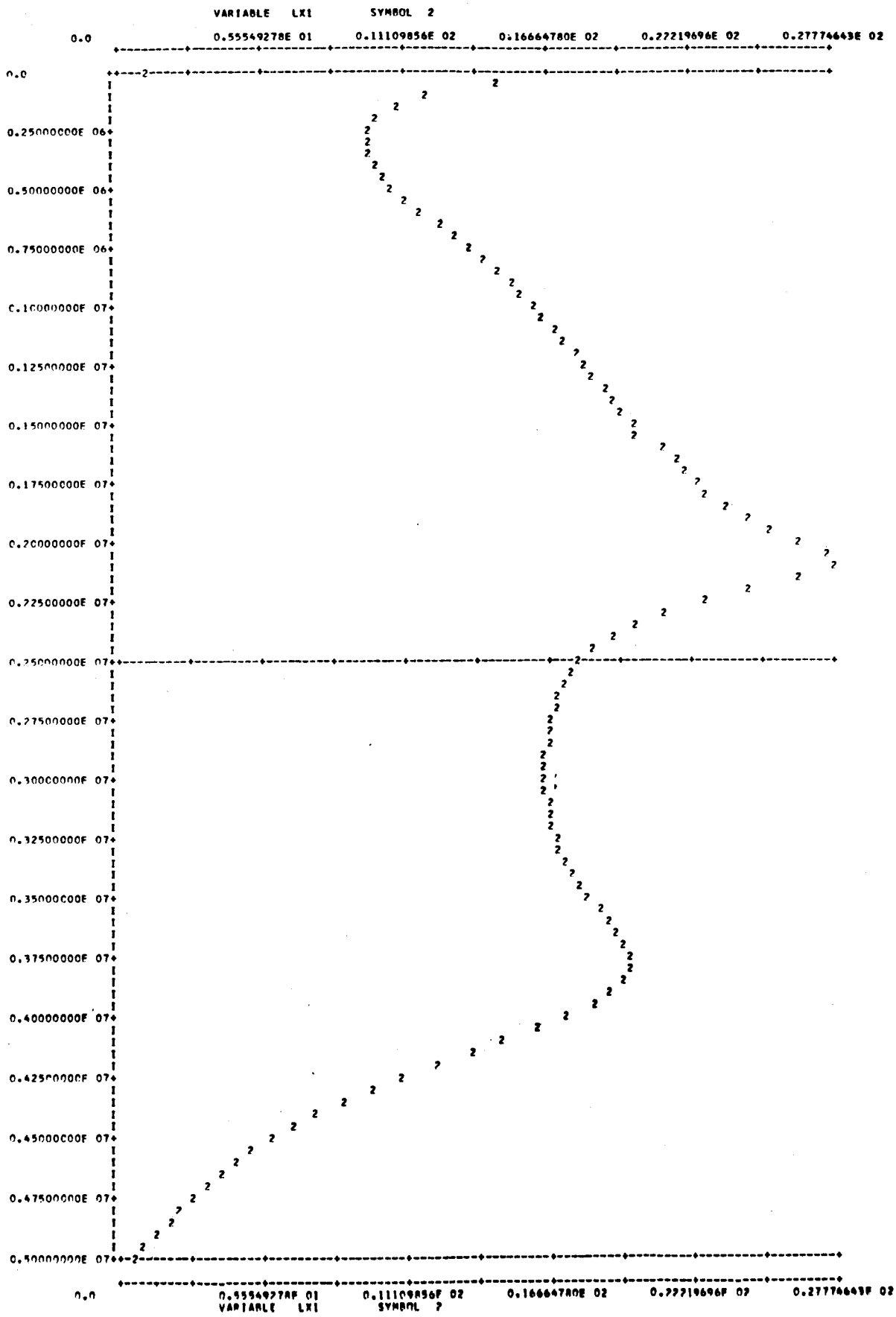

Figure B-153. System G1-P1-IG1

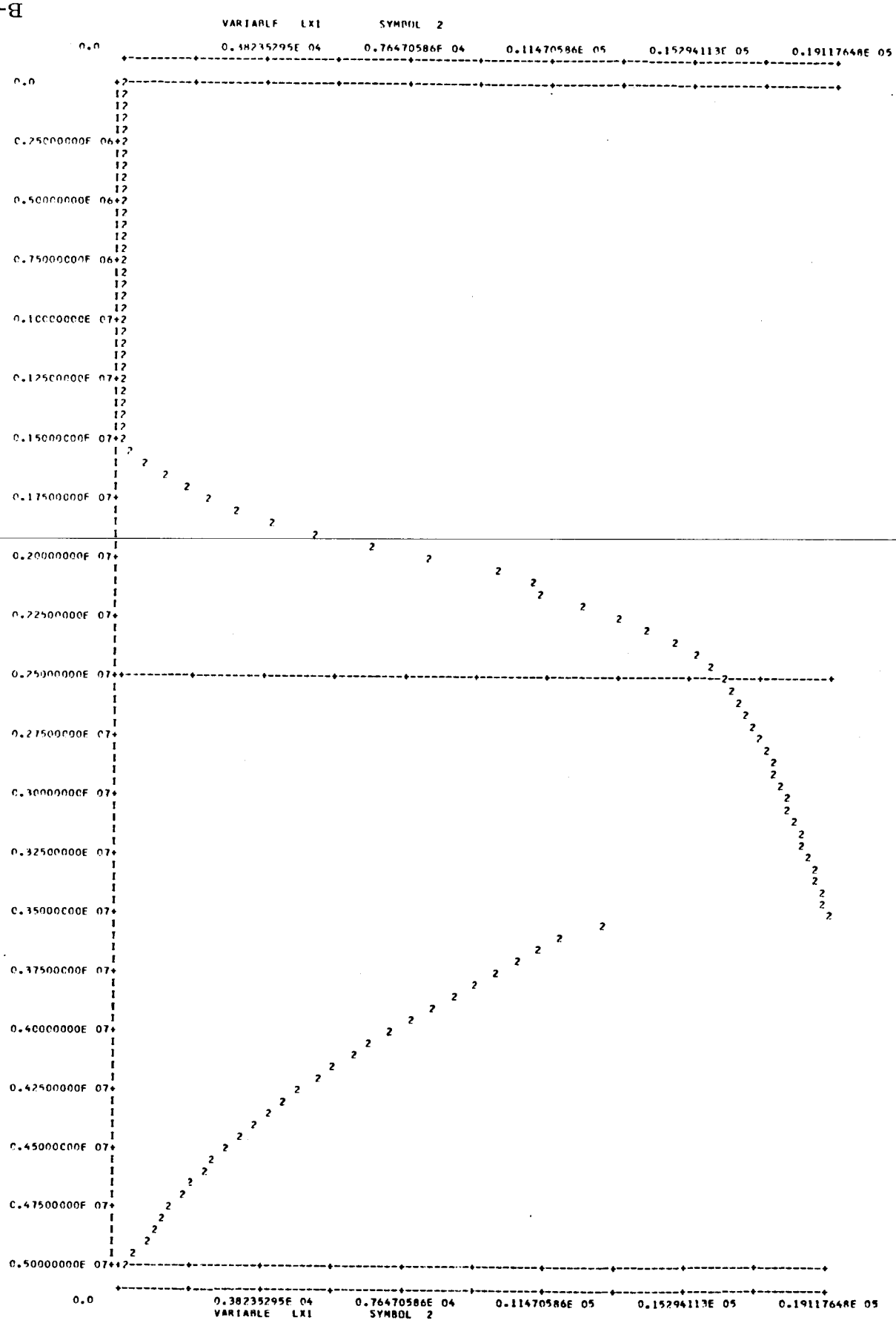

Figure B-154. System P1 with Normal Initial Error

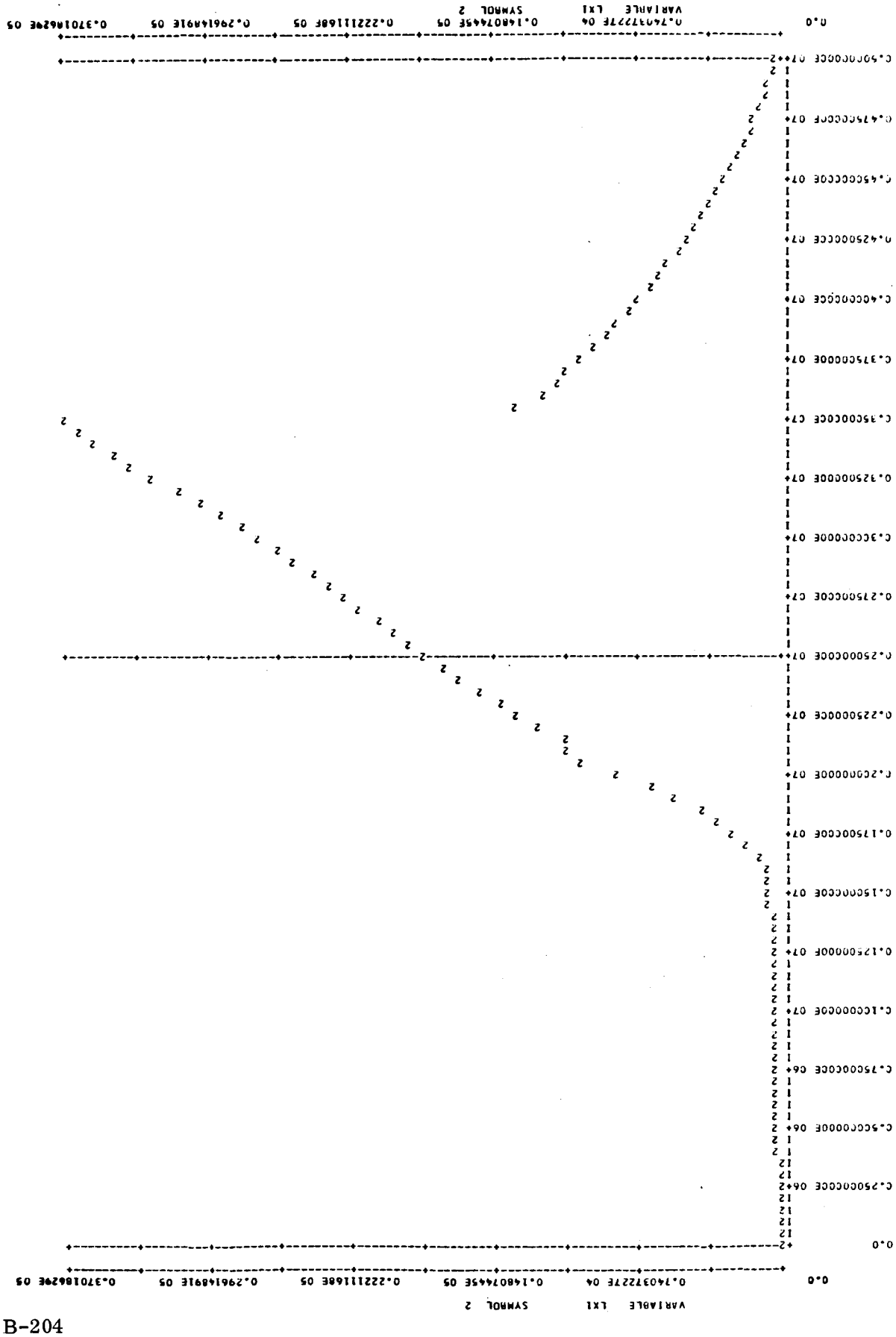

Figure B-155. P1 with Initial Error PO2

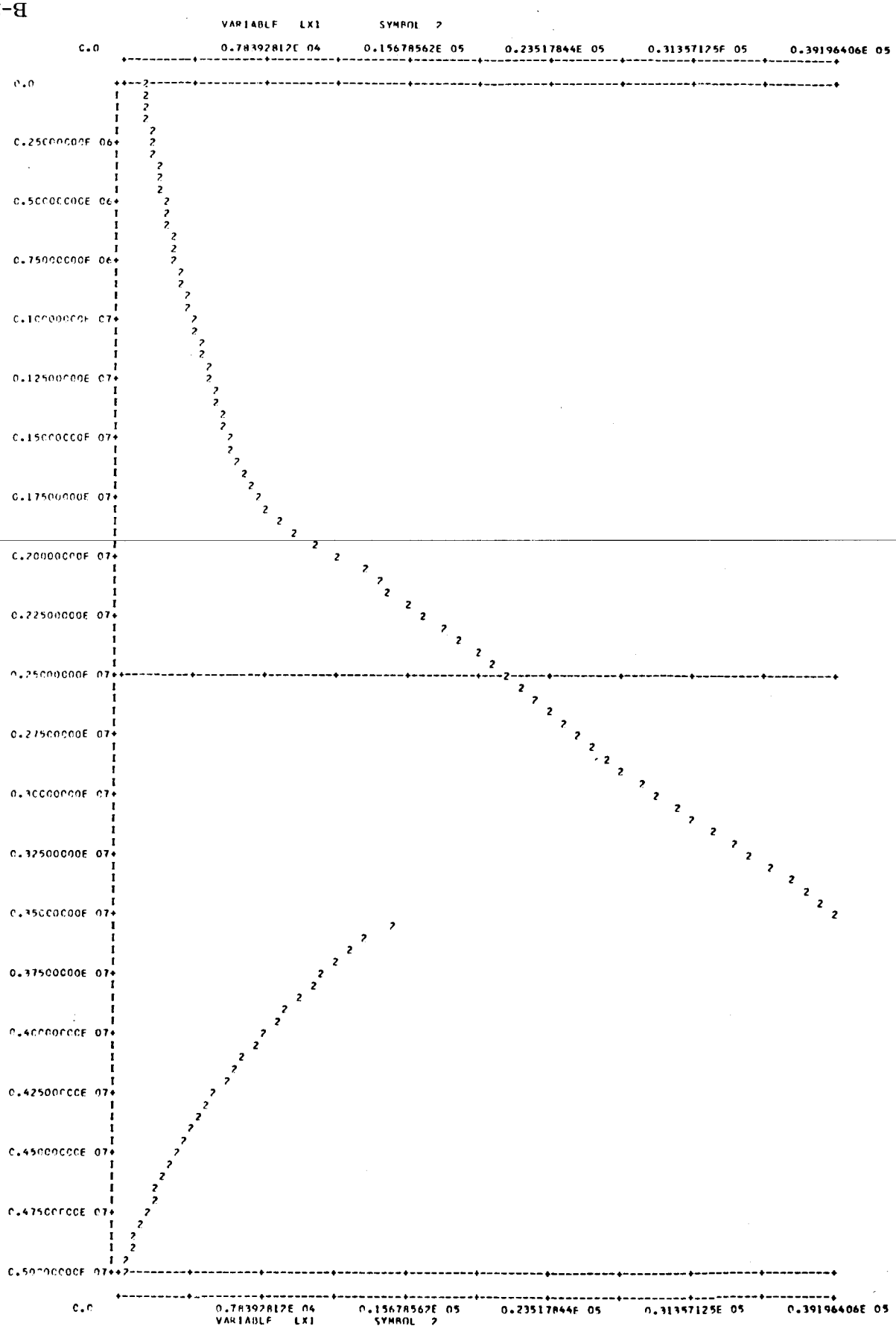

Figure B-156. System P1 with Initial Error PO3

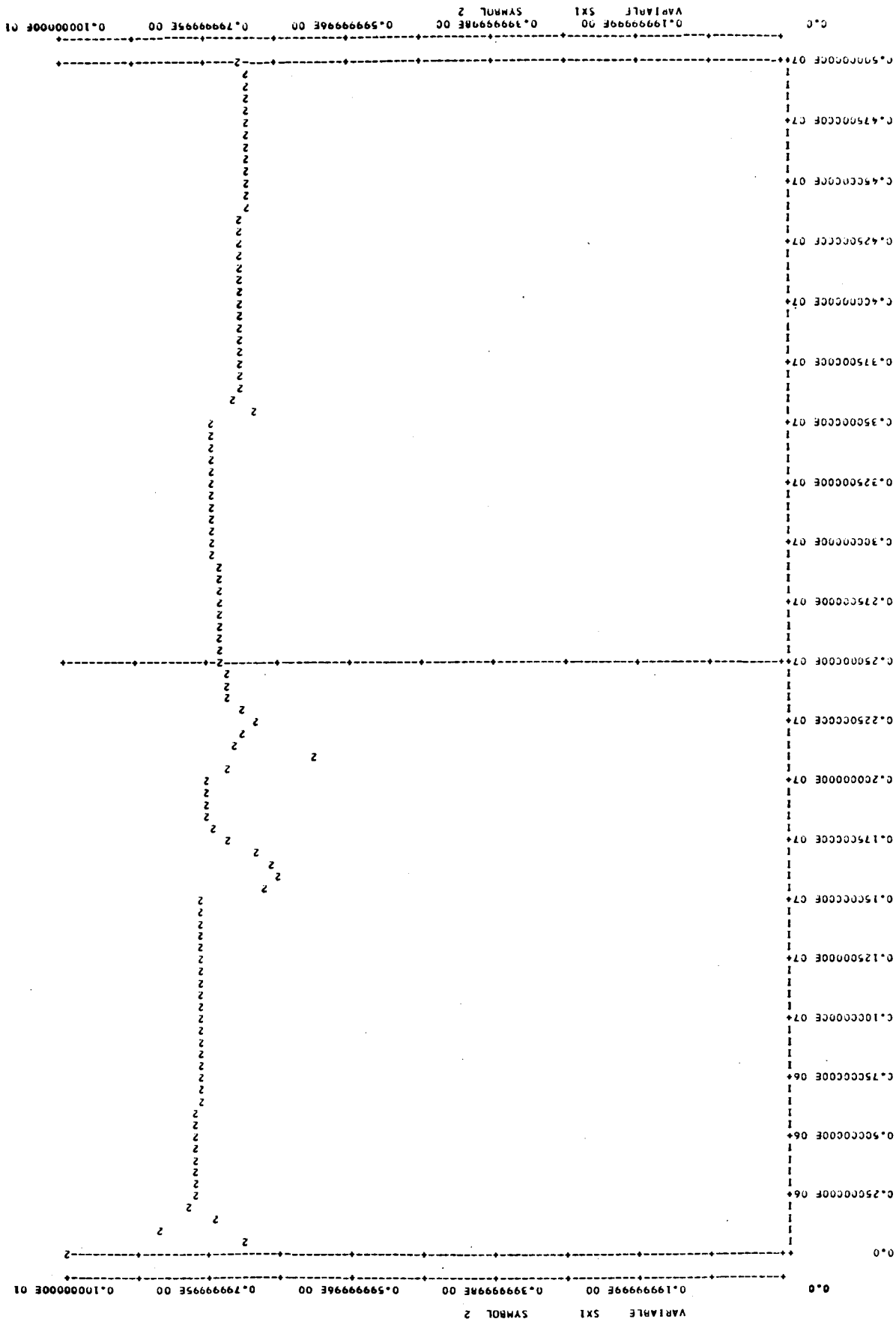

Figure B-157. Sensitivity to 4σ Error of P1

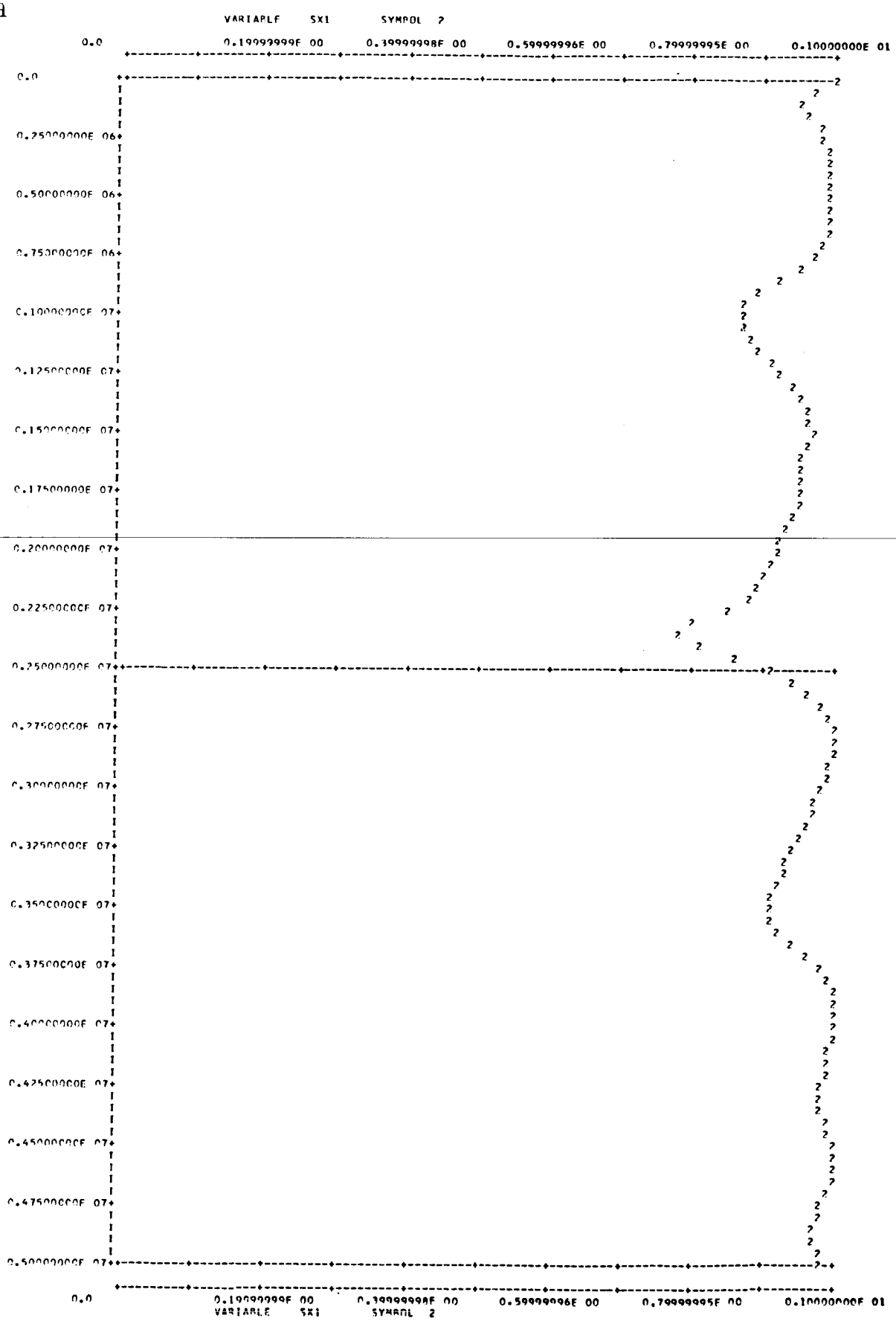

Figure B-158. Sensitivity to 4σ-P1, 5σ-IG1

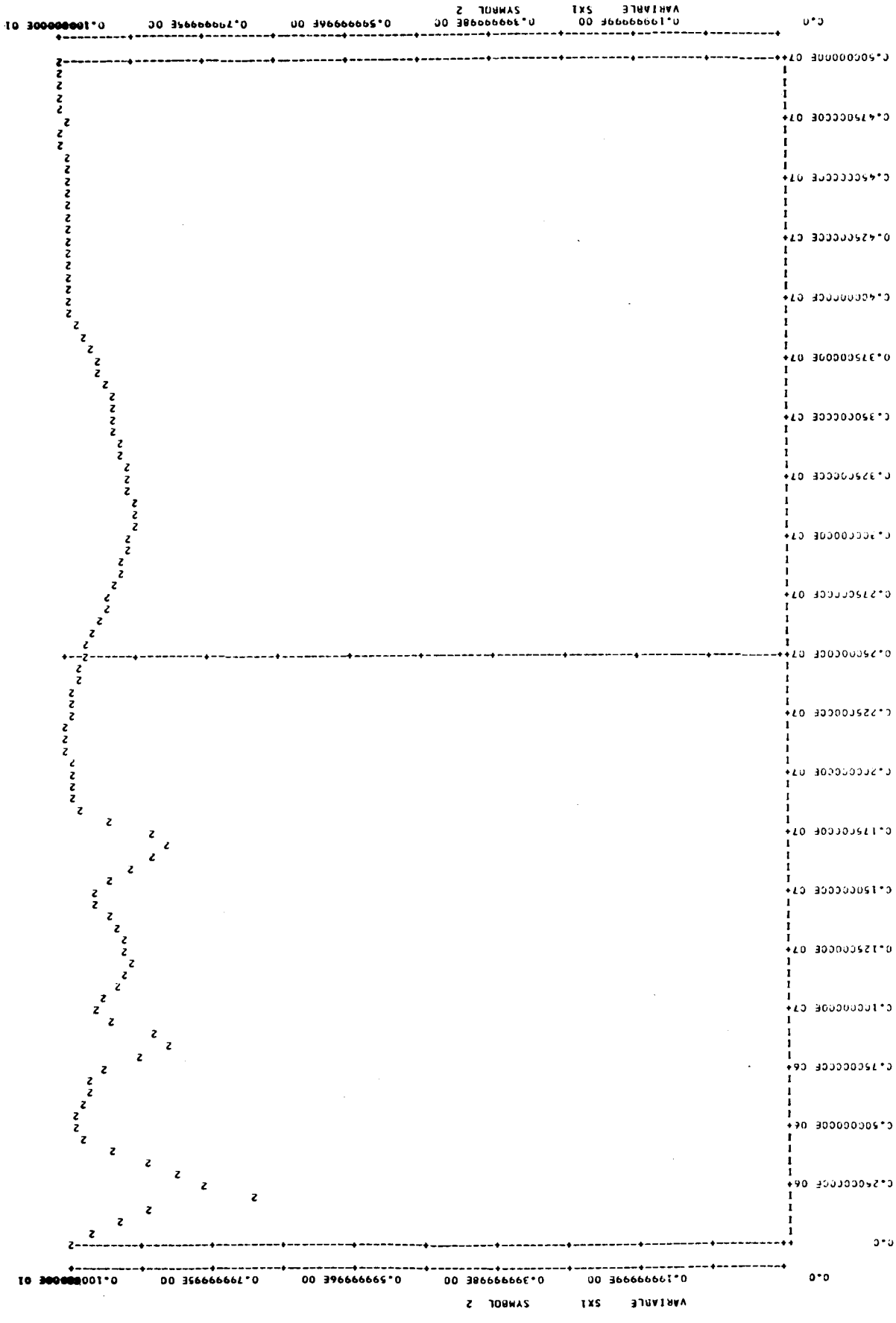

Figure B-159. Sensitivity to 4σ-P1, 5σ-IC1

Figure B-160. Sensitivity to 4σ-G1, 5σ-IG1

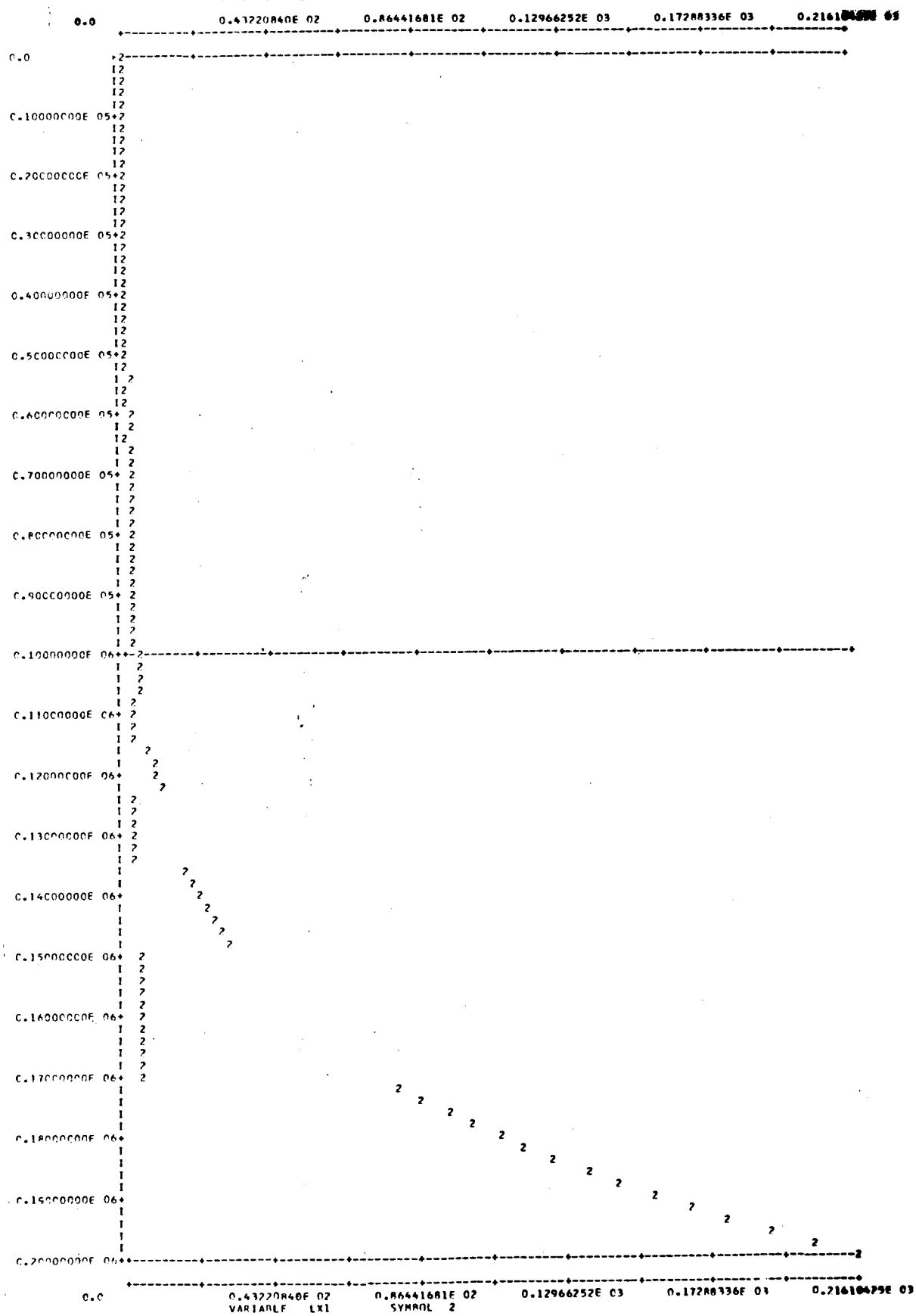

Figure B-161. Spiral Out at Mars with P1

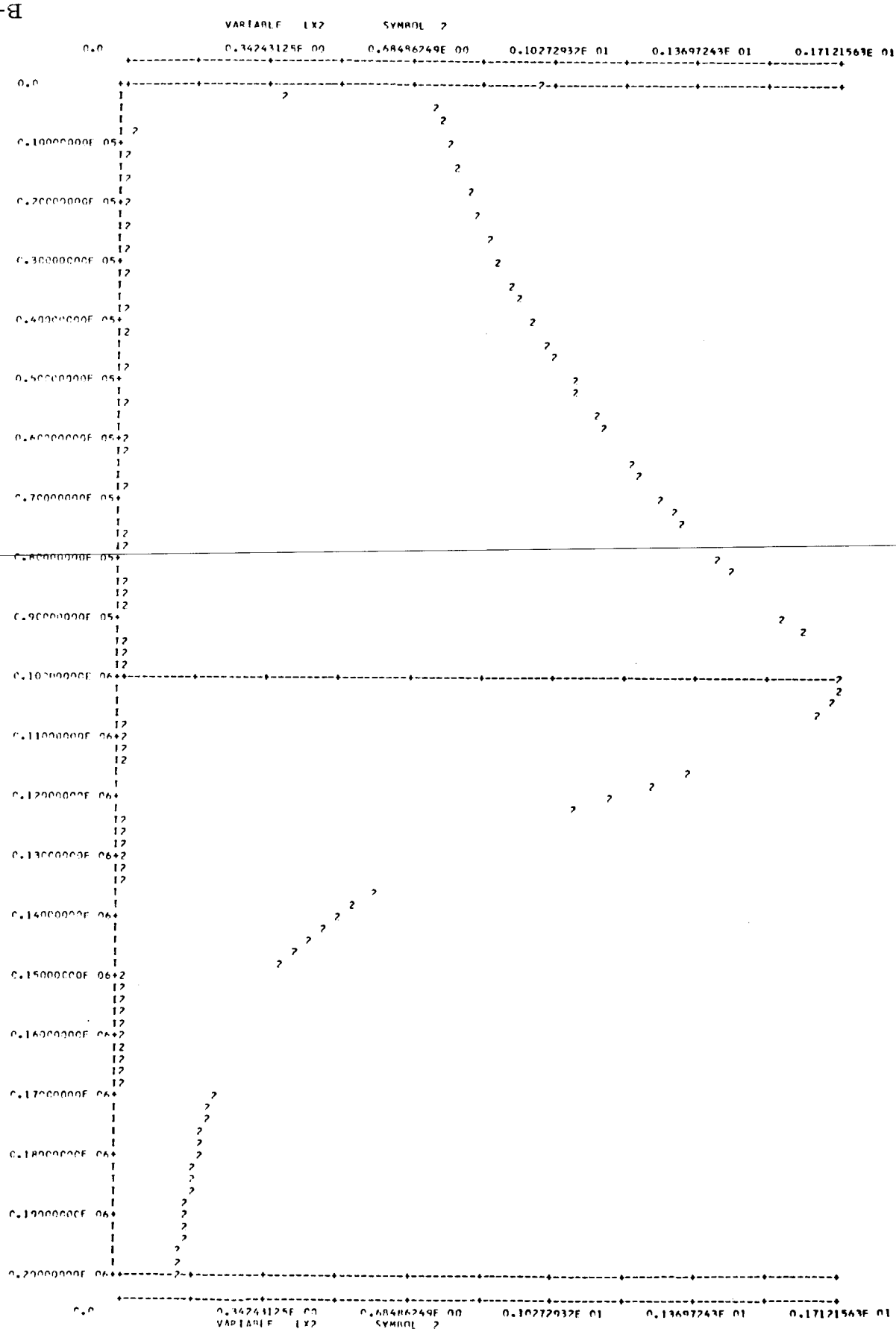

Figure B-162. Spiral Out at Mars with P1-IG1

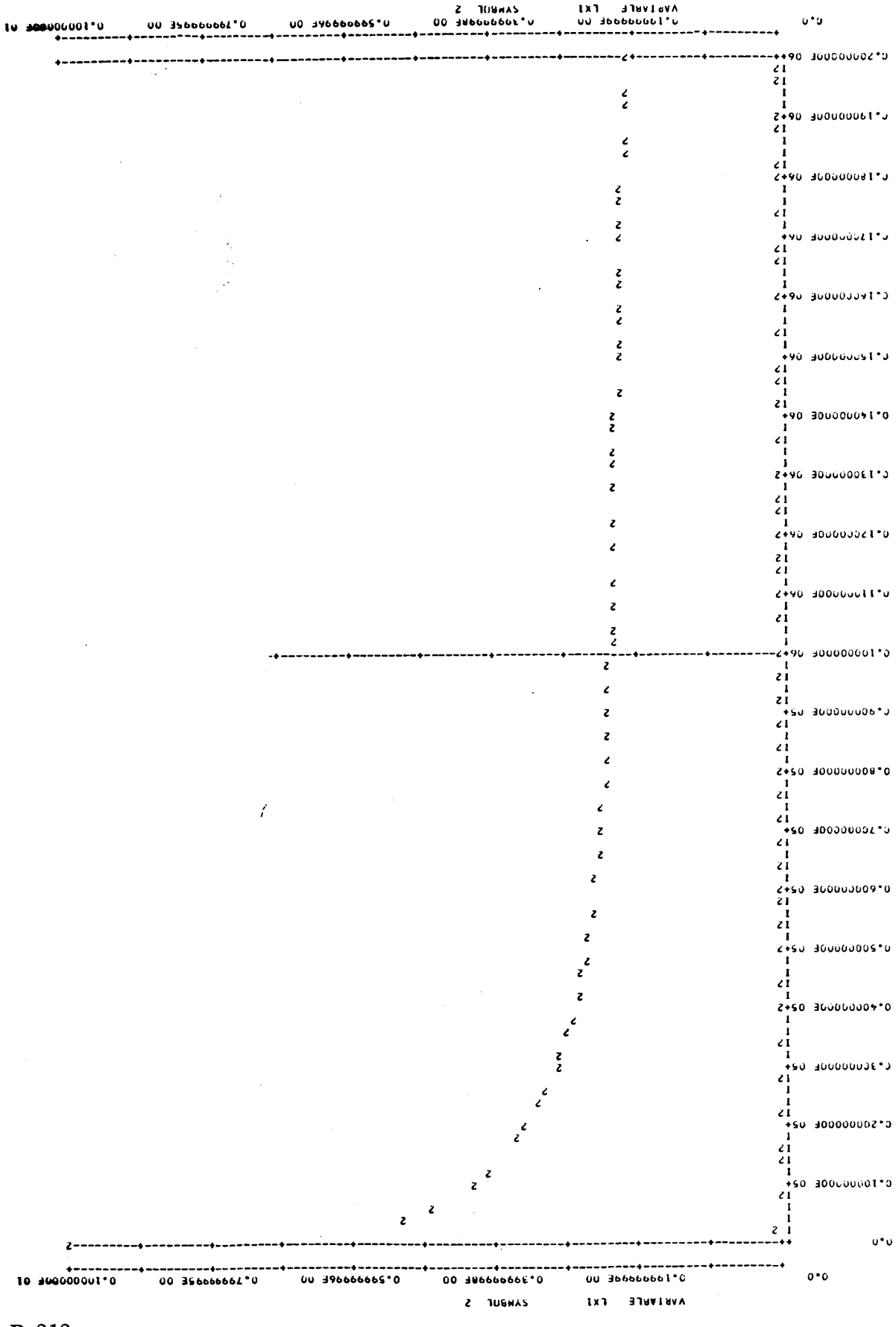

Figure B-163. Spiral Out at Earth with G1-P1-IG1